Ninth International Conference on Permafrost

Proceedings of the Ninth International Conference on Permafrost
University of Alaska Fairbanks
June 29–July 3, 2008

Ninth International Conference on Permafrost

Edited by Douglas L. Kane and Kenneth M. Hinkel

Volume 1

Institute of Northern Engineering
University of Alaska Fairbanks
2008

Ninth International Conference on Permafrost
Edited by Douglas L. Kane and Kenneth M. Hinkel

Printed in the United States of America

Elmer E. Rasmuson Library Cataloging in Publication Data
International Conference on Permafrost (9th : 2008 : Fairbanks, Alaska)
Ninth International Conference on Permafrost /
edited by Douglas L. Kane and Kenneth M. Hinkel.
— Fairbanks, Alaska : Institute of Northern Engineering,
University of Alaska Fairbanks, 2008.
2 v., : ill., maps ; cm.
Includes bibliographical references and index.
June 29–July 3, 2008
1. Permafrost–Congresses. 2. Frozen ground–Congresses.
I. Title. II. Kane, Douglas L. II. Hinkel, Kenneth M.

GB641.I6 2008

ISBN 978-0-9800179-2-2 (v.1)
ISBN 978-0-9800179-3-9 (v.2)

Production Editors: Thomas Alton and Fran Pedersen

Kane, D.L. & Hinkel, K.M. (eds). 2008. *Ninth International Conference on Permafrost.* Institute of Northern Engineering, University of Alaska Fairbanks (2 Vols.), 2140 pp.

Contents

Volume 1

Volume 2

Preface

Since the first International Permafrost Conference convened in 1963, we have sustained an international scientific and engineering collaborative effort until we now are immersed in this, the Ninth International Conference on Permafrost (NICOP). Considerable change has occurred over the past 45 years, resulting in heightened interest in the permafrost environment and understanding of its many aspects. Participation by engineers and scientists in advancing our knowledge of permafrost as a thermally impacted medium has continued to grow in the wake of both resource development and climate change.

The University of Alaska Fairbanks (America's Arctic University) is an excellent choice for the location of this conference. Permafrost is ubiquitous in Interior Alaska, and it influences many aspects of our society. Our local field trips are arranged around some of the most interesting phenomena here in the zone of discontinuous permafrost, including the world famous Permafrost Tunnel, the Trans Alaska Oil Pipeline, evidence of anthropogenic impacts on permafrost, and thermokarsting of warm permafrost. Fairbanks is also a good starting point for trips to other parts of Alaska, including the North Slope, Seward Peninsula, Denali National Park (Mount McKinley), and many other adventures. We have also taken this opportunity to offer courses related to the permafrost environment for high school and elementary teachers, advanced graduate students, and working professionals.

The University of Alaska Fairbanks hosted the Fourth International Conference on Permafrost in 1983. It was at this meeting that the International Permafrost Association (IPA) was formally established. IPA members are truly pleased with the strong international flavor of this year's conference, with approximately 30 countries participating. IPA's uninterrupted activities over the past 25 years are partially responsible for this concerted effort to expand our understanding of the permafrost environment, both spatially and temporally. It is also, however, abundantly clear that much of our current interest in this environment is driven by climate change.

Currently, many aspects of permafrost research are receiving considerable attention. These include carbon release into the atmosphere, discharge from catchments dominated with permafrost, the role of gas hydrates in cold environments, degrading permafrost and thermokarsting, infrastructure design in a changing environment, and the overarching issue of climate change on this thermally sensitive environment. It is essential that our scientific and engineering communities help our societies adapt to living and working on warming permafrost. Permafrost degradation will affect all aspects of life in the high latitudes and high elevations. We must anticipate the changes in ecology, hydrology, and infrastructure construction that will accompany degradation of permafrost with a warming climate. That is the challenge facing permafrost scientists and engineers. It is our hope that by sharing our knowledge and understanding, we may better serve our nations and people.

Enjoy the conference. We hope you will go home with increased knowledge and an invigorated appetite for expanding our understanding of the environment we call "permafrost."

—Douglas L. Kane
Water and Environmental Research Center, Institute of Northern Engineering
—Larry D. Hinzman
International Arctic Research Center

Acknowledgments

We, the organizers of the Ninth International Conference on Permafrost (NICOP), cannot sufficiently express our gratitude to those who have made NICOP both possible and successful. There are those who contributed financially by keeping the cost of the registration low, supporting young investigators, helping defer the cost of the proceedings, and sustaining many other behind-the-scenes activities. There are those who served on the numerous committees associated with this conference at the local, national, and international levels; we hope they found this exercise to be professionally rewarding. Finally, there are those who served as associate editors and reviewers of the more than 400 papers submitted. This conference is advertised as an International Conference; to be truly successful, much work must be done to overcome language barriers. While not always finding success in bringing a paper to publication, the associate editors and reviewers performed in a very commendable manner. Thank you all for your help.

—Douglas Kane, Larry Hinzman, and the Local Organizing Committee

NICOP Organizing Team Members

General Chair	Douglas Kane
Co-Chair	Larry Hinzman
Publications	Douglas Kane, Kenneth Hinkel, Thomas Alton, Fran Pedersen
Conference Facilitator	Elizabeth Lilly
Technical Program	Larry Hinzman
Short Courses	Larry Hinzman, Michael Lilly, Yuri Shur
Exhibits - Trade Show	Michael Lilly
Public Affairs	Marmian Grimes, Jenn Wagaman, Cherie Solie
Fundraising	Dave Norton, Jerry Brown, Larry Hinzman, Michael Lilly, James Rooney, Douglas Kane
Finance	Michael Lilly
Website	Gary Whitton
Special Events/Social	Elizabeth Lilly, Deborah Bennett, Melanie Jackson, Chris Lace
Young Researchers	Guido Grosse, Katey Walter, Andrew Balsar, Oliver Frauenfeld
ICOP-IPA-IPY Celebration	Jerry Brown, Jess Walker, John Zarling
Field Trip Guides	Deanne Stevens

U.S. Permafrost Association Board of Directors

Kenneth Hinkel, President
Yuri Shur, President-Elect
Oliver Frauenfeld, Secretary
Michael Lilly, Treasurer
Anna Klene, Member
Jennifer Harden, Member
Larry Hinzman, IPA Representative
Jon Zufelt, Past President

NICOP Program Committee

Larry Hinzman, Chair
Jerry Brown
Doug Goering
Jennifer Harden
Kenneth Hinkel
Douglas Kane
Frederick Nelson
Vladimir Romanovsky
Katey Walter
Jon Zufelt

Local Field Trip Organizers

James Begét
Deb Bennett
Nancy Bigelow
Patty Burns
Ed Clarke
Billy Connor
Charles Collins
Tom Douglas
Doug Goering
Jack Hébert
Melanie Jackson
Elden Johnson
Torre Jorgenson
Elizabeth Lilly
Michael Lilly
O.D. Odsather
Vladimir Romanovsky
Yuri Shur
Diana Solie
Katey Walter
Kenji Yoshikawa

Extended Field Trip Organizers

Donald “Skip” Walker
Tom Hamilton
Bill Streever
Chien-Lu Ping
Robert Gieck
Gary Michaelson
Torre Jorgensen
Jesse Walker
Caryn Rae
Kenneth Hinkel
Jerry Brown
Deanne Stevens
Jim Beget
Chris Burn
Antoni Lewkowicz
Tom Krzewinski
Phil Brease
Nel Caine
Koren Nydick
Elden Johnson
John Zarling
Ed Clarke
O.D. Odsather
Lee Schoen

Additional people who have assisted in NICOP Organization

Danielle Jamieson
Dan White
Michelle Bartlett
Wendy Warnick
Helga Wilm

U.S. National Committee

Jerry Brown, Chair
Roger Barry
Julie Brigham-Grette
Jody Deming
Craig Dorman
Kenneth Hinkel
Larry Hinzman
Douglas Kane
Frederick Nelson
Vladimir Romanovsky
Bill Streever
Rupert "Bucky" Tart
Patrick Webber
Jon Zufelt

International Organizing Committee

Antoni Lewkowicz, Chair
David Gilichinsky
Huijun Jin
Truls Mølmann
Marcia Phillips

NICOP Sponsors

Universities
University of Alaska International Polar Year (Gold plus)
University of Alaska President's Fund (Gold)
Alaska University Transportation Center (Gold)
University of Alaska Fairbanks Institute of Northern Engineering (Silver)
University of Alaska Fairbanks International Arctic Research Center (Silver)
University of Alaska Fairbanks Experimental Program to Stimulate Competitive Research (EPSCoR) (Bronze)
University of Colorado-National Snow and Ice Data Center (Contributor)

Government Agencies
Alaska Division of Geological & Geophysical Surveys, Fairbanks (Gold)
U.S. National Science Foundation (Silver)
U.S. Geological Survey (Silver)
U.S. Army Cold Regions Research and Engineering Laboratory (Bronze)
U.S. Department of Energy (Bronze)
U.S. Arctic Research Commission (Brass)
U.S. Bureau of Land Management (Brass)
Denali Commission (Brass)
North Slope Science Initiative (Brass)
U.S. Minerals Management Service (Contributor plus)
U.S. Fish & Wildlife Service, Fairbanks Field Office (Brass)

Corporate and Non-Governmental Organizations
Arctic Foundations, Inc., Anchorage (Gold)
Alyeska Pipeline Company, Anchorage (Silver)
BP Foundation (Bronze)
International Permafrost Association (Bronze plus)
GW Scientific, Fairbanks (Bronze)
Duane Miller & Associates, Anchorage (Bronze)
CH2MHILL Energy & Power, Anchorage (Brass)
ConocoPhillips Alaska (Brass)
EBA Engineering Consultants Ltd., Canada (Brass)
Golder Associates, Anchorage (Brass)
Shannon & Wilson, Inc. Seattle (Brass)
BeadedStream, LLC, Anchorage (Contributor)
Hawk Consultants, LLC, Anchorage (Contributor)
Houston Advanced Research Center (HARC) (Contributor)
Northern Engineering & Scientific (Contributor)
Northern Geotechnical Engineering, Inc., Anchorage (Contributor)
R&M Consultants, Inc., Anchorage (Contributor)
Tryck Nyman Hayes, Inc., Anchorage (Contributor)
Resource Data, Inc., Anchorage (Sustaining)
URS Corporation, Anchorage (Sustaining)
Usibelli Foundation (Sustaining)
Harley H. Hightower, FAIA, Anchorage (Sustaining)

ICOP Donor Circle (Contributor)
Jerry and Celia Brown
Edwin Clarke
Hugh M. French
Don W. Hayley
C.W. "Bill" Lovell
J. Ross Mackay (Honorary Member)
Michael C. Metz
Frederick E. Nelson
Jim and Florence Rooney
Rupert "Bucky" Tart
Ted B. Trueblood
H. Jess Walker
John Zarling

Individuals
Joe Malen

In-Kind Sponsors
ABR, Inc., Environmental Research and Services
Mountain Studies Institute
Pogo Mine, Teck Cominco Limited
University of Alaska Toolik Field Station
University of Cincinnati
University of Colorado, Institute of Arctic and Alpine Research
U.S. Army CRREL Permafrost Tunnel
U.S. Geological Survey
U.S. National Park Service

Associate Editors

Lukas Arenson, BGC Engineering, Canada
James Bockheim, University of Wisconsin, US
Julie Brigham-Grette, University of Massachusetts, US
Sherry Cady, Portland State University, US
Billy Connor, University of Alaska Fairbanks, US
Scott Dallimore, Geological Survey of Canada, CA
Claude Duguay, University of Waterloo, CA
Oliver Frauenfeld, University of Colorado, US
Hugh French, University of Ottawa, CA
Guido Grosse, University of Alaska Fairbanks, US
Stephan Gruber, University of Zurich, CH
Jennifer Harden, U.S. Geological Survey, US
Charles Harris, Cardiff University, UK
Christian Hauck, University of Karlsruhe, DE
Don Hayley, EBA Engineering Consultants, Ltd., CA
David Hik, University of Alberta, CA
Kenneth Hinkel, University of Cincinnati, USA
Hans-Wolfgang Hubberten, Alfred Wegener Institute, DE
Ole Humlum, University of Oslo, NO
Elden Johnson, Alyeska Pipeline Service Company, US
Torre Jorgenson, ABR Inc., US
John Kimble, Consulting Soil Scientist, US
Peter Kuhry, Stockholm University, SE
Philip Marsh, Environment Canada, CA
Chris McKay, NASA, US
James McNamara, Boise State University, US
Julian Murton, University of Sussex, UK
Frederick Nelson, University of Delaware, US
Mark Parsons, University of Colorado, US
Marcia Phillips, Swiss Federal Institute for Snow and Avalanche, CH
Volker Rachold, International Arctic Science Committee, SE
Vladimir Romanovsky, University of Alaska Fairbanks, US
Sharon Smith, Geological Survey of Canada, CA
Steve Solomon, Geological Survey of Canada, CA
Ted Vinson, Oregon State University, US
Daniel Vonder Mühll, ETH Zurich, CH
Patrick Webber, Michigan State University, US
John Zarling, Zarling Aero and Engineering, US

Reviewers

Clint Adler, Alaska DOT&PF, US
Thomas A. Ager, US Geological Survey, US
H. Jonas Akerman, Lund University, SE
Michel Allard, Université Laval, CA
Dale T. Andersen, NASA Ames, US
Lesleigh Anderson, US Geological Survey, US
Pat Anderson, University of Washington, US
Oleg A. Anisimov, State Hydrological Institute, RU
Lukas U. Arenson, BGC Engineering, CA
Arnold Arnoldusson, Norwegian Inst. of Land Inventory, NO
Valery Astakhov, National Research Inst. of Remote Sensing, RU
Tezera F. Azmatch, University of Alberta, CA
Megan Balks, University of Waikato, NZ
Andrew W. Balser, University of Alaska Fairbanks, US
Rene Barendregt, University of Lethbridge, CA
Brian Barnes, University of Alaska Fairbanks, US
David L. Barnes, University of Alaska Fairbanks, US
William Barr, University of Calgary, CA
Roger G. Barry, National Snow and Ice Data Center, US
Doug Benn, University Centre in Svalbard, NO
Bruce Bennett, Yukon Department of Environment, CA
Ivar Berthling, Norwegian University of Sci.and Tech., NO
Peter Blanken, University of Colorado, US
James Bockheim, University of Wisconsin, US
Xavier Bodin, University Paris/Joseph Fourier University, FR
Jan Boelhouwers, Uppsala University Uppsala, SE
Julia Boike, Alfred Wegener Institute, DE
W. Robert Bolton, Alfred Wegener Institute, DE
Christian Bommer, Swiss Fed. Inst. for Snow …, CH
Philip Bonnaventure, University of Ottawa, CA
Matthew T. Bray, University of Alaska Fairbanks, US
Alexander Brenning, University of Waterloo, CA
Gabriele Broll, University of Vechta, DE
Troy Brosten, Boise State University, US
Jerry Brown, International Permafrost Association, US
Bruce Brunette, Alaska DOT&PF, US
Margo M. Burgess, Geological Survey of Canada, CA
Christopher R. Burn, Carleton University, CA
Fabrice Calmels, University of Alberta, CA
Philip Camill, Carlton College, US
Iain B. Campbell, Land & Soil Consultancy Services, NZ
Sean K. Carey, Carleton University, CA
James W. Cassie, BGC Engineering Inc., CA
Beata Casto, University of Buffalo, US
Jessica E. Cherry, University of Alaska Fairbanks, US
Jens H. Christensen, Danish Meteorological Institute, DK
Hanne H. Christiansen, University Centre in Svalbard, NO
Evgenii Chuvilin, Moscow State University, RU
Graeme G.C. Claridge, Land & Soil Consultancy Services, NZ
Edwin S. Clark, Soils Alaska, US
Ian D. Clark, University of Ottawa, CA
Mark Clark, Natural Resources Conservation Service, US
Peter Cleall, University of Cardiff, UK
Gary D. Clow, US Geological Survey, US
Michael Cole, ABR Inc., US
Charles Collins, US Army, ERDC/CRREL, US

Jean Côté, Université Laval Québec, CA
Michelle Côté, Geological Survey of Canada, CA
Nicole Couture, McGill University, CA
Patrick Crill, Stockholm University, SE
Ronald P. Daanen, University of Alaska Fairbanks, US
Scott Dallimore, Geological Survey of Canada, CA
Debendra K. Das, University of Alaska Fairbanks, US
Simon Davies, Colorado School of Mines, US
Gregory P. De Pascale, William Lettis & Assoc. Inc., US
Reynald Delaloye, University of Fribourg, CH
Philip Deline, Université de Savoie, FR
Jack Dennett, EBA Engineering Consultants Ltd., CA
Alexander Derevyagin, Moscow State University, RU
Bernhard Diekmann, Alfred Wegener Institute, DE
Wojciech Dobinski, University of Silesia, PL
Yongtao Dong, University of Alaska Fairbanks, US
Guy Dore, Universite Laval, CA
D.S. Drozdov, Earth Cryosphere Institute, RU
Caroline Duchesne, Geological Survey of Canada, CA
Alejandra Duk-Rodkin, Geological Survey of, CA
Larry Dyke, Geological Survey of Canada, CA
Mark Ednie, Geological Survey of Canada, CA
Markus Egli, University of Zurich, CH
Olaf Eisen, Alfred Wegener Institute, DE
Wendy Eisner, University of Cincinnati, US
David Esch, Alaska DOT&PF (retired), US
Bernd Etzelmüller, University of Oslo, NO
Eugenie Euskirchen, University of Alaska Fairbanks, US
Zhaosheng Fan, University of Colorado, US
Herman Farbrot, University of Oslo, NO
Alexander N. Fedorov, Melnikov Permafrost Institute, RU
Michael G. Ferrick, US Army, ERDC/CRREL, US
Javier Fochesatto, International Arctic Research Center, US
Steven L. Forman, University of Illinois-Chicago, US
Daniel Fortier, University of Alaska Fairbanks, US
Richard Fortier, Université Laval, CA
Walter J. Fourie, University of Alaska Fairbanks, US
Pierre Francus, Inst. National de la Recherche Scientifique, CA
Oliver W. Frauenfeld, University of Colorado, US
Regula Frauenfelder, University of Oslo, NO
Barry M. Freifeld, Lawrence Berkeley National Laboratory, US
Hugh M. French, University of Ottawa, CA
Duane Froese, University of Alberta, CA
Rina Garcia, Stockholm University, SE
Gunther Ghysels, Ghent University, BE
I. Gidley, University of Calgary, CA
Robert E. Gieck, University of Alaska Fairbanks, US
Ted Goebel, Texas A&M University, US
Douglas J. Goering, University of Alaska Fairbanks, US
Jules M. Goldspiel, Cornell University, US
Michael Gooseff, Pennsylvania State University, US
Jacob Gorelik, Earth Cryosphere Inst. SB RAS, RU
Sergey Goryachkin, Geography Institute, Moscow, RU
Raoul Granger, National Hydrology Research Centre, CA
Mikhail N. Grigoriev, Permafrost Institute Yakutsk, RU
Guido Grosse, University of Alaska Fairbanks, US
Ed Grozic, EBA Engineering Consultants Ltd., CA
Jocelyn Grozic, University of Calgary, CA
Hansueli Gubler, AlpuG Davos, CH
Mauro Guglielmin, Insubria University Varese, IT
Steve D. Gurney, University of Reading, UK
Örjan Gustafsson, Stockholm University, SE
Spencer Guthrie, Brigham Young University, US
Wilfried Haeberli, University of Zurich, CH
Birgit Hagedorn, University of Alaska Anchorage, US
Tristram C. Hales, Cardiff University, UK
Svein-Erik Hamran, University of Oslo, NO
Chris Hanks, Alexco Resource Corp., US
Jennifer Harden, US Geological Survey, US
Charles Harris, University of Cardiff, UK
Robert N. Harris, Oregon State University, US
Stuart A. Harris, Calgary Alberta, CA
Bent Hasholt, University of Copenhagen, DK
Andreas Hasler, University of Zurich, CH
Steven Hastings, San Diego State University, US
C. Haththatowa, University of Calgary, CA
Christian Hauck, Karlsruhe Institute of Technology, DE
Helmut Hausmann, Technical University of Vienna, AT
Jennifer Heldmann, NASA Ames, US
Karen S. Henry, ERDC/CRREL, US
Rita Hermanns, Friedlipartner AG, CH
Thomas Herz, University of Giessen, DE
Ulrike Herzschuh, Alfred Wegener Institute, DE
Gloria Hicks, National Snow and Ice Data Center, US
Christin Hilbich, Friedrich-Schiller-Universität Jena, DE
Kenneth M. Hinkel, University of Cincinnati, US
Larry Hinzman, University of Alaska Fairbanks, US
Richard Hodgkins, Loughborough University, UK
Martin Hoelzle, University of Zurich, CH
Ed T. Hoeve, EBA Engineering Consultants Ltd., CA
Igor Holubec, I. Holubec Consulting Inc., CA
Anne Hormes, University Centre in Svalbard, NO
William T. Horne, EBA Engineering Consultants Ltd., CA
Hans-Wolfgang Hubberten, Alfred Wegener Institute, DE
Leroy Hulsey, University of Alaska Fairbanks, US
Ole Humlun, University of Oslo, NO
James Hunter, Geological Survey of Canada, CA
Atsushi Ikeda, University of Tsukuba, JP
Thomas Ingeman-Nielsen, Tech. University of Denmark, DK
Arne Instanes, Opticonsult Bergen, NO
Kenneth C. Irving, University of Alaska Fairbanks, US
Ketil Isaksen, Norwegian Meteorological Institute, NO
Mamoru Ishikawa, Hokkaido University, JP
Michel Jaboyedoff, University of Lausnne, CH
Matthias Jakob, BGC Engineering, CA
Richard Janowicz, Yukon Dept. of Environment, CA
Alexander Jarosch, University of British Columbia, CA
A. Jayasinghe, University of Calgary, CA
Margareta Johansson, Lund University, SE
Elden R. Johnson, Alyeska Pipeline Service Co., US
Ken Johnston, Earth Tech, CA
H. Jonas Akerman, Lund University, SE
Ben Jones, US Geological Survey, US
Kevin W. Jones, EBA Engineering Consultants Ltd., CA
Torre Jorgenson, ABR Inc., US
Håvard Juliussen, University Centre in Svalbard, NO
Andreas Kääb, University of Oslo, NO
Mikhail Kanevskiy, University of Alaska Fairbanks, US
Julian Kanigan, Indian and Northern Affairs, CA
Kumari Karunaratne, Carleton University, CA
Andreas Kellerer-Pirklbauer, University of Graz, AT
Martina Kern-Luetschg, Cardiff University, UK
Maureen Ketzler, US Forest Service, US
Alexander Kholodov, University of Alaska Fairbanks, US
John Kimble, Consulting Soil Scientist, US
Lorenz King, University of Giessen, DE

Kurt Kjær, University of Iceland, IS
Anna E. Klene, University of Montana, US
Michael Knapp, Alaska DOT&PF, US
Christof Kneisel Universität Würzburg, DE
Steven V. Kokelj, Indian and Northern Affairs, CA
Else Kolstrup, University of Uppsala, SE
Vladimir S. Kolunin, Earth Cryosphere Institute, RU
P.Y. Konstantinov, Melnikov Permafrost Institute, RU
Demitri Konyushkev, Docuchaev Soils Institute, RU
Michael Krautblatter, University of Bonn, DE
Thomas Krzewinski, Golder & Associates, US
Bernd Kulessa, Swansea University, UK
Anna N. Kurchatova, Tyumen State Oil and Gas University, RU
Denis Lacelle, Canadian Space Agency, CA
Branko Ladanyi, Polytechnique Montréal, CA
Christophe Lambiel, University of Lausanne, CH
Hugues Lantuit, Alfred Wegener Institute Potsdam, DE
David M. Lawrence, NCAR, US
Daniel Lawson, US Army, ERDC/CRREL, US
Marc Lebeau, Université Laval Québec QC, CA
Anne-Marie LeBlanc, Université Laval, CA
Jonah Lee, University of Alaska Fairbanks, US
Marina Leibman, Earth Cryosphere Institute, RU
Mathias Leopold, University of Jena, DE
David W. Leverington, Texas Tech University, US
Antoni Lewkowicz, University of Ottawa, CA
Xin Li, World Data Center for Glaciology Lanzhou, CN
Jenny Liu, University of Alaska Fairbanks, US
Shuhuang Liu, US Geological Survey, US
Jerónimo López-Martínez, University of Madrid, ES
Lorene A. Lynn, University of Alaska Fairbanks, US
Jacek Majorowicz, Northern Geothermal Consultants, CA
Galina Malkova, Russian Academy of Sciences, RU
Michael Manga, University of California Berkeley, US
Jan Mangerud, University of Bergen, NO
William F. Manley, University of Colorado, US
Gavin K. Manson, Natural Resources, CA
Sergei Marchenko, University of Alaska Fairbanks, US
Laurent Marescot, ETH Zuerich, CH
Margarita Marinonva, California Inst. of Technology, US
Philip Marsh, Nat. Hydrology Res. Centre Environment, CA
Irene Marzloff, Johann Wolfgang Goethe Univ., DE
Norikazu Matsuoka, University of Tsukuba, JP
Hansruedi Maurer, ETH Zurich, CH
Galina G. Mazhitova, Komi Science Centre, RU
William D. McCoy, Univ. of Massachusetts, US
Les McFadden, University of New Mexico, US
A. David McGuire, University of Alaska Fairbanks, US
Robert McHattie, Alaska DOT&PF (retired), US
Christopher McKay, NASA Ames Research Center, US
Fiona McLaughlin, Dept. of Fisheries and Oceans, CA
Malcolm McLeod, Landcare Research Hamilton, NZ
Nicola McLoughlin, University of Bergen, NO
Michael C. Metz, M.C. Metz Associates, US
Franz Meyer, Alaska Satellite Facility Fairbanks, US
Hanno Meyer, Alfred Wegener Institute, DE
Keith Meyer, Michael Baker Jr. Corp., US
Gary J. Michaelson, University of Alaska Fairbanks, US
Fred A. Michel, Carlton University Ottawa, CA
Nicole Mölders, University of Alaska Fairbanks, US
Jack D. Mollard, J.D. Mollard and Associates, CA
Dan Moore, University of British Columbia, CA
George Moridis, Lawrence Berkeley Laboratories, US
Thomas Moses, Alaska DOT&PF (retired), US
Michael Mungoven, USDA-NRCS, US
Julian B. Murton, University of Sussex, UK
Mark Musial, Golder Associates, US
Philippe Nater, GeoNum GmbH, CH
Frederick E. Nelson, University of Delaware, US
William G. Nelson, University of Alaska Anchorage, US
Heng Joo Ng, Schlumberger, CA
Derick Nixon, Nixon Geotech Ltd., CA
F. Mark Nixon, Geological Survey of Canada, CA
Jeannette Noetzli, University of Zurich, CH
Rune S. Ødegård, University of Gjovik, NO
Jonathan O'Donnell, University of Alaska Fairbanks, US
Stanislav Ogorodov, Moscow State University, RU
C. Ordonez, University of Calgary, CA
Kirk Osadetz, Geological Survey of Canada, CA
Thomas Osterkamp, University of Alaska Fairbanks, US
Jim M. Oswell, Naviq Consulting Inc., CA
Sam Outcalt, University of Michigan (retired), US
P. Paul Overduin, Alfred Wegener Institute, DE
Ron Paetzold, Geo-Watersheds Scientific, US
Michael Palmer, Indian and Northern Affairs, CA
Charles Paull, Monterey Bay Aquarium Research Inst., US
David Payer, US Fish and Wildlife Service, US
Rorik Peterson, University of Alaska Fairbanks, US
Richard Petrone, Wilfred Laurier University, CA
Eva-Maria Pfeiffer, University of Hamburg, DE
Marcia Phillips, Swiss Fed. Inst. for Snow …, CH
Ryan D. Phillips, C-CORE St John's Newfoundland, CA
Chien-Lu Ping, University of Alaska Fairbanks, US
Albert Pissart, Université de Liege, BE
Vladimir V. Pitulko, Inst. for History of Mat. Culture, RU
Lawrence J. Plug, Dalhousie University, CA
Stefan Pohl, Nat. Hydrology Res. Centre Environment, CA
Wayne Pollard, McGill University, CA
Olga Ponomareva, Earth Cryosphere Institute, RU
Anupma Prakash, University of Alaska Fairbanks, US
Jon Price, University of Waterloo, CA
William Quinton, Wilfred Laurier University, CA
Charles Racine, US Army, ERDC/CRREL (retired), US
Miguel Ramos, University of Alcala, ES
Gareth Rees, Scott Polar Research Institute, UK
J. Repelewska-Pękala, University of Maria Curie, PL
Anette Rinke, Alfred Wegener Institute, DE
Dan Riseborough, Geological Survey of Canada, CA
Armin Rist, Swiss Fed. Inst. for Snow …, CH
Stephen D. Robinson, St. Lawrence University, US
Isabelle Roer, University of Zurich, CH
Vladimir Romanovsky, University of Alaska Fairbanks, US
Bård Romstad, University of Oslo, NO
Vladislav Roujanski, EBA Engineering Consultants Ltd., CA
Stephan Saboundjain, Alaska DOT&PF, US
Torsten Sachs, Alfred Wagener Institute, DE
Kazuyuki Saito, University of Alaska Fairbanks, US
Michael Schirmer, Swiss Fed. Inst. for Snow …, CH
Lutz Schirrmeister, Alfred Wegener Institute, DE
Michael Schlegel, GeoEngineers Inc., US
Martin Schnebelli, Swiss Fed. Inst. for Snow …, CH
Edward A.G. Schuur, University of Florida, US
Georg Schwamborn, Alfred Wegner Institute, DE
Charles A. Schweger, University of Alberta, CA
Dmitry Sergeev, Institute of Environmental Geoscience, RU
Enrique Serrano, University of Valladolid, ES

Jack Seto, BGC Engineering Inc., CA
Natsagdorj Sharkhuu, Mongolian Academy of Sciences, MN
Nicolai I. Shiklomanov, University of Delaware, US
Yuri Shur, University of Alaska Fairbanks, US
Andrew G. Slater, University of Colorado, US
Lee Slater, Rutgers University, US
Chuck Slaughter, University of Idaho, US
Bruce Smith, Worley Parsons, CA
Orson P. Smith, University of Alaska Anchorage, US
Scott Smith, Research Branch Agriculture and Agri-Food, CA
Sharon Smith, Geological Survey of Canada, CA
Chris Spence, National Hydrology Research Centre, CA
Sarah M. Springman, ETH Zurich, CH
Blaire Steven, University of Wyoming, US
Christopher W. Stevens, University of Calgary, CA
De Anne Stevens, Alaska Dept. of Natural Resources, US
Marc Stiglitz, Georgia Institute of Technology, US
Vladimir Stolbovoy, Joint Research Centre of European …, IT
Dmity Streletskiy, University of Delaware, US
Robert Striegle, US Geological Survey, US
Tetsuo Sueyoshi, Hokkaido University, JP
Brad Sutter, NASA Ames Research Center, US
John Inge Svendssen, University of Bergen, NO
David Swanson, US Forest Service, US
Eors Szathmary, Eötvös Loránd University , HU
Pavel A. Tarasov, Free University of Berlin, DE
Charles Tarnocai, Agriculture and Agri-Food, CA
Rupert G. Tart, Golder Associates Ltd., US
Alan E. Taylor, ASL Environmental Sciences Inc., CA
Robert O. Taylor, Natural Resources, CA
Randi Thompson, BGC Engineering Inc., CA
Gennady S. Tipenko, Russian Academy of Sciences, RU
Horacio Toniolo, University of Alaska Fairbanks, US
J. Kenneth Torrance, University of Carleton, CA
Thomas P. Trainor, Univeristy of Alaska Fairbanks, US
Richard Trimble, EBA Engineering Consultants Ltd., CA
Dario Trombotto, Ianigla-Cricyt-Conicet, AR
Merritt R. Turetsky, Michigan State University, US
Craig Tweedie, University of Texas El Paso, US
William Ussler, Monterey Bay Aquarium Res. Inst., US
Jef Vandenberghe, Vrije Universiteit, NL
B. Van Vliet-Lanoë, Univ. Sciences et Tech. de Lille, FR
Yurij K. Vasilchuk, Moscow State University, RU
Alexander Vasiliev, Earth Cryosphere Institute, RU
Gonçalo Vieira, University of Lisbon, PT
Ted Vinson, Oregon State University, US
Jason G. Vogel, University of Florida, US
Daniel Vonder Mühll, ETH Zurich, CH
William Waite, US Geological Survey, US
Mark Waldrop, US Geological Survey, US
Donald Walker, University of Alaska Fairbanks, US
Katey Walter, University of Alaska Fairbanks, US
James Walters, University of Northern Iowa, US
B. Wang, Geological Survey of Canada, CA
KaiCun Wang, University of Maryland, US
Jeff Warburton, University of Durham, UK
Patrick J. Webber, Michigan State University, US
Matthias Wegmann, Institute of Safety and Security, CH
Malte Westerhaus, University of Karlsruhe, DE
Kimberly Wickland, US Geological Survey, US
Jacek Wierzchos, University of Lleida, ES
Cort J. Willmott, University of Delaware, US
William Winters, US Geological Survey, US
Stephen A. Wolfe, Geological Survey of Canada, CA
Ute Wollschlaeger, University of Heidelberg, DE
Ming-ko Woo, McMaster University, CA
Fred Wright, Geological Survey of Canada, CA
Yladimir Yakushev, VNIIGAZ, RU
Daqing Yang, University of Alaska Fairbanks, US
Edward Yarmak, Arctic Foundations, Inc., US
Shiqiang Ye, BC Hydro, CA
Kenji Yoshikawa, University of Alaska Fairbanks, US
Kathy Young, York University, CA
Dmitry Zamolodchikov, Ctr. for Ecol. and Prod. of Forests, RU
John P. Zarling, Zarling Aero and Engineering, US
Jay Zarnetske, Oregon State University, US
Aining Zhang, Natural Resources, CA
Gordon Zhang, EBA Engineering Consultants Ltd., CA
Tingjun Zhang, University of Colorado Boulder, US
Xiong Zhang, University of Alaska Fairbanks, US
Yu Zhang, Natural Resources, CA
Shu-ping, Zhao, CAREERI CAS, CN
Sergei Zimov, Northeast Science Station, RU
Jon E. Zufelt, US Army ERDC/CRREL, US

Initial Disturbance and Recovery Measurements from Military Vehicle Traffic on Seasonal and Permafrost Terrain

Rosa T. Affleck
U.S. Army Engineer Research and Development Center, Cold Regions Research and Engineering Laboratory
Sally A. Shoop
U.S. Army Engineer Research and Development Center, Cold Regions Research and Engineering Laboratory
Charles M. Collins
U.S. Army Engineer Research and Development Center, Cold Regions Research and Engineering Laboratory
Ellen Clark
U.S. Army Garrison Alaska, Center for Environmental Management of Military Lands, Colorado State University

Abstract

Disturbance from off-road vehicle operations was measured to determine damage to the soil and the vegetation. A 20-ton Stryker vehicle was used for maneuver impact tests on various terrains at a training land in Alaska during winter and spring. The trafficking consisted of both single and multiple passes for straight and turning maneuvers. The wintertime maneuver test was conducted on frozen terrain with 10 cm of snow cover. The initial disturbance to the soil and vegetation was observed to be minimal during the winter maneuver test, which showed limited vegetative shearing or soil disturbance in the vehicle tracks. The initial disturbances during the spring maneuver tests were observed to be minimal on shallow thawed terrain and significant in some areas with deep thaw depth, high moisture content, and sparse vegetation cover. The locations where the initial survey points were taken were revisited during the growing season to measure the recovery. The recovery was measured almost every year for up to four years in some locations to examine and assess the rebounding of the vegetation and healing of the ruts. Soil erosion from flooding and soil slumping were observed on ruts or tracks during the first recovery visit. The results showed significant vegetation rebound after three years. Recovery rates varied significantly depending on the terrain, ground and soil conditions, and initial impact severity.

Keywords: permafrost; rutting; seasonal terrain; thawing condition; vegetation recovery; vehicle disturbance.

Introduction

A 20-ton Stryker was newly introduced to U.S. Army Alaska (USARAK) training lands to train and support the Stryker Brigade Combat Team (SBCT3) (Shoop et al. 2004). Vegetation recovery rates on non-seasonal terrain have been examined after being disturbed by military vehicles (Howard et al. 2007). However, disturbance information from this type of vehicle was limited and unknown on Alaska training lands, especially since USARAK used light vehicles prior to SBCT. The initial question was how much impact could be expected from the Stryker vehicle. Secondly, what are the expected recovery rates from various types of disturbance? These questions were important for the training land managers for planning, suitability, and rehabilitation management. Maneuver impact tests using a 20-ton Stryker vehicle were conducted in March and May of 2003. The tests were conducted at one location during winter with frozen ground and snow cover and at three locations during the spring breakup when soil strength was at its annual minimum immediately following the melting of seasonal frost. This study was an attempt to quantify the initial disturbance generated by 20-ton Stryker vehicle (Affleck et al. 2004, Affleck 2005). The test in March 2003 was conducted on a permafrost terrain, while the tests in May 2003 were conducted on a permafrost area and on two sites with seasonal frost.

Prior to this study, there had been few studies conducted on the long- and short-term effects of off-road vehicle traffic on arctic tundra and subarctic alpine tundra soils (Abele et al. 1984, Walker et al. 1977, 1987, Sparrow et al. 1978, Slaughter et al. 1990). These studies concluded that poorly drained soils underlain by permafrost are often most heavily damaged, and soil bulk densities were higher on traffic areas than on the undisturbed areas. In addition, their findings included that the disturbances were based on many factors, including vehicle type, acceleration, turning radius, speed, time of summer, number of passes, slope, and vegetation. However, these off-road vehicles are mainly used for recreational and transportation purposes in Alaska, are lighter in weight (less than 10,000 kg), and have lower contact pressures than the Stryker vehicle.

Approach

The maneuver impact tests were composed of spiral and multi-pass tests. For the spiral test, the vehicle performed turning maneuvers by traversing from a large radius to a small radius to examine the disturbance generated when the vehicle is turning. The multi-pass tests were composed of lanes with 1, 4, 8, and 13 passes. The maneuver impact tests were conducted at three locations in May 2003 during spring and in one location in March 2003 during winter.

Test Vehicle

The Stryker vehicle used during the test was an infantry carrier vehicle (ICV) with no additional armor; it weighed approximately 18,000 kg (40,000 lbs) when loaded. The vehicle configurations listed for the Stryker are based on one of its variants (Table 1). The eight-wheel-drive Stryker is a combat vehicle and consists of four axles with 44.3 cm (17.43 in.) of ground clearance (Fig. 1). Although the vehicle has the capacity to run under cross-country tire inflation, it was operated using on-road tire pressures of 550 kPa (80 psi) on all eight tires.

A Global Positioning System (GPS) unit was mounted on the Stryker vehicle to track its position. The GPS unit recorded the position data of the test at 1-s intervals. The GPS data were used to determine vehicle speed and turning radius.

The terrain disturbance measurement categories included an imprint, a scrape, or a combination of both, and a pile (Ayers et al. 2000, Haugen 2002, Haugen et al. 2002, Affleck 2005). An imprint is where soil and vegetation are compressed in the vehicle track. A scrape is where the soil and vegetation have been stripped away from the vehicle track. A pile disturbance is where soil and vegetation have been displaced from the vehicle track and piled on the side(s). The impact severity was characterized by the amount of vegetation disturbed and removed, and the amount of bare soil exposed along the track.

Test locations and conditions

The test sites are described in detail by Affleck (2005) and Affleck et al. (2004). The sites include Arkansas Range, Eddy Drop Zone, and Texas Range. The test conditions during the trafficking to quantify terrain disturbance are briefly described in Table 2. There was only one test site during winter season on limited snow cover.

Initial disturbance

The initial disturbance to soil and vegetation along the vehicle tracks in the maneuver test area was measured in August 2003. The guidelines were established using impact severity and its corresponding disturbed width using guidelines (Ayers et al. 2000, Haugen 2002, Haugen et al. 2002). Although the initial survey was conducted a few months after the maneuver tracking, changes in vegetation in terms of recovery were considered minimal or almost zero. The initial disturbances from the Stryker maneuver tests were thoroughly described by Affleck (2005) and Affleck et al. (2004).

Recovery measurements

Recovery surveys were conducted in May 2004, August 2006, and June 2007. Guidelines used to measure the recovery of the soil and vegetation were established using impact severity and its corresponding disturbed width, based on work by Ayers et al. (2000), Haugen (2002), and Haugen et al. (2002), and modified for seasonal and permafrost areas as listed in Table 3.

Percent recovery and recovery rate

An overall assessment is quantified based on percent recovery and recovery rate. Percent recovery is measured in terms of the soil and vegetation rebound for each monitoring

Table 1. Stryker vehicle mobility parameters.

Width, cm (in.)	265.4 (104.5)
Length, cm (in.)	693 (273)
Weight, kg (lb)	17,745 (39,120)
Contact pressure, kPa (psi)	193 (27.94)
Tractive force, asphalt, kN (lb)	125.8 (28,283)
Tractive force, ice, kN (lb)	17.4 (3,912)
Ground clearance, cm (in.)	44.3 (17.43)
% Slope performance: Frontal, side	60, 30
Cross-country tire pressure, kPa (psi)	275.8 (40)

Figure 1. Stryker disturbance test in March 2003 at the Texas Range site.

Table 2. Test site locations, terrain description, and conditions during tracking.

Test Sites		Arkansas Range (AR)		Eddy Drop Zone (EDZ)		Texas Range (TR)
Terrain description		Flat, seasonal		Flat, seasonal		Gently sloping permafrost
Vegetation		Grass and short bushes		Sphagnum moss, sedge, tall grass and thick bushes	Tall grass, bare ground	Sphagnum moss, sedge
Soil type		Silty sand (SM)		Silty sand (SM) with thick organic layer in dense vegetative areas		Peat, organics
Test section conditions		Wet	Dry	Dense vegetation	Sparse vegetation	Ice-rich, high water content
Spring thaw	Avg. water content (%)	49.3	33.9	94.5	36.2	315.7
	Avg. thaw depth (cm)	28.8	23.4	14.5	44.5	7.6
Winter	Snow depth (cm)	—	—	—	—	10.0

Table 3. Modified recovery impact severity guidelines for seasonal terrain.

Impact Severity (%)	*Guidelines*
0	No visible disturbance as compared to surrounding vegetation/area; **no depression of vehicle track or rutting**
100	Slight leaning of vegetation; vegetation may be leaning in the direction of the vehicle track instead of standing straight compared to surrounding vegetation; **minimal compression of vegetation and organic mat and depression of vehicle track or rutting still exist [≤ 7.6 cm (3 in.)] but vegetation cover** similar or same in size as surrounding vegetation; vehicle track only slightly visible
200	Leaning of vegetation, likely in the direction of vehicle tracking compared to surrounding vegetation; **depression of vehicle track or rutting still exists but vegetation cover** similar in size to surrounding vegetation; visibility of tracks; little to no disturbance of soil visible
40	Depression of vehicle track **narrowing and more shallow due to soil slumping, movement, or erosion**; bare soil visible; over one third of the vegetation not present compared to surrounding; vegetation growing in track not as fully grown or as large as surrounding vegetation **or other vegetation types growing along the tracks** (e.g., moss); if rocky soil, some rock visible in bare soil; **organic matter accumulating in tracks**
600	About one third of the area with growing vegetation; vegetation smaller than surrounding vegetation **or sign of other vegetation types growing along the tracks** (e.g., moss, dominant or invasive vegetation); significant amount of bare soil still exposed; if rocky soil, rocks visible on soil surface; depression of track visible; sign of **soil slumping, movement, or erosion in tracks**
800	Few vegetative species growing on vehicle path; vegetation present is much smaller and less developed than surrounding vegetation; depression of track visible; if in a rocky soil, increasing amount of rocks visible in track
100	Track is bare soil with no vegetation growing; depression of track visible; if in a rocky soil, rocks highly visible in track

time with respect to the initial disturbance at the same location. The equation used to calculate percent recovery for each monitoring time (or measurement date) is

$$\%\text{Recovery}_t = \left(\frac{IS_i - IS_t}{IS_i}\right)100 \qquad (1)$$

where IS_i is the impact severity during initial time and IS_t is the impact severity at the time of interest.

Recovery rate can be obtained by plotting the percent recovery with the time.

Results

Permafrost terrain

The disturbance from the Stryker vehicle during the winter test at Texas Range (TR) was generally in the imprint category in which the snow and vegetation were compressed by the tires, showing bare ground in some areas along the tracks (Fig. 2a). The initial impact severity values were mostly near 10%, with vegetation being flattened and with broken stems or branches as shown in Figure 2b. Because the ground was frozen during the test (and had sufficient bearing capacity), the ground showed no rutting or depression. Tracks were still visible after a year (Fig. 2c). However, it was fully recovered after 3.42 years, when tracks were very hard to find (Fig. 2d).

Because the thaw depth was minimal during the test, the initial impact severity during the spring test at Texas Range was mainly compression of the vegetation and organic layer down to the frozen layer, where some vegetation had been sheared off the track at a few locations due to the vehicle turning.

Seasonal terrain

The initial impact severity (IS_i) during the spring test at Arkansas Range and Eddy DZ varied tremendously depending on the soil condition and vegetation cover. In the wet section at Arkansas Range and the sparse vegetation areas at Eddy DZ, the IS_i was up to 100%, resulting in complete removal of the vegetation and displacement of soil with significant ruts along the tracks (Fig. 3a). Soil slumping occurred during the following spring thaw, and possibly soil settlement from water ponding in the area made the soil fill in the tracks as shown in Figure 3b. At Arkansas Range, soil slumping on the ruts' side walls occurred, possibly due to freezing and thawing effects. Both the soil erosion and slumping processes made the ruts more shallow and narrow over time. In addition, organics (dead leaves) accumulated on the tracks. Over time, other vegetation types were observed growing in the tracks (e.g., moss, dominant or invasive vegetation), as seen in Figure 3c, for example, and adjacent vegetation sprawled into the tracks. In dense vegetative areas and dry soil locations at both Arkansas Range and Eddy DZ, the initial disturbance ranged from minimal compression of vegetation and organic mat to slight vegetation removal, to deep ruts with some shearing of plant at roots and some bare soil exposed.

Recovery

The disturbances were grouped based on the initial impact severity. IS_i >50% was considered to be high initial impact, while IS_i <50% was defined as low initial impact. The percent recovery values were obtained using Equation 1, and then an average value was taken from both inner and outer tracks and for each measurement date.

The percent recovery varied significantly depending on the terrain, ground and soil conditions, and initial impact severity (Fig. 4).

(a) March 2003, initial disturbance.

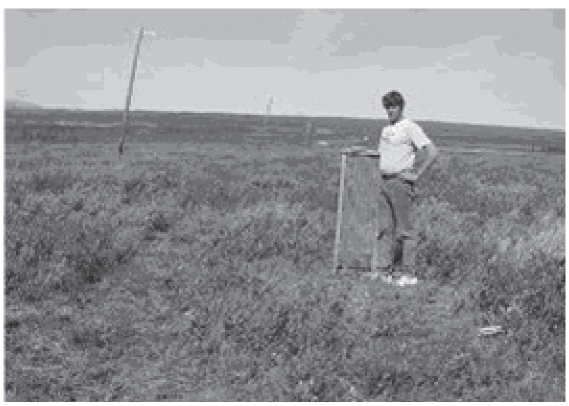

(b) Five months after trafficking.

(c) May 2004, one year and two months after trafficking. The area had just had a controlled burn.

Figure 2. Disturbance and recovery on tracks at Texas Range on permafrost.

(d) August 2006, 3.42 year after trafficking.

Figure 2. Continued.

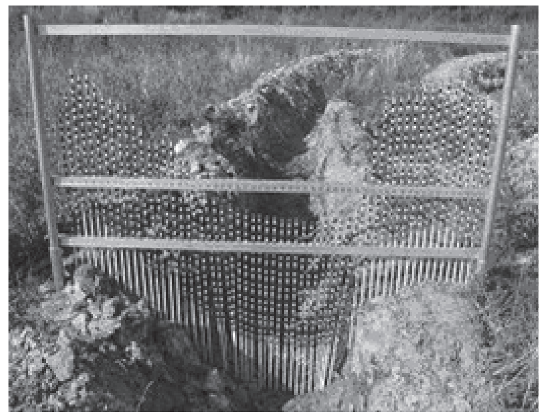

(a) August 2003, initial survey.

(b) May 2004, one year after.

(c) August 2006, 3.25 years after.

Figure 3. Left track disturbance and recovery on a track at Eddy DZ after 13 passes.

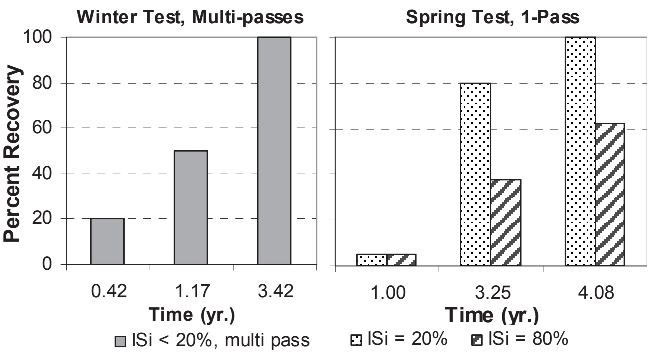

(a) Texas Range, permafrost terrain.

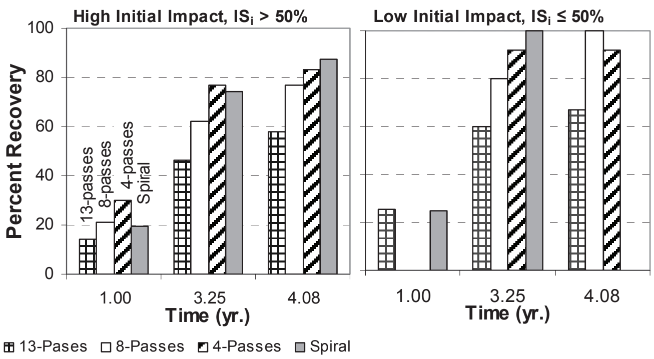

(b) Spring test disturbance at Arkansas Range.

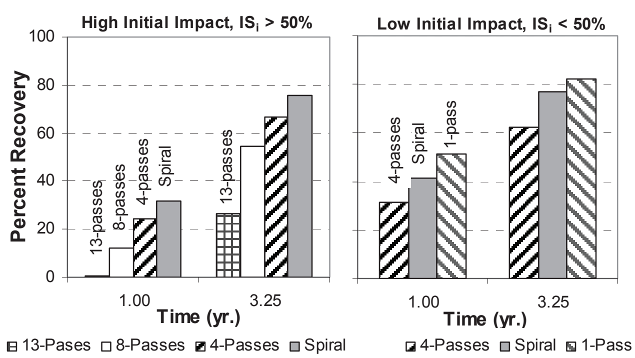

(c) Spring test disturbance at Eddy DZ, seasonal terrain.

Figure 4. Recovery rates at various locations from disturbance during winter and spring tests.

At the permafrost site (Texas Range), the recovery from the disturbance during the winter test produced a correlation with a rapid recovery of 100% after 3.42 year (Fig. 4a, left chart). On the other hand, the recovery for the spring test depended on the severity of the initial disturbance (Fig. 4a, right chart). 100% and 60% of recovery were found after 4 years for disturbances with initial impact severity of 20% and 80%, respectively.

Considerable differences in recovery rates were found at Arkansas Range and Eddy DZ from the disturbance generated by the Stryker vehicle during the spring tests (Figs. 4b & 4c). The percent recovery was higher and at a higher rate when the initial impact was less, but it also depended on the number of passes (Fig. 4b). For example, for initial high impact (severity of greater than 50%) after 4 years, approximately 58% and 87% recovery had occurred for the 13 passes and the spiral (single pass), respectively. However, with low initial impact (severity of less than 50%), the recovery rates were approximately 66% and 100% for the 13 passes after 4 years and for the spiral after 3.25 years, respectively.

Only up to 3.25 years of monitoring were conducted at Eddy DZ. The percent recovery was very limited for the 13-pass tracks, with zero recovery after the first year and only 26% after 3.25 years. During trafficking, the 13-pass tracks had less vegetation with bare ground compared to the rest of area at Eddy DZ. Overall, the recovery seemed to increase with a decreasing number of passes for initial impact severities greater than 50% (Fig. 4c, left chart). The recovery was a bit higher for low initial impact (severity less than 50%, Fig. 4c, right chart), and these tracks were in the dense vegetation area.

Summary and Conclusion

The initial disturbance from a Stryker vehicle at various sites and terrain conditions was assessed. Vegetation and surface recovery were monitored for up to 4 years in some sites. Percent recovery was quantified based on the impact severity for each measurement date with respect to the initial impact severity. Findings about the recovery can be summarized with the following:

1) The percent recovery and recovery rates varied significantly depending initial disturbance, which is a function of the terrain, ground and soil conditions and maneuver types (number of passes, tracks on turns and straight).

2) Recovery was rapid when the initial disturbance was low during winter with a snow cover on permafrost.

3) A higher rate of recovery was observed on areas with low initial disturbance of less that 50% impact severity.

4) There was very slow recovery after multi-pass trafficking and turns when the trafficking was on sparse vegetation, wet soils, and higher thaw depth areas.

5) The initial disturbance decreases and recovery rates increase with decreasing number of passes.

6) Overall the recovery from the vehicle impact of the Stryker vehicle is very promising as long as the tracks are allowed to heal over time.

Acknowledgments

Funding for the study was provided by the U.S. Army Garrison Alaska Directorate of Public Works and from AT42 High-Performance Ground Platform and Terrain Mechanics Modeling. The authors thank Jerry Reagan of the Cold Region Testing Center and his crew for conducting the Stryker maneuver tests at Donnelly Training Area. Technical support from U.S. Army Alaska staff, including Gary Larsen, Kevin Gardner, and Michael Davis; U.S. Army Alaska, Donnelly Training Area Range Control; and Sarah Brobst was greatly appreciated. We gratefully acknowledge Paul Ayers and Katie Simmons of the University of Tennessee for their technical support. The authors gratefully acknowledge the support provided by ERDC-CRREL staff, including Paul Richmond, Christopher Berini, Garrett Quillia, Maj. Douglas Anderson, the late Judy Strange, and Thomas Douglas.

References

Abele, G., Brown, J. & Brewer, M.C. 1984. Long-term effects of off-road vehicle traffic on tundra terrain. *Journal of Terramechanics* 21(3): 283–294.

Affleck, R.T. 2005. *Disturbance Measurements From Off-road Vehicles on Seasonal Terrain.* ERDC/CRREL Report TR-05-12. Hanover, NH: U.S. Army Engineer Research and Development Center, Cold Regions Research and Engineering Laboratory.

Affleck, R.T., Shoop, S., Simmons, K. & Ayers, P. 2004. Disturbance from off-road vehicle during spring thaw. *Proceedings, 12th American Society of Civil Engineers, International Winter Construction Symposium and Expo on Cold Regions Engineering, Alberta, Canada, 16–19 May 2004*.

Ayers, P., Vance, M., Haugen, L. & Anderson, A.B. 2000. *An Evaluation of DGPS-based Continuously Operating Vehicle Monitoring Systems to Determine Site-specific Event Severity Factors.* ERDC/CERL Technical Report TR-00-43. Champaign, IL: U.S. Army Engineer Research and Development Center, Construction Engineering Research Laboratory.

Haugen, L. 2002. *Design and Testing of a Vehicle Tracking System for Monitoring Environmental Impact at U.S. Army Training Installations.* M.S. Thesis. Fort Collins, CO: Colorado State University.

Haugen, L.B., Ayers, P.D., Anderson, A.B. & Nissen, P.E. 2002. Using GPS to evaluate movement patterns and impacts during training maneuvers. *Proceedings, 14th International Society for Terrain-Vehicle Systems (ISTVS), Vicksburg, Mississippi.*

Howard, H.R., Ayers, P.D. & Simmons, K.J. 2007. Vegetation rates after military training. *Proceedings, Joint North America, Asia-Pacific ISTVS Conference and Annual Meeting of Japanese Society for Terramechanics, Fairbanks, Alaska, June 23-26, 2007.*

Shoop, S., Affleck, R., Collins, C., Larsen, G. & Sullivan, P. 2004. Maneuver analysis methodology to assess vehicle impacts on training lands. *Journal of Terramechanics.*

Slaughter, C.W., Racine, C.H., Walker, D.A., Johnson, L.A. & Abele, G. 1990. Use of off-road vehicles and mitigation of effects of Alaska permafrost environments: a review. *Environmental Management* 14: 63–72.

Sparrow, S.D., Wooding, F.J. & Whiting, E.H. 1978. Effects of off-road vehicle traffic on soils and vegetation in the Denali Highway Region of Alaska. *Journal of Soil and Water Conservation* 33: 20–27.

Walker, D.A., Webber, P.J., Everett, K.R. & Brown, J. 1977. *The Effects of Low-pressure Wheeled Vehicles on Plant Communities and Soils at Prudhoe Bay, Alaska.* Special Report 77-17. Hanover, NH: U.S. Army Cold Regions Research and Engineering Laboratory.

Walker, D.A., Cate, D., Brown, J. & Racine, C. 1987. *Disturbance and Recovery of Arctic Alaskan Tundra Terrain: A Review of Recent Investigations.* CRREL Report 87-11. Hanover, NH: U.S. Army Cold Regions Research and Engineering Laboratory.

Erosion of the Barrow Environmental Observatory Coastline 2003–2007, Northern Alaska

A. Aguirre
The University of Texas at El Paso, El Paso, Texas, USA

C.E. Tweedie
The University of Texas at El Paso, El Paso, Texas, USA

J. Brown
International Permafrost Association, Woods Hole, MA, USA

A. Gaylord
Nuna Technologies, Homer, Alaska, USA

Abstract

The Barrow Environmental Observatory (BEO) is bounded to the east by the 10.7 km long Elson Lagoon shoreline of the Beaufort Sea. Rates of erosion along the 2 to 4 m high, ice and organic rich permafrost bluffs have been monitored annually at 14 transects since 2002 as part of the Arctic Coastal Dynamics (ACD) program. Continuous, ground-based Differential Global Positioning System (DPGS) surveys were conducted along the entire length of the BEO coastline in 2003, 2006, and 2007. The mean erosion rate during the four-year period was 2.3 m per year. A comparison of fall and summer erosion rates calculated from repeat DGPS surveys indicate similar amounts of erosion during fall 2006 (between August 2006 and June 2007, 8120 m^2) and summer 2007 (between June and August 2007, 7934 m^2). The total area lost to erosion during the four-year period was 9.8 hectares (average 2.5 ha/yr), which is almost twice the rate (1.3 ha/yr) calculated for the period 1979–2000 by previous studies

Keywords: ACD; bathymetry; coastal erosion; DGPS; ground ice; permafrost.

Introduction

Erosion of ice-rich, permafrost coastlines in the Arctic is limited to periods of ice-free seas. The duration and extent of seasonal ice-free seas in the Arctic is increasing (Serreze et al. 2007, Stroeve et al. 2007) and it is predicted that this in combination with increased storminess could increase rates of erosion experienced along arctic coastlines (Atkinson 2005). Increased rates of coastal erosion can impact communities, affect industry, and alter ecosystem structure and function in coastal terrestrial and marine ecosystems. Evidence supporting increased rates of erosion in the Arctic remain relatively scant and until recently the relationship between seasonal and interannual variations in erosion and storminess has been poorly studied. This study, linked to the Arctic Coastal Dynamics (ACD) program, documents the seasonal and interannual variations in coastal erosion along the Elson Lagoon coastline of the Barrow Environmental Observatory (BEO) situated on the Beaufort Sea coast of northern Alaska.

The Elson Lagoon shoreline is an ideal location to observe changing shoreline conditions. Coastal erosion research along this coastline dates back to 1948, is associated with the ACD program, and is situated on the BEO, a 7466 research preserve set aside by local land owners for research. Because of the availability of historical quantitative erosion data, there is potential in creating predictive models for shorelines with similar characteristics. Observing rapid change in high latitude shorelines creates urgency for these models to be developed. Until recently, observations have relied on measurements from sequential, high resolution imagery and repeat line-transect measurements made perpendicular to the coastline. Our additional results reported here are based on repeat, ground-based Differential Global Positioning System (DPGS) surveys that were conducted along the 10.7 kilometer length of the BEO coastline in August of 2003, 2006, and 2007. A similar survey was also conducted in June 2007 to begin to ascertain seasonal variations in the coastal erosion. This paper provides an update from on-going field studies, initial results presented at the eighth international permafrost conference in Zurich (Brown et al. 2003), and observations reported in the proceedings of the Arctic Coastal Dynamics workshops held in 2003 in St. Petersburg and in 2004 in Montreal (Serbin et al. 2004, Francis-Chythlook 2004, 2005, Francis-Chythlook & Brown 2005). Several papers report on regional erosion rates along the Chukchi Sea coast (Sturtevant et al 2005), the entire Beaufort Sea coast (Jorgenson & Brown 2005) and for a section of the Beaufort Sea coastline to the east that is directly exposed to the ocean (Mars & Houseknecht 2007).

The objectives of this continuing ACD project are to improve our understanding of rates and causes of coastal erosion and to assess their contributions to offshore sediment and carbon budgets and the impacts on living resources (Rachold 2004). Like many ACD-affiliated projects, this project also serves as a training ground for a new generation of young researchers and contributes to the International Polar Year and its legacy. Data from this project has been incorporated into the interactive and freely available Barrow Area Information Database-Internet Map Server (www.baidims.org) (Graves et al. 2004).

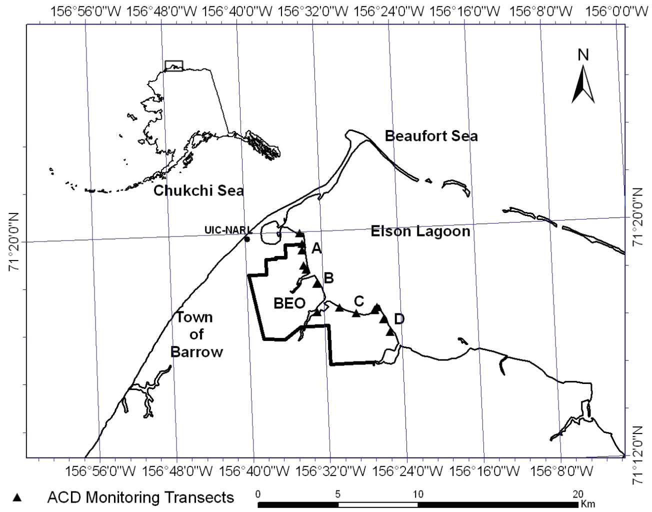

Figure 1. Location of the ACD observatory and key sites on the Elson Lagoon coastline of the BEO near Barrow, Alaska.

Study Area

The Barrow Environmental Observatory (BEO) is bounded on the east by the 10.7 kilometer-long Elson Lagoon shoreline (71°19'53", 156°34'4", Fig. 1). Elevations range from sea level to 4.4 m along this coastal stretch. Terrain is composed of ice wedge polygons, shallow elliptically shaped lakes, drained lake basins, and small ponds (Brown et. al 1980). The area is mainly composed of moist and wet tundra with acidic soils. The ACD observatory on the BEO coastline is divided into four segments with sections A, B, and D facing eastward and section C facing predominantly north. Water depth in Elson Lagoon ranges from 0.5 m to 3.5 m. The lagoon is bounded to the northeast by a series of low elevation barrier islands. Shallow but submerged bars lie at the mouth of most creeks draining from the BEO to Elson Lagoon and a submerged shoal extends northwest from Tekegakrok Point, which marks the junction between Sections C and D of the coastal observatory. Fourteen permanent ACD transect sites are oriented perpendicular to the coastline along the Elson Lagoon coast.

Methods

Field data collection utilized a Trimble NetRS GPS receiver with a Zephyr Geodetic antenna as a fixed Geodetic GPS base station located at the Barrow Arctic Science Consortium (BASC). This base station provides differential correction of data files at 1 second intervals as well as real time correction to field rover GPS units within approximately five kilometers and in line of sight of site of the Trimble HPB450 radio transmitter that is connected to the base station . The base station was upgraded in 2005 from a Trimble GPS 5800, which was used during the 2003 coastal survey described below. The rover system used for 2007 surveys included a Trimble R7 with internal radio that communicated with the base station radio transmitter for real time DGPS correction and a TSC2 survey controller that logged field data. Field surveys in 2003 and 2006 utilized a Trimble 5700 receiver,

Figure 2. Segment C facing east.

Zephyr antenna, and a Trimble TSC1 controller. All DGPS equipment was provided by UNAVCO (www.unavco.org) to the local science logistics provider (BASC).

A total of four surveys of the 10.7 kilometer ACD BEO observatory were conducted. These included August 2003, 2006, and 2007 and June 2007. During each survey, field personnel walked along the top of the coastal bluff edge. The initial surveys for the 2003 season were conducted by Serbin et al (2003). In subsequent years surveys were conducted by the lead author of this paper following previously documented survey methodology documented in Serbin et al. (2003). For field surveys, the rover receiver was installed in a standard Trimble backpack configuration with the GPS antenna mounted on the bluff side of the backpack. After antenna height was corrected for the height of the field observer, this configuration allowed for the location of the horizontal and vertical position of the coastal bluff edge to be documented (Fig. 2).

Two survey methods were used. Real Time Kinematic (RTK) surveys were conducted whenever possible. This required a radio link to the base station. RTK surveys allow for instant DGPS processing and the acquisition of centimeter-accuracy horizontal and vertical location data. The second method utilized a Post-Processed Kinematic (PPK) survey style, which did not require a radio link, but instead relied on an unobstructed On-The-Fly (OTF) initialization period and post-survey differential correction with GPS data logged at the base station to provide field survey data with centimeter accuracy. For both survey types, the rover receiver was set to log data at a high resolution of one-second intervals to more accurately delineate the generally irregular coastal bluff edge. Repeat surveys using these vertically and horizontally centimeter-accurate field methods provide a means to accurately monitor the geospatial dynamics of the coastal bluff edge as it changes with coastal erosion.

DGPS survey data was downloaded from the controller and imported into Trimble Geomatic Office Software version 1.63 (TGO). Data was exported in text files suitable for ingestion by ESRI's ArcGIS (Workstation 9.2) Geographic Information System (GIS) software. Data from PPK surveys were processed by downloading base station files that were utilized for differentially correcting data collected by the

Table 1. Section length calculated for each DGPS survey.

Segment	Length (meters)			
	2003	2006	Jun-07	Aug-07
A	2923	2774	2683	2710
B	1666	1658	1568	1633
C	3449	3464	3377	3419
D	2643	2728	2651	2667
Total	**10681**	**10624**	**10279**	**10429**

Table 2. Total land area lost to erosion between sampling periods.

Segment	Erosion Area (m^2)				
	Aug 03- Aug 07	Aug 03- Aug 06	Aug 06- Aug 07	Aug 06- June 07	June 07- Aug 07
A	16118	14143	1975	1375	600
B	9540	4584	4956	3156	1797
C	19237	16652	2584	666	1918
D	53130	46592	6539	2920	3619
Total	98025	81971	16055	8120	7934

Table 3. Total land area lost to erosion expressed as an annual rate.

Segment	Erosion Area (m^2/year)		
	Aug 03– Aug 07	Aug 03– Aug -06	Aug 06– Aug 07
Years	4	3	1
A	4030	4714	1975
B	2385	1528	4956
C	4809	5551	2584
D	13282	15531	6539
Total	24506	27324	16055

Table 4. Total land area lost to erosion expressed as an annual rate per meter length of coastline.

Segment	Erosion Area (m^2/year/segment length)		
	Aug 03– Aug 07	Aug 03– Aug -06	Aug 06– Aug 07
A	1.5	1.6	0.7
B	1.5	0.9	3.0
C	1.4	1.6	0.7
D	5.0	5.9	2.4
Mean	2.3	2.5	1.7

rover GPS unit using standard DGPS correction procedures. Processed data were exported as for that of the RTK surveys.

Processed DGPS survey data were imported to ArcGIS as X, Y point data and saved to a point shapefile. Erroneous points that resulted from poor GPS signal when field personnel traversed small coastal gullies were deleted. Using the polyline conversion tool in the ArcGIS extension AlaskaPak Version 2.0 for ArcGIS 9.2, point shapefiles were converted to polyline shapefiles. For each survey, the length of the coastline was computed for each of the four monitoring segments using the attribute data field calculator tool associated with the ArcGIS polyline tool (Table 1). Using the polyline shapefiles as a determinant location of the coastal bluff at each survey time, polygon shapefiles were created to establish the area of coastline lost to erosion for each monitoring segment for the following survey periods: August 2003 to August 2007, August 2003 to August 2006, August 2003 to June 2007, and June to August 2007. The area of each polygon shapefile was computed using the calculate area command from ArcGIS Toolbox. Rates of erosion were calculated for the following five periods by subtracting the total area of a preceding survey period from that of the most recent survey period: August 2003 to August 2007, August 2003 to August 2006, August 2006 to August 2007, August 2006 to June 2007, and June 2007 to August 2007. To enhance inter-comparison of erosion rates between segments of different lengths and different sampling periods, results were normalized by the length of the coastal segment at the earliest survey associated with a given survey period and reduced to a year-long time frame for survey periods spanning the 2003 to 2006 and 2007 periods (Table 4).

The establishment of the 14 coastal erosion monitoring transects (Fig. 1) oriented perpendicular to the coastline has been previously described by Brown et al. (2003). Since 2002, the distance from fixed markers along these linear transects to the coastal bluff and thaw depths have been measured. In 2003, 2006, and 2007, these measurements were made on the same day as the August DGPS surveys. While these survey methods do not permit the geospatial elucidation permissible from the repeat DGPS surveys, they are easy to perform, are part of the long-term ACD monitoring protocol, and are an excellent measurement to cross-check the accuracy of the DGPS surveys.

Results

Table 1 details the length of each coastal segment at each survey time. Section lengths were longest for Segments A and B in 2003 and Segments C and D in 2006. Lengths of the coastal bluff were shortest for Segments A, B, and C in June 2007 and for Segment D in 2003. Segment length is determined by the irregularity of the coastal bluff during each survey time period.

The calculated rates of total loss to erosion are given in Table 2. Overall, 9.8 hectares of tundra were lost to erosion between August 2003 and August 2007. Higher erosion rates were documented for Segments C and D in summer 2007 than in the Fall of 2006. Erosion loss was greatest in Segment D followed by Segments C, A, and B.

Mean annual erosion for all segments except Segment B was greater between 2003 to 2006 than between 2006 and August 2007 (Tables 3, 4). Erosion rates calculated for Segment B were greater between August 2006 and 2007 than during the period 2003 to 2006. Rates of erosion were greater in the Fall of 2006 for Segments A and B than in summer of 2007. As previously reported, Segment D had the highest rate of erosion when normalized by length of

Table 5. Distance between permanent markers and the coastal bluff edge since 2002 at ACD permanent line transects depicted in Figure 1.

Annual, total and average loss of coastline at permanent ACD line transects (m)								
Transect	2002	2003	2004	2005	2006	2007	total loss	m/yr
A1	92.2	89.2	88.1	86.2	76.0	75.0	17.2	2.9
A2	45.9	44.1	41.3	40.5	36.5	35.5	10.4	1.7
A3	110.4	109.1	-	107.3	105.0	103.9	6.5	1.1
A4	143.0	142.4	-	141.2	139.0	136.6	6.4	1.1
A5	56.0	55.0	-	53.6	53.2	50.8	5.2	0.9
B1	101.8	-	-	96.5	95.7	92.7	9.1	1.5
C1	-	72.4	70.9	-	68.8	68.2	4.2*	1.1
C2	-	37.7	-	-	29.3	28.6^	9.1*	2.3
C3	-	34.0	31.2	-	28.2	26.4^	7.6*	1.9
C4	-	97.3	95.6	91.9	88.0	80.8	16.5*	4.1
C5	38.0	37.0	34.6	34.8	-	34.3	3.7	0.6
D1	52.0	49.0	41.6	34.5	16.7	14.3	37.7	6.3
D2	54.9	53.2	51.5	44.7	38.7	35.6	19.3	3.2
D3	64.5	59.7	57.1	49.3	34.6	26.3	38.2	6.2

* Indicates total loss calculated between 2003 and 2007 instead of 2002 and 2007.
^ Indicates measurements made using the ArcGIS measuring tool due to erroneous field measurements.

coastline (Table 4). This rate is over three times the rate of loss recorded for the other segments during the period August 2003 and August 2007.

Annual rates of coastal retreat recorded using DGPS methods (Table 4) are similar to those measured using line-transect methods (Table 5).

Discussion

Similar to other studies focused on coastal erosion along Elson Lagoon (Brown et al. 2003, Serbin et al. 2004), this study documents substantial spatial and temporal variability in the rates of erosion. Within the 2003–2007 study period no segment monitored maintained a consistent temporal trend in the rate of erosion measured. Nonetheless, the DGPS study reported above has identified rates of erosion that are comparable to those that have used linear transect methods (Table 5) and GIS interpolation (Brown et al. 2003, Francis-Chythlook & Brown 2005, Serbin et al. 2004). Figure 3 illustrates a section of segment D on 2002 Quickbird panchromatic satellite image (Manley et al. 2005). The location of the coastline identified by DGPS surveys in 2003, 2006, and August 2007 are labeled. Relatively small scale sub decimeter-scale variability in the degree of coastal retreat between sampling periods can be observed. It appears that the variability in the rate of coastal erosion documented in this and other local studies is strongly related to this spatiotemporal heterogeneity.

Seasonally, erosion can begin as soon as the coastal bluffs thaw and Elson Lagoon becomes partially ice-free. This generally occurs around July 11th (Craig George unpublished data). Erosion ceases as bluffs freeze and the lagoon becomes ice covered, which has occurred around the 8th of October since 1988 (Craig George unpublished data). The process of shoreline retreat is enhanced by the undercutting of the coastal bluffs (thermo-erosion notches or niches) and removal by wave action of the slumped and thawed materials that can otherwise protect the coast from additional retreat (Walker 1991). Diurnal tidal movements are not considered to influence erosion in the Barrow area because they approximate only 0.3 m (Beal 1968, Mathews 1970). Brown et al. (2003) suggest the frequency, intensity, and duration of storms, and high water events affect seasonal to multi-decadal rates of retreat, whereas local spatial differences in erosion are generally attributed to the spatial variations in bluff elevation, ice and organic contents of exposed sediments, water depth, and wave fetch (Brown et al. 2003).

To better understand factors controlling the spatiotemporal variability in the patterns of coastal erosion along the Elson Lagoon coastline, a more thorough analysis of the interplay between the spatiotemporal dynamics of coastal erosion and other physical and climatic factors needs to be considered. These include the density of polygons and ice wedges, differences in land cover types, soil characteristics, and the elevation of the eroding coastline. The orientation of the coastline, offshore bathymetry, and the timing of freezing and thawing of the bluff, degree of storminess within a given sampling period are also important. These considerations fall beyond the scope of the current work, which is focused on updating the ACD time series for this section of coastline, but will be explored in a graduate thesis currently being developed by the lead author of this paper. Variations in seasonal soil thaw depths do not appear to play a role in erosion as regional thaw depths have been relatively consistent during the sample period (Nelson et al. 2008).

The DGPS survey method employed for this study demonstrates a potentially excellent method for further understanding how small-scale processes may control coastal erosion. Compared to line transect methods and GIS analysis, DGPS methods permit a greater consistency of measurement along the coast, provide better documentation of coastal shapes, provide more accurate and detailed products, and permit potentially more accurate volumetric calculations of erosion loss. DGPS surveys also appear to be more cost-effective than the acquisition and georectification of aerial or satellite imagery for the study area. The acquisition of imagery is costly and can be difficult to obtain due to the cloudy conditions that prevail during the arctic summer period. Nonetheless, DGPS surveys can be time consuming, require advanced training, and need to be performed at a relatively high frequency (at least twice in the summer, snow-free period) in order to best understand how climate and sea-state controls the seasonal and spatial dynamics of erosion. Products obtained from DGPS surveys are also particularly well suited to the development of process models that may help to predict future erosion patterns in the Barrow area and elsewhere along the arctic coastlines.

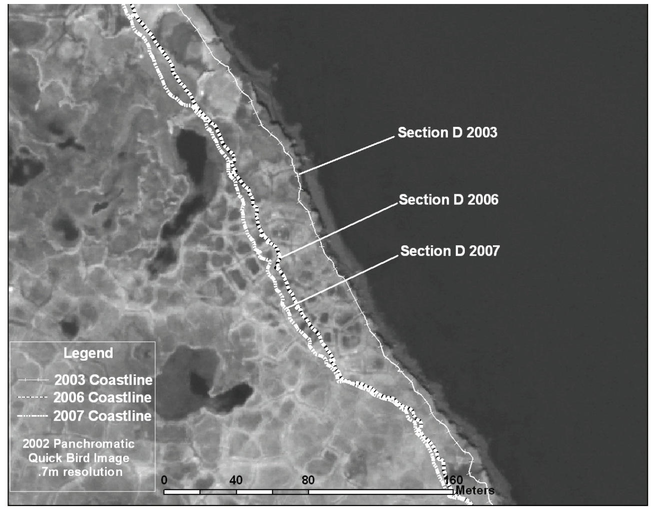

Figure 3. A section of segment D showing the location of the coastline in 2003, 2006, and August 2007 determined from DGPS surveys of the coastal bluff edge

Conclusion

Erosion rates along the Elson Lagoon coastline of the Barrow Environmental Observatory in northern Alaska, continue to be monitored as key contributions to the Arctic Coastal Dynamics Program, the International Polar Year, and a sustainable Arctic Observing Network. The Differential Global Positioning Systems approach employed provides a high-accuracy method to track coastline changes and to compute area and potentially volumetric losses due to erosion. The rates of coastal erosion documented in this study, like others in the Barrow area, confirm highly variable rates over time and space. Mean annual rates of erosion documented in this study are consistent with earlier reports, which further support the use of DGPS to monitor coastlines. Similar to Brown et al. 2003, who reported erosion rates between 1948–1949 and 1962–1964 we continue to document erosions rates for the Elson Lagoon between 1–3 m/yr. With the application of DGPS, however, we believe we can better determine where the higher erosion rates along this coastline are occurring and explore further questions such as why some areas are more vulnerable than others. We are currently evaluating the USGS Digital Shoreline Analysis System (DSAS) extension tool for ArcGIS to automate and standardize future analysis. Further research is needed to better affirm the primary controls of coastal erosion along this and similar sections of arctic coastline. This paper is a contribution to the International Polar Year (Project 90) by a member (lead author) of the Permafrost Young Researchers Network (PYRN).

Acknowledgments

The land occupied by the Barrow Environmental Observatory is owned by the Ukpeagvik Iñupiat Corporation (UIC) and has been designated for research and long-term observations. The Barrow Arctic Science Consortium (BASC), a non-profit organization dedicated to scientist/community collaboration, was designated by UIC to manage the BEO with support from the U.S. National Science Foundation (NSF). We are grateful to both UIC and BASC for the opportunity to establish and maintain our sites. NSF grants OPP9906692 and OPP0454996 (BAID) provided support. We also express appreciation to several undergraduate and graduate participants who assisted the authors in the field and with GIS support (Shawn Serbin, David Zaks, Eric Hammerbacher, Edith Jaurrieta Amorita Armendariz, Paulo Olivas, Ryan Cody, Rob Wielder, Sandra Villarreal, Santonu Goswami, and G. Walker Johnson). UNAVCO has generously provided DGPS support and training to field parties since 2002. Any opinions, findings, conclusion, or recommendations expressed in this paper are those of the authors and do not necessarily reflect the views of the National Science Foundation. Identification of specific products and manufacturers in the text does not imply endorsement by the National Science Foundation.

References

Atkinson, D.E. 2005. Observed storminess patterns and trends in the circum-Arctic coastal regime. *Geo-Marine Letters* 25: 98-109.

Beal, M.A. 1968. The seasonal variation in sea level at Barrow, Alaska. In: J.E. Sater (coord.), *Arctic Drifting Stations, 327-341.*

Brown J., Miller, P.C., Tieszen L. & Bunnell, F.L. 1980. *An Arctic Ecosystem: The Coastal Tundra at Barrow Alaska*. Stroudsburg, Pennsylvania: Dowden, Hutchinson and Ross, Inc., 571 pp.

Brown, J., Jorgenson, M.T., Smith, O.P. & Lee, W. 2003. Long-term rates of erosion and carbon input, Elson Lagoon, Barrow, Alaska. In: M. Phillips, S.M. Springman & L.U. Arenson, (eds.), *ICOP 2003 Permafrost: Proceedings of the 8th International Conference on Permafrost*. Netherlands: A.A. Balkema Publishers, 101-106.

Francis-Chythlook, O.P., 2004. *Coastal processes in Elson Lagoon, Barrow, Alaska*, M.S. Thesis. University of Alaska Anchorage, 130 pp.

Francis-Chythlook, O. 2005. Results of a wave climate study for Elson Lagoon, Barrow, Alaska. *ACD-Arctic Coastal Dynamics, 5th International Workshop, October 13-16, 2004, McGill University, Montreal, Canada. Reports on Polar and Marine Research* 506: 44-45.

Francis-Chythlook, O. & Brown, J. 2005. Additional erosion observations for the Elson Lagoon key site, Barrow, Alaska, *ACD-Arctic Coastal Dynamics, 5th International Workshop, October 13-16, 2004, McGill University, Montreal, Canada*, *Reports on Polar and Marine Research* 506: 38-41.

Graves, A., Tweedie, C.E., Zaks, D., Serbin, S., Manley, W., Brown, J. & Bulger, B. 2004. Spatial data infrastructure supports long term measurements to detect Arctic change. *Arctic Coastal Dynamics, Report of the 4rd International International Workshop. St. Petersburg, Russia, 10-13 November 2003.Reports on Polar and Marine Research.* 482: 29-30.

Jorgenson, M.T. & Brown, J. 2005. Classification of the Alaskan Beaufort Sea Coast and estimation of carbon and sediment inputs from coastal erosion. *Geo-Marine Letters* 25: 69-80.

Manley, W.F., Lestak, L.R., Tweedie, C.E. & Maslanik, J.A. 2005. *High-resolution Radar Imagery, Digital Elevation Models and Related GIS Layers for Barrow, Alaska.* Boulder, CO: National Snow and Ice Data Center. DVD.

Mars, J.C. & Houseknecht, D.W. 2007. Quantitative remote sensing study indicates doubling of coastal erosion rate in past 50 yr along a segment of the Arctic coast of Alaska. *Geology* 35: 583–586.

Matthews, J.B 1970. Tides at Point Barrow. *Northern Engineers* 2(2): 12-13.

Nelson, F.E., Shiklomanov, N.I., Streletskiy, D.A., Romanovsky, V.E., Yoshikawa,K., Hinkel, K.M. & Brown, J. 2008. A Permafrost Observatory at Barrow, Alaska: Long-term Observations of Active Layer Thicknesses and Permafrost Temperatures *Proceedings of the Ninth International Conference on Permafrost, Fairbanks, Alaska, June 29–July 3, 2008* (this proceedings).

Rachold V., Are, F.E., Atkinson, D.E., Cherkashov, G. & Solomon, S.M. 2004. Arctic Coastal Dynamics (ACD): an introduction. *Geo-Marine Letters* 25: 63-68.

Serbin, S., Graves, A., Zaks, A.D., Brown, J. & Tweedie, C.E. 2004. The utility of survey grade Differential Global Positioning Systems (DGPS) technology for monitoring coastal erosion. *Arctic Coastal Dynamics, Report of the 4rd International Workshop. St. Petersburg, Russia, 10-13 November 2003. Reports on Polar and Marine Research* 482: 52-56.

Serreze, M.C., Holland, M.M. & Stroeve, J. 2007. Perspectives on the Arctic's shrinking sea-ice cover. *Science* 31(5818): 1533-1536.

Stroeve, J., Holland, M.M., Mier, W., Scambos, T. & Serreze, M. 2007. Arctic sea ice decline: faster than forecast. *Geophysical Research Letters* 34(9): Art. No. L09501.

Sturtevant, P.M., Lestak, L.R., Manley, W.F. & Maslanik, J.A. 2005. Coastal erosion along the Chukchi coast due to an extreme storm event at Barrow, Alaska. *5th International Workshop, October 13-16, 2004, McGill University, Montreal, Canada. Reports on Polar and Marine Research.* 506:114-118.

Walker, H.J. 1991. Bluff erosion at Point Barrow and Wainwright, Arctic Alaska. *Z. Geomorh. N.F. Suppl.-Bd.* 81: 53-61.

Pore Water and Effective Pressure in the Frozen Fringe During Soil Freezing

Satoshi Akagawa
Hokkaido University, Sapporo, Japan

Syuhei Hiasa
West Nippon Expressway Co. Ltd., Osaka Japan

Syunji Kanie
Hokkaido University, Sapporo, Japan

Scott L. Huang
University of Alaska Fairbanks, Fairbanks, USA

Abstract

A model pipe (75 mm diameter, 29.5 mm length) is placed in NSF clay. Thin thermocouples attached to pressure gauges and markers monitor temperature. Five pressure gauges are placed along the pipe centerline and below the pipe: three in the vertical/radial direction, and two in the horizontal/hoop direction. As the frost bulb grows, the pipe moves up by 29 mm. Markers move away along the direction of heat flow during the early stage, but move upward with the model pipe once contained within the frost bulb. The pore-water pressure depresses in a temperature range corresponding to that of the frozen fringe. As the pore-water pressure depression reaches 35 kPa, the temperature is lowered by about 0.12°C. The effective pressure in the frozen fringe increases as temperature decreases, with the magnitude in the radial direction twice that in the hoop direction. The decrease of pore-water pressure is considered the driving force for ice lens formation, and the increase of effective pressure is the driving force for soil consolidation in the frozen fringe.

Keywords: effective pressure; frost heave mechanism; frozen fringe; unfrozen pore-water pressure.

Introduction

The subject of frost heave mechanism has been discussed and studied for a long time, yet it still attracts the attentions of scientists in the 21st century. Several models of the frost heave mechanism were proposed in the 1970s and 1980s (Miller 1978, Gilpin 1980, Takagi 1980), but they have not yet been verified empirically. The authors have attempted to verify those frost heave models empirically, and present results of the lab experiment in this paper.

Taber (1929) foresaw pore-water pressure depression in front of the segregating ice lens. Chamberlain and Gow (1978) speculated that the high consolidation of thawed sub-sea permafrost was due to the pore-water pressure depression as the ground became frozen. Gilpin (1980) and Miller (1978) proposed their frost heave models, and mentioned that the pore-water pressure depression in frozen fringe was the driving force sucking the water to the segregating ice lens. Akagawa (1988) observed consolidation in the frozen fringe during frost heaving with X-ray radiography technology and concluded that the consolidation was caused by pore-water pressure depression at the segregating ice lens.

Direct measurement of the pore-water pressure depression in the frozen fringe was first made by Radd and Oertle (1973) but was under closed system frost heave tests. Miyata and Akagawa (1998) tried to measure unfrozen pore-water pressure at the segregating ice lens in open system frost heave tests and concluded that the pore-water pressure depression was one-half of the value given by Generalized-Clausius-Clapeyron-Equation.

Despite intensive efforts taken to reveal the pore-water pressure depression at the segregating ice lens experimentally, none of them have received wide acceptance so far.

In this paper the total pressure and pore-water pressure in soil are presented. The pressure changes were monitored with frost heave tests in a 2D model. The relationship between the pressure measurements and the pressures depression in frozen fringe is discussed.

Experiment

Test apparatus and thermal condition

The experiment was conducted with an insulated soil box as shown in Figure 1 that was placed in a cold room in which temperature was maintained at 1.50 ± 0.5°C.

The box has inner dimensions of 500 mm in height, 500 mm in width, and 300 mm in depth. Two sides, the rear, and the bottom of the container were thermally insulated with Expanded Poly-Styrene. The front was covered with double Plexiglas to provide transparency and thermal insulation. The top side of the box was open to the air.

The experiment was initiated by circulating -10°C coolant as "thermal-shock," and then the temperature was warmed to and kept at -4°C.

Monitored items and methods

During the experiment total pressure, pore-water pressure, soil deformation, and temperature of the model ground were monitored.

The total pressure gauge is 23 mm in diameter and 5 mm

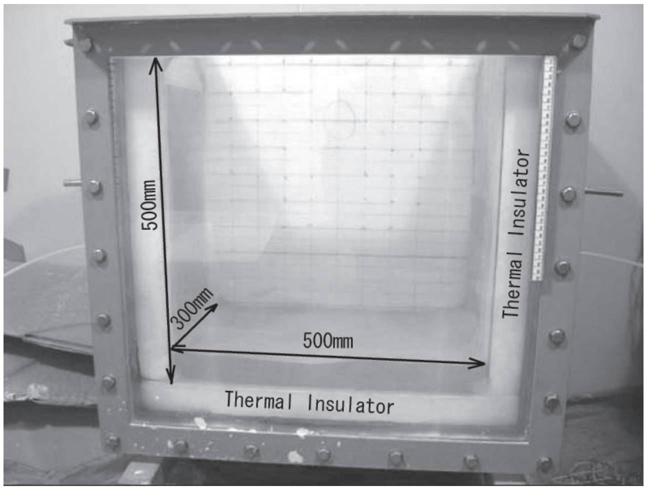

Figure 1. Insulated box used in axial-cylindrical frost heave test.

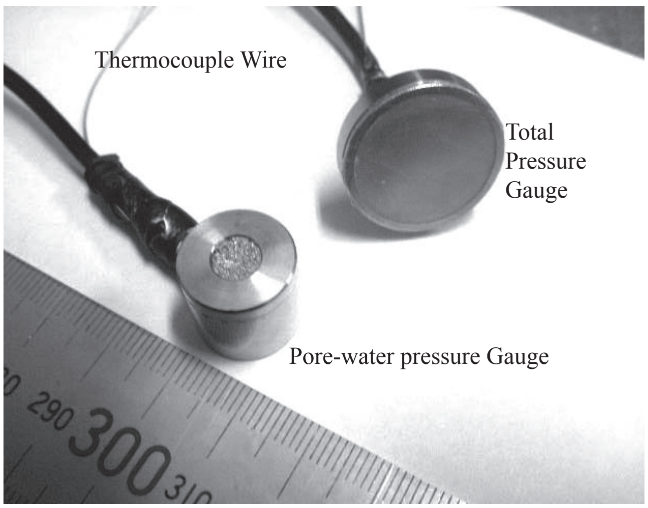

Figure 2. Total pressure and pore-water pressure gauges.

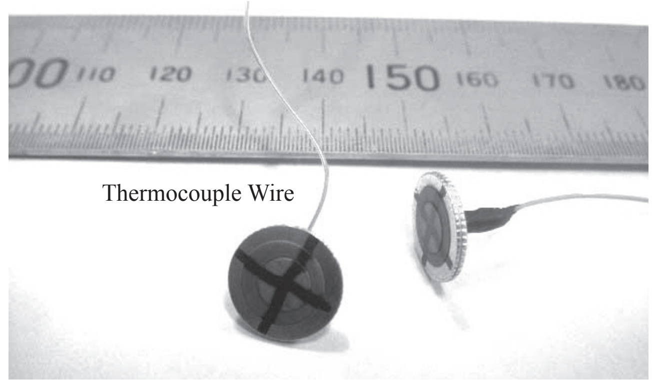

Figure 3. Marker with thin thermocouple.

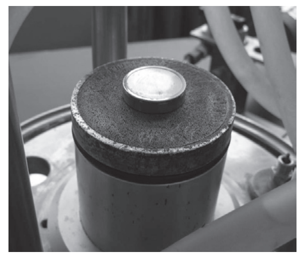

a) Total pressure gauge on the lower pedestal.

b) Cylindrical Plexiglas as soil container.

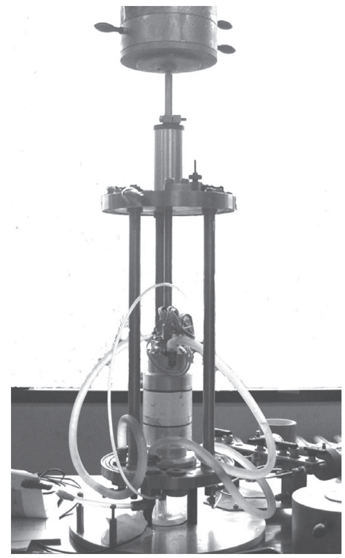

c) Pressure applied by dead weight through soil to total pressure gauge.

Figure 4. Total pressure gauge calibration.

in thickness, and the pore-water pressure gauge is 15 mm in diameter and 15 mm in thickness, as shown in Figure 2. The capacity of both types of transducers is 100 kPa.

Soil deformation was monitored with markers, which were placed between the front Plexiglas and test soil with a coating of grease to reduce the friction, as shown in Figure 3.

All the total pressure gauges were calibrated with the apparatus shown in Figure 4. One of the typical results obtained is shown in Figure 5. According to the calibration, the linearity of loading and unloading processes is considerably good, but it has hysteresis in loading and unloading.

Because the size of the experiment box was not large enough to utilize common thermocouples, the authors have used thin thermocouples, such as Omega TT-T-36, instead. Thin thermocouples, were attached to the pressure gauges and 20 of the markers as shown in Figures 2 and 3, in order to monitor the gauge and marker temperatures and to ensure the proper distance between the gauges and the cooling model pipe.

The temperature measurement method utilized in the experiment was traditional as shown in the Figure 6. However, the authors have confirmed the absolute accuracy of ± 0.02°C with this method by traceability.

The gauges and markers, with attached thermocouples, were placed in the model soil as shown in Figure 7.

In the vertical direction, five total pressure gauges were placed. Three of them were for vertical or radial total pressure, and the remaining two were for total pressure in horizontal or hoop direction. At about 12.5 mm below the model pipe, two total pressure gauges for radial and hoop direction and one pore-water pressure gauge were placed.

In the following sections, data obtained with these three groups of gauges are discussed.

Soil used and its preparation

Soil utilized in this experiment is commonly known as NSF clay with mineral composition of Pyrophyllite. This clay has relatively high frost heave susceptibility.

NSF clay powder was first mixed with distilled water with water content 1.5 times its liquid limit. It was then poured into the soil box in layers of 5 cm thick, and finally consolidated by dead weights with 10 kPa pressure. The front views of the

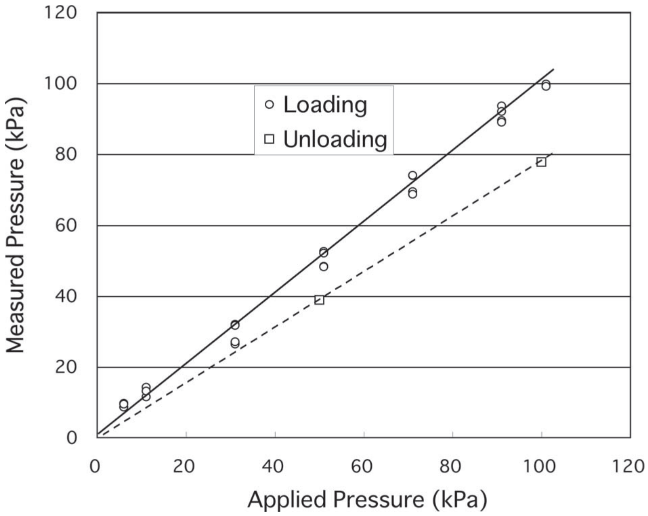

Figure 5. Typical calibration result of the total pressure gauge.

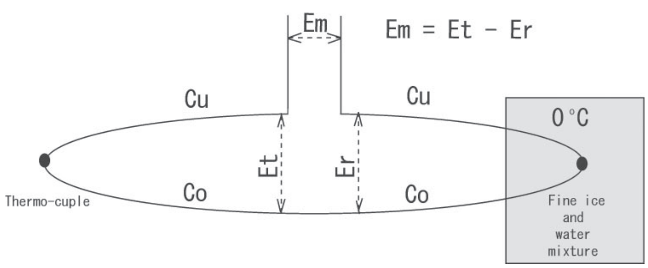

Figure 6. Thermocouple wiring.

soil box right after filling and at the end of consolidation are shown in Figure 8.

The consolidation behavior of NSF clay is shown in Figure 9. According to the e-log *P* relationship, the model soil made of NSF clay is normally consolidated and may cause a considerable amount of consolidation in frozen fringe when it freezes.

Thermal two-dimensionality

Prior to the main experiment the authors conducted a freezing test using agar instead of soil. Through this test we could verify the thermal dimensionality in 2D by checking the shape of the cylindrical frozen agar, which mimics growth of the "frost bulb" by a buried chilled gas pipeline in the arctic regions. As shown in Figure 10, the frost bulb is laterally symmetrical, and the lateral thermal two-dimensionality is presumed satisfied. In addition, the diameter of the frost bulb is almost the same in the middle and the rear end; the two-dimensionality in the pipe direction is considered satisfied for the rear half.

Test Results

Frost bulb growth

The frost bulb growth in elapsed time is shown in Figure 11. As time elapses, the diameter of the frost bulb is getting larger.

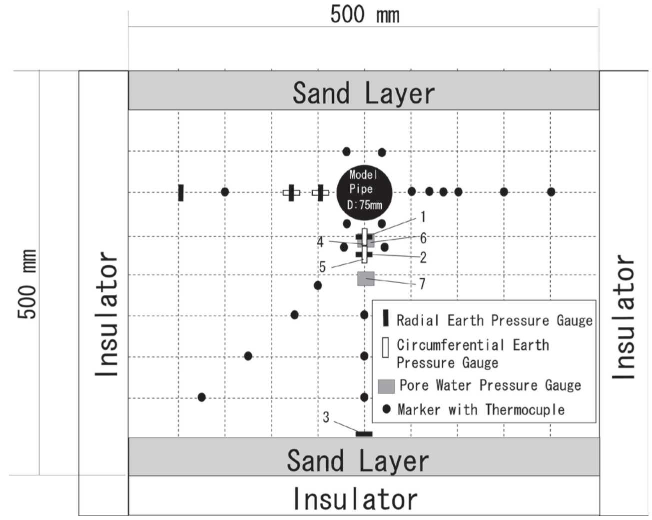

Figure 7. Locations of installed gauges and markers.

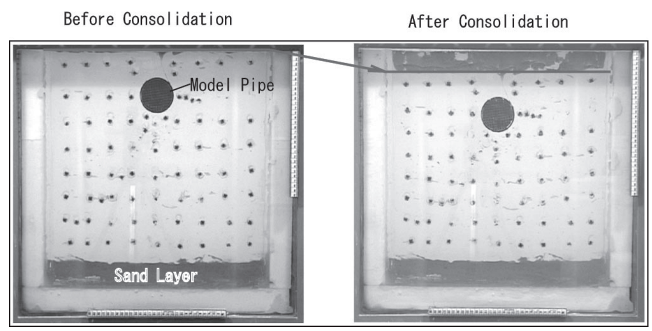

Figure 8. Initial and final condition of pre-consolidation at 10kPa pressure.

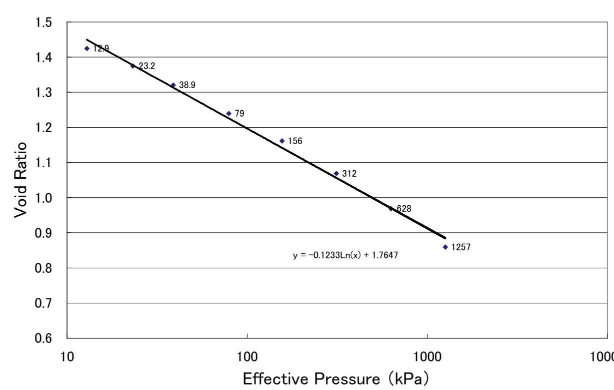

Figure 9. Consolidation behavior of saturated NSF model soil.

Upward movement of model pipe

Analyzing (x, y) coordinates of the markers, which were originally placed at the grid centers with 50 mm spacing on the front Plexiglas, 2D deformations of the model soil were recorded and are shown in Figure 12. As the frost bulb becomes larger, the model pipe is pushed up by 29 mm vertically, as shown in the figure. The movement of the markers during the experiment is also shown in the figure. Before the markers were enclosed by the growing frost bulb, they moved away along the direction of heat flow. However, as the markers were within the frost bulb, they moved upward with the model pipe.

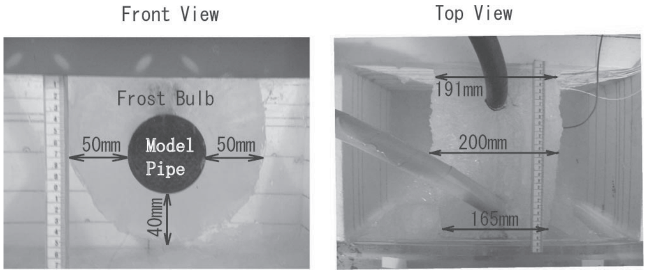

Figure 10. Frost bulb observed in preliminary experiment.

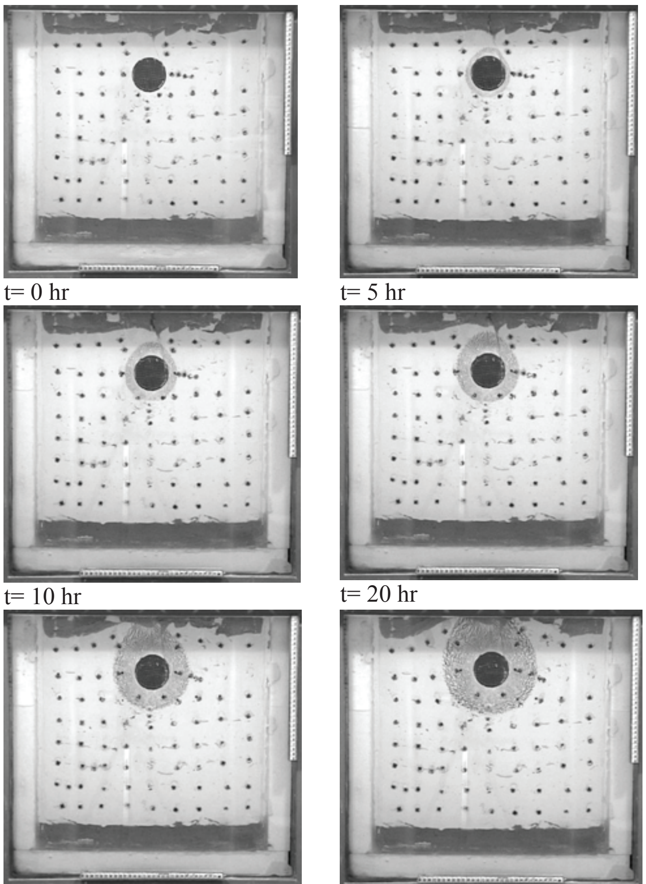

Figure 11. Frost bulb growth in elapsed time.

Monitored total and pore-water pressures

Three radial total pressures monitored with gauges Number 1–3, which were placed along the vertical pipe centerline are shown in Figure 13. The most adjacent gauge to the model pipe, Number 1, was captured by the frozen fringe at about 40 hours. This was recognized by its temperature shown in the figure. The frost bulb, however, did not enclose the other two gauges, Numbers 2 and 3, during the experiment. It is clearly shown in the figure that the radial total pressure rapidly increases when its temperature drops slightly below 0°C. It reaches a maximum pressure at about 60 hours, and then starts to decrease as the temperature approaches -0.2°C. Since this temperature range corresponds to that of a frozen fringe, the radial total pressure is presumed to have a sharp increase in frozen fringe and to decline in the much colder frozen portion in axial-symmetric freezing.

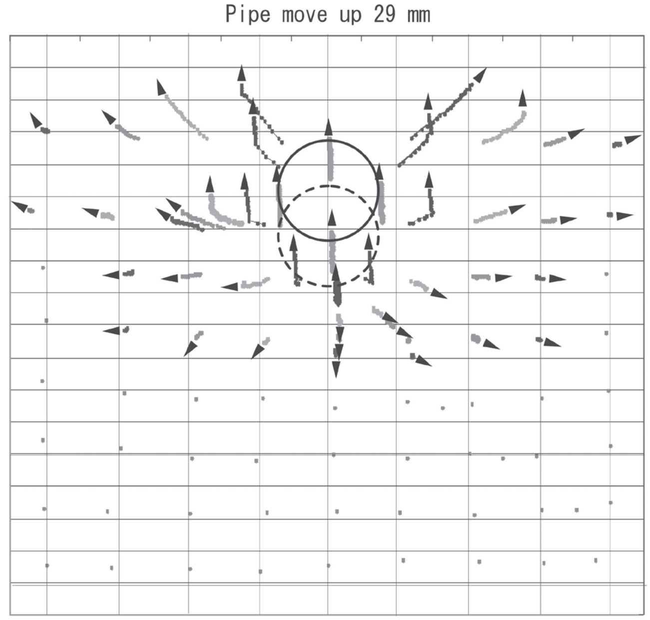

Figure 12. Model soil deformation with frost bulb growth.

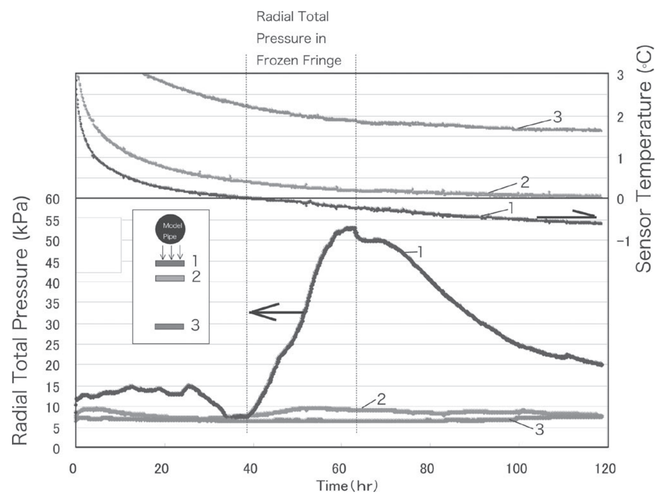

Figure 13. Radial total pressure below model pipe.

Two hoop total pressures, monitored with gauges Numbers 4 and 5, which were arrayed along the vertical pipe centerline, are shown in Figure 14. The frozen fringe captures the gauge next to the model pipe, Number 4, at about 40 hours. Similar to gauge Number 1, this is determined by its temperature at 0°C, as shown in the figure. Gauge Number 5 was not included in the frost bulb during the experiment.

A sharp increase of the hoop total pressure as its temperature dropped below 0°C was not seen in this case. However, a clear increase of the hoop total pressure was recorded after the gauge temperature fell below about -0.2°C, and it continued until the end of the experiment.

According to the data mentioned above, the hoop total pressure did not seem to change in the frozen fringe. Instead, it increased as the temperature dropped in the frozen soil.

Two pore-water pressures monitored with gauges Numbers 6 and 7, which also were placed along the vertical

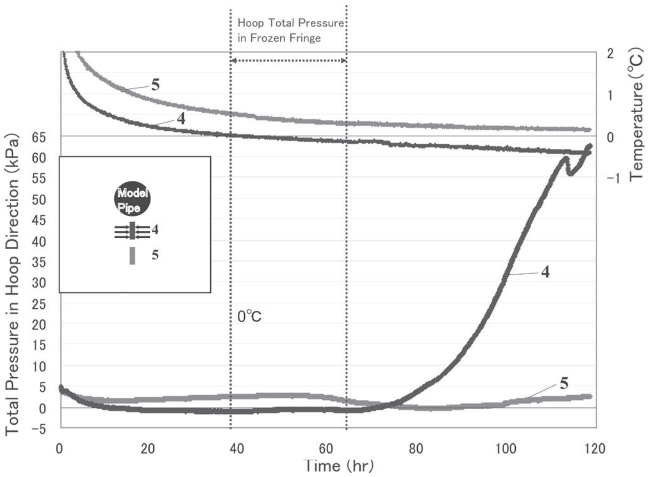

Figure 14. Hoop total pressure below model pipe.

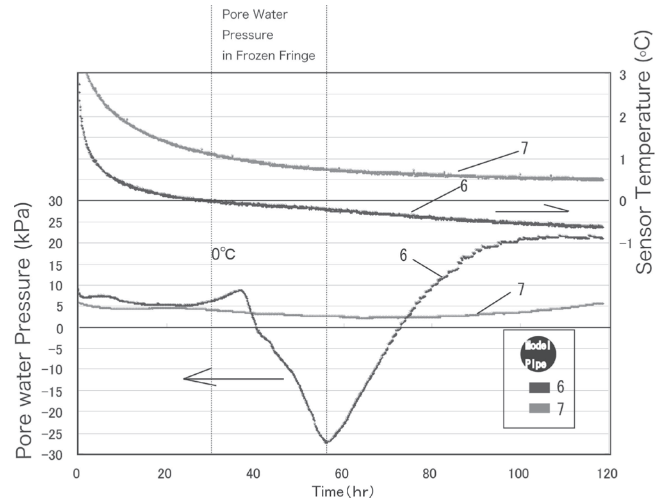

Figure 15. Pore-water pressure below model pipe.

pipe centerline, are shown in Figure 15. The most adjacent gauge to the model pipe, Number 6, was captured by the frozen fringe at about 40 hours. This is recognized by its temperature shown in the figure. Gauge Number 7 was not captured by the frost bulb during the experiment. It is clearly seen in the figure that the pore-water pressure, or unfrozen water pressure, in the frozen fringe sharply decreases when its temperature drops below 0°C and then starts to increase at about -0.2°C.

Discussion

Pore-water pressure in frozen fringe

As is clearly shown in Figure 15, the pore-water pressure depresses in a temperature range corresponding to that of the frozen fringe. Therefore, it infers that the unfrozen water pressure in the frozen fringe decreases as the local soil temperature becomes lower. During the period the unfrozen water pressure depression reached 35 kPa, temperature of the pressure gauge was lowered by about 0.12°C. This relationship between unfrozen water pressure and temperature seems not in good agreement with Generalized-Clausius-Clapeyron-Equation. However, if a certain amount of ice pressure is generated in the frozen fringe, it might likely agree with Generalized-Clausius-Clapeyron–Equation.

Effective pressure in the frozen fringe

The effective pressures in the radial and hoop directions calculated with the measured total soil and pore-water pressures are shown in Figure 16. As is clearly seen in the figure, the effective pressure in the frozen fringe increases as its temperature decreases. However, the magnitude of the effective pressure in the radial direction is about twice of that in the hoop direction.

Another noteworthy trend seen in the figure is that the effective pressure in the hoop direction after 90 hours, which corresponds to a well-frozen soil, continues to increase as time elapses and temperature becomes lower, whereas the effective pressure in the radial direction continues the decreasing trend.

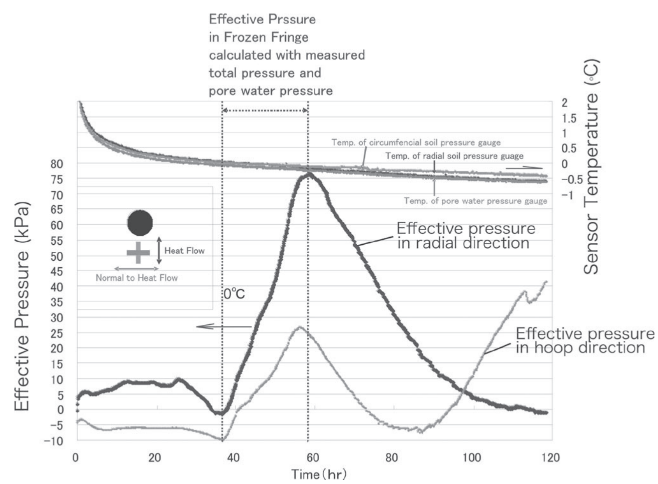

Figure 16. Effective pressures in radial and hoop directions in the frozen fringe.

Conclusions

Total pressure and pore-water pressure were directly measured in freezing soil during the 2D-model chilled gas pipeline experiments.

Because many features, such as frost bulb growth and upward movement of the model pipe, agreed well with the field experiment (Huang et al 2004), the observed pressures seem to be an indication of the real phenomena in freezing ground.

A significant finding from this experiment is that the pore-water pressure gauge has measured a clear pressure depression while it was in the frozen fringe. In addition, the effective pressures in the radial and hoop directions, which were calculated with the total pressure and pore-water pressure, showed steep increases in the frozen fringe.

The decrease of pore-water pressure was considered the driving force for ice lens formation, and the increase of the effective pressure was the driving force for consolidation in the frozen fringe.

References

Akagawa, S. 1988. Experimental study of frozen fringe characteristics. *Cold Regions Science and Technology* 15: 209-223.

Chamberlain, E.J. & Gow, A.J. 1978. Effect of freezing and thawing on the permeability and structure of soils. *Engineering Geology* 13: 73-92.

Gilpin, R.R. 1980. A model for the prediction of ice lensing and frost heave in soils. *Water Resources Research* 16(5): 918-930.

Huang S.L., Bray M.Y., Akagawa S. & Fukuda M. 2004. Field Investigation of Soil Heave by a Large Diameter Chilled Gas Pipeline Experiment, Fairbanks, Alaska. *J. Cold Regions Engineering* 18(1): 2-34.

Miller, R.D. 1978. Frost heaving in non-colloidal soils. *Proceedings of the Third International Conference on Permafrost, Edmonton*: 708-713.

Miyata Y. & Akagawa S. 1998. An experimental study of dynamic solid-liquid phase equilibrium in a porous medium. *JSME International Journal Series B* 41(3): 590-600.

Radd, F.J. & Oertle, D.H. 1973. Experimental pressure studies of frost heave mechanics and growth fusion behavior of ice. *Proceedings of the Second International Conference on Permafrost*: 377-384.

Taber, S. 1929. Frost heaving. *Journal of Geology* 37: 428-461.

Takagi, S. 1980. The adsorption force theory of frost heaving. *Cold Regions Science and Technology* 3: 57-81.

Coastal Processes and Their Influence Upon Discharge Characteristics of the Strokdammane Plain, West Spitsbergen, Svalbard

H. Jonas Akerman

Department of Physical Geography and Ecosystems Analysis, Lund University, Sweden

Abstract

Changes in Arctic sea ice conditions have affected conditions ashore along the west coast of Svalbard. Effects upon the discharge characteristics of a drainage basin close to the seashore are discussed. The area studied lies on the strandflat plain, south of Kapp Linné (78°04′N, 13°38′E). The anomalous discharge pattern of the Fyrsjöen Lake catchment area is described. Some years the outlet is blocked by ice-cemented storm ridges, delaying the spring peak flow several weeks and raising the lake level dramatically. Vast areas are flooded, affecting snowmelt, vegetation, and breeding birds of the area. The lake is then tapped during a few days with heavy flow, after which the discharge pattern returns to normal. This process is not unique, but rather common along the west coast of Spitsbergen. The special hydrographic and discharge conditions have an influence on the active layer, the permafrost, the vegetation, and the bird colonies of the area.

Keywords: arctic ecology; arctic sea ice; breeding birds; costal processes; polar hydrology; Svalbard.

Introduction

Sea ice is regarded as a key indicator and vital factor of climate change processes and has received much attention owing to the apparent reduction in coverage in the Arctic Sea (Parkinson et al. 1999, IPCC 2001, ACIA 2004). Since the potential impacts of these changes on climate, ecosystems, and lithosphere processes are great, sea ice is an important variable in any study of Arctic environmental change. The reduction in sea ice over the past several decades varies by region and season (Johannessen et al. 1995, 1999, Serreze et al. 2000, Serreze et al. 2003). The decrease in sea ice extent on the west coast of Svalbard is consistent with the general regional observations (Vinje 1976, 2001a, 2001b), and the periods with ice-free conditions have increased substantially. This has affected the hydrological and ecological environment of the Fyrsjöen catchment, which lies within an area where periglacial studies have been performed 1972–2004 (Åkerman 1980, 1992, 2005). Hydrological effects upon the active layer, river discharge, water balance, and the breeding birds also were monitored as a subproject.

A special focus has been directed toward changes in extreme runoff and floods that are likely to affect the depth of the active layer and the stability of the permafrost. This may lead to thermokarst processes and alter biological production and biodiversity within catchments near the coast. The status of ponds and wetlands, for which water levels are critical, determines whether these wetlands will become sources or sinks of CO_2 and CH_4.

Investigation Area

The investigation area is situated on the southern shore of the westernmost part of Isfjorden, central Spitsbergen (Fig. 1). The central west coast of Spitsbergen lies on the periphery of the extreme arctic zone. The moderating influence of the North Atlantic Ocean reduces temperature extremes and

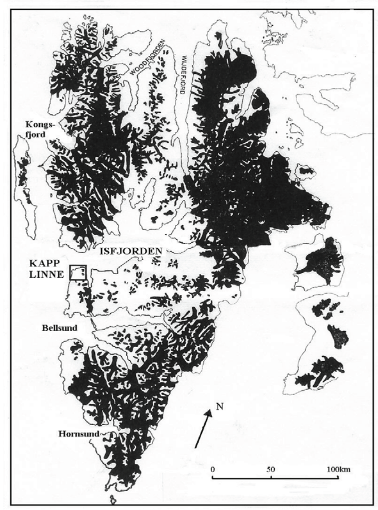

Figure 1. Svalbard and Spitsbergen with its glacial cover in black. The investigation area is indicated by a square

also brings more precipitation than is experienced at similar latitudes (Førland et al. 1997, Humlum 2002, Humlum et al. 2003).

The position on the border between maritime arctic and more continental arctic conditions explains the very great local climatic variations in Spitsbergen (Førland et al. 1997, Humlum et al. 2003). This is important for the interpretation of geomorphological and hydrological processes in an area with very few weather stations. The investigation area, however, offers the advantage of a permanent weather station situated not more than 6 km from the most distant monitoring site. The basic meteorological and climatological data have been obtained from this station.

The MAAT in the study area is -4.6°C, as measured at Isfjord Radio Station for the period 1935–1976 (Steffensen 1969, 1982, Førland et al. 1997 (Table 1). The estimated value for the normal period 1961–90 is -5.1°C (Førland et al 1997). The mean annual precipitation is 435 mm for the post-war period 1951–1975 (Steffensen 1982), and 443 mm during the full official record period (1935–1976), with a data gap during the war 1941–46. The estimated value for the normal period 1961–90 is 480 mm (Førland et al. 1997).

The official weather station was terminated in summer 1976, but an automatic station was established in 1996. After the termination of the official station in 1976, the author continued measurements of metrological and hydrological data within the study and catchment area. The records are covering the period up to 2003 with only minor gaps in the air temperature measurements. Unfortunately, there are long gaps in the measurements of precipitation. The annual course of air temperature and precipitation for Isfjord Radio are given as monthly means in Table 1 (c.f. also Akerman 1980, pp. 14-45, and Steffensen 1969, 1982, Førland et al 1997, Akerman 2005).

Objectives

The main objectives of this study are:

- To describe some of the hydrographical characteristics of the Fyrsjöen Lake catchment area.
- To give a simple description of the water balance of the catchment area.
- Describe how the blocking storm ridges are affecting the discharge pattern and the flooding of the catchment area.
- Illustrate how the flooding has affected the active layer in a small bog within the catchment.
- Investigate how the years of flooding have affected the breeding birds within the catchment.

Methods

Meteorological data have been obtained from the weather station at the nearby Kapp Linné station (Isfjord Radio). Additional precipitation data have been collected within the catchment during intensive study periods by the use of standard pluviometers and collectors. Winter precipitation and the effect of drifting snow (import to the catchment) have been studied through detailed snow surveys in late winters. The discharge in the outlet river needed different techniques during the violent peak flow and gentle normal flow. Water level has been measured with a fixed level gauge plus a recording level gauge put on the only rock outcrop along the short river. Propeller-type current meters applied in a simple traverse cableway have measured water speed during medium and peak flow. At lower flows, the water speed had to be measured with floats.

The highly variable cross-sectional area has been mapped every year or upon demand after “dam break flow” events (Pritchard & Hogg 2002). The dam break flow has here also been named “flush flow” in accordance with the terminology used for quick initial discharge in urban catchments. (Bertrand et al. 2002). Measurements started the first week of June and ended the first week of September. Hardly any flow was missed in May, but some years, flow in September has been missed.

Table 1. Official monthly and annual air temperature (°C) and precipitation (mm) (1935–1975) for Isfjord Radio. Data from Norsk Meteorlogisk Institutt, Oslo, Norway (Steffensen 1982).

Month	Temp °C	Precipitation (mm)
Jan	-10.7	37
Feb	-11.5	34
March	-12.2	34
April	-9.3	24
May	-3.3	25
June	+1.7	28
July	+4.7	38
August	+4.3	53
September	+1.1	47
October	-3.2	44
November	-6.8	40
December	-8.9	39
Annual	-4.6	443

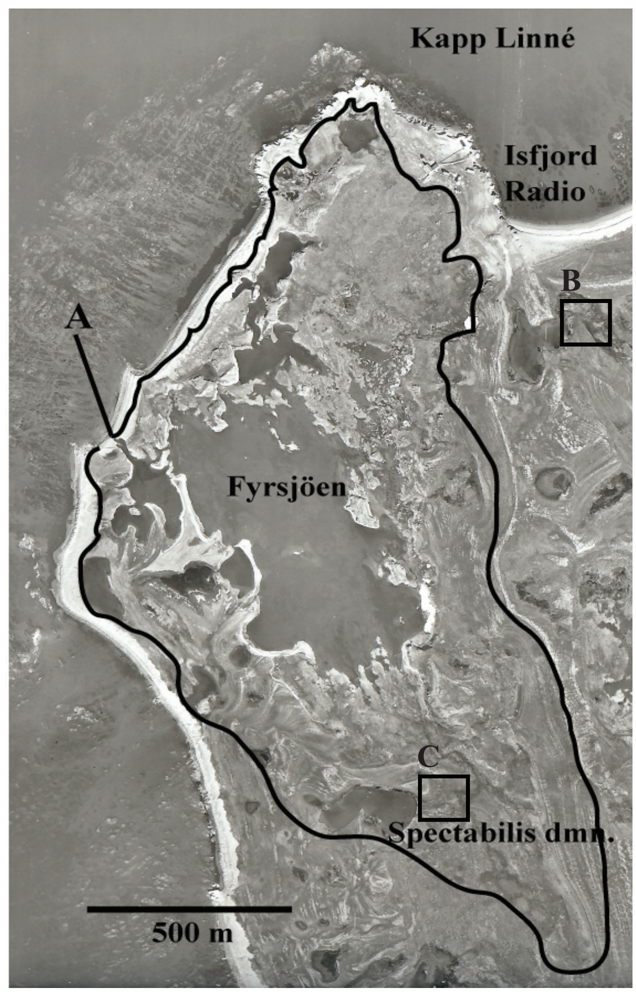

Figure 2. The Fyrsjöen catchment area. *A* indicates the short outlet river through the storm ridges; *B* shows the IPA active layer monitoring site AL3; and *C* is the active layer monitoring site next to the ”Spectabilis” pond. (Aerial photograph; Norwegian Polar Institute, No. S69 2431, August 19, 1969.)

The active layer measurements followed the IPA methodology, but here only within a 20 x 40 m area (Brown et al. 2000). Readings were taken the last week of August. The nearest IPA standard site is 1.5 km away.

The breeding success and failure is based upon a nest inventory within the catchment prior to flooding events. This inventory has only been performed along the easily accessible bogs and shores and not upon the islands of the Fyrsjöen Lake. The post-flooding inventory was based upon the position of nests plotted on the 1:7000 topographical map in relation to the maximum water level (Akerman 1980). This makes the result of this part of the investigation relative only, but for the species studied it makes only a minor difference to the result.

Observations

Discharge and water balance

The annual course of flow in the catchment follows a characteristic pattern. In a normal year, the flow in June starts gradually along with the onset of the snowmelt. The catchment has no connection with higher levels (the water divide is 12–14 m. a. s. l.), nor has it connection with any glacier. The June part of the annual discharge is, as a mean, 16.1% (Figs. 3, 4), while July has 64.6%, August 19.2%, and September, only 0.01%. During flooding years, the dam breaks through, and flow normally does not start until July, giving July 77.7%, August 21.9%, and September 0.4% of the annual discharge. The low amounts in September are mainly explained by the fact that the catchment receives no contribution from meltwater from a glacier (cf. Killingtveit et al. 2003). The September precipitation and the active layer discharge flow are quantitatively of little importance. Typical daily discharge graphs are shown in Figure 5.

Despite some clear shortcomings in the measurements and gaps in the background meteorological data, an attempt to illustrate the water balance of the catchment has been performed. A common formula of the common water balance equation can be:

$$P - Q_{river} - Q_{ground} - ET \pm \Delta S = \epsilon \qquad (1)$$

where P is precipitation, Q_{river} is the river discharge, Q_{ground} is the groundwater discharge, ET is the evapotranspiration, ΔS is the storage changes, and ϵ is the error, all expressed in mm water. The error should end up close to 0 if all variables are measured correctly.

In this case the groundwater discharge can be ignored as we, as far as known, have permafrost in the entire catchment. There might be some uncertainties as we are close to the sea and the Lake itself might have some groundwater leakages. There is also a small karst sinkhole within the catchment, but this is, as far as can be judged, of minor quantitative importance.

Regarding evapotranspiration, the figure 80 mm/yr, used by Killingtveit et al. (2003), has been adopted. The storage component S is considered to be constant, as the water level in the lake at the end of the drainage season is down to a

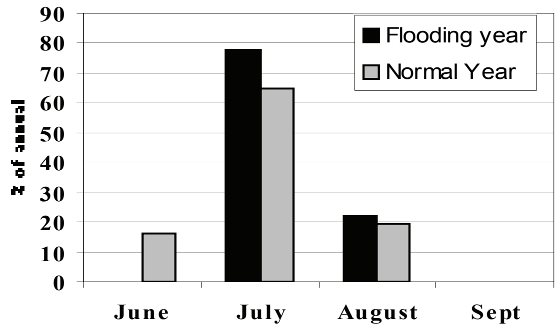

Figure 3. Runoff in the Fyrsjöen Lake catchment per month in % of the total 1974–2001. Note that September might be too low, as measurements some years could not be continued into this month.

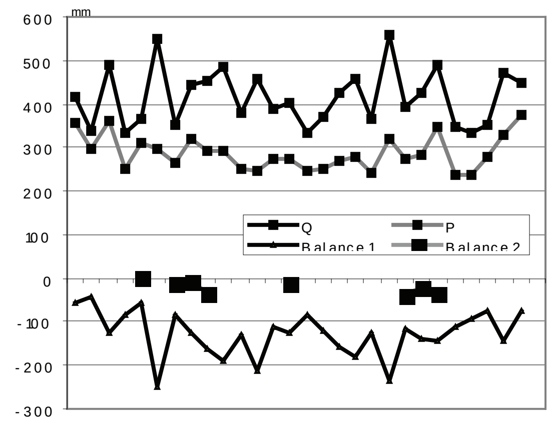

Figure 4. Runoff, precipitation, and hydrological balance for the Fyrsjöen Lake catchment area during the hydrological years (Sept–Aug) 1973/74 to 1999/2000. Q = discharge, P = precipitation-ET, water balance 1 = P–Q, and balance 2 = corrected water balance (considering the snow drift import) in mm during the hydrological years (Sept–Aug) 1974/75 to 1999/2000.

constant level with only marginal variations from year to year. Considering the annual budget, other storage components in this catchment are also of minor importance.

The discharge characteristic of the Fyrsjöen Lake catchment is shown in Figures 4 and 5 and Table 2, in which simple water balance figures are given also. The balance for each and every hydrological year is found negative—on an average -127 mm. The reasons for this lies partly in the precipitation or discharge figures, which may have some errors built in. But there is one factor not considered which became evident during the snow cover surveys within the catchment. Snow cover surveys have been performed in late winter during 8 different years.

The results are given in Figure 4 and Table 2. We find that the catchments contain on an average 100 mm more water equivalents than the winter precipitation measured indicates. The reason for this is the large amount of drifting snow that is accumulated in drifts mainly along the eastern “slopes” of the basin. The shallow basin gets a “precipitation import” through snowdrift mainly from the prevailing easterly winter winds.

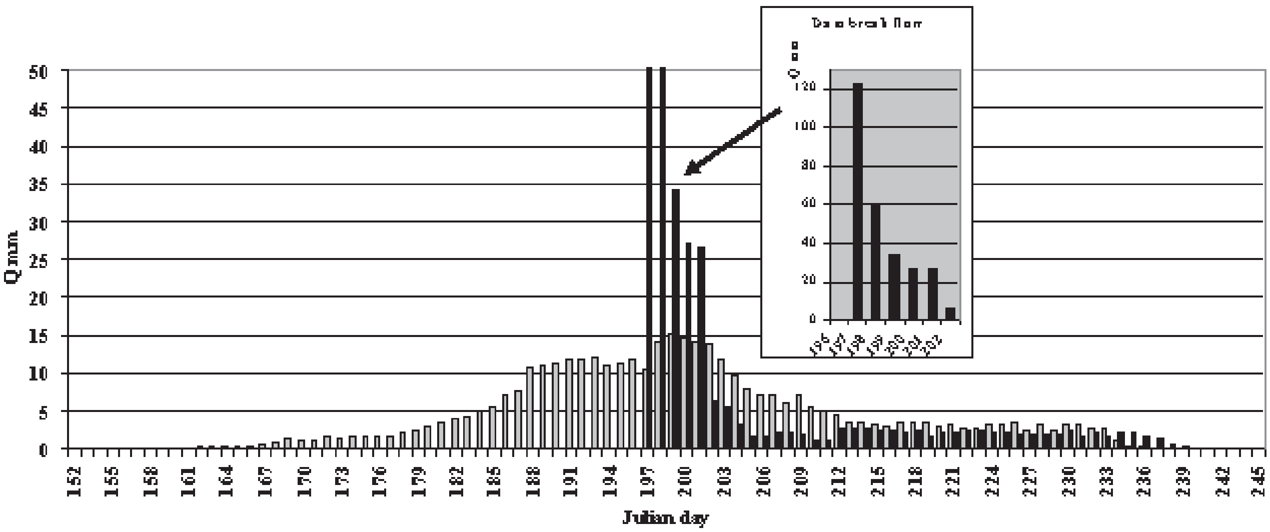

Figure 5. Daily discharge in the Fyrsjöen Lake outlet channel during a "normal" year—in this case 1995 (grey bars)—and a "flooding" year—in this case 1994 (black bars). A "flooding year "is a year with less sea ice and hence unprotected shores along which high blocking storm ridges are formed. Note that the discharge scale for the dam break flow days is different, with up to 120 mm the first day of the "flush."

Storm ridges

The storm ridges that are the cause of the blocked and delayed drainage of Fyrsjöen Lake are built up by the autumn and winter storms. These types of ridges have been observed in the mapping of the Svalbard coasts (Etzelmüller et al. 2003) and are by no means unique. In the coastal geomorphological mapping of Svalbard, they are classified as barriers (Ødegård et al. 1987, Høgvard & Sollid 1988). What is notable is that they now are formed almost every winter as a result of less sea ice along the coast (Fig. 6). Despite that this is indirect observation, they correspond well with the regional sea ice dynamics observed and monitored through RS (e.g., Vinje 1976, 2001, Shapiro et al. 2003).

The barriers vary in height according to the site, but in general they reach between 4 and 6 m above mean seawater level. They are built by coarse beach gravel, sand, and cobbles, typically with a large amount of seaweeds (kelp) mixed in and/or as a cover. In the frozen state, the ridges are like a concrete wall very resistant to melting. During melting, thermokarst features like collapsed thermokarst dolines appear in the surface, and some piping with a low amount of seepage may also occur. This seepage has not been measured, but is of minor importance.

Active layer

The active layer measured in the small bog next to the "Spectabilis dammen" pond follows the same general pattern as the active layer in the IPA bog site some 1.5 km to the north. The small "Spectabilis dammen" bog belongs to one of the bogs and other areas within the catchment that are flooded for years with a blocking storm ridge. The active layer during the investigation period is shown in Figure 7. The two bogs, which apart from size are as similar as can be, show the same general pattern regarding the active layer; that is, a gradual shallower active layer during the period 1972 to the mid-1980s, followed by an equally clear trend of increasing active layer depths. This pattern goes in perfect correspondence with the summer temperature DDT (degree days thaw) that is included in the figure.

However, if we separate the "normal years" and the "flooding years," we find that the "Spectabilis" bog has a deeper active layer (on an average 7 cm deeper) during a flooding year. This clearly indicates the importance of flooding also for the processes in the active layer and the top of the permafrost.

Table 2. Corrected hydrological balance for the Fyrsjöen Lake catchment area based upon snow surveys.

Hy.year	Vinter P mm	Balance mm	Snow in mm	Diff. mm	Corr. Balance
1977/78	267	-55	326	59	4
1979/80	292	-86	368	76	-10
1980/81	261	-123	378	117	-6
1981/82	304	-161	429	125	-36
1986/87	278	-125	391	113	-12
1993/94	298	-119	379	81	-38
1994/95	282	-141	402	120	-21
1995/96	287	-142	397	110	-32

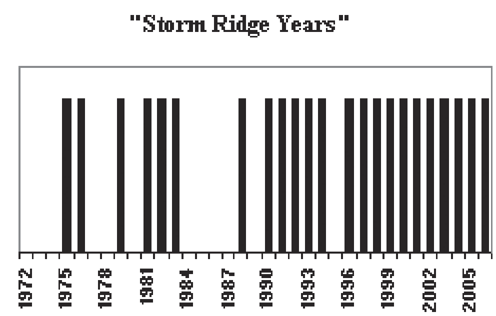

Figure 6. Years with and without larger storm ridges blocking the outlet river from the Fyrsjöen Lake catchment.

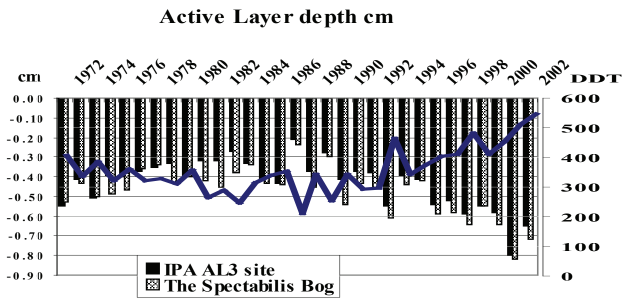

Figure 7. The active layer and the summer climate expressed in DDT (degree days thaw) 1972 to 2002 in the IPA monitoring site AL3 and in the "Spectabilis Bog."

Table 3. Breeding failure during a flooding year (1994) for seven regular breeding species within the Fyrsjöen catchment area.

Species	Nests/Failure	%
Stercorarius parasiticus	1/1	100
Sterna paradisea	26/5	21
Phalaropus fulicarius	6/3	50
Calidris maritima	3/2	66
Somateria molissima	26/5	21
Somateria spectabilis	10/4	40
Gavia stellata	2/2	100

Breeding birds

The breeding birds of the catchment area that have been monitored are shown in Table 3. We find that the Red-throated Diver (*G. stellata*) and the Arctic Skua (*S. parasiticus*) are the species strongest influenced in this case; but the Grey Phalarope (*P. fulicarius*), the less common King Eider (*S. spectabilis*), and the Purple Sandpiper (*C. maritima*) may also locally suffer a loss of 40 to 60% due to the flooding here.

This is, of course, only a very marginal loss considering the total population of these species along the coasts of Svalbard, but considering that this scenario is a trend that prevails, it might be of importance (Fig. 8).

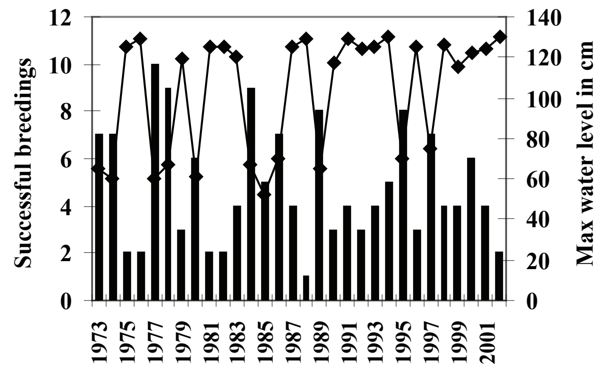

Figure 8. Successfully breeding pairs of King Eider in the Fyrsjöen catchment (bars) compared with the annual maximum water level above mean in cm.

Table 4. Line of observed related "events" from the global scale down to the species level.

A changing climate – a warmer Arctic
Less sea ice
Unprotected shores during winter storms
High ice-cemented storm ridges
Blocked river outlets
Blocked/delayed spring discharges
Anomalous drainage pattern
Flooding of floodplains, lakes, and bogs
Deepening of active layers
Changes in greenhouse gas exchanges
Disturbed plant communities
Breeding failures with birds

Discussion

Changes in the duration of the open-water season will be critical to the future impacts of coastal and near-coastal processes and environments in the Arctic. An increasing storm frequency and sea level rise are the most well-known possible consequences of climate change, and the fate of sea ice may be equally or more important to natural and human coastal systems (Kerr 2002).

The stability of any coast is a function of the interaction between meteorological and oceanographic forces and the physical properties of coastal materials. The interaction between the atmosphere and the ocean that produces waves and storm surges is mediated by the presence and concentration of sea ice, while coastal materials are either strengthened or destabilized by the presence of permafrost, the abundance of ground ice, and associated temperature regimes (Are 1988; Kobayashi et al., 1999).

Coastal wetlands are likely to move farther inland, and coastal flood events will increase. Salinity might increase in coastal marine ecosystems that are now freshened by terrestrial water discharge. If storm surges and coastal flood events increase in frequency and/or intensity, ecosystems in the affected areas are likely to be affected adversely.

This study, which may be summarized in Table 4, is an example of some of these problems.

Acknowledgments

Financial support was received from the Swedish Natural Sciences Research Council (NFR G.GU 3445 106-117), the Royal Physiographic Society in Lund and The Swedish Society for Anthropology and Geography.

References

ACIA. 2004. *Impacts of a Warming Arctic – Arctic Climate Impact Assessment*. Cambridge, UK: Cambridge University Press.

Akerman, H.J. 1980. *Studies on Periglacial Geomorphology in West Spitsbergen*. PhD thesis. Lunds Univ. Geografiska Inst. Ser. Avh. LXXXIX, 297 pp.

Akerman, H.J. 1992. Hydrographic characteristics of the Strokdammane Plain, West Spitsbergen, Svalbard. *Geografiska Annaler* (74A):2-3: 169-182.

Akerman, H.J. 2005. Slow slope processes and active layer 1972-2002, Kapp Linné, Svalbard. *Nor. Geogr. J.* 59: 116-128. Oslo. ISSN 0029-1951.

Are, F.A. 1988. Thermal abrasion of sea coasts (parts I & II) *Polar Geography and Geology* 12: 1-57.

Bertrand, J.L., Chebbo, G. & Saget, A. 1998. Distribution of pollutant mass vs volume in storm water discharge and the first flush. *Water Res.* 32: 2341-2356.

Brown, J., Hinkel, K.N. & Nelsson, P.E. 2000. The circumpolar active layer monitoring (CALM) programme: research design and initial results. *Polar Geography and Geology* 24: 165-258.

Etzelmüller, B., ØÅrd R.S. & Sollid, J.L. 2003. The spatial distribution of coast types on Svalbard. In: V. Rachold et al. (eds.), *Arctic Coastal Dynamics Report of the Third International Workshop, University of Oslo, Norway, 2–5 December 2002*. Bremerhaven: Alfred Wegener Institute for Polar and Marine Research.

Førland, E.J., Hanssen-Bauer, I. & Nordli, P.Ø. 1997. Climate statistics and long-term series of temperature and precipitation at Svalbard and Jan Mayen. *Klima* 21/97. Oslo: Norwegian Meteorological Institute.

IPCC. 2001. *Climate Change 2001: Synthesis Report. A Contribution of Working Groups I, II, and III to the Third Assessment Report of the IPCC.* Cambridge, UK, and New York, USA: Cambridge University Press, 398 pp.

Høgvard, K. & Sollid J.L. 1988. *Coastal map Svalbard B4 Bellsund,* 1:200,000. Department of Physical Geography, University of Oslo, Norway.

Humlum, O., Instanes, A. & Sollid, J.L. 2002. Modeling late 20th century precipitation in Nordenskiöld Land, Central Spitsbergen, Svalbard by geomorphological means. *Nor. Geogr. J.* 56: 96-103.

Humlum, O. et al. 2003. Permafrost in Svalbard: A review of research history, climatic background, and engineering challenges. *Polar Research* 22(2): 191-215.

Kerr, R. 2002. A warmer Arctic means change for all. *Science* 297: 1490-1492.

Kobayashi, N.J., Vidrine, C., Narin, R.B. & Solomon, S.M. 1999. Erosion of frozen cliffs due to storm surge on the Beaufort Sea Coast. *J. of Coastal Research* 15: 332-344.

Ødegard, R., Sollid, J.L. & Trollvik, J.A. 1987. *Coastal map Svalbard A3 Forlandssundet* 1:200,000. Department of Physical Geography, University of Oslo, Norway.

Parkinson, C.L., Cavalieri, D.J., Gloersen, P., Zwally, H.J. & Comiso, J.C. 1999: Arctic sea ice extents, areas, and trends, 1978-1996. *J. Geophys. Res*. 104: 20837-20856.

Johannessen, O.M., Miles, M. & Bj¢rgo, E. 1995. The Arctic's shrinking sea ice. *Nature* 376: 126-127.

Johannessen, O.M., Shalina, E. & Miles, M.W. 1999. Satellite evidence for an Arctic sea ice cover in transformation. *Science* 286: 1937-1939.

Killingtveit, Å., Pettersson, L.E. & Sand, K. 2003. Water balance investigations in Svalbard. *Polar Research* 22(2): 161-174.

Prichard, D. & Hogg, A.J. 2002. On sediment transport under dam-break flow. *J. Fluid Mech*. 4783: 265-274.

Serreze, M.C., Walsh, J.E., Chapin III, F.S., Osterkamp, T., Dyurgerov, M., Romanovsky, V., Oechel, W.C., Morison, J., Zbang, T. & Barry, R.G. 2000. Observational evidence of recent change in the northern high-latitude environment. *Climatic Change* 46(1-2): 159-207.

Serreze, M.C., Maslanik, J.A., Scambos, T.A., Fetterer, F., Stroeve, J., Knowles, K., Fowler, C., Drobot, S., Barry, R.G. & Haran, T.M. 2003. A record minimum arctic sea ice extent and area in 2002. *Geophysical Res. Letters* 30(3): 1110, doi:10.1029/2002GL016406, 2003.

Shapiro, I., Colony, R. & Vinje, T. 2003. April sea ice extent in the Barents Sea, 1850-2001. *Polar Research* 22(1): 5-10.

Steffensen, E. 1969. The climate and its recent variations at the Norwegian Arctic stations. *Metorol. Annaler* 5(8).

Steffensen, E. 1982. The climate at the Norwegian Arctic stations. *Klima* 5: 1-44.

Vinje, T. 1976: Sea ice conditions in the European sector of the marginal seas of the Arctic, 1966-1975. *Norsk Polarinst. Arbok* 1975, Norwegian Polar Institute: 163-174.

Vinje, T. 2001a Anomalies and trends of sea-ice extent and atmospheric circulation in the Nordic Seas during the period 1864-1998, *Journal of Climate* 14(3): 255-267.

Vinje, T. 2001b: Anomalies and trends of sea-ice extent and atmospheric circulation in the Nordic seas during the period 1864-1998. *Journal of Climate* 14: 255-266.

Forecasting Chemical Thawing of Frozen Soil as a Result of Interaction with Cryopegs

V.I. Aksenov
FSUE Fundamentproect, Moscow, Russia
N.G. Bubnov
Limited company Neivo, St.Peterburg, Russia
G.I. Klinova
FSUE Fundamentproect, Moscow, Russia
A.V. Iospa
FSUE Fundamentproect, Moscow, Russia
S.G. Gevorkyan
FSUE Fundamentproect, Moscow, Russia

Abstract

This paper suggests methods of forecasting chemical thawing of frozen soils interacting with cryopegs. We have performed experiments on chemical thawing of frozen soils at negative temperatures and have conducted theoretical research on the interaction between cryopegs and frozen soils. The results of our study are as follows: (1) Peculiarities of cryopeg occurrences across the Yamal Peninsula have been discovered; (2) Five types of cryopeg occurring throughout the Yamal Peninsula have been discovered, and cryopeg classification has been elaborated; (3) Basic patterns of chemical thawing of frozen soils have been identified; thus, experiments have shown the migration of unfrozen water and salt ions from the brine (mineralized water) to the frozen soil; (4) Three models of the most typical cryopeg occurrences across the Yamal Peninsula have been designed, and can be used for engineering purposes; and (5) New methods of forecasting the process of chemical thawing of frozen soils interacting with cryopegs have been suggested and are based on the empiric calculation formula (7) given in this paper.

Keywords: chemical thaw; cryopeg; frozen soil;, highly mineralized groundwater; pile; saline permafrost; saline soil; salt migration; thaw settlement.

Introduction

Yamal Peninsula (Western Siberia, Russia) (Fig.1) is one of the most promising Russian regions currently under intensive development. Primarily this involves exploration of a number of large oil and gas fields.

Modern marine and alluvial-marine deposits in the Pleistocene marine terraces and the deep Pre-Quaternary deposits scattered across Yamal Peninsula are rich in cryopegs.

Cryopegs are highly mineralized (saline) groundwater existing at temperatures below 0°C. Their temperature ranges from -12°C to almost 0°C. A change of temperature entails a change in the degree of cryopeg mineralization, which typically varies from 10 to 150 g/l (promille), but sometimes may be as high as 200 g/l.

Cryopegs pose a significant threat to pile foundations built in the permafrost region. Local thawing of soil adjacent to a brine lens may trigger further thawing of the soil along a pile trestle or a borehole. Such thawing is of chemical nature and occurs at temperatures below 0°C.

This paper deals with the interaction between natural brines (cryopegs) and frozen soil under continental conditions. These are characterized by lower temperatures compared to the subaqueous frost, as well as by certain peculiarities of the structure and composition of the rock mass. This difference can have a considerable effect on the interaction between the brines and the frost.

Cryopeg Distribution and Conditions for their Formation

In practice, civil engineers most commonly have to deal with "near-surface" cryopegs located at shallow depths. Such cryopegs are widely spread on laida (littoral marshy area flooded during the incoming tide and dry during tidal fall) and in the low reaches of rivers exposed to tide and surge, as well as at marine terraces formed by saline soils. However, they rarely occur at temperatures below -4ºC.

The laida and flood plain cryopegs were formed mainly as a result of decrease of temperature and freezing of enclosing deposits. They are located in areas adjacent to river flood plains, on sand spits, and in the rear part of flood plains. On laida the soil strata may be composed of just cooled soil containing cryopegs, of soil freezing only from the surface, or in form of soil frozen throughout the investigation depth interbedded by cooled soil lenses containing cryopegs.

The laida cryopegs feature the highest degree of salinity (up to 150 g/l) and, as a rule, low (up 10 m) water heads (Fig.1).

The flood plain cryopegs are characterized by a lower

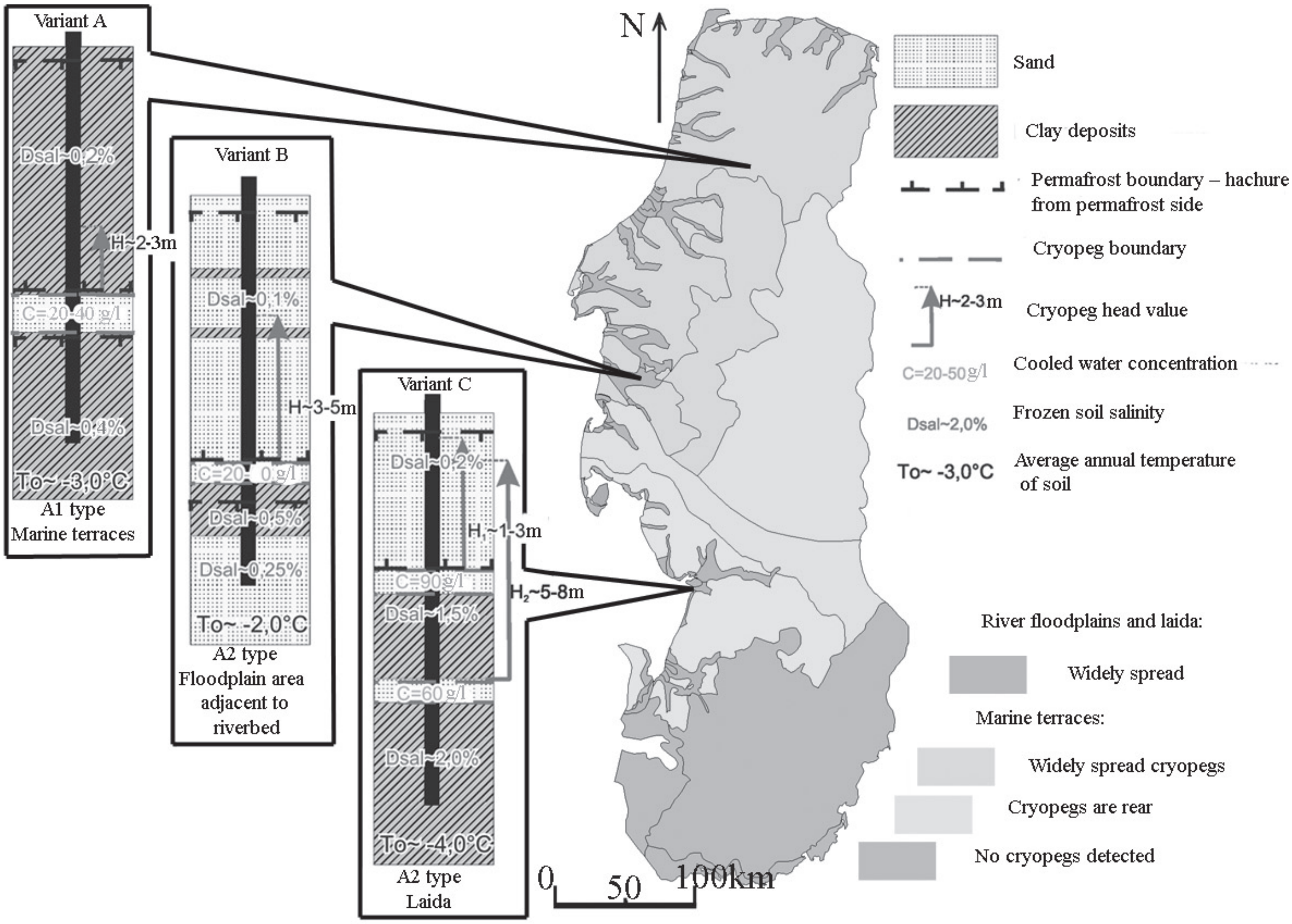

Figure 1. Distribution of cryopegs at Yamal Peninsula.

degree of mineralization (as a rule within 40–70 g/l), but slightly higher water heads. An upper layer of non-saline frozen soil 4–8 m thick is clearly distinguishable in the flood plain deposit profile. In laida this layer is of discontinuous nature and is thinner (2–6 m).

The marine terrace cryopegs occur in the form of relatively thin lenses at various depths and are confined to certain areas featured by enhanced salinity. Within these areas they are confined to local zones with temperatures higher than the background temperature. They are striped on the gently sloping hills, in depressions, on hasyrey (the bottoms of modern and ancient drained lakes), and in areas covered by shrub.

Over the last 40 years a number of researchers have studied cryopegs. As a result of their efforts several systems for classifying cryopegs according to their formation and distribution patterns were proposed and published. The most detailed classifications were proposed by N.V. Ivanova (Ivanova et al. 1992) and one suggested by I.D. Streletskaya (1991). In this paper we take the Streletskaya classification as the basis for our research, but we have modified it slightly to be consistent to the purposes of this study.

This classification is based on the conditions of cryopeg formation. All cryopegs are divided into groups, types, and sub-types (Table 1).

The groups are identified depending on cryopeg position in cryogenic strata (areas of active and passive cryodiagenesis). The cryopeg types are distinguished based on a set of genetic specificities, where the main attribute is the dynamic (period) of change of the cryogenic strata temperature. The sub-types are also identified based on the set of genetic specificities, but the main attribute is the trend (increase or decrease) of the cryogenic strata temperature.

The lenses are up to several meters thick and stretch for 100–300 m. They are featured by hydrostatic and cryogenic heads (10–36 m). The degree of cryopeg salinity is 5–35 g/l; water chemical composition is dominated by sodium chloride. The enclosing ground is represented by various types of sandy-clayey soils (D_{sal} = 0.1-1.0%). The salinity of cryopegs at all levels is 50–80 g/l, and their chemical composition is dominated by sodium chloride.

Cryopeg Impact on Ground Base

Cryopegs occur along the arctic sea coast at depths ranging from several meters to several hundred meters.

Two main factors are decisive in terms of modern distribution of frozen soils and cryopegs with marine-type salinity. The first factor involves sea water percolation through permafrost with the follow-on freezing. The second factor has to do with physical and chemical changes and desalination of the upper layer of permafrost during local warming. The frozen soil thawing and freezing processes are accompanied by salt differentiation between the liquid and solid phases as well as by change of the interstitial solution's concentration. As the interstitial water freezes, a small portion of salt dissolved in it is captured by ice crystals while another portion precipitates and the third portion is squeezed out into the underlying ground. All this enhances mineralization of the residual solution, which, in its turn, facilitates the formation of cryopegs.

In terms of chemical composition, the arctic coast cryopegs are similar to the sea water composition. They have marine-type salinity with the following ion concentration ratio:

$$Cl > SO_4 > HCO_3 ;$$
$$Na > Mg > Ca.$$

The volume of cryopeg lenses in permafrost varies and depends on conditions under which such lenses are formed. Volume of the brine containing lenses formed in tectonic fractures may be large enough. Small lenses containing non-freezing brine solutions may be formed as a result of sea water percolation through the soft ground. The mechanism of their occurrence is as follows. When soil freezes due to the squeezing of salt out from the phase boundary, an area with low freezing temperature is formed near such a boundary. If the rate of salt diffusion is lower than that of freezing, the conditions favorable for normal crystallization occur below the enhanced salt concentration area. This triggers formation of a new ice sub-layer. Such overcooling of the brine solution caused by enhancement of salt concentration during soil freezing is one of the conditions for formation of a striped structure of frozen soil. In a situation where the brine solution remains unfrozen and the frozen soil enclosing a lens does not thaw, the cryopeg temperature should be the same as that of the enclosing frozen soil. But if the brine solution temperature differs from that of the frozen soil, their contact, depending on the external conditions, should result either in further overcooling of the brine solution with the follow-on freezing, or in thawing of the frozen soil (Gorelik & Kolunin 2002, Grigoryan et al. 1987).

Until now the processes of interaction between frozen soil and saline solutions were under researched. For a long time it was supposed that frozen soils were impenetrable to both water and brine solutions. But in recent years new information has been obtained on the development of the physical-chemical and the mass exchange processes occurring in frozen soils as a result of interaction with the saline solutions (Gorelik & Kolunin 2002, Grigoryan et al. 1987). Recently it was discovered that unfrozen moisture and salt ions migrate from a brine solution into a frozen soil. And here several mechanisms of ion migration are operating: diffusion, convection, and adsorption.

Depending on values and ratio of moisture potential gradient to that of ion concentration, moisture and salt migrate to and from the frozen soil. When brine solution concentration reaches the critical value, the dynamic equilibrium occurs, which leads to termination of the mass exchange process. These critical values of concentration depend on texture, mineral, and chemical composition of the frozen soils, as well as on their temperature. In case of sands interacting with the sodium chloride solution, such critical concentration is not less than 0.1 gram·mol per liter, and for clays it is equal to 5 gram·mol per liter.

The research results show that water and salt migration flows change with time. At the initial stage salt ions migrate and an insignificant amount of moisture is being transferred. Salt ions invading the frozen soil interact with soil mineral particles and with molecules of attached water and ice. Cations interact with the negatively charged surface of mineral particles, while anions interact with the positively charged surface of interstitial ice. In the beginning of the salt transfer process, intensity of anions migration in frozen soil is higher than that of cations. But later on, intensities of migration of anions and cations become almost the same.

Capacity of frozen soil to selectively transfer or hold certain types of ions plays an important role in the salt transport process. Such capacity of frozen soil depends on valence and mass of migrating ions, their hydratability, as well as on a structure of frozen soil pore space. And the structure of pore space of frozen soil, in its turn, depends on temperature and cryogenic morphology of frozen soil.

Mass transfer in frozen soils is possible only if there is a system of continuous water films oriented in the direction of the migration forces. Formation of segregated ice or ice-cement bands results in discontinuity of the active part of pore space participating in the mass transfer processes. This in its turn entails decrease of migration flow rate. This is why structure of pore space plays an important role in the migration processes.

If initial temperatures of soil and brine solution are the same, the phase changes associated with dissolution of interstitial ice contained in frozen soil occur at the interface of soil and brine solution. As a result the temperature of frozen soil will decrease.

In non-saline soils at temperatures below freezing point the relationship between unfrozen water W_w and temperature T is definitely described by the "unfrozen moisture curve." But in the case of saline soils the amount of unfrozen moisture (W_w) depends not just on temperature but also on concentration of interstitial solution. During the phase change process, concentration of interstitial solution changes according to the following formula:

$$C = \frac{C_O \cdot W}{W_w} \tag{1}$$

where W – total humidity of frozen soil; W_w – content of frozen moisture in frozen soil; Co – initial concentration of interstitial solution. The W_w value can be easily determined from the formula proposed by Aksenov (1980):

$$W_w = 0{,}25 \cdot W_P + (W - 0{,}25 \cdot W_P) \cdot \frac{T_{bf}}{T} \tag{2}$$

where W_p – humidity at plasticity limit; T_{bf} – temperature at which interstitial solution starts to freeze, determined from the formula:

Table 1. Classification of the North-Western Yamal Cryopegs (according to I.D. Streletskaya with partial modification).

Group	Type (Dynamics of cryogenic formation temperature)	Sub-type (Trend of cryogenic formation temperature)	Geomorphological level	Age and genesis of enclosing deposits	Composition of enclosing deposits and salinity of soils, D_{sal},%	Enclosing soil temperature, °C	Depth and absolute height, m	Head, m	Thickness lens,, m	Mineralization,, g/l
Active cryodiagenesis zone	A. Short term (average annual, 2 – 5 years, 11 years fluctuations of temperature)	$A_{1.}$ Soil temperature rise	Marine terraces	m,pm I-II, sd II-IV	Sandy-loam and clayey Ds=0.2 - 0.8	-0.5÷-4	3 -12 0 ÷ +40	0.5-5.0	0,2-0,5	20-60
			Flood plain	am, lm IV	Sandy-loam and clayey Ds=0.05 - 0.5	-0.5÷-3	3 -10 0 ÷ +5	0.5-5.0	0,1-0,5	7-50
		$A_{2.}$ Soil temperature drop	Flood plain (adjacent to river bed)	am IV	Sandy and sandy-loam Ds=0.05 - 0.7	-0.5÷-3	5-10 0 ÷ +5	2-6	0,1-0,5	7-50
			Flood plain (spit)	am IV	Sandy and clayey Ds=0.1 - 0.7	-3÷-5	6-10 0 ÷ +5	3-4	0,1-0,5	80-90
			Flood plain (hasyrey)	lmIV	Sandy-loam and clayey Ds=0.1 - 0.7	-3÷-5	2-10 0 ÷ -5	0.1-7	0,1-0,3	60-100
			Laida	mIV	Sandy and clayey Ds=0.5 - 3	-4÷-8	1-15 0 ÷ -10	0-10	0,1-0,5	70-150
Passive Cryodiagen. zone	B. Medium term (40-90 years fluctuations of temperature)	B_1-$B_{2.}$ Soil temperature rise and drop	All levels	m,pm III	Sandy and sandy-loam Ds=0, 1-0,6	-3÷-5	15-40 -10÷ -40	10-35	0,3-12	50-80

$$T_{bf} = -1{,}83 \cdot \frac{C_O}{\mu} \tag{3}$$

where μ – molecular mass of dissolved salt.

Patterns of Chemical Thawing of Frozen Soil as a Result of Interaction with Cryopegs

We conducted experimental research of a process of interaction between the NaCl solution and a frozen soil. Soil samples were placed into a 5 sm tall cylindrical container being 2 sm in diameter and were kept in a constant-temperature cabinet at a given temperature (below 0°C) during 2–3 days until soil phase changes were completed.

After that, a brine solution with the same temperature was poured on the upper surface of the sample. The soil container was sealed by a lid with a capillary. Soil thawing dynamics was assessed by rate of descent of the solution in the capillary. The side surface of the cylindrical container was covered by thermal insulating material, while the temperature at the container's upper and bottom surfaces was the same as the experiment temperature. By this we simulated one-dimensional interaction between the brine solution and the soil. Similar equipment and procedure of experiments were used by Gaidaenko (1990) and Ostroumov (1990).

Table 2. Constant factors of the formula (7).

	The opened system		The closed system	
	Case of sand	Heavy clay loam	Case of sand	Heavy clay loam
A_1	0,0752	- 0,3062	- 0,0692	– 0,0447
A_2	0,0588	- 1,0633	- 0,2205	0,0008
A_3	1,6036	0,7064	1,8014	1,7719
B_1	- 0,3029	1,9217	0,5746	0,3467
B_2	0,8455	8,0137	2,9339	1,0402
B_3	- 3,3278	2,0932	- 4,8438	- 6,6717

The results of our experiments are as follows. When temperature T = -1.8°C, a contact between frozen sand and brine solution (with concentration of 50 g/l) leads to a situation where chemical thawing of soil occurs during the first 20 hours. After that, interstitial moisture starts to refreeze. If solution concentration is 100 g/l, chemical thawing of soil proceeds continuously. In this case, when temperature T = -1.8°C, refreezing does not occur.

In the case of frozen clay, when temperature T = -1.8°C and brine solution concentration C = 100 g/l, the rate of chemical thawing is twice lower that for frozen sand, while refreezing starts in about 40 hours.

The rate of chemical thawing of frozen soils is influenced by a value of salt diffusion coefficient, which, in its turn, depends on many parameters. Primarily it depends on type of

Table 3. Rate and depth of chemical thawing of frozen soils as a result of interaction with cryopegs.

Cryopeg type and sub-type	Geomorphological level	Composition of enclosing deposits	Salinity, g/l	Enclosing soil temperature T, °C	Heat transfer system	Thawing rate V, sm/day	Thawing depth per 0.5 years h, m	Thawing depth per 1 year h, m
A_1	Marine terrace, flood plain	Clay loam	40	-1.5 < -2.0	Opened "	0.46 0	0.85 0	1,70 0
A_2	Floodplain (area adjacent to riverbed)	Sand	40	-1.5 -2.0 < -2.5	Opened " "	0.94 0.36 0	1.71 0.66 0	3,42 1,32 0
A_2	Floodplain (hasyrey)	Clay loam	80	< -3.0	Closed	0	0	0
B	All levels	Sand	80	< -3.0	Closed	0	0	0

soil, thickness of water films in soil voids (pores), geometry and relative position of water films and ice crystals. For example, continuous ice beds prevent penetration of salt into soil. The coefficient of salt diffusion in frozen soil is calculated using the following formula:

$$D = W \cdot D_O \tag{4}$$

where D_O is the coefficient of salt diffusion in free water; in case of a NaCl, D_O is approximately 0.04–0.05 sm/h.

The rate of chemical thawing of frozen soil also depends on average density of brine solution-as brine solution density decreases, the duration of chemical thawing of soil increases.

We obtained a simple function that allows for calculating depth of chemical thawing of frozen soil exposed to saline solution:

$$h = h_1 \cdot \sqrt{t} \tag{5}$$

where h is the depth of soil layer thawed during an estimated time t; h_1 is the depth of soil layer thawed during the first day.

Our research demonstrates that when the temperature of brine solution is the same as temperature of frozen soil, the rate of chemical thawing of frozen soil depends on brine solution temperature and concentration in the following manner:

$$f(C,T) = (A_1 \cdot \ln C + B_1) \cdot T^2 + (A_2 \cdot \ln C + B_2) \cdot T + (A_3 \cdot \ln C + B_3) \tag{6}$$

where

$$V = \begin{cases} f(C,T) & at \quad f(C,T) \geq 0, \\ 0 & at \quad f(C,T) < 0; \end{cases} \tag{7}$$

where V is the soil thawing rate (sm/day); C is the brine solution concentration expressed in promille; T is the air temperature expressed in degrees Celsius. The factors A_i and B_i (i = 1, 2, 3) – constant values (experimentally obtained) (see Table 2).

The process of chemical thawing of soil described above will also occur under the foot of a pile driven into a borehole. When a borehole is being drilled, natural pressure of rock formation is released in the area where a pile is driven in.

Practical Examples

Physical and mechanical properties (strength and deformability) of marine deposits scattered along the Arctic coast depend on temperature, salinity, particle-size distribution, and humidity of marine sediments.

Depending on their deformability the Yamal Peninsula soils include hard frozen, plastic frozen, or cooled soils. Plasticity depends on soil type, temperature, and salinity that determine phase composition of interstitial solution and degree of soil cementation by interstitial ice. That is why it is expedient to link boundary of soil state change to phase composition of soil moisture.

Various states of frozen soils (hard frozen, plastic frozen, and cooled soil) also depend on interactions between the ground base and cryopegs. Chemical thawing of frozen soil is triggered by such interactions.

The comprehensive approach to studying distribution and classification of cryopegs, adopted by us, allowed for revealing patterns of cryopegs distribution within ground strata along the western coast of Yamal Peninsula. This makes it possible to assess soil variants as a base for pile foundations.

Let us consider these variants from the viewpoint of the possible load bearing capacity of piles.

Examples are based on typical soil conditions (in accordance with the survey of the Obskaya-Harasaway road (see Fig. 1).

Variant "a" (Fig. 1, variant A). A pile driven into frozen clay, saline soil taps low-pressurized low-mineralized cryopeg lens (C = 20–40 g/l) at a depth of H = 2–3 m. The temperature (T_o) of the saline clay soil of the marine terrace is minus 3°C. As a result, the pile surface is wetted with mineralized water (either fully or partially). Under such conditions the rate of chemical thawing of the soil amounts to zero (Table 3). However, given the above mineralization and temperature, there will be just a film of fresh ice forming in the pile contact area. In general, the bearing capacity of the pile will be largely unaffected. Tables containing construction standards can be used to calculate the bearing capacity.

Thus, if the temperature is minus 3°C and the salinity of clay soil is ~ 0.2%, shearing resistance of the soil adfreezing with the metal pile can be assumed equal to R_{af} = 150 kPa. If the temperature remains unchanged and the salinity amounts to 0.4%, design pressure under the pile butt-end can reach R = 550 kPa, which will ensure the bearing capacity of the pile.

Variant "b" (Fig. 1, variant B). A pile is driven into a frozen ground strata in the laida area adjacent to a riverbed. The upper part of the strata consists of slightly saline sands (D_{sal} = 0.1–0.15%). The bottom part is composed by clayey saline soils (D_{sal}=0.5%). A cryopeg lens penetrated by the pile is featured by high salinity (up to 70g/l). The pile driven into such a borehole is unlikely to have proper load bearing capacity since the rate of chemical thawing is high and equals to 0.36 sm/day (Table 3). Over half a year, chemical thawing along the level (r) can reach 0. 66 m (see Table 3). Bearing capacity of the pile in the lower part across the lateral adfreezing surface of saline (D_{sal} = 0.5%) clay soil is just as small. At a temperature of minus 2°C, R_{af} can amount to 30 kPa. In general, in the upper part of the pile, since soil is not frozen, sand will be thawed due to chemical thawing. In the bottom part of the pile there are plastic frozen soils with weak strength properties. Installation of a pile in such conditions is inexpedient and should be avoided. In such circumstances cooling systems may be used as a last resort.

Variant "c" (Fig. 1, variant C). A pile is driven into cooled soil in the bottom part of the section. The upper layer consisting of frozen sand may be 2–4 m thick. As a result of exposure to highly saline head water, chemical thawing of this layer may occur. The clayey saline soil strata (D_{sal} = 2.0%) may be interbedded by sand containing highly saline head cryopegs. In this situation a construction method based on preliminary thawing of ground strata should be used. The construction standards for thawed ground shall be used for determining strength properties.

Conclusion

Despite insufficient knowledge of the subject under investigation, limited experimental data, and challenges in meeting the set objectives, the research and studies performed by us allow for the first time to reveal basic patterns of change of physical and mechanical properties of frozen soil as a result of their interaction with cryopegs.

Our study comprised a number of experiments on chemical thawing of soils at a temperature ranging between -1.5°C and -6.0°C and with brine concentration ranging between 40 and 80 g/l. The analysis of the results yielded by our experiments enabled us to:

(1) discover basic interaction patterns between frozen soils and mineralized waters at below-zero temperatures;

(2) compile tables and devise formulas for calculating the rates of chemical thawing of frozen soils (see Formula (7), Table 4);

(3) suggest methods of assessing the bearing capacity of piles driven into the rock mass with cryopeg lenses. This allows us to determine whether it is possible to ensure the bearing capacity of pile bases (if there are any cryopegs present), or whether such a possibility is completely ruled out.

References

Aksenov, V.I. 1980. *Study on Mechanical Properties of Saline Soil as Building Bases.* Moscow: MISI, 24.

Gaidaenko, E.I. 1990. Effect of saline liquids on frozen soils and mortars. *Frozen Saline Soils as Foundations for Buildings*. Moscow: Nauka, 62-70.

Gorelik, Ya.B. & Kolunin, V.S. 2002. *Physics and Modeling of Cryogenic Processes in Crust.* Novosibirsk. Publishing House of Siberian Branch of Academy of Sciences, 317.

Grigoryan, S.S., Krass, M.S., Guseva, E.V. & Gevorkyan, S.G. 1987. *Quantitative Theory of Geocryological Forecast.* Moscow: Publishing House of Moscow University, 266.

Ivanova, N.V. et al. 1992. Patterns of cryopegs formation within Kara cryoartesian basin. *Formation of Cryolithozone Ground Water.* Yakutsk: Publishing House of Siberian Branch of Academy of Sciences, 18-34.

Ostroumov, V.E. 1990. Salt transfer in dispersed frozen soils under the influence of temperature gradient. *Frozen Saline Soils as Foundations for Buildings.* Moscow: Nauka, 45-55.

Streletskaya, I.D. 1991. *Patterns of distribution and Formation of Saline Frozen Soil and Cryopegs in North Western Yamal.* Moscow: Moscow State University, 21.

Permafrost and Cryopegs of the Anabar Shield

Sergey V. Alexeev
Institute of the Earth's Crust SB RAS, Irkutsk, Russia
Ludmila P. Alexeeva
Institute of the Earth's Crust SB RAS, Irkutsk, Russia
Alexander M. Kononov
Institute of the Earth's Crust SB RAS, Irkutsk, Russia

Abstract

The Anabar shield is characterized by continuous permafrost. The mean annual temperature of rocks reaches -15ºC, and the zero isotherm position is detected at depth 1000 m. According to the scheme of geocryological zonation, the ice-rich permafrost, underlain by dry permafrost, occurs down to a depth of 200 m; but the hydrogeological studies performed recently on the margins of the shield indicate possible availability of fresh groundwater within its field. Remarkably, this paper for the first time offers the theoretical model of cryopeg formation in crystalline rocks and a new type of permafrost structure. The study suggests that glaciation and marine transgressions have been identified as truly crucial events in the Pleistocene history of the shield. The glacial complexes experienced the processes of seawater-frozen rocks interaction, ground ice melting, and replacement of fresh groundwater with seawater. As a consequence, appropriate conditions were created for ice-rich permafrost and subpermafrost cryopegs to be derived in cryochrons.

Keywords: Anabar shield; brines; cryopegs; glaciation; permafrost; seawater.

Introduction

The Siberian platform is the most ancient and largest geological unit of Eurasia, in which a sustainable portion of rocks have been in a perennially frozen state since Early-Middle Pleistocene. Its northeastern part is occupied by the basement uplift that is the Anabar shield and is characterized by truly complicated natural and geocryological-hydrogeological conditions.

Lack of geocryological and hydrogeological information on the Anabar shield is primarily explained by its remoteness, as well as unavailability of data on deep drilling accomplished within the shield, and targeted survey. Therefore, identification of the main parameters of the Anabar shield permafrost and features of its evolution are key scientific goals. The profound knowledge to be gained will ensure understanding of the general pattern of the continental crust formation on Earth in the Late Cenozoic. The authors of this paper have compiled available data on geological features and the geocryological and hydrogeological settings of the Anabar shield. Paleogeocryological interpretation of these sources of information defined morphological and genetic specifics of the shield permafrost and the major phases of its evolution in the Late Cenozoic, as well as new types of the cryolithozone structure.

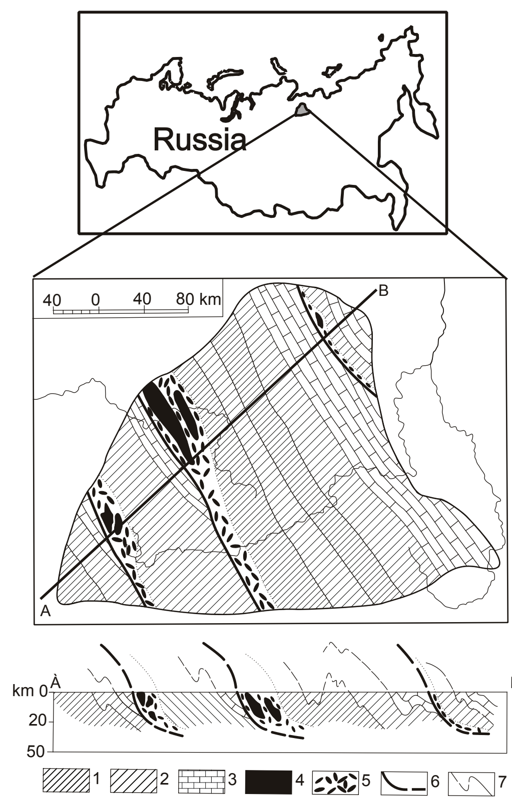

Figure 1. Geological structure of the Anabar shield (Rozen et al. 1986). 1 – Daldyn series, 2 – upper Anabar series, 3 – Khapchan series, 4 – cataclasite, phyllonite and diaphthorite of deep-seated shear zone and diaphthoresis, 5 – faults (mylonite and blastomylonite), 7 – folded structure (shown on section A–B).

Presentation and Discussion of Results

Geology, geomorphology, and climate

The Anabar shield is composed of the Archean metamorphosed rocks of the granulite complex; for example, gneisses and crystalline schists (Fig. 1). They make up some

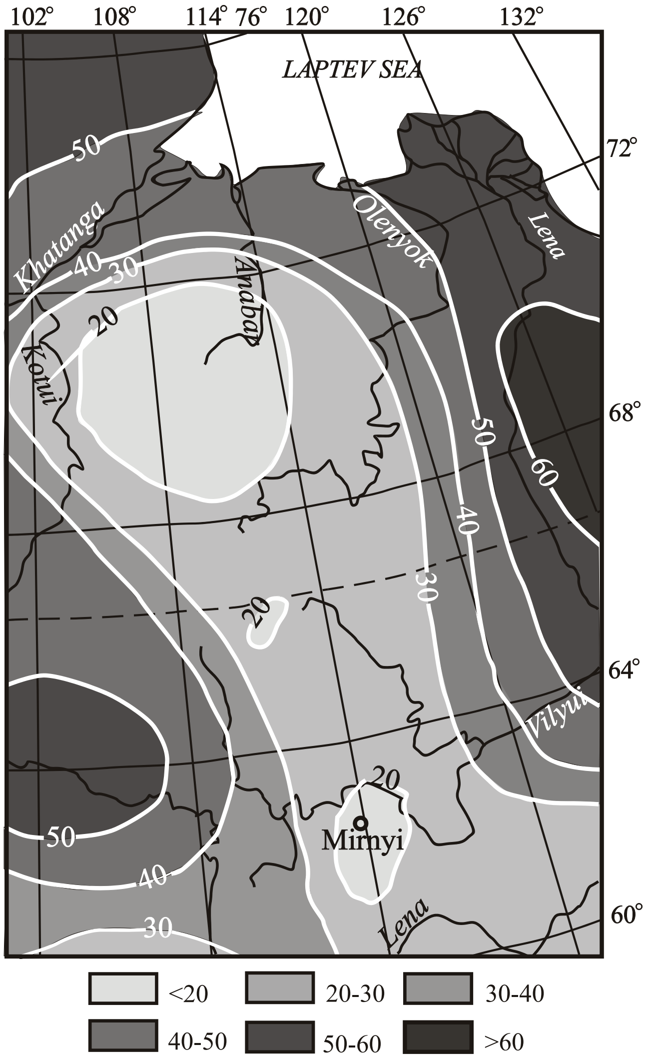

Figure 2. Heat flow values (mW/m^2) in the north of the Siberian platform (*Temperature, cryolithozone…* 1994)

rigid blocks, for instance, the Magan, Daldyn and Khapchan terrains, divided by thick zones of shearing and splitting striking towards the northwest (Rozen et al. 2002).

The Anabar shield is rimmed with a zone of flatly lying Proterozoic (peridotites, amphibolites, and pyroxenites) and Cambrian sedimentary rocks. Quaternary sediments are thin and are not widespread. The ancient magmatic rocks (granites and anorthosites) were formed in the Archean and Proterozoic cycles of volcanism, while young rocks represent Permian-Triassic "Siberian traps" making up thick covers, sills, and dykes. The common units of the Anabar shield structure are large fault dislocations.

The Anabar shield is one of the largest uplifts of the Mid-Siberian plateau. In relief the uplift looks like a deformed flat cupola with massive prominences separated by incised river valleys. A typical structural relief of the plateau was formed over the sedimentary rocks of monoclinal bedding composing the edges of the Anabar uplift. The maximum altitude of the plateau is 900 m in its central and southwestern parts. In the south and northeast, it reaches 600 m; in the southeast, it is 300–350 m; and near the eastern border, it is close to 200 m. The river valleys commonly occur in the zones of tectonic dislocations. They lack such forms of accumulation relief as the first floodplain terrace, river sand bars, spits, and flood lands.

The Anabar shield lies within the Siberian part of the sub-Arctic zone having a sharply continental climate. In the cold period, the climate is much affected by the Asian barometric maximum. The mean annual temperature of air varies from -13 to -15, while the mean minimum of air temperature ranges from -18 to -21°C (Gavrilova 1998). The amplitude of temperature variations reaches 56°C. In time of anticyclone, the air temperature inversion leads to a marked cooling of river valley bottoms. The annual amount of precipitation decreases south to north from 266 to 194 mm/yr. The steady snow cover is formed by early October, and it melts down in late May. On the wind-protected sites, the snow cover is commonly 66–73 cm deep, whereas in the open parts its depth decreases to 46–57 cm. The average value of snow density is 0.16–0.22 g/cm^3.

Geocryology and hydrogeology

The Anabar shield is located in the northern geocryological zone where permafrost is ubiquitous. Knowledge about the thermal status of frozen ground is insufficient and poor, because deep wells applicable for geothermal observations were not drilled. The highest mean annual temperature of rocks (-7…-9 °C) is typical for river valleys, gently sloping shores, and low interfluvial areas overlain with sandy and loam sandy fluvioglacial sediments. On the high, steep slopes and tops of the Anabar plateau, the mean annual temperature of rocks reaches -13…-15°C (Ershov 1989).

Considering geothermal parameters, the Anabar shield is regarded as the region with the coldest crust and the lowest heat flow (Balobaev et al. 1983). The temperature of rocks at depth 500 m amounts to -3…-5, and at depth 1000 m, it raises to -1…+1 °C. The heat flow values vary from 15 to 20 mWt/m^2 (Fig. 2).

It is currently believed that within the Anabar shield the cryolithozone has two layers. In the upper part of the shield and on its slopes, the thickness of permafrost reaches 150–200 m. It is underlain by dry rocks with negative temperature. Groundwater can occur only in the seasonally thawed layer and within closed taliks within river valleys. The total thickness of the cryolithozone is estimated to be over 1000 m (Fotiev 1978, Ershov 1989).

The authors of this paper propose that the sequence of perennially frozen rocks is composed of disconnected blocks and boulders bound by interstitial ice and dispersed material. The ice inclusions basically fill fractures of cleavage, chipping, as well as fractures of slip. The rocks of the Anabar shield inherit fractured and fracture-vein cryogenic structures producing shlierens, nests, and extensive veins. The pattern of fractures and ice-filled cracks essentially changes in massive rocks, and it is defined by the lithological, petrographic, and tectonic factors. In basalts, the net of cracks looks like columnar or pillar jointing (Fig. 3a). In granites and sandstones, the ice-containing cracks produce a system net (Fig. 3b), while in schists this is a wavy net (Fig.

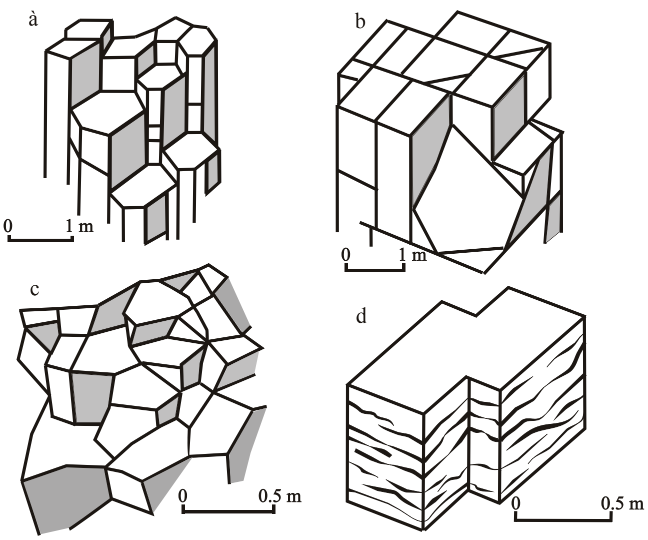

Figure 3. Structures of ice-filled fractures of the Anabar shield: a – polygonal (basalt), b – system (granite), c – chaotic (dolerite), d – wavy (schists).

3d), both occurring on the folds of longitudinal compression and near faults. In the fault zone, next to the ruptures and contact of intrusive rocks the dolerites display a chaotic net of cracks (Fig. 3c). The structure-forming ground ice has cement, infiltration, and sublimation genesis.

Hydrogeological studies performed recently on the margins of the Anabar shield indicate possible availability of fresh groundwater within its inner field (Solopanov & Tolstov 1996). This statement can be exemplified by the Tomtor pluton, hosting the unique deposit of rare-metal ores, located about 180 km east of the shield. The massif is composed of ultrabasic, alkaline, and carbonatite rocks. Geophysical surveys suggest that subpermafrost waters exist within the Anabar shield (Kalinin & Yakupov 1989).

At depths of 170–400 m, the wells penetrated artesian subpermarost waters of chloride-hydrocarbonate sodium composition with salinity of 225–770 mg/L. The head over the aquifer roof was 120–360 m. The well flow rate ranges from 2.4 to 7.0 m^3/day (Solopanov & Tolstov 1996). The geothermal observations in wells indicate that the temperature of rocks at the depth of zero ranges from -6.1 to -8.4°C, which corresponds to calculated estimates of mean annual temperature of rocks of the Anabar shield. The temperatures were measured at the Chair of Geocryology at Moscow State University.

Discussion

The interior of large massifs of crystalline rocks, for example, Baltic, Canadian, and Brazilian shields, contains chloride saline waters and brines of different salinity. Researchers have proposed alternative processes of evaporative concentration of seawaters and dissolution of halogene formations. In recent years, a number of published papers reported formation of chloride brines of the Baltic and Canadian shields due to cryogenic concentration of seawater (Herut et al. 1990, Szilder et al. 1995, Bottomley et al. 1999,

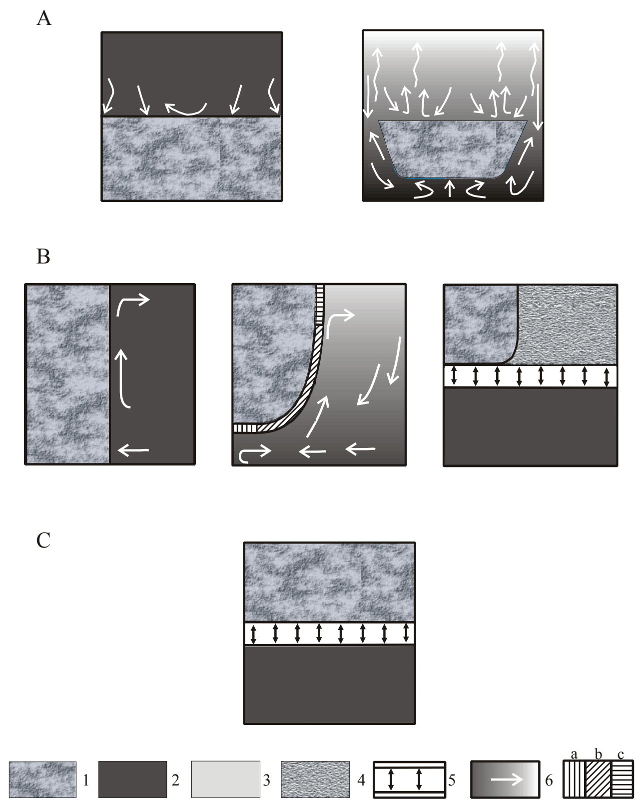

Figure 4. Phase interaction scheme in the brine-ice system (Alexeev 2000): 1 – initial ice, 2 – brine, 3 – diluted solution, 4 – secondary ice, layer of local equilibrium in the system and phase interaction at molecular diffusion, 6 – direction of density convection, 7 – hydrodynamic layer: a) zone of convection beginning and of the most active ice melting, b) zone of decreasing unequilibrium to ice, c) zone of neutral phase contact.

Marion et al. 1999, Starinsky & Katz 2003).

The principally new scenario is proposed as to how cryopegs could possibly be formed in the crystalline rocks of the Anabar shield. The theoretical background of the authors is based on some principal points.

1. Glaciation of the Anabar shield is an important factor of Pleistocene history. It resulted in formation of the thick glacial covers of the Antarctic type, or typical mountain-valley glaciers (Ershov 1990, 1998, Romanovsky 1993). Glaciation left a series of terminal moraines enclosed in each other. The glacier tongues also left moraines behind in the mountain valleys. The glaciers continuously covered the northern part of the Anabar plateau. Deglaciation caused formation of peculiar glacial complexes. They consist of the tongue basin or central depression.

2. The Pleistocene stage of the Anabar shield evolution is responsible for a significant number of marine transgressions, preconditioned by either active tectonic movements or glacial eustatic rises of the ocean level. The sea repeatedly reached the northern margin of the Anabar shield.

3. Marine transgressions proceeded with seawater of different salinity interacting with ice-rich frozen rocks. The phases interacted within the systems: "brine above ice" and "brine in the lateral contact with ice" (Alexeev 2000) (Fig. 4).

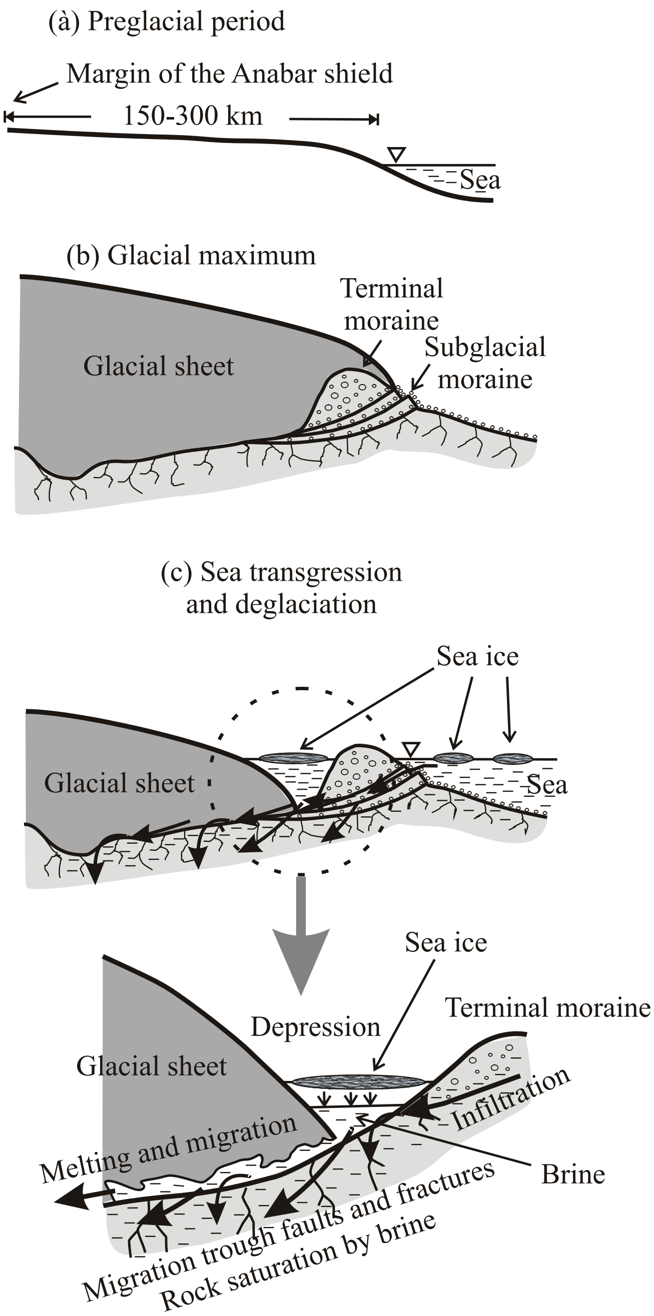

Figure 5. Cryopeg formation in crystalline rocks of the Anabar shield.

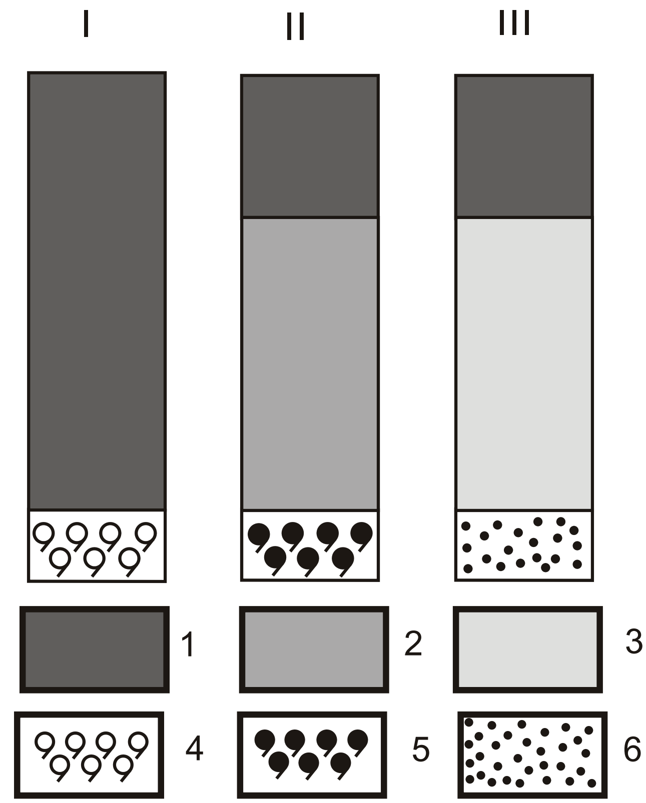

Figure 6. Permafrost structure of the Anabar shield (I and II are new types of permafrost structure, III – commonly accepted type). 1 – ice-rich frozen rocks, 2 – rocks filled by cryopegs, 3 – dry frozen rocks, 4 – rocks filled by subpermafrost fresh water, 5 – rocks filled by saline waters with positive temperature, 6 – dry rocks with positive temperature.

With sub-freezing air temperatures, the flooded part of the shelf turned into a peculiar cryogenic basin. Considering its functioning and final salinity, the cryogenic basin is similar to the classic sea evaporitic lagoon. However, the H_2O-solvent was removed due to the ice formation combined with sublimation, and it induced the change of the liquid phase volume and concentration of seawaters. Thus, in the time of glaciation and deglaciation it is suggested that the Anabar shield experienced the following events.

In the preglacial period, the Anabar shield and sea were separated by a narrow zone of intercalating continental and marine sediments extending for 150–300 km (Fig. 5). In time of glaciation, the entire marine material was dragged by a glacier to its termination. While advancing, it displaced a wide and massive terminal moraine forward. The bottom moraine formed in the base of a glacier. It consisted of weathering crust fragments and debris.

The glacier retreated when the climate turned warm, or if the amount of solid sediment diminished. Due to ice melting, the moraine material piled on the former glacier bed as a moraine line oriented across the valley.

The depression was formed between the glacier and deposited moraine. In the period of transgression, this depression was gradually filled with seawater infiltrating through a moraine either over the planes of scaly overthrusts or over the contact of rocks and lenses of dead ice. Their subsequent cooling was accompanied by ice formation in the near-surface space of depression, concentration, and subsidence of denser brine waters onto the water reservoir bottom. The stronger brines further migrated onto the dislocated bed of the ice shield through steeply dipping fractures of the tectonic zones and exogenous fracturing. If fissures in rocks were filled with ice, it actively melted, and a convective mass transfer took place. The brines also migrated towards the center of the depression along the thawed glacier base. The brines flew out of the depression, and the outflow was made up for new portions of seawater supplied from the moraine line.

During several tens of thousands of years of a transgressive regime, the crystalline rocks could have enclosed a considerable volume of brines. At the next stage of the Anabar shield evolution, the liquid phase in the crystalline rocks was stratified according to the density. This resulted in formation of a peculiar zonation marked by an increase of groundwater salinity at depth. Fresh and saline waters were frozen through, while the brines, when cooled, were transformed into cryopegs. We suggest that this scenario describes how conditions were created for formation of the cryolithozone, which consists of frozen and cryopeg-filled rocks.

Conclusions

Important conclusions have been derived due to the study performed:

1. The glaciation event was an important stage in the Late Cenozoic history of the Anabar shield development. The subsequently occurring deglaciation and transgression of the sea created conditions appropriate for formation in the crystalline rocks of the brines genetically related to seawater, which was infiltrated into crystalline rocks on the glacier/sea border.

2. In the Late Pleistocene cryochrons, the permafrost sequences were derived within the zone of exogenous fracturing. The profound cooling of crystalline rocks brought about cryogenic concentration of groundwater, increase in salinity, and formation of a thick zone of subpermafrost cryopegs.

Therefore, the formerly existing concept that groundwater is lacking within the shield is to be essentially reconsidered. Having considered available data, the proposal is to distinguish two alternatives types of cryolithozone structure with variable ratios of rocks having negative temperature (Fig. 6). The figure displays the relationships between different stages of cryogenic rocks.

When compiling a new map of geocryological conditions in East Siberia the newly recognized types (columns I and II) of cryolithozone, with possible presence of fresh groundwater and brines, should be included.

Acknowledgments

The authors express sincere gratitude to Tatiana Bounaeva for translation of the Russian text into English. The authors would like to thank the anonymous reviewers for the constructive comments and additional language improvement. This research has been carried out with the financial support of the Russian Fund for Basic Research (project 08-05-00086), Scientific School (9542.2006.5), and Polar Earth Science Program, Office of Polar Programs, National Science Foundation (ARC-0632400, ARC-0520578).

References

Alexeev, S.V. 2000. *The cryogenesis of groundwater and rocks as exemplified by the Daldyn-Alakit region of Western Yakutia.* Novosibirsk: Publ. SPC UIGGM SB RAS, 119 pp. (in Russian).

Balobaev, V.T., Pavlov, A.V., Perlshtein, G.Z. et al. 1983. *Thermal-physical researches of Siberian cryolithozone.* Novosibirsk: Nauka, 22-34 (in Russian).

Bottomley, D. J., Katz, A., Chan, L. H. et al. 1999. The origin and evolution of Canadian Shield brines: evaporation or freezing of seawater? New lithium isotope and geochemical evidence from the Slave Craton. *Chem. Geology* 155: 295-320.

Ershov, E.D. (ed.). 1989. *Geocryology of the USSR. Central Siberia.* Moscow: Nedra, 414 pp. (in Russian).

Ershov, E.D. 1990. *General Geocryology*. Moscow: Nedra, 559 pp. (in Russian).

Ershov, E.D. (ed.) 1998. *The Bases of Geocryology. Part 3. Regional and Historical Earth's Geocryology.* Moscow: Publ. of Moscow State University, 575 pp. (in Russian).

Fotiev, S.M. 1978. *Hydrogeothermal Peculiarities of the Permafrost of USSR.* Moscow: Nauka, 236 pp. (in Russian).

Gavrilova, M.K. 1998. *The Climates of the Earth Cold Regions.* Yakutsk: Publ. SB RAS, 206 pp. (in Russian).

Herut, B., Starinsky, A., Katz, A. et al. 1990. The role of seawater freezing in the formation of subsurface brines. *Geochim. Cosmochim. Acta* 54: 13-21.

Kalinin, V.M. & Yakupov, V.S. 1989. *Regional regularities of permafrost thickness behavior*. Yakutsk: Publ. SB RAS, 142 pp. (in Russian).

Marion, G.M., Farren, R.E. & Komrowski, A.J. 1999. Alternative pathways for seawater freezing. *Cold Regions Sci. Tech.* 29: 259-266.

Romanovsky, N.N. 1993. *The Bases of Lithosphere Cryogenesis.* Moscow: Publ. of Moscow State University, 335 pp. (in Russian).

Rozen, O.M., Vishnevsky, A.N., Glukhovsky, M.Z. et al. 1986. *Structure of the Anabar Shield Earth Crust.* Moscow: Nauka, 198 pp. (in Russian).

Rozen, O.M., Serenko, V.P., Spetsius, Z.V. et al. 2002. The Yakutian kimberlite province: disposition in the Siberian craton structure, composition peculiarities of the upper and lower crust. *Geology and Geophysics* 43(1): 3-26 (in Russian).

Solopanov, A.T. & Tolstov, A.V. 1996. Cryohydrogeological conditions of the Tomtor massif. Cryolithozone and groundwaters of Siberia. *Groundwaters and Icings*. Yakutsk: PI of SB RAS: 87-94 (in Russian).

Starinsky, A. & Katz, A. 2003. The formation of natural cryogenic brines. *Geochim. et Cosmochim. Acta* 67(54): 1475-1484.

Szilder, K., Lozowski, E.P. & Forest, T.W. 1995. One-dimensional freezing of seawater in constrained volume. *Can. Geotechn. Journal* 32, 1: 122-127.

Tectonics, geodynamics and metallogeny of the Sakha Republic (Yakutia) territory. 2001. Moscow: Nauka (Interperiodika), 571 pp. (in Russian).

Temperature, cryolithozone and radiogenic heat generation in the earth crust of the Northern Asia. Novosibirsk: Publ. SPC UIGGM SB RAS, 141 pp. (in Russian).

A First Estimate of Mountain Permafrost Distribution in the Mount Cook Region of New Zealand's Southern Alps

Simon Allen
Department of Geography, University of Canterbury, Christchurch, New Zealand
Ian Owens
Department of Geography, University of Canterbury, Christchurch, New Zealand
Christian Huggel
Glaciology, Geomorphodynamics & Geochronology, Department of Geography, University of Zurich, Zurich, Switzerland

Abstract

The heavily glaciated Mount Cook Region of New Zealand has experienced several recent large rock instabilities, but permafrost conditions related to these events remain unknown. This work presents the first systematic approach for investigating the distribution of mountain permafrost in New Zealand. At this level of the investigation, a first-order estimate is based upon the adaptation of established topo-climatic relationships from the European Alps. In the southeast of the study region, the permafrost estimate gives a reasonable correspondence with mapped rock glacier distribution but the maximum elevation of vegetation growth is situated 200 m beneath the lower limit of estimated permafrost. Extreme climate gradients exist and towards the humid northwest, where rock glaciers are absent and vegetation patterns give an unclear climate signal, large uncertainties remain. Data currently being recorded from a network of rock wall temperature measurements will help remove this uncertainty, and will allow distribution modeling that better accounts for the topographic complexities of this steep alpine region.

Keywords: permafrost distribution; rock instabilities; spatial modeling; Southern Alps; New Zealand.

Introduction

Internationally, mountain permafrost is a well recognized phenomenon in relatively low-angled debris-covered terrain where active rock glaciers produce distinctive landforms that indicate perennially frozen ground beneath. Previous research based upon the identification of active rock glaciers in the Southern Alps of New Zealand has suggested that permafrost probably occurs only sporadically within a very narrow altitudinal zone in the more arid areas of the Alps (Brazier et al. 1998). However, there has been no scientific consideration in New Zealand given to the likely wider distribution of permafrost within bedrock slopes, and in particular, on steep slopes which dominate at higher elevations throughout the Mount Cook Region (MCR). Recent large rock avalanches, including the spectacular summit failure of Mount Cook (McSaveney 2002) have awoken interest in the understanding of permafrost and slope stability interactions in the region. This paper aims to present the first results from permafrost distribution modeling for the MCR, based upon local application and calibration of topo-climatic relationships established in the European Alps. Initial validation of the estimated permafrost distribution is discussed on the basis of a rock glacier inventory and remote sensing-based vegetation mapping, and future research towards improved modeling in this region is introduced.

Background

Studies of permafrost processes in New Zealand are limited (Soons & Price 1990), with only a few detailed studies emerging from the identification and dating of rock glaciers within the Southern Alps. These studies have served to improve the chronology of Holocene glacial activity in the region (McGregor 1967, Birkeland 1982) and offer some insights regarding possible climate sensitivities of rock glaciers (Jeanneret 1975, Kirkbride & Brazier 1995). From the mapping and classification of periglacial landforms in the Ben Ohau Range, Brazier et al. (1998) suggested that permafrost distribution was more limited than would be expected based upon climatic boundaries identified in the European Alps (Haeberli 1985). In the driest, generally low-elevation mountains east of the Southern Alps, rock glaciers are absent and ice-free talus slopes dominate. In the more humid, maritime regions to the west where precipitation exceeds 10000 mm y^{-1}, glacier equilibrium line altitudes (ELAs) are low and temperate mountain glaciers dominate, with no active permafrost landforms evident (Augustinus 2002). Between these two extremes, within a narrow zone where precipitation does not exceed 1500 mm y^{-1} ELAs are higher, glacial ice is limited to debris-covered cirques, and more numerous permafrost landforms are found (Brazier et al. 1998).

Understanding permafrost distribution within complex steep mountain terrain is a relatively new field of scientific research largely stemming from European-based studies in relation to climate warming, permafrost degradation and related slope instability hazards (Gruber & Haeberli 2007). During the past 50 years, several large rock avalanche events have occurred within the MCR (McSaveney 2002), but in the complete absence of data regarding permafrost distribution in the steep terrain of the Southern Alps, the possible role of permafrost weakening within past or future detachment zones is uncertain.

In complex mountain terrain, variations in topography and related permafrost factors such as snow cover result in the necessary use of spatial modeling to achieve any realistic estimate of permafrost distribution (Etzelmüller et al. 2001). A hierarchy of modeling procedures has therefore been developed over recent years (Hoelzle et al. 2001). Readily applied empirical-statistical approaches relate documented permafrost occurrences to easily measured topo-climatic factors such as altitude, slope and aspect, air temperature, and solar radiation (e.g., Imhof 1996) and are particularly well suited for preliminary assessment and planning in relation to geotechnical hazards (Harris et al. 2001). A useful, and essential first step in these studies has been the adaptation of Haeberli's (1975) original topo-climatic key for predicting permafrost occurrence, which provides an immediate impression of likely permafrost distribution, and a basis from which local validation and more advanced modeling can proceed.

Study Region

The MCR is broadly defined here to encompass the 700 km^2 Aoraki Mount Cook National Park, extending west of the Main Divide into the Westland National Park and south to include the Ben Ohau Range (Fig. 1A). The region includes the highest mountains and the most heavily glacierised terrain of New Zealand's Southern Alps. Permanent snow covered peaks are found between 2500 and 3754 m a.s.l., with local relief in the order of 1000–2700 m. Moist westerly airflow perpendicular to the Main Divide, generates very high orographic rainfall amounts and creates an extreme precipitation gradient leeward of the Alps (Griffiths & McSaveney 1983). Glacial retreat since the Little Ice Age maximum has been most rapid during the mid 20th Century, leading to a 25% loss of total ice area in the Southern Alps during this past century, although some highly responsive glaciers have had notable periods of advancement over recent years (Chinn 1996).

Estimating Permafrost Distribution

Based on extensive geophysical and morphological investigations of rock glacier phenomena in the eastern Swiss Alps during the 1970s, Haeberli (1975) developed 'rules of thumb' for predicting permafrost occurrence. Stemming from these rules was the empirical topo-climatic key, incorporating the primary physical factors which influence permafrost distribution, determining both a zone of probable permafrost and the permafrost limit within a transitional zone termed "possible permafrost." These physical factors include significant aspect dependent radiation effects, altitudinal changes in air temperature, and topographically related snow cover variation (Etzelmüller et al. 2001). In relation to snow cover, gentle terrain situated at the foot of steeper slopes where long-lasting avalanche snow may accumulate can maintain cooler ground surface temperatures than steeper slopes of the same aspect. On flat terrain, the local permafrost distribution is determined more by air

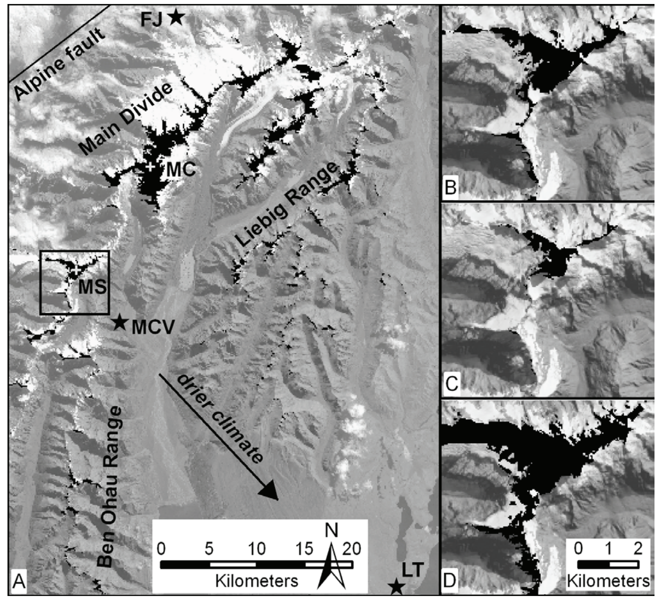

Figure 1. A) GIS-based modeling of possible steep permafrost distribution (black) in the MCR based upon adjustment of the original topo-climatic key (Haeberli 1975) using MAAT calculated from the Franz Josef (FJ), Mount Cook Village (MCV) and Lake Tekapo (LT) climate stations. Also shown are the locations of Mount Cook (MC, 3754 m) and Mount Sefton (MS, 3151 m), B) Closer view of the estimated permafrost terrain around the summit area of Mount Sefton, C) repeated for a 0°C isotherm rise of 200 m, and D) a 0°C isotherm lowering of 200 m. The base image used is an ASTER satellite mosaic from 2007.

temperature and snow cover than by radiation. Calibration of the key to local conditions in the MCR was based upon calculation of mean annual air temperature (MAAT) for the years 1982–2007 and the local 0°C isotherm elevation using daily temperature data from three climate stations located across the region (Fig 1A). For the eight primary slope aspects, the original elevation zones given in the topo-climatic key were either raised or lowered based upon the difference between the local elevation of the 0°C isotherm and the equivalent value from the Swiss Alps where the key was established. Topographic values for all analyses were extracted from the Landcare Research 25 m resolution South Island digital terrain model (DTM).

In an attempt to account for the significant climate gradients associated with the föhn effect which results from initially moist airflow across the Main Divide, the 0°C isotherm was calculated independently using MAAT measured at each of the three climate stations. Hydrological studies in the region have shown that rainfall gradients are approximately parallel to the Main Divide, with maximum rainfall measurements associated with the steepened terrain along the alpine fault (e.g., Griffiths & McSaveney 1983). Because of the effects of decreasing moisture towards the southeast on environmental lapse rates, the following values were used: Franz Josef, 0.005°C m^{-1} (Anderson 2003), Mount Cook Village, 0.0065°C m^{-1} , and Lake Tekapo, 0.0075°C m^{-1}. The latter two rates have not been directly measured, but were inferred from the nearest available

Table 1. Topo-climatic key for the estimation of permafrost distribution in the MCR adapted from Haeberli (1975).

Aspect	Permafrost possible		Permafrost probable	
	Steep slopes	Foot of slopes	Steep slopes	Foot of slopes
S	2280	1980	2480	2430
SE	2330	2180	2480	2580
E	2480	2280	2880	2580
NE	2730	2180	2880	2580
N	2880	2130	2880	2480
NW	2580	2030	2780	2430
W	2380	1980	2480	2330
SW	2230	1930	2280	2280
Flat Areas				
Wind-exposed		2480		2580
Wind-shielded		2530		2880
Variability				
Franz Josef (0.005 °C m^{-1})			270 m higher	
Lake Tekapo (0.0075 °C m^{-1})			190 m lower	

All elevations are given in metres above sea level (m). Values are based upon MAAT at Mount Cook Village (765 m) and an air temperature lapse rate of 0.0065°C m^{-1}. Variability is calculated using MAAT at Franz Josef (155 m) and Lake Tekapo climate stations (762 m) with given lapse rates.

measured locations where precipitation and humidity values are comparable (Brazier et al. 1998). Using a GIS procedure, the 0°C isotherm elevations were then interpolated between the three climate stations in a southeastern direction based upon distance from the alpine fault (Fig 1A). This modeling of 0°C isotherm elevations is a crude simplification, but for the purposes of an initial permafrost estimate, it is able to provide an approximation for the influence of moisture gradients prevailing across this region of the Alps.

Table 1 gives the adjusted permafrost elevation limits based upon the 0°C isotherm elevation of 2114 m calculated at the Mount Cook Village. This establishes a lower limit of permafrost in steep terrain (on slopes >20°) of 2880 m on sunny northern aspects, decreasing to 2230 m on shaded southern aspects. At Franz Josef, where a strong maritime climate prevails, the 0°C isotherm could be positioned up to 270 m higher, with a corresponding rise of the permafrost limits by the same amount, whereas these limits may be 190 m lower towards the drier climate at Lake Tekapo. At the foot of slopes (<20°), permafrost may be possible up to 750 m lower than on corresponding steeper slopes, but is probable at elevations only 400 m lower.

At elevations where possible steep permafrost is predicted along the Main Divide, glacial ice dominates much of the terrain with only limited exposed bedrock around ridge tops, on steep faces and rock outcrops (Fig 1A). In this region of the Alps, the average ELA is around 2000 m, well below the lower boundary of permafrost such that temperate glacial ice dominates, but areas of polythermal ice and associated permafrost interactions are likely within the higher elevation cliff and hanging glaciers (Etzelmüller & Hagen 2005). In the drier southeast, glacial growth is restricted with both talus and bedrock surfaces featuring prominently at elevations within the estimated permafrost terrain.

The accuracy of the selected lapse rates, MAAT, and resulting 0°C isotherm calculations will have a significant influence on the permafrost distribution estimate. This sensitivity is well illustrated for the area of the Main Divide around Mount Sefton (Figs. 1B-D). The current model estimates widespread permafrost surrounding the summit pyramid and along the ridges to the west and northeast. However, a 200 m lowering of the isotherm due to a colder MAAT or greater lapse rate selection would significantly increase the estimated possible permafrost distribution along all surrounding ridgelines and on all slope aspects. Under the scenario of a warmer MAAT or lower selected lapse rate resulting in a 200 m rise of the isotherm, the estimated permafrost terrain becomes mostly limited to the shaded aspects high on the summit area of Mount Sefton. While illustrating the sensitivity of the topo-climatic key to local calibration, this also gives some indication of the effect future climate warming could have on permafrost distribution in the region.

Local Validation Using Rock Glacier Inventory

Active and fossil periglacial landforms have been previously mapped in the Ben Ohau Range using a threefold classification of debris-covered glaciers, cirque-floor lobe forms, and talus rock glaciers (Brazier et al. 1998, Appendix 1). Although the Ben Ohau Range comprises only a small area of the much larger study region, it does contain the only known active permafrost forms in the region, and therefore is able to provide some initial local-scale validation of the permafrost distribution estimate. The original mapped landform data were transferred into a GIS inventory of active and fossil permafrost forms, with some positions and measurements reassessed using high resolution (0.61 m) QuickBird satellite imagery in combination with a DTM. A total of 70 permafrost forms were mapped according to their Rock Glacier Initiation Line Altitude (RGILA) position as measured from the foot of the talus. Active debris-covered glaciers are not necessarily indicative of permafrost conditions, but are included here to further illustrate the distinct landform zonation that occurs along this range (Brazier et al. 1998).

The active permafrost forms predominate on shaded aspects within a narrow 8.2 km north-south zone towards the centre of the Ben Ohau Range where the highest peaks are just above 2400 m (Fig. 2A). The RGILA of all active landforms would therefore be expected to lie mid-way between the permafrost limits estimated at the southern and northern ends of the range, but instead are positioned at altitudes 20 to 180 m lower (Fig. 2B). Permafrost originating at the foot of slopes might account for the preservation of some of these forms at lower elevations, but the possibility that the model estimate is too high within this area of the study region must also be considered. Although data are unavailable for northerly aspects, the aspect-related variability of the model from east through to west appears to match the distribution of active rock glaciers. No fossil permafrost forms are located within

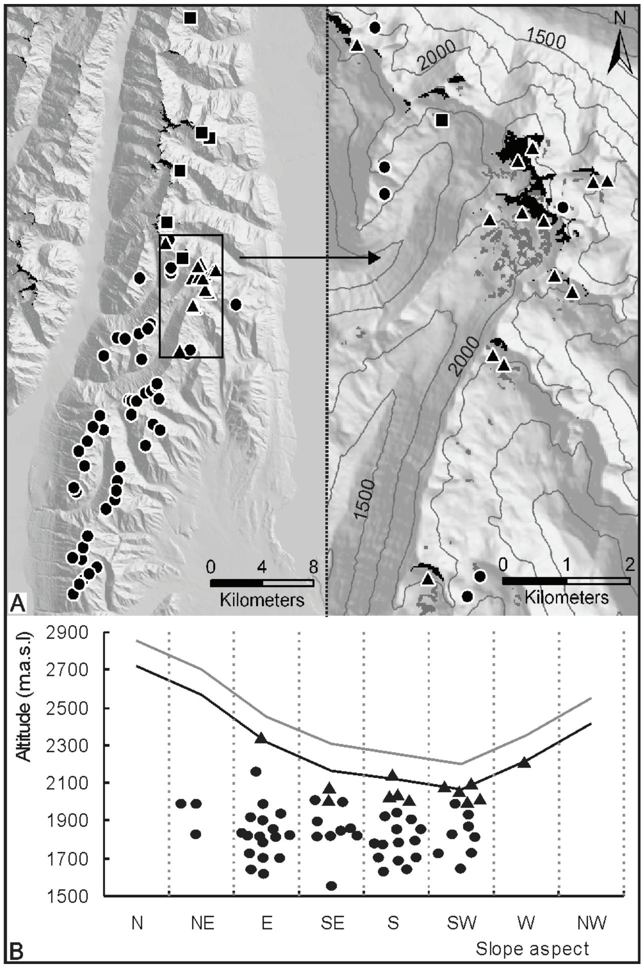

Figure 2. A) Modeled permafrost distribution on steep slopes (black) along the Ben Ohau Range compared with an inventory of active (triangle) and fossil (circle) rock glacier forms, and debris covered glaciers (square). Permafrost modeled at the foot of slopes is also shown (grey), based on slope curvature analyses. B) The spatial distribution of rock glacier forms is compared to steep permafrost lower elevation limits at the northern (grey) and southern (black) ends of the Ben Ohau Range.

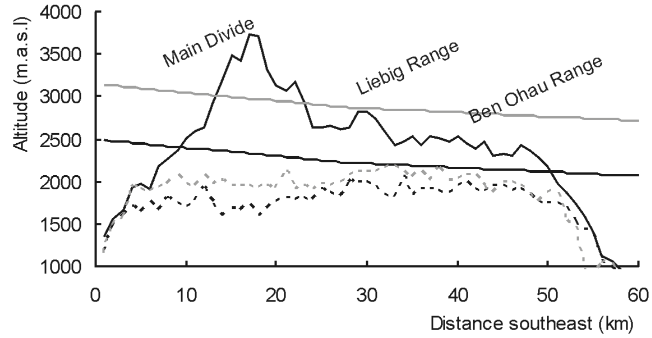

Figure 3. MAV (dashed) and corresponding minimum elevation of estimated permafrost distribution (solid lines) are plotted for steep northern (grey) and southwestern slopes (black) from northwest-southeast across the study region. The topographic profile with main mountain ranges labeled is also provided.

the estimated permafrost terrain and most are positioned more than 200 m below the estimated boundary, which is greater than can be expected from 20th Century temperature warming in this region (Salinger 1979). The numerous fossil forms mapped at the southern end of the range are located at much lower altitudes, with surface dating suggesting that many of these forms are periglacial relics from the late Pleistocene (Birkeland 1982). Towards the northern end of the range, increased snowfall combined with topographic effects enables the growth of heavily debris covered cirque glaciers at higher elevations and neither active nor fossil permafrost forms are observed here.

Comparison with Vegetation Mapping

Modern remote sensing-based mapping techniques are able to provide a crude, indirect indication of likely permafrost distribution (Etzelmüller et al. 2001). The presence or absence of alpine vegetation is a particularly well known indicator of permafrost distribution in mid-latitude mountains (Haeberli 1975), and the inclusion of vegetation abundance mapping from satellite imagery has proven a useful parameter for improved distribution modeling (Gruber & Hoelzle 2001). In the current study, orthorectified 15 m resolution Advanced Spaceborne Thermal Emission and Reflection Radiometer (ASTER) imagery from 2007 was used to create a map of vegetation distribution for the entire study region. To achieve this, the Normalised Difference Vegetation Index (NDVI) was used, which is based upon the contrasting spectral response of healthy vegetation between the red and near infrared (NIR) wavelengths. Combined with a DTM, altitudinal patterns in vegetation distribution were analysed and compared with the estimated permafrost distribution. A comparison is made between the maximum altitude of alpine vegetation growth (MAV) and the estimated lower limit of steep permafrost distribution within every 1 km zone in a northwestern to southeastern direction across the Southern Alps, parallel to the climatic gradient (Fig. 3). To examine the influence of slope aspect on vegetation patterns and any relationship there might be to permafrost distribution patterns, analyses are included for both sunny northern aspects and shaded southwestern aspects. A slope curvature threshold was incorporated to ensure that only pixels with a small change in aspect were included, minimizing the risk of erroneous measurements around sharp terrain features.

In the drier mountains east of the Main Divide, such as the Liebig and Ben Ohau Ranges, the MAV on steep southwestern aspects is positioned at around 2000 m, and is consistently 200 m lower than the estimated lower boundary of possible permafrost for these slopes. Closer towards the Main Divide, this difference increases to over 400 m as the rise in permafrost limits is not matched by any rise in MAV. In fact, the fluctuating MAV decreases closer to the Main Divide possibly as a function of large maritime snowfalls combined with the effects of geomorphic and glacial disturbances. On northern slope aspects the MAV averages 150 m higher than on southwestern aspects, with some greater differences measured nearer to the Main Divide, but never coming close to reflecting the much greater differences that are expected between permafrost limits on these contrasting slope aspects. The lack of any strong MAV pattern across the study region suggests that the usefulness of vegetation as an indicator of likely permafrost distribution is very limited in the Southern Alps of New Zealand. While the presence of vegetation confirms the absence of permafrost, the absence of vegetation offers very little conclusive information as to the distribution of permafrost, particularly nearer towards the Main Divide.

Discussion

Application of topo-climatic relationships established within the Swiss Alps to a more maritime alpine region characterized by extreme climate gradients produces many challenges. MAAT and lapse-rate calibration parameters used here are based on low-elevation climate stations located some distance from the Main Divide, and with the absence of additional data, climate gradients across the highest terrain cannot be modeled with certainty. A current study is suggesting that maximum precipitation might exist very close to, and even leeward to the Main Divide (Kerr et al. 2007), which would likely raise the estimated permafrost limits near to this region. In addition to the effect that climate gradients will have on local MAAT, associated differences in factors such as cloudiness and precipitation will also influence the amount of variation within the topo-climatic key from northern to southern aspects. Heavy snowfall and maritime cloud cover near the Main Divide will influence solar radiation patterns at the ground surface, which largely determine the aspect variation within the key. Therefore, the assumption of uniform variation between slope aspects across the study region must be reconsidered in a more advanced approach to modeling permafrost distribution.

Comparison of modeled permafrost distribution with rock glacier inventories is a well-established approach (e.g., Imhof 1996), but was restricted in the current study by the limited spatial distribution of these landforms. Modern earth imagery such as QuickBird has significantly improved the ability to recognize and map permafrost features, but some subjectivity and potential for error remains in determining active from inactive landforms and defining parameters such as the RGILA. Vegetation patterns in relation to climate gradients and permafrost distribution were explored here on the fundamental basis of being absent or present, but given the ecological diversity that exists across the Southern Alps, more useful patterns might be observed within individual species or by using the NDVI to explore topographic patterns in plant biomass (Gruber & Hoelzle 2001).

Recent large rock failures in the European Alps have suggested that permafrost degradation is a serious concern in relation to climate warming and slope instability (Gruber et al. 2004). In the Southern Alps of New Zealand, the summit collapse of Mount Cook in 1991 detached from a maximum elevation of 3720 m on an eastern exposition (McSaveney 2002). This is well above the estimated lower boundaries of possible permafrost where 20th Century thawing may be expected. However, the large rock buttress involved in the failure extended down to a much lower elevation, and in complex, steep topography, the effects of three-dimensional thermal gradients must also be considered because of contrasting temperatures between colder and much warmer sunny slope expositions of the terrain (Noetzli et al. 2007). Furthermore, bedrock temperatures are complicated by the presence of steep ice bodies because heat exchanges associated with surface melting can induce significant thermal anomalies within the underlying bedrock (Huggel et al. 2008). Of the other large rock avalanche events occurring in the region over the past 50 years, three originated from within the estimated permafrost terrain, while another was initiated from an elevation approximately 140 m below the estimated lower permafrost boundary. In addition, two recent fatal rockfall events near the summits of Mount Cook and Mount Sealy further south, have also originated from within the estimated permafrost terrain.

On the basis of this initial estimate of permafrost distribution and the uncertainties it has raised, a field campaign was initiated during November 2007 measuring the spatial variation of rock surface temperatures on steep bedrock slopes over a 12-month period. Following the methodologies developed by Gruber et al. (2003), 15 miniature temperature data loggers were installed at elevations ranging from 2400 m to 3150 m on various slope aspects both immediately on the Main Divide and on the drier Liebig Range towards the southeast. In addition, a series of high elevation air temperature loggers have been installed across the region to better establish relationships with the low elevation, long term records from the Mount Cook Village climate station. Information regarding the spatial distribution of rock surface temperatures will be used to more accurately model and validate permafrost distribution across the region.

Conclusions

A first-order approach for permafrost distribution mapping in the Mount Cook Region of New Zealand's Southern Alps has been presented. Towards the southeast of the region a drier, more continental climate prevails, and the permafrost estimate gives reasonable correspondence with the limited distribution of active and fossil rock glaciers. Closer towards the Main Divide where conditions are more humid, the lower boundary of permafrost distribution is expected to be significantly higher, but rock glaciers are absent here preventing any potential for local validation. Similarly, modeled vegetation altitudinal limits across the region showed no relationship with the climatic gradients which are expected to influence permafrost distribution. Future modeling will incorporate rock wall temperature data to facilitate permafrost modeling which better accounts for the effects of solar radiation and topographic shading in this complex, steep mountain environment.

Acknowledgments

This paper has benefited significantly from support provided by the Glaciology, Geomorphodynamics & Geochronology Group, Department of Geography, University of Zurich. In particular, Stephan Gruber and Martin Hoelzle are thanked for their suggestions and advice. Fieldwork for this project is funded by the New Zealand Earthquake Commission. We thank Ray Bellringer of the Department of Conservation for his project support. Three anonymous reviewers provided thoughtful suggestions for an improved manuscript.

References

Anderson, B. 2003. *The response of Ka Roimata o Hine Hukatere Franz Josef Glacier to climate change.* Unpublished PhD Thesis, University of Canterbury.

Augustinus, P. 2002. Periglacial research in New Zealand: a review. *South African Journal of Science* 98: 64-70.

Birkeland, P.W. 1982. Subdivision of Holocene glacial deposits, Ben Ohau Range, New Zealand, using relative dating methods. *Geological Society of America Bulletin* 93: 433-449.

Brazier, V., Kirkbride, M.P. & Owens, I.F. 1998. The relationship between climate and rock glacier distribution in the Ben Ohau Range, New Zealand. *Geografiska Annaler* 80 A(3-4): 193-207.

Chinn, T.J.H. 1996. New Zealand glacier responses to climate change in the past century. *New Zealand Journal of Geology and Geophysics* 39: 415-428.

Etzelmüller, B. & Hagen, J.O. 2005. Glacier-permafrost interaction in arctic and alpine mountain environments with examples from southern Norway and Svalbard. In: C. Harris and J.B. Murton (eds.), *Crysopheric Systems: Glaciers and Permafrost. Geological Society Special Publication No. 242*, London.

Etzelmüller, B., Hoelzle, M., Heggem, E.S.F., Isaksen, K., Mittaz, C., Vonder Mühll, D., Odegard, R.S., Haeberli, W. & Sollid, J.L. 2001. Mapping and modeling the occurrence and distribution of mountain permafrost. *Norwegian Journal of Geography* 55: 186-194.

Griffiths, G.A. & McSaveney, M.J. 1983. Distribution of mean annual precipitation across some steepland regions of New Zealand. *New Zealand Journal of Science* 26: 197-209.

Gruber, S. & Haeberli, W. 2007. Permafrost in steep bedrock slopes and its temperature-related destabilization following climate change. *Journal of Geophysical Research* 112, doi:10.1029/2006 JF000547.

Gruber, S. & Hoelzle, M. 2001. Statistical modeling of mountain permafrost distribution: Local calibration and incorporation of remotely sensed data. *Permafrost and Periglacial Processes* 12: 69-77.

Gruber, S., Hoelzle, M. & Haeberli, W. 2004. Permafrost thaw and destabilization of Alpine rock walls in the hot summer of 2003. *Geophysical Research Letters* 31:L13504.

Gruber, S., Peter, M., Hoelzle, M., Woodhatch, I. & Haeberli, W. 2003. Surface temperatures in steep alpine rock faces-a strategy for regional-scale measurement and modeling. *PERMAFROST, Proceedings of the Eighth International Conference on Permafrost 2003*. Zurich: Swets & Zeitlinger, 325-330.

Haeberli, W. 1975. Untersuchungen zur Verbreitung von Permafrost zwischen Fluelapass und Piz Grialetsch (Graubunden). *Mitteilungen der Versuchsanstalt für Wasserbau, Hydrologie und Glaziologie der ETH Zurich* 17: 221.

Haeberli, W. 1985. Creep of mountain permafrost: internal structure and flow of alpine rock glaciers. *Mitteilungen der Versuchsanstalt für Wasserbau, Hydrologie und Glaziologie der ETH Zurich* 77: 142.

Harris, C., Davies, M.C.R. & Etzelmüller B., 2001. The assessment of potential geotechnical hazards associated with mountain permafrost in a warming global climate. *Permafrost and Periglacial Processes* 12: 145-156.

Hoelzle, M., Mittaz, C., Etzelmüller, B. & Haeberli, W. 2001. Surface energy fluxes and distribution models of permafrost in European mountain areas: an overview of current developments. *Permafrost and Periglacial Processes* 12: 53-68.

Huggel, C., Caplan-Auerbach, J., Gruber, S., Molnia, B. & Wessels, R. 2008. The 2005 Mt. Steller, Alaska, rock-ice avalanche: A large slope failure in cold permafrost. *Proceedings of the Ninth International Conference on Permafrost, June 28–July 3, 2008, Fairbanks, Alaska.*

Imhof, M. 1996. Modeling and verification of the permafrost distribution in the Bernese Alps, Western Switzerland. *Permafrost and Periglacial Processes* 7: 267-280.

Jeanneret, F. 1975. Blockgletcher in den Südalpen Neuseelands. *Zeitschrift für Geomorphologie. NF* 19: 83-94.

Kerr, T., Owens, I. & Henderson, R. 2007. An extreme average annual precipitation gradient measured in a lee mountain catchment, South Island, New Zealand. *Geophysical Research Abstracts* 9(11607).

Kirkbride, M. & Brazier, V. 1995. On the sensitivity of Holocene talus-derived rock glaciers to climate change in the Ben Ohau Range, New Zealand. *Journal of Quarternary Science* 10: 353-365.

McGregor, V.R. 1967. Holocene moraines and rock glaciers in the central Ben Ohau Range, South Canterbury, New Zealand. *Journal of Glaciology* 6: 737-747.

McSaveney, M.J. 2002. Recent rockfalls and rock avalanches in Mount Cook National Park, New Zealand. *Geology Society of America, Reviews in Engineering Geology, XV*: 35-69.

Noetzli, J., Gruber, S., Kohl, T., Salzmann, N. & Haeberli, W. 2007. Three-dimensional distribution and evolution of permafrost temperatures in idealized high-mountain topography. *Journal of Geophysical Research* 112, doi:10.1029/2006JF000545.

Salinger, M.J. 1979. New Zealand climate: the temperature record, historical data and some agricultural implications. *Climate Change* 2: 109-126.

Soons, J.M. & Price, L.W. 1990. Periglacial phenomena in New Zealand. *Permafrost and Periglacial Processes* 1: 145-159.

The Perennial Springs of Axel Heiberg Island as an Analogue for Groundwater Discharge on Mars

Dale T. Andersen
Carl Sagan Center for the Study of Life in the Universe, SETI Institute, Mountain View, CA 94043, USA
Wayne H. Pollard
Department of Geography, McGill University, Montre´al, Que´bec, H3A 2K6, Canada
Christopher P. McKay
NASA Ames Research Center, Moffett Field, CA 94061, USA

Abstract

There are several regions on Earth where mean annual temperatures are well below freezing and yet liquid water persists. Such polar regions provide excellent analogues to study the hydrological cycle under conditions that have prevailed in the polar desert environment of Mars. In regions of continuous permafrost, fluxes of energy and water are strongly linked. However, most scientific studies of northern hydrology have been limited to surface process studies focusing on precipitation, snowmelt, evaporation, slope runoff, and stream flow. The springs located at Axel Heiberg Island provide insights into the limits of physical and biological processes associated with groundwater in cold polar deserts. These qualities make them valuable as analogues for groundwater activity on Mars. This paper summarizes the biophysical characteristics of several groups of perennial springs located in a range of settings on Axel Heiberg Island. Included are past and current hydrologic, microbiologic and geomorphic research and climate studies and their application as Mars analogues.

Keywords: astrobiology; groundwater; High Arctic; Mars; perennial springs; permafrost.

Introduction

Groundwater in regions of thick continuous permafrost

Several research groups have reported the occurrence of springs in the High Arctic. Spitsbergen, the largest island in the Svalbard archipelago, resides between 77° and 80°N where permafrost depths are estimated at 100–400 m. Roughly 60% of the island is covered in glaciers and a number of springs occur from Bockfjord in the northernmost part of the island to Sørkapp in the south (Banks et al. 1999, Lauritzen & Bottrell 1994). The Trollosen spring, a thermoglacial karst spring in South Spitsbergen, has a reported discharge rate of about 18 m^3/s of a turbid, 4°C water during the summer. Its flow is thought to originate from moulins on a glacier about 5 km distant. Nearby springs discharge water that is 12–15°C and seem to have a separate hydrothermal source with a subsurface temperature in the deep aquifer of at least 30°C (Lauritzen & Bottrell 1994). The thermal springs at Bockfjord are associated with local volcanic sources and geochemical evidence suggests that temperatures at depth reach between 130–180°C. They form travertine terraces with coatings of biofilms at the surface, and work is presently underway regarding the biological aspects of these springs primarily by the interdisciplinary, international Arctic Mars Analogue Svalbard Expedition (AMASE) team, which is creating a sampling and analysis strategy that could be used for future Mars research (Amundsen et al. 2004, Steele et al. 2004).

Grasby et al. (2003) have reported supraglacial sulfur springs located at 81°019′N, 81°359′W, in Borup Fiord Pass on northern Ellesmere Island in the Canadian high Arctic. Ten spring outlets were observed discharging from the surface of a 200 m thick glacier with active discharges estimated at 1 l/min at some locations and diffuse seeps elsewhere. The origins of the water were not reported, but a large ice-dammed lake located to the north of the spring sites may be a potential source along with basal melting of the glacier. To date, it is not clear if these springs are perennial or are seasonal. The spring outflows are located about 500 m from the terminus of the glacier depositing native sulfur, gypsum, and calcite onto precipitate mounds on top of the ice surface. Grasby et al. (2003) measured outflow temperatures of 1–2°C and reported smelling H_2S in and around the outlets. The water chemistry of the springs is different from local melt water with higher pH and conductivity values than local melt. Light and electron microscopy and culture-independent molecular methods provide evidence of a microbial community associated with the springs. The only other known perennial springs at these high latitudes are those located on Axel Heiberg Island in the Canadian high Arctic. We have identified several groups of perennial springs in a range of settings on Axel Heiberg Island located near the McGill Arctic Research Station (M.A.R.S.); the purpose of this paper is to describe these sites and review the research activities associated with them.

Study Site

Axel Heiberg Island

Axel Heiberg Island (Fig. 1) resides within the Sverdrup Basin, a pericratonic sedimentary trough encompassing roughly 313,000 km^2 and located within the Arctic Archipelago (Pollard et al. 1999). The axis of the basin strikes northeasterly from the Sabine Peninsula on Melville Island to the northwestern region of Ellesmere Island. Axel Heiberg is geologically complex, consisting of folded and faulted sedimentary rocks ranging

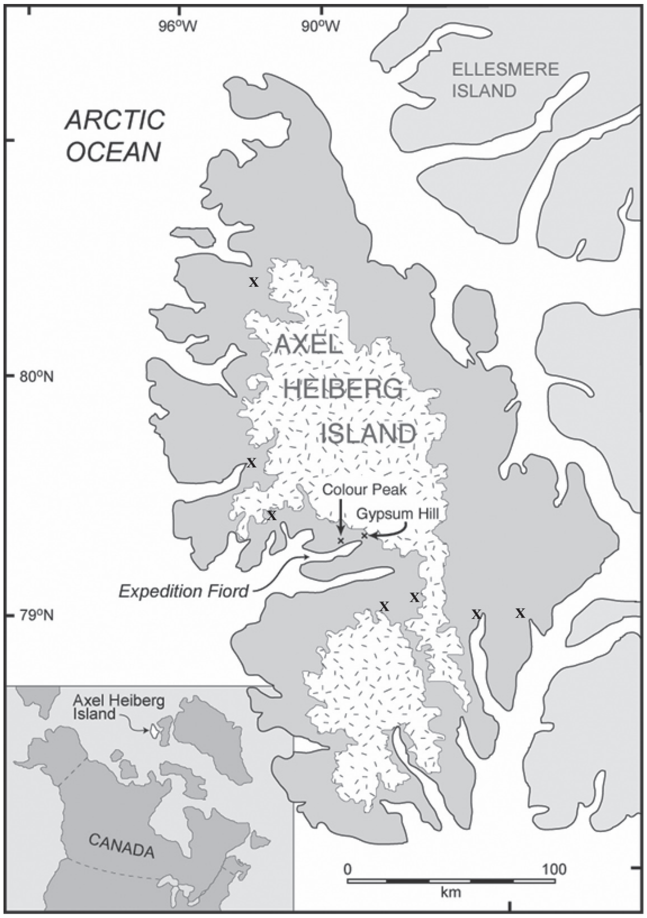

Figure 1. Map of Axel Heiberg Island. The x-marks show approximate locations of perennial springs.

from Triassic to Tertiary in age. Late Paleozoic evaporites locally intrude the overlying sedimentary/clastic rocks in a series of exposed piercement structures that occur mainly in line with the basin axis (Stephenson et al. 1992). The intrusions of the evaporites are typically associated with early Tertiary (Innuitian) orogenic activity and are mapped as Tertiary (Otto Fiord Formation) by Thornsteinsson (1971). However, the emplacement of the anhydrite structures at Expedition Fiord took place during an earlier tectonic phase prior to the mid Cretaceous (Embry & Osadetz 1988, Stephenson et al. 1992). Quaternary stream, deltaic, marine, and glacial sediments cover the valley floors and form raised shorelines.

There is considerable relief near the head of Expedition Fiord with peaks approximately 2000 m a.s.l. that decrease toward the fiord mouth. Breached anticlines produce asymmetrical ridges characterized by steep (70–80°) scarp faces and 25–35° dip slopes. In some locations, piercement structures create more regular and symmetrical hill and mountain features. Weathering of gypsum and anhydrite outcrops has given the diapirs very ragged, serrated profiles. Resistant volcanic sills and dikes have differentially eroded, leading to steep slopes mantled with coarse angular talus.

Glaciers currently cover 30–35% of Axel Heiberg Island, including the Stacie and Müller (McGill) Ice Caps and numerous outlet and valley glaciers. Small ice caps and isolated cirque and valley glaciers are widespread. At Expedition Fiord, the

	1998	1999	2000	2001	2002
January	-31.96	-32.6	-31.16	-32.42	-33.4
February	-34.38	-27.86	-23.83	-33.76	-35.24
March	-28.48	-17.89	-15.94	-30.02	-31.02
April	-16.65	-4.68	-4.88	-20.8	-25.07
May	-5.47	5.17	6.82	-10.13	-6.26
June	5.39	9.55	6.64	2.3	1.98
July	7.36	0.29	-2.64	5.23	4.42
August	2.86	-9.68	-13.88	3.34	4.08
September	0.1	-25.34	-23.89	-5.92	-2.61
October	-15.27	-31.69	-25.7	-20.3	-10.07
November	-23.55	-35.03	-24.48	-23.53	-26.93
December	-33.33	-35.58	-22.1	-26.28	-24.08
Mean	-14.45	-17.11	-14.59	-16.02	-15.35

Table 1a Mean Temp 1998-2002: -15.50 ¡C

	1998	1999	2000	2001	2002
January	0	0	0	0	0
February	0	0	0	0	0
March	0	0	0	0	0
April	1.07	10	17.65	0	0
May	7.79	160.68	211.4	2.7	4.65
June	162.13	286.55	207.19	92.62	83.51
July	228.66	57.35	20.62	163.09	135.61
August	91.36	0.29	0	114.09	128.17
September	36.51	0	0	7.89	13.34
October	0	0	0	0	8.96
November	0	0	0	0	0
December	0	0	0	0	0
Total	527.52	514.87	456.86	380.39	374.24

Table 1b Thawing index

	1998	1999	2000	2001	2002
January	-990.7	- 1010.57	-965.81	- 1004.93	- 1035.31
February	-962.77	-780.15	-690.93	-945.34	-986.78
March	-882.79	-554.66	-494.18	-930.57	-961.77
April	-500.69	-150.44	-164.06	-624.09	-752.15
May	-176.43	-0.46	-0.07	-316.71	-198.68
June	-0.53	0	-8.12	-23.67	-25.12
July	-0.36	-48.27	-102.42	-1.03	-1.19
August	-2.8	-300.44	-430.37	-10.69	-1.72
September	-33.6	-760.32	-716.74	-185.55	-91.62
October	-473.34	-982.51	-796.72	-629.34	-321.25
November	-706.5	-1050.9	-734.33	-705.98	-807.98
December	-1033.3	-1102.8	-685.04	-814.7	-746.61
Total	-5763.8	-6741.6	-5788.8	-6192.6	-5930.2

Table 1c Freezing index

Figure 2. Gypsum Hill Springs, "Little Black Pond."

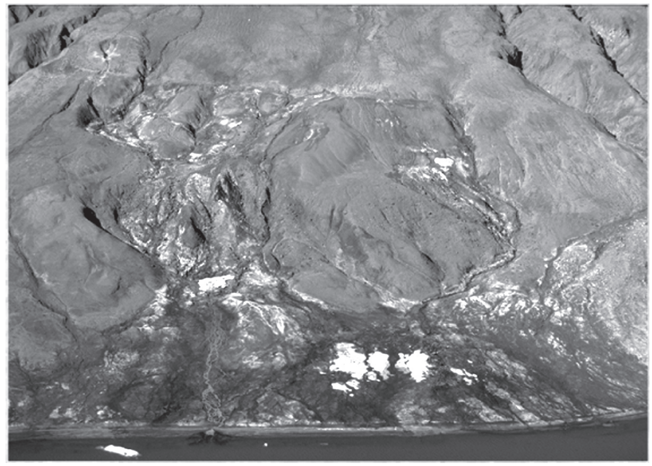

Figure 3. Colour Peak Springs.

White and Thompson glaciers converge roughly 10 km up valley from the head of the fiord, while the terminus of Crusoe glacier lies only a few kilometers west of the Expedition River Valley.

Climate/permafrost

The north and northwest Arctic Archipelago is characterized by polar desert conditions displaying very cold, dry winters and cool summers with maximum precipitation occurring in July. Intermittent climate records for the Expedition Fiord locale are available for the last 47 years, with a more complete record for the last 17 years.

Year-round data from an automatic weather station at Colour Lake (elevation 64 m a.s.l.) has been collected since 1992 indicates a mean annual temperature of -15.5°C with approximately 451 thawing degree-days and 6083 freezing degree-days during an average year (Andersen et al., this study). Tables 1a, 1b, and 1c list the mean average temperatures, thawing, and freezing index (degree-days below and above freezing) for each month during the years 1998–2002.

Permafrost depth has not been measured directly at Expedition Fiord; however, a permafrost thickness of > 400 m was documented in an exploration well at Mokka Fiord on the east side of Axel Heiberg Island, roughly 60 km from Expedition Fiord (Andersen 2004). Other exploration wells in the area reveal that permafrost is generally between 400–600 m thick. Permafrost features include extensive polygonal ice wedge development in unconsolidated fluvial and colluvial deposits at lower elevations.

McGill Arctic Research Station (M.A.R.S.)

The McGill Arctic Research Station is located 8 km inland at Expedition Fiord, Nunavut, on Central Axel Heiberg Island in the Canadian High Arctic (approximately 79º26′N, 90°46′W). Established in 1960 on the shores of Colour Lake, M.A.R.S. is one of the longest-operating seasonal field research facilities in the High Arctic, providing access to glacier, ice cap, and polar desert and tundra environments. Researchers utilizing M.A.R.S. have accumulated the longest continuous mass balance record for any High Arctic glacier (White Glacier). Past and current research conducted at the various springs has been carried out with support of this facility. The geomorphology, climate, chemistry and microbiology of the Gypsum Hill and Colour Peak Springs have been previously described by Pollard et al. (1999), Pollard (2005), Andersen et al. (2002), Heldmann et al. (2005a, b), Omelon et al. (2006) and Perreault et al. (2007), respectively.

Gypsum Hill springs: N79°24.247′, W090°43.968′

The Gypsum Hill spring site (Fig. 2) consists of approximately 40 springs and seeps on the northeast side of Expedition River, discharging along a band nearly 300 m long and 30 m wide between 10–20 m a.s.l. The springs are concentrated at the break in slope where bouldery colluvial materials overlap sandy outwash. The surface around the springs is littered by large boulders from both the till and exposed anhydrite. The area immediately surrounding the springs consists of small mounds separated by shallow gullies. There are outflows occurring in Expedition River; however, thick ice and snow in the winter and high stream flows during the summer have prevented determination of their exact locations. Pollard et al. (1999) estimated the total discharge of the Gypsum Hill Springs to be approximately 10–15 l/s. Spring outflow temperatures range from -0.5°C to 7°C. Major ion chemistry of the spring water is listed in Table 2. Analysis of the dissolved gases and bubbles in the spring water indicates that the source of the water is likely to be a combination of subglacial melt and lake water (Andersen 2004). Two nearby glacially-dammed alpine lakes, Phantom Lake and Astro Lake, provide large reservoirs of water and have basins residing upon gypsum-anhydrite piercement structures. Lake water is transported into the subsurface via permeable strata associated with the piercement structures. The water continues to flow along the subsurface salt strata to the spring sites, accumulating dissolved salts as it flows through this subsurface layer.

The composition of dissolved gases in the springs indicates that only 50% of the water comes from lake water and that the other 50% comes from glacial ice that has melted while isolated from the atmosphere. The dissolved gases in lake water reflect the equilibrium with the atmosphere based on the relative solubility of each gas. In contrast, air trapped in glacial

Table 2. Major ion chemistry of the spring water collected at Colour Peak, Gypsum Hill and Stolz Diapir outlets. *ORP values are reported as mV normalized to a hydrogen electrode (NHE).

	Colour Peak spring	Gypsum Hill spring	Stolz Diapir spring
Temperature (°C)	6.4	6.6	-1.05
pH	6.82	7.66	6.70
ORP (mV, NHE)*	-122.4	-97.1	--
Conductivity (mS/cm)	170	105	640
Density (g/cm^3)	1.114	1.056	--
Ca^{2+} (all in mol/kg)	0.0905	0.0574	0.032
Mg^{2+}	0.0130	0.0049	LDL
Na^+	2.30	1.5043	5.217
K^+	0.0048	0.0015	0.003
Cl^-	1.9324	1.0732	5.127
SO_4^{2-}	0.0240	0.0385	0.44
PO_4^{3-}	<0.5 mg/l	<0.5 mg/l	<0.5 mg/l
NO_3^-	0.001	LDL	LDL
DIC (mmol/l)	0.278	0.389	6.09
DOC (mg/l)	<0.2 mg/l	<0.2 mg/l	2.050
Alkalinity	0.0184	0.0155	--

ice has an atmospheric composition other than for Ne and He. These latter two gases are soluble in ice and would therefore be expected to diffuse through the ice. As an example, the ratio of N_2/Ar in lake water in equilibrium with the atmosphere is 37 while for air it is 84.

Colour Peak springs: N79°22.866', W091°16.270'

The Colour Peak Springs (Fig. 3) are located on the south-facing slope of Colour Peak at an approximate elevation of 100 m a.s.l., emerging from the top of the slope along a line nearly 400 m long. These springs are grouped into three distinct topographically controlled areas with 20 vents discharging directly into Expedition Fiord 300 m down slope. Major ion chemistry of the spring water is listed in Table 2. Interestingly, the springs on Axel Heiberg Island flow all year with little variation in their temperature and are not associated with volcanic activity.

Andersen et al. (2002) show that this can be explained by considering the flow through the subsurface salt layers. The flow enters the subsurface via the permeable strata associated with the salt diapirs that reside beneath the lakes, glaciers, and ice cap. At this depth the groundwater temperature is 0°C. The flow then proceeds below the surface to depths of at least 600 m and is warmed by the local geothermal gradient to temperatures up to 6°C. The flow rate to the surface is rapid enough that the temperature of the emerging groundwater does not change significantly from its initial value at depth.

Perreault et al. (2007) have speculated that sulfur-based metabolism may be the major source of biological energy production in these environments. Surveys of the microbial diversity in the sediments of these springs were conducted by

Figure 4. Wolf Diapir Springs.

analyzing denaturing gradient gel electrophoresis (DGGE) and clone libraries of 16S rRNA genes amplified with Bacteria and Archaea-specific primers. Dendrogram analysis of the DGGE banding patterns divided the springs into two clusters based on their geographic origin. Bacterial 16S rRNA clone sequences from the Gypsum Hill library (spring GH-4) classified into seven phyla (Actinobacteria, Bacteroidetes, Firmicutes, Gemmatimonadetes, Proteobacteria, Spirochaetes, Verrucomicrobia); δ- and γ-Proteobacteria sequences represented half of the clone library. Sequences related to Proteobacteria (82%), Firmicutes (9%), and Bacteroidetes (6%) constituted 97% of the bacterial clone library from Colour Peak (spring CP-1). Most GH-4 archaeal clone sequences (79%) were related to the Crenarchaeota while half of the CP-1 sequences were related to orders Halobacteriales and Methanosarcinales of the Euryarchaeota. Sequences related to the sulfur-oxidizing bacterium Thiomicrospira psychrophila dominated both GH-4 (19%) and CP-1 (45%) bacterial libraries and 56-76% of the bacterial sequences were from potential sulfur-metabolizing bacteria.

Skaare Fiord Springs: N78°56.702', W088°17.666'

Sub-glacial discharge has been observed at an alpine glacier near the northeastern end of Skaare Fiord. The flow was discovered by Twin Otter pilots flying over the glacier during April 2002 when air temperatures were still well below freezing. Initial reconnaissance during the summer found an icing that was approximately 0.5km in diameter with red-tinted fine sediments covering the surface. The discharge was flowing from the central area of the icing at a rate of ~250 ml/sec, the water tasting strongly of iron, but not saline.

East Fiord springs: N79°30.109', W093°25.716'

In April 2007 during a wildlife survey, biologists from the Canadian Department of Environment reported to our research team a reddish staining on a glacier in the vicinity of East Fiord. Subsequent exploration of the area by helicopter located a large icing, stained with an iron-rich precipitate forming on and draping over the north edge of the unnamed glacier. Water was observed to be flowing from a series of outlets on top of the glacier about 20 m from the edge.

Figure 5. Stolz Diapir Spring

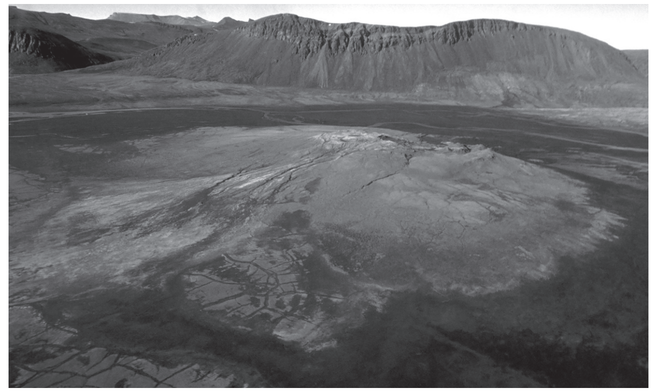

Figure 6. Middle Fiord Pingo with active outflow.

Wolf Diapir springs: N79°04.285', W090°12.755'

The Wolf Diapir site is characterized by a large mound of salt 3m in height and 3m in diameter that forms "fumarole-like" structure (Fig. 4). A saltpan extends about 0.5 km to the west. Water is present as a pool in the central portion of the structure, and during the winter months as temperatures decrease, the water level builds up and flows out and over the top producing a series of small terraces and rim pools on the NNE side of the structure. Increasing air temperatures in the summer allow for the dissolution of the salts (such as hydrohalite), and the spring water breaks through the sides and is released at the base lowering the water level. During July 2004, water flowing beneath and through the side of the structure was saline with a temperature of -3.5°C, pH of 6.4, and ORP of 60.0 (mV, NHE). Hydrogen sulfide was present in and around the discharge site.

Nine km SW of the Wolf Diapir Spring, a saline stream originating from beneath a landslide deposit with a flow rate of a flow of 10–12 L l/ss^{-1} occurs in the vicinity of Junction Diapir, originating on the south side of the dome and bounded by the Steacie Ice Cap. It has not been determined if this flow is perennial.

Stolz Diapir Springs: N79°05.343', W87°02.228'

At Whitsunday Bay a single spring discharges approximately 150 m up the south east side of Stolz Diapir and flows along a deep valley for 200m before it fans onto the Whitsunday River plain (Fig. 5). The position of the outflow moves up and down slope from year to year. Discharge is fairly constant at 40–50 l s^{-1} and the discharge temperature is constant at 1.2°C. Major ion chemistry of the spring water is listed in Table 2. In some years the outflow is marked by a single well-defined vent 40–50 cm in diameter while in others the outflow permeates through a layer of colluvial debris. This hypersaline spring produces a salt tufa deposit up to 5 m thick near the spring outlet and 1m thick near the valley mouth. In winter hydrohalite ($NaCl \cdot 2H_2O$) precipitates form a series of pool and barrage structures that staircase down the outflow channel. Several pools up to 10m wide and 3–5 m deep allow the water to cool in stages as it works its way down the valley with temperatures ranging from -10°C to -17°C in pools near the outlet to the eutectic point of the salts on the floodplain. The hydrohalite deposit merges with a fan-shaped icing that spreads on to the Whitsunday river flood plain. The source of recharge for the spring appears to be snowmelt that flows into and through the dome on the north west side of the diapir. The inflowing water is fresh, low conductivity (58.3 μS/cm) and near neutral pH (6.9). The inflowing water picks up the salts via dissolution of halite, which is present as large deposits at and near the surface of the diapir.

Bunde Fiord Ssprings: N80°22.749', W93°57.584'

Approximately 16 km SSW of Bunde Fiord, a large rectangular icing fills an east-west trending river channel where it dissects the northern edge of an anhydrite diapir abutting the far northwest end of the Mueller Ice Cap. The icing is roughly 200 m by 100 m, 2 m thick, and covered with a thick paste of precipitates and evaporates. The icing forms as a result of perennial flow from a series of small springs that exit the diapir 10–20 m above the base. The discharge is saline and flows into a small stream where it mixes with meltwater from local glacial sources. The stream contains numerous filamentous brown mats consisting of pennate diatoms.

Middle Fiord pingo: N79°43.653', W94°13.794'

At Middle Fiord a small spring flows from the side of a large pingo situated in the middle of a large floodplain 3 km downstream from Middle Fiord Glacier (Fig. 9). The pingo is 110 m in diameter and 20m high and is composed entirely of medium-grained sand and fine gravel. Water discharges at 0.5 to 1.2 l/s and at a temperature of 1.2°C from two or three closely-spaced outlets midway up the west side of the pingo.

Mars

Groundwater and the search for life on Mars

Despite the vast differences between the two planets today, Mars and Earth may have been much more similar early in their histories. If life developed on Mars as it did on early Earth, it may have faced an untimely extinction as the cryosphere of Mars enveloped the entire planet, its atmosphere thinned, and liquid water ceased to exist at the surface; or perhaps it has retreated to subsurface refugia. Nonetheless, even when Mars was wet it was probably cold. Thus the hydrological cycle in the coldest regions on Earth provides the best analog for a Martian hydrology. From studies of springs, rivers, and lakes in the polar regions, quantitative models have been developed that show how liquid water could have persisted on Mars even if mean annual temperatures were below freezing (Lee et al. 2001, Andersen et al. 2002, Heldmann et al. 2005a, b, McKay et al. 2004).

Springs, residual icings, pingos, and massive ground-ice deposits located in the Arctic (and Antarctic) provide opportunities to study microbial ecosystems in extreme polar environments. The ranges in temperature, pH, redox, nutrient availability, and the large seasonal variations in light have undoubtedly shaped the structure and function of the ecosystem as well as impacting the biological record left in the sediments. The planet Mars may have once hosted microbial ecosystems in a physical setting not too dissimilar to the Earth's polar regions. Determining the nature of the early Martian climate, the existence of subsurface water, or whether Mars ever gave rise to life will be aided by studies of terrestrial microbial ecosystems in regions of thick, continuous permafrost.

Acknowledgments

The authors acknowledge the support for fieldwork by the Canadian Polar Continental Shelf Project. The authors also wish to acknowledge support provided by NASA's Exobiology program, the Canadian Space Agency, the McGill University High Arctic Research Station, and the Natural Sciences and Engineering Research Council of Canada. Additional funding for student research was provided by the Department of Indian and Northern Affairs, Northern Scientific Training Program, and the McGill University Centre for Climate and Global Change Research.

References

Amundsen, H., Steele, A., Fogel, M., Mysen, B., Kiehle, J., Schweizer, M., Toporski, J. & Treiman, A. 2004. Life in a Mars analogue: Microbial activity associated with carbonate cemented lava breccia from NW Spitsbergen [Abstract]. *Fourteenth Annual V.M. Goldschmidt-Conference. Geochimica et Cosmochimica Acta 68 (11, Supplement 1):* A804.

Andersen, D. 2004. *Perennial springs in the Canadian High Arctic: Analogs of Martian hydrothermal systems*. Ph.D. Thesis. McGill University, Montreal.

Andersen D., Pollard W., McKay C., & Heldmann, J. 2002. Cold springs in permafrost on Earth and Mars. *J. Geophys. Res.* 10: 1029/2000JE001436.

Banks, D., Sletten, R.S., Haldorsen, S., Dale, B., Heim, M. & Swensen, B. 1998. The thermal springs of Bockfjord, Svalbard: occurrence and major ion hydrochemistry. *Geothermics* 27:445-467.

Embry, A.F. & Osadetz, K.G. 1988. Stratigraphy and tectonic significance of Cretaceous volcanism in the Queen Elizabeth Islands, Canadian Arctic Archipelago. *Can. J. Earth Sci.* 25: 1209-1219.

Gilichinsky, D., Rivkina, E., Bakermans, C., Shcherbakova, V., Petrovskaya, L., Ozerskaya, S., Ivanushkina, N., Kochkina, G., Laurinavichuis, K., Pecheritsina, S., Fattakhova, R. & Tiedje, J. 2005. *Biodiversity of cryopegs in permafrost. FEMS Microbiol. Ecol.* 53(1): 117-128.

Grasby, S.E., Allen, C.C., Longazo, T.G., Lisle, J.T., Griffin, D.W. & Beauchamp, B. 2003. Supraglacial sulfur springs and associated biological activity in the Canadian high arctic-signs of life beneath the ice. *Astrobiology* 3(3): 583-596.

Heldmann, J.L., Toon, O.B., Pollard, W.H., Mellon, M.T., Pitlick, J., McKay, C.P. & Andersen, D.T. 2005a. Formation of Martian gullies by the action of liquid water flowing under current Martian environmental conditions, *J. Geophys. Res.* 110: E05004, doi: 10.1029/2004JE002261.

Heldmann, J.L., Pollard, W.H., McKay, C.P., Andersen, D.T. & Toon, O.B. 2005b. Annual development cycle of an icing deposit and associated perennial spring activity on Axel Heiberg Island, Canadian High Arctic. *Arctic, Antarctic and Alpine Research* 37(1): 127-135.

Lauritzen, S.E. & Bottrell, S. 1994. Microbiological activity in thermoglacial karst springs, South Spitsbergen. *Geomicrobiology Journal* 12:161-173.

Lee, P., Cockell, C., Marinova, M., McKay, C. & Rice, J. 2001. Snow and ice melt flow features on Devon Island, Nunavut, Arctic Canada as possible analogs for recent slope flow features on Mars. Abstract #1809. *Lunar & Planetary Science Conference XXXII, March 2001*.

McKay, C., Andersen, D., Pollard, W.H., Heldmann, J., Doran, P., Fritsen, C. & Priscu, J. 2004. Polar Lakes, Streams, and Springs as Analogs for the Hydrological Cycle on Mars. In: T. Tokano (ed.), *Water on Mars and Life.* Berlin: Springer-Verlag, 219-233.

Omelon, C., Pollard, W. & Andersen, D. 2006. Geochemical evolution of perennial springs and the formation of travertines at Expedition Fiord Canadian High Arctic. *Applied Geochemistry* 21, 1-15.

Perreault, N., Andersen, D.T., Pollard, W.H., Greer, C.W. & Whyte, L.G. 2007. Culture independent analyses of microbial biodiversity in cold saline perrenial springs in the Canadian High Arctic. *Applied and Environmental Microbiology* 73(5): 1532-1543.

Pollard, W.H. 2005. Icing processes associated with high arctic perennial springs on Axel Heiberg Island. *Permafrost and Periglacial Processes* 16: 51-68.

Pollard W.H., Omelon, C., Andersen, D.T. & McKay, C.P. 1999. Perennial spring occurrence in the Expedition Fiord area of Western Axel Heiberg Island, Canadian High Arctic. *Canadian J. Earth Sci.* 36: 1-16.

Steele, A., Schweizer, M., Amundsen, H. & Wainwright, N. 2004. In-field testing of life detection instruments and protocols in a Mars analogue arctic environment [Abstract]. AbSciCon 2004, NASA Ames Research Center, Moffett Field, CA. *International Journal of Astrobiology, Supplement 1 (March)*: 24.

Stephenson, R., VanBerkel, J. & Cloethingh, S. 1992. Relation between salt diapirism and tectonic history of the Sverdrup Basin, Arctic Canada. *Canadian Journal of Earth Sciences* 29: 2640–2652.

Thorsteinsson, R. 1971. *Geology of Strand Fiord, District of Franklin.* 1:250,000. Map 1301A. Geological Survey of Canada. Map 1301A, scale 1: 250,000.

Geotechnical Considerations For Cut-Off Wall in Warm Permafrost

Steven L. Anderson, P.E.
Senior Geotechnical Engineer and Associate, Golder Associates Inc., Anchorage, AK
Thomas G. Krzewinski, P.E.
Senior Geotechnical Engineering Consultant and Principal, Golder Associates Inc., Anchorage, AK
Jim Swendseid, P.E.
Senior Mine Engineer, Teck Cominco Alaska Inc.

Abstract

A cut-off wall back dam has been designed for the existing tailings impoundment at the Red Dog Mine, Alaska. The planned cut-off wall, which is about 5,000 ft long and up to 170 ft deep, is located in an area of warm permafrost that consists of colluvium and alluvial materials overlying shale bedrock. The geotechnical program included a total of 41 boreholes on either side of the cut-off wall alignment. Geotechnical considerations included ice-rich and organic materials up to 19 ft thick and establishing design depths for the cut-off wall in frozen shale. These geotechnical issues have been addressed through a stable embankment design and deep excavation technology. Instrumentation and monitoring will be used to monitor the performance of the cut-off wall after construction is completed in the next two years.

Keywords: cut-off wall; dam design; geotechnical investigation; trench cutter.

Introduction

Teck Cominco Alaska Inc. (TCAK) commissioned Golder Associates (Golder) to design a Back Dam to minimize the potential for seepage at the southern end of the tailings impoundment at Red Dog Mine, Alaska. The Back Dam was designed for an elevation of 960 ft with a planned closure elevation of 986 ft.

The Red Dog Mine is located approximately 90 miles north of Kotzebue, Alaska at about 68 degrees latitude. The proposed Back Dam is located at the north end of the Overburden Stockpile, as shown in Figures 1 and 2.

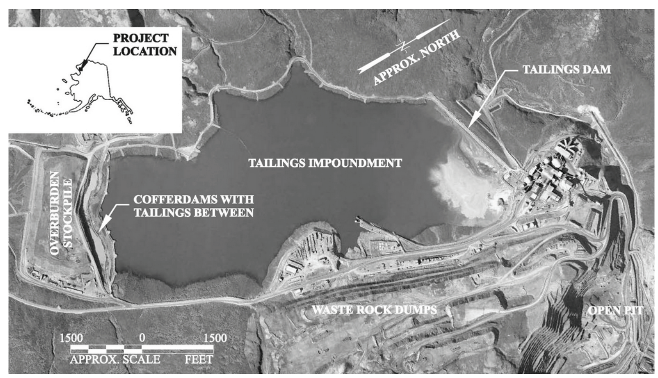

Figure 1: Back Dam location.

Background

Since 2002, the Back Dam design progressed through several stages and several options for reducing the seepage potential were reviewed. The initial design concept included construction of a cofferdam and installing a geomembrane liner on the upstream face of the Overburden Stockpile that would be keyed into silty native soil of relatively low permeability. Subsequently, TCAK constructed two waste rock cofferdams with a layer of geotextile and tailings placed between and a geotechnical investigation was performed by Golder in 2004 to verify the engineering parameters and assumptions used in the design. Based on the 2004 investigation results, ice-rich and organic materials were encountered below the proposed geomembrane liner and highly fractured bedrock was found near the liner key-in elevations.

During revision of the Back Dam design to account for the findings of the 2004 investigation, TCAK requested that the design should incorporate a cut-off to low permeability bedrock to reduce the risk of long-term seepage through the native materials and weathered bedrock. Several cut-off wall options were evaluated such as grouting, deep soil mixing, sheet piles, vibrated beam, a slurry trench, extending the geomembrane liner into a trench, and using a Bauer Cutter Soil Mixer (CSM). The option selected included constructing the cut-off wall with the Bauer CSM through an embankment between the Overburden Stockpile and the cofferdams.

In 2005 and 2006, Golder performed another geotechnical investigation along the southern cofferdam to determine the depth to low permeability bedrock. Ice-rich materials and organics were also encountered during this investigation and the low permeability bedrock was found to be up to about 170 ft below the proposed dam crest elevation of 960 ft.

Following the geotechnical investigation, the Bauer CSM was withdrawn as an option due to its very low production rates through rock and the amount of rock excavation expected. The Bauer CSM was replaced by a Bauer Trench Cutter.

Site Characteristics

Climate

The climate at the Red Dog Mine is characterized by long, cold winters and moderately warm, windy and somewhat rainy summers. The average annual temperature is 24°F (-4°C) with an air freezing index (AFI) of 4731°F-days and an air thawing index (ATI) of 1899°F-days. Total precipitation is generally between 10 to 13 inches per year and the average annual snowfall is 48 inches.

Thermal conditions

In the early 1980s the Red Dog Mine site was the subject of various feasibility and design studies. During this timeframe, approximately 50 thermistor strings were installed in geotechnical boreholes to provide information on the subsurface thermal regime of the area. These early readings are summarized in a monograph produced by the American Society of Civil Engineers (ASCE) (Hammer et al. 1985) that indicated relatively warm permafrost was present at the mine site and that surface water and shallow groundwater greatly influenced the thermal stability of the permafrost soils. Significant thaw bulbs were delineated surrounding streams in the area and the average temperature in a given area was significantly increased by poor drainage conditions and/or exposure to sunlight. In shaded areas with good drainage, temperatures averaged as low as 25°F (-3.9°C). In exposed areas with poor drainage, temperatures averaged as high as 31°F (-0.6°C) in frozen soils and some very poorly drained exposed areas found no permafrost present (to the depths explored).

Between 1995 and 1997, seven thermistor strings were installed within the Overburden Stockpile. Temperature readings from these thermistor strings indicate the permafrost has aggraded into portions of the stockpile and the depth to the top of permafrost varied between about 15 ft to 70 ft below the ground surface (Water Management Consultants 1999).

Thermistor readings were also taken during the 2005/2006 geotechnical investigation that indicated an average thaw depth of 18 ft below the native soil surface and average permafrost temperatures of about 31°F (-0.6°C). The deepest thaw depths were located near historic drainages.

Geology

The Overburden Stockpile site is reported to be generally underlain by a layer of unconsolidated, ice-rich, colluvial deposits, and interbedded Cretaceous age shale with inclusions of dark grey to brown sandstone.

Subsurface conditions

Subsurface conditions have been characterized near the proposed cut-off wall location from the geotechnical investigations performed in 2004 through 2006 that included 15 boreholes near the north face of the Overburden Stockpile and 26 boreholes along the southern cofferdam and near the abutments. The locations of these boreholes are shown in Figure 2 with subsurface profiles shown in Figures 3 and 4. These investigations also included test pits, thermistor string readings, packer tests, and laboratory testing.

- Fill materials were encountered on the haul roads, cofferdam, and Overburden Stockpile. The waste rock fill materials at the haul road and cofferdam generally had a composition of silty gravelly soil with occasional cobbles and boulders. Fill materials at the Overburden Stockpile mainly consist of Kivalina shale that had been stripped from the mining area.
- The native soils are colluvial and alluvial materials comprised of organic soil, ice and ice-rich soil, silty clayey soil and sandy gravelly soil.
    - Ice-rich and organic materials up to 14 ft and 19 ft thick were encountered near the cut-off wall alignment and below the Overburden Stockpile, respectively.
    - The silty clayey soil was loose to compact when thawed, averaged about 6 ft thick and generally thinned out toward the east.
    - The sandy and gravelly soil consists of silty sands to poorly graded sands and gravels that were typically compact to dense when thawed.
- The shale bedrock underlying the colluvial and alluvial materials was typically highly to completely weathered near the contact surface and became fresher with depth. The rock was generally fractured with a rock quality designation (RQD) of less than 20%. Rock strengths varied from weak (R2) to very strong (R5) with estimated uniaxial compressive strengths (UCS) up to 22,010 psi. The majority of bedrock encountered, about 75%, had a UCS less than 7,500 psi.

Design Considerations

Cut-off wall alignment

The cut-off wall alignment was selected to limit the amount of excavation into the Overburden Stockpile and minimize disturbance of the cofferdam. Using an excavation surface derived from the borehole and ground topography data, an alignment for the cut-off wall was developed based on the criteria that included:

- Maintaining the cut-off wall within the center of the constructed embankment to protect the cut-off wall from slope instability issues.
- Using 1H:2V (horizontal to vertical) slopes for the excavation prism starting a distance of 1.5 ft out from the alignment centerline at an elevation of 986 ft. The offset distance was based on a 3 ft cut-off wall width and the slope angle was based on the 2 to 1 stress distribution method, which is an empirical approach based on the assumption that the area over which the load acts increases in a systematic way with depth.

Cut slopes were developed based on natural slope angles with flatter cut slopes expected on the northern side of the alignment within the impoundment area. A limited amount of excavation into the cofferdam was considered tolerable depending on the seepage flows encountered after dewatering.

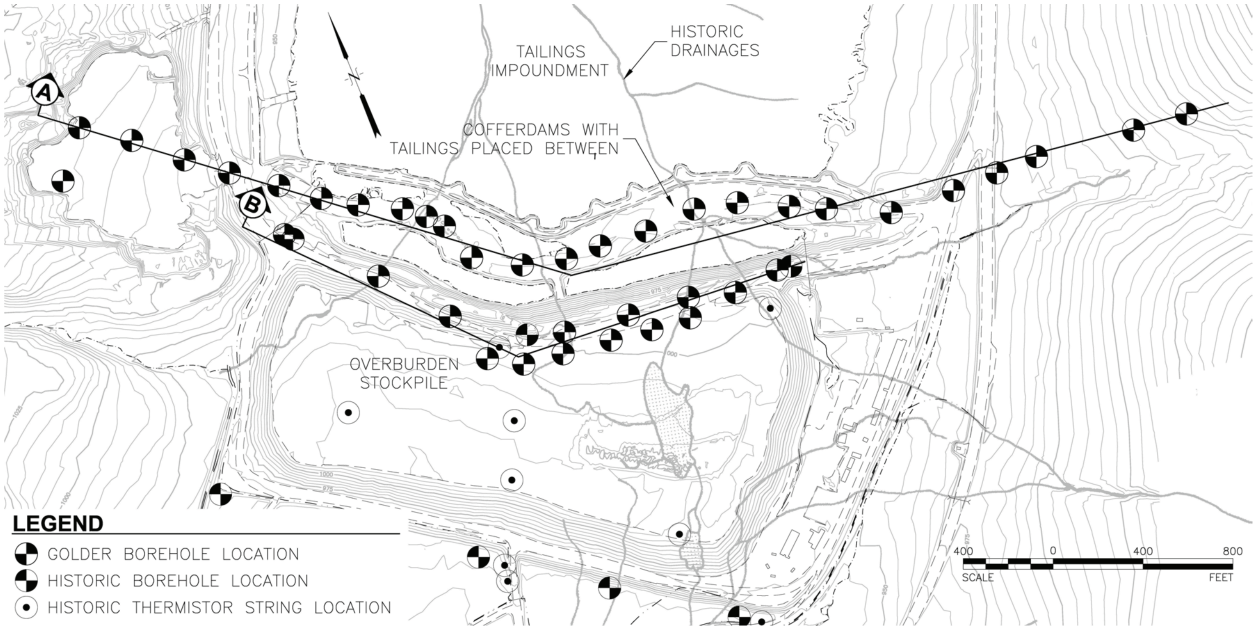

Figure 2. Borehole locations.

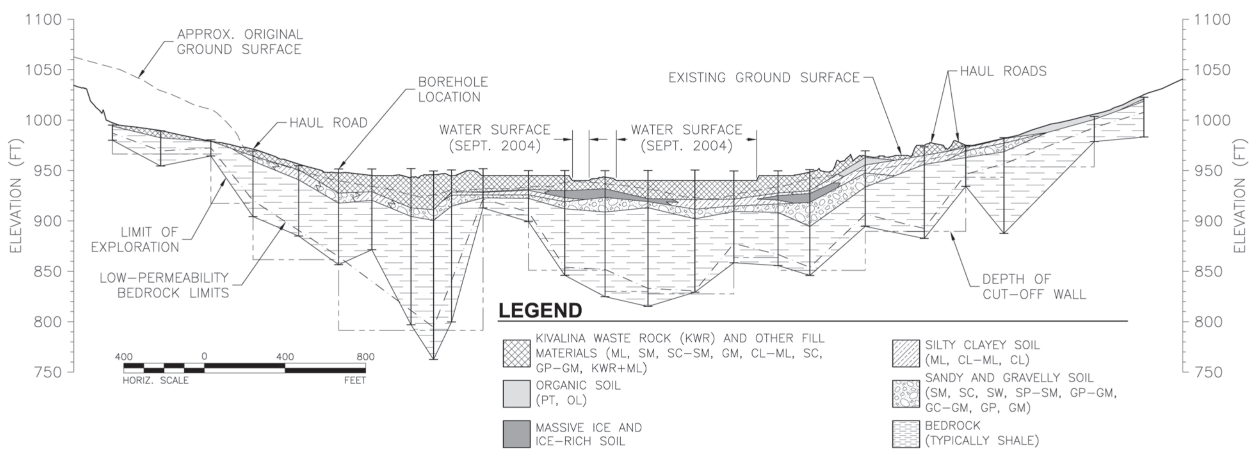

Figure 3. Section A through cofferdam.

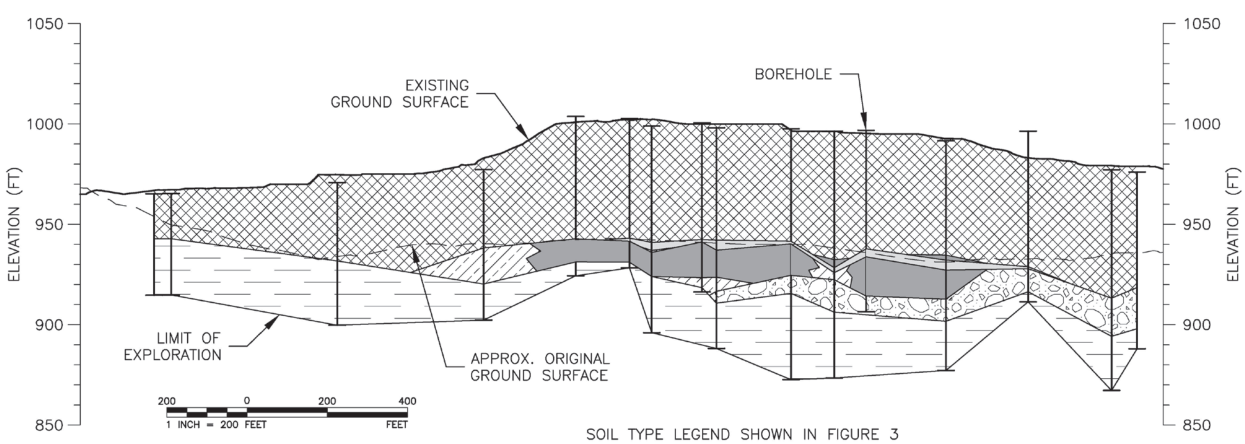

Figure 4. Section B through Overburden Stockpile.

Cut-off wall embankment section

The cut-off wall embankment will consist of a central section composed of select fill produced from screened crushed rock and compacted in controlled lifts to 95% maximum dry density (Modified proctor) to optimize strength and limit impacts from settlement. The select fill width was arbitrarily set at 20 ft for crest elevations of 986 ft and higher with 1H:3V side slopes. This provides a base width equivalent to the estimated deepest fill height (a criterion similar to what is used for impervious core dams) and keeps the select fill within the base excavation limits. The 20 ft width also allows for future raises, if required.

Rockfill, placed in controlled lifts and compacted with a minimum number of passes with a roller, will be used as fill outside of the select fill prism to provide additional stability with 3H:1V side slopes. The rockfill materials will be produced from waste rock from the mining operations or borrowed from other rock quarry areas. Acid producing rock will only be allowed on the upstream side of the cut-off wall. Some maintenance and additional fill placement is expected as the underlying ice-rich materials slowly thaw and consolidate, including some small slope failures and slumping due to as much as 9 ft of differential settlement, especially if the ice thaws quickly. The integrity of the cut-off wall, which is supported by the select fill section, will not be affected as these deformations will occur within the fill materials outside of the select fill section.

The proposed trench cutter and base carrier need a minimum work area of about 30 ft from the centerline of the cut-off wall alignment; therefore, the width of the embankment crest will be about 60 ft to keep the cut-off wall within the center of the embankment. As the cut-off wall construction needs a level work surface, stepped benches are required as the elevation increases at the abutments. In addition, a stepped bench is required at the deepest wall section due to the excavation limits of the proposed trench cutter. These benches were extended in stages to overlap gaps in the cut-off wall.

Cut-off wall panel target depths

The depth to low permeability bedrock, which was defined as having a permeability of 1 x 10^{-6} cm/sec or lower, was established during the 2005/06 geotechnical investigation. Permeability of the bedrock was typically determined using visual methods instead of the planned packer testing due to the frozen state of the rock. The visual criterion for apparent low permeability was one or less tight fractures per foot for a minimum length of three feet. Based on this criterion, the depth to apparent low permeability bedrock is shown in Figure 2. The cut-off wall panels will be keyed 3 ft into the apparent low permeability bedrock.

The deepest panel areas are located near historic drainages. These deeper zones of higher permeability bedrock are believed to be caused by freeze/thaw cycles and other weathering affects. The shallower panels are located outside of these historic drainages and in areas where the bedrock surface was encountered at a higher elevation. Therefore, these higher areas have not been exposed to the same degree of weathering and are less fractured at depth.

Thermal considerations

The cut-off wall is expected to be susceptible to degradation from freeze-thaw cycles; therefore, an insulated section will be installed to keep the frost penetration above the top of the cut-off wall. The insulation must also be wide enough to control frost penetration from the sides.

Due to the warm permafrost temperatures, which are near 31°F, the frozen conditions are not expected to affect the cut-off wall installation.

Instrumentation and monitoring

Instrumentation including thermistor strings, piezometers, and survey monuments will be important to monitor the performance of the seepage reduction structure. Thermistor strings will be installed to monitor degradation or aggradation of the permafrost. Standpipe piezometers will be installed to monitor water levels and seepage potential across the cut-off wall. Surficial survey monuments will be used to monitor settlement. Additional instruments installed within the cut-off wall itself, such as inclinometers and extensiometers to monitor vertical and horizontal movements, are important to monitor the performance of the cut-off wall.

Contingency options

In the event the cut-off wall does not perform as intended, as indicated by an increased head drop across the cut-off wall, some contingency options include jet grouting and permeation grouting. Jet grouting would likely be used for repairing higher than expected seepage in the fill and soils above the bedrock and possibly within the completely to highly weathered bedrock. Permeation grouting would be used to repair the bedrock. Water tests are typically performed prior to permeation grouting to evaluate the permeability of the rock and select the starting mix; therefore, this option would be the most successful under thawed conditions.

After the cut-off wall has been constructed, we expect the permafrost will aggrade into the fill embankment as it did into the Overburden Stockpile. Therefore, these contingency options will be considered following monitoring of the piezometers and thermistors strings.

Engineering Analyses

Engineering analyses performed for the design included seepage modeling, slope stability analyses (for the constructed embankment and cofferdam), hydrology and hydraulic analyses, thermal modeling, settlement, trench stability, and mix design of the cut-off wall materials. The following sections describe the results of the seepage analyses and mix design testing.

Seepage modeling

Potential seepage rates based on the cut-off wall design and future closure options were evaluated using the 2-D finite element program SEEP/W®. Analyses were carried out to evaluate seepage through the deepest section and the average section along the alignment. Some of the variables evaluated included:

- Changing the depth of the cut-off wall at the deepest section from 50 ft below the embankment to a 3 ft key into low permeability bedrock (10^{-6} cm/sec).
- Changing the hydraulic conductivity of the cut-off wall between 10^{-6} cm/sec and 5 x 10^{-7} cm/sec.
- Changing the hydraulic conductivity of the native soils and weathered/fractured bedrock, which were assumed to have the same permeability, between 10^{-3} cm/sec to 10^{-5} cm/sec (worst to best case).
- Changing the closure option from no tailings beach to a 900 ft tailings beach using 300 ft increments.

Results from the seepage modeling included the following:

- Keying the cut-off wall into low permeability bedrock decreased the flux values substantially assuming the worst-case (1 x 10^{-3} cm/sec) for the hydraulic conductivity of the native soils and weathered/fractured bedrock.
- For the best case native soils and weathered/fractured bedrock hydraulic conductivity, there was essentially no difference in flux values if the cut-off wall is installed at least 50 ft below the embankment fill whether it is keyed into the low permeability bedrock or not. Increasing the hydraulic conductivity of the native soils and weathered/fractured bedrock by an order of magnitude (average case of 1 x 10^{-4} cm/sec) about doubled the flux values.
- Assuming the native soils and weathered/fractured bedrock have at least a hydraulic conductivity of 1 x 10^{-4} cm/sec or less, seepage rates will still be relatively low if the cut-off wall terminates above the target depths.
- Adding a tailings beach may reduce the seepage flows up to 50%. A tailings beach that is 600 ft to 900 ft long will reduce seepage flows about 20% more than a tailings beach that is 300 ft long.
- The head drop across the wall could vary from 7 ft to 32 ft. The average head drop across the wall for all cases was 19 ft.
- Under completely thawed conditions, seepage flows should be expected to vary from about 30 gpm to 80 gpm for the entire cut-off wall alignment. Lower seepage values should be anticipated if:
    - The cut-off wall target depths can be achieved during construction;
    - The hydraulic conductivity of the cut-off wall or the low permeability bedrock is less than the design permeability of 1 x 10^{-6} cm/sec; and/or,
    - A tailings beach is constructed.

Mix design

The performance goals for the mix design were developed based on the engineering analyses described above. As settlements and stability are not expected to be a design concern, the minimum mix design compressive strength and deformity was determined qualitatively to be 100 psi and 5% strain, respectively, which should be greater than the surrounding soil. A minimum permeability of 1 x 10^{-6} cm/sec was selected based on the seepage analyses; however, a performance specification was provided based on a flux value of 0.007 gpm/ft width for a head loss of 23 ft and a minimum wall thickness of 2.6 ft to possibly reduce material quantities and save costs. This specification should provide a maximum flow rate of about 40 gpm across the entire cut-off wall.

Mix design testing was performed at Golder's laboratory in Burnaby, British Columbia, Canada using the following available materials:

- Potable water available at site (pH = 7)
- Type I cement meeting ASTM C150
- Bentonite meeting API 13A, Section 9
- ¾-inch minus crushed rock from site, which was passed through LA abrasion devise to simulate cuttings from the Trench Cutter

The mix design results are shown in Table 1. Based on the mix design testing results, Mix Design No. 4, which is 19% water, 10% cement, 3% bentonite, and 68% aggregate, met the performance criteria of 100 psi minimum compressive strength and a maximum permeability of 1 x 10^{-6} cm/sec at a strain of 5%. Additional testing will be performed by the contractor during construction to verify the field mixture continued to meet the performance specifications.

Current Construction Highlights

Excavation and embankment construction

Excavation and embankment construction is being performed by TCAK with construction quality control (CQC) provided by Golder. To date, the embankment has been constructed for about half the alignment and excavation depths have been similar to what was estimated from the design drawings. An example of some of the ice-rich materials encountered during the excavation is shown in Figure 5.

Slope stability was monitored on a daily basis during the embankment construction and slopes were flattened as necessary. Seepage flows through the cofferdam were generally low and easily controlled. However, seepage flows through the Overburden Stockpile were higher than expected and required construction of drainage trenches. A photograph of the constructed embankment is shown in Figure 6. Construction of the embankment is planned for next year with the majority of excavation occurring in the winter.

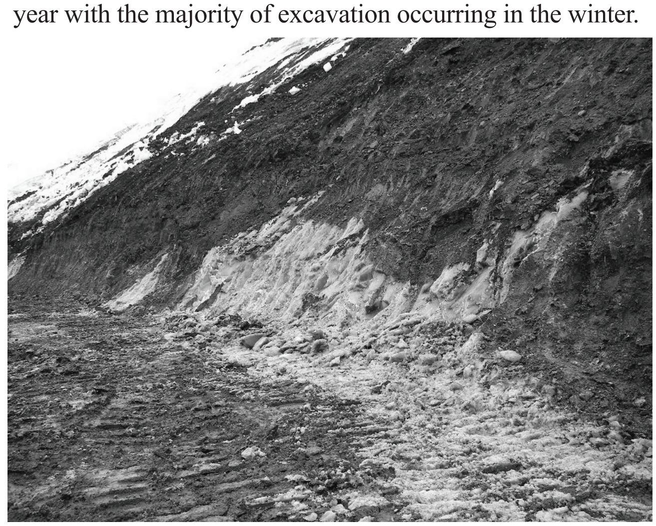

Figure 5. Massive ice encountered during excavation.

Table 1. Mix design results.

Mix Type	Sample Number	Age (days)	Wet Density (cm/sec)	Permeability Before Strain (cm/sec)	Maximum Deviator Stress (psi)	Tangent Modulus (tsf)	Maximum Strain (%)	Permeability After Strain (cm/sec)
Plastic Cement	1A	46	83	2.6E-07	231	2109	8.3	2.8E-7
	3A	19	78	6.3E-06	26	829	8.1	8.6E-6
Plastic Concrete	4B	42	129	6.8E-08	452	5127	7.7	8.4E-7
	4A	80	129	6.0E-08	514	3592	17.7	1.8E-6
	5A	19	131	3.5E-08	749	8135	1	6.9E-7

Strain of Sample 5A limited by capacity of load cell

Figure 6. Embankment with Bauer trench cutter.

Figure 7. Bauer cutter heads.

Cut-off wall construction

The cut-off wall is being constructed by Golder Associates Innovative Applications (GAIA), a wholly owned subsidiary of Golder's Canadian company providing specialized contracting services, with assistance from Bauer Maschinen. About 65 linear ft of cut-off wall has been constructed in 2007 to evaluate the performance of the cutter heads (Fig. 7), the slurry transport systems, and the mix design. Cut-off wall construction is scheduled to continue next year with two 12-hour shifts from May to October. The project is expected to be completed in 2009.

The cut-off wall is constructed by installing a series of primary and secondary panels. Construction begins by installing reinforced concrete guide walls to help support the near surface soils and provide alignment and continuity for the cut-off wall. Slurry is then introduced into the shallow trench between the guide walls and the panel is pre-excavated further to submerge the slurry pump on the trench cutter. Excavation continues with the trench cutter to the design depths. During this excavation, the slurry is recycled through a desander. The working slurry in the excavated column is then replaced with fresh slurry and the panel is completed by backfilling the column with tremied plastic concrete.

Conclusions

Based on the results of geotechnical investigations performed in warm permafrost for a cut-off wall in northwestern Alaska, ice-rich materials up to 19 ft thick were encountered in the overburden materials along the proposed alignment. In lieu of packer testing, which could not be performed in the frozen ground, a visual criterion was also developed to determine cut-off wall target depths in apparent low permeability bedrock. A cut-off wall up to 170 ft deep was required based on the borehole data.

To address the potential settlement issues from the melting ice-rich soils, a stable embankment design was developed that included excavating the ice-rich materials and constructing the central part of the embankment with select engineered fill. The cut-off wall will be constructed using a Bauer Trench Cutter that is capable of excavating into the bedrock to the design target depths. Plastic concrete slurry composed of aggregate, cement and bentonite will be used to backfill the excavation. Instrumentation and monitoring will be used to monitor the performance of the cut-off wall after construction is completed.

References

Hammer, T.A. et al. 1985. Ground temperature observations. *Thermal Design Considerations in Frozen Ground Engineering*: 8-52.

Water Management Consultants. 1999. The Phase II Hydrologic Characterization of the Tailings Impoundment. Report to Teck Cominco Alaska Inc.

Water Chemistry of Hydrogenous Taliks in the Middle Lena

N.P. Anisimova
Melnikov Permafrost Institute, SB RAS, Yakutsk, Russia
N.A. Pavlova
Melnikov Permafrost Institute, SB RAS, Yakutsk, Russia

Abstract

Based on the results of long-term investigation, this paper outlines the chemistry of groundwater of open and suprapermafrost taliks, occurring beneath the channel and arms, as well as in the low terraces of the Middle Lena River. This paper also illustrates the character of changes in the groundwater chemistry within the vertical profile and along the stretch of channel sediments forming an open talik under the Lena River; how these changes depend on surface water TDS fluctuations during the year-cycle; and specific features of mineral content of underlying bedrock. We have also regarded the impact of permafrost processes and human contamination in change of suprapermafrost talik groundwater chemistry.

Keywords: chemistry; hydrogenous taliks; open river talik; suprapermafrost talik.

Introduction

In Central Yakutia, with prevailing continuous permafrost, the groundwater in taliks is widely distributed under the Lena River channel, under lakes, cut-off meanders, and small rivers. Their chemistry is considerably affected by the geological and structural pattern of the territory, terrain type, geocryologic conditions, and the composition of recharge water.

There has been a thorough investigation of peculiarities of groundwater chemistry origins for taliks in the Middle Lena, where the river passes on from the Prilensky plateau region to the Central Yakutia lowland area. The valley's profile changes correspondingly from a narrow valley with steep rock sides to a vast terraced accumulative valley. The widest terraced part of the river valley situated on the western bank between the Tabaga and Kangalass bedrock fold is known as Tuymaada. It is 6–8 km wide. It includes two terraces and a flood plain which is separated from the main channel by numerous arms and islands. The width of the main channel of the Lena River at the town of Yakutsk is about 3 km. The Lena River flood plain is annually inundated by floodwater, its level above mean water reaching 8–10 m, according to long-term assessment. The flood plain topography is hilly, complicated by numerous narrow, semi-cut-off depressions and arcs. Arcs are made of fine and medium sand of channel facies, its surface covered by flood plain sabulous-loamy sediments 0.5–2.5 m thick. In the upper part of the cross section of semi-cut-off depressions and scourways we can identify a sabulous-loamy layer, up to 5 m thick. The combined thickness of the alluvial sediments, forming the flood plain, reaches 10–15 m.

Alluvial sediments in the Tuymaada region occur in Middle Jurassic rocks, upper layers of which are composed by clayey siltstone interbedded by fissured sandstones. Upstream the river, the thickness of Lower Jurassic terrigenous sediments is gradually diminishing; starting in the town of Pokrovsk the channel alluvium is underlain by carbonates.

The eastern low terraces are separated from the fourth one (Bestyakh) by a bench up to 20 m high. The depth of the river in the middle is 3–5 m, reaching 15–20 m along the fairway.

The spring flood of the river typically brings a rapid and high level rising. The main yield falls in the warm season. The winter period witnesses 9%–11% of the total yield. The river is completely frozen from the first half of November until the second half of May. It is mostly meltwater-recharged (50%), up to 35% rainfall-recharged, and about 15% of the recharge comes from ground water.

In the studied area permafrost covers all the territory, except for the Lena River channel and large lakes which are underlain by open taliks. The thickness of permafrost ranges from 20 to 450 m. The minimal thickness (20–50 m) is identified within low flood plain, under islands, and under some lake taliks. In the first and second fluvial terraces of the eastern bank (opposite Pokrovsk), separated from the channel by wide flood plain, the thickness of permafrost reaches 250–350 m; in the first fluvial terrace of the western bank (Yakutsk and suburbs) it makes 216–270 m, extending northwards up to 475 m (Khatyryk). Seasonal thawing depth depends on the general climate and a number of local factors: lithological composition of soils, their water-saturation, water permeability, shading effect, type of vegetation, the stage of the area in terrain, underlying bedrock temperature, etc. Depending on these factors the thickness of the seasonally thawing layer varies within quite a wide range (from 0.3 to 4.5 m).

The temperature of the permafrost within fluvial terraces is not uniform. The lowest temperatures (from -2.5°C to -4°C) occur in the ground that forms the flood plain, the surface of which is considerably swamped and peated. Within the first and second fluvial terraces the temperature is lower (from -0.9°C to -2.5°C), only in swamped and peated areas in the rear sides of the terraces the temperature falls to -3.6°C.

Research Methods

The existence of taliks in Lena River frozen ground is caused by the warming effect of river-, lake-, and suprapermafrost waters. According to the stage in the terrain, taliks are subdivided into river taliks, occurring in active channel sediments and bedrock immediately under the river, and terrace taliks, formed under flood plain and dead-channel lakes, or in depressions at the floors of arcs, ridges, and terrace slopes.

Initiated in the mid 1950s by the Permafrost Institute long-term investigations on water chemistry of hydrogenous taliks in the middle Lena valley have been continued. The investigations include drilling, water, and ground sampling for chemical analyses, temperature measurements in instrumented boreholes, as well as long-term observations of groundwater level and chemistry in taliks. Data obtained from long-term hydrogeochemical studies of open and suprapermafrost taliks occurring beneath the river channel and arms, as well as in the low and medium terraces in the Middle Lena valley were analyzed. This allowed us to determine variations in groundwater chemistry in relation to the dissolved solids concentration in source surface water in an annual cycle and to the composition of the underlying bedrock. An understanding was gained on the effects of cryogenic processes and anthropogenic contamination on talik water chemistry.

Results and Discussion

Open talik under the Lena River

The Lena River open talik was first tested in 1958 by a Gidroproekt Institute expedition in the Pokrovsk area. The 70–200 m deep drill holes completed on the islands and in the channel penetrated 27 m thick sandy-pebbled sediments and underlying fissured Cambrian limestone. During further investigation the groundwater of the Lena River talik was revealed in the Peschany island opposite Tabaga Point at the interval of 10.4–105.8 m, the water level settled at the depth of 4.37 m from earth surface. Among the water-bearing materials in Peschany island are anisometric quartzo-feldspathic sands, Quaternary gravels, and underlying fissured sands and Lower Jurassic siltstone. In channel sediments where there is no permafrost the water is non-artesian, and in the islands in conditions of active suprapermafrost forming, waters revealed in channel sediments have a slight pressure.

On the projection, the open talik zone contour repeats the contour of the channel zone. Its width ranges from 2.0 to 2.7 km.

Total dissolved solids (TDS) and chemistry of Lena River talik groundwater are not homogeneous judging by alluvial sediments cross section. In upper layers of channel sediments the chemistry of the water varies during the year according to the changes occurring in the composition of recharging surface water.

In winter water TDS reaches 500 mg/l with hydrocarbonate-chloride composition, and during the warm period it reduces down to 70–150 mg/l, when calcium and magnesium hydrocarbonates start prevailing.

In the bottom layers of the river talik alluvial zone the chemistry of water is affected by the mineralogical composition of the underlying bedrock. South from Pokrovsk, where channel sediments overlie Cambrian limestone, the chemistry of the bottom alluvial zone water is dominated by calcium and magnesium hydrocarbonates, and the TDS makes 330–570 mg/l (interval 33–70 m).

Downstream where Cambrian limestone dips below Jurassic sandstone in the basal levels of channel sediments, water, classified by the dominant dissolved ions, is mostly hydrocarbonate and natrium type with a TDS of 350–490 mg/l (Fig. 1).

The temperature in the Lena River channel ranges from 1°C to 4°C. On the old islands the soil is frozen down to 15-60 m deep. In the underlying talik, bedrock water is slightly over-mineralized. Thus, in fissured Cambrian limestone on the island opposing Pokrovsk, water TDS under the permafrost at a depth of 15 m made 500 mg/l, and its composition was hydrocarbonate magnesium-calcium; and on Ponomarev Island, opposing Yakutsk, under 25 m of permafrost, water revealed in Jurassic sandstone had a hydrocarbonate natrium composition, an increased content of chlorides, and TDS of about 1 g/l. Such composition occurs as a result of poor permeability under the permafrost.

The analysis of water chemistry in channel sediments of an open talik under the Middle Lena River (from Bulgunnyakhtakh to Namtsy) showed that there is no mineralized groundwater discharge into the channel from bedrock. The chemistry of the water revealed in the well under 173 m of permafrost in Jurassic sandstone in the western bank flood plain at Tabaga Point according is a bicarbonate-chloride sodium type (hereafter the water type name is given in increasing order of components), and TDS is 1.6 g/l.

Subpermafrost water of Middle Cambrian sediments, revealed in the well on the eastern bank of the Lena River (Krasny Ruchei, southern part of the studied territory) at a depth of 350 m is a bicarbonate-sulfate-chloride sodium type and TDS is 2 m/l.

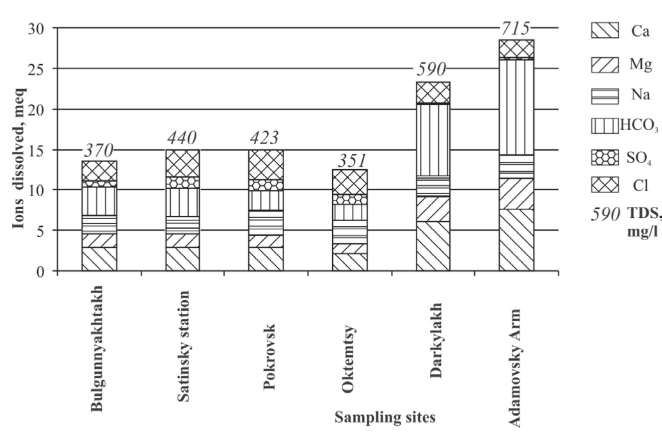

Figure 1. Changes in chemistry of groundwater under the Middle Lena.

Table 1. Water Chemistry of the Lena Riverside Arms in Tuymaada Valley (Makarov 1996).

Arm	pH	Minerals total, mg/l	Unit	Ca^{2+}	Mg^{2+}	$(Na+K)^+$	NH_4^+	HCO_3^-	SO_4^{2-}	Cl^-
Tabaga	7.5	178	mg/l	18	5.5	22	1.2	48	75	32
			meq%	39	20	41		24	48	28
Khatass	7.3	186	mg/l	30	8	27	1	82	36	43
			meq%	44	19	37		41	23	37
Khatass	5.9	163	mg/l	21	6	21.5	0.7	9	77	29
			meq%	42	20	38		6	62	32
Prigorodnaya	7.4	143	mg/l	24	6	21.5	1.2	55	41	25
			meq%	46	19	35		37	35	29
Zhatai	8.1	112	mg/l	17	6	17.5	0.7	54	21	24
			meq%	40	23	36		44	22	34
Tulagino	8.2	115	mg/l	21	7	13	0.4	78	17	18
			meq%	48	26	26		60	17	24

Although this water is high pressure artesian, its discharge to the surface is impeded by aquitard in the overlying zone (Beletsky & Kyrbasov 1972). The drilling of the aquitard consisting of marls interbedded with dolomites and limestone more than 100 m thick was completed starting from the depth of 50–75 m.

Suprapermafrost taliks

The suprapermafrost river talik under the arms of the Lena River was revealed during drilling by *Kommunvodstroi* Institution expeditions in 1932–1934. In 1960–1961 the Yakutsk Geological Board completed 15 drill holes with depths ranging from 12 to 76 m, aimed at estimating groundwater abundance under the Lena River channel near Yakutsk. The wide accumulative flood plain of the Lena River has numerous arms and lakes, flooded in spring. The taliks under them are closed. They are up to 40 m thick. The chemistry of talik water mostly depends on the surface water composition, but the discharges of surface- and suprapermafrost water from terraces also affects it.

Surface water TDS in the Tabaga, Khatass, Yakutsk, Zhatai, and Darkylakh arms situated on the western bank opposite Yakutsk, makes 50–60 mg/l in June, with an ionic composition dominated by calcium hydrocarbonates. At the end of summer it rises up to 170–180 mg/l, and natrium chlorides and sulphates prevail (Table 1). The highest values of water TDS in the river arms (up to 500 mg/l with dominating natrium chlorides) as well as in the main channel, are registered at the end of winter. In the river talik of the Adamovsky arm opposite Yakutsk the composition and mineralization of groundwater in winter (February) varies slightly along its profile; in the upper part (6–9 m deep) TDS makes about 620 mg/l with natrium and magnesium hydrocarbonates dominating, and in deeper layer (at interval of 12–15 m) it is slightly lower (470 mg/l) and has a natrium hydrocarbonate composition.

In the talik under the Darkylakh arm situated downstream, in the upper part of alluvial layer at a depth of 1–9 m, the TDS of the groundwater in April is about 500 mg/l; it has hydrocarbonate-chloride composition, not homogeneous by cations it contains.

The chemistry of water in suprapermafrost taliks under arms of the river which are close to Yakutsk is affected by contaminated suprapermafrost water runoff from urban areas to the alluvium. This is proven by an increased content of chlorine in the talik water and by its increased oxidability of 9.4 mg O_2/dm^3.

Increased accumulation of contaminants in alluvial sediments of river arms usually accompanies low permeability. Thus, for example, while constructing District 202 of Yakutsk, after an inwash of sand on the flood plain surface, TDS in channel sediments increased up to 1–2 g/l with a dominance of natrium chlorides and sulphates, which were being introduced with contaminated suprapermafrost water from the first fluvial terrace and were concentrating at permafrost table.

In the sediments making up the Lena River fluvial terrace suprapermafrost water-bearing taliks underlying minor arms and lakes are widely distributed. In the lower reaches of minor eastern-bank tributaries (Tamma, Lutenka, Menda, Suola) the thickness of river taliks in well-draining sandy-pebbled sediments makes 30–60 m and in some cases extends deeper into underlying bedrock. The maximal water-bearing capability of such arm taliks is indicated under minor arms within the Bestyakh terrace. Even though the channel is not wide (10–20 m) and surface flow is not permanent, here river taliks sustain during the winter as well, due to their increased water drainage and comparatively the high temperature of the permafrost. Thus, for example, water in a talik under the Tamma River dried channel in April (before flood) at a depth of 3–13 m has TDS of 200–300 mg/l. Its type is hydrocarbonate calcium-magnesium.

Increased thickness of river taliks under the Lena's eastern tributaries is indicated in the areas underlain by sandy-pebbled sediments covering fissured bedrock. Thus, in the lower reach of the Menda River the thickness of the aquifer talik reaches 60 m. At August testing the yield made 1.8 l/s, TDS – 200 mg/l, and the chemistry was dominated by calcium hydrocarbonates. The underflows beneath minor eastern tributaries discharge into the Lena River talik. In some cases, icing forms in areas near outlets of such rivers.

Minor western tributaries in Tuymaada Valley

(Shestakovka, Khatynnakh, Markhinka, and Zolotinka) do not have a year-round discharge, therefore during winter small river taliks sustain only in isolated, deep parts of the channels. In one of these river taliks in the lower reach of Markhinka at the end of winter (April) at a depth of 1.5 m, water had TDS of 238 mg/l, hydrocarbonate natrium-magnesium-calcium composition, and a high concentration of organic substances. Shestakovka River taliks occur under the lake-like widening of its channel in the lower reach. Here, TDS in water from the talik, revealed in sands in the interval of 1.0–4.5 m, varies during the year from 510 to 780 mg/l, while TDS in the river is considerably lower (50–95 mg/l). Talik water quality deterioration results from organic matter inflow from the seasonally freezing layer of the catchment area and from overlying stratum in the dried part of the channel.

Suprapermafrost aquifers in the first and second terraces of the Lena River also occur under lakes and cut-off meanders. The groundwater occurrence depth in lake taliks is subject to the depth of lake and in dried frozen parts of the basin corresponds to the thickness of newly formed permafrost. The thickness of taliks under small shallow lakes does not exceed 20 m and at a depth of 2–3 m and a width of 100–200 m it increases up to 30–40 m.

In taliks underlying continuously or periodically discharging lakes water TDS is not higher than 400–700 mg/l. The dissolved ionic type is hydrocarbonate, calcium, magnesium, and sporadically natrium. Under small static lakes no deeper than 1 m, taliks are thin (0.5–1.5 m). Their water TDS is often more than 1 g/l.

The majority of cut-off lakes in low terraces forming a beaded drainage become interconnected during high water. Nevertheless, the connection between their taliks is presently interrupted as a result of permafrost forming between the lakes in dry parts where there are roads.

In lower western terraces of the Lena River where saline lands are widely distributed under drying basins we can often indicate small freezing lake taliks with TDS of 2.5–4 g/l. In relict lake taliks under completely dried basins the TDS in some cases reaches up to 60 g/l, and the ionic composition is dominated by sulphates and chlorides, natrium and magnesium.

Increased salinity of the groundwater in lake taliks within the densely populated part of Tuymaada Valley is affected by human contamination of the territory (Anisimova et al. 2005).

The good quality of water in lakes and their taliks will retain only in case of them being non-stagnant and recharged by meltwater and slightly saline suprapermafrost water. On the western bank such lakes occur at the floor of the alluvial valley slope and on the eastern bank – at the floor of the fourth Bestyakh fluvial terrace. Such are, for instance, lakes to the south of Pavlovsk, where they are recharged not only by precipitation water, but also by intrapermafrost taliks occurring in the Bestyakh terrace. Said taliks discharge either in creek valleys, forming year-round flowing springs or forming submerged crop outs in some low-terrace lakes (Buluus, for instance). This thick intrapermafrost taliks' water is of low TDS and is hydrocarbonate magnesium-calcium and hydrocarbonate natrium type, but it cannot discharge into the Lena River talik due to the impedance of thick layers of low-terrace permafrost.

Conclusions

All stated above demonstrates that there are two crucial factors that affect the quality of water in open and suprapermafrost taliks: permeability rate determined by water circulation, and rechargeability with good quality water. Within the studied area the required properties are indicated only in one Lena River talik upstream from Pokrovsk where channel sediments are underlain by fissured limestone, and in the river taliks under right tributaries of Lena (Menda, Tamma, Lutenga).

In the Tuymaada Valley area, under the arms, yield horizon is confined only by the channel sediments zone. But in the vicinity of Yakutsk, the water chemistry of the river taliks deteriorates as a result of contaminated groundwater runoff of the active layer and suprapermafrost taliks from the urban area.

Acknowledgments

This study was supported by the RFBR grant 06-05-96087.

The authors are grateful to two anonymous reviewers for their helpful comments.

References

Anisimova, N.P., Pavlova, N.A. & Stambovskaya, Y.V. 2005. The influence of anthropogenic Contamination on groundwater chemistry in flood plain taliks and riverbed, Middle Lena River. Fundamental issues of water resources research and utilization. *Proceedings of a Scientific Conference, Irkutsk, Russia, September 20-24, 2005:* 339-340.

Beletsky, V.L. & Kyrbasov, P.V. 1972. *Saline Water in Middle Cambrian Sediments by the Lena River Streamside // Geocryological and Hydrogeological Research of Siberia.* Yakutsk: Yakutsk Book Publishing House, 164-167.

Makarov, V.N. 1996. *Environmental and Geochemical Profile of Tuymaada Valley //Environmental and Geochemical Issues in the Permafrost Region*. Yakutsk: SB RAS Institute of Permafrost Press, 3-34.

A New Hypothesis on Ice Lens Formation in Frost-Susceptible Soils

Lukas U. Arenson
BGC Engineering Inc., Vancouver, BC
Tezera Firew Azmatch
UofA Geotechnical Centre, Department of Civil and Environmental Engineering – University of Alberta,Edmonton, AB, Canada
David C. Sego
UofA Geotechnical Centre, Department of Civil and Environmental Engineering – University of Alberta,Edmonton, AB, Canada

Abstract

Generally it is accepted that frost heave is a one-dimensional process assuming that the ground conditions are homogeneous and the temperature gradient is one-dimensional. Unfrozen water is attracted to the base of the warmest ice lens for it to grow. Recent laboratory investigations suggest that the growth of ice lenses is more complex. Vertical ice veins form through the frozen fringe in a regular, hexagonal pattern reaching the freezing front. Based on these observations, a new hypothesis for ice lens formation is suggested. As suction builds within the frozen fringe, thin vertical cracks form that do not completely fill with ice, allowing a thin film of water to migrate from the unfrozen zone to the warmest ice lens. The existence of these vertical channels helps explain the measured ice lens growth considering the decreasing hydraulic conductivity in the frozen fringe as voids fill with ice. The tensile strength and the stress state of the soil that governs the crack pattern, therefore, control the ice lens growth and hence frost heave.

Keywords: frost heave; frost susceptibility; ice lens formation; hexagonal cracks.

Introduction

Saturated fine grained soils are known to form horizontal ice lenses when subjected to sub-zero temperatures. These ice lenses change the structure of the soil, generally associated with frost heaving. This change in structure as well as the expansion of these so-called frost-susceptible soils hasve to be taken into consideration when encountering such a soil as a construction or foundation material.

Phenomena associated with frost-susceptible soils have long been recognized by many researchers (e.g., Beskow 1935, Miller 1973, Penner 1959, Penner 1972, Taber 1929, Taber 1930). The basic mechanisms involved in frost heave were identified in the early days based on experimental evidences. Ice lenses form at a certain distance above the freezing front, and water from the unfrozen zone migrates towards the ice lens. Under thermal steady state the warmest ice lens continues to grow as long as water is available. Under transient conditions (penetrating frost front) the ice lens grows until, under some conditions still being debated, a new ice lens starts to form at a location below the initial one. By eliminating the water accessibility or reducing the hydraulic conductivity of the soil, frost heave is significantly reduced. In other words, the water migration towards the ice lens and its amount are the governing factors that contribute to ice lens development and frost heave under thermal steady state.

Based on experimental evidence this paper proposes a new hypothesis on ice lens growth, in particular on how water migrates towards the growing ice lens. The hypothesis assumes that the water migration from the unfrozen zone towards the ice lens is not a simple one-dimensional process. It is further thought that this new hypothesis may explain the phenomenon of frost heave better and may help in better quantifying the frost susceptibility and frost heave potential of freezing ground.

Ideas Behind Frost Heave Theories

Several theories and ideas have been proposed over the years that describe the thermodynamic processes involved in frost heave. Henry (2000) presents a thorough overview of available frost heave concepts. To date two main concepts are widely used to predict frost heave: (1) the segregation potential (SP) concept that was introduced by Konrad & Morgenstern (1980, 1982) and (2) the discrete ice lens theory proposed by Nixon (1991), which is an extension and modification of the rigid ice model by Gilpin (1980) and O'Neill & Miller (1985). Figure 1 shows the idealized frost heave concept generally used. Under a constant thermal gradient, the warm side of the ice lens at a certain time is at a temperature T_l slightly colder than the temperature at the pore freezing front at the base of the frozen fringe, the partially frozen zone between the warmest ice lens and the freezing front. Water migrates through the unfrozen zone and the frozen fringe towards the warm side of the ice lens. Under saturated condition it can be assumed that the increase in pore water pressure in the unfrozen zone with depth is constant. At the interface between the ice lens and the water, the thermodynamic equilibrium requires that free energy of the ice equals that of the water. By using the Clapeyron equation, the suction at the interface between the ice and the water can be calculated. For example, if the temperature at the bottom of the ice lens is -0.1°C, the suction is -125 kPa

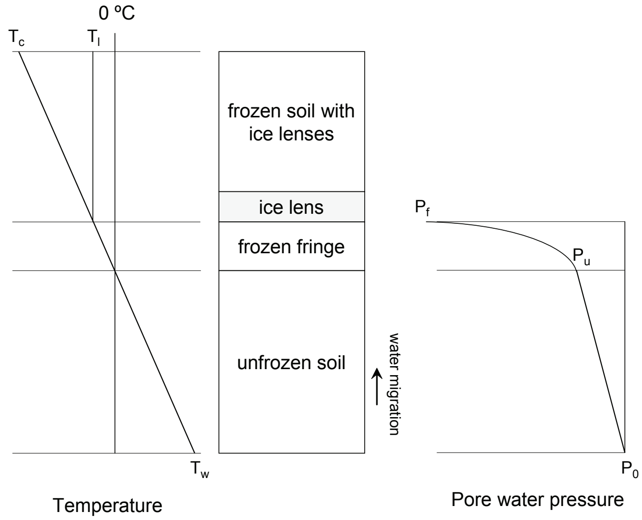

Figure 1. Temperature gradient and pore water pressure distribution und an idealized, one-dimensional ice lens growth scenario after Konrad (1989) and Nixon (1991). Significant suction is noted in the frozen fringe.

and for -0.2°C, the suction is -250 kPa. In order to satisfy the thermodynamic equilibrium, significant suction is required that rapidly decreases within the frozen fringe (Fig. 1).

Experimental Evidence

Recently a series of frost heave tests have beenwere carried out at the University of Alberta using novel visualization techniques. The one-dimensional freezing tests were performed on frost-susceptible Devon silt (Xia 2006). High resolution digital images were further utilized to measure ice lens growth with time under different temperature and stress conditions. Later, particle image velocimetry was applied to measure ice lens growth and soil consolidation during freezing on a microscopic scale (Arenson et al. 2007).

Ice lens structure and growth

The freezing tests clearly demonstrated that ice lens growth is not a simple one-dimensional process, but rather more complex. A snapshot from an early freezing stage (Fig. 2) shows that vertical ice veins precede the formation of the horizontal ice lens. The thin vertical ice vein nearly reaches down to the unfrozen zone through the frozen fringe. Even though the ice veins are not necessarily continuous, they grow more or less vertically on a continuous line. The thin nature of the ice veins makes them difficult to extract using digital image techniques (Fig. 3). However, it can be noted that the thickness of the ice veins does not change much with time in contrast to horizontal ice lenses.

The vertical ice lens structure was also observed when the sample was split at the end of the test (Fig. 4). The vertical ice veins of the frozen segment where well attached to the upper half, whereas a crack pattern was observed in the unfrozen half. The separation of the two halves occurred just below the final horizontal ice lens. In other words one sees on top of the frozen fringe when looking at the unfrozen section

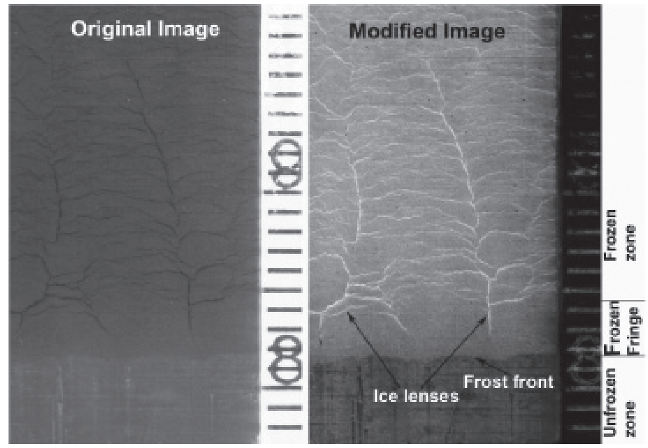

Figure 2. Original and modified image of ice lenses during one-dimensional freezing. The image was taken early during a freezing test at a high cooling rate. Scale in mm (after Xia, 2006).

(e.g., Fig. 4 right). The fact that the unfrozen part could be separated easily from the frozen part with the vertical ice veins attached to the frozen side indicates that there is only a weak bond between the unfrozen soil and the ice within the frozen fringe.

Analysis of the cross section confirms observations that were previously described during observations from the side as the sample froze. A regular pattern of vertical ice veins is formed along the height of the frozen section (Fig. 2). The existence of the vertical ice veins that precede horizontal ice lens formations is not a boundary effect occurring at the outer limit of the circular freezing test. On the contrary, a regular, hexagonal pattern forms throughout the whole cross section. Similar patterns were observed by Mackay (1974, McRoberts & Nixon 1975) for lake and marine clays, glacial tills, and mudflow deposits in permafrost areas of northern Canada. They also provide some theories of the reticulate ice lens growth mainly based on the idea of water being sucked from the clay resulting in suction cracks. Chamberlain and Gow (1979) also presented images of frozen silt that show the reticulate ice structure. They further suggest that there is a direct connection between the vertical ice veins and the vertical hydraulic conductivity of the freezing and frozen soil. However, no evidence or connection is shown between the vertical ice veins and the horizontal ice lenses.

The hexagonal pattern that was observed in the frozen fringe, i.e. the unfrozen side of the sample has a very strong resemblance to drying soils (Fig. 5). The size of the hexagonal elements in the freezing tests further depends on initial conditions, such as consolidation pressure or pore water salinity, and the boundary condition, such as temperature gradient or water availability. Figure 6 shows cross sections from three additional freezing tests. Test #1 (Fig. 4) was consolidated at a vertical pressure of 100 kPa, but frozen at 0 kPa pressure. Tests #4, #5, and #6 in Figure 6, on the other hand, were frozen under the consolidation pressures of 100 kPa, 200 kPa and 400 kPa, respectively. The horizontal ice lens and the frost heave rates decreased with increasing consolidation pressure as expected. In

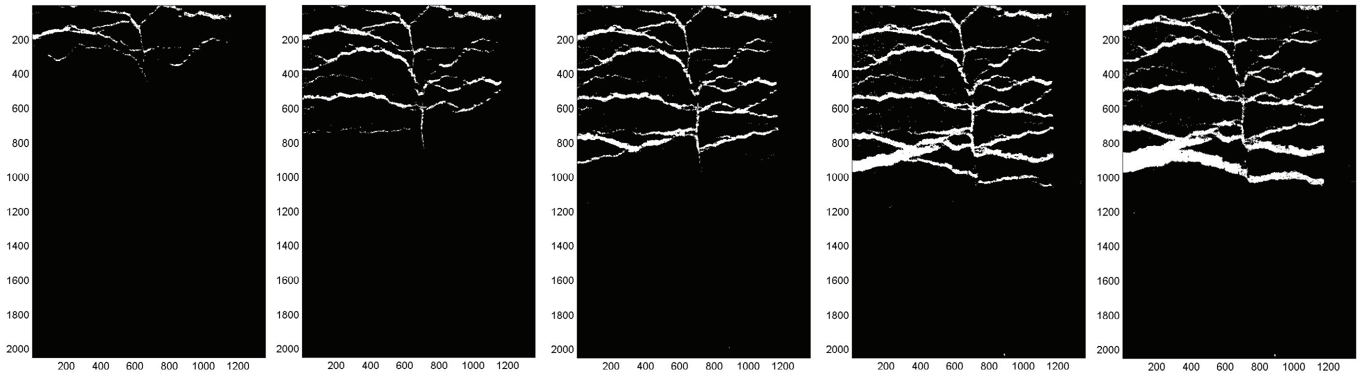

Figure 3. Digitally extracted ice lens structure with time for freezing test. The sequence shows the initiation of the final ice lens (Arenson et al. 2007).

addition, a change in the vertical ice structure can be noted. The size of the hexagonal elements increases with increasing pressure, i.e. the distance between the vertical ice veins increases. This was also visible in the pictures taken from the side of the freezing cell. The change in element size can be quantified by counting the number of full elements within a 50 mm x 50 mm square in the centre of the cross section. Even though the measure is quite rough it shows that with decreasing number of elements, i.e. increasing distance between the vertical ice veins, the final ice lens growth rate decreases. Test #1 and #4 showed similar heave rates of $2.64 \cdot 10^{-6}$ mm/s and Test #5 and #6 displayed values of 1.53 and $1.51 \cdot 10^{-6}$ mm/s, respectively (Xia 2006). The element count gives 18, 17, 11 and 10 hexagonal elements in the centre of the cross section. Even though only four tests are available the trend is convincing.

Hydraulic conductivity and water demand

The one-dimensional ice lens growth hypothesis assumes that all the water at the base of the growing ice lens migrates from the unfrozen soil through the partially frozen soil in the frozen fringe. Experiments on the hydraulic conductivity of partially frozen soils have shown that the permeability decreases rapidly as soon as pore ice forms (Aguirre-Puente and Gruson, 1983; Chamberlain and Gow, 1979; Konrad and Samson, 2000a; Konrad and Samson, 2000b; Williams and Burt, 1974). This reduction is caused by the decrease in void ratio as the pore water freezes and water migration to an ice lens is hindered. Williams and Burt (1974) present data for hydraulic conductivities k of silt as a function of temperature that show the rapid decrease in k from 10^{-6} m/s at -0.1°C to 10^{-11} m/s at -0.4°C, i.e. 5 orders of magnitude for 0.3°C temperature change. This decrease is not linear. A decrease of four orders of magnitude was actually recorded for the temperature drop from -0.1°C to -0.2°C. Similar trends were obtained by Horoguchi & Miller (1980). They further show a hysteresis effect that depends on whether the silt undergoes freezing or thawing. The hydraulic conductivities of the frozen silt (4-8μ) measured by Horoguchi & Miller (1980) ranged from $2 \cdot 10^{-8}$ m/s (0°C) to 10^{-12} m/s (-0.15°C). The rate of Williams & Burt (1974) are probably affected by the presence of lactose used in their experimental setup, indicating the challenges in measuring the hydraulic conductivity for partially frozen soils.

The authors are not aware of any experimental study that measures the hydraulic conductivity in the frozen fringe. A simple approach is therefore used to estimate the change in hydraulic conductivity k within the frozen fringe based on the soil-water characteristic curve (SWCC). Because the freezing process is somewhat similar to the drying process, the SWCC approach was judged to be suitable to estimate this change. The problem of using temperature dependent approximations, such as the temperature dependent permeability function suggested by Gilpin (1980), is that three-dimensional effects are excluded, and vertical flow of water from the unfrozen zone towards the growing ice lens is implied.

The Devon silt used for these investigations has an unfrozen, saturated hydraulic conductivity of $9.9 \cdot 10^{-10}$ m/s at an effective stress of 100 kPa. The moisture content at saturation was 26% with a porosity n of 40% (Xia, 2006). The volumetric water content changes in the frozen fringe when suction builds up (Fig. 1). Hence, the hydraulic conductivity changes. The hydraulic conductivity can, for example, be calculated after Fredlund and Xing (1994). The following parameters were utilized to calculate the hydraulic conductivity distribution (Fig. 7):

$a = 1.948$	parameter for Fredlund and Xing (1994)
$n = 2.708$	"
$m = 1.084$	"
$k_{sat} = 9.9 \times 10^{-10}$ m/s	saturated hydr. conductivity
$\theta = 15.6\%$	saturated vol. water content

The water requirement at the final ice lens can be calculated from the ice lens growth rate. For test #1 2.9×10^{-9} m³/s has to migrate from the unfrozen zone through the frozen fringe. Konrad (1994) showed that for temperatures close to 0°, theoretically the suction at an ice lens under atmospheric pressure increases linearly with decreasing temperature at a rate of 1250 kPa/°C. In test #1, a temperature gradient of 0.058°C/mm is applied at thermal steady state. With a frozen fringe thickness of 6 mm, the suction at the ice lens base is estimated to 438 kPa to satisfy the thermodynamic

Figure 4. Hexagonal structure of the vertical ice lenses. The frozen section is on the left, the unfrozen section on the right. The sample diameter is about 100 mm (Xia 2006).

Figure 5. Cracked earth inside the Ubehebe Crater, California (www.tawbaware.com).

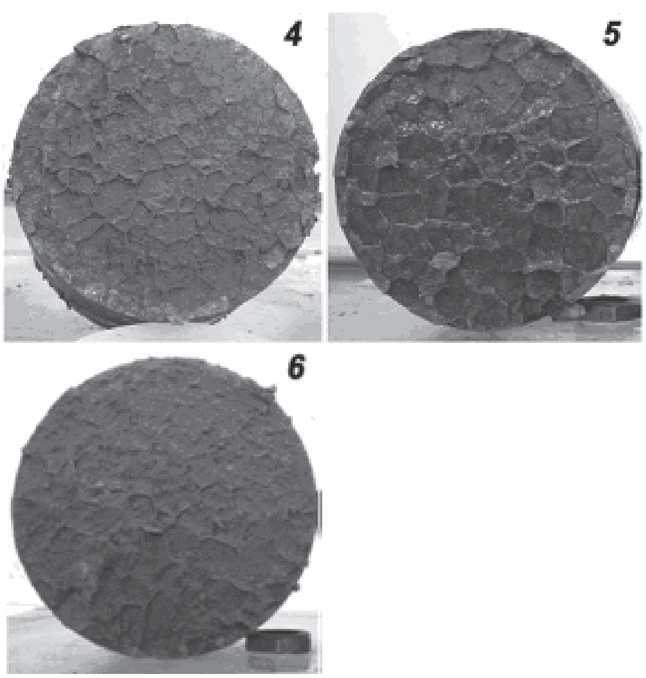

Figure 6. Cross sections after freezing for tests under different vertical pressure: #4: 100 kPa, #5: 200 kPa, #6: 400 kPa.

equilibrium. In an unfrozen state such suction would reduce the hydraulic conductivity in the Devon silt by more than 70%.

In order to estimate the amount of water flowing through the frozen fringe, an average value had to be determined. The average hydraulic conductivity k_{mv} can be calculated by assuming flow through a series of layers with changing hydraulic permeability and using Equation 1:

$$k_{mv} = \frac{\sum d_i}{\sum \frac{d_i}{k_i}} \tag{1}$$

Where d_i is the layer thickness and k_i the permeability. An exponential decrease in pore water pressure is further assumed in the frozen fringe towards the ice lens with no suction at the freezing front. This is a conservative approach since suction is most likely to penetrate into the unfrozen soil (Seto & Konrad 1994). Under these conditions, k_{mv} = 1.7 x 10^{-16} m/s, and a minimum of 8 x 10^{-18} m/s at the ice lens is determined for the frozen fringe in test #1 (Fig. 8). Utilizing Darcy's law a hydraulic gradient can be estimated. The average hydraulic gradient required in order to attract the necessary amount of water would be 17 x 10^6. This is significantly higher than the hydraulic gradient (~7000) that can be generated over the frozen fringe with a suction of 438 kPa.

Using the suction development at the ice lens and the SWCC may underestimate the hydraulic conductivity of the soil. However, even if the minimum hydraulic conductivity was capped at 1 x 10^{-14} m/s, the gradient would be in the order of 80,000. Such a cap would represent values measured for hydraulic permeability in frozen soils (Williams & Burt 1974).

Even though several assumptions had to be made that need further confirmation, and it may even be possible that the suction generated at the ice lens is capable of attracting enough water towards the ice lens, some concerns remain. If the suction reaches values of approximately 900 kPa it is possible that cavitation occurs under atmospheric conditions, i.e. as it reaches its vapor pressure, the pore fluid vaporizes and forms small bubbles of gas. According to the authors' knowledge no experimental evidence is available that shows the formation of gas bubbles at an ice lens.

New Ice Lens Growth Hypothesis

Based on recent laboratory investigations a new concept behind ice lens growth and frost heave is proposed. In 1979, Chamberlain & Gow (1979) presented similar ideas and experimental evidences. They showed that freezing and thawing caused a reduction in void ratio and an increase in vertical conductivity. The later was attributed to the formation of polygonal shrinkage cracks. However, no definite relationship could be established and the mechanisms observed have not been connected to ice lens formation and growth.

The new idea is based on water flow along vertical ice

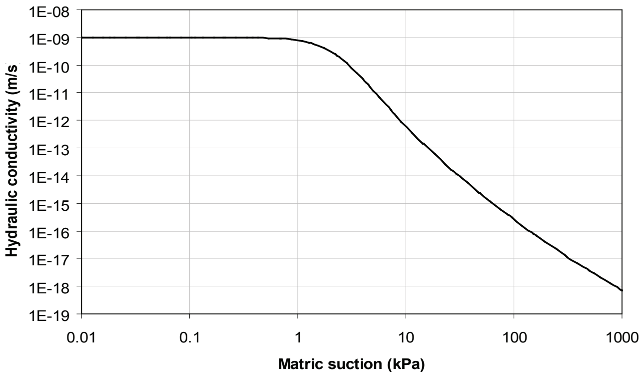

Figure 7. Hydraulic conductivity as a function of suction. Curve determined after Fredlund and Xing (1994).

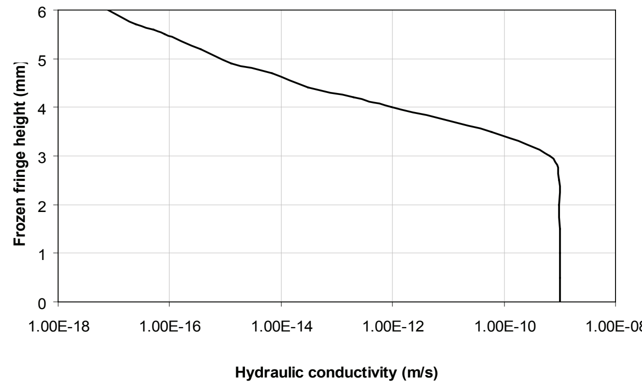

Figure 8. Hydraulic conductivity in the frozen fringe.

veins. As suction builds within the frozen fringe and the unfrozen soil below the freezing front, the soil reaching its tensile strength resulting in thin vertical cracks. These cracks are originally filled with water but will freeze rapidly as the freezing front penetrates. Between the vertical ice vein and the soil, a water film forms. This film is not the same as a water film that would form around a soil particle at thermal steady state, and may only be 60–100 nm thick at 0.1°C.

Instead of a one-dimensional water flow through the frozen fringe, that has a low hydraulic conductivity, water from the unfrozen zone migrates along the vertical ice veins towards the growing horizontal ice lens. By assuming laminar, incompressible, steady flow between two parallel plates (e.g., Streeter and Wylie 1985), a layer of 3 µm and a suction of 100 kPa would be enough to allow the necessary amount of water flow towards the ice lens in test #1. This simple calculation shows that significantly more water can migrate from the unfrozen soil to the growing ice lens along these ice veins at a much lower suction gradient than if it has to migrate through partially frozen pores of the frozen fringe. The thickness of the vertical ice lens did not change with time. It is assumed that no ice accumulation occurs because of the moving water film at the interface between the soil and the ice. Further, there is no major heat loss perpendicular to the ice vein that could lead to horizontal crystal growth. Figure 9 shows a schematic of the flow scheme based on this new concept.

Because water flow along vertical ice lenses controls the amount of water that migrates through the frozen fringe, it is basically the tensile strength of the soil at a certain stress state that governs ice lens growth. In order to attract sufficient water the suction may reach values that would cause tension cracking of the soil below the warmest ice lens. With a higher tensile strength, fewer vertical cracks can form, and therefore a lower number of preferential flow paths are available for water to migrate towards the ice lens. The application of a vertical stress, for example, changes the stress state of the Devon silt resulting in fewer cracks and therefore slower frost heave.

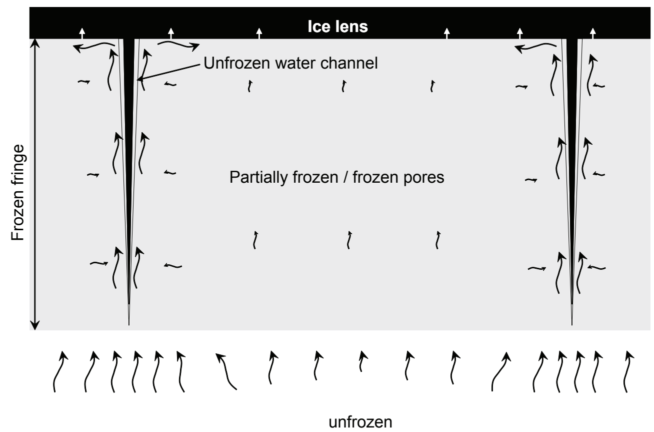

Figure 9. Water migration in freezing soils.

Conclusions

Based on experimental evidence a new hypothesis for a frost heave mechanism is proposed. The existence of vertical channels can explain the measured growth of the horizontal ice lenses considering the consolidation and the decreasing hydraulic conductivity in the frozen fringe. To date it is not clear how these vertical ice veins and water channels form. The tensile strength of the unfrozen soil may be reached as suction occurs. In addition, strain compatibility in the consolidation soil may also trigger the formation of vertical cracks.

However, the stress state and tensile strength of a soil basically govern ice lens growth because they controls the number of vertical cracks and vertical ice lenses that form in the frozen fringe.

A new series of one-dimensional freezing tests is currently being carried out at the University of Alberta Geotechnical Centre to improve our understanding of the hypothesis presented. The relationship between the hexagonal element sizes and frost heave rate will be studied in more detail using different soils as well as saline pore water. Saline pore water is known to change the size and shape of the ice lens pattern as well as the frost heave behavior (Arenson et al. 2006). The goal of this future research is to couple the tensile strength of a soil directly with frost heave potential.

Even though intense research has to be carried out in the future to support these ideas, the authors believe that it is time to move from a one-dimensional frost heave model towards a three-dimensional concept, even for one-dimensional freezing conditions.

Acknowledgments

The authors wish to acknowledge the valuable contributions obtained from three independent reviewers. They would further like to thank Andy Take from Queen's University for his support with the GeoPIV analysis. Tezera Firew Azmatch appreciated the financial support through the NSERC Discovery Grant held by Dr. Sego.

References

Aguirre-Puente, J. & Gruson, J. 1983. Measurement of permeabilities of frozen soils. In: T.L. Péwé and J. Brown (eds.), *4th International Conference on Permafrost, Fairbanks, AK, United States, July 17-22, 1983*: 5-9.

Arenson, L.U., Sego, D.C. & Take, W.A. 2007. Measurement of ice lens growth and soil consoliodation during frost penetration using particle image velocimetry (PIV), *60th Canadian Geotechnical Conference, Ottawa, ON*: 2046-2053.

Arenson, L.U., Xia, D., Sego, D.C. & Biggar, K.W. 2006. Change in ice lens formation for saline and non-saline Devon silt as a function of temperature and pressure. In: M. Davies & J.E. Zufelt (eds.), 1*3th International Conference on Cold Regions Engineering. American Society of Civil Engineers (ASCE), Orono, Maine, USA*: CD-Rom.

Beskow, G. 1935. Soil freezing and frost heaving with special applications to roads and railroads. *Swedish Geological Society, C, No. 375, Year Book No. 3*, Cold Region Research and Engineering Laboratory, Special Report 91-23: 41-157.

Chamberlain, E.J. & Gow, A.J. 1979. Effect of freezing and thawing on the permeability and structure of soils. *Engineering Geology* 13(1-4): 73-92.

Fredlund, D.G. & Xing, A.Q. 1994. Equations for the soil-water characteristic curve. *Canadian Geotechnical Journal* 31(4): 521-532.

Gilpin, R.R. 1980. A model for prediction of ice lensing and frost heave in soils. *Water Resources Research*, 16(5): 918-930.

Henry, K.S. 2000. *A Review of the Thermodynamics of Frost Heave.* CRREL Technical Report (TR 00-16): 25.

Horiguchi, K. & Miller, R.D., 1980. Experimental studies with frozen soil in an "ice sandwich" permeameter. *Cold Regions Science and Technology* 3(2-3): 177-183.

Konrad, J.M. 1989. Pore water-pressure at an ice lens: Its measurement and interpretation. *Cold Regions Science and Technology* 16(1): 63-74.

Konrad, J.M. 1994. 16th Canadian Geotechnical Colloquium - Frost Heave in Soils - Concepts and Engineering. *Canadian Geotechnical Journal* 31(2): 223-245.

Konrad, J.M. & Morgenstern, N.R. 1980. A mechanistic theory of ice lens formation in fine-grained soils. *Canadian Geotechnical Journal* 17(4): 473-486.

Konrad, J.M. & Morgenstern, N.R. 1982. Effects of applied pressure on freezing soils. *Canadian Geotechnical Journal* 19(4): 494-505.

Konrad, J.M. & Samson, M. 2000a. Hydraulic conductivity of kaolinite-silt mixtures subjected to closed-system freezing and thaw consolidation. *Canadian Geotechnical Journal* 37(4): 857-869.

Konrad, J.M. & Samson, M. 2000b. Influence of freezing temperature on hydraulic conductivity of silty clay. *Journal of Geotechnical and Geoenvironmental Engineering* 126(2): 180-187.

Mackay, J.R. 1974. Reticulate ice veins in permafrost, Northern Canada. *Canadian Geotechnical Journal* 11(2): 230-237.

McRoberts, E.C. & Nixon, J.F. 1975. Reticulate ice veins in permafrost, Northern Canada - Discussion. *Canadian Geotechnical Journal* 12(1): 159-162.

Miller, R.D. 1973. Soil freezing in relation to pore water pressure and temperature, *Second International Conference of Permafrost. Natl. Acad. Sci., Washington., Yakutsk, Siberia*: 344–352.

Nixon, J.F.D. 1991. Discrete ice lens theory for frost heave in soils. *Canadian Geotechnical Journal* 28(6): 843-859.

O'Neill, K. & Miller, R.D. 1985. Exploration of a rigid ice model of frozet heave. *Water Resources Research* 21(3): 281-296.

Penner, E. 1959. *The Mechanism of Frost Heaving in Soils.* Bulletin 225, U.S. Highway Research Board.

Penner, E. 1972. *Influence of Freezing Rate on Frost Heaving*. Highway Research Record 393, U.S. Highway Research Board.

Seto, J.T.C. & Konrad, J.M. 1994. Pore pressure measurements during freezing of an overconsolidated clayey silt. *Cold Regions Science and Technology* 22(4): 319-338.

Streeter, V.L. & Wylie, E.B. 1985. *Fluid Mechanics*. McGraw-Hill Book Company, 586 pp.

Taber, S. 1929. Frost heaving. *Journal of Geology* 37(5): 428-461.

Taber, S. 1930. The mechanics of frost heaving. *Journal of Geology* 38: 303-317.

Williams, P.J. & Burt, T.P. 1974. Measurement of hydraulic conductivity of frozen soils. *Canadian Geotechnical Journal* 11(4): 647-650.

Xia, D. 2006. *Frost Heave Studies Using Digital Photographic Technique.* M.S. Thesis. Edmonton, AB, Canada: University of Alberta, 165 pp.

Impact of the August 2000 Storm on the Soil Thermal Regime, Alaska North Slope

David E. Atkinson

International Arctic Research Center, University of Alaska Fairbanks, Fairbanks, Alaska 99775, USA

Larry Hinzman

International Arctic Research Center, University of Alaska Fairbanks, Fairbanks, Alaska 99775, USA

Abstract

The impact of a severe Alaska North Slope storm (August 2000) on the ground thermal regime along a north-south/coastal-inland transect was investigated. Using data gathered by the Water and Engineering Research Center at the University of Alaska Fairbanks, the storm was found to have a strong and widespread effect. Briefly, the storm initiated rapid cooling that was fairly uniformly expressed at all sites, despite their varying distances from the coast. At all of the sites 30 cm ground temperature dropped from 4°C to 1°C which, at the coastal sites, did not return to pre-storm summer levels before the initiation of winter despite two subsequent warm periods.

Keywords: Alaska; arctic storms; coastal; ground thermal regime.

Introduction

Storms in the arctic coastal zones have well-documented impacts on infrastructure and coastal morphometry via waves and storm surges (Rahold et al. 2005); however, the associated impacts on the ground thermal regime are not well documented. Gaining further insight into this issue is especially important in ice-rich regions where the seasonal freeze-thaw cycle is a critical underpinning to many derivative studies. A primary impact of storm passage is a rapid cooling of the entire active layer. This can act to prematurely shorten the thaw season by initiating early fall cooling. Focusing on a particularly severe storm (August 2000) and using a north-south/coastal-interior transect of meteorological and ground temperature data, this issue, one that has received virtually no specific treatment in the literature, is explored in detail.

The North Slope storm of August 10–12, 2000

In August of 2000, a strong storm moved from the north Chukotka coast, across the Chukchi Sea over to Alaska, and eastward along the North Slope coast. The storm strengthened to 996 millibars by August 11, when its center was positioned north of Prudhoe Bay (Fig. 1), and it developed a very strong pressure gradient to the west. The strong pressure gradient generated observed winds of 70 kts (36m/s), which caused the storm to develop heavy sea states that included a moderate surge and high waves. This event caused $7.7 million dollars in infrastructure damages along the North Slope, including the sinking of a barge (Koslow 2000). Unusual for Alaska, this event also caused substantial wind damage in the form of roof failure on many structures in Barrow.

The strength and orientation of the storm circulation (Fig. 2) allowed it to tap into a cold air mass situated over the mid/north Beaufort Sea (Fig. 3) and to draw it over and well south into the north Alaskan landmass. This rapid influx of cold air reduced air temperatures by up to 10°C in coastal areas (Fig. 4), from well above zero in the +6°C to +8°C range to below the freezing point, within a day.

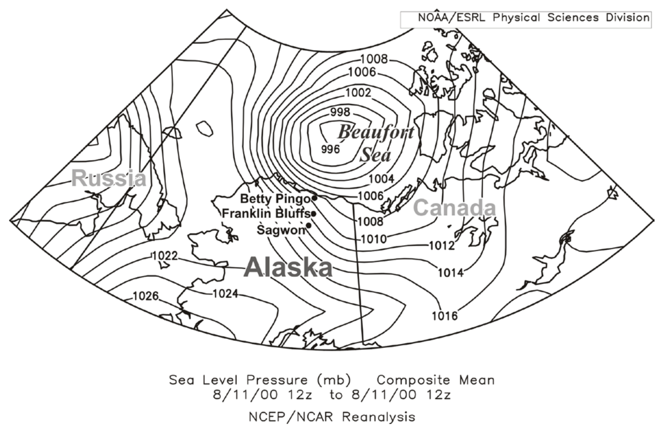

Figure 1. A plot of surface mean sea level pressure showing the August 2000 storm at peak intensity, 0300 AKT on August 11, 2000. The three ground temperature sites from which ground thermal and meteorological data were drawn are indicated. These locations are operated by the Water and Engineering Research Center at the University of Alaska Fairbanks as part of the "Kuparuk River Watershed Studies" project. Note closely-spaced pressure contours to the west of storm center. This flow pattern advected cold air over the North Slope region. (Pressure pattern data from the National Centers for Environmental Prediction/Department of Energy Reanalysis II, plotted at the National Oceanic and Atmospheric Administration's Earth Systems Research Laboratory [NOAA-ESRL]). AKT refers to Alaska Time.

Given its effect on air temperatures, the influx of cold air also likely had an impact on the ground thermal regime. It is the objective of this paper to examine the nature of this response at several locations in the North Slope of Alaska and to assess its possible impact at the seasonal time-frame.

Data and Methods

Meteorological and ground temperature data were obtained from monitoring sites operated as part of the Kuparuk River Watershed project by the Water and Engineering Research Center (WERC) at the University of Alaska Fairbanks (Kane & Hinzman 2000, Kane et al. 2000, Romanovsky

Table 1: The three main locations from which soil temperature profile data were drawn. The abbreviation for each station used in the text is given.

Site	*Sub-sites*	*Distance to coast (Prudhoe Bay)*
Betty Pingo	Upland (BPU)	12 km
	Wetland (BPW)	
Franklin Bluffs (FB)	--	70km
Sagwon (SW)	--	100km

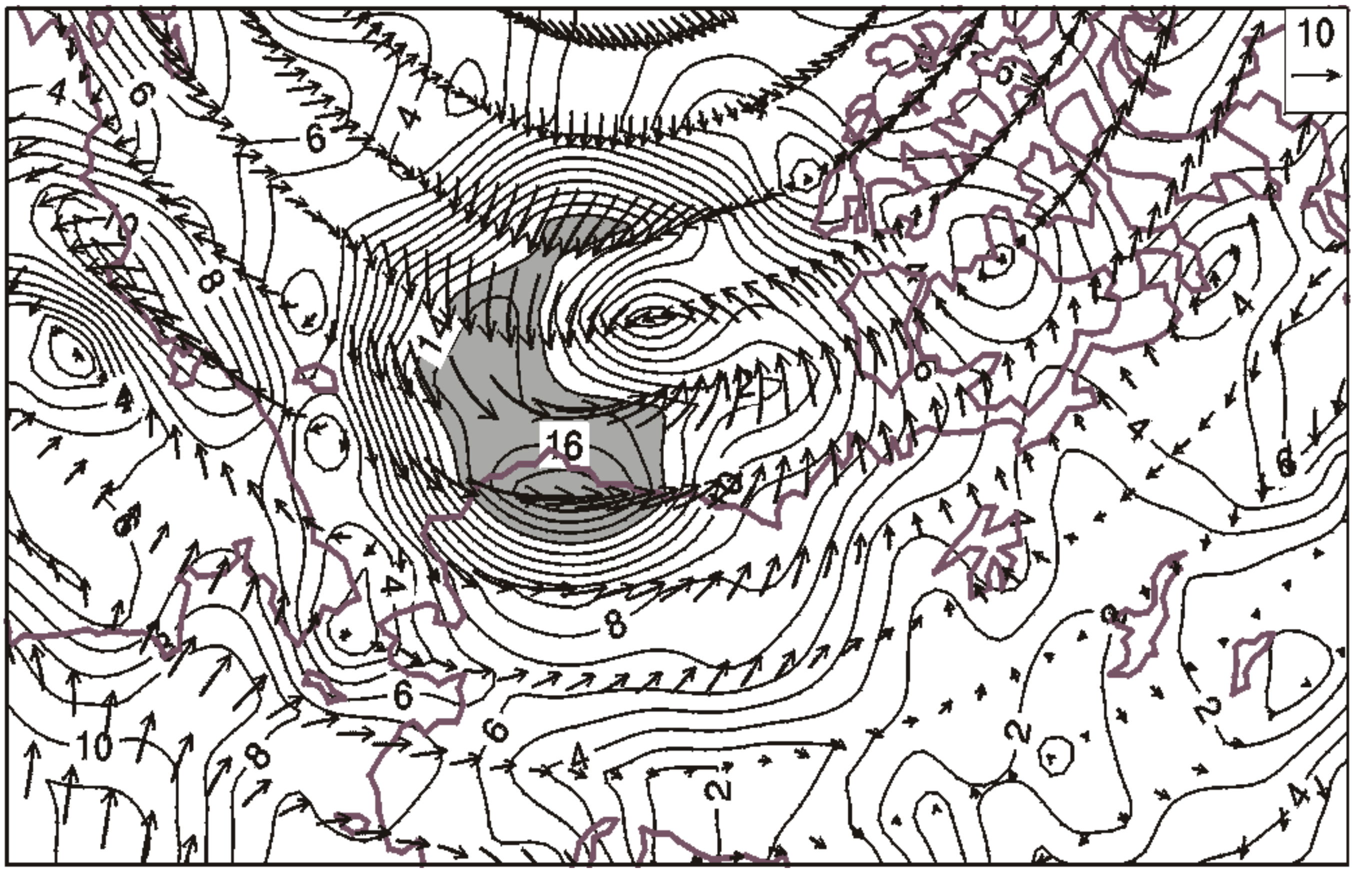

Figure 2. Wind speed isotachs (m/s) and direction vectors at the height of the storm (Aug. 10, 2100AKT). Shaded zone represents wind speeds exceeding 14 m/s.

& Osterkamp 2006). Four data sets were used from three separate locations (Table 1, Fig. 1).

This sampling methodology allowed a north-south transect to be examined with the three locations at successively greater distances from the coast. Storm winds and the strength of an advective temperature change can decrease with distance away from the coast due to a reduction of wind speed, brought about by increased surface roughness, and reduction of air/ground temperature gradient due to a longer exposure of the air mass to the modifying effects of the surface underneath (Wallace & Hobbs 2006, 404). In addition, the two locations at the Betty Pingo site allowed comparisons to be made between a saturated ("Wetland site") and non-saturated ("Upland site") ground. Data are available online at the WERC website (Kane & Hinzman 2000).

Analysis consisted of a direct examination of selected time series and a comparison between sites and between specific elements for the period of time surrounding the storm to determine timing and magnitude of temperature change at different levels. This was performed using a comprehensive plot on which time series from the four stations were laid out side-by-side (Fig. 5). Ground thermal data were recorded hourly at BPU and BPW and once daily at the FB and SW locations. At all locations, meteorological data were recorded once per hour; however, they were subset to once per day at FB and SW for comparison with the ground thermal data.

Results

The ground thermal regime at BPW and BPU responded rapidly to the initiation of cold air advection by the storm winds. The regular daytime cooling that was underway by mid-afternoon, August 10 (all time references are local time) was extended well below the daytime minimum (approximately 6–7°C) at the two sites compared to the preceding days. This coincided with the establishment of

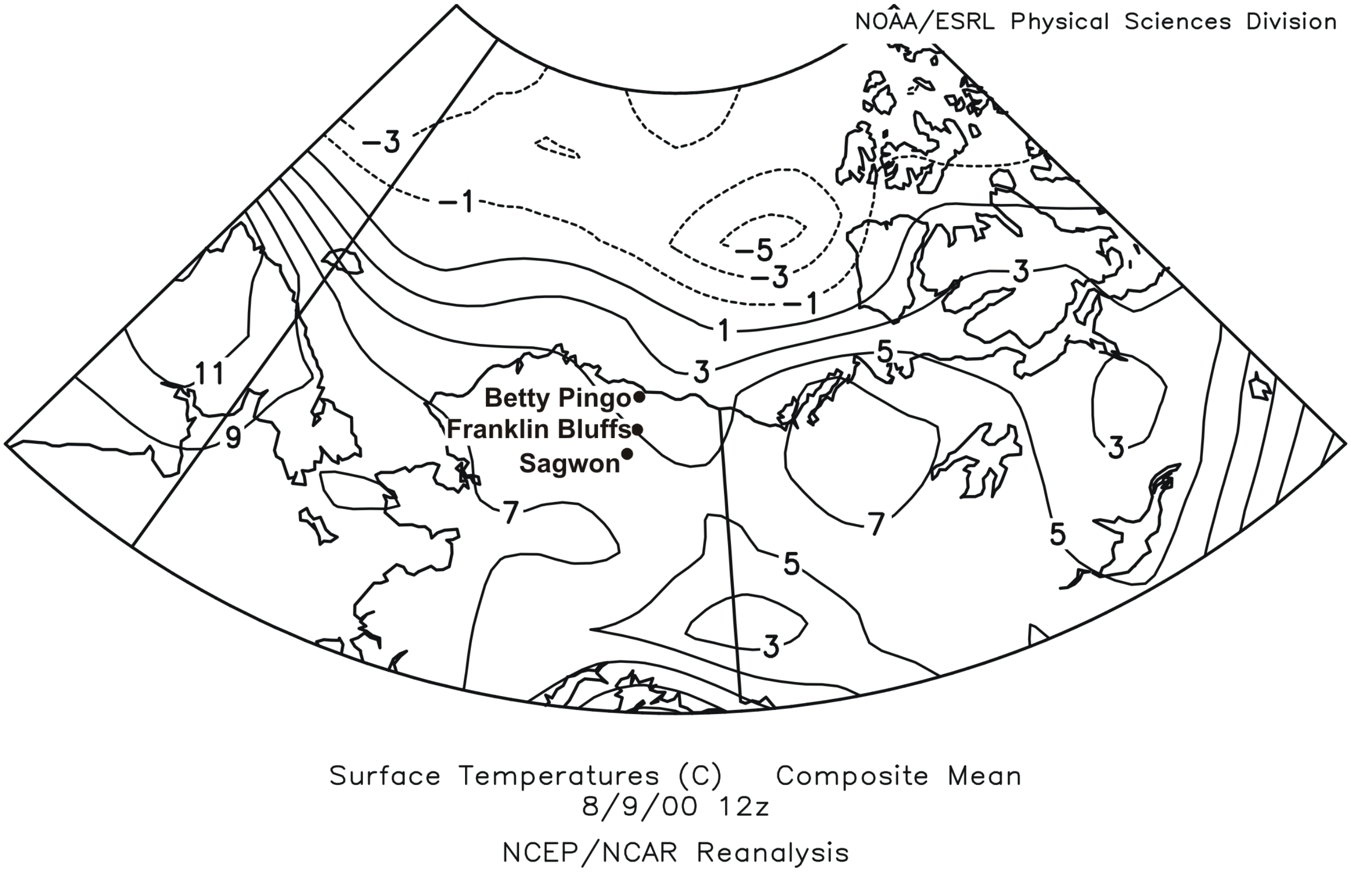

Figure 3: Surface air temperature distribution two days before the storm. Dashed isotherms indicate negative temperatures. Note the cold zone over the north/west Beaufort (circled). Rapid advection of this air mass along the trajectory indicated by the heavy arrow occurred as the storm moved along the north coast.

strong, persistent winds out of the west (Fig. 6 – BPU and BPW). At BPW air temperatures dropped 16°C, to -2°C, within one day and then dropped further the next day. The 5 cm soil depth temperature responded with a drop from ~7°C to 2°C in a 36-hour period. The 30 cm soil depth temperature dropped from 4°C to 2°C, and then further, down to 1°C, over the next few days. Similar patterns were observed at BPU, although at this location the air temperature drop was not as large, which meant the corresponding decrease in ground temperatures occurred slightly later. The main response difference observed between the BP wetland and upland sites was that soil temperatures at the wetland site exhibited a greater sensitivity to the air temperature forcing, especially 30 cm depth, from 5°C to 1°C at the upland site, whereas at the wetland site the 30 cm temperature change was from 4°C to 1.5°C. This is despite the fact that the upland site sensor is positioned slightly deeper, at 35 cm, and not 30cm. It was interesting to note, however, that the temperature drop at the 5 cm depth was greater at the wetland site, from 8°C to 2°C, whereas at the upland site, the 5 cm temperature change was from 7°C to 2°C.

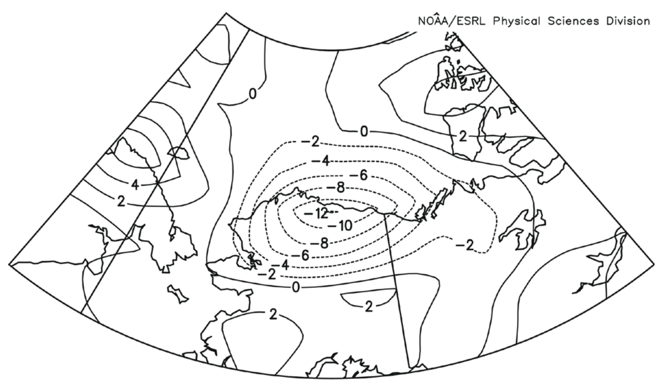

Figure 4. Surface air temperature difference plot, Aug. 11, 0900 AKT minus Aug. 10, 0900 AKT. This indicates the magnitude of temperature change in a 24-hour period over the north Alaska landmass. Dashed lines indicate negative temperature isotherms.

The data availably at FB and SW limited the detail of analysis but the major patterns were apparent. The same pattern of wind speed and direction observed at the BP sites prevailed at FB and SW—a strong peak in wind speeds developed out of the west. Although the two sites started with different air temperatures, at both locations air temperature had dropped to -2°C by the second day, representing decreases of 12°C (FB) and 10°C (SW). At both sites a drop in the 5 cm soil temperatures from 6°C to 2°C (FB) and from 9°C to ~1°C (SW) was observed, and in the 30 cm soil temperatures from 4°C to 1°C was observed.

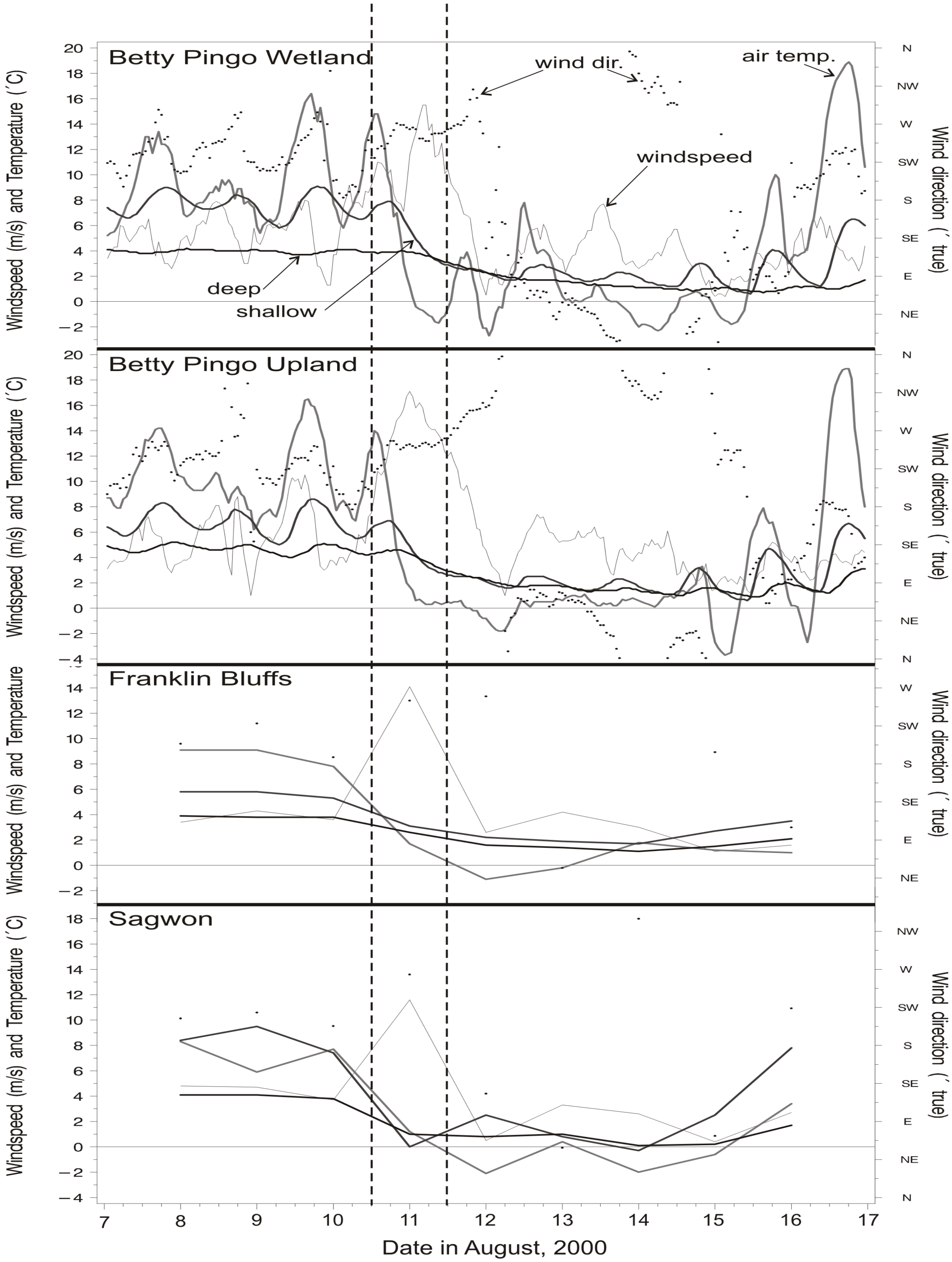

Figure 5. Winds, air temperature, and ground temperatures at the four sites. The following formatting scheme is applied to each plot: the dots represent wind direction observations in degrees true heading (vertical scale on the right), the thin black line represents wind speed (m/s), the thick light grey line represents air temperature (°C), the thick medium grey line represents a "shallow" ground temperature (°C), the thick black line represents a "deep" ground temperature (°C). The distinction "shallow" refers to the 5 cm soil depth at all sites and "deep" refers to 30 cm soil depth at all sites except Betty Upland, where it is 35 cm depth. The two vertical dashed lines represent the core of the storm from 1200 AKT, August 10 to 1200 AKT, August 11, 2007.

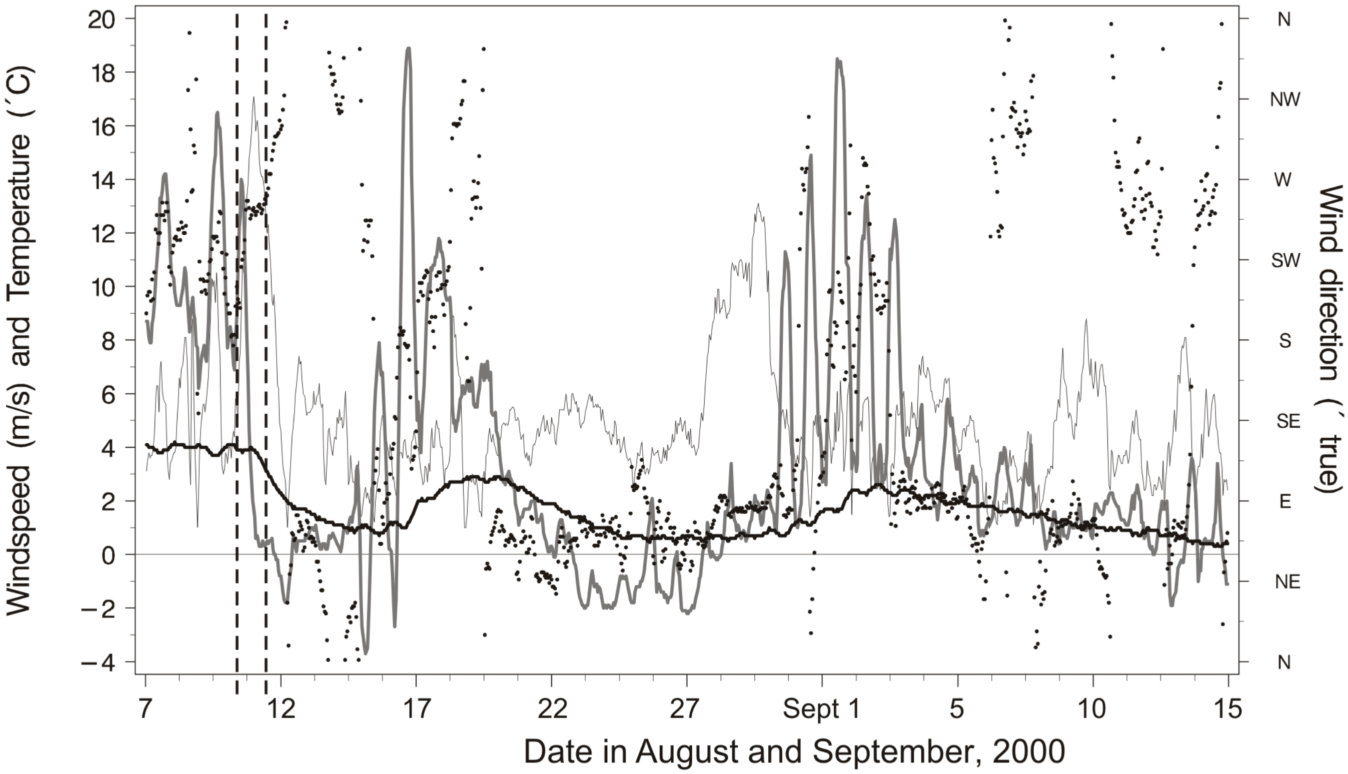

Figure 6. Wind speed and direction, air temperature, and 30 cm ground temperature at Betty Pingo Wetland. Storm time frame is indicated by the vertical dashed lines. Line schema is identical to that used in Figure 5.

Discussion and Conclusions

Examination of the longer-term implications of the storm-induced temperature drop at BPW site shows that, despite two very warm spells (air temperatures >15°C), the temperature at 30 cm does not again reach its summer levels (Fig. 7). This suggests that the influx of cold air from the storm was sufficient to set the stage for winter freeze-up; that is, it may be argued that without the contribution of this storm event, ground freeze-up would have occurred later in the fall. A more frequent occurrence of such storm events, which might accompany conditions of reduced sea-ice cover, could have the paradoxical effect of checking a summer ground thermal warming trend. Cooling did not seem to be quite as prominent at the inland sites (not shown): during the two warm episodes, 30 cm temperatures did warm to return almost to their pre-storm levels, although, as noted below, all sites cooled to a uniform extent.

Overall, the reach of the storm was considerable—marked effects on ground thermal regime were noted 100 km inland at Sagwon site, situated effectively at the foothills of the Brooks Range. Typically when an air mass is advected a long way over a surface, the lowest atmospheric layers begin to take on the temperature and moisture characteristics of the surface. In this case, that means the air mass should warm as it moves inland. However, the lowest air temperature reached during the event (start of August 12) at all four sites—that is, ~-2°C, was essentially the same. The ground thermal response was likewise uniform: at all sites the 30 cm soil temperature dropped to 1°C. This is indicative of the strength and persistence of the wind, that the air was moved so rapidly into the region that it underwent little modification in its lowest layers. Even though the peak wind speeds were progressively lower with increasing distance inland, they were still sufficient to move the advected air rapidly enough. Thus this one event affected soil temperatures to at least 30 cm depth over the bulk of the Alaska North Slope.

It is important to note that this particular event possessed unusual strength, which means it is unlikely that similar events observed on the north coast would be exert an influence as far inland as this event did. This is a question, however, that should be pursued in more detail to better understand the potential of increased summer storm activity on the ground thermal regime of the Alaska North Slope. It is clear that broader consideration of advected air masses and their relative frequency of occurrence over time could be a useful component of ground thermal regime to consider in more detail.

References

Kane, D.L., Hinzman, L.D., McNamara, J.P., Zhang, Z. & Benson, C.S. 2000. An Overview of a Nested Watershed Study in Arctic Alaska. *Nordic Hydrology* 31: 245-266.

Kane, D.L. & Hinzman, L.D. 2000. *Climate data from the North Slope Hydrology Research project*. University of Alaska Fairbanks, Water and Environmental Research Center. http://www.uaf.edu/water/projects/NorthSlope/ Fairbanks, Alaska, variously paged.

Koslow, M. 2000. *Climatology of Low Pressure Systems near Barrow, Alaska*. Unpublished monograph. University of Colorado, 18 pp.

Rahold, V., Are, F.E., Atkinson, D.E., Cherkashov, G. & Solomon, S.M. 2005. Arctic Coastal Dynamics: an introduction. *GeoMarine Letters* 25: 2-3.

Romanovsky, V. & Osterkamp, T. 2006. Interannual variations of the thermal regime of the active layer and near-surface permafrost in northern Alaska. *Permafrost and Periglacial Processes* 6: 316-335.

Wallace, J.M. & Hobbs, P.V. 2006. *Atmospheric Science: An Introductory Survey* (2nd ed.). New York: Academic Press, 483pp.

Global Simulation of Permafrost Distribution in the Past, Present, and Future Using the Frost Number Method

Tim Aus der Beek, Ellen Teichert
CESR, Center for Environmental Systems Research, University of Kassel, Germany

Abstract

Currently, about 39 mil km² of the world (including Antarctica) are covered by permafrost. One aim of this modeling experiment is to compare the current global permafrost distribution with its extent in the past and in future projections by integrating the well-known Frost Number method into the global hydrological and water-use model WaterGAP. The Frost Number is related to the zonal arrangement of permafrost and was slightly modified to test its receptivity of different snow parameter formulations. For past extents the Frost Number was averaged for 1901–1930 and set in contrast to present permafrost spreading (1971–2000). The future time slice was computed by averaging permafrost extent for 2071–2100, and was yet again compared with present and past permafrost extents. From the wide variety of climate scenarios, two contrasting IPCC-SRES scenarios, A1B and B1, were chosen. CO_2 and CH_4 feedback loops of melting permafrost were not considered in the model. To account for the specific variability of General Circulation Models (GCMs), two different GCMs were applied for both IPCC-SRES scenarios. Model results imply that the area of global permafrost occurrence decreased by 7% between past and present conditions, and future scenarios project that 30%–45% of the contemporary extent could be diminished by 2100. The application of different snow-parameter formulations yielded only minor changes in the quantification of the Frost Number.

Keywords: climate scenarios; Frost Number; global modeling; permafrost distribution; WaterGAP.

Introduction

The well-known Frost Number has proven its suitability for application to large geographical domains (Anisimov & Nelson 1997), but has never been operated on the global scale. The study presented hereby examines permafrost spreading on the global scale and, contrary to most other modeling efforts, considers three different time periods between 1901 and 2100. Future permafrost zonation is also used to roughly estimate the increase of atmospheric carbon content, released from formerly frozen grounds. The Frost Number method has been applied to several regions, such as the Northern Hemisphere (Anisimov & Nelson 1997), and has proven its suitability for the prediction of permafrost over large geographical domains by comparison with hard data (Anisimov & Nelson 1997). The Frost Number applied in this study relies on freezing and thawing indices based on air temperature (Frauenfeld et al. 2007) instead of modeled soil temperature, as in Stendel & Christensen (2002) or Lawrence & Slater (2005). Therefore, soil water processes and relic permafrost are not considered in the model.

Snow density, which is supposed to be crucial for the computation of snow cover and thus permafrost occurrence, was kept constant in earlier analyses (Anisimov & Nelson 1997). This model experiment also tests the variability of the Frost Number method by employing a snow-density routine. Furthermore, it introduces two different algorithms for the calculation of thermal conductivity of snow.

Methods

WaterGAP and data

To allow for a global application of the Frost Number method, it was incorporated into the hydrology and water-use model WaterGAP 2.1f (Water-Global Assessment and Prognosis), which computes daily water balances for a global 0.5°x0.5° grid with monthly hydrological outputs, such as river runoff and evapotranspiration (Döll et al. 2003). Due to its implemented soil routine, WaterGAP also offers good prerequisites for potential modeling of future active layer permafrost thawing. However, in this study the soil and runoff generation routine has not yet been linked to permafrost modeling.

The input data for past and current climate conditions used in this study consists of the CRU dataset (version TS 2.1, Mitchell & Jones. 2005), which has been compiled and regionalized by the Climate Research Unit (CRU) of the University of East Anglia, Norwich, UK. Air temperature and precipitation for both future scenarios were calculated by two different transient atmospheric General Circulation Models (GCMs) to account for the spatial variability of climate patterns in GCMs. The first GCM projection of air temperature and precipitation applied in WaterGAP is calculated by the Hadley Center Coupled Model (HadCM3), which has been developed at the Hadley Center for Climate Predictions and Observations in Exeter, UK (Gordon et al. 2000). ECHAM5, the second GCM, has been developed by the Max-Planck Institute for Meteorology (MPI) in Hamburg, Germany (Roeckner et al. 2006). Both GCMs have been scaled with the IPCC-SRES (Intergovernmental Panel on Climate Change – Special Report on Emission Scenarios) scenarios A1B and B1 (IPCC 2001). The A1B scenario is driven by very high economical outputs and energy demands, which nearly double today's CO_2 emissions and lead to an air temperature increase of 4.4°C (multi-model global mean) between 2000 and 2100. On the contrary, the B1 scenario projects CO_2 emissions slightly lower than today and an average air temperature increase of 3.1°C (multi-model global mean for 2100), which occurs in combination with a balanced economy and usage of alternative energy systems. CO_2 and CH_4 feedback loops of melting permafrost are not included in the data or model.

The Frost Number

The Frost Number method was developed by Nelson & Outcalt (1983, 1987) to predict and regionalize the presence and absence of permafrost on a large scale by calculation of degree-days of freezing (DDF) and thawing (DDT). The physical derivation and all computational details of the three different Frost Numbers (Air, Surface and Soil) are given in Nelson & Outcalt (1987).

The here-applied *Surface Frost Number* F_+ (equation 1) includes variables from the *Air Frost Number*, such as DDF and DDT, which are estimated from air temperature data for each grid cell. Furthermore, it also considers snow-cover properties at the earth surface, which can have large impacts on the process of soil freezing (Osokin et al. 2001). The *Surface Frost Number* has been applied in this study to analyze permafrost distribution for three different time periods: 1901–1930, 1971–2000, and 2071–2100. For all three time margins, F_+ has been averaged to a single value for each global grid cell to eliminate input inaccuracies caused by annual air temperature variations. The *Surface Frost Number* F_+ can be derived by

$$F_+ = \frac{DDF_+^{1/2}}{DDF_+^{1/2} + DDT^{1/2}} \quad (1)$$

where DDF_+ and DDT_+ are degree days of "surface" freezing and thawing (°C days). Due to this definition, F_+ ranges between 0 and 1, for which Nelson and Outcalt (1987) further derived threshold boundaries for different permafrost types, such as continuous ($F_+ \geq 0.67$), extensive discontinuous ($0.67 > F_+ \geq 0.6$), sporadic discontinuous ($0.6 > F_+ \geq 0.5$) and no permafrost ($F_+ < 0.5$).

We will only explain selected important formulations of the derivation of DDF_+ and DDT_+ to not repeat Nelson & Outcalt (1987). The main feature of F_+ is the integration of the snow cover, which is calculated by

$$\overline{Z}_s = \sin^2 \phi \{\sum_{i=1}^{k} [(P_i / \rho_r)(k-(i-1))]/k\} \quad (2)$$

where $\overline{Z}_s$ is the average winter snow-cover depth, P_i is water-equivalent precipitation for months i (i = 1, 2, …, k), ρ_r is relative snow density of each cell, and Φ is the cell's latitude. The trigonometric function of equation (2) determines shorter and less pronounced thaws with increasing latitude, whereas the latter term weights snow falling early in the year at higher latitudes, simulating a more realistic snow-cover distribution. A description of the influence of intra-annual variability of snowfall on permafrost occurrence can be found in Zhang et al. (2001).

As snow density was kept constant in earlier applications of the Frost Number, this study explores the effects of applying two different formulations of snow density for the 1971–2000 period. First, snow density is set constant to 100 kg m^{-3} for all cells and F_+ is being calculated. For the second case, snow density ρ_s (in kg m^{-3}) for each cell is computed by

$$\rho_s = 545 * (5 - \overline{T})^{-1.15} + 50 \quad (3)$$

where $\overline{T}$ is the mean winter air temperature in °C. Equation (3) was defined by Meister (1986), who derived this air temperature–fresh snow density relationship by analyzing more than 850 snow-density measurements for three different climate regions. He also showed that, for stations below 1500 m.a.s.l., wind effects are negligible for the computation of snow density. In this study, snow density calculated by equation (3) has been limited to a maximum of 700 kg m^{-3}, which is concordant with the findings of Mellor & Mellor (1988). In general, equation (3) yields slightly higher snow-density values than in well-known functions described by Jordan (1991) and Hedstrom & Pomeroy (1998). Another modification from the original set of formulations provided by Nelson & Outcalt (1987) is the application of two regression functions of snow density and snow thermal conductivity (equations 4 and 5). Both methods have been applied for both versions of snow-density derivation for 1971–2000, resulting in a total of four different global computations of the Surface Frost Number for that period. Here and in previous studies on F_+, thermal conductivity of snow λ_s (in W m^{-1} K^{-1}) has been calculated with the formulation of Van Dusen (Paterson 1994: 205):

$$\lambda_s = 2.1*10^{-2} + 4.2*10^{-4} \rho_s + 2.2*10^{-9} \rho_s^{\,3} \quad (4)$$

where snow density ρ_s is in kg m^{-3}. The second method of obtaining λ_s is given in Sturm et al. (1997) who found the following regression by the statistical evaluation of nearly 500 snow thermal conductivity measurements:

$$\lambda_s = 0.023 + 0.234 * \rho_s \quad \text{for } \rho_s \leq 0.156 \quad (5)$$
$$\lambda_s = 0.138 - 1.01 * \rho_s + 3.233 * \rho_s^{\,2} \quad \text{for } \rho_s > 0.156$$

Equation (5) requires ρ_s in g cm^{-3} and yields λ_s in W m^{-1} K^{-1}. The computation of F_+ for all three time slices has been carried out with equations (3) and (5), whereas present conditions were additionally calculated by three combinations of constant ρ_s and equations (3) to (5).

So far, the Surface Frost Number has been applied to Canada (Nelson 1986), Russia, and the Northern Hemisphere (Anisimov & Nelson 1996, 1997). All modeling results were validated by comparison with measured permafrost extents and generally showed good agreements. A sensitivity analysis for the Surface Frost Number in combination with climate change scenarios has been conducted by Anisimov & Nelson (1996).

Results

The modeled global distribution of permafrost for all three time periods is shown in Figure 1. The zonal extent of all

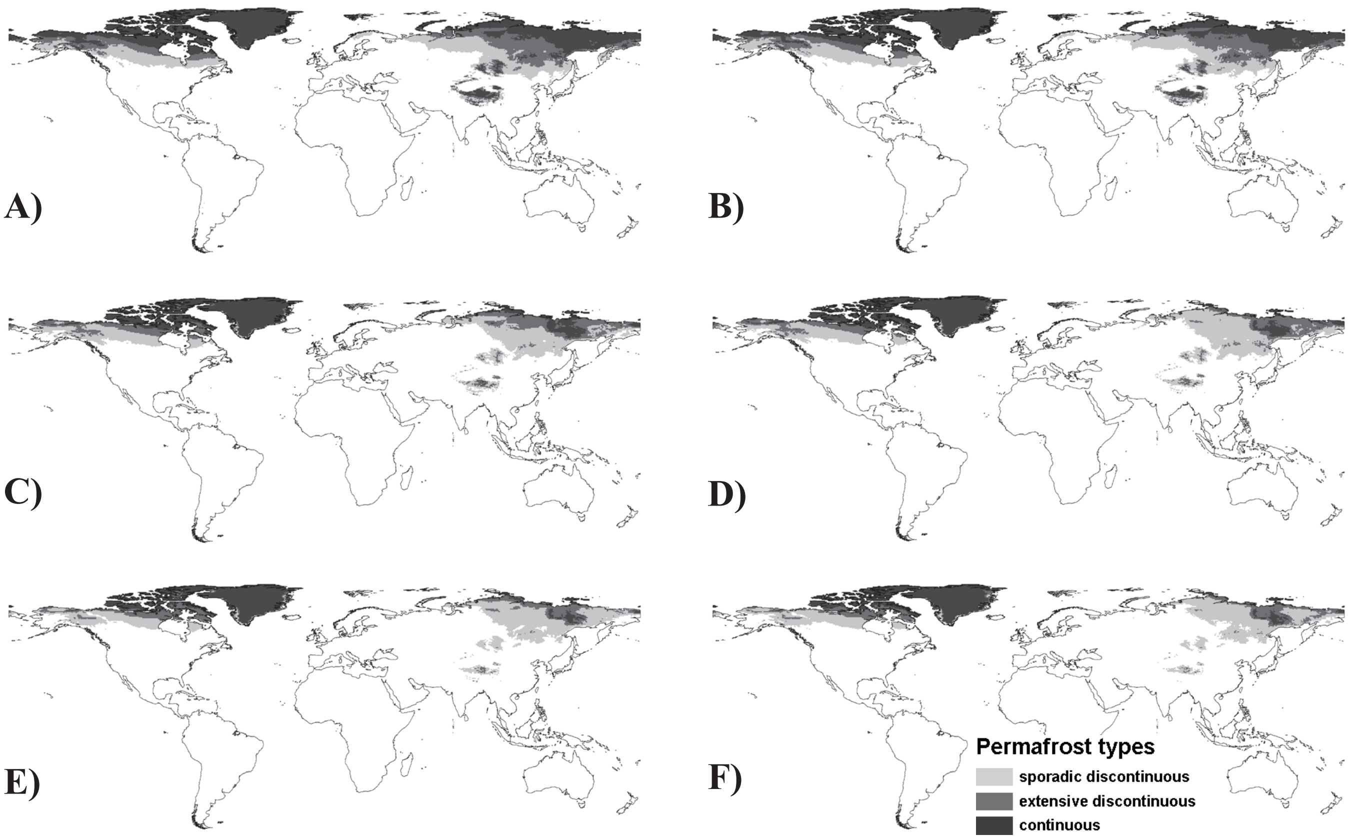

Figure 1. Global permafrost distribution modeling results (Surface Frost Number, using equations (3) and (5)). A): 1901-1930. B): 1971-2000. C): 2071-2100 (B1, HadCM3). D): 2071-2100 (B1, ECHAM5). E): 2071-2100 (A1B, HadCM3). F): 2071-2100 (A1B, ECHAM5).

permafrost calculations is given in Table 1. When comparing past and present conditions (Fig. 1A and 1B), it is noticeable that both, continuous and discontinuous permafrost boundaries, experience a moderate northeast shift. Due to the continental climate of the Eurasian permafrost regions, its degradation is more pronounced than for its North American counterpart. According to Table 1, the time period 1901–1930 featured 13% more continuous and 9% more discontinuous permafrost than today. An explanation for these findings can be derived by the analysis of air temperature data. Data analysis revealed that global average temperature in this modeling experiment increased by 0.5°C between both time periods, whereas the increase for permafrost regions averaged 0.7°C. Rising air temperature is strongly related to CO_2 emissions, which drastically increased since begin of industrialization.

Validation of present permafrost distribution

In order to assess the accuracy of the model results, we compared the Northern Hemisphere permafrost map of Brown et al. (1998) with the calculated present permafrost distribution. This was achieved by scaling the map to the 0.5° grid of WaterGAP. In general, total permafrost occurrence is underestimated by 7% (see Table 2), which could partially be explained by the model's inability to represent relic permafrost. The prediction of continuous and discontinuous permafrost cells is less accurate. However, this could be improved by adjusting the empirical threshold boundaries of the Frost Number. Additionally, we applied the map comparison algorithm *Kappa* (Pontius 2000) to contrast our results with the permafrost map. *Kappa* can vary between -1 and 1, where 1 describes a perfect fit and -1 is equivalent to a negative correlation of both maps. The global comparison yields a *Kappa* value of 0.67, whereas the comparison of the different permafrost zones yields a still acceptable value of 0.5.

A validation of simulated past permafrost distribution is not possible, as no permafrost map of this time period is available. However, as model results for past permafrost occurrence rely on the same climate data source as the validated present results, we can assume the results to be reasonable. In addition, Romanovsky (2005) found increasing permafrost temperatures for the last few decades at a multitude of boreholes. These outcomes support our model results of melting permafrost.

Future projections of permafrost distribution

The comparison of present and future permafrost occurrences (Fig. 1B versus 1C to 1F) can be discussed exemplarily for the HadCM3 climate forcing datasets. The pessimistic IPCC-SRES A1B scenario reveals significant zonal permafrost reductions of about 42% for the HadCM3 dataset (Fig. 1E). Once again, the impacts of climate change are more evident for the Eurasian continent, where continuous and extensive discontinuous permafrost is reduced to patches at the northeastern shoreline. Further, continuous permafrost with mid-continental exposition, such as in Mongolia and China, will be nonexistent. On the other side of the globe, modeled permafrost formations in Canada and Alaska undergo a northbound shift of 500 to 700 km. These findings can again be attributed to global warming. Thus, mean air temperature values of contemporary permafrost areas were compared to scenario temperatures for the same area. This revealed that the temperature increase was 15% (HadCM3) and 23% (ECHAM5) higher than the global average. Generally, the GCM ECHAM5 generates higher average air temperatures than HadCM3, and its combination with the IPCC-SRES A1B scenario yields with 11.6 million km² or -45% the strongest decrease of zonal permafrost arrangements of all four scenarios (see Table 1 and Fig. 1).

On the contrary, the optimistic IPCC-SRES B1 scenario indicates permafrost degradation of about 30% for both GCMs, whereas ECHAM5 again predicts higher losses than HadCM3. Since ECHAM5 triggers higher air temperature, much more continuous and extensive discontinuous permafrost is transformed to sporadic permafrost, which causes an increase of sporadic permafrost for this scenario. The spatial distribution of permafrost shows a less severe but yet significant shift of permafrost boundaries to the northeast. In contrast to the A1B scenario, northern Siberia still features a thick band of extensive discontinuous permafrost.

The conversion from continuous to discontinuous to no permafrost will have large impacts on society and climate. Nelson et al. (2002) describe how the permafrost-thawing processes already apparent cause soil instabilities; for example, by thermokarst, which render streets and buildings in Alaska and Canada useless. As permafrost regions are projected to be diminished by 7.7 to 11.6 million km² (see Table 1) during the next 100 years, the economical infrastructure expenses will rise dramatically for all circum-Arctic countries. In addition, large quantities of carbon are fixed in today's frozen ground which, if set free, can give impetus to feedback loops of an even more rapidly increasing climate. Zimov et al. (2006) state that the atmospheric global carbon budget rose by ~170 gigatons (GT) from preindustrial times to ~730 GT today. They further estimate that currently some 1980 GT are retained in glacier moraines, sediments beneath ice sheets, frozen Siberian loess, and steppe-tundra soils. If permafrost degradation follows the prediction of our analysis, about 600–900 GT of formerly frozen carbon will be released into the atmosphere and enhance already existent global warming until 2100.

The modeling results also suggest that the future rate of permafrost degradation will quadruple compared to today. During the last 70 years, annual global permafrost decline averaged ~23,000 km² per year, whereas the next 100 years will face an average loss of ~95,000 km² per year. In combination with the already described intensified global warming by carbon release from frozen ground, it is likely, that this average rate will rise even higher.

The Southern Hemisphere

Due to the fact that WaterGAP does not include Antarctica, Southern Hemisphere permafrost is very rare. The past time slice displays a total of four model grid cells containing discontinuous permafrost, which are reduced to three cells for contemporary conditions, and to none for all four future scenarios. The location of these cells in Argentina is concordant with the position of mountainous permafrost-

Table 1. Global area occupied by discontinuous and continuous permafrost in million km² (using equations 3 and 5). Values in parenthesis indicate percentage change to modeled 1971–2000 conditions.

	1901 – 1930	1971 - 2000	2071 – 2100 A1B, HadCM3	2071 – 2100 A1B, ECHAM5	2071 – 2100 B1, HadCM3	2071 – 2100 B1, ECHAM5
Sporadic discontinuous	9.5 (+ 2)	9.4 (0)	8.7 (-8)	8.2 (-13)	9.1 (-4)	9.5 (+1)
Extensive discontinuous	7.1 (+7)	6.7 (0)	2.9 (-56)	2.6 (-61)	4.3 (-35)	3.9 (-41)
Continuous	10.5 (+13)	9.4 (0)	3.1 (-67)	3.1 (-67)	4.4 (- 53)	4.1 (-56)
All permafrost regions	27.1 (+7)	25.5 (0)	14.7 (-42)	13.9 (-45)	17.8 (-30)	17.5 (-31)

Table 2. Global area occupied by discontinuous and continuous permafrost in million km² for 1971–2000 and comparison of different snow density ρ_s and thermal conductivity λ_s equations for the calculation of permafrost. Values in parenthesis indicate percentage change relative to permafrost map compiled by Brown et al. (1998). Anisimov & Nelson (1997) used different climate input and modeled Northern Hemisphere permafrost distribution (F_+) for 1961–1990 (using constant ρ_s (300 kg m^{-3}) and equation 4).

	ρ_s: equation (3) λ_s: equation (5)	ρ_s: constant λ_s: equation (5)	ρ_s: equation (3) λ_s: equation (4)	ρ_s: constant λ_s: equation (4)	Anisimov & Nelson (1997)	Permafrost map (Brown et al. 1998)
Sporadic discontinuous	9.4 (-17)	8.9 (-22)	9.7 (-15)	9.1 (-20)	8.1	11.4 (0)
Extensive discontinuous	6.7 (+24)	6.6 (+23)	6.8 (+26)	6.7 (+25)	5.6	5.4 (0)
Continuous	9.4 (-12)	9.7 (-9)	9.6 (-10)	9.9 (-7)	11.7	10.6 (0)
All permafrost regions	25.5 (-7)	25.2 (-8)	26.1 (-5)	25.7 (-6)	25.5	27.4 (0)

monitoring boreholes; for example, *Balcon I* at 32°57'43"S, 69°22'19"W (Trombotta et al. 1997), which are operated by the Global Terrestrial Network for Permafrost (GTNP).

Modification of the surface Frost Number

The aim of this model application was not only to predict global permafrost distribution, but also to test the framework of the Frost Number for the implementation of different formulations for snow density ρ_s and thermal conductivity λ_s. Table 2 compares the influence of these formulations on global permafrost distribution for contemporary conditions. The variation of total permafrost occurrence is rather small and lies within the range of one million km², whereas the combination of equations (3) (ρ_s calculated) and (4) (λ_s according to Van Dusen) yields the largest permafrost extent. Thus, as total permafrost occurrence is generally underestimated by the model, this combination of equations yields the smallest divergence (-5%) to the map of Brown et al. (1998). The lowest extent has been predicted by combining constant ρ_s and equation (5) (λ_s according to Sturm et al. 1997). The integration of equations (3) and (5) in the Frost Number calculations, which have also been used for the scenario estimates, generates mid-range permafrost spreading compared to other combinations. However, with 9.4 million km² of modeled continuous permafrost area, it also provides the smallest zonation of all four combinations.

Thermal conductivity of snow λ_s has been calculated using two different formulations, of which equation (5) generally yields lower values than equation (4) for ρ_s smaller than 345 kg m^{-3}, which holds true for most cells in this analysis. Table 2 shows that all permafrost calculations conducted with equation (5) feature smaller discontinuous and continuous permafrost extents than its counterpart equation (4). When snowfall occurs in the early stages of winter, low λ_s and thick snow layers can cause an insulation of the upper soil layer and thus prevent permafrost occurrence (Zhang et al. 2001). This effect is partially accounted for in equation (2), where snowfall early in the year is weighted higher than late snowfall.

There are two more options of snow-depth modeling, which could be applied for further studies on the Surface Frost Number. First, a physically detailed approach, which considers snow metamorphism and overburden (Jordan 1991). Secondly, if necessary input data are not available, a conceptual approach, as in Pomeroy et al. (1998), who suggest initializing annual snow density with 100 kg m^{-3} and add 25 kg m^{-3} for each month colder than 0°C.

In general, the comparison with results from a similar study conducted by Anisimov & Nelson (1997) shows good agreement for total permafrost extent. However, continuous permafrost is 25% lower, and discontinuous permafrost spreading is 15% higher in the current study. This could be explained by different climate data input, higher constant snow density, and an earlier and colder time period. Thus, in between the climate normal 1961–90 and 1971–2000, air temperature increase caused a transformation from continuous to discontinuous permafrost, which could explain some of the differences between both studies.

Conclusions

This model experiment projects that, due to climate change, increasing air temperatures do have a significant impact on global permafrost distribution and thawing. According to the model results, which esteem from two IPCC-SRES scenarios and two GCMs, future continuous permafrost will suffer the largest zonal reductions, which vary between -53% and -67% compared to today. Discontinuous permafrost faces two different pathways of decay, depending on its type. On the one hand, extensive discontinuous permafrost experiences losses between -35% and -61%. On the other hand, sporadic discontinuous permafrost faces moderate spatial changes between +1% and -13%, which is due to the conversion from continuous and extensive discontinuous to sporadic discontinuous permafrost. These thawing processes can have large impacts on urban infrastructure and can trigger feedback loops of enhanced global warming. The modeling results also show, that permafrost degradation in the next 100 years will progress much faster than during the last 70 years.

In this study, a validation of the Frost Number for present total permafrost occurrence has been carried out successfully. The general underestimation of modeled global permafrost extent can probably be addressed to the existence of relic permafrost which is not considered by the model.

The incorporation of additional snow parameter equations showed little sensitivity to the calculation of the Surface Frost Number.

Although the Surface Frost Number has proven its suitability to display contemporary permafrost distribution to some extent, the interpretation of all modeling results should be regarded with caution. Especially the interaction of transient GCMs, climate change scenarios, climate data-input uncertainties, and empirical model functions can lead to large inaccuracies in the prediction of permafrost occurrence. In this study, the main disadvantage of the Surface Frost Number can be seen in its dependence on climate input solely. Further, snow property calculations, such as modeled snow depth, should be subject to more physical approaches, which also consider snow typical processes, such as snow compaction (e.g., as in Jordan 1991). It is recommended further studies integrate soil properties, relic permafrost, and carbon and methane cycling in the assessment of climate change driven permafrost thawing. Potential candidates for the integration of soil features are formulations such as the Stefan Frost Number (Nelson & Outcalt 1987) or the more detailed Kudryavtsev solution, which is described in Anisimov et al. (2007).

Acknowledgments

We thank our colleagues, especially Florian Wimmer and Frank Voß, at the Center for Environmental Systems Research (CESR) for valuable discussions about the thermal properties of snow. We also gratefully acknowledge the helpful comments by two anonymous reviewers. This work was funded by the German Federal Ministry of Education and Research (FKZ:033762A).

References

Anisimov, O.A., Lobanov, V.A., Reneva, S.A., Shiklomanov, N.I., Zhang, T. & Nelson, F.E. 2007. Uncertainties in gridded air temperature fields and effects on predictive active layer modeling. *Journal of Geophysical Research* 112: F02S14.

Anisimov, O.A. & Nelson, F.E. 1997. Permafrost zonation and climate change in the northern hemisphere: results from transient general circulation models. *Climatic Change* 35: 241-258.

Anisimov, O.A. & Nelson, F.E. 1996. Permafrost distribution in the northern hemisphere under scenarios of climatic change. *Global and Planetary Change* 14(1-2): 59-72

Brown, J., Ferrians, O.J., Heginbottom, J.A. & Melnikov, E.S. 1998. *Digital Circum-Arctic Map of Permafrost and Ground-Ice Conditions*. Int. Permafrost Association Data and Information Working Group, Circumpolar Active-Layer Permafrost System, CD-ROM version 1.0. National Snow and Ice Data Center, U. of Colorado, Boulder, Colorado.

Döll, P., Kaspar, F. & Lehner, B. 2003. A global hydrological model for deriving water availability indicators: model tuning and validation. *Journal of Hydrology* 270: 105-134.

Frauenfeld, O.W., Zhang, T. & McCreight, J.L. 2007. Northern hemisphere freezing/thawing index variations over the twentieth century. *International Journal of Climatology* 27(1): 47-63.

Gordon, C.; Cooper, C., Senior, C.A., Banks, H., Gregory, J.M., Johns, T.C., Mitchell, J.F.B. & Wood, R.A. 2000. The simulation of SST, sea ice extents and ocean heat transports in a version of the Hadley Centre coupled model without flux adjustments. *Climate Dynamics* 16: 147-168.

Hedstrom, N.R. & Pomeroy, J.W. 1998. Measurements and modeling of snow interception in the boreal forest. *Hydrological Processes* 12: 1611-1625.

IPCC. 2001. *Special Report on Emissions Scenarios*. Cambridge: Cambridge University Press, 570pp.

Jordan, R. 1991. A one-dimensional temperature model for a snow cover. Technical documentation for SNTHERM.89. U.S. Army Corps of Engineers*, Cold Reg. Res. and Eng. Lab.*. Special Report 91-16.

Lawrence, D.M. & Slater, A.G. 2005. A projection of severe near-surface permafrost degradation during the 21st century. *Geoph. Res. Lett*. 32: L24401.

Mellor, M. & Mellor, A. 1988. Some characteristics of falling snow. *Cold Reg. Sc. and Tech.* 15: 201-206.

Meister, R. 1986. Density of new snow and its dependence on air temperature and wind. *Zürcher Geografische Schriften* 23: 73-79.

Mitchell, T.D. & Jones, P.D. 2005. An improved method of constructing a database of monthly climate observations and associated high resolution grids. *International Journal of Climatology* 25(6):693-712.

Nelson, F.E. 1986. Permafrost distribution in Central Canada: applications of a climate-based predictive model. *Annals of the Association of American Geographers* 76(4): 550-569.

Nelson, F.E., Anisimov, O.A. & Shiklomanov, N.I. 2002. Climate change and hazard zonation in the Circum-Arctic permafrost regions. *Nat. Hazards* 26:203-225.

Nelson, F.E. & Outcalt, S.I. 1987. A computational method for prediction and regionalization of permafrost. *Arctic and Alpine Research* 19(3): 279-288.

Nelson, F.E. & Outcalt, S.I. 1983. A frost index number for spatial prediction of ground-frost zones. *Permafrost: Fourth International Conference Proceedings*, I. Washington, DC: National Academy Press: 907-911.

Osokin, N.I., Samoylov, R.S., Sosnovskiy, A.V., Sokratov, S.A. & Zhidkov, V.A. 2000. Model of the influence of snow cover on soil freezing. *A. of Glaciology* 31: 417-421.

Paterson, W.S.B. 1994. *The physics of glaciers*. 3rd edition. Oxford: Pergamon Press, 481pp.

Pomeroy, J.W., Gray, D.M., Shook, K.R., Toth, P., Essery, R.L.H., Pietroniro, A. & Hedstrom, N. 1998. An evaluation of snow accumulation and ablation processes for land surface modelling. *Hydrological Processes* 12: 2339-2367.

Pontius, R.G. 2000. Quantification error versus location error in comparison of categorical maps. *Photogram. Engineering & Remote Sensing* 66(8): 1011-1016.

Roeckner, E., Brokopf, R., Esch, M., Giorgetta, M., Hagemann, S., Kornblueh, L., Manzini, E., Schlese, U. & Schulzweida, U. 2006. Sensitivity of simulated climate to horizontal and vertical resolution in the ECHAM5 atmosphere model. *J. of Climate* 19: 3771-3791.

Romanovsky, V.E. 2005. *How rapidly is permafrost changing and what are the impacts of these changes?* http://www.arctic.noaa.gov/essay_romanovsky.html.

Stendel, M. & Christensen, J.H. 2002. Impact of global warming on permafrost conditions in a coupled GCM. *Geophysical Research Letters* 29(13):1632.

Sturm, M. , Holmgren, J, Koenig, M. & Morris, K. 1997. The thermal conductivity of snow. *Journal of Glaciology* 43: 26-41.

Trombotto, D., Buk, E. & Hernandez, J. 1997. Monitoring of mountain permafrost in the Central Andes, Argentina. *Permafrost & Perigl. Proc* 8: 123-129.

Zhang, T., Barry, R.G. & Haeberli, W. 2001. Numerical simulations of the influence of the seasonal snow cover on the occurrence of permafrost at high latitudes. *Norsk geogr. Tidsskr*. 55: 261-266.

Zimov, S.A., Schuur, E.A.G. & Chapin III, F.S. 2006. Permafrost and the global carbon budget. *Science* 312(5780): 1612-1613.

Remote Sensing Data for Monitoring Periglacial Processes in Permafrost Areas: Terrestrial Laser Scanning at the Hinteres Langtalkar Rock Glacier, Austria

Michael Avian
Institute of Remote Sensing and Photogrammetry, Graz University of Technology, Austria
Andreas Kellerer-Pirklbauer
Institute of Geography and Regional Science, University of Graz, Austria
Arnold Bauer
Institute of Digital Image Processing, JOANNEUM RESEARCH, Graz, Austria

Abstract

This article discusses long-range terrestrial laser scanning (TLS) as a monitoring technique focusing on recent geomorphic changes at the near-terminus zone of the Hinteres Langtalkar rock glacier (46°59′N, 12°47′E). This rock glacier is characterised by extraordinarily high movement rates at its lower part since the mid-1990s. The surface of this collapsing part of the rock glacier is characterised by a very disturbed topography, which causes problems for terrestrial as well as remote sensing monitoring methods. The lack of textural information makes approaches such as optical flow detection in grey-scale images non-applicable at this study area. Long-range TLS is completing the dataset with distance measurements leading to 3D point clouds, which are afterwards converted into accurate 3D models. Analysis of surface kinematics derived from five digital elevation models (DEM) obtained during TLS campaigns between 2001–2006 shows promising results covering this lack of data in unfavourable terrain.

Keywords: Austrian Alps; high-resolution DEM; LIDAR; rock glacier kinematics; terrestrial laser scanning.

Introduction

Surface dynamics of rock glaciers are of increasing interest due to a high relationship to thermal conditions of permafrost areas. A few rock glaciers in the Alpine arc reacted to increasing air temperatures with extraordinarily high movement rates over several years (Roer et al. 2003). Most of them now show decreasing surface velocities (Delaloye et al. 2008). The Hinteres Langtalkar rock glacier changed its behavior most likely in 1994, moving over a prominent bedrock ridge into steeper terrain (Avian et al. 2005). Despite the remoteness of the location, a comprehensive monitoring network has been installed to get a better understanding of present processes, such as a geodetic survey (annually since 1998; Kienast & Kaufmann 2004), monitoring of the near-surface and surface thermal regime (since 2006 within the project ALPCHANGE), terrestrial laser scanning (2x2000, 2x2001, 2004, 2005, 2006, and 2007; cf. Bauer et al. 2003), and digital photogrammetry (1969, 1974, 1983, and 1997; cf. Kaufmann & Ladstädter 2004), providing data of different nature and in different resolutions in time and space. Long-range TLS ought to monitor the lowest part of the rock glacier to gather information about vertical surface changes and 3D movement rates.

Geographical Setting

The cirque-system Hinteres Langtalkar (46°59′N, 12°47′E) is situated in the Schober Mountains within the Hohe Tauern Range (Central Alps, Austria) (Fig. 1). The cirque-system is a hanging valley at the orographic right side of the Gössnitz Valley. The cirque covers an altitudinal range between 2300–3019 m a.s.l. The northwest facing tongue-shaped rock glacier itself covers the entire upper cirque floor with a lower margin at 2455 m a.s.l., root zones beginning in appr. 2700 m a.s.l, and a geometry of 600x300 m (Fig. 2). In general, rock glaciers are numerous in the Schober Mountains due to favorable geological conditions, leading to a total number of 77 intact rock glaciers (*cf.* Lieb 1998). Furthermore, the main range of the Central Alps (10 km to the N) causes pronounced continental climatic characteristics with a mean annual air temperature (MAAT) of 0°C at 2200 m a.s.l. and precipitation of ~1500 mm at 2000 m a.s.l. Glaciation in the Schober Mountains is developed only in some cirques and decreased rapidly during the last decades due to atmospheric warming (Kellerer-Pirklbauer & Kaufmann 2007). Auer et al. (2002) report a rising of the MAAT of 1.6°C since 1886 at the Hoher Sonnblick Meteorological Station (3106 m a.s.l., 15 km E of Hinteres Langtalkar) which is above the global average of 0.74°C (*cf.* IPCC 2007).

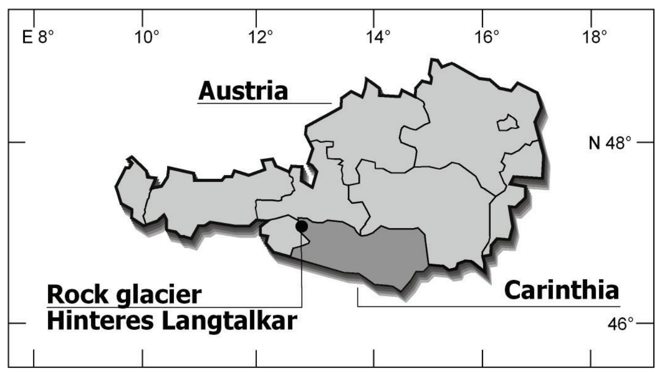

Figure 1. Location of Hinteres Langtalkar within Austria.

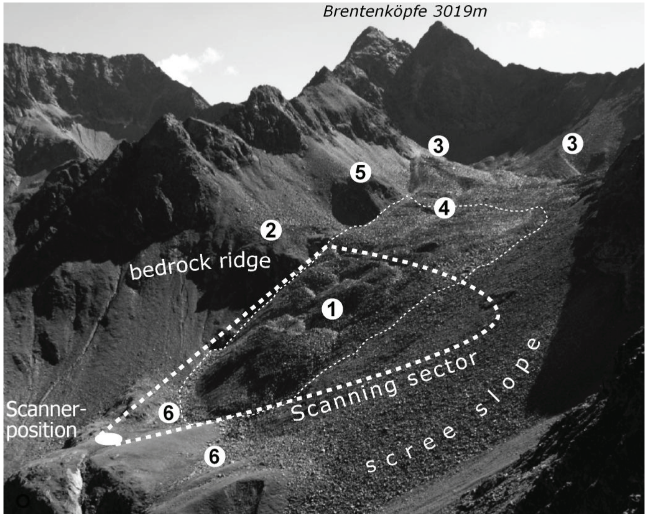

Figure 2. The cirque-system Hinteres Langtalkar including the monitoring configuration. Codes in photograph: (1) Area of intensive rock glacier movement and disintegration, (2) prominent bedrock ridge partly covered by periglacially weathered debris, (3) latero-terminal moraine ridges dating from the Little Ice Age (~1850 AD), (4) crevasses on rock glacier indicating high strain rates, (5) meteorological station and (6) fresh boulders spreading over alpine meadows adjacent to the rock glacier front. The thin dashed line comprises the recently fast-moving part of the rock glacier. Scanner position is in a distance of ~90 m to the rock glacier front (Photograph by Viktor Kaufmann 24.08.2003).

Methods

Laser scanning or LiDAR (Light detection and ranging) data have been used intensively for high mountain applications during the last decade. Examples are monitoring of glacier surface elevation changes by Airborne Laser Scanning/ALS (e.g., Baltsavias et al. 2001, Würländer et al. 2004) or TLS (e.g., Avian et al. 2007), monitoring of periglacial processes using TLS (e.g., Bodin et al. 2008), hazard monitoring by TLS (e.g., Conforti et al. 2005, Rabatel et al. 2007) or snow cover monitoring using TLS (Prokop 2007). Primary resulting digital elevation models (DEM) are used to consider surface elevation variations to quantify, for instance, glacier dynamics. Determination of horizontal flow fields with high-resolution DEMs was presented by e.g., Bucher et al. (2006) with the aid of the software IMCORR, using concepts from aerial image matching (cross correlation in grey-scale images).

The ability of TLS to acquire high-resolution 3D data of surface structures makes this technique an interesting instrument for measuring high mountain environments. The integrated measurement system is capable of describing 3D motion and deformation of rock glacier surface within a few hours measurement. It is a time-of-flight system that measures the elapsed time of the pulse emitted by a photo-diode until it returns to the receiver optics. Maximum range depends on the reflectivity of surface (which is favourable for snow and debris-covered terrain) and atmospheric visibility (best for clear visibility, bad for haze and fog). A measuring range of up to 2000 m allows hazardous sites to be easily measured from a safe distance. Since each single measurement consists of a multitude of laser-pulses, different measurement modes ("first pulse," "last pulse," "strongest pulse") give proper results even during bad weather conditions and on poor surfaces like vegetated, moist, or roughly structured terrain that might otherwise lead to ambiguous measurements. Table 1 gives an overview of technical information concerning the long-range TLS Riegl LPM-2k.

Table 1. Scanner parameters and values of the used instrumentation Riegl LPM-2k Long-range Laser Scanner.

Scanner parameter	Value (range)
Measuring range for:	
- good diffusely reflective targets	up to 2500m
- bad diffusely reflective targets	>800m
Ranging accuracy	+50mm
Positing accuracy	+0.01gon
Measuring time / point	0.25s to 1s
Measuring beam divergence	1.2mrad
Laser wavelength	900nm
Scanning range	
- horizontal	400gon
- vertical	180gon
Laser safety class	3B, EN 60825-1
Power supply	11-18V DC, 10VA
Operation temperature range	-10 to +50°C

The measurement

Information at each individual measurement point includes the distance to the surface, the exact angular positions, the reflectance, and an estimated root mean square error (RMSE) of the distance measurement for reliability check. Measurements with an accuracy of distance better than 5 cm are automatically combined to a measurement grid. In general, several methodological, technical, and logistical problems are to be encountered when establishing an integrated monitoring system in this high alpine environment. These include among others the stability of device control software, the automatic sensor orientation, the high number of measurements, the compensation of weather influences, and the selection of reliable measurements. In addition, it is of particular importance to consider the highly heterogeneous surface in terms of material (rock, vegetation, and humidity in general) and structure. Many years of experience in the field of TLS (beginning in 2000) result in the development of a well-engineered, stable acquisition and analysis system, which in combination with expert field work, copes with all the conditions.

Data processing

The TLS dataset is converted to a DEM, which is a digital raster representation of surface topography. In general, a horizontal reference surface is used. However, topology is often highly varying in terms of inclination; for example, most of the potentially insecure surfaces are characterized by comparable steep fronts. In order to represent the surface data in best resolution, we generalize the DEM to an analytical reference model that best describes the global shape of the observed surface. To raster, a regularly spaced grid is defined on the reference model, and the "height" on every pixel is processed as normal distance to the reference surface. This data structure complies well with practical requirements such as difference measuring, volume change evaluation, and various visualization tasks. Neighbourhood relations of measured data points are directly described in the DEM structure; therefore, operating on DEMs allows quick access to the surface heights in a well-defined geometry. Direct mapping from the sensor spherical system to the DEM cartesian coordinate space would result in a sparse and non-uniform elevation map, especially at great distances. To avoid interpolation artefacts, the Laser Locus Method (Kweon et al. 1992) for DEM (Bauer et al. 1999) generation proves to be a robust tool for data acquisition from flat angles and supports error detection and utilization of additional confidence values provided by the range sensor. Since the DEMs of (temporally) different surface measurements are geo-referenced, simple differences between the DEMs reflect the changes in elevation. In consequence we can derive a full description of change in volume, spatial distribution of shape, or arbitrary profiles on the surface.

Single time-of-flight measurements are automatically combined to a measurement grid that enables the generation of a dense, enhanced DEM of the rock glacier surface. Repeatable sensor orientation is performed using reflective targets fixed on stable surfaces somewhere in the spherical field of view of the sensor. TLS measures the position of a theoretical, stable point on the surface within a given reference system.

Surface motion analysis

The DEM differences primarily only describe the vertical distance of the surface change. In order to understand the complex kinematics of rock glacier deformation – like the highly dynamic lowest part of the Hinteres Langtalkar rock glacier – further knowledge about the 3D surface motion patterns is required. Among others, Kääb et al. (2003) and Kaufmann & Ladstädter (2004) provide solutions to calculate the 3D motion by means of optical flow detection on the grey level images using correlation-based matching. This method is not applicable to the current laser scanning configuration, since similar reflectance conditions cannot be assured (basic requirement for robust matching). Tracking of objects on the surface can still be performed by the high-resolution surficial morphology provided by the DEM (despite the lack of textural information). Only on surfaces, where the structural surface changes are relatively small, state-of-art matching methods (cf. Paar & Almer 1993) obtain dense tracking vectors. In combination with the primarily obtained DEM differences mentioned above, this results in a three-dimensional vector field that describes the kinematic state of the rock glacier surface within the given periods.

Table 2: Periods of data acquisition and quality parameters. Data used for analysis discussed in this study are indicated in bold.

Period	total pts	used pts	PR (1)	OA (2)
07/2000	27048	26381	0.98	0.07
08/2000	**27048**	**26437**	**0.98**	**0.06**
07/2001	27048	26274	0.97	0.02
08/2001	**26910**	**26312**	**0.98**	**0.02**
08/2004	**20424**	**19818**	**0.97**	**0.02**
08/2005	**27048**	**17843**	**0.65**	**0.02**
09 2006	**7836**	**6048**	**0.77**	**0.02**
07/2007	6384	5739	0.90	0.02

(1) PR: point ratio = numbers of points used/total number of points measured. (2) OA: orientation accuracy [m].

Cross check with auxiliary data

To control the significance of the image matching data, cross checking with displacement rates from adjacent parts of the rock glacier were considered. Geodetic survey has been carried out in the middle part of the rock glacier (data kindly provided by V. Kaufmann) with its lower measurement boundary at the disintegrated lower part of the rock glacier. These campaigns provide verification data for the displacement vectors derived from image matching (Tab. 2). Some limitations in interpretation have to be considered due to distances of up to 60 m between scanning area and respective control points.

Results

Quality of data from image matching

To get more information about interpretability, a review of data quality is essential. In 2000–2005 the total number of acquired points is high with 20,000 to 30,000 per campaign. The surface topography of a rock glacier consists of boulders with sizes between a few decimeters up to some metres. This is of crucial importance in the face of a true reproduction of the real surface and subsequently in receiving reasonable results in terms of surface motion patterns. Due to problems with energy supply in 2006 and 2007, the scanning increment had to be reduced during these campaigns, leading to total point numbers below 10,000. This low number is unfavourable for interpolation and obtaining a DEM for an area-wide precise motion analysis. Orientation accuracy is satisfying for all periods with 0.02–0.07 m (Table 2).

Annual displacements from image matching

Results of the rock glacier motion analysis are given in mean annual horizontal displacement rates.

2000–2001: The stepped lowest part differentiates clearly in velocity patterns. The ridges show mean annual displacement rates of 0.78 ma^{-1} (max. 1.38 ma^{-1}) (Fig. 3A; zone 1), 0.95 ma^{-1} (max. 1.73 ma^{-1}) (Fig. 3A; zone 2), 1.38 ma^{-1} (max. 1.64 ma^{-1}) (Fig. 3A; zone 3), and 1.35 ma^{-1} (max. 1.75 ma^{-1}) (Fig. 3A; zone 4). The adjacent scree slope at the orographic left side of the rock glacier shows constant movement rates of 0.02–0.06 ma^{-1} over the entire scanning area.

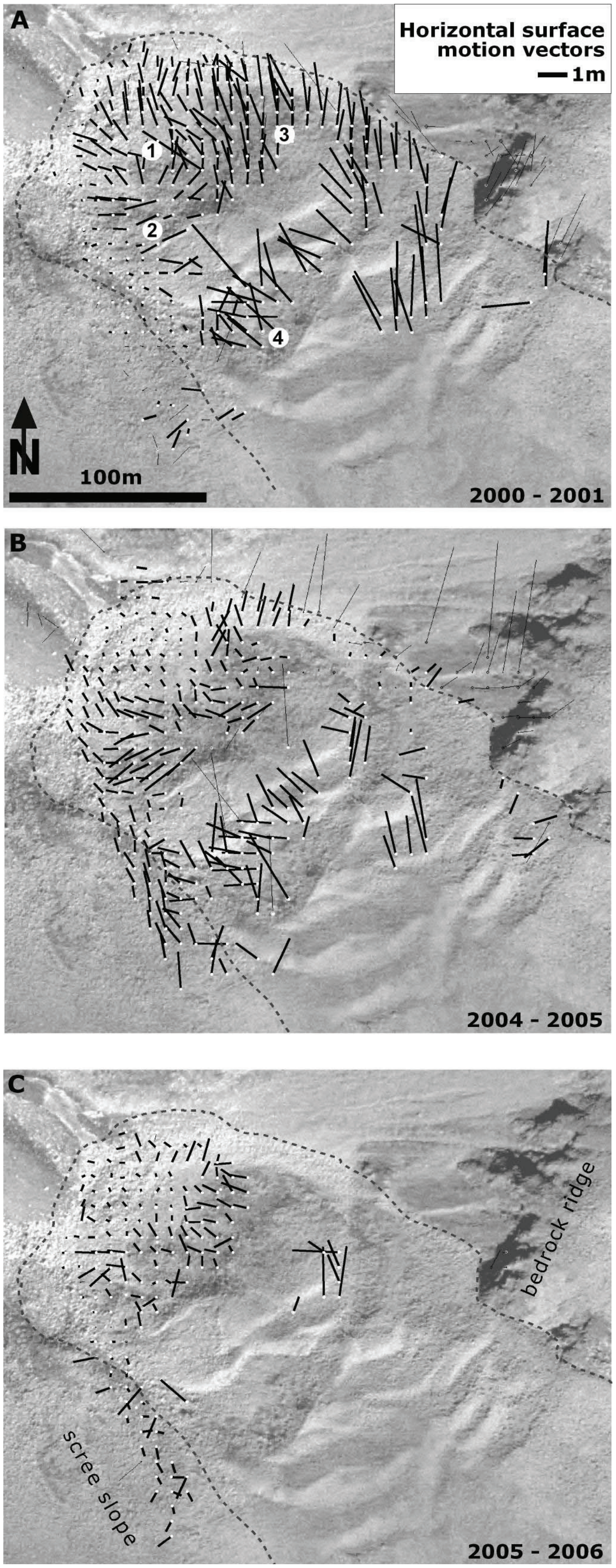

Figure 3. Horizontal displacement rates [ma^{-1}] for three annual periods: (A) 2000/01, (B) 2004/05 and (C) 2005/06. Motion vectors are obtained from DEM differences, DEMs were derived from TLS data. Numbers (1-4) indicate zones of different behaviour in terms of surface velocity; for details refer to text (Orthophotograph ©Nationalpark Hohe Tauern, 1998).

2004–2005: Quality of velocity data from this period tends to be unsatisfying in some areas. Distinct differentiation between obviously moving and akinetic areas at the margin of the rock glacier is not possible. Velocity patterns do not indicate a distinct border between the scree slope and the rock glacier body. Furthermore, displacement rates of 0.35–0.40 ma^{-1} seem to be unreasonable for this particular area. Surface topography on the rock glacier itself can be deduced from flow fields properly, as they show similar patterns as in the other periods.

2005–2006: Flow velocities and patterns are more difficult to interpret, although the ridges are detectable due to higher displacement rates (0.75 ma^{-1}). The main front shows rates around 0.15 ma^{-1}, the left margin is distinguishable towards the non-moving scree slope. Coarse point resolution leading to small spots of areal data does not allow reasonable interpretation of the upper part of the rock glacier tongue (cf. uppermost scanning area in Fig.2).

Direction of annual displacement vectors

Direction of movement at the terminus zone of the rock glacier shows outward movement of displacement vectors as expected. The ongoing development of the imbrication and the distinct shifting of detritus is visible in abrupt changes of the magnitude and direction of velocity vectors (Fig. 3, A-C, 1-4).

Cross checking with results from geodetic survey

Surface displacements derived from geodetic surveys in both periods at least coincide with displacement ranges obtained from TLS image matching (Tab. 3). However, substantial controlling is not possible due to poor data overlap. The main problems are hazardous working conditions for terrestrial monitoring, making geodetic or GPS surveys hardly feasible in the fast-moving sections of this rock glacier (up to 2.38 ma^{-1} in 2003–2004). The steep rock glacier's front surface changes rapidly in shape, texture, and object distribution. This results in unfavorable conditions for analysis of optical data; viewing angles nearly vertical or area-wide changes in surface cause problems in automatic detection).

High values at some areas of the right margin of the rock glacier, the bedrock, and vegetated areas are results due to unfavorable scanning geometry and therefore are not taken into account as the exact rock glacier extent is known from fieldwork.

Discussion and Conclusions

High-resolution DEMs derived from long-range terrestrial laser scanning are a good data basis for monitoring permafrost processes related to geo-hazards. Derivates like surface elevation changes and displacement vectors (in case of the availability of multi-temporal high-resolution DEMs) provide useful information about 3D surface dynamics. However, the quality of dataset s and concepts for calculating morphometric parameters have to be assessed critically. Point density is a crucial factor (cf. Bodin et al. 2008) as is the quality of the measurement itself (high point ratio and total point number). Remoteness (sufficient energy supply) and atmospheric conditions (e.g., air humidity) are crucial limiting factors. The exemplary study of the Hinteres Langtalkar rock glacier demonstrates the importance of independent control data for evaluation, and the problems in acquisition of the latter. High landscape dynamics – frequent shifting of material, block falls – inhibit terrestrial surveys. Methodological problems in automatic data interpretation (e.g., inadequate texture for photogrammetry) complicate remote sensing approaches. The current monitoring configuration lacks additional control targets in the vicinity of the upper rock glacier tongue on the bedrock. Large differences in velocity values of different periods do not allow the interpretation of recent processes precisely at present.

In terms of velocity patterns, topography, and surface modification, some considerations are appropriate. In the lowest section of the rock glacier front, the surface velocity is decreasing to the margin as expected. Flow patterns are detectable in step-like relief which geomorphodynamically results in a distinct surface topography (Figs. 2, 3). High velocities within ridges and sharp limits at the ridge fronts to slower areas support this assumption. The formation of the micro-relief within ridges is also visible in the displacement patterns. Surface velocity patterns also exhibit distinct differences between the main rock glacier body and adjacent permafrost areas at the orographically left side. At the beginning of the steeper part of the lower rock glacier tongue, varying directed vectors in both periods indicate non-laminar movement of that particular part and are therefore interpreted as intense modification and frequent shifting of the disturbed surface.

As this particular rock glacier shows extraordinary surface velocity rates (cf. Avian et al 2005, Roer et al. 2005), upcoming TLS campaigns on the middle and upper section of the rock glacier would enhance knowledge about methodological problems due to the availability of independent data derived from geodetic measurements.

Acknowledgments

These activities were carried out within the framework of the project ALPCHANGE (www.alpchange.at) funded by the Austrian Science Fund (FWF) through project no. FWF P18304-N10. We kindly acknowledge the help of Viktor Kaufmann (Institute of Remote Sensing and Photogrammetry, Graz University of Technology) for providing data from geodetic surveys. We also thank students of the Institute of Geography and Regional Science, University of Graz and the Institute of Remote Sensing, Graz University of Technology, Austria as well as several volunteers of the Nationalpark Hohe Tauern for their support during field campaigns.

Table 3. Annual horizontal displacement rates from geodetic measurements (based on unpublished data by V. Kaufmann) and image matching of adjacent areas.

Image matching	Geodetic survey	
displacement range [ma^{-1}]	Points	displacement [ma^{-1}]
2000/2001		
0.99 – 2.04	24	1.504
0.92 – 1.88	25	1.468
1.26 – 1.93	27	1.720
1.56 – 2.29	28	1.683
2004/2005		
1.05 - 1.98	24	2.017
0.97 – 1.89	25	1.734
no data	27	1.967
1.23 – 2.32	28	1.947

References

Auer, I., Böhm, R., Leymüller, M. & Schöner, W. 2002. Das Klima des Sonnblicks–Klimaatlas and Klimageographie der GAW-Station Sonnblick einschließlich der umgebenden Gebirgsregion. *Österreichische Beiträge zur Meteorologie und Geophysik* 28: 305 pp.

Avian, M., Kaufmann, V. & Lieb, G.K. 2005. Recent and Holocene dynamics of a rock glacier system–the example of Langtalkar (Central Alps, Austria). *Norsk Geografisk Tidsskrift* (Norwegian Journal of Geography) 59: 149-156.

Avian, M., Lieb, G.K., Kellerer-Pirklbauer, A. & Bauer, A. 2007. Variations of Pasterze Glacier (Austria) between 1994 and 2006 - Combination of Different Data Sets for Spatial Analysis. *Proceedings of the 9th International Symposium High Mountain Remote Sensing Cartography (HMRSC), Graz, Austria, September 14–22, 2006*: 79-88.

Baltsavias, E.P., Favey, E., Bauder, A., Boesch, H. & Pateraki, M. 2001. Digital surface modelling by airborne laser scannino and digital photogrammetry for glacier monitoring. *Photogrammetric Record* 17, 98: 243-273.

Bauer, A. & Paar, G. 1999. Elevation Modeling in Real Time Using Active 3D Sensors. *Proceedings of the 23rd Workshop of the Austrian Association for Pattern Recognition, AAPR, Robust Vision for Industrial Applications 1999. Steyr, Austria. May 27-28, 1999, Schriftenreihe der Österreichischen Computer Gesellschaft* 128: 89-98.

Bauer, A, Paar, G. & Kaufmann, V. 2003. Terrestrial laser scanning for rock glacier monitoring. *Proceedings of the Eighth International Conference on Permafrost, Zurich, Switzerland, 21-25 July 2003:* 55-60.

Bodin, X., Schoeneich, P. & Jaillet, S. 2008. High Resolution DEM Extraction from Terrestrial LIDAR Topometry and Surface Kinematics of the Creeping Alpine Permafrost: the Laurichard Rockglacier Case Study (French Southern Alps). *Proceedings of the Ninth International Conference on Permafrost, Fairbanks, Alaska, June 29–July 3, 2008* (this proceedings).

Bucher, K., Geist, Th. & Stötter, J. 2006. Ableitung der horizontalen Gletscherbewegung aus multitemporalen Laserscanning-Daten Fallbeispiel: Hintereisferner/Ötztaler Alpen. *Proceedings of Angewandte Geoinformatik 2006 – Beiträge zum AGIT-Symposium Salzburg, Salzburg, Austria, July 5-7, 2006*: 277-286.

Conforti, D., Deline, P., Mortasa, G. & Tamburini, A. 2005. Terrestrial scanning LiDAR technology applied to study the evolution of the ice contact Miage glacier (Mont Blanc, Italy). *Proceedings of the 9th Alpine Glaciological Meeting, Milano, Italy, February 24–25, 2005*: (digital media)

Delaloye, R., Perruchoud, E., Avian, M., Kaufmann, V., Bodin, X., Ikeda, A., Hausmann, H., Kääb, A., Kellerer-Pirklbauer, A., Krainer, K., Lambiel, C., Mihajlovic, D., Staub, B., Roer, I. & Thibert, E. 2008. Recent interannual variations of rock glaciers creep in the European Alps. *Proceedings of the Ninth International Conference on Permafrost, Fairbanks, Alaska, June 29–July 3, 2008* (this proceedings).

IPCC. 2007. *Climate Change 2007: The Physical Science Basis. Contribution of Working Group I to the Fourth Assessment Report of the Intergovernmental Panel on Climate Change.* S. Solomon, D. Qin, M. Manning, Z. Chen, M. Marquis, K.B. Averyt, M.Tignor and H.L. Miller (eds.). Cambridge, United Kingdom and New York, NY, USA: Cambridge University Press.

Kääb, A., Kaufmann, V., Ladstädter, R. & Eiken, T. 2003. Rock glacier dynamics: implications from high-resolution measurements of surface velocity fields. In: *Proceedings of the Eighth International Conference on Permafrost, 21-25 July 2003, Zurich, Switzerland* 1:501-506.

Kaufmann, V. & Ladstädter, R. 2004. Documentation of the movement of the Hinteres Langtalkar rock glacier. *Proceedings of the 20th Congress of the International Society for Photogrammetry and Remote Sensing, Istanbul, Turkey, July 12–23, 2004, IAPRS, 35, Part B7*: 893-898.

Kellerer-Pirklbauer, A. & Kaufmann, V. 2007. Paraglacial talus instability in recently deglaciated cirques: Schober group, Austria. *Proceedings of the 9th International Symposium High Mountain Remote Sensing Cartography (HMRSC), Graz, Austria, September 14–22, 2006:* 121-130.

Kienast, G. & Kaufmann, V. 2004. Geodetic measurements on glaciers and rock glaciers in the Hohe Tauern National park (Austria). *Proceedings of the 4th ICA Mountain Cartography Workshop*, *Vall de Núria, Catalonia, Spain, September 30–October 2, 2004*, Monografies tècniques 8, Institut Cartogràfic de Catalunya, Barcelona: 101–108.

Kweon, I.S. & Kanade, T. 1992. High-resolution terrain map from multiple sensor data. *IEEE Transactions on Pattern Analysis and Machine Intelligence* 14(2): 278-292.

Lieb, G.K. 1998. High mountain permafrost in the Austrian Alps. *Proceedings of the Seventh International Conference on Permafrost, Yellowknife, Canada, June 23–27, 1998*: 663-668.

Paar, G. & Almer, A. 1993. Fast hierarchical stereo reconstruction. In: *Proceedings of the Second Conference on Optical 3-D Measurement Techniques, Zurich, Switzerland*: 460-466,

Prokop, A. 2007. The application of terrestrial laser scanning for snow depth observation. *Geophysical Research Abstracts* 9: 07074.

Rabatel, A., Deline, P., Ravanel, L. & Jaillet, S. 2007. The use of laser scanning and terrestrial photogrammetry to quantify rock falls/avalanches in steep high-alpine rock walls. *Geophysical Research Abstracts* 9: 07170.

Roer, I., Avian, M., Delaloye, R., Lambiel, C., Dousse, J.-P., Bodin, X., Thibert, E., Kääb, A., Kaufmann, V., Damm, B. & Langer, M. 2005. Rock glacier ”speed-up” throughout European Alps - a climatic signal? *Proceedings of the Second European Conference on Permafrost, Potsdam, Germany, June 12–16, 2005*: 101-102.

Würländer, R., Eder, K. & Geist, Th. 2004. High quality DEMs for glacier monitoring – image matching versus laser scanning. *International archives of Photogrammetry, Remote Sensing and spatial information science* XXXV (B7): 753-758.

Permafrost Temperatures and Erosion Protection at Shishmaref, Alaska

Mary T. Azelton
U.S Army Corps of Engineers, Alaska District, Anchorage, AK, USA
Jon E. Zufelt, PhD, PE
U.S Army Corps of Engineers, Engineer Research and Development Center Cold Regions Research and Engineering Laboratory, Ft. Richardson, AK, USA

Abstract

Shishmaref, Alaska, is located on Sarichef Island in the Chukchi Sea. Sarichef Island is composed of very fine-grained sand permafrost, most likely wind-blown deposits formed as dunes when global sea levels were much lower. With present-day sea levels and changing climatic conditions in the region, these permafrost soils are more susceptible to erosion from wind, wave, and ice forces. In recent years, erosion at Shishmaref has been more pronounced due to the changing climatic conditions in the region. To combat this erosion, several local protection projects have been constructed with varying degrees of success. In an effort to learn more about the thermal conditions of the permafrost at Shishmaref, ERDC-CRREL and the Alaska District installed a series of thermistor strings beneath these revetments. This data will allow us to gain an understanding of the temperature of the permafrost throughout the year and during periods of intense fall storm events.

Keywords: convective cooling; permafrost; Shishmaref.

Introduction

Shishmaref, Alaska is located on Sarichef Island, in the Chukchi Sea, just north of the Seward Peninsula. Shishmaref is 8.5 km from mainland Alaska, 210 km north of Nome, and 170 km southwest of Kotzebue. Shishmaref has a population of approximately 615, most of whom are Inupiat Eskimo. The people of Shishmaref live a traditional subsistence lifestyle.

Sarichef Island is a barrier island 4 km long by 0.7 km wide. The island is one of a string of barrier islands separating the Chukchi Sea from the Alaskan mainland. These islands are composed of very fine-grained sand-permafrost, most likely wind-blown deposits formed as dunes when global sea levels were much lower. With present-day sea levels and changing climatic conditions in the region, these permafrost soils are more susceptible to erosion from wind, wave, and ice forces.

Short period waves from locally generated storms appear to be the most problematic for the island. The shoreline is directly exposed to the southwesterly and northwesterly fetches across the Chukchi Sea and can experience moderately high waves under storm conditions. Such waves are generally in the 1.5 to 2.5 m high range with periods of 4 to 5 seconds based on observations at the bluff. Events with waves as high as 3 m have been estimated from observations during extreme storm conditions. These waves can cause severe erosion when coupled with high storm surge events. Fall storms can cause extreme erosion to the shoreline at Shishmaref. The wave action caused by these storms cuts into the banks and in the spring the banks that were undercut will thaw, drop, and wash away, thus exposing more frozen soils. Figures 1 and 2 illustrate how much damage can occur to the shoreline at Shishmaref due to one storm. Figure 3 illustrates the permafrost degradation seen at Shishmaref.

Figure 1. Shoreline fronting the Teacher's Quarters in July of 2004. Note steps to grass-covered bluff.

Figure 2. Shoreline fronting the Teacher's Quarters after storm of October of 2004.

Figure 3. Permafrost degradation at Shishmaref, Alaska showing exposed permafrost horizon.

The frozen horizon can be clearly seen at the base of the bluff. Documented history of storm damage and coastal erosion problems at Shishmaref extends back more than 50 years and includes numerous reports by various consultants and State and Federal agencies, including the Alaska District, U.S. Army Corps of Engineers (USACE).

Erosion Protection

The community has tried many techniques throughout the years to arrest the erosion of their coastline including barrels, gabions, sandbags, and articulated concrete mat (AMC). All of these proved to be only temporary solutions as wave action and high water level events have all but destroyed these structures. Because the shoreline continues to recede, the community has moved houses and other structures back from the shoreline but they are quickly running out of room due to Shishmaref's limited size and soil conditions.

To combat the erosion several local erosion protection projects have been constructed with varying degrees of success. In 2004 the Bureau of Indian Affairs (BIA) constructed approximately 150 m of rock revetment. The Alaska District constructed approximately 70 m of rock revetment in the summer/fall of 2005, with the City of Shishmaref extending this effort by constructing an additional length of rock protection. In a continuing effort to protect the shoreline, the Alaska District will complete another 200 m of rock revetment in the fall of 2007 and summer of 2008. Figures 4 and 5 illustrate these construction efforts. Eventually the community would like to see their entire shoreline protected.

Permafrost Temperature Measurement

In an effort to learn more about the thermal properties of the permafrost at Shishmaref, the U.S. Army Corps of Engineers Engineer Research and Development Center-Cold Regions Research and Engineering Laboratory (ERDC-CRREL) and the Alaska District have installed a series of thermistor strings beneath several of the rock revetments placed at Shishmaref. This data will enhance existing knowledge of the temperature of the permafrost throughout the year

Figure 4. USACE revetment fronting the Teacher's Quarters – summer 2005.

Figure 5. USACE revetment construction fall of 2007.

at Shishmaref, as well as during intense fall storm events. With a better understanding of the permafrost conditions on Sarichef Island, USACE and other agencies will have more information with which to design stable erosion protection measures.

The Alaska District and CRREL installed the first thermistor string in the summer of 2005, coinciding with the construction of the USACE revetment fronting the school property. Figure 6 illustrates the placement of this thermistor string prior to covering with core rock. In addition, in the summer of 2006 a string of thermistors was placed beneath a gabion revetment built by the City of Shishmaref. Both of these strings were placed beneath the filter fabric prior to the placement of the core rock or the gabion baskets. The gabion revetment has subsequently been covered by the USACE rock revetment in the fall of 2007. In July of 2007 a vertical string, descending approximately 3.3 m was placed near Nayokpuk store and in August of 2007, a string was placed beneath the new USACE revetment along the shore fronting Nayokpuk store. This string was also placed between the filter fabric and the parent soil material.

All of the thermistor strings are connected to and read by Campbell Scientific CR10X data loggers and powered by three deep discharge gel-cell marine batteries. The thermistor strings are constructed from a multi-conductor cable with one of the conductors used as a common leg for the resistance measurement of each precision glass bead thermistor. Each thermistor location is isolated and waterproofed. The multi-conductor cable is protected by an outer conduit. The initial installation at the school property used a reinforced washing machine hose while later cables were protected with non-metallic liqui-tight conduit. Figure 7 shows the approximate location of each string on the island. Also included in this figure is the location of a proposed thermistor string in a relatively undisturbed portion of the shoreline. This string is intended to provide data on soil temperatures where convective cooling is not possible due to the native soil conditions and would be one of the last portions of the shoreline to be protected.

Figure 6. Thermistor string installation in the USACE revetment fronting the Teacher's Quarters.

Potential for convective cooling

There are several pieces of information that the Alaska District and CRREL hope to obtain from the data acquired from these thermistor strings. The first is a better understanding of the thermal interaction between the rock revetment and the natural soil materials at Shishmaref. The hope is to be able to establish where the active layer is generally located at the shoreline. The data will also be used to determine how the permafrost reacts to fall storm events. The data should show whether or not there are thermal fluxes in the soil temperatures during fall storms. Knowing whether or not the soil temperature fluctuates during these fall storms can enable a better understanding of when and what causes the shoreline permafrost to degrade and thus cause erosion.

Data provided by the thermistor strings may also provide knowledge of the link between the temperature of the permafrost and convective cooling. The fact that natural convection can have a large impact on heat transfer in a porous medium is well known (Goering 1995). In order to maintain stable permafrost, it is generally necessary to ensure that the mean annual surface temperature (MAST) is maintained below 0°C (Goering 1998). While the rock and gap sizes are greater than those recommended for efficient convective cooling, it is surmised that after a period of stabilization the revetment will help to maintain the MAST below 0°C, thus thermally stabilizing the permafrost.

Convective cooling is heat transfer by the natural upward flow of air from the relatively warmer object being cooled. Convective cooling techniques have been used with varying

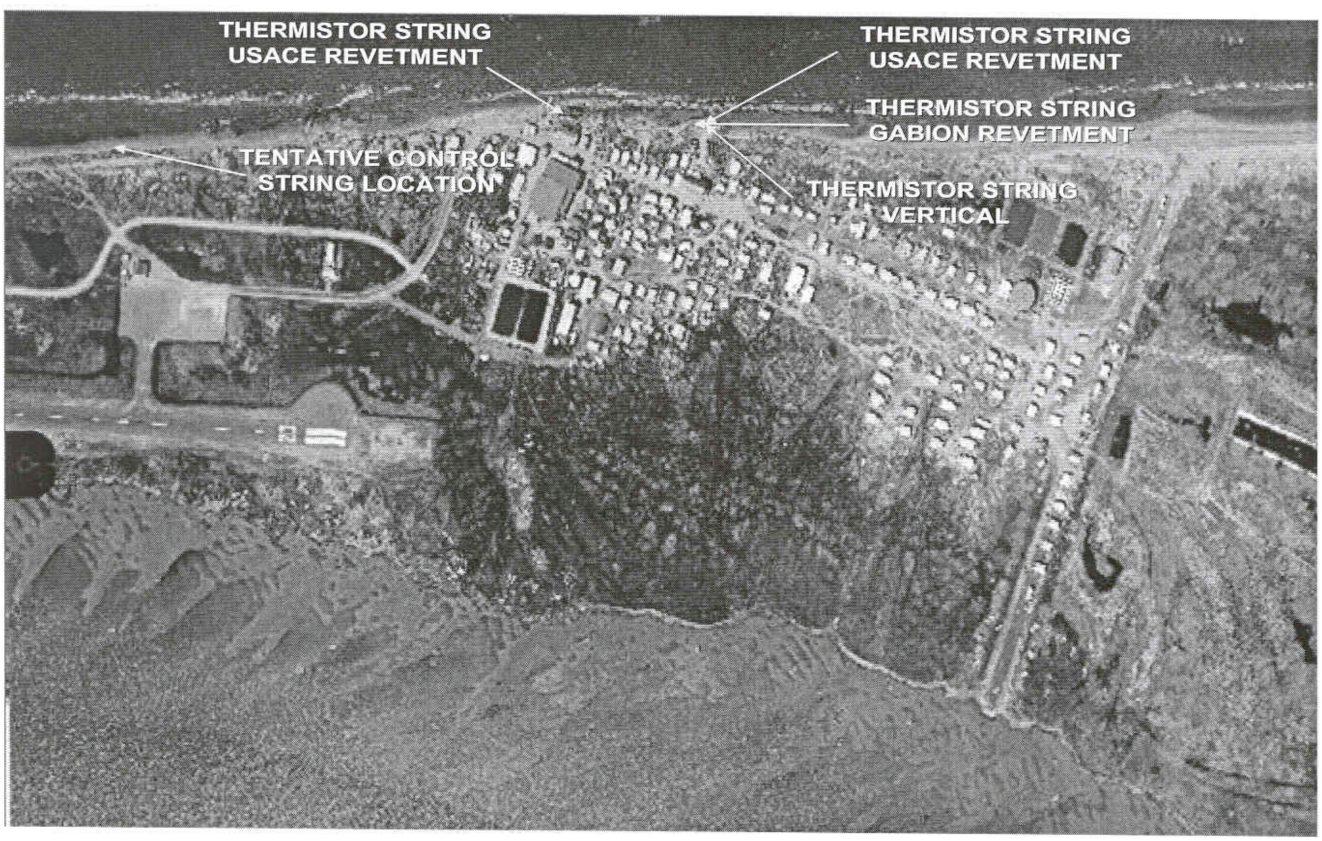

Figure 7. Thermistor string locations at Shishmaref.

degrees of success in road embankments in the Fairbanks, Alaska area. Several studies have previously been conducted on the use of Air Convection Embankments (ACE), which allow for natural convection of the pore air to occur within the embankment during the winter months (Goering 1998). Convection enhances the upward transport of heat out of the embankment during the winter months thus cooling the lower portions of the embankment and underlying foundation soil (Goering 1998). The cooling effect is achieved by maintaining a relatively small temperature difference during the winter compared with the summer. During the winter, colder pore air in the upper potion of the embankment will descend due to its greater density while warm pore air from the embankment base rises. This results in a pattern of convection cells within the embankment.

With the aid of convective cooling, the permafrost table should begin to rise. In order to achieve this cooling effect the embankment must be composed of a rock and gravel matrix, which is railroad ballast sized (0.05 to 0.075 m), poorly graded, and with a very low fines content (Goering 2003). Due to time, materials available, funding constraints, and coastal conditions the USACE revetments do not fully meet the criteria that best enhances convective cooling. It is still uncertain how much heat transfer will occur from the relative impermeable embankment base to the permeable revetment. The revetment that fronts the teacher's quarters at Shishmaref does not have a poorly graded rock/gravel matrix. The core layer in this revetment consists of dredge spoils with a high fines content. What may enhance convective cooling in this revetment is the armor rock layer. The armor layer in this revetment was constructed using selective placement. Selective placement is the careful selection and placement of individual armor stones to achieve a higher degree of interlocking. This 1 meter (approximate) thick layer of tightly knit rock may help to facilitate convection within the revetment. In the revetment fronting Nayokpuk store, once again the gradation of the gravel layer was not ideal to aid in convective cooling. Instead of a poorly graded material, the gravel in this revetment is closer to well-graded gravel. While not poorly graded gravel, the material used in the revetment should be clean enough (marginal amount of fines) to provide ample void space for convection to occur. It is hoped that the effects of convective cooling will be seen on the landward side of the revetment where a gravel layer has been placed to a thickness of 0.70 m. Water infiltration within the revetment during the spring and summer months may decrease the effects of convective cooling within the system. Presently there is not enough information to determine whether these revetments are helping combat permafrost degradation. Within 5 to 6 years enough data will have been collected so that the Alaska District and CRREL can do further analysis and then re-evaluate the effects of convective cooling.

Temperature data

The data gathered from the vertical thermistor string should allow us to confirm the general location of the active layer. It will also show the maximum and minimum annual permafrost temperatures. Preliminary data for the vertical string, and the string beneath the newest USACE revetment

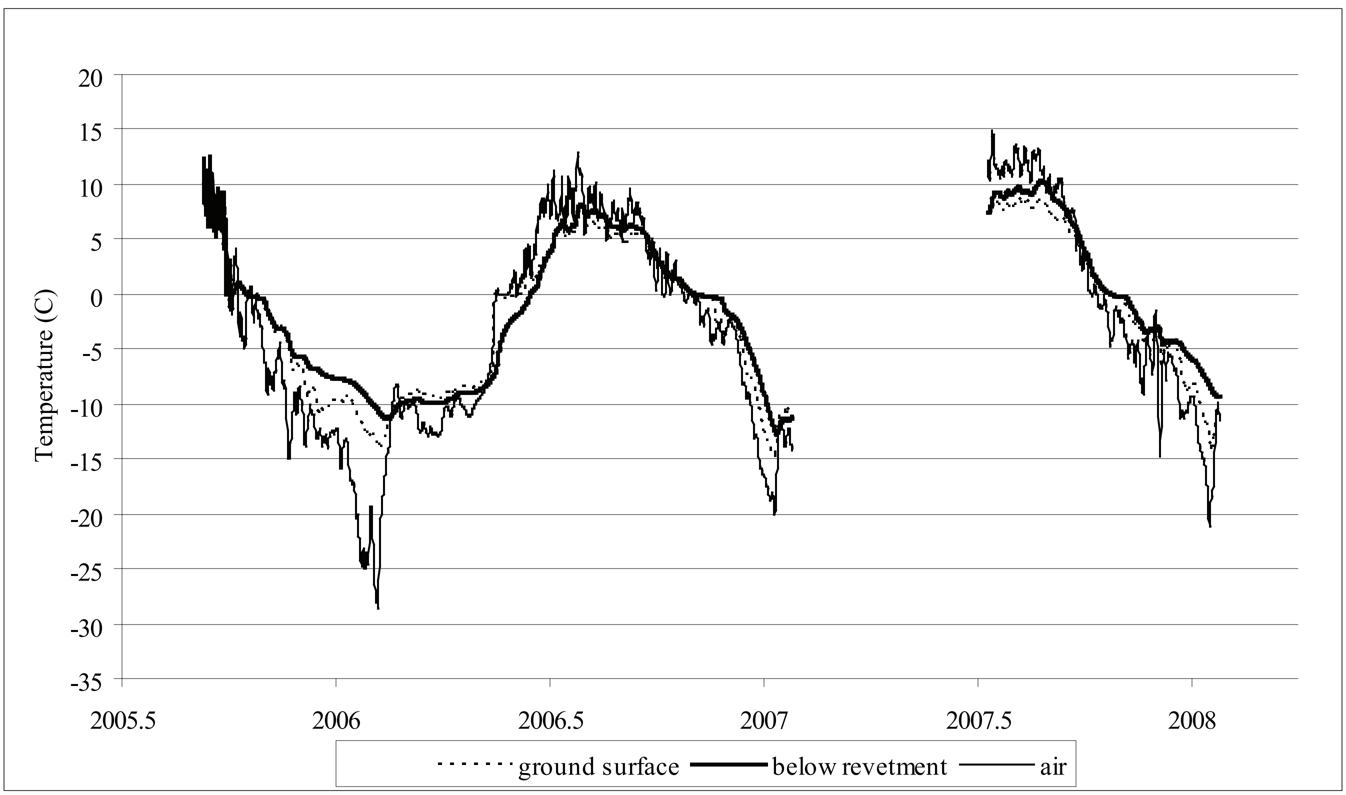

Figure 8. Graph of Temperature vs. Date for the thermistor string placed in the USACE revetment fronting the Teacher's Quarters.

should be available by the time of the presentation of this paper.

Figure 8 shows a graph of the data collected from the thermistor string beneath the USACE revetment fronting the Teacher's Quarters from September 2005 until January 2008. Gaps in data are due to power source difficulties. The data logger was originally placed on a trickle charger to keep the internal battery charged. Due to problems with power source reliability and the desire to keep the system maintenance-free, it was removed from line voltage and placed on the three deep discharge gel-cell marine batteries described above. From the data collected at this point it is apparent that the ground is staying relatively cool. The location of this thermistor string is beneath the filter cloth and just above the native soil. The core rock and armor stone of the shore protection are located vertically above the thermistors. Plotted on Figure 8 are the air temperature from a thermistor located approximately 3 m from the Teacher's Quarters, the ground temperature approximately 0.20 m below the surface, and the temperature beneath the core rock and armor stone. At the time of construction of this revetment, the native soil was contoured to match the final slope of the armor stone which resulted in the native soil, core rock, and armor stone attaining a temperature equivalent to the air temperature. Over the next month, all three temperatures on Figure 8 can be seen to follow the general decline of the air temperature. It can be seen from the period corresponding to the annual cycle of late 2005 to late 2006, the time that the soil temperatures were below 0^{o}C are longer than they were above 0^{o}C. This indicates that the mean annual soil temperature (both beneath the revetment and 0.2 m below the ground surface) is below 0^{o}C, one of the goals of convective cooling. There are some variations noted from year to year for the data presented. The maximum soil temperature beneath the revetment was approximately 8°C in the summer of 2006 and approximately 10°C in the summer of 2007. Similarly, the minimum soil temperature beneath the revetment was approximately -11°C in early 2006, -13°C in early 2007, and was still dropping at -9.6°C in mid-January 2008. This indicates that the base of the revetment is not below the permafrost table but within the active layer. Further data will allow the determination of whether the revetment is acting as an Air Convection Embankment

Summary

ERDC-CRREL and the Alaska District have installed several thermistor strings beneath shore protection projects at Shishmaref, Alaska on Sarichef Island. Data from the strings are beginning to show the variations in the temperature experienced over the annual cycle in the native soil beneath the revetment projects. It is hoped that the grading and selective placement of the armor stone of these revetments causes them to act as an Air Convection Embankment. An additional string placed vertically will supply information about the depth to the permafrost table and the thickness of the active layer.

In the future, along with continual data collection for the 4 strings currently in place a control string of thermistors will be placed at Shishmaref. Due to timing and funding constraints, the control string will be the final thermistor string placed on Sharichef Island. This string will be tentatively placed along the shoreline in the vicinity of the landing strip (as shown in Fig. 7). This area was chosen as a probable location because it will be one of the last areas impacted by revetment construction. Therefore, it should give us the longest period of record for temperatures on the unreveted shoreline. In April of 2008 a Ground Penetrating Radar (GPR) study will be will be conducted by the Alaska District and CRREL to aid in permafrost delineation, including depth to the permafrost table and the thickness of the permafrost layer. When this work is completed the Alaska District and ERDC-CRREL should have a through understanding of permafrost conditions in the vicinity of Shishmaref on Sarichef Island. Knowing the potential stability of the permafrost soils on Sharichef Island will enable the Alaska District and other Federal and State agencies make informed decisions regarding future shore protection and development opportunities.

References

Goering, D.J. 1998. Experimental Investigation of Air Convection Embankments for Permafrost-Resistant Roadway Design. *Proceeding of the 7th International Conference on Permafrost, Yellowknife, Canada, 1998*: 319-326.

Goering, D.J. 2003. Passively cooled railway Embankments for Use in Permafrost Areas. *Journal of Cold Regions Engineering* 17(3): 119-133.

Goering, D.J. & Kumar, P. 1995. Winter-time Convection in open-graded embankments. *Cold Regions Science and Technology* 24: 57-74.

Measuring Ice Lens Growth and Development of Soil Strains during Frost Penetration Using Particle Image Velocimetry (GeoPIV)

Tezera Firew Azmatch

UofA Geotechnical Centre, Department of Civil and Environmental Engineering, University of Alberta, Edmonton, AB, Canada

Lukas U. Arenson

BGC Engineering Inc., Vancouver, BC

David C. Sego

UofA Geotechnical Centre, Department of Civil and Environmental Engineering, University of Alberta, Edmonton, AB, Canada

Kevin W. Biggar

BGC Engineering Inc., Edmonton, AB

Abstract

The formation of ice lenses and the water migration during freezing of frost susceptible, fine-grained soils is a dynamic and complex process. Horizontal ice lenses and vertical ice veins form at different spacing, intervals, and growth rates as the pore freezing front penetrates into the ground forming a three dimensional ice lens pattern. One-dimensional step-freezing tests were carried out in a transparent freeze cell with frost susceptible Devon silt to study this effect in detail. Time-lapse photography and particle image velocimetry are used to identify the dynamics of the freezing processes. Three dimensional movements are used to measure the changes in ice lens growth and axial soil strain in-between ice lenses with time. The formation and growth rate of vertical ice veins are studied and local vertical strains are determined. Horizontal soil deformations are also investigated. The detailed strains and ice lens growth rates within freezing soils help in improving formulations for frost heave, strength, and deformation behavior of freezing and frozen soils.

Keywords: frost heave; frost susceptibility; ice lens formation.

Introduction

The formation of ice lenses and the water migration during freezing of frost susceptible, fine-grained soils is a dynamic and complex process. Horizontal ice lenses and vertical ice veins form at different spacing, intervals, and growth rates as the freezing front penetrates into the ground forming a three dimensional ice lens pattern. This pattern and the growth rates of the ice lenses strongly depend on the freezing boundary conditions, such as temperature gradient, cooling rate, or vertical pressures, and the characteristics of the soil, i.e. the grain size distribution, hydraulic conductivity, water availability, and pore water salinity (Konrad & Morgenstern 1982, Konrad 1994, Miller 1973, Penner 1972).

The formation of ice lenses is possible with the presence and migration of unfrozen water at temperatures below its freezing point (Konrad and Morgenstern 1980). It is believed that migration of the free water is induced by a temperature gradient within the soil that induces suction. The suction then drives the movement of free water to the growing ice lens. The flow of water towards the warmest ice lens is assisted by the formation of tension cracks, which increase the vertical hydraulic conductivity of the soil (Chamberlain & Gow 1979).

Freezing tests conducted at the University of Alberta (Xia 2006) have shown that ice lens growth is not a one-dimensional process. Horizontal ice lenses as well as vertical ice veins form as the soil freezes. The vertical ice veins develop a hexagonal crack pattern similar to that observed in drying soils (Arenson et al. in press).

The reticulate ice structure, also observed under natural freezing conditions (Mackay 1974), during freezing deforms the soil horizontally and vertically. When the final ice lens starts to form, part of the soil below the final ice lens consolidates, and part of the soil above the final ice lens heaves. Arenson et al. (2007) measured the vertical deformations in freezing soil and were able to explain the freezing process using these deformation results.

This work was continued, and this paper focuses on the formation of the vertical ice veins and the horizontal soil deformations. Results from the time-lapse photography presented by Xia et al. (2005) are re-analyzed using particle image velocimetery (PIV) to develop a better understanding of the formation and growth of ice structures.

Laboratory Tests

One-dimensional open system (access to water) step-freezing tests were carried out on Devon silt under different boundary conditions. The Devon silt has a liquid limit of 32%, plastic limit of 20%, and specific gravity of 2.65. The samples were frozen from the top downward. Two temperature baths control the temperature conditions at the top and the bottom of the sample to establish one dimensional

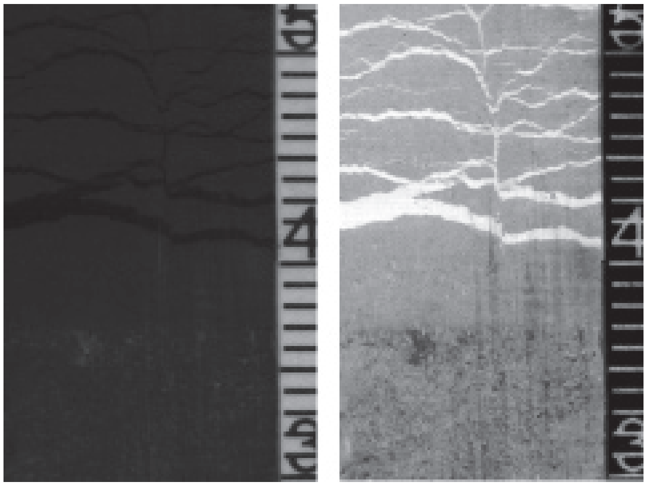

Figure 1. Original picture (left), and visible ice lens structure (right).

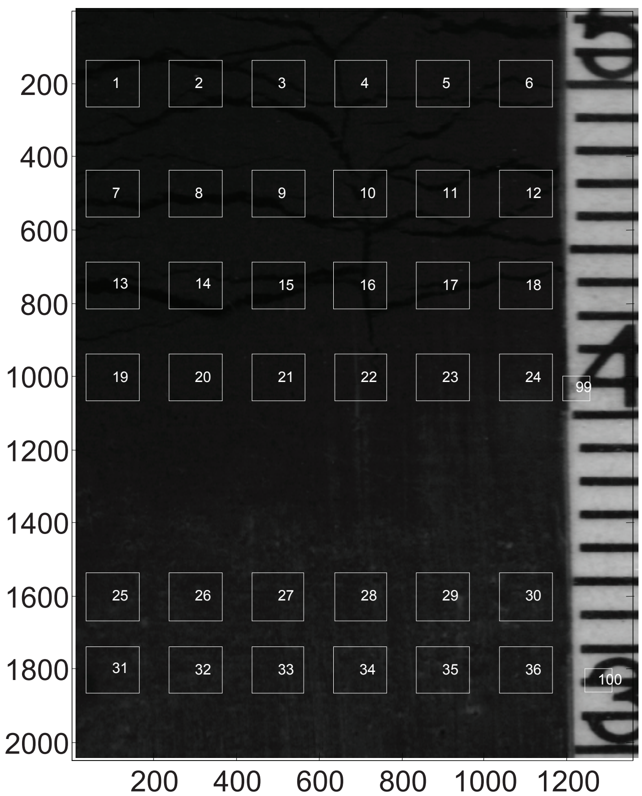

Figure 2. Initial patch locations; the scale is in pixels (1 pixel ~10 μm).

vertical freezing from the top downward.

A fluorescent tracer ($C_{20}H_{12}O_5$), which appears green in unfrozen water but colorless in ice under ultra violet light (Arenson & Sego 2006), was used to determine the frozen and unfrozen zone of the sample during freezing.

Time-lapse photography provided digital photo records to visually observe and document the freezing process. Details of the time-lapse photography technique and of the laboratory freezing tests used herein are presented in Xia et al. (2005) and Xia (2006).

Table 1. Test conditions.

Test #	T_{grad}[1] (°C/m)	S[2] (g/L)	σ[3] (kPa)
1	58	0	0
4	58	0	100
8	58	10.2	0

[1] Temperature gradient at thermal steady state
[2] Salinity (NaCl)
[3] Vertical pressures during freezing

Image Analysis using GeoPIV

The digital images were analyzed using GeoPIV software, a MatLab module which implements particle image velocimetery (PIV) in a manner suited to geotechnical testing. This code has been programmed and successfully used for geotechnical laboratory testing to measure deformations in soils (White et al. 2003). It has also been used to determine the deformations in freezing soils (Arenson et al. 2007).

Figure 1 shows the original image and the corresponding ice lens structure for one of the images.

GeoPIV was used to measure the soil deformation. Geo PIV uses image texture to follow patches over a time series of pictures. A number of patches were defined on the sample and their movement was followed over time (Fig. 2).

Test Results and Image Analysis Results

Three tests from Xia et al. (2005) were analyzed in this paper. These tests were chosen because of their well defined vertical ice veins. The freezing test conditions are shown in Table 1. All the samples were initially consolidated at 100 kPa vertical pressure.

Ice Lens Growth and Deformation

The reticulate ice structures and cross sections of the frozen samples showing the hexagonal ice vein pattern are presented in Arenson et al. (in press). Figures 3 through 10 show various deformation results.

Vertical deformations

In the plots for vertical deformations (Figs. 3, 7) positive values indicate heave and negative values indicate consolidation.

It can be seen from Figure 3 (Test #1) that heaving starts at about 42 hours after the start of the test. By the time heaving has started the consolidation process is nearly complete. This means that heaving and consolidation are not occurring in parallel. Heaving starts almost after consolidation is complete. The heave rate and the consolidation rate are constant.

Figure 3 also indicates that P10 is undergoing heaving, and P22, P24, and P25 are consolidating. Hence, row 2 (containing patches P7–P12) is heaving, and row 4 (containing patches P19–P24) is consolidating. The final ice lens for this test is located between row 2 and row 4. This

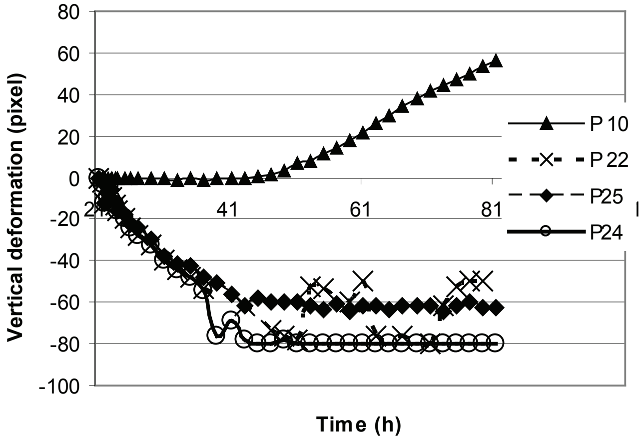

Figure 3. Vertical deformations for Test #1. P10 is located above the final ice lens. P22, P24 and P25 are located below the final ice lens.

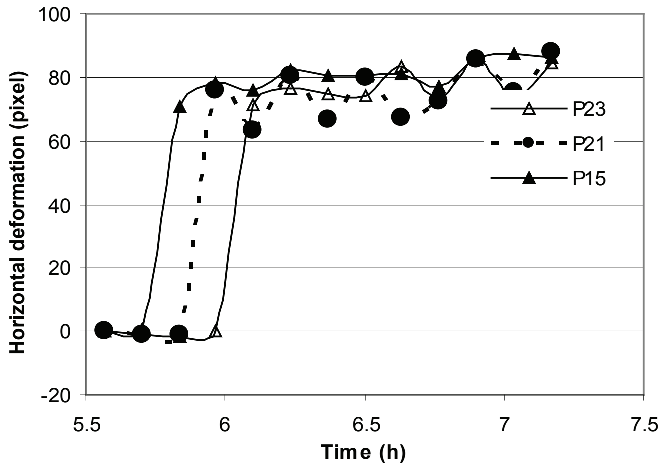

Figure 4. Horizontal deformations for Test #1.

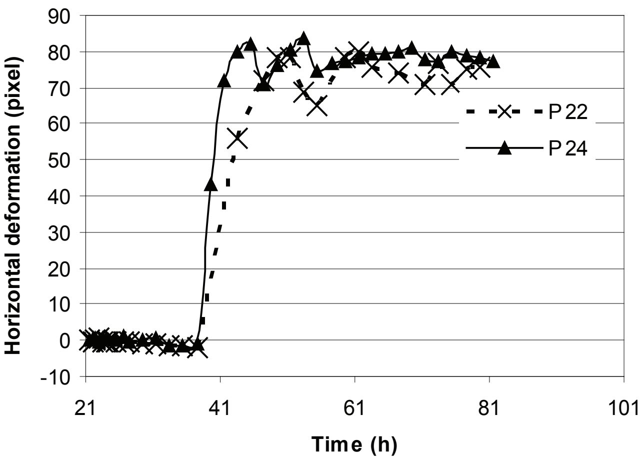

Figure 5. Horizontal deformations while a final vertical ice vein is being formed for Test #4.

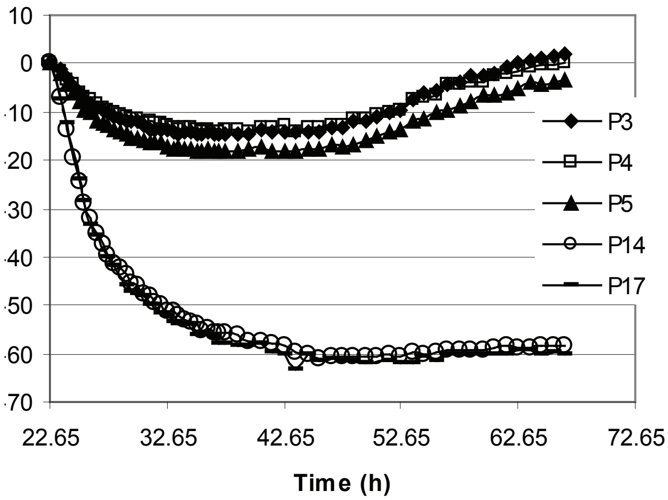

Figure 6. Horizontal deformations while an intermediate vertical ice vein is being formed for Test #4.

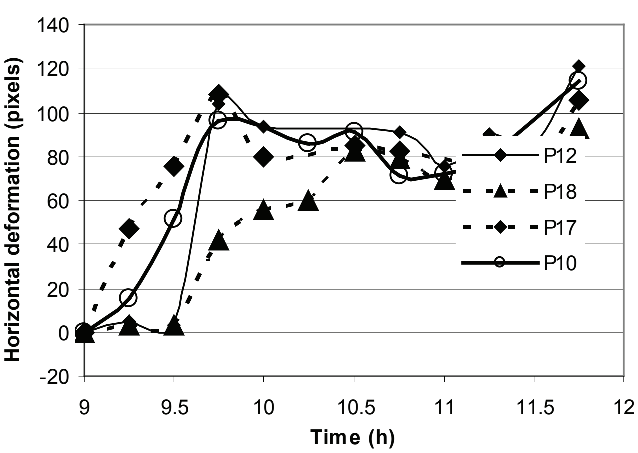

Figure 7. Vertical deformations while the final ice lenses are being formed for Test #8. P3, P4 and P5 are located above the final ice lens. P14 and P17 are located below the final ice lens.

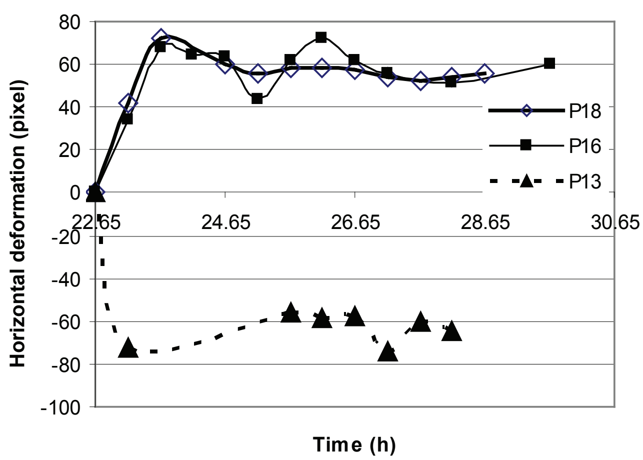

Figure 8. Horizontal deformations while a final vertical ice vein is being formed for Test #8. P13 is located to the left of the vertical ice vein. P16 and P18 are to the right of the vertical ice vein.

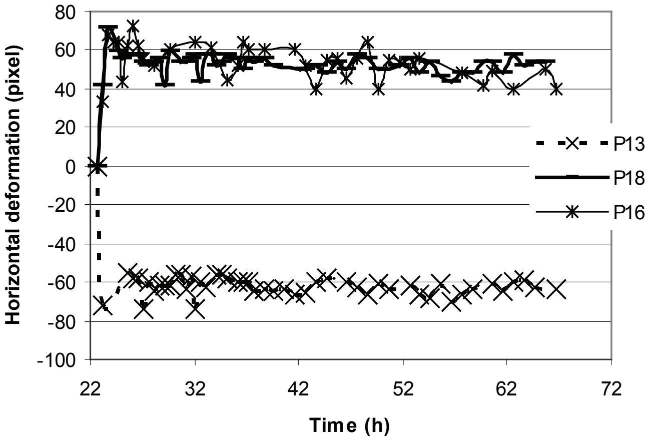

Figure 9. Horizontal deformations while a final horizontal ice lens is being formed for Test #8. P13 is located to the left of the vertical ice vein. P16 and P18 are to the right of the vertical ice vein.

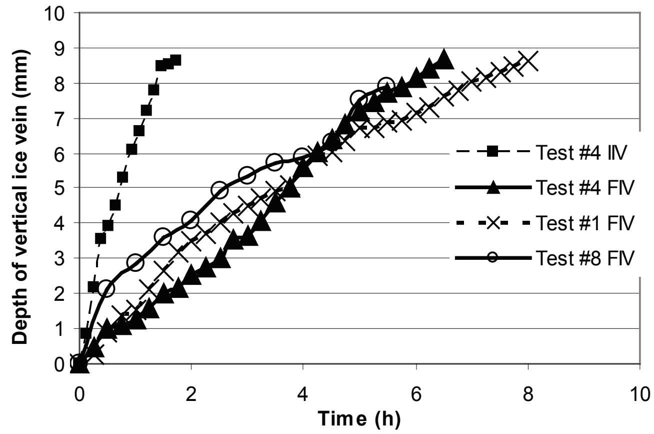

Figure 10. Rate of growth of the vertical ice veins (FIV=Final Ice Vein, IIV=Intermediate Ice Vein).

explains that water is being drawn from the region below the final ice lens. This water is then used to form the final ice lens. As the final ice lens forms, the regions above it start to heave, as observed by the movement of P10. Similar trends have also been observed by tracing other patches in the same test.

In Figure 7, all the patches are consolidating during the first 42 hours. After 42 hours, patches P3 and P4 start heaving, and patches P14 and P17 do not deform anymore. The final ice lens for this test started forming after about 42 hours. This indicates that the development of the final ice lens, hence frost heave, starts after the consolidation is complete. The final ice lens for this test is located between row 2 (containing patches P7–P12) and row 3 (containing patches P13–P18)

Figures 3 and 7 also indicate that the rate of heaving is smaller than the rate of consolidation. It can be concluded that the rate of ice formation is lower than the rate of water extraction from the soils.

Horizontal deformations

In Figure 3, it can be seen that heaving starts around 42 hours after the start of the test. This implies that the final horizontal ice lens starts to form after 42 hours. In Figure 4, it can be noted that the horizontal strains remain constant while the final ice lens is being formed. The same observation can be made in Figures 5, 6, and 8. This implies that the horizontal strains are due to the formation of the tension cracks and not due to the formation of the final horizontal ice lenses. The horizontal strains could therefore be assumed to originate from the formation of the vertical tension cracks, which are a result of the suction created by the temperature gradient. According to the authors, the mechanism of the formation of the vertical ice veins can be described as follows: First, suction is created in the frozen fringe, and tension cracks form; these tension cracks are then filled with water being removed from the soil, and finally, part of the water in the tension cracks freezes to form the vertical ice veins and part of it moves up to form the horizontal ice lenses behind the vertical ice veins. The formation of the tension cracks facilitates the flow of water by increasing the hydraulic conductivity of the soil. It is observed that tension cracks are formed prior to the formation of horizontal ice lenses (Arenson et al. in press).

While the soils are straining horizontally, water is being drawn to form the vertical ice veins and the horizontal ice lenses above their crack tip. Mackay (1974) states, "The vertical and horizontal ice veins are believed to have grown in shrinkage cracks with much of the water being derived from the adjoining clay."

In most of the tests, the magnitude of the horizontal displacement is between 60 and 80 pixels (approximately 0.6–0.8 mmm). These could indicate that the thickness of the vertical tension cracks formed is almost constant. It can be observed from the digital images that the thickness of the vertical ice veins is the same for almost all the tests.

From Figures 8 and 9, it can be observed that the movements of P13 are in the opposite direction to that of P16 and P18. This is because the patches are located on different sides of the vertical ice vein. P13 is located to the left of the vertical ice vein, and P16 and P18 are located to the right of the vertical ice vein. Hence, their corresponding horizontal displacement is in a different direction but it displaces the same amount, indicating the opening of the vertical crack and the formation of the ice vein.

Rate of growth of vertical ice veins

Tension cracks always formed before the horizontal ice lenses. These tension cracks, which facilitate the flow of unfrozen water, are then filled partly by vertical ice veins.

Figure 10 shows the rate of growth of the vertical ice veins. The final ice veins (FIV) are defined as the vertical ice veins that form immediately before the start of the formation of the final horizontal ice lens. The intermediate ice veins are the vertical ice veins that form before the FIV. The rate of growth of the final vertical ice veins ranges from 1.22 mm/h to 1.57 mm/h. For Test #4, the rate of growth of the intermediate ice vein is 5.78 mm/h. Hence, the rate of growth

Table 2. Depth and growth rate of vertical ice veins.

Test #		Height of vertical ice vein (mm)	Growth rate (mm/h)
1	FIV	8.60	1.22
4	FIV	8.67	1.37
	IIV	8.60	5.78
8	FIV	7.91	1.57

of the IIV is higher than the rate of growth of the FIV.

The height of the vertical ice veins for the tests under consideration is about the same for all tests.

Conclusions

Particle image velocimetry (PIV) was used to measure soil deformations. Patches with a distinct characteristic were followed as the ice lenses formed and grew. The deformations measured were used to explain the freezing process and the resulting ice being formed.

The heaving process and the consolidation process were observed to take place at different times. Heaving followed immediately after consolidation was complete.

The horizontal strains were observed to be a result of the formation of the vertical tension cracks as the freezing front advanced.

The suction produced as a result of the temperature gradient caused tension cracks in the soil. The tension cracks, which increase the vertical permeability of the soil, were then filled with water. A channel formed where water can migrate from the unfrozen zone to the warmest ice lens. Part of the water moved up enhancing the development of a horizontal ice lens above the crack, and part of it froze inside the cracks, leading to the formation of the vertical ice veins.

The vertical tension cracks always formed before the horizontal ice lenses formed. Thus, the formation of the tension cracks, and hence the tensile strength of the soils, play a very important role in the freezing process.

Acknowledgments

The authors would like to thank Dr. Andy Take from Queens University for his support with the GeoPIV analysis. Tezera Firew Azmatch appreciated the funding through the NSERC Discovery Grant held by Dr. Sego.

References

Arenson, L.U., Firew Azmatch T. & Sego, D.C. 2008. A new hypothesis on ice lens formation in frost susceptible soils. *Proceedings of the Ninth International Conference on Permafrost, Fairbanks, Alaska, June 29–July 3, 2008* (this proceedings).

Arenson, L.U., Sego, D.C. & Take, W.A. 2007. Measurement of ice lens growth and soil consolidation during frost penetration using particle image velocimetry (PIV). *60th Canadian Geotechnical Conference, Ottawa, ON, October 21–24, 2007*: in press.

Arenson, L.U., Xia, D., Sego, D.C. & Biggar, K.W. 2006. Change in ice lens formation for saline and non-saline Devon silt as a function of temperature and pressure. *13th International Conference on Cold Regions Engineering. American Society of Civil Engineers (ASCE), Orono, Maine, USA*: CD-Rom.

Arenson, L.U. & Sego, D.C. 2006. The effect of salinity on freezing of coarse grained sands. *Canadian Geotechnical Journal* 43(3): 325-337.

Chamberlain, E.J. & Gow, A.J. 1979. Effect of freezing and thawing on the permeability and structure of soils. *Engineering Geology* 13(1-4): 73-92.

Konrad, J.M. 1989. Pore water-pressure at an ice lens: Its measurement and interpretation. *Cold Regions Science and Technology* 16(1): 63-74.

Konrad, J.M. 1994. 16th Canadian Geotechnical Colloquium - Frost Heave in Soils - Concepts and Engineering. *Canadian Geotechnical Journal* 31(2): 223-245.

Konrad, J.M. & Morgenstern, N.R. 1980. A mechanistic theory of ice lens formation in fine-grained soils. *Canadian Geotechnical Journal* 17(4): 473-486.

Konrad, J.M. & Morgenstern, N.R. 1982. Effects of applied pressure on freezing soils. *Canadian Geotechnical Journal* 19(4): 494-505.

Mackay, J.R. 1974. Reticulate ice veins in permafrost, Northern Canada. *Canadian Geotechnical Journal* 11(2): 230-237.

Miller, R.D. 1973. Soil freezing in relation to pore water pressure and temperature, *Second International Conference on Permafrost. National Academy of Sciences, Washington, Yakutsk, Siberia*: 344-352.

Nixon, J.F.D. 1991. Discrete ice lens theory for frost heave in soils. *Canadian Geotechnical Journal* 28(6): 843-859.

Penner, E. 1959. *The Mechanism of Frost Heaving in Soils.* Bulletin 225, U.S. Highway Research Board.

Penner, E. 1972. *Influence of Freezing Rate on Frost Heaving.* Highway Research Record 393, U.S. Highway Research Board.

Taber, S. 1930. The mechanics of frost heaving. *Journal of Geology* 38: 303-317.

White, D.J., Take, W.A. & Bolton, M.D. 2003. Soil deformation measurement using particle image velocimetry (PIV) and photogrammetry. *Geotechnique* 53(7): 619-631

Xia, D. 2006. *Frost Heave Studies Using Digital Photographic Technique.* M.S. Thesis. Edmonton, AB, Canada: University of Alberta, 165 pp.

Xia, D., Arenson, L.U., Biggar, K.W. & Sego, D.C. 2005. Freezing process in Devon silt – using time-lapse photography. *Proceedings, 58th Canadian Geotechnical Conference, Saskatoon, Saskatchewan. September 18–21.* CD-ROM

Evidence of Permafrost Formation Two Million Years Ago in Central Alaska

James E. Beget, Paul Layer, David Stone, Jeffrey Benowitz, Jason Addison
Department of Geology and Geophysics, University of Alaska Fairbanks, Fairbanks, AK, USA

Abstract

Ice wedge casts and thermokarst deposits near the base of loess cliffs at Gold Hill record a previously unrecognized cycle of transient climate cooling and permafrost formation followed by an interval of climate warming and permafrost degradation. The ice wedge casts and thermokarst features occur below the PA tephra (ca. 2.02 myr) and begin above loess recording the Reunion paleomagnetic excursion (ca. 2.14 myr). The dates indicate colder conditions and permafrost formation in central Alaska 2.14–2.02 million years ago and can be correlated with marine isotope stage 77, a time of significant global glaciation and cooling. Warmer conditions during marine isotope stage 76 thawed the permafrost and generated the ice wedge casts and thermokarst sediments preserved at Gold Hill today. Climate and permafrost in Alaska were responding rapidly to global climate forcing by two million years ago.

Keywords: Alaska; climate change; geochronology; loess, permafrost; Quaternary.

Introduction

Loess deposits are common across central Alaska, especially in low-lying areas near the Tanana and Yukon and other glacier-fed rivers. Large areas of ice-rich frozen ground in valley bottoms in central Alaska have formed in loess and reworked eolian silts. River erosion or human disturbance of loess at building, mining, and other construction sites sometimes reveal spectacular views of ice wedges, ice lenses, and other varieties of permafrost.

Pewe (1951) first recognized that the silts that blanket hillslopes and form thick deposits in valley bottoms near Fairbanks and other areas were eolian in origin, and suggested that the ice wedges and other periglacial features found in the loess were produced during the last ice age.

Large areas of valley-filling loess deposits were washed away and destroyed by hydraulic excavation and dredging during 20th century industrial scale gold mining operations near Fairbanks, Ester, Chicken, and other mining areas in central Alaska. When the mining operations stopped, cliffs of loess and other sediments 10–50 m thick were left in some areas. As a result of the gold mining, numerous bones and occasional frozen carcasses of bison, mammoths, and other extinct Pleistocene megafauna were collected from the loess and the alluvial gravels beneath the loess (Guthrie 1990).

The Troy L. Pewe Climatic Change Permafrost Reserve is located along the north side of the Parks Highway beginning about 3 km southwest of the University of Alaska Fairbanks campus. The site preserves the eastern part of an almost continuous vertical bluff of loess almost 5 km long produced by hydraulic mining in the Fairbanks area. The highest cliffs and the oldest deposits of loess occur at the eastern end of the Gold Hill exposure. The original surface of the loess sloped gently downwards to the south, and small "islands" of the original loess valley fill left by the mining operations are preserved on the south side of the Parks Highway.

Pewe (1975a, b) divided the loess at Gold Hill into four main stratigraphic units. A buried horizon containing logs and branches found near the middle of some loess sections was named the Eva Creek Forest Bed, while the upper loess was assigned to the Goldstream Formation and the lower loess to the Gold Hill Formation. A basal forest bed occurred in a few sites and was named the Dawson Cut Forest Bed (Pewe 1975b). Pewe also recognized that numerous tephras are preserved in the loess. The base of the entire 30-m-thick loess section was originally estimated to be "Illinoian" in age, i.e., less than 200,000 years old (Pewe 1975a, Pewe & Reger 1989).

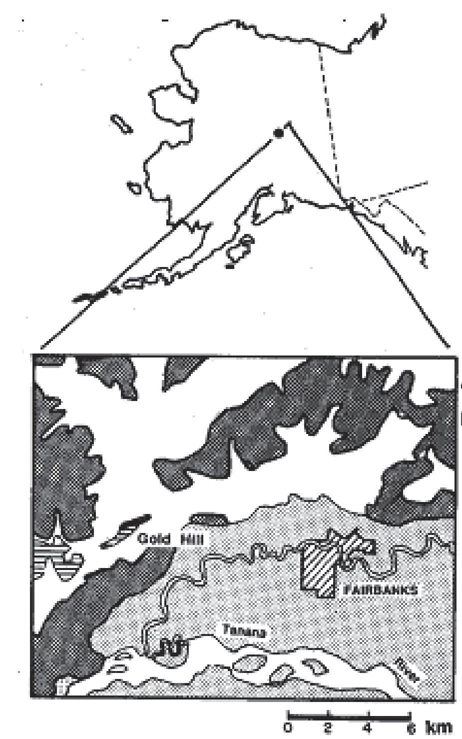

Figure 1. Location of the study site at Gold Hill and simplified Quaternary geology of the Fairbanks area. Light stiple = alluvium, dark stiple = pre-Quaternary bedrock, white = loess deposits, horizontally lined = gravel deposits exposed by mining. Figure modified from Westgate et al. (1990).

The first indication that Alaskan loess deposits might be much older came from the discovery that the loess

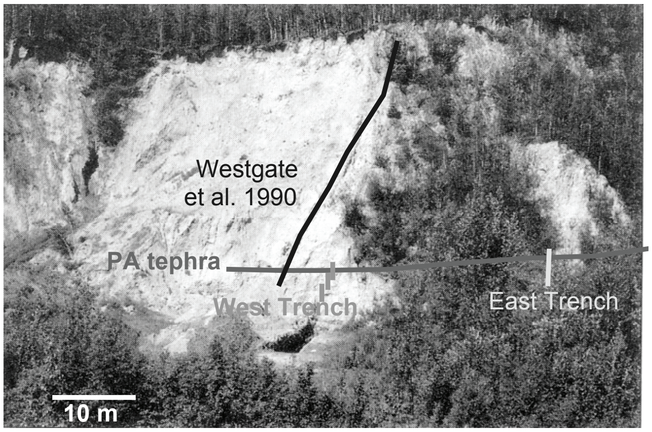

Figure 2. Location of the PA tephra and trenches excavated for stratigraphic and paleomagnetic studies at Gold Hill.

contained numerous paleosols, in addition to the Eva Creek and Bonanza Creek Forest Beds (Beget 1988, 1991). The sequences of multiple paleosols and interstratified loess deposits found at Gold Hill and other sites were interpreted as glacial-interglacial cycles, requiring an age for the loess significantly older than originally inferred by Pewe. These interpretations were supported by geophysical studies that demonstrated that loess deposited in glacial and interglacial periods had different magnetic properties, and that changes in environmental magnetic signals recorded in the loess could be used to produce proxy climate records through loess sections in Alaska that correlated with Milankovitch models of insolation changes and marine isotope records (Beget and Hawkins 1989, Beget et al. 1990, Beget 1996).

Westgate et al. (1990) used tephrochronology and paleomagnetic stratigraphy to determine that the PA tephra found at ca. 21 m depth at Gold Hill was deposited ca. 1.9 million years ago, and loess at the base of the Gold Hill section was as much as 3.1 million years old. Westgate and his co-workers took samples at 10 cm intervals, and found the upper loess was normally magnetized and correlative with the Brunhes paleomagnetic epoch. The lower part of the loess recorded mainly reversed magnetic fields, but in the overall reversely polarized section, there were magnetic reversals back to normal polarity at about 2.5 meters, 3.5 meters, 5.5 meters, and 8.2 meters below the PA tephra layer. The initial transition from normal to the reversely magnetized loess was correlated with the Brunhes-Matuyama boundary, and the two normal epochs below the PA tephra were assigned to the two Reunion subchrons (also known as the Huckleberry Ridge and Reunion events) in the Matuyama Paleomagnetic Chron. More recent work indicates the age of the PA tephra is 2.02 +/- 0.14 Ma (Westgate et al. 2003).

Here we report on the discovery of ice wedge casts, thermokarst features, and interstratified loess and paleosol sequences found below the PA tephra near the base of the Gold Hill section. We also present new paleomagnetic dates for the Gold Hill loess. Our data show that Alaskan loess deposits are surprisingly good recorders of short-lived geologic events, including transient shifts in climate and fluctuations in the earth's magnetic field. Paleoclimatic records from loess deposits are an important source of information about events in terrestrial areas of Alaska.

Field and Laboratory Methods

The PA tephra layer is located 11 m from the bottom of the loess section, and forms a distinctive marker bed that can be traced for more than 30 m across the lower part of the Gold Hill loess. The tephra bed is as much as 5 cm thick, although in most places it is broken into pods or two or more thinner layers. It was used as a datum from which local stratigraphic field measurements were taken at various points along the section.

Trenching and sampling were done to generate two new stratigraphic sequences: one about 5 m east of the long section studied by Westgate et al. (1990) and the second about 20 m to the east (Fig. 2). Both trenches were excavated to a depth of about 4 m and studied with the help of enthusiastic students (Naibert et al. 2005). The newly created loess exposures were then photographed and stratigraphically logged. At both sites, oriented samples were collected beginning at the PA tephra and continuing down to the bottom of the trenches. During sampling, a series of platforms were cut along the excavated exposure, and oriented plastic cube samples were taken at 5 cm intervals from undisturbed loess exposed in the face of the trenches for paleomagnetic analyses. Plastic vials of loose material were also collected every 2 cm for magnetic susceptibility measurements.

The oriented cubes were taken to the Paleomagnetic Laboratory at the University of Alaska Fairbanks, and successive alternating field demagnetization (11 steps) up to 100mT was applied to strip away the modern magnetic overprint and to determine the original polarity of the magnetic field at the time the loess was deposited. After some primary data analysis to locate points of interest in the section, the loess was sampled again with plastic cubes at 2 cm intervals from depths of 0.9 to 1.1 m, and from 2.9 to 3.1 m, for a more detailed examination of changes in magnetic inclination using alternating field demagnetization.

Stratigraphy and Structure

During the initial trenching and logging, it became apparent that loess just below the PA tephra had been locally involved in a series of post-depositional collapses. The PA tephra was deposited on the ground surface ca. 2 million years ago, and thus the topography and slumps that occurred near that time at Gold Hill can be reconstructed from the taphonomy of the PA tepha deposits. We note that a veneer of loose colluvium from 0.1–0.5 m thick is present on the surface at Gold Hill, but our excavations cut completely through the colluvium to expose the much more indurate early Quaternary loess. Our trenching sites were chosen specifically to determine the relationship between the deposits and stratigraphy in the trenches and the PA tephra.

Our excavations reveal the PA tephra was incorporated in local depressions and slumps in 4 distinct areas along the

30-m-long exposure. At the eastern pit, the tephra and the intercalated loess, which elsewhere are preserved in sub-horizontal beds, abruptly began to drop in elevation on each side of a 2-m-wide V-shaped depression, indicating the collapse had formed after the tephra was deposited, and that tephra and loess at the margin of the V-shaped depression was progressively slumping into the depression. Further excavations found pellets of the tephra and blocks of loess in a compact silt matrix within the depression. The V-shaped depression was excavated to a depth of 2 m where it became narrow and terminated. The morphology of the V-shaped depression, and the deformation of the sediment at the margins of the pit, are identical to modern ice wedge casts in the Fairbanks area, and the feature is interpreted as a 2 myr old ice-wedge cast.

At the western pit, a well-developed organic-rich paleosol occurs about 20–60 m thick above the PA tephra. This paleosol can be traced along much of the exposure above the PA tephra. The excavations in the western trench found bedded organic-rich sediment and loess and pods of PA tephra that had apparently collapsed into a broad depression. The organic material occurs in beds at angles up to 70°, together with loess and small pods of the PA tephra (Fig. 3). The depression is interpreted as having formed as part of a thermokarst zone.

At the far eastern of the PA exposure, a loess cliff exposed a 3-m-thick diamicton that could be traced 5 m across the section. The diamicton contained rounded to elongate silt and multi-colored paleosol clasts ranging from 0.5–10 cm in diameter disseminated in a dense, fine-grained matrix. The eastern margin of this deposit cuts across undisturbed loess below the PA tephra, and itself locally underlies the PA tephra and incorporates pods of the tephra. We interpret the diamicton as having formed by progressive collapse of wet, thawed pellets and blocks of sediment into a large thermokarst pit. Similar large pits are forming today at sites where frozen loess is thawing near Fairbanks (Shur et al. 2000). Bits of thawed ground can frequently be heard falling into thermokarst pits, and we suggest the abundant rounded clasts in this deposit accumulated in similar fashion in an ancient thermokarst collapse 2.0 million years ago.

The presence of ice wedge casts and thermokarst features below the PA tephra indicates climate in the Fairbanks cooled sufficiently prior to the deposition of the PA tephra to allow the formation of permafrost. The climate must have subsequently warmed and caused the permafrost to degrade and the thermokarst features to form. The warm period is tentatively correlated with the well-developed paleosol just above the PA tephra, as the presence of the strong paleosol records an interglacial period that occurred just after the PA tephra fall.

Paleomagnetic Record from the Trenches

New paleomagnetic data help to constrain the age of the periglacial features and the climate flucations recorded at the base of Gold Hill. The paleomagnetic data from our two new trenches predominantly display reversed magnetization, as expected in the Matuyama reversed polarity chron. Our data are generally consistent with the previously published age of the PA tephra and the paleomagnetic data from Westgate et al. (1990), and confirms that the loess below the PA tephra is indeed older than 2 million years. However, a comparison of the paleomagnetic data from our two new trenches and the trench of Westgate and his co-workers, reveals some differences. Our two new sections both contain a number of normally magnetized polarity samples that can be interpreted as recording a brief magnetic reversal within the upper part of the Matuyama chron that was not recognized in the trench studied by Westgate and his co-workers. This introduces the possibility that the creation and thawing of ice wedges and other kinds of permafrost may have disrupted the original loess deposits and affected the lateral continuity and preservation of the paleomagnetic record at Gold Hill.

Figure 3. Organic-rich silts and blocks of gleyed and unaltered loess filling a collapsed zone stratigraphically below the PA tephra in the western trench.

Our eastern trench contains a zone of magnetic polarity samples at 0.7 m below the PA tephra. The reversed signal occurs in five successive samples, leaving little doubt that it is a real reversal. Our western trench also produced evidence of this episode of normal magnetization, although it occurred in only one sample. Westgate et al. (1990) also found one point near this depth below the PA that appeared to record a transition to normal polarity, but they decided not to assign a reversal to this normal horizon. Based on the excellent signal in our eastern trench and the appearance of the same event in the two other trenches, we believe this is real polarity event. Because this is the first reversal below the PA tephra, we interpret this event as the Reunion event, dated to 2.14 million years ago.

The variability in the character of the magnetic signal between our two trenches and the Westgate trench is consistent with our recognition of ice wedge casts and thermokarst features in the loess at this depth in the loess. Since the loess below the PA tephra was locally disturbed by a cycle of formation and destruction of ground ice, the sedimentation rate and mode of deposition should vary from place to place across the exposure, just as we observe. Similarly, the low inclinations that both we and Westgate et al. (1990) observed in this area, likely reflect deformation of the sediment during the intrusion of ice wedges and slumping and relaxation of the sediment as the ground ice thawed. Indeed, when the sample locations of the paleomagnetic cubes are compared to the stratigraphic interpretations of the two trenches, it is clear the paleomagnetic samples from the eastern trench, where the Reunion event is best recorded, were taken from loess adjacent to an ice wedge cast, while paleomagnetic sampling in the western trench was inadvertently done partly excavated through a thermokarst deposit.

The short duration of the reversal ca. 0.7 m below the PA tephra in the Gold Hill loess is also consistent with our interpretation that this marks the Reunion event, as the Reunion event is consistently characterized as having been brief and transient where observed elsewhere on earth. The apparent brevity of the reversal and the lateral paleomagnetic inhomogeneity we find across the section is, therefore, supportive of our conclusion that permafrost, including ice wedges, formed and then thawed ca. 2.05 million years ago, shortly after the Reunion Chron.

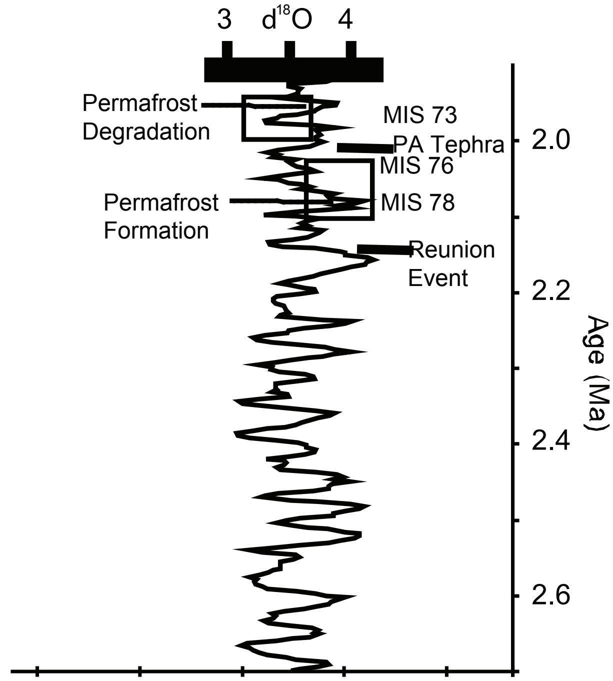

Figure 4. Standardized global marine isotopic record from Shakleton et al. (1995) covering the time period of the recorded by loess near the PA tephra at Gold Hill. Ground ice formed during a cold interval soon after the Reunion Chron (2.14 million years) and was destroyed during a subsequent interglacial interval. We correlate the cold interval with MIS 76–78 and the warm interval with MIS 73.

Environmental Reconstruction

We collected samples for magnetic susceptibility measurements from both the eastern and western trenches. The susceptibility values averaged about 10 SI units, but systematic variations in magnetic susceptibility occurred through the sections, with massive unaltered loess having higher susceptibilities than loess from the paleosol zones. The pattern of environmental magnetism 2 million years ago closely resembles that from middle and late Quaternary loess sequences, suggesting that the susceptibility signal records both primary variations in wind strength and subsequent pedogenic alteration of the magnetic minerals in the loess (Beget 2001).

We used the ages of the PA tephra and the Reunion chron to control a linear interpolation model to estimate ages of sediments between these two well-dated points in our trenches at Gold Hill, and to evaluate the paleoclimatic inferences from the environmental magnetic record and the evidence of permafrost formation and disappearance.

The PA tephra occurs in a high susceptibility zone, and the age of the PA correlates well with a glacial interval recorded by marine isotope stage MIS 74 in global marine records (Shackelton et al. 1995). The paleosol just above the PA tephra has low susceptibility and is correlated with an interglacial episode recoded by MIS 73. The Reunion chron occurs during the MIS82-81 transition in the marine record, which is followed by a long and sustained global glacial event during MIS78 to MIS 76.

The top of the ice wedge casts and thermokarst features occurs between the PA tephra and the Reunion paleomagnetic chron, and the formation of ice wedges recorded at Gold Hill is therefore correlated with the unusually sustained glacial interval recorded by MIS 78–76. This glacial event produced a significant interval of cold climate 2.1 million years ago in central Alaska. The marine isotopic data suggests that the MIS 78–76 glaciation was one of the longest and most intense until Middle Pleistocene time, resulting in as much as 70 m of sea level drop due to ice sheet growth on land (Pillans et al. 1998).

The fact that the PA tephra is locally incorporated in the ice wedge casts and thermokarst deposits, indicates warming and destruction of the ice wedges occurred after the PA tephra was deposited. We suggest this interval is correlative with MIS 73, a global warm interval recorded in marine records at about 1.9 million years ago. The correlations suggested by our discovery of ice wedge casts and thermokarst features, and our new age-dating model at Gold Hill, link evidence of rapid climate change in Alaska ca. 2 million years ago with the environmental magnetic proxy record of climate change from the loess, the paleosol evidence, the sedimentological record of permafrost formation and degradation, and the standard global climate record from isotopic studies of marine cores. We believe the excellent temporal correlations support the validity of our approach and the reliability of our conclusions.

Summary and Conclusions

We carried out stratigraphic, sedimentologic, and paleomagnetic studies of sediments in the lower part of the Gold Hill loess deposit, 3 km southwest of the University of Alaska Fairbanks. We report here on work done in two new trenches that were hand excavated by students participating in an NSF summer institute and by undergraduate and graduate students enrolled in the Geology and Geophysics program at the University of Alaska (Naibert et al. 2005).

The exposures in the two new trenches were photographed and stratigraphically logged. Oriented cubes and cylindrical cores were collected at regular intervals through the two new loess sections, starting from the prominent PA Tephra and extending down ca. 4 m.

The PA tephra, recently redated at 2.02 +/- 0.14 myr (Westgate et al. 2003), can be traced laterally across the exposure for 30 m, but the trenching revealed that the tephra layer was locally displaced by collapses, and was incorporated in deposits that had collected in small depressions stratigraphically below the level of the primary ash deposit. Excavation through the collapse deposits indicate that some of the collapse features are V-shaped and are interpreted as ice wedge casts, while others are broader, with irregular boundaries, and are interpreted as the products of thermokarst collapse pits.

The remnant magnetization recorded in the sets of oriented cubes and cylindrical cores taken from the two loess sections was measured at the University of Alaska-Fairbanks using a cryogenic magnetometer. Both alternating field and thermal demagnetization techniques were employed. Our data show that the section records predominantly reversed polarity, consistent with an age assignment within the Matuyama Reversed Chron. We identified a thin horizon of normal polarity at 0.7 m below the PA tephra. This event is well-preserved in our easternmost trench, but is recorded by only one point in our western trench. We correlate this event with the Reunion Chron dated to 2.14 million years ago. A transient normal polarity event at about the same stratigraphic position appears to be present in the paleomagnetic record of Westgate et al. (1990), although they did not assign it to any chron.

The variations between the paleomagnetic record of the Reunion event in these three trenches, excavated about 30 m apart, demonstrates that loess stratigraphy in this part of the Gold Hill section is complex and disturbed. This is consistent with the recognition of ice wedge casts and thermokarst features below the PA tephra. The strongest and thickest expression of the Reunion event occurs in samples taken down through undisturbed loess adjacent to an ice wedge cast in our eastern trench, while samples from our western trench intersect a thermokarst pit and show a weaker signal. More evidence of disturbance in this part of the loess section comes from low magnetic inclinations that characterize samples from this part of the section. The low inclinations are interpreted as a record of post-depositional deformation of the sediment associated with the growth of ice wedges and subsequent slumping and relaxation of the sediment as the ground ice thawed.

We also found systematic variations between magnetic susceptibility values from unaltered loess and those measured from loessic paleosols similar to those found in late Quaternary loess (Beget and Hawkins 1988; Beget 2001). The Reunion Chron and the PA tephra were used to develop a linear sedimentation rate model and to produce age estimates for the environmental magnetic record and unaltered loess interpreted as a glacial deposit and paleosols interpreted as interglacial deposits.

The stratigraphy and geochronology indicate ice wedges formed in central Alaska ca. 2.1 million years ago. The marine oxygen isotope record records a major, global glacial event at the same time, during MIS 78–76 (Shackleton et al. 1995, Pillans et al. 1998), suggesting the permafrost formed in response to global forcing. The permafrost degraded ca. 1.95 million years ago, at the same time as MIS 73, a global period of mild, interglacial temperatures.

Our study indicates that Alaskan permafrost was forming and degrading in response to changing global climate forcing by 2.14 million years ago. Some prior studies have suggested that the onset of glacial conditions in the Arctic was slow and gradual. In contrast, our work on permafrost history at Gold Hill indicates that Arctic climates have been fluctuating at the same rates and at the same times as global climate changes since earliest Pleistocene times.

Acknowledgments

Layer and Stone acknowledge funding from the National Science Foundation. Beget acknowledges funding from the U.S. Dept. of the Interior. Addison received funding from a University of Alaska Graduate Fellowship. Benowitz, also received funding from a University of Alaska Graduate Fellowship as well as additional funding from the Department of Geology and Geophysics of the University of Alaska Fairbanks.

References

Beget, J.E. 1988. Tephras and sedimentology of frozen loess: In: I.K Senneset (ed.), *Proceedings of the Fifth International Permafrost Conference, Trondheim, Norway, August 2-5, 1988*: 672-677.

Beget, J.E. 1991. Paleoclimatic significance of high latitude loess deposits. In: G. Weller (ed.), *Proceedings of the International Conference of the Role of the Polar Regions in Global Change, Fairbanks, Alaska, June 11–15, 1990*: 594-598.

Beget, J.E. 1996. Tephrochronology and paleoclimatology of the last interglacial-glacial cycle recorded in Alaskan loess deposits. *Quaternary International* 34–36: 121-126.

Beget, J.E., 2001. Continuous late Quaternary proxy climate records from loess in Beringia. *Quaternary Science Reviews* 20: 499-507.

Beget J.E. & Hawkins, D. 1989. Influence of orbital parameters on Pleistocene loess deposition in central Alaska. *Nature* 337: 151-153.

Beget, J.E., Stone, D.E. & Hawkins, D. 1990. Paleoclimatic forcing of magnetic susceptibility variations in Alaskan loess. *Geology* 18: 40-43.

Guthrie, D.R.. 1990. *Frozen Fauna of the Mammoth Steppe: The Story of Blue Babe*. Univ. Chicago Press, 338 pp.

Naibert, T.J., Domeier, M.M., Robertson, K.L., Fallon, J.F., Stone, D.B., Beget, J.E. & Layer, P.W. 2005. Re-evaluation of the magnetostratigraphy of the Gold Hill loess, Interior Alaska. American Geophysical Union. AGU Fall Meeting Abstracts, p. A96.

Pewe, T.L. 1951. An observation on wind-blown silt. *Journal of Geology* 59: 399-401.

Pewe, T.L. 1975a. Quaternary geology of Alaska. *U.S. Geological Survey Professional Paper 835*, 145 pp.

Pewe, T.L. 1975b. Quaternary stratigraphic nomenclature in central Alaska. *U.S. Geological Survey Professional Paper 862*, 32 pp.

Pewe, T.L., Berger, G.W., Westgate, J.A., Brown, P.M. & Leavitt, S. W. 1997. Eva interglaciation forest bed, unglaciated East-Central Alaska: global warming 125,000 years ago. *Geological Society of America Special Paper 319*, 54 pp.

Pewe, T.L.& Reger, D. 1989. Quaternary Geology and Permafrost along the Richardson and Glenn Highways between Fairbanks and Anchorage, Alaska. Fieldtrip Guidebook T102. *28th International Geological Congress*, Washington D.C., American Geophysical Union, 54 pp.

Pillans, B., Chappell, J., & Naish, T. R. 1998. A review of the Milankovitch climatic beat: template for Plio–Pleistocene sea-level changes and sequence stratigraphy. *Sedimentary Geology* 122: 5-21.

Shackleton, N.J, Crowhurst, S., Hagelberg, T., Pisias, N.G. & Schneider, D.A. 1995. A new Late Neogene time scale: application to leg 138 sites, *Proc. ODP Sci. Results* 138, 3-101.

Westgate, J.A., Stemper, B.A. & Péwé, T.L. 1990, A 3 m.y. record of Pliocene-Pleistocene loess in Interior Alaska: *Geology* 18: 858-861.

Westgate, J.A., Preece, S.J. & Pewe, T.L. 2003. The Dawson cut forest bed in the Fairbanks area, Alaska, is about 2 million years old. *Quaternary Research* 60(1): 2-8.

Recent Advances in Mapping Deep Permafrost and Gas Hydrate Occurrences Using Industry Seismic Data, Richards Island Area, Northwest Territories, Canada

Gilles Bellefleur
Geological Survey of Canada
Kumar Ramachandran
University of Tulsa
Michael Riedel
McGill University
Tom Brent
Geological Survey of Canada
Scott Dallimore
Geological Survey of Canada

Abstract

A 3D seismic reflection survey acquired by industry over the Mallik area in 2002 is used to map heterogeneities in permafrost and to determine the extent of gas hydrate occurrences beneath it. Seismic amplitude anomalies associated with lakes and drainage systems are observed in the 3D seismic data. Beneath lakes, the seismic data show weaker amplitudes, locally compromising images of the geology within and below the permafrost. On Richards Island, many of the lakes are deeper than the thickness of winter ice and have taliks that penetrate permafrost. Amplitude effects on the seismic data arise from velocity and attenuation variations associated with frozen and unfrozen parts of the permafrost. A 3D travel-time tomography algorithm was used to produce a map of the permafrost velocity structure. The 3D velocity map clearly reveals a heterogeneous velocity distribution, primarily related to thermal variations within the permafrost.

Keywords: gas hydrates; Mallik; Richards Island; seismic data; talik; tomography.

Introduction

The Mackenzie Delta area is characterized by a remarkable variability in permafrost conditions. In the central Mackenzie Delta, permafrost may be less than 80 m thick whereas in northern Richards Island it may be more than 700 m thick (Judge et al. 1987). This variability in part reflects a complex Quaternary history of surface temperatures and geologic processes (Taylor et al. 1996). As elaborated in more detail by Wright et al. (2008), lakes which cover between 20% and 50% of the landscape of the Mackenzie Delta area have played an important role in conditioning ground temperatures. Positive mean annual temperatures beneath the lakes (and indeed river channels or the ocean), if imposed for a significant amount of time, can thaw the permafrost, creating a thermal talik (above 0°C). More common perhaps, warmer permafrost beneath lakes affects the proportion of liquid water versus ice within the sediment matrix. Both conditions can modify the physical properties of sediments, affecting the propagation of seismic waves. Sediments with ice in the pore space are stiffer and characterized by higher seismic velocities whereas unfrozen sediments have lower velocities (Zimmermann & King 1986). Here, we show some effects of deep taliks on a 3D seismic reflection dataset acquired near the Mallik area on Richards Island (Fig. 1). Beneath lakes, the seismic data show weaker amplitudes, which locally compromise images of the geology within and below the permafrost. Direct seismic arrivals are used to produce a 3D velocity map of the permafrost. This map reveals a heterogeneous distribution of velocities, mostly related to variations in ice bonding within the permafrost. The 3D seismic data are also used to image and characterize gas hydrate accumulations beneath the permafrost.

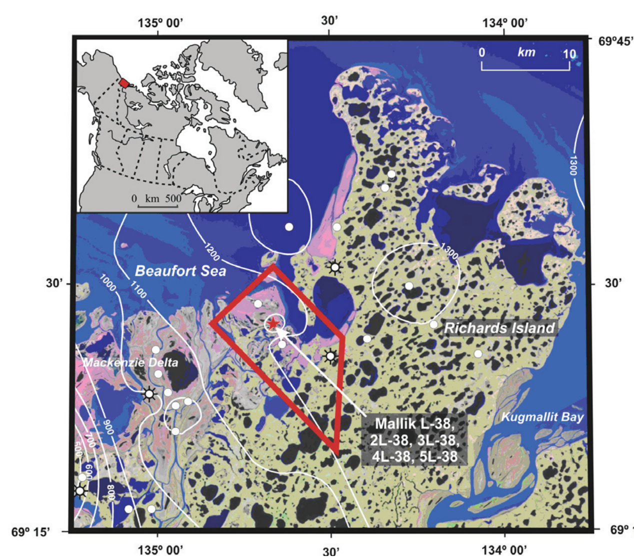

Figure 1. Location map showing the Mallik area in the Mackenzie Delta. The red polygon outlines the area covered by the 3D seismic survey used in this study. Small circles indicate well locations whereas larger circles with ticks show wells that intersected gas hydrate. Contours represent the base of the gas hydrate stability field.

Geological Setting

The 3D seismic survey used in this study is located in the western part of Richards Island in the Mackenzie River Delta on the coast of the Beaufort Sea (Fig. 1). The area straddles two physiographic regions identified by Rampton (1988), the Big Lake Delta Plain to the west which is influenced by active Mackenzie River deltaic deposition and older upland terrain referred to as the Tuktoyaktuk Coastlands. A shallow water embayment of the Beaufort Sea, referred to here as Mallik Bay, is also a dominant feature. Pleistocene sediments consisting mainly of glacial, marine, and fluvio-deltaic sediments are exposed at shallow depth beneath the Big Lake Delta plain and outcrop at the surface in the Tuktoyaktuk Coastlands. These deposits are underlain by older deformed deltaic Tertiary strata (Dixon 1995).

Interpretations of geophysical well logs from exploration wells in the area suggest that ice bonded permafrost beneath terrestrial areas is 600 to 650 m deep and that gas hydrates can occur to depths of 1150 m (Judge et al. 1987). Two major gas hydrate research well programs have been conducted at the Mallik site (Dallimore & Collett 2005) which is located at the apex of a regional anticline structure. Core studies and geophysical interpretations document that gas hydrate occurs in coarse-grained sandy sediments of the Mackenzie Bay and Kugmalit Tertiary sequences from 870 to 1100 m depth. The gas hydrate-bearing sediments are interbedded with silty sediments with little or no gas hydrate.

Approximately 50% of the surface area within the 3D seismic survey is affected by lakes, river channels, or the Mallik Bay. While no detailed bathymetric data are available, point soundings suggest water depths varying from less than 0.5 m to more than 6 m.

3D Seismic Data

The upper 2 s of a 3D seismic reflection dataset acquired during winter in 2002 has been made available to the Mallik 5L-38 science program through partnership with a joint venture of BP Canada Energy, Chevron Canada Resources, and Burlington Resources Canada. The 3D data were acquired with a combination of vibroseis and dynamite and covers approximately 130 km^2 that include four gas hydrate targeted wells and four industry wells drilled in the 1970s. The 3D acquisition geometry was designed to image conventional hydrocarbon accumulations located beneath permafrost and gas-hydrate zones (deeper than 1100 m). The initial data processing also focused on the imaging of the conventional gas-bearing structures, and the resulting 3D volume provides poor reflection images of the permafrost (above 600 m) and low fold in common-depth-point gathers in the gas-hydrate depth range (900–1100 m). For this study, we chose a dataset reprocessed to maintain the relative true-amplitude character of the data (Riedel et al. 2006).

Several areas of reduced seismic amplitude are observed in the true-amplitude 3D seismic dataset at depths exceeding 1 km (Fig. 2). Understanding these low-amplitude anomalies

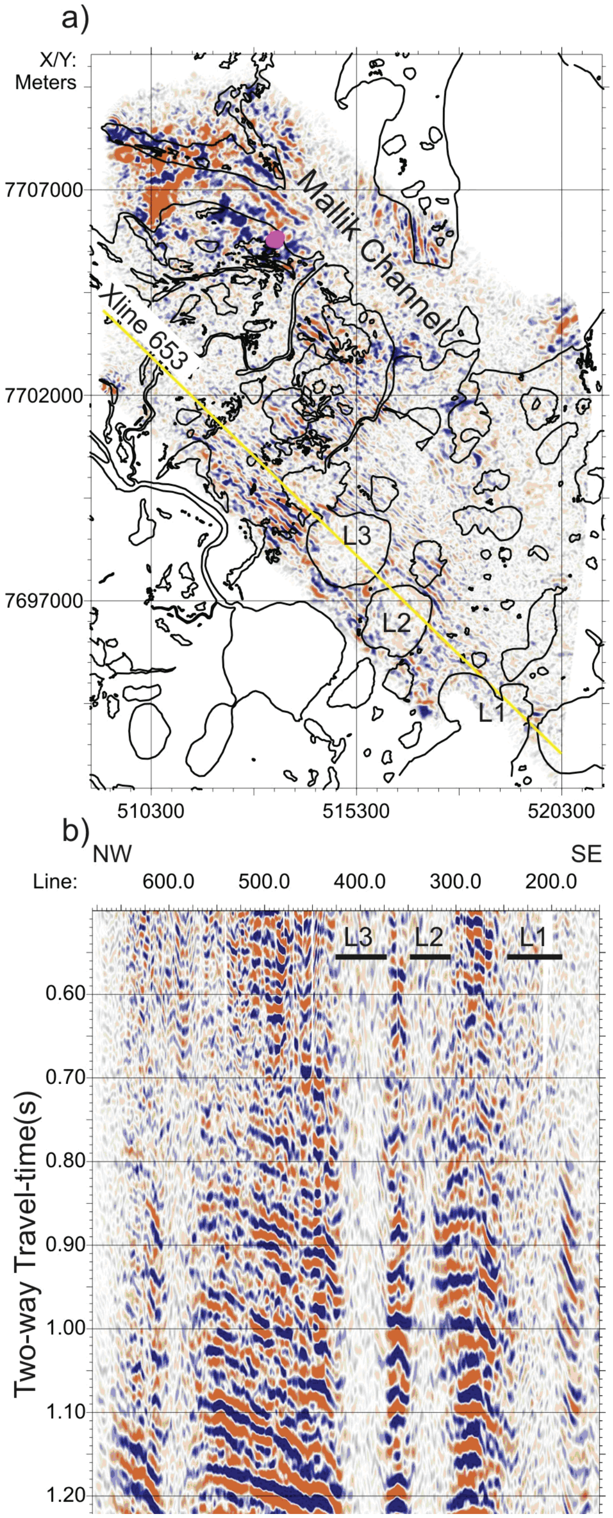

Figure 2. (a) Time slice from the true-amplitude 3D seismic data at 800 ms (approximately 1100 m). The purple dot shows the location of the Mallik wells. (b) Cross-line 653 showing reduction of amplitude beneath the lakes. The location of cross-line 653 is shown in (a) (yellow line). Colors represent seismic amplitudes (blue: negative amplitude; red: positive amplitude).

(also referred to as washout zones) is important for any gas-hydrate related interpretation. In the marine environment, wide-spread amplitude blanking has often been attributed to the presence of gas hydrate (Holbrook et al. 2001). At Mallik, the low seismic amplitude areas in the gas hydrate stability field (200 to 1100 m) may not indicate the presence of gas hydrates but instead likely result from variations of physical properties in permafrost, and more specifically to property changes associated with deep taliks.

A time slice from the 3D true-amplitude dataset, with an overlay of the hydrology, is shown in Figure 2. The time slice is located beneath the permafrost near the base of the gas hydrate stability field at 800 ms (approximately 1100 m depth). Areas of seismic blanking or reduced seismic amplitude are coincident with the location of large lakes. A seismic cross-section (Fig. 2b) shows that the reduced amplitudes beneath the lakes extend down to 1.3 seconds. Some reflections are also truncated underneath water bodies. This is particularly evident near the Mallik channel (Fig. 2a) and near lakes located in the southeast part of the time slice (L1, L2 and L3 on Figs. 2a, b). Some deeper water areas of Mallik Channel do show a response similar to that seen beneath the lakes (Fig. 2a). However, the river channels and many smaller lakes less than 300-400 m in diameter show no seismic amplitude reduction. Similar observations are made for shallow water areas located offshore.

The effect of ice bonding on seismic velocity is well documented. In water-saturated and unconsolidated sediments, velocity of P-waves varies significantly as a function of the fraction of pore water that is unfrozen (Zimmermann & King, 1986). Sediments with only ice in the pore space can have P-wave velocity as high as 4200 m/s whereas as sediments mostly filled with water have velocities near 1800 m/s. Other factors such as composition, density, porosity, and pressure also affect P-wave velocity of sediments. As reviewed by Wright et al. (2008) large lakes in the Richards Island area can have a significant talik beneath them. It is expected that sediments beneath those lakes will have a larger proportion of unfrozen water in the pore space and will be characterized by lower P-wave velocities. The unfrozen or partially unfrozen areas also attenuate seismic waves propagating through them more severely (the amplitude of waves in those areas is reduced more rapidly than within frozen permafrost) producing low amplitude areas in Figure 2.

Areas with lower velocity delay seismic waves propagating down to and up from deeper reflective geological structures. These delays, because they occur at shallow depths, must be taken into account during data processing to produce the most accurate images of deeper geological structures, and quantitative information about the velocity distribution of the permafrost is required to estimate proper static corrections. The velocity distribution can also provide information about the internal structure of the permafrost.

Velocity Structure of Permafrost

Direct P-wave travel-time tomography is used to produce a 3D velocity map of the permafrost. Tomographic inversion of first arrival travel-time data is a non-linear problem since both the velocity of the medium and the ray paths in the medium are unknown. The final solution is typically obtained by repeated applications of linearized inversion until model parameters (velocities) explain the observations (travel-times) within satisfactory criteria. More details about the tomography method can be found in Ramachandran et al. (2005).

The tomographic inversion of direct seismic arrivals resulted in a velocity model covering the area of the 3D survey and extending down to a depth of 500 m which is about 100 m above the base of permafrost. This model is divided into 50 m cubes. Approximately one million direct arrival travel-times were manually picked and used in the tomography. Figure 3 displays two depth slices from the reconstructed velocity model. The shallowest slice at 100 m shows a heterogeneous permafrost with P-wave velocities ranging from 1500 to 5000 m/s. As expected, lower velocities are found underneath lakes and drainage system and they likely correspond to areas of unfrozen permafrost. The deeper slice at 250 m is more homogeneous but still shows lower velocities beneath some lakes and the Mallik channel. At that depth, velocities beneath most lakes are slightly higher and may indicate the presence of a greater proportion of ice in the pore space of sediments, possibly related to a thermal gradient within some taliks. Some of the low-velocity areas beneath the lakes extend down to approximately 300 m (not shown) and have an inverted-cone shape (Fig. 4).

One way to assess the constraint on the velocity model is to count the number of rays passing through each cell. A large number of rays per cell is usually indicative of a well-constrained velocity. Figure 5 shows a depth slice at 100 m with the number of rays per cell. At this depth, all cells are cut by a large number of rays, except at the edge of the 3D velocity slice. At greater depths, the number of rays per cell is significantly lower. This is a result of the maximum source-receiver separation used during data acquisition. Larger source-receiver separations would be required to map velocity variations near the base of permafrost with travel-time tomography.

Gas Hydrates

Gas hydrate accumulations located onshore in Arctic permafrost regions are seen as a potential source of natural gas. Most known gas-hydrate occurrences in the Mackenzie Delta and Beaufort Sea areas were indirectly discovered or inferred from conventional hydrocarbon exploration programs. One of these occurrences, the Mallik gas hydrate field (Fig. 2), has received particular attention over the last 10 years. Two internationally-partnered research well programs have intersected three intervals of gas hydrates and have successfully extracted sub-permafrost core samples with significant amounts of gas hydrates (Dallimore & Collett

2005). The gas hydrate intervals are up to 40 m in thickness and have high gas hydrate saturation sometimes exceeding 80% of pore volume of unconsolidated sand with average porosities ranging from 25% to 40%. The gas hydrate intervals are located on the crest of the anticline between 900 m and 1100 m depths and do not exhibit large dips. Here, we refer to the three gas hydrate intervals as Zones A, B, and C (Dallimore & Collett 2005). Zone A is the shallowest gas hydrate interval whereas Zone C marks the base of the gas-hydrate occurrence at Mallik.

Sonic logging data acquired in two boreholes at Mallik show that P-wave velocity of sediments increases with concentration of gas hydrates (Guerin & Goldberg 2005).

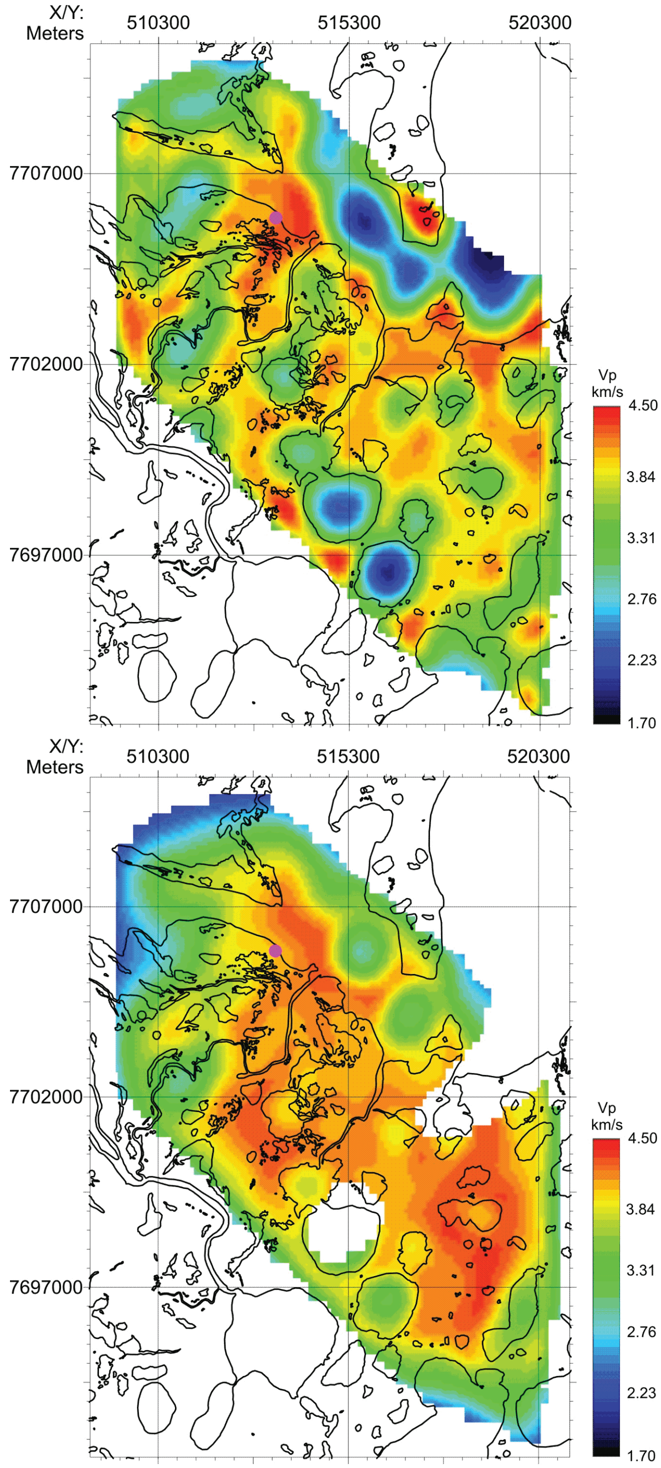

Figure 3. Depth slices through the 3D velocity model obtained from direct arrival travel-time tomography (top: depth slice at 100 m; bottom: depth slice at 200 m). Low-velocity areas are found beneath large lakes and deep water channels. The no-data areas on the deeper slice correspond to low-velocity zones not traversed by first-arrival rays which follow the fastest trajectory. Low-velocity zones will tend to be under-sampled as depth and source-receiver separation increase.

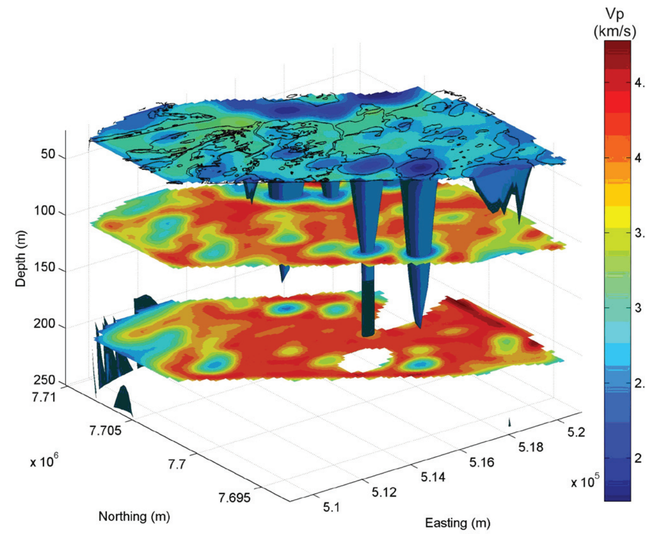

Figure 4. Plunge view to the NE showing three velocity slices (at 25 m, 100 m, and 200 m), natural drainage system and iso-surfaces set at 2.4 km/s. The iso-surfaces have an inverted-cone shape and are located beneath lakes and the Mallik water channel.

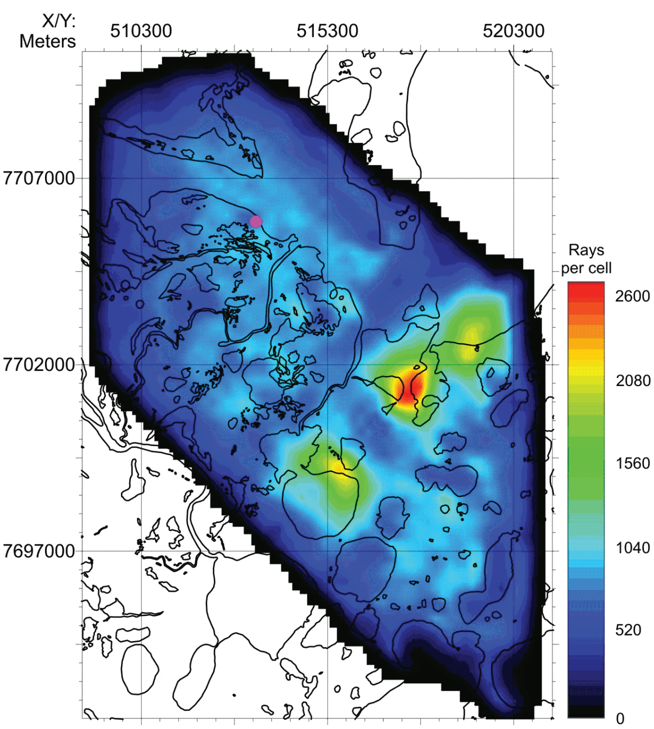

Figure 5. Depth slice at 100 m showing the number of rays per cell that constrained the velocity model shown in Figure 3. A large number of rays per cell is an indication of well-constrained velocity.

P-wave velocities range from 2400 m/s in sediments having no gas hydrates to 3200 m/s in strata with 80% pore occupancy by gas hydrate. This strong velocity contrast makes gas hydrates detectable with surface seismic reflection methods when they are found beneath the permafrost. They are difficult to detect when located within permafrost because of the limited or lack of velocity contrast with frozen sediments. On Mallik seismic records, the hydrate-bearing sediments are seen as bright reflections relative to a lower-amplitude surrounding background. Fortunately, there are no deep lakes close enough to the Mallik well site to distort seismic images.

While successfully used for determining in-situ properties of gas hydrates, boreholes alone cannot confirm lateral continuity of any of the three hydrate zones, which is required to provide reliable estimates of the resource in place. Here, we also used the 3D seismic data to assess the seismic characteristics of the zones to help define the lateral extent of the gas hydrates away from the wells. At the same time, we also wish to assess the influence of the local geology on the distribution of gas hydrates. Our seismic characterization approach relies strongly on well-log data in the gas hydrate intervals, seismic-to-well correlation, and acoustic impedance inversion. The seismic inversion generated an acoustic impedance (product of density and velocity) image of approximately 1.5 km^2 area around Mallik 5L-38 by matching a reflectivity model to the seismic data. We further extracted P-wave velocities from the impedances assuming no lateral variability in the density of the sediments. Overall the density is relatively constant throughout the entire gas hydrate interval and averages 2100 kg/m^3. We have attempted to convert P-wave velocity to gas hydrate concentration in pore-space by using the effective medium theory by Helgerud et al. (1999), in which gas hydrate supports the sediment matrix but does not cement sediment grains. In general, a very good correlation between the Mallik 5L-38 P-wave velocity logs and the inverted P-wave section is found for Zones B and C. Figure 6 shows maps of the inverted P-wave velocity for Zones B and C. Zone C reveals a complex pattern with large variation in P-wave velocity over distances less than a few hundred meters. This complex pattern could certainly be explained by lateral sediment heterogeneity and by spatial limitations of small-scale faults and other discontinuities. Zone C is more continuous and extends over a larger area than Zone B. P-wave velocities locally exceed 2900 m/s and correspond to sediments with high gas hydrate saturation (above 60%). These highly saturated sediments cover approximately 0.25 km^2. The area of highest gas hydrate concentrations for Zone B follows a N-S trend. Zone B is less continuous than Zone C and covers an area of approximately 0.1 km^2. The extent and geometry of Zones B and C defined from impedance inversion suggest that local geology plays a significant role in the distribution of gas hydrate at Mallik.

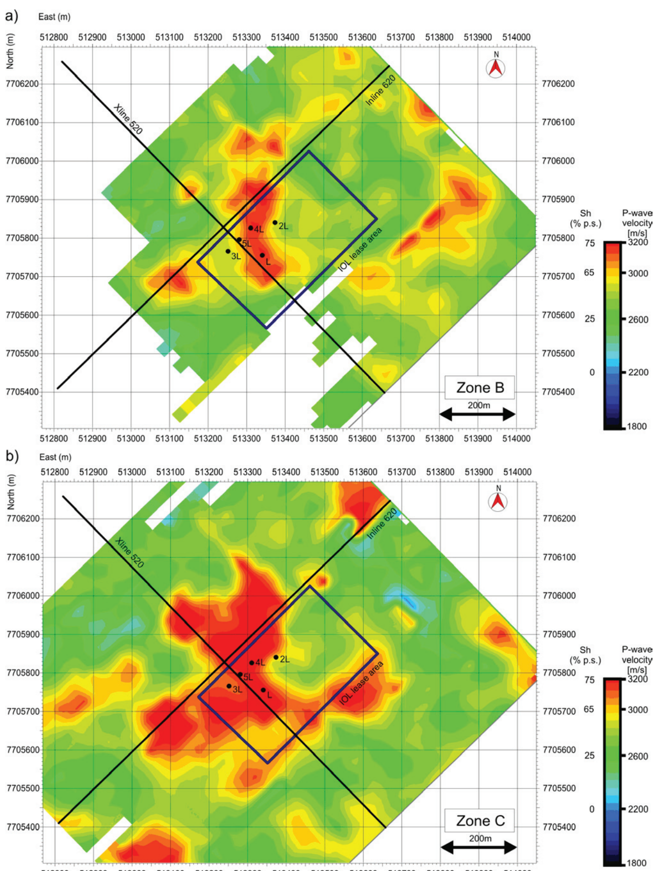

Figure 6. Velocity Map obtained from acoustic impedance inversion showing the extent of gas hydrate Zones B (top) and C (bottom). Color code shows P-wave velocity in m/s and gas hydrate concentration in percent of pore space (% p.s.). Gas hydrate Zone C is structurally complex with a center area of highest P-wave velocity and related gas hydrate concentration underneath the Mallik well sites. Zone B extends over a much smaller area than Zone C and is distributed along a N-S axis.

Conclusions

Lower seismic amplitudes are observed on the 3D Mallik data beneath some lakes and water channels. Amplitude effects on the seismic data arise from velocity and attenuation variations associated with frozen and unfrozen parts of the permafrost. A 3D velocity map of the permafrost obtained with direct arrival travel-time tomography indicates that some of the low-velocity areas beneath the lakes have an inverted-cone shape and extend down to approximately 300 m. Beneath the permafrost, results from acoustic impedance inversion indicate that sediments with high gas hydrate saturation near the Mallik well site extend over an area of 0.25 km^2 and suggest that lateral and depth-dependent geology variations play a significant role in the distribution of gas hydrates.

Acknowledgments

We acknowledge the international partnership that undertook the Mallik 2002 Gas Hydrate Production Research Well Program: the Geological Survey of Canada, Japan National Oil Corporation, GeoForschungsZentrum

Potsdam, U.S. Geological Survey, India Ministry of Petroleum and Natural Gas, BP/ChevronTexaco/Burlington joint venture parties, U.S. Department of Energy. The first 2 s of the Mallik 3D seismic data has been made available to the Mallik science program through partnership with the BP/ChevronTexaco/Burlington joint venture parties. Geological Survey of Canada contribution 20070388.

References

Dallimore, S.R. & Collett, T.S. 2005. Summary and implications of the Mallik 2002 gas hydrate production research well program. In: S.R. Dallimore & T.S. Collett (eds.), *Scientific Results from the Mallik 2002 Gas Hydrate Production Research Well Program, Mackenzie Delta, Northwest Territories, Canada.* Geological Survey of Canada. Bulletin 585: 36 pp.

Dixon, J. 19*95. Geological Atlas of the Beaufort-Mackenzie Area.* Geological Survey of Canada. Miscellaneous Report 59: 173 pp.

Guerin, G. & Goldberg, D. 2005. Modeling of acoustic wave dissipation in gas hydrate–bearing sediments, *Geochem. Geophys. Geosyst.* 6: Q07010, DOI: 10.1029/2005GC000918.

Helgerud, M., Dvorkin, J., Nur, A., Sakai, A. & Collett, T. 1999. Elastic-wave velocity in marine sediments with gas hydrates: Effective medium modeling. *Geophysical Research Letters* 26: 2021-2024.

Holbrook, W.S. 2001. Seismic studies of the Blake Ridge: Implications for hydrate distribution, methane expulsion, and free gas dynamics. In: C.K. Paull & W.P. Dillon (eds.), *Natural Gas Hydrates, Occurrence, Distribution and Detection.* AGU Geophysical Monograph Series 124: 235-256.

Judge, A.S., Pelletier, B.R. & Norquay, I. 1987. Permafrost base and distribution of gas hydrates. In: B.R. Pelletier (ed.), *Marine Sciences Atlas of the Beaufort Sea-Geology and Geophysics.* Geological Survey of Canada Miscellaneous Report 40: 39 pp.

Ramachandran K., Dosso, S.E., Spence, G.D., Hyndman, R.D. & Brocher, T.M. 2005. Forearc structure beneath southwestern British Columbia: A three-dimensional tomographic velocity model. *J. Geophys. Res.* 110: B02303, DOI: 10.1029/2004JB003258.

Rampton, V.N. 1988. *Quaternary Geology of the Tuktoyaktuk Coastlands, Northwest Territories.* Geological Survey of Canada, Memoir, 423 pp.

Riedel, M., Bellefleur, G., Brent, T., Dallimore, S.R. & Collett, T.S. 2006. Amplitude and frequency anomalies in 3D seismic data from the Mallik 5L-38 research site. *Geophysics*, 71: B183-B191, DOI: 10.1190/1.2338332.

Taylor, A.E., Dallimore, S.R. & Judge, A.S. 1996. Late Quaternary history of the Mackenzie-Beaufort region, Arctic Canada, from modelling of permafrost temperature, part 2--The Mackenzie Delta-Tuktoyaktuk coastlands. *Canadian Journal of Earth Science* 33: 62-71

Wright, J.F., Taylor, A.E. & Dallimore, S.R. 2008. Thermal impact of Holocene lakes on a permafrost landscape, Mackenzie Delta, Canada. *Proceedings of the Ninth International Conference on Permafrost, Fairbanks, Alaska, June 29-July 3, 2008* (this proceedings).

Zimmerman, R.W & King, M.S. 1986. The effect of the extent of freezing on seismic velocities in unconsolidated permafrost. *Geophysics* 51: 1285-1290.

Massive Ground Ice on the Ural Coast of Baydaratskaya Bay, Kara Sea, Russia

N.G. Belova, V.I. Solomatin, F.A. Romanenko
Lomonosov Moscow State University, Faculty of Geography, Moscow, Russia

Abstract

Massive ground ice on the coast of Baydaratskaya Bay (Kara Sea) is exposed on the western (Yugorski) side near the mouth of the Ngoyu-Yacha River. It reaches 7 m in thickness and lies in sandy stratum. The isotopic and chemical composition of the ice, complicated ice structure with several types of ice, ice deformations, and the lacustrine-alluvial origin of host sediments suggest a burial origin for the massive ice beds. Sands with massive ice are underlayed by clayey stratum which is related to the Kara diamicton stratigraphic unit. Massive ice beds are supposed to be the remains of outlet glaciers from Pai Khoi or Polar Ural, which were buried in lacustrine-alluvial (fluvioglacial) sediments in the Late Weichselian; this area wasn't covered by the Barents-Kara Ice Sheet at that time.

Keywords: Barents-Kara Ice Sheet; Late Weichselian glacial maximum; massive ground ice; paleogeography; Russian Arctic.

Introduction

It is now known that massive ground ice exposures on the coast of Baydaratskaya Bay (Kara Sea) are found in just one section – on Yugorski (western) side near the mouth of the Ngoyu-Yacha River (Fig. 1). The origin of these ice formations remains sharply controversial both locally and globally. There are two main points of view on massive ice origin: it could be buried glacial ice (in particular, basal ice of ice sheets) or intrasedimental ice, formed in pre-existing sediments. Any paleoreconstructions in this area would be imperfect without taking into account the origin of massive ice. For the purpose of making the question of massive ice origin clear at a local scale, an integrated study of thick (up to 7 m) massive ice beds was conducted 2005–2007 along the coastal bluffs of the area. The host strata and the relation to massive ice, ice structure, chemical composition of ice and host sediments, and isotopic composition of the ice have been studied to solve this problem.

Quaternary history of the study area

The Yugorski peninsula was supposed to be overridden by the Barents-Kara Ice Sheet no later than 90–80 ka BP, Marine Isotope Stage 5a–b (MIS 5a–b), i.e., at Early Weichselian. The Late Weichselian glacier limit didn't attain this area (see Fig. 1; based on Svendsen at al. 2004). During Holocene warming, this region was essentially reshaped by increased thermokarst activity (Romanenko et al. 2001).

Host Sediments: Stratigraphy and Relation with Massive Ground Ice

Composition and stratigraphy of host sediments

Near the mouth of the Ngoyu-Yacha River, the ridgy plain with an altitude of 27–35 m above sea level (a.s.l.) comes out to the Baydaratskaya Bay coast. In the coastal zone, this surface is strongly dissected by numerous thermokarst depressions known locally as "khasyreys" (The term is of Nenets origin (northwestern Siberia); an analogous term of Yakut origin is "alas"). The altitudes of many khasyreys are lower: up to 15–20 m. The elevated surfaces that have remained unaffected by thermokarst occupy a minor area compared to dissected ones.

The stratum of heavy consolidated fractured clays with scarce rounded boulders underlies many sections (Fig. 2), but on most of studied area it lies below sea level. In the upper part, clays are silty and contain occasional thin sand laminas (up to 0.5 cm thick) with fragments of shells.

Composite sandy stratum with clay bands, folds, lenses of well-rounded pebbles and gravel with fragments of sea shells overlap the clay unit at a stratigraphic disconformity (Fig. 2). The chemical composition of aqueous extract shows that this stratum is fresh (Fig. 6). The stratification features indicate the formation of these sediments by fluctuating stream activity. The alternating pebbly gravel layers with clayey layers, as well as the results of chemical analysis, indicates continental and coastal formational environments. Z.V. Aleshinskaya (pers. com.) came to the conclusion about the alluvial origin of the sandy stratum following analysis of diatom composition. On the pollen and spore diagram, the redeposited pollen of *Betula* sect*. Albae*, and *Pinus* is rather abundant, and there exists pollen of *Fagus* and *Juglans*. Spectra of a similar composition were detected in deposits of the Eemian-Early Weichselian (MIS 5d–e, c. 100–130 ka BP) of the Pai Khoi Ridge (Northern Ural); this may imply that a considerable part of spores and pollen was redeposited from older Pleistocene sediments (Andreev et al. 1998).

Gravel lenses and bands in the sandy stratum perhaps represent erosion activation phases on adjacent areas of the Polar Ural. Numerous facies boundaries in sandy-gravelly-pebbled stratum are possibly determined by alluvial redeposition on the lacustrine-alluvial plain. The ^{14}C dates from sandy sediments unaffected by thermokarst were 22 500±400 (detritus, GIN-13795) and 44 900±1100 (wood, GIN-13796) ^{14}C years BP. Peat lenses, which were formed during increased thermokarst activity at the surface of the sandy stratum, is characterized by a continuous

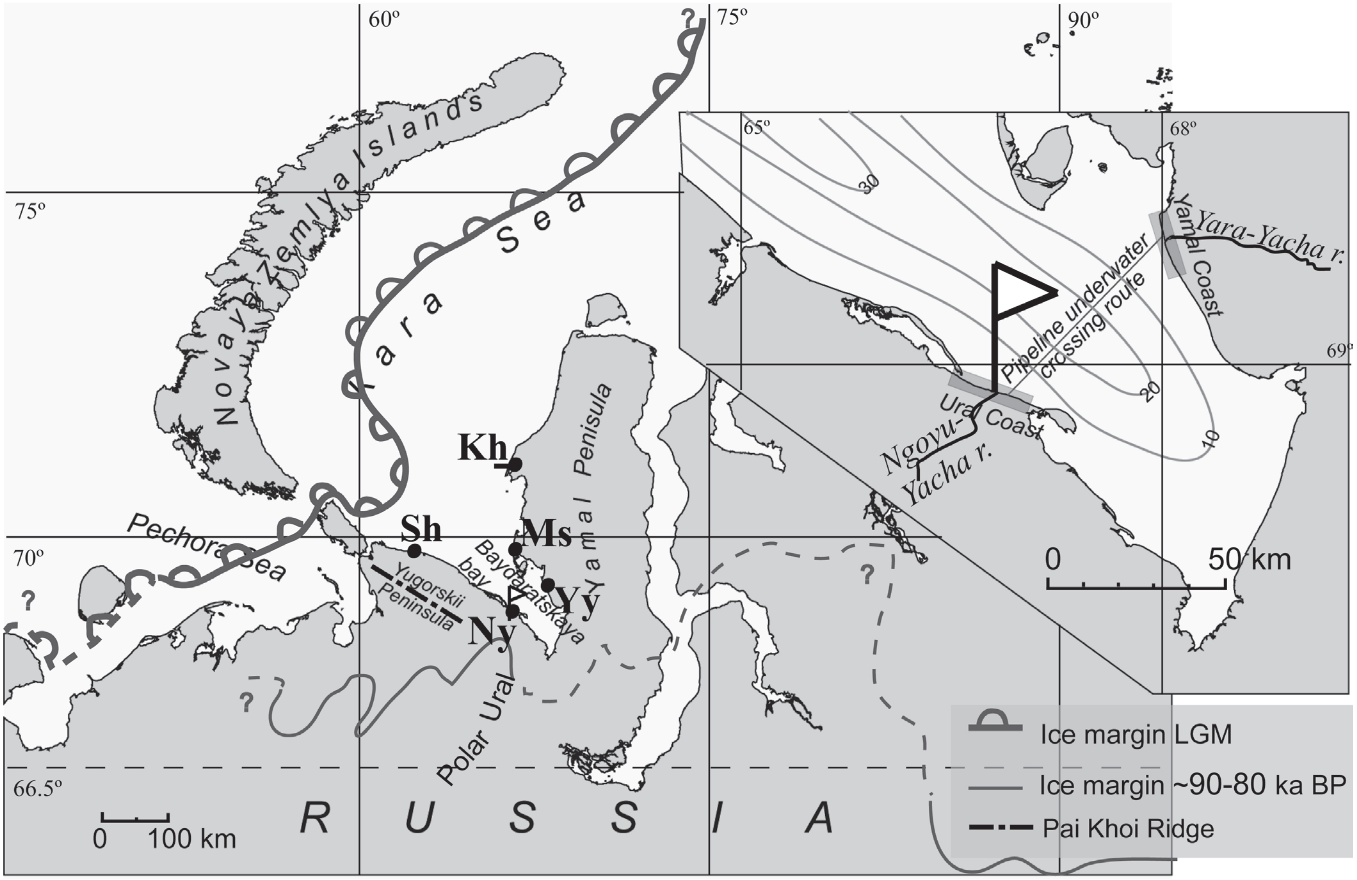

Figure 1. The area of investigations (marked by flag). Ice limits of the Late Weichselian glacial maximum (LGM) and Early Weichselian glacial maximum (90–80 ka BP) according to Svendsen et al. (2004). Ny – Ngoyu-Yacha River, Kh – Kharasavey River (northern Kara diamicton limit), Sh – Cape Shpindler, Ms – Marresale Station, Yy – Yara-Yacha River.

dated series (9 dates) from 10,900±120 (MSU-1362) and 8,210±110 (GIN-7862) to 4,140±70 (WAT-2895) ^{14}C years BP (Romanenko et al. 2001). It confines the period of sandy stratum formation at 11,000 yr BP.

On the opposite coast of Baydaratskaya Bay, near the mouth of the Yara-Yacha River, the same sandy stratum is exposed on coastal bluffs. Radiocarbon analysis using two *in situ* peat samples from lake sediments yielded an AMS radiocarbon age of 28 650±280 (AA-20 497) and 29 750±520 (AA-20 498) ^{14}C years BP (Gataullin & Forman 1997); and 19 560±330 ^{14}C years BP (GIN-8561) (Romanenko et al. 2001). It could be formed in the Middle-Late Weichselian (Romanenko et al. 2001). This confirms Middle-Late Weichselian age of sandy stratum on investigated area.

Relations between massive ground ice and host sediments

The principal singularity of the sandy stratum, which forms the surface with altitudes of 27–35 m a.s.l., is massive ground ice. Ice bodies are confined mainly to the highest parts of the unit that are least modified by thermokarst. They are recovered as close to the water edge, as near the highest altitudes of this surface – up to 15 m a.s.l.. Maximum dimensions of these massive ground ice bodies is up to 7 m thick (Fig. 3) and 150 m along the coastline.

Massive ground ice lies generally conformably with host strata. But fairly often the upper contact cuts the layers in the massive ice; in other words, this contact is erosional or it is a thaw unconformity. The erosional nature of the contact is obvious when massive ice is overlaid by several meters of sands with clear fluvial bedding (Fig. 4). Sometimes the upper contact is marked by c. 0.2 m of clay; thus it can be secondary.

At the lateral contact the ice bed is tapering out by ice layers, which are also conformable with host deposits (Fig. 2). Directly under the massive ground ice the deformed ice bands, dykes and elongated lenses are found with thicknesses up to 0.7 m; they disrupt the sand stratification or lie conformable with enclosing sediments. The ice of the bands and lenses is mostly transparent, often laminated owing to inclusions of host sediments, which lie in laminas parallel to ice bands. Tubular bubbles (c. 1 mm diameter and ≤2cm long) were often observed orthogonal to ice bands.

Cryostructures of Massive Ground Ice

Massive ice beds are composed of several types of ice. The majority of ice beds consists of laminated ice. This ice type is characterized by close alternation of layers (with 5–15 cm average thickness) of relatively transparent ice and muddy ice. The latter is due to suspended sand, clay

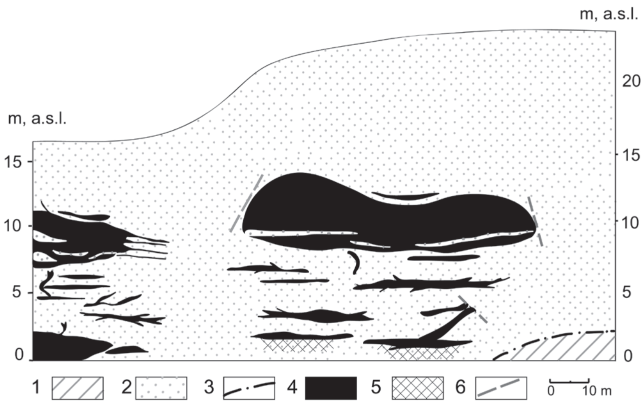

Figure 2. Stratigraphy of coastal bluffs (general scheme). 1- clays with boulders, 2 - sandy stratum, 3 – sediments strata's boundaries, 4 – ice, 5 – icy sediments, 6 - unclarified ice boundaries.

and silt aggregates, several mm in diameter, and rounded or amorphous silty-clayey fragments up to several cm across (Fig. 5 a,b).

In the lower parts of the ice beds the mud content is usually higher than in the upper parts, and the laminations therefore become less distinct. Here it can be distinguished as the muddy ice subtype. Clay, silt and sand material in the ice beds corresponds to sands, silts and clays which enclose the massive ground ice. Generally, the layering of massive ground ice is subhorizontal, although it is more correct to note that it is subparallel to the upper ice bed boundary. Laminated ice has an average crystal diameter of 0.5–1.0 cm, and crystals are mostly isomorphic. In muddy ice layers with a great amount of sandy particles, the crystal size is much smaller. The laminated ice type becomes more complicated in places due to folds of different scales (Fig.5b), transparent ice inclusions, or sandy and clayey layers.

Thus, at the upper contact of the thickest massive ice bed, the upper 2 m of laminated ice are crumpled in recumbent folds above a subhorizontal shear plane. The limbs of the folds have amplitude of about 1 m.

Besides the laminated ice in the massive ice beds, there are also transparent and bubbly ice types (Fig. 5 c,d). Bubbly ice (bubbles are usually spherical, 0.5–3.0 mm diameter) is typical of the upper ice beds, and in the coastal section it gradually replaces laminated ice. By contrast, the transparent ice appears often to break through and sometimes draw apart the subhorizontal ice lamina. The thickness of such seams is up to 0.5 m; they often lie nearly vertically and sometimes bifurcate along several subparallel seams. In section they can have the form of a fold (Fig.6).

Transparent ice in its middle part often includes clay bands parallel to its boundaries (Fig. 5d, 6). The crystals of transparent ice can be 25 cm across.

For massive ground ice, independent of the ice type, clayey and sandy layers of different thickness (from several cm up to 0.5 m, usually about 10–20 cm) are typical. Thick ground layers are more frequent in the lower reaches of the ice beds; these layers can lie parallel to each other, form lenticular structures, and sometimes cut the subhorizontal ice layers.

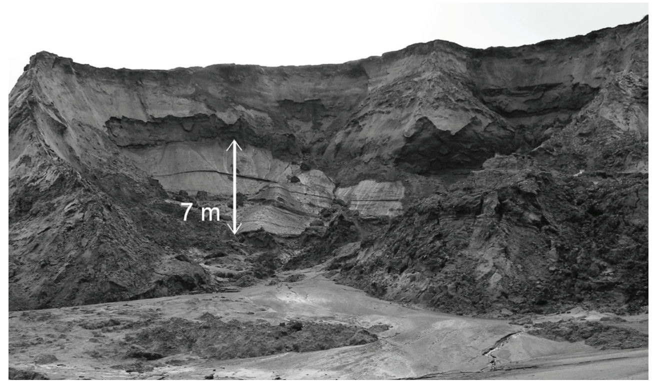

Figure 3. The thickest bed of massive ice (Photo by A.S. Iosimov).

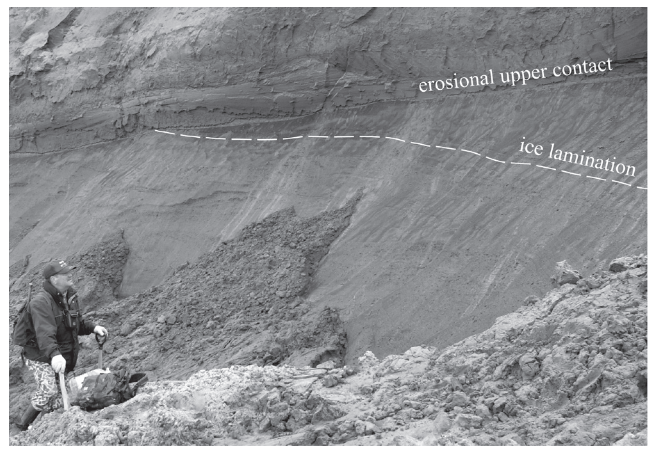

Figure 4. Erosional upper contact of massive ground ice (4 m thick). Ice bed is overlain by 8 m of sands.

Chemical and Isotopic Composition

Chemical analysis

In 2005–2007, the massive ice beds, ice bands and lenses in the underlying sediments (melt ice) and host sediments (from sediments aqueous extract) were sampled for chemical analysis. All the samples turned out to be fresh water– the mineralization of all of them is less than 200 mg/l. But composition and the ratio between different chemical ions varies substantially (Fig. 7). In massive ground ice, Ca^{2+} and Na^{+} cations and HCO_3^{-} (rarely SO_4^{2-}) are predominant. But in ice bands and lenses from below the massive ice beds HCO_3^{-} is completely absent. Aqueous extract from sediments shows that here chemical composition is somewhat different – Ca^{2+}, K^{+}, Na^{+} and SO_4^{2-} predominate.

Isotopic analysis

The first results of stable isotope measurements in massive ice beds near the mouth of the Ngoyu-Yacha River were obtained concurrent with discover in 1990 (Konyakhin et al. 1991). Based on this data, the ^{18}O isotope values vary from -17.5 to -25.5‰ (relative to SMOW standard) in transparent ice and from -18.4 to -22.4‰ in bubbled ice. The analytical results of samples from 2006 confirmed the significant spread

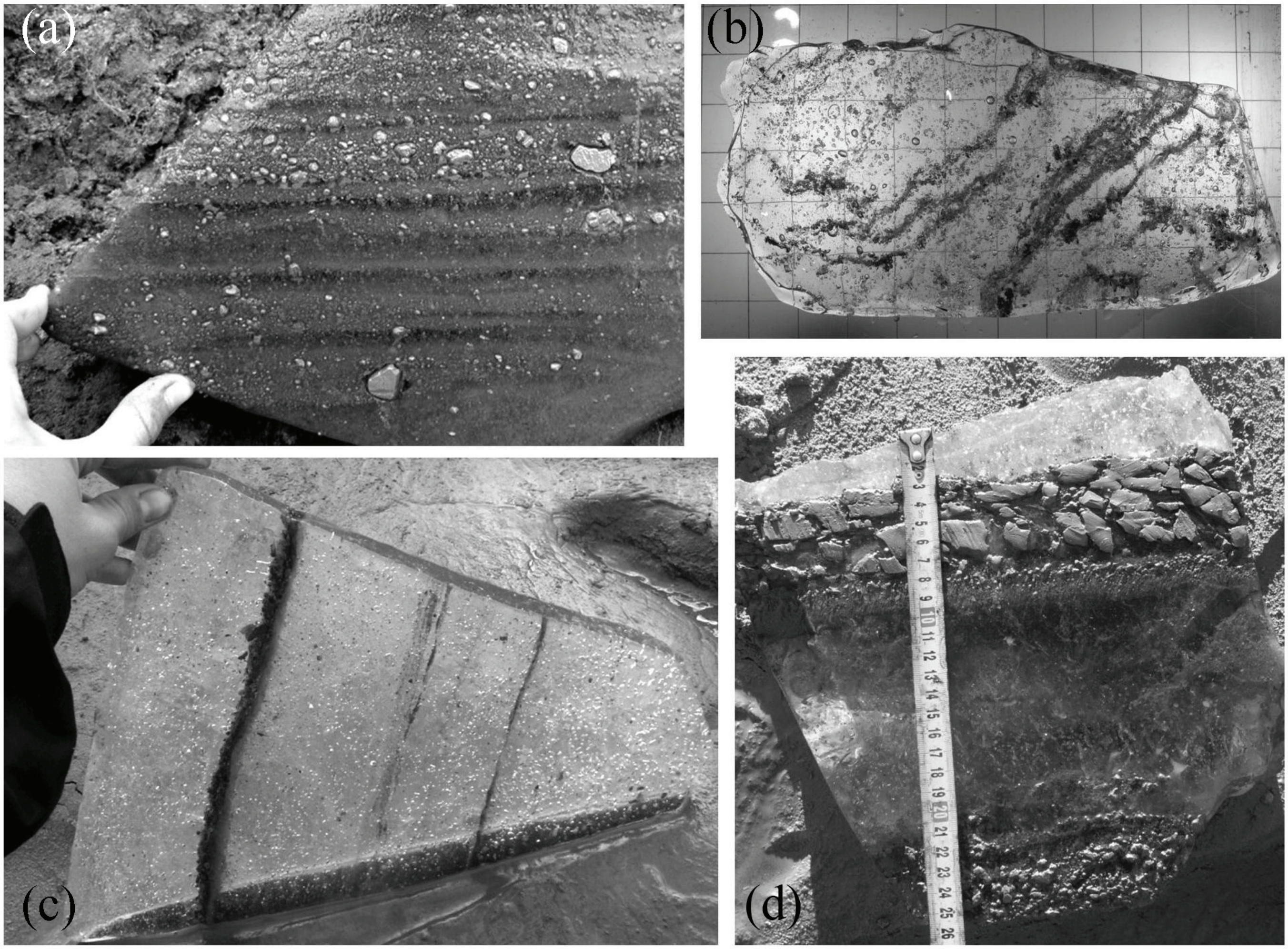

Figure 5. Types of massive ice: (a) laminated ice; (b) laminated deformed ice (1 cm mesh); (c) bubbly ice; (d) transparent ice with clayey band.

of values established earlier. A massive ice bed, 3.5 m in thickness, has been sampled in one vertical section at every 30–40 cm (Belova et al. 2007). Sampled ice is homogeneous; it is presented by laminated type except for the upper 30 cm where it slips into laminated, but clearer, bubbly ice. Here the dispersion turned out to be significant—at about 7‰ for $\delta^{18}O$ and about 45‰ for δD (Fig. 8).

Interpretation and Discussion

Composition and stratigraphy of host sediments

The lowest stratigraphic unit in the sections studied is represented by clays with boulders, and this unit can be related to the Kara diamicton. It is an informal stratigraphic unit first defined near Marresale station by V.N. Gataullin (Gataullin 1988; see Fig. 1). Kara diamicton is widespread on the western Yamal Peninsula, but has yet to be identified north of 70º50′N (Kharasavey River mouth; Forman et al. 2002). Near the Marresale station its uppermost facies is represented by massive to crudely stratified clayey silty diamicton without any glaciotectonic structures and with random pebbles and occasional sand horizons <1 cm thick. This description is almost identical to that for one of the clay units near the mouth of the Ngoyu-Yacha River. At Marresale station, the upper facies of the diamicton is interpreted by investigators as a supraglacial meltout till formed by the release of glacial debris from stagnant glacier ice. Based on finite radiocarbon and luminescence ages of ca. 35,000 to 45,000 yr obtained from the immediately overlying Kara diamicton Varjakha peat and silt (informal unit), the last glaciation was >40,000 yr ago (Forman et al. 2002). Thus, at the study area, the last large-scale glaciation was presumably also earlier than Middle Weichselian.

In such a case, massive ice beds in a sandy unit overlying what is probably Kara diamicton couldn't be the remains of a large ice sheet. Furthermore, they lie in lacustrine-alluvial sediments, so the lack of typical moraine deposits can be explained by their origin as remains of local glaciers (probably outlet glaciers of local Ural glaciation). This fact is confirmed by implication of spore-pollen spectra data, which is similar to Eemian-Early Weichselian one in Pai Khoi Ridge deposits (central part of Yugorski peninsula, northern part of Ural). Based on dates of the enclosing sediments, this glaciation could have occurred in Late Weichselian (MIS 2).

In the northern part of the Yugirski peninsula at Cape

Figure 6. Fold formed by transparent ice in laminated ice with subhorizontal bedding.

Shpindler (Fig. 1), a somewhat similar assumption was made. Possibly glacier ice was flowing northward from the hills in the Pai-Hoi uplands on the Yugorski Peninsula, 468m a.s.l., which may have acted as an ice sheet nucleation area during the Early Weichselian glaciation (Svendsen et al. 2004). However, at the study area it is difficult to assume the same scenario because typical moraine sediments are absent.

The unconformable upper contact of the massive ice unit in some places can be the result of thaw layer deepening or increased thermokarst activity during Holocene warming. But in many sections where the surface is unaffected by thermokarst and massive ice is overlaid by more than 8 m of sediments, this unconformity was evidently formed at the same time as the massive ground ice. This fact contradicts the intrasedimental hypothesis of massive ice formation but can be explained within the framework of a burial origin.

The ice bands and lenses and dykes in the host sediments most likely were formed by segregation and injection processes during permafrost aggradation following the burial of portions of the outlet glaciers.

Ice structure

The ice types described here can be observed in the case of buried glacier or under intrasedimental ice origin. Similar ice types were described in other massive ice exposures; for example, in massive ice at Tuktoyaktuk Coastlands in western Arctic Canada, which is supposed to be buried basal ice of the Laurentide Ice Sheet (Murton et al. 2005). There the laminated type of ice from this study can be related to aggregate-poor ice facies altering with pure ice facies.

Ice deformations, which are poorly explained by the intrasedimental hypothesis of massive ice origin, provide much stronger evidence of massive ice burial. For example, the observed folded transparent band could be formed as a result of ice removal in horizontal flatness, which deformed a previously intact band (such transparent bands form in bodies of contemporary glaciers).

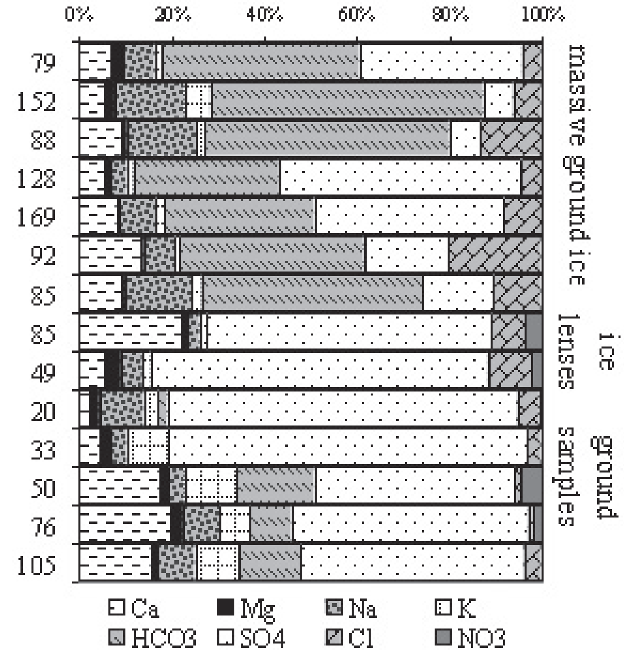

Figure 7. Mineralization (Y-axis, mg/l) and percentage of chemical components in massive ice, host sediments and ice bands and lenses in host sediments.

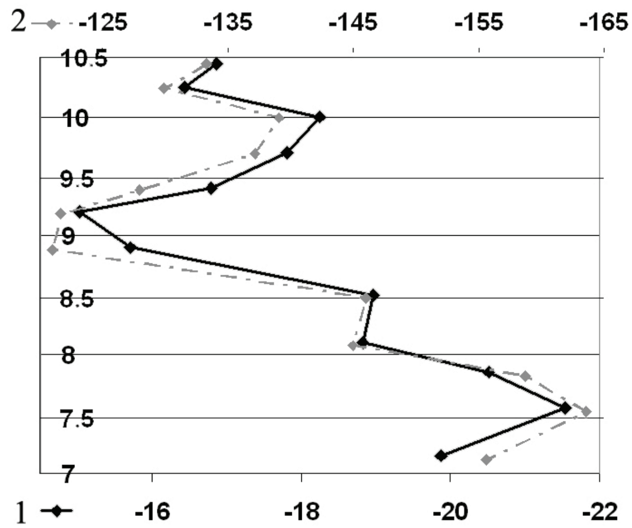

Figure 8. Vertical profiles of the ^{18}O (1) and D (2) isotope values in the massive ground ice body 3.5 m thick. Y-axis shows altitudes, a.s.l.

Chemical and isotopic composition

The chemical composition of massive ice and host sediments is slightly different, which testifies against the hypotheses of underground origin of massive ground ice.

Ice bands and lenses are similar to sandy strata by the ratio of chemical components' content, which confirms their intrasedimental origin. The absence of HCO_3^- in these ice formations is typical for stagnant water (Alekin 1970). It supports the formation of these lenses in a closed system during freezing and consolidation of enclosing lacustrine-alluvial sediments.

The rather large amplitude of oscillation of the ^{18}O and D isotope values tells about the impossibility of this massive intrasedimental ice bed forming only by the segregation process. On the contrary, this data doesn't contradict the possibility of basal glacial ice burial.

Conclusions

Based on these data, we can suppose that the complicated sandy-pebble stratum, which encloses massive ground ice, was formed in conditions of periglacial lacustrine-alluvial flat with the demolition of the material from adjacent parts of the Polar Ural. During Middle-Late Weichselian, as the result of intensive entry of alluvial-proluvial or fluvioglacial sediments and reformation of river channels ice bodies, apparently remnants of Ural's outlet glaciers could be buried. Later on they were periodically destroyed by thermokarst and buried again, which caused complicated construction of ice beds. The last regional glaciation occurred earlier in this area, probably during Early Weichselian.

Acknowledgments

We are grateful to S.A. Ogorodov for logistical support of fieldwork, and to the Russian Foundation of Basic Research, projects 05-05-64883 and 05-05-64872, for financial support.

References

Alekin, O.A. 1970. The foundations of hydrochemistry. Leningrad: Hydrometeorology Publishing, 442 pp. (in Russian).

Andreev, A.A., Tarasov, P.E., Romanenko, F.A., Sulerzhitskii, L.D. & Terekhov, K.I. 1998. Vegetation of the western coast of Baydaratskaya Bay at the end of the Late Pleistocene. *Stratigraphy and Geological Correlation* 6(5): 520-525.

Belova, N.G., Solomatin, V.I., Romanenko, F.A., Olyunina, O.S. & Ogorodov, S.A. 2007. New materials on massive ground ice at the eastern coast of Yugorski peninsula. *Proceedings of the international conference "Cryogenic resources of polar regions"*. Salekhard: Vol.1: 198-200 (in Russian).

Forman, S.L., Ingólfsson, Ó., Gataullin, V., Manley, W.F. & Lokrantz, H. 2002. Late Quaternary stratigraphy, glacial limits, and paleoenvironments of the Marresale area, western Yamal Peninsula, Russia. *Quaternary Research* 57: 355–370.

Gataullin, V.N. 1988. Upper Quaternary Deposits of the Western Coast of the Yamal Peninsula, Russia.// Ph.D. thesis abstract, Federal Geological Institute, 26 pp. (in Russian).

Gataullin, V.N. & Forman, S.L. 1997. Stratigraphy of upper Quaternary sediments in Western Yamal as a key for last glacial paleogeography reconstructions. // Problems of the cryolithology of Earth. International conference proceedings. Pushchino, 1997: 246-249.

Konyakhin, M.A., Ampleeva, T.V. & Nikolaev, V.I. 1991. An occurrence of massive ground ice in Upper Pleistocene deposits, the Uralian Coast of the Baydaratskaya Bay. *Materials of Glaciological Researches* 72: 227-228 (in Russian).

Murton, J.B., Whiteman, C.A., Waller, R.I., Pollard, W.H., Clark, I.D. & Dallimore, S.R. 2005. Basal ice facies and supraglacial melt-out till of the Laurentide Ice Sheet, Tuktoyaktuk Coastlands, western Arctic Canada. *Quaternary Science Reviews* 24: 681-708.

Svendsen, J.I., Alexanderson, H., Astakhov, V.I., Demidov, I., Dowdeswell, J.A., Funder, S., Gataullin, V., Henriksen, M., Hjort, C., Houmark-Nielsen, M., Hubberten, H.W., Ingólfsson, Ó., Jakobsson, M., Kjær, K.H., Larsen, E., Lokrantz, H., Lunka, J.P., Lysa, A., Mangerud, J., Matiouchkov, A., Murray, A., Möller, P., Niessen, F., Nikolskaya, O., Polyak, L., Saarnisto, M., Siegert, C., Siegert, M.J., Spielhagen, R.F. & Stein, R. 2004. Late quaternary ice sheet history of northern Eurasia. *Quaternary Science Reviews* 23: 1229-1271.

Romanenko, F.A., Voskresenskiy, K.S., Tarasov, P.E., Andreev, A.A., Nikolaev, V.I. & Sulerzhitskiy, L.D. 2001. The relief and loose sediments forming features on the Western Yamal and Baydaratskaya Bay coast (Kara Sea). *Problems of general and applied geoecology of the North.* Moscow: MSU Publishing, 41-68 (in Russian).

A Direct Method for Obtaining Thermal Conductivity of Gravel Using TP02 Probes

Hui Bing
State Key Laboratory of Frozen Soil Engineering, Cold and Arid Regions Environmental and Engineering Research Institute, CAS, Lanzhou, China

Ping He
Tunnel and Underground Engineering Research Center, Ministry of Education, Beijing Jiaotong University, Beijin, China

Norbert I. Koemle
Space Research Institute, Austrian Academy of Science, Graz, Austria

Wenjie Feng
State Key Laboratory of Frozen Soil Engineering, Cold and Arid Regions Environmental and Engineering Research Institute, CAS, Lanzhou, China

Abstract

Gravel was used as one of the effective measures to decrease the temperature of embankment during construction of the Qinghai-Tibet Railway. Thermal conductivity is one of the most relevant material parameters needed for the design and construction of roads and railways, especially in permafrost regions. We report on the measurement of the thermal conductivity of gravel (with grain size between 5 cm and 8 cm, which was widely adopted during construction of the Qinghai-Tibet Railway) using Thermal Properties sensors (TP02) made in Netherlands, which allowed a direct measurement of local thermal conductivity. Two conditions of the gravel are preformed: (1) natural convection exists in the gravel, and (2) there is only heat conductivity in the gravel by setting the boundary temperature and constrained convection using agar gel embedded in the gravel. We describe the data evaluation and present the results of the experiments.

Keywords: agar gel; gravel; natural convection; permafrost regions; Qinghai-Tibet Railway; thermal conductivity.

Introduction

In many physical and engineering problems thermal conductivity of the materials used is one of the key parameters that, to a high extent, control the thermo-physical behavior of the system. For example, during construction, the distribution of artificial or naturally generated underground heat determines the stability of the roadbed and thus the safety of the pathways. This is especially important in permafrost regions, like the areas transected by the Qinghai-Tibet Railway. The permafrost layer of the road contains high ice content, making it susceptible to consolidation if thawing occurs. If thawing consolidation takes place beneath engineering structures such as roadway embankments and buildings, the consolidation of the foundation soils typically results in instability and failure of the structures.

Thawing-unstable permafrost provides a very significant challenge to engineers working on the Qinghai-Tibet Railway. Over the years, techniques for avoiding damage to engineering structures because of thaw settlement have remained high on the research agenda for the Chinese government and scientific researchers, although the railway was test run on July 1, 2006. Roadbed embankments typically have a large influence on the thermal regime of the ground when they are constructed in permafrost regions. In order to maintain the stability of the embankments, gravel embankments and slopes are used to avoid thawing-settlement in permafrost regions. But there is some dispute over temperature decreasing degree of various conditions for the complicity of the thermal conductivity determination.

Goering (1996, 2000) studied temperature decreasing of gravel embankments in winter using the dynamic of porous medium. Temperature reductions will reduce or eliminate the tendency for the subsurface permafrost to thaw, thereby protecting the embankment structure from damage due to thaw-settlement. Due to the macropore characteristic of the gravel, cool and warm air in winter and summer can change reciprocally, shielding heat (Sun & Ma 2003). Under the condition of temperature fluctuation and knowing the heat diffusion coefficient of the gravel, thermal conductivity can be obtained by calculating the equivalent heat capacity (Sun et al. 2002, 2005). Therefore, thermal conductivity is a key heat parameter in indicating the heat condition for designing the gravel embankments and slopes. Thermal conductivity of the various materials can be obtained by experiment, but it is difficult to gain the conductivity for gravel of large grain size. However, Thermal Properties sensors (TP02) supplied by IWF and produced by the Hukseflux company allow direct measurement of local thermal conductivity. This research has resulted in a number of indoor experimental studies which can be utilized in field research and numerical modeling of the convection embankments for protecting a wide variety of structures from thawing-settlement damage. Nevertheless, many unsolved problems still remain.

Experimental Apparatus and Materials

Experimental apparatus

The goal of our experiments was to measure the thermal conductivity of gravel used in roadbed engineering. The tests were performed in a thermally controlled environment, namely a climate chamber (Fig. 1). The chamber allowed establishment of a homogeneous temperature environment in the range of -40°C to +70°C. The inner size of the chamber is approximately 100 cm × 100 cm × 100 cm. Two big fans on the inside back of the chamber are used to control the temperature of the chamber to a prescribed value. Also, the air humidity inside the chamber can be controlled externally and set to a given temperature. During operation the power device of the chamber must be cooled by a cold water circuit.

The second major device used in the experiments was the sample container (Fig. 2). It is of rectangular shape (70 cm × 70 cm × 35 cm) and its sides are thermally insulated. The bottom of the container is connected to a circuit which connects to a cooling machine working with alcohol as the cooling agent. The bottom temperature of the container can be set to a certain value, so the upper and bottom temperature of the sample in the container can be controlled by setting the temperature on the chamber and the cooling machine to whatever temperature gradient wanted for the experiments.

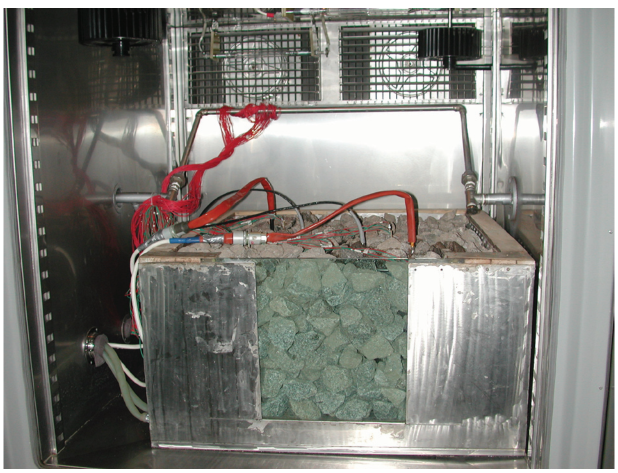

Figure 1. Climate chamber and container used in the experiments.

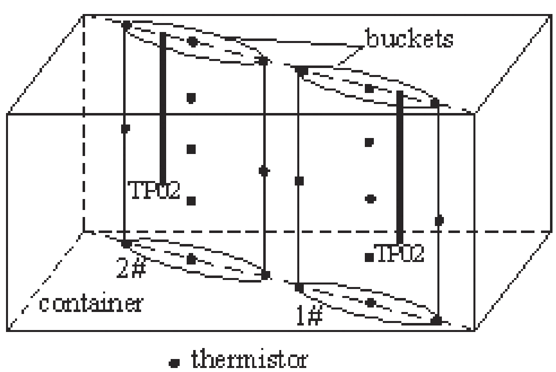

Figure 2. Schematic charts of the experimental apparatus.

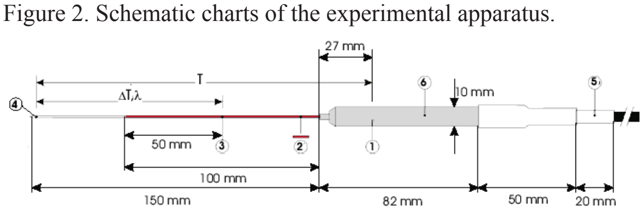

Figure 3. Dimension and buildup of Hukseflux TP02 thermal conductivity probes, which were used to obtain the thermal conductivity data presented in this paper. The sensors including the needle are hermetically sealed in a stainless steel casing, which makes them suitable also for vacuum application.

The third device used was two big stainless steel buckets 32 cm in inner diameter and 30 cm in height. The buckets were filled with gravel and put in the diagonal place of the container; the container was filled with gravel, too.

Measurement sensors

Two types of sensors inserted in the gravel were used in our experiments for measuring the thermal conductivity λ. Thermistors were distributed among the gravel uniformly, which can be seen in Figure 2, to monitor the temperature variations of the gravel during the periods of cooling and heating. The other sensors are two TP02 probes (Fig. 3), which were put in the two buckets. It allows a classical method of getting the thermal conductivity value. The sensor needle of the Hukseflux TP02 probe consists of a needle with two thermocouple junctions (one of which acts as a reference) and a heating wire. It is inserted into the medium that is investigated. In the base, a temperature sensor is mounted. The probe has a heater resistance per meter of 75.52 Ω, a length of 150 mm, and a diameter of 1.5 mm. Its maximum operating temperature is T_{max} = 135°C. To get reasonable results of thermal conductivity, the sensor has to be inserted into the sample at least to the upper end of the thin needle, better up to the base. The principle relies on the unique property of a line source: after a short transient period the temperature rise, ΔT, only depends on heater power, Q, and medium thermal conductivity, λ:

$$\Delta T = (Q/4\pi\lambda)(\ln t + B) \tag{1}$$

with ΔT in K, Q in W/m, λ in W/mK, t the time in s and B a constant.

The thermal conductivity can be calculated from two measurements at t_1 and t_2 (Seiferlin et al. 1996). For TP02, both t_1 and t_2 are higher than 60s, and typically 100s apart. Now ΔT the temperature difference between t_1 and t_2

$$\lambda = (Q/4\pi\Delta T)\ln(t_2/t_1) \tag{2}$$

The signal of TP02 is the function of the natural logarithm of time. The different steps of signal analysis for evaluating the thermal conductivity from the measured temperature signal of a heated thin-wire sensor can be seen in Figure 4. In every individual measurement, the graph in the logarithmic time scale should also be visually inspected to see where the linear part heat can be used for the evaluation of λ.

To estimate the length of the transient part of the signal, one can use the following formula (Hukseflux TP02 manual):

$$t_{transient} = \frac{10D^2}{a} \tag{3}$$

Hereby, the transient time is proportional to the medium thermal diffusivity a, and the probe cross section (D is the diameter).

Experimental procedure

The gravel we used in our experiment is widely adopted in the convection roadbed along Qinghai-Tibet Railway. The porosity of the gravel with grain size of 5 cm–8 cm has been experimentally determined as n = 0.48. Figure 2 also shows the schematic charts of the experimental apparatus used in our experiment. We filled the two buckets (#1 and #2) and the container with gravel at random. It was possible to make a large number of measurements over a number of days under this condition, when the cooling fans of the chamber were switched off temporarily and thus no forced air convection took place in the chamber.

In order to investigate the thermal conductivity of gravel without convection, we used agar gel, filling the pores of gravel. It was also used for calibration in the experiments. This is a water gel, of which the ingredients can be bought in every pharmacy. The agar itself does not significantly influence the thermal, but eliminates the effects of convection. At 20°C and 0°C, its thermal conductivity is 0.60 W/mK and 0.57 W/mK, respectively. The temperature dependence of the thermal conductivity is 0.0015 W/mK/°C.

Two different grain size gravel measurements were done at room temperature. After the investigation, the calibration of the probes was performed.

Data Evaluation

The criterion for natural convection

The Rayleigh number is a key similarity parameter investigating the natural convection in the porous medium (Sun et al. 2004). Whether natural convection will take place depends on the shape and the boundary of the porous medium. Based on the research on the convection of gravel, the Rayleigh number is defined as

$$R_a = \frac{\rho_0 g \beta K H \Delta \theta}{\mu \alpha_t} \tag{4}$$

It is the product of Darcy number $D_a = K/H^2$ and the Rayleigh number of pure fluid $Ra' = \beta g\ H^3 \Delta\theta / \mu a_t$, where ρ_0 is the density of the pore air (kg·m^{-3}), g is gravity acceleration (m·s^{-2}), β is the coefficient of thermal expansion (K^{-1}), and K is the permeability of the gravel (m^2), which is difficult to obtain, and generally it is estimated by the semi-rational formula as follows (Goering, 1998):

$$K = \frac{1}{5}\left[\frac{(1-n)^2}{n^3}\left(\frac{f_0}{100}\sum \frac{p_m}{d_m}\right)^2\right]^{-1} \tag{5}$$

where f_0 is the shape factor of gravel ranging from 6.0 of sphere to 7.7 of corner edge shape, and p_m is the percent of average grain size, d_m, in gravel. In the experiments, the permeability of the gravel is 4.83 × 10^{-6}m^2 determined experimentally. H is the height of the gravel (m), and $\Delta\theta$ is the temperature difference between the lower and upper boundary in the experiment (K); μ is dynamic viscosity of the pore air (N·s·m^{-2}) influenced by temperature, and it is of 1.158 × 10^{-5} N·s·m^{-2}～1.700 × 10^{-5} N·s·m^{-2} under the temperature of between -20° to 40°, and a_t is the volumetric heat capacity of the pore air (m^2·s^{-1}).

There is a critical Rayleigh number, Ra_c, depending on the shape and boundary conditions of the porous medium (Bear 1972). When Ra is less than Ra_c, the component of air among gravel is zero, so there is only pure heat conductivity; however, natural convection is taking place when Ra is greater than or equal to Ra_c. The critical Rayleigh number Ra_c can be calculated under different boundary conditions (Kong et al. 1996). In the experiments, it is a two-dimensional square region, all-around waterproof, and boundary temperatures are stable with side insulation, so $Ra_c = 4\pi^2 = 39.47$. The Rayleigh number, Ra, is 67.83 in the minimum temperature difference between the lower and upper boundary, greater than the critical Rayleigh number, Ra, 39.47; so before filled with agar gel during the experiment, heat conductivity exists in the gravel, but natural convection as well.

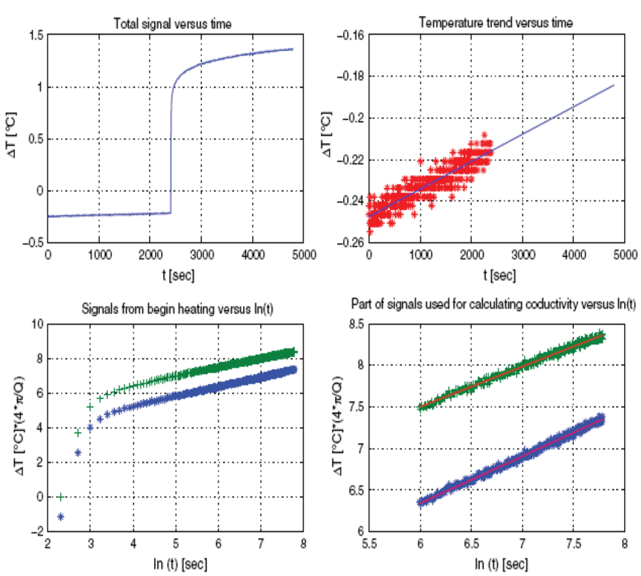

Figure 4. Different steps of signal analysis for evaluating the thermal conductivity from the measured temperature signal of a needle probe. Upper left: measured temperature increase in response to sensor heating. Upper right: evaluation of the general temperature trend in the sample before heating. Lower left: corrected (green) and uncorrected (blue) temperature increase in response to sensor heating over a logarithmic time coordinate; only the heated part of the signal is plotted here. Lower right: part of the signal used for the evaluation of the thermal conductivity.

Thermal conductivity of gravel with convection

Figure 5 shows the variation of thermal conductivity of existing natural convection in gravel. It can be seen that the thermal conductivity increases in positive temperature and decreases in negative temperature, so it is good for heat exchange in summertime for road stability in permafrost regions. There is the same trend in the temperature gradient (Fig. 6). It means that there exists natural convection to a negative temperature gradient (bottom temperature is grater than the upper temperature), and there is only heat conductivity to a positive temperature gradient (bottom temperature is lower than the upper temperature). Under this condition, the bottom temperature is higher than the upper boundary temperature. Due to the existence of natural convection, the heat transferred from the lower to upper is greater than the conditions where there is only heat conductivity. With the increasing of the temperature gradient, the effect is more obvious. The advantage of gravel roadbeds and slopes is active protection of the permafrost, especially in summertime with high temperatures. The results can be used in numerical modeling of the variation of temperature field of the roadbed.

From the experiment graph of the thermal conductivity of gravel with convection, we know the thermal conductivity with convection, but in our experiment using TP02 probes, we do not know how much the convection affects the thermal conductivity, namely temperature.

Thermal conductivity of gravel filled with agar

Our experiments with gravel, agar gel, and the composite sample (gravel with air, and gravel with agar gel filled) offer the possibility to test some simple formulas predicting the conductivity of two component samples practically, since we have both conductivity measurements of the single components and measurements of the sample containing both components in a known volume ratio.

In order to eliminate the effects of convection, the thermal conductivity measurements were done by filling the gravel with agar gel. The thermal conductivity of the composite sample is 1.6 W/mK in positive temperature, and 3.0 W/mK when freezing. Then the simplest way to predict the effective conductivity of the composite sample would be

$$\lambda = n\lambda_a + (1-n)\lambda_s \tag{6}$$

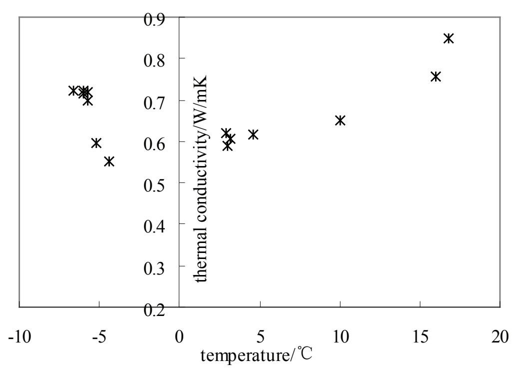

Figure 5. The variation of thermal conductivity with temperature when there is existing natural convection.

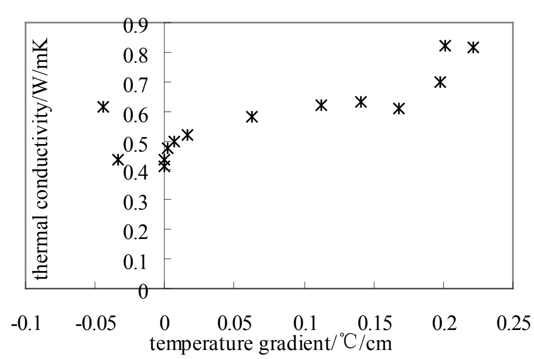

Figure 6. The variation of thermal conductivity of gravel with temperature gradient.

where n is the porosity of the gravel (equivalently n is the volume ratio filled with the agar gel); λ_a is the thermal conductivity of agar gel, and the change is very little with temperature; and λ_s is the conductivity of granite stones.

The porosity n of the composite sample (respectively the fraction filled by the agar gel) has been experimentally determined as $n = 0.48$. The calculation value of the thermal conductivity of gravel filled with agar gel is 1.692 W/mK in positive temperature, and 2.964 W/mK when freezing.

Different grain-size thermal conductivity measurement at room temperature

At room temperature, different grain size gravel measurements were done. One is of grain size between 1 cm and 2 cm, and the porosity of it is 37.9%; the other is of grain size between 2 cm and 4 cm, and the porosity is 40%. It can be seen from Figure 7 that the bigger the grain size or porosity, the greater is the thermal conductivity.

Conclusions

1. The thermal conductivity measurements of gravel using TP02 probes give a simple and direct way to obtain results. To the temperature and the temperature gradient with air convection, the thermal conductivity increases in positive, and decreases in negative.
2. With the agar gel filled and using one simple formula, the calculation value of the thermal conductivity of gravel is 1.692 W/mK in positive temperature, and 2.964 W/mK when freezing.
3. The bigger the grain size or porosity, the greater is the thermal conductivity.
4. We studied the thermal conductivity of gravel with air convection, but it is still a question as to how much the convection affects the thermal conductivity and the temperature in the roadbed. A solution to this is expected in our future work.

Acknowledgments

Funding for this work was provided by the National Key Basic Research and Development Foundation of the Ministry of Sciences and Technology of China (Grant No. 2002CB412704), National Natural Science Foundation of

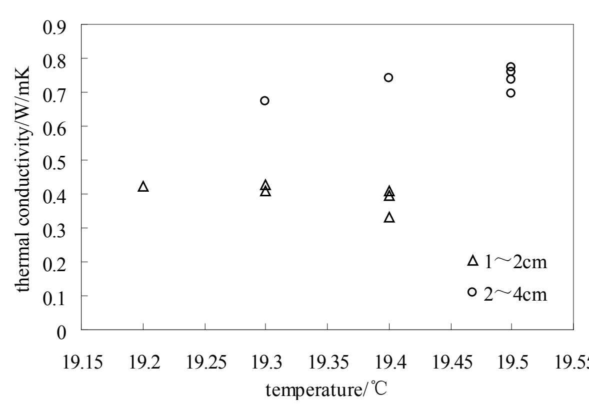

Figure 7. Thermal conductivity of different grain sizes.

China (No. 50778012, No. 40501016), the National Natural Science Foundation for Basic Talents Training in Special Subject of Glaciology and Cryopedology (No. J0630966).

References

Bear, J. 1972. *Dynamics of Fluids in Porous Medium*. New York: Elsevier.

Goering, D.J. 1998. Experimental investigation of air convection embankment for permafrost-resistant roadway design. *Proceeding of the Seventh International Conference on Permafrost. Yellowknife, NWT, Canada*.

Goering, D.J. & Kumar, P. 1996. Winter-time convection in open-graded embankments. *Cold Regions Science and Technology* 24: 57-74.

Goering, D.J., Instanes, A. & Knudsen, S. 2000. Convective heat transfer in railway embankment ballast, *Proceedings of the International Symposium on Ground Freezing and Frost Action Soils, Louvain-la-Neuve, Belgium. A.A. Balkema, Rotterdam*, 31-36.

Hukseflux Thermal Sensors: TP02 probe for thermal conductivity measurement, 2003. User manual, 26 pp.

Kong, X.Y., Lu, D.T., Xu, X.Z. & Wang X.D. 1996. Study on convection in porous medium. *Advances in Mechanics* 26: 510-520.

Seiferlin, K., Koemle, N.I., Kargl, G. & Spohn, T. 1996. Tine heat source measurements of the thermal conductivity of porous HO ice, CO ice and mineral powders under space conditions. *Planet Space Science* 44: 691-704.

Sun, X.B., Xu, X.Z., Lai, Y.M. & Li, D.Q. 2002. Determination of thermal diffusivity and conductivity on ballast. *Journal of Glaciology and Geocryology* 24: 790-795.

Sun, Z.Z. & Ma, W. 2003. Effects of ballasts on temperature of embankment in permafrost region. *Journal of Railway Engineering Society* 4: 59-61.

Sun, X.B., Xu, X.Z., Lai, Y.M., Li, D.Q., Wang, S.J. & Zhang, J.Z. 2004. Experimental research of thermal diffusivity and conductivity in embankment ballast under periodically fluctuating temperature, *Cold Regions Science and Technology* 38: 219-227.

Sun, X.B., Xu, X.Z., Lai, Y.M. & Fang, M.X. 2005. Evaluation of fractured rock layer heights in ballast railway embankment based on cooling effect of natural convection in cold regions. *Cold Regions Science and Technology* 42: 120-144.

The Effect of Near-Freezing Temperatures on the Stability of an Underground Excavation in Permafrost

Kevin L. Bjella , P.E.
Cold Regions Research and Engineering Laboratory, Fairbanks, AK, USA

Abstract

Changes in tunnel geometry have occurred to the Cold Regions Research and Engineering Laboratory (CRREL) Permafrost Tunnel in Fox, Alaska, since excavation in the mid-1960s. Frozen silt deformation has occurred in the rear of the horizontal adit, and a portion of the gravel roof in the lower winze chamber has detached from the silt strata above. Both of these deformations are attributable to thermal changes in the facility that have raised the overall temperature to near-freezing. Temporary modifications to the air-chilling system have decreased the temperature to an average of -7.0°C for the winter months and -3.5°C for the summer months, and early data from a monitoring program indicate the creep rate has slowed significantly.

Keywords: creep; frozen gravel; frozen loess; ice wedges; massive ice; permafrost tunnel.

Introduction

The CRREL Permafrost tunnel is located 16 km north of Fairbanks in Fox, Alaska (Fig. 1).The facility consists of a 110 m long horizontal adit excavated in frozen loess and a 45 m long winze that extends obliquely down to the underlying frozen gravels. Changes have occurred to the geometry of the tunnel since the excavation was conducted in the mid to late 1960s. Specifically deformation of the frozen silt has occurred in the rear of the adit, and a rooffall of the gravel layer has occurred in the room at the bottom of the winze. Investigation of the deformation was conducted in May of 2006 to ascertain what measures could be taken to prevent further deformation (Bjella et al., in press).

Background

This tunnel is composed of two portions: the adit (a nearly horizontal passage from the surface into a mine), which was driven by the U.S. Army Corps of Engineers using continuous mining methods in the winters of 1963–64, 1964–65, and 1965–66 (Sellman 1967), and the winze (an inclined adit), which was driven by the U.S. Bureau of Mines from 1968 to 1969 using drill and blast, thermal relaxation, and hydraulic relaxation methods (Chester & Frank 1969).

The adit was driven into a nearly vertical silt escarpment at the margin of Goldstream Creek Valley. This valley was historically mined for placer gold, and the escarpment was created by this activity. The geology consists of silt deposits that are Wisconsin to recent in age and eolian in nature derived from the Alaska Range. The silts overlie gravels of Nebraskan age derived from the surrounding hills of the Yukon–Tanana Upland terrain, and they in turn overlie Pre-Cambrian Birch Creek schist bedrock (Sellman 1967). The natural surface over the axis of the tunnel rises gently from the top of the 10 m escarpment and preferentially drains towards Goldstream Creek to the west and Glenn Creek to the north. The overburden is approximately 8 m deep at the rib-sets near the portal, 12 m deep at the rear of the adit, and approximately 17 m deep over the gravel room.

The tunnel contains many periglacial features found in fine-grained permafrost, such as thick segregated ice, massive ice (ice wedges and thaw ponds), and erosional and climate change boundaries marking depositional events, all of which are readily seen in the walls and roof of the adit and winze. The mode of permafrost formation was generally syngenetic, and the ice wedges are probably segments of larger ice wedge polygon complexes. Sellman (1967) suggested that two major silt units with separate ice wedge development exist in the adit. Moisture contents for the silt range from 39% to 120% with an average of 77% (Sellman 1967). The lower winze gravels have an average moisture content of 13.5% (Law 1987).

When the tunnel was constructed, it was realized that warm summer temperatures would adversely affect the stability of the facility, and therefore a mechanical air-chilling unit was installed. This unit, which is housed outdoors,

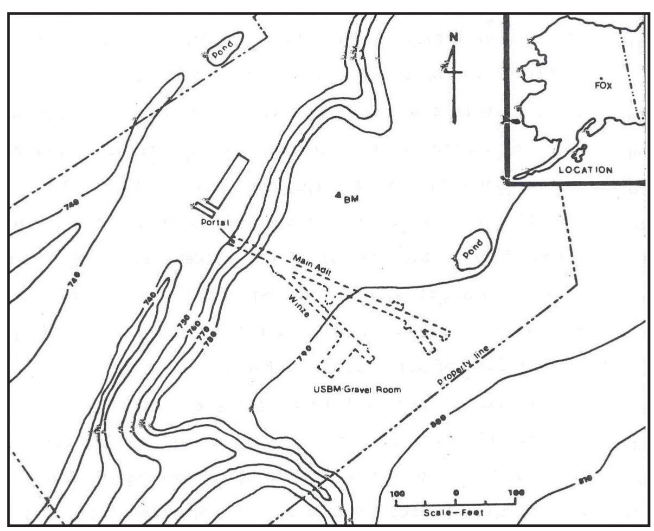

Figure 1. Plan view of the CRREL permafrost tunnel (after Pettibone & Wadde, 1969; scale in feet).

circulates liquid refrigerant through a series of loops that are embedded in the active layer over the portal bulkhead. One of these loops is circulated through a blower unit that hangs inside the tunnel between the bulkhead and the rib-sets and this serves to cool the interior air. This mechanical system was designed to run only during the months when outdoor ambient temperatures are above freezing.

Now inaccessible at the end of the adit are three approximately 1 m diameter ventilation shafts that were augured down from the surface to the tunnel. These were designed to aid in natural convection cooling in the winter while the portal doors were opened. These were problematic to maintain, as surface water would migrate along the shaft, thaw the permafrost, and form a conduit for surface water to travel to the tunnel, eventually occluding the vent. Each subsequent vent was installed after the failure of the previous. Sometime after 1993, the last of the three vents froze shut and has not been operable since. To aid in cooling the rear of the adit since that time, fans have been used to circulate the winter air after opening the portal doors.

The continuous mining method utilizing the Alkirk Miner simultaneously cut two 2 m circular arcs, side by side. After this pass was complete to the end of the adit at 110+00 (110 m, where 0+00 is the inside wooden bulkhead), a portion of the floor was lowered using a Joy 10 RU coal cutter, which resembled a large, multi-angle chainsaw. This started near the bulkhead and continued to approximately midway at 50+00, where the floor begins to incline noticeably to meet the elevation of the Alkirk pass at 62+0.5. The winze begins at 30+00 and drops obliquely at an incline of 14% for 45 m, passing into the gravel unit and ultimately into the weathered bedrock, where the Gravel Room was excavated (Pettibone 1973). At the time of excavation, portions of the Gravel Room roof consisted of a gravel layer up to 2 m thick below the overlying silt unit (Garbeil 1983).

Silt deformation

Beginning at the portal and moving towards the face (rear), the adit retains the original excavated geometry. An examination of the area near the portal reveals that this location has not experienced any appreciable deformation, probably because of the proximity to the portal doors during winter cooling and the proximity to the mechanical chilling unit during summer cooling. At 50+00, the “switch room,” measuring 6×6 m, was excavated on the south side of the adit, and it appears that the roof in this area may have dropped some amount corresponding to the 12 m roof span. A transverse-oriented crack, about 4 cm wide, crosses the roof in this area. It is ice-filled, which suggests a cyrostructural origin and not a tension crack from deformation. Otherwise, from the portal to approximately 75+00, there is no perceptible deformation to suggest structural instability. In fact, for most of this portion of the adit, the Alkirk Miner profile is still visible in the roof, suggesting that the material is relatively stable and has not moved or deformed since the time of excavation.

At approximately 75+00 the roof begins to perceptibly sag and at 80+00 fallen slabs of silt up to 0.25 m in thickness are lying on the floor; the adit is then completely blocked by low-hanging and fallen soil layers at 90+00 (Fig. 2). The overhead layers of soil delaminate from the bedded soil above and creep down towards the floor hanging from the wall/roof intersection. This portion of the adit has evidence of paleo-alluvial deposition and erosion (Sellman 1967) where the poorly-graded silt contains interbedded layers of gravelly sandy silt, millimeters to centimeters in thickness. These layers are the preferential locations of the overhead detachment yielding the laminated structure (Bjella et al., in press). The slow deformation towards the floor can then give way to an abrupt release of portions up to 4 m^2 when the tensile strength of the soil is exceeded on either end of the catenary. Except near the portal, approaching the face, and in close proximity to cryological ice features, the silt in the adit and upper 30 m of the winze appears to have undergone little deformation since emplacement and retains a massive cryological structure appearance. No subsidence is noticed at the surface directly above this deformation.

The winze was excavated using drill and blast methods starting at a low hanging ledge at 30+00. This ledge was the pullout location for the shuttle car used to move waste material out of the adit from the Alkirk machine. Because of the excavation method, the winze retains a much rougher appearance than the adit and is shallower in geometry. There is no evidence through the entire length that this ramp has undergone deformation to any significant degree.

Gravel deformation

The Gravel Room, which is located at the foot of the winze and extends to the southwest, was the focus of subsurface mining studies in the late 1960s. The room is 9×21 m and was excavated in the gravel and bedrock below the overlying silt unit. This silt/gravel boundary at the time of excavation was approximately 2 m above the level of the roof of the Gravel Room. It was recognized that this gravel material, with its much higher unit weight than the silt unit to which it is bonded (2080 kg/m^3 for the gravel vs. 1600 kg/m^3 for the silt), could separate and fall in rooms of large roof span.

Investigators have repeatedly studied this parting potential through the years, with two investigations utilizing a warming study to understand the temperature dependence on creep and separation of the two soil units (Pettibone 1973, Garbeil 1983, Huang 1985, 1986). Two multiple-position borehole extensometers were installed during the 1983 study, with one end anchored in the silt unit and the other anchored in the gravel roof. Specific parting of 0.0084 mm/d was noted between the silt and gravel units when temperatures achieved their highest readings of -1.9°C during the study. Overall vertical closure rates for the room during April 1983 were 0.010 mm/day at -3.7°C, and in July 1983 the closure accelerated to 0.053 mm/d at -1.9°C.

The Gravel Room roof fell to the floor, approximately 25 m^3, after a 6.2 Richter magnitude earthquake struck the Fairbanks region in October 1995. The boundary of the dropped material is coincident with the wall that was installed to facilitate warming of the roof in 1983 and is shown in Figure 2. No subsidence is noticed at the surface due to this roof fall.

Additional observations

On the north side of the adit at 80+00 is a 5×5 m side area referred to as Sayles's Room (also called the Crystal Room). It is divided from the adit by a lumber frame and a heavy tarpaulin, and inspection revealed a large ice wedge on the western wall that widens where it meets the roof and then spreads out to almost room-width across the roof towards the adit. The adit at this stationing is overlain by massive ice, but to what degree is uncertain. The roof in Sayles's Room is supported by a 3 m long steel beam resting on 15×15 cm timbers, which are the remnants of previous creep testing.

Opposite Sayles's Room on the southeast end of the adit, at approximately 95+00, a 16×6 m crosscut exists that departs at a 36° angle. This room is now inaccessible because of the deformation in the adit, and anecdotal information implies that an ice wedge feature is exposed in the southwest wall of this room adjacent to the adit. Also, in the north wall of the adit at 75+00, there is a complex configuration of massive ice consisting of ice wedges, pond ice, and 5 to 15 cm -thick ice lenses. Because of the close proximity of the adit deformation, the Sayles's Room ice wedge, the cross-cut ice wedge, and the massive ice complex at 75+00; and based on the polygonal nature of ice wedge complexes (Williams & Smith 1989, Murton & French 1994), this intersection may be coincident with the near-center of an ice wedge polygon complex (Bjella et al., in press).

Analysis

Creep reference locations

Creep reference locations were installed in May of 2006 to specifically measure the change in dimension of selected areas of the facility. Seven were established in the adit and two in the winze and were designed to be measured with a metal tape extensometer which measures the relative distance to the nearest 0.01 mm. Each location consists of four attachment points of 0.95 cm diameter × 20 cm long lag eye-bolts screwed into the soil. Two of the points are located at mid-height of opposing walls, approximately perpendicular to the axis of the tunnel. The other two are located in the roof and floor in the same plane as the wall points, and are approximately mid-distance between the walls. The locations are prefixed with *A* for adit or *W* for winze and numbered starting with "1" continuing toward the face. Location A3 consists of only floor and roof points.

The creep stations are shown in Figure 2 and listed in Table 1 with distances from the bulkhead. The stations in the winze are measured from adit location A1. There have been three measurements conducted at all locations starting in May of 2006, with the most recent in July of 2007. The results of the measurements are listed in Table 1. On either side wall near

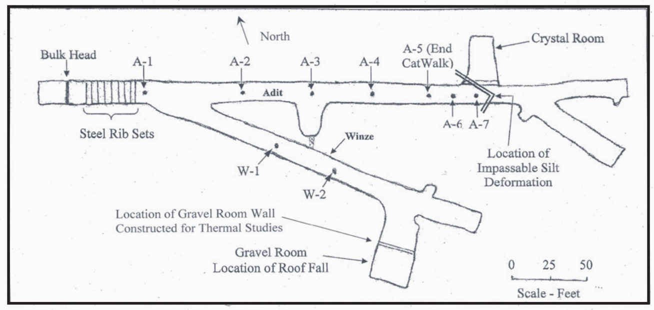

Figure 2. Detailed tunnel plan showing locations of deformation and creep monitoring locations (scale in feet).

the bulkhead are 0.95 cm lag bolts located in vertical 10×10 cm timber posts and these serve as a permanent extensometer reference location to verify continued accuracy of the tape extensometer measurements.

Wu (1985) measured nineteen vertical and nine horizontal convergence stations in both the adit and winze over a 287-day period. Four vertical and two horizontal points appear to have been within approximately 3 m of the newly established creep reference locations in the adit. Two vertical and two horizontal points appear to have been within these same limits of the newly created creep reference locations in the winze. Wu's locations, total convergence, and rate are listed in Table 1.

Temperatures

In May of 2006, temperature measurements were taken utilizing thermistors located approximately every 3.0 m horizontally and at 1.0 m vertically from the floor, both in the air and at soil depths of 0.15 m, 0.40 m, and 0.60 m. The tunnel air near the portal was approximately -3.0°C, and the rear adit air was approximately -1.7°C. The temperature gradient near the portal was 5.6°C/m with depth into the wall, with the ambient air colder than the wall. The gradient at 83+00 was 0.42°C/m, with the ambient air warmer than the wall. The crossover (0°C/m) where the temperature of the ambient air is the same as the wall temperature takes place at approximately 75+00, where the silt deformation begins. The temperature at the top of the winze was -3.0°C, the bottom of winze -2.7°C, and the Gravel Room measured -2.2°C. The mechanical cooling unit was delivering approximately -5.0°C air, and it is unknown at what depth into the wall the soil temperature reaches equilibrium with the local permafrost.

Pettibone (1973) reported that in February of 1969 the gravel room was approximately -8.3°C, and in March it was -6.7°C. During the period mid-April to mid-June 1969 the temperature was -3.9°C. Linnell & Lobacz (1978) reportthat immediately after tunnel excavation the face experienced temperatures down to -9.0°C in the winter months when natural convection was being utilized through the vent system.

Temperatures measured by Wu from October 4, 1983, to February 28, 1984, show that the adit roof in the area corresponding to A4 to A7 ranged from -3.8 to -2.5°C with

Table 1. Creep measurements.

Location	Stationing (m)	*Creep (mm)	*Rate (mm/day)	†Creep (mm)	†Rate (mm/day)	‡Wu ID	‡Creep (mm)	‡Rate (mm/day)
A1 Vertical	16+50	-1.35	0.004	-0.07	0.006			
A1 Horizontal		-0.05	0.000	-0.65	0.005			
A2 Vertical	40+00	-5.35	0.017	-0.30	0.003			
A2 Horizontal		-4.95	0.016	-0.05	0.000			
A3 Vertical	54+00	-9.75	0.031	-0.85	0.007			
A4 Vertical	63+00	-9.80	0.031	-0.20	0.002	VA8	-3.96	0.014
A4 Horizontal		-5.70	0.018	-1.25	0.010			
A5 Vertical	75+00	-14.4	0.045	-.850	0.007	VA5	-5.16	0.018
A5 Horizontal		-14.3	0.045	-2.60	0.022	HA3	-3.53	0.012
A6 Vertical	80+00	-25.9	0.082	-2.80	0.023	VA4	-7.29	0.025
A6 Horizontal		-21.9	0.069	-2.30	0.019	HA2	-6.65	0.023
A7 Vertical	85+00	-51.2	0.161	-7.55	0.063	VA3	-14.2	0.050
A7 Horizontal		-31.5	0.099	-4.50	0.038			
W1 Vertical	30+00	-10.9	0.034	-2.70	0.023	VB3	-4.72	0.017
W1 Horizontal		-22.7	0.071	-4.05	0.034	HB2	-5.72	0.020
W2 Vertical	42+00	-15.9	0.050	-2.25	0.019	VB6	-5.41	0.019
W2 Horizontal		-17.5	0.055	-3.25	0.027	HB3	-5.38	0.019
Reference	0+00	-1.70	0.005	-1.00	-0.008			

* 5/17/2006 to 3/31/2007 (318 days)
† 3/31/2007 to 7/29/2007 (120 days)
‡ 5/17/1983 to 2/28/1984 (287 days)

the warmest temperatures at the end of the measurement period. The winze roof temperatures in the area of W1 to W2 for the same period ranged from -5.2 to -3.1°C, again with the warmest temperatures at the end of the period. Johanssen (1993) details the beginning of silt deformation that has altered the wooden frame for the door leading into Sayles room, and he reports the rear of the adit is approaching 0.0°C. At that time the vent system was operable; therefore, this system must have become unusable after that date. It is unknown if the mechanical system has degraded over the years, but it could be assumed that the system has only decreased in efficiency.

The temperature distribution measured in May of 2006 (-3.0°C at the portal, -1.7°C rear of adit) demonstrated that the air delivered in the summer from the chilling unit and the winter ambient air from the open portal doors was not being circulated to the rear of the adit or bottom of the winze in an effective manner. Because of this, starting on July 17, 2006, air temperatures at the front of the adit near A1, back of the adit near A6, and bottom of the winze near W2 have been recorded daily. The wall soil temperature near A4 at a wall depth of 0.15 m and 1.5 m above the floor has also been measured since that time. A plot of this data from Jan. 1, 2007 to March 19, 2007 is shown in Figure 3. Previous studies (Wu 1985, Law 1987) have shown considerable seasonal temperature variations of approximately 4°C, and daily variations of up to 1.0°C, and this was confirmed by our measurements.

Discussion

The larger scale deformation that has been occurring in the CRREL Tunnel for the last two decades appears to be attributable to the gradual increase in tunnel temperatures due to air-handling issues. No measurements or comparisons have been made to determine if a correlation exists with recent climate change. In an effort to slow deformation, a portable blower unit with 45 cm -diameter flexible ducting delivering approximately 0.55 m^3/sec was placed outdoors of the portal and routed approximately 60 m down the adit in February of 2007. The blower unit was moved inside the tunnel under the chilling unit when the chilling unit was turned on for the summer season. The point in time when the blower was first added is shown in Figure 3, and the temperatures decreased substantially to -7.5°C at the back of the adit by March 19, 2007, twelve days prior to the second creep reference location measurements. The temperatures during the third creep reference location measurements on July 29, 2007, averaged -3.5°C for the air near station A6. The creep rate at the rear of the tunnel has slowed by a factor of approximately 3 from the second measurement to the third, and the rate for the winze locations during the same period has slowed by approximately a factor of 2. This creep rate reduction corresponds with the modifications to the cooling system.

To illustrate temperature sensitivity in the near freezing range from -2.0° to -1.0°C for ice-rich fine-grained soil, we compare three uniaxial constant-stress tests (creep) conducted by the author on intact CRREL Tunnel cores

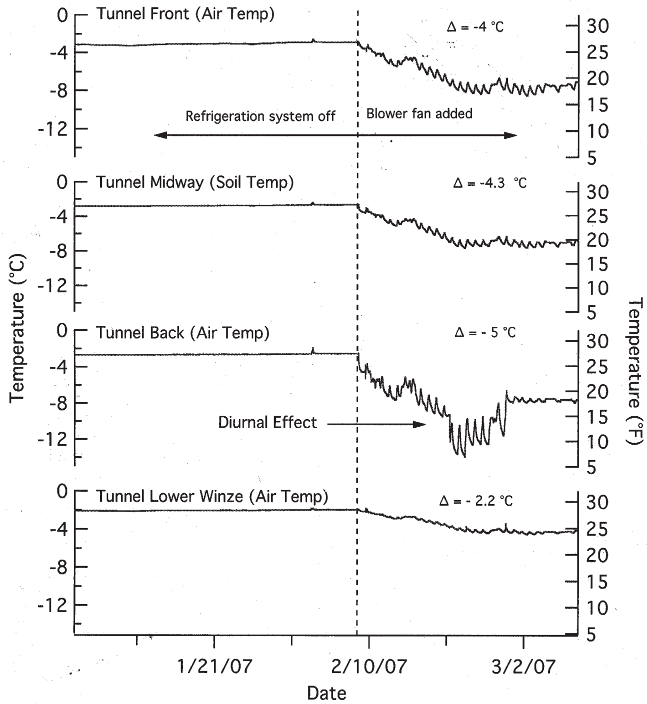

Figure 3. Tunnel facility temperatures.

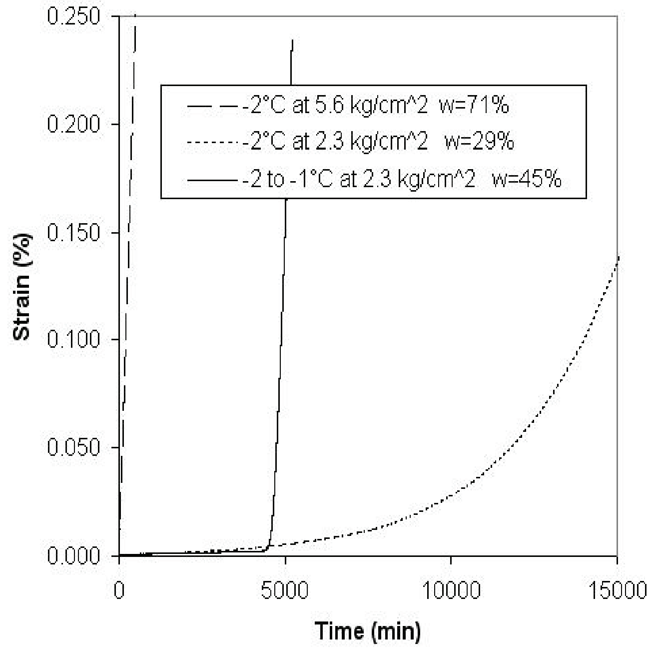

Figure 4. Temperature dependence of tunnel silt.

measuring 100.0 mm in length and 55.0 mm in diameter. These cores were taken from the left wall at approximately 74+00 and 0.3 m above the floor. One test was conducted at an axial stress of 5.6 kg/cm^2, and the second at 2.3 kg/cm^2 (approx. stress due to overburden), both at a constant -2.0°C. The third test was conducted at 2.3 kg/cm^2 with a temperature step from -2.0 to -1.0°C at 4500 min. For the third test the strain rate accelerates from 4.0 x 10^{-9} (s^{-1}) to 3.0 x 10^{-6} (s^{-1}) in 18 hr (Fig. 4).

In another example of temperature sensitivity, Zhu & Carbee (1987) conducted uniaxial constant-stress tests with remolded CRREL Tunnel silt. For medium density samples of approximately 1.2 g/cm^2 and moisture contents of 43%, it was found that for an applied stress of approximately 7.0 kg/cm^2, the time to failure dropped from 29,000 min at -2.0°C, to 70 min at a temperature of -1.0°C.

Conclusions

The adit deformation coincides with the reduction of facility cooling via natural convection and forced mechanical chilling, which has raised the rear adit air temperature to near freezing. This is in comparison to temperatures measured after excavation in the late 1960s. In addition it appears the rear of the adit is composed of a higher density of cryological structures than is evident in the rest of the facility. Exactly how the structural integrity of the frozen silt with emplaced massive ice bodies is affected by warmer temperatures is at best very complex. However, it can be assumed that across the soil mass as a whole, the non-homogenous thermal conductivity and strength properties due to these ice bodies, and the silt deformation caused by the emplacement, only serves to weaken the total soil mass, especially at the soil/ice margins.

This higher density of massive ice features is coincident with a change in soil gradation towards the rear of the adit, from poorly-graded silt, to poorly-graded silt with interbedded layers of larger grain size, resulting in preferentially weaker -bonded frozen soil. These weaker bonds and massive ice/soil margins are the location for detachment when the temperature is raised to near zero.

The winze and Gravel Room experience warmer temperatures than historical for the same reasons as the adit. These warmer temperatures have weakened the bond between the frozen gravel comprising the roof and the silt unit above, causing detachment during a past dynamic event. These warmer temperatures, large roof span, and historical parting studies have contributed to this parting.

Due to the addition of the blower and ductwork, there has been a reduction in rear adit temperature to an average -7.0°C for the winter months, and -3.5°C for the summer months, which has reduced the creep movement by a factor of 3. The temperature reduction in the winze has reduced the creep by a factor of 2. Continued reduction of the temperature to a maximum of -5.0°C for all portions of the facility during all seasons would be expected to reduce the deformation to the slower rates experienced prior to the extreme deformation of the rear of the adit.

Acknowledgments

Stephanie Saari and Art Gelvin of CRREL contributed greatly to the information provided in this report. The tunnel upgrades and ongoing data collection would not have been as successful and efficient without their specific and dedicated technical expertise.

Also, we wish to thank Dr. Gang Chen of the University of Alaska Fairbanks, Department of Mining Engineering, and Dr. Scott Huang of the University of Alaska Fairbanks, Department of Geological Engineering, for the use of the tape extensometer and general comments.

References

Bjella, K.L., Tantillo, T.J, Weale, J.C. & Lever, J.H. 2006. *The CRREL Permafrost Tunnel.* Technical Report (in press). Hanover, NH: Cold Regions Research and Engineering Laboratory, 69 pp.

Chester, J.W. & Frank, J.N. 1969. *Fairbanks placers fragmentation research final report*. Minneapolis: Twin Cities Mining Research Center, U.S. Bureau of Mines, Heavy Metals Program, 52 pp.

Garbeil, H.M. 1983. *Temperature effects upon the closure of a gravel room in permafrost.* M.S. Thesis. University of Alaska Fairbanks, 134 pp.

Huang, S.L. 1985. Temperature and time effects on the closure of a gravel room in permafrost. *Bulletin of Association of Engineering Geologists* 22(2): 53-65.

Huang, S.L. & Aughenbaugh, N.B. 1986. Stability study of CRREL Permafrost Tunnel. *ASCE Journal of Geotechnical Engineering* 112(8): 777-790.

Johansen, N.I. (1993.) *CRREL Permafrost tunnel after event*. Video.

Johansen, N.I. & Ryer, J.W. 1982. Permafrost creep measurements in the CRREL tunnel. *Proceedings of the Third International Symposium on Ground Freezing, Hanover, New Hampshire.* Hanover, New Hampshire: U.S. Army CRREL, 61-63.

Law, K.H. 1987. *Time-dependent bearing capacity of frozen ground*. M.S. Thesis. University of Alaska Fairbanks, 129 pp.

Linell, K.A. & Lobacz, E.F. 1978. Some experiences with tunnel entrances in permafrost. *Proceedings of the Third International Conference on Permafrost, 1978, Edmonton, Alberta:* 814-819.

Murton, J. B. & French, H.M. 1994. Cryostructures in permafrost, Tuktoyaktuk coastlands, western arctic Canada. *Canadian Journal of Earth Sciences* 31: 737-747.

Pettibone, H.C. 1973. Stability of an underground room in frozen gravel. In *Permafrost: North American contribution to the Second International Conference*, Washington: National Academy of Sciences, 699-706.

Pettibone, H.C. & Waddell, G.G. 1969. Stability of an underground room in frozen, gold-bearing strata, Fairbanks, Alaska. *Seventh Annual Northwest Mining Association Convention, Spokane, Washington*. U.S. Bureau of Mines Heavy Metals Program, 14 pp.

Sellmann, P.V. 1967. *Geology of the USA CRREL Permafrost Tunnel in Fairbanks, Alaska*. Technical Report 199. Hanover, NH: Cold Regions Research and Engineering Laboratory, 22 pp.

Williams, P.J. & Smith, M.W. 1989. *The frozen earth: Fundamentals in geocryology*. Cambridge, U.K.: Cambridge University Press.

Wu, M.C. 1985. *The temperature and geometry influences on an underground opening in the frozen ground*. M.S. Thesis. University of Alaska Fairbanks, 186 pp.

Zhu, Y. & Carbee, D.L. 1987. *Creep and Strength Behavior of Frozen Silt in Uniaxial Compression.* CRREL Report 87-10. Hanover, NH: Cold Regions Research and Engineering Laboratory, 67 pp.

Distribution of Permafrost Types and Buried Ice in Ice-Free Areas of Antarctica

J.G. Bockheim
University of Wisconsin, Madison, WI, USA

I.B. Campbell
Land & Soil Consultancy Services, Nelson, New Zealand

M. Guglielmin
Insubria University, Varese, Italy

J. López-Martínez
University of Madrid, Madrid, Spain

Abstract

Only 0.35% (49,800 km^2) of Antarctica is ice-free. We have divided the continent into nine major ice-free regions and estimated the distribution of permafrost by form: (i) buried ice within the upper 100 cm; (ii) ice-cemented permafrost with the surface within the upper 70 cm; (iii) ice-cemented permafrost with the surface below 70 cm; and (iv) dry-frozen permafrost with the surface below 70 cm. For each of these categories, permafrost distribution was divided into continuous, discontinuous, and sporadic or no permafrost. Based on preliminary analysis, 43% of the ice-free areas contain ice-cemented permafrost in the upper 70 cm, followed by dry-frozen permafrost (41%), and buried ice (13%). Permafrost is continuous throughout East Antarctica and along the Antarctic Peninsula and the surrounding islands at elevations generally above 40 m a.sl. Along the Antarctic Peninsula, discontinuous permafrost exists at elevations between 40 and 20 m a.s.l, and permafrost is either sporadic or lacking below 20 m a.s.l.

Keywords: ANTPAS; Antarctica; dry-frozen permafrost; ice-cemented permafrost; permafrost mapping.

Introduction

Only 0.35% or 49,800 km^2 of the Antarctic region (≥60ºS) is ice-free (Fig. 1). At 24,200 km^2 the Transantarctic Mountains (TAM), which extend 2,600 km from North Victoria Land (69ºS) to the Roberts Massif in the upper Scott Glacier region (86º30′S), are the largest ice-free area (Table 1).

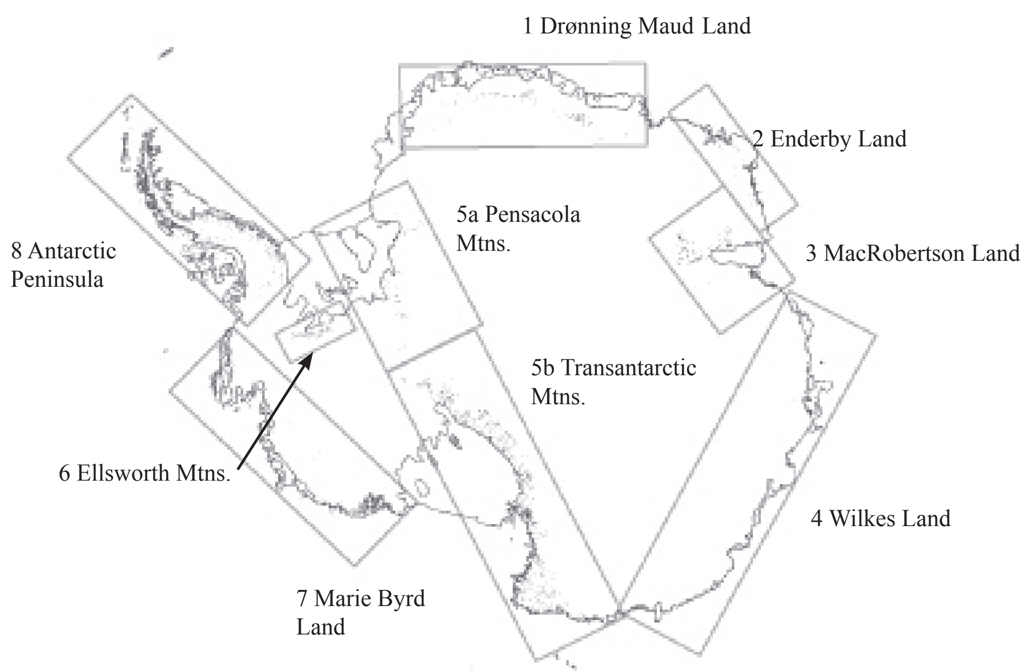

Figure 1. Major ice-free regions of Antarctica (after Greene et al. 1967). Ice-free areas are shown with dots, with each dot accounting for 15 km^2. Areas delineated using the Antarctic Digital Database V. 4.0 and ArcGIS V. 9.1 by D. Smith of the Australian Antarctic Division.

The Antarctic Peninsula and its offshore islands constitute the next largest ice-free region at 10,000 km2 (Table 1), followed by MacRobertson Land, Drønning Maud Land, and the Ellsworth Mountains. The Pensacola Mountains, Enderby Land, Marie Byrd Land, and Wilkes Land each contain 1500 km2 of ice-free area, or less.

Bockheim (1995) prepared the first permafrost map of ice-free areas in Antarctica. He showed that permafrost was limited to ice-free areas and that all of East Antarctica and most of West Antarctica contain continuous permafrost. Discontinuous permafrost was present from 66ºS to 63ºS along the Antarctic Peninsula and its offshore islands. Sporadic permafrost was limited to the South Orkney Islands. Zotikov (1963) showed the distribution of subglacial permafrost in Antarctica.

The following is a review of permafrost conditions in Antarctica by region. In the Sør Rondane Mountains of Drønning Maud Land (region 1), ice-cemented permafrost occurs at depths ranging from 7 to 80 cm, and dry permafrost is common (Sekyra 1969, Vtyurin 1986, Matsuoka et al. 2006). McNamara (1969) reported the top of ice-cemented permafrost at 75 cm in Enderby Land (region 2) and a limited amount of dry-frozen permafrost. Since the climate in MacRobertson Land (region 3) is comparable to that of Enderby Land, we suggest that the permafrost conditions are likewise comparable. It is likely that dry-frozen permafrost exists in the southern Prince Charles Mountains. Wilkes Land (region 4) contains two major ice-free areas, the Bunger Hills and the Windmill Islands. According to Blume & others (2002), the top of ice-cemented permafrost occurs at 30 to 80 cm throughout the Windmill Islands.

Observations from the Pensacola Mountains (region 5a) (Parker et al. 1982) imply that the ice-cemented permafrost surface occurs at 20 to 45 cm. In that dry-frozen permafrost exists in the Ellsworth Mountains, which occur at a similar latitude and proximity to the Ronne Ice Shelf, it is likely that dry-frozen permafrost exists in portions of region 5a.

For convenience we subdivided the Transantarctic Mountains (TAM; region 5b) into three subregions based on latitude: North Victoria Land (69º30′–75ºS), the central TAM (75º–80º30′S), and the southern TAM (80º30′–86º30′S). Campbell & Claridge (2006) reviewed permafrost properties throughout the TAM, noting that the active layer ranges from <5 cm in inland and upland regions to 80 cm in coastal areas. The moisture content of ice-cemented permafrost is greatest in coastal areas, where snowfall and regelation are common, and lowest in inland areas, where the moisture content may be <1%. In North Victoria Land (NVL), the active layer ranges from 10 to 30 cm in thickness (Guglielmin 2006). Whereas ice-cemented permafrost and buried ice are common, dry-frozen permafrost was not observed in NVL (Guglielmin & French 2004). However, in the Rennick Glacier-Talos Dome areas of interior NVL, ice-cored moraines are common beside blue-ice glacier margins (Denton et al. 1986). Elsewhere the surface of ice-cemented permafrost occurs at 8 to 70 cm; dry-frozen permafrost exists in the Morozumi Range.

Early permafrost studies in the central TAM largely were limited to observations and measurements of the growth of patterned ground (Berg & Black 1966, Black 1973), and core logs collected in 1970–1975 during the Dry Valley Drilling Project (DVDP) (McGinnis 1981). Using a combined dataset that included nearly 1000 shallow (<1.5 m) excavations, Bockheim & others (2007) provided a map at a scale of 1:2 million showing the distribution of permafrost in the MDVs. Their data suggested that about 55% of the permafrost was ice-cemented, 43% was dry-frozen, and buried ice comprised at least 2% of the ice-free area. Permafrost form was related to climatic zone, age of sediments, and local site factors.

The Ellsworth Mountains (region 6) can be divided into the Heritage Range, which contains localized areas of glacial drift, and the Sentinel Range, which contains primarily arétes and nunataks (Denton et al. 1992). We were unable to find information about permafrost conditions in Marie Byrd Land (region 7).

The Antarctic Peninsula (region 8) can be divided into five latitudinal subregions: (1) Palmer Land and Alexander Island (68–76ºS), (2) Graham Land and the Palmer Archipelago (63–68ºS), (3) the James Ross Archipelago (65º30–67ºS), (4) the South Shetland Islands (61–63ºS), and (5) the South Orkney Islands (60–61ºS). Permafrost depths bear a strong relation to latitude along the Antarctic Peninsula. Along the Trinity Peninsula and offshore islands, the surface of ice-cemented permafrost occurs at 25 cm (Everett 1976). In the South Shetland Islands, the top of ice-cemented permafrost exists at 25 cm to more than 100 cm, with about 50% of sites examined having permafrost in the upper 70 cm (López-Martínez et al. 1996, Serrano et al. 1996, Bölter et al. 1997, Blume et al. 2002, López-Martínez & Serrano 2002, Vieira et al. 2007). The surface of ice-cemented permafrost occurs at 40 to 200 cm in the South Orkney Islands (Holdgate et al. 1967, O'Brien et al. 1979).

To address the need for a permafrost map for Antarctica, a joint committee was appointed at the Seventh International Conference on Permafrost in Zurich by the International Permafrost Association (IPA) and the Scientific Committee on Antarctic Research (SCAR). In November 2004 the International Workshop on Antarctic Permafrost and Soils, sponsored by the U.S. National Science Foundation, was held in Madison, Wisconsin. A task force under the auspices of ANTPAS, the Antarctic Permafrost and Soils group (http://erth.waikato.ac.nz/antpas/) was established to begin preparing a permafrost and ground-ice map of Antarctica, with subgroups responsible for key ice-free areas. This manuscript is in response to this mandate and is intended to accompany these maps.

Methods

Ice-free areas in Antarctica, defined here according to the Antarctic Treaty (http://www.scar.org/treaty) as all lands >60ºS, were delineated using the Antarctic Digital Database version 4.0 (http://www.add.scar.org/) and ArcGIS 9.1 by D. Smith of the Australian Antarctic Division. Ice-free areas were divided into nine regions using the subdivisions of

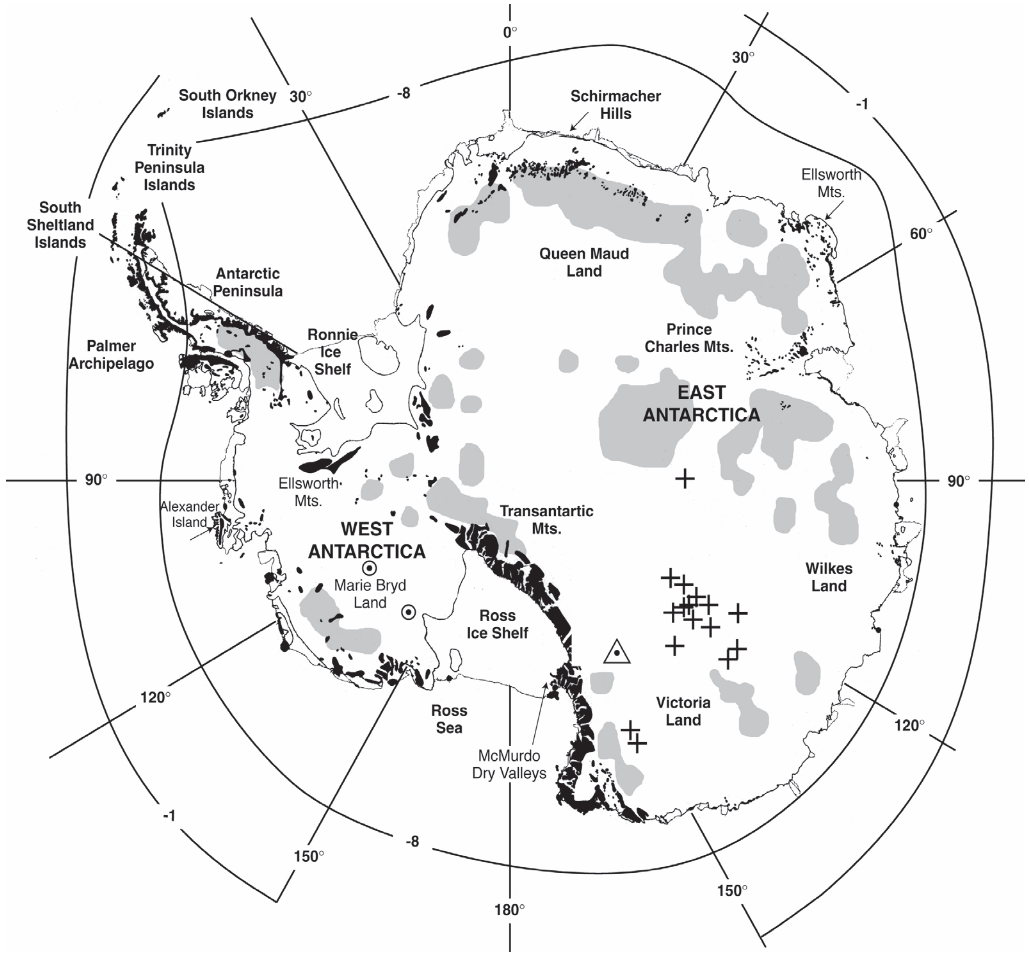

Figure 2. Provisional distribution of permafrost in Antarctica. Ice-free areas are shown in black; grey areas represent the likely location of subglacial permafrost; and crosses indicate the existence of subglacial lakes. The -1°C and -8°C isotherms represent the likely distribution of discontinuous and continuous permafrost, respectively, based on correlations from the Northern Hemisphere (Bockheim 1995).

Greene & others (1967) (Fig. 2). Expert permafrost scientists working in Antarctica were contacted and asked to assist in preparing the following legend: (i) buried ice within the upper 100 cm; (ii) ice-cemented permafrost with the surface within the upper 70 cm; (iii) ice-cemented permafrost with the surface greater than 70 cm; and (iv) dry-frozen permafrost with the surface below 70 cm. For each of these categories, permafrost distribution was divided into

(i) continuous, (ii) discontinuous, and (iii) sporadic or no permafrost. The legend included a color scheme for permafrost maps. In Antarctica, the active layer either grades into ice-cemented permafrost or, in dry areas, into dry-frozen permafrost. In the latter case, the active layer can only be differentiated from dry-frozen permafrost from temperature monitoring.

The distribution of permafrost form by region was determined from the ANTPAS database for regions 4, 5b, 6, and 8 (Table 1). To determine permafrost distribution for the remaining regions, we utilized published data from regions 1, 2, 3, and 7 and inferences from diagnostic ground criteria for regions 5b and 7. These criteria included a stippled pattern and medial moraines on 1:250,000 topographic maps for ice-cored drift and strongly developed patterned ground on high-resolution land satellite images and proximity to stream, lakes, and ponds for ice-cemented permafrost. The remaining areas, particularly in interior mountains and broad central valleys, were assigned to dry-frozen permafrost. The 20 m contour was used to delineate areas where the top of ice-cemented permafrost occurred below 70 cm along the Antarctic Peninsula and its offshore islands.

We were unable to locate sufficient permafrost information for mapping regions 2 (Enderby Land), 3 (MacRobertson Land), 5a (Pensacola Mountains), and 7 (Marie Byrd Land); however, we provide brief summaries of information existing for these areas. Maps (not included in this brief report) were developed for the more-studied regions 1, 4, 5b, 6, and 8, which account for about 38,000 km2 or 85% of the ice-free areas in Antarctica. Because of insufficient data, we were unable to show permafrost thickness and temperatures on the maps.

Table 1. Database and proposed map scales for permafrost mapping in Antarctica.[1]

No.	Region	Subregion	Proposed Map scale	Data available Soils	Data available Permafrost	Electronic data archive	GIS
1	Queen Maude Land	Fimbulheimen	1:1000K	?	?	?	?
		Sør Rondane Mtns.	1:500K	Y	Y	?	?
2	Enderby Land	Scott Mtns.-Amundsen Bay	1:500K	?	?	?	?
3	MacRobertson Land	Mawson Escarpment	1:250K	?	?	?	?
		Prince Charles Mtns.	1:500K	?	?	?	?
		Grove Mtns.	1:250K	Y	Y	?	?
4	Wilkes Land	Windmill Islands	1:50K	Y	Y	?	?
5a	Pensacola Mtns.	Shackleton Range	1:500K	N	N	N	N
		Paxutent Range	1:500K	N	N	N	N
		Thiel Mtns.	1:250K	N	N	N	N
5b	Transantarctic Mtns.	North Victoria Land (69–75ºS)	1:1000K	Y	Y	Y	Y
		Central Victoria Land (75–80º30'S)	1:1000K	Y	Y	Y	Y
		S. Victoria Land (80º30'–86º30'S)	1:1000K	Y	Y	Y	Y
6	Ellsworth Mtns.	Heritage Range	1:500K	Y	Y	Y	N
		Sentinel Range	1:500K	Y	Y	Y	N
7	Marie Byrd Land	Ford Ranges	1:250K	?	?	?	?
8	Antarctic Peninsula	Palmer Land & Alexander Island	1:1000K	?	?	?	?
		Graham Land & Palmer Archipelago	1:1000K	?	?	?	?
		James Ross Archipelago	1:200K	Y	Y	Y	Y
		South Shetland Islands	1:200K	Y	Y	Y	Y
		South Orkney Islands	1:200K	Y	Y	Y	Y

[1] ? = availability of data uncertain; Y = data available; N = data not available; electronic data archive = data available in spreadsheets; GIS = Geographic Information System.

Results

More than 80% of the ice-free area of Antarctica contains continuous permafrost (Table 2). Discontinuous and sporadic permafrost occurs only along the tip of the Antarctic Peninsula and its offshore islands.

The dominant permafrost form is ice-cemented permafrost within 70 cm of the surface, accounting for 43% of the ice-free area in Antarctica. Ice-cemented permafrost is prevalent in coastal areas, including Wilkes Land, Enderby Land, and the Antarctic Peninsula and its offshore islands, and accounts for 60%–93% of the area (Table 2). In terms of total area, ice-cemented permafrost within 70 cm of the surface is most abundant in the Transantarctic Mountains (8000 km^2) and the Antarctic Peninsula (6000 km^2).

Dry-frozen permafrost accounts for 41% of the total ice-free area (Table 3) and is most abundant in Queen Maud Land, the Pensacola Mountains, and the Ellsworth Mountains, accounting for 59%–65% of the area (Table 1). The Transantarctic Mountains contain 11,600 km^2 of dry-frozen permafrost, 57% of the total area.

The total area of buried ice is not completely known. We suggest that this form of permafrost comprises 13% of the total ice-free area (Table 2). Buried ice is most abundant in the Transantarctic Mountains and along the Antarctic Peninsula. Deep (>70 cm) ice-cemented permafrost primarily occurs in coastal areas of East Antarctica and along the Antarctic Peninsula

Table 2. Preliminary estimation of permafrost distribution in Antarctica by region (bold face = estimates).

Region	Area (km^2)	% Ground ice	% Ice-cemented <70 cm	% Ice-cemented >70 cm	% Dry frozen
1	3400	2	58	4	36
2	1500	2	60	30	8
3	5400	6	44	2	48
4	700	2	93	5	0
5a	1500	6	32	0	60
5b	24200	18	33	1	48
6	2100	6	35	1	59
7	1000	2	33	0	65
8	10000	15	60	5	20
Total	49800				

Discussion

Permafrost is dominant in ice-free areas of Antarctica, which contain till-covered and bedrock surfaces occupying 49,800 km^2 of the entire continent. The distribution of permafrost in continental Antarctica is continuous except along the outer Antarctic Peninsula (ca. ≤63ºS) with the

Table 3. Estimated permafrost areas in Antarctica by subregion.

	km²			
Region	Ground ice	Ice-cemented <70 cm	Ice-cemented >70 cm	Dry frozen
1	68	1972	136	1224
2	30	900	450	120
3	324	2376	108	2592
4	14	651	35	0
5a	90	480	30	900
5b	4356	7986	242	11616
6	126	735	0	1239
7	20	330	0	650
8	1500	6000	500	2000
Total	6828	21430	1501	20341
	13.1	*43.0*	*3.0*	*40.8*

northern boundary roughly following the -8ºC isotherm for mean annual air temperature. Recent findings (Serrano & López-Martinez 2000, Vieira et al. 2006) have validated Bockheim's (1995) proposal that the southern limit is defined by the -1ºC isotherm for mean annual air temperature. In the South Shetland Islands discontinuous permafrost exists at elevations between 40 and 20 m a.s.l, and permafrost is either sporadic or lacking below 20 m. In this area, altitude, topography, soil characteristics, and slope orientation affect permafrost occurrence and distribution.

In the South Shetland and South Orkney Islands, the active layer thickness appears to be strictly related to surface characteristics such as snow distribution and vegetation type and coverage (Cannone et al. 2006).

Ice-cemented permafrost within the upper 70 cm is the dominant form in Antarctica, accounting for 43% of the ice-free area. This type of permafrost occurs in coastal areas and adjacent to water bodies and on predominantly younger land surfaces throughout the continent. Dry-frozen permafrost is unique to Antarctica and occurs on predominantly older land surfaces especially in broad valleys in the McMurdo Sound area and inland mountains throughout the continent. It accounts for 41% of the ice-free area. Buried ice is ubiquitous in Antarctica in ice-cored moraines of Holocene age along major outlet glaciers and the coast. Ice buried by drift occurs along the Polar Plateau. Buried ice overlain by ablation till occurs sporadically and in places in thought to be of Miocene age (Sugden et al. 1999).

Conclusions

This text is intended to accompany maps at different scales depicting permafrost and buried ice of the Antarctic region (≥60ºS). Based on our analysis, 43% of the ice-free areas contain ice-cemented permafrost in the upper 70 cm, followed by dry-frozen permafrost (41%), and buried ice (13%). Permafrost is continuous throughout East Antarctica and along the Antarctic Peninsula and the surrounding islands at elevations above 40 m. Discontinuous permafrost exists at elevations between 40 and 20 m, and permafrost is either sporadic or lacking in coastal areas below 20 m.

Acknowledgments

This report is the collective effort of the IPA working group on Antarctic Permafrost and Periglacial Environments. The authors gratefully acknowledge the contributions of ANPAS members, including M. Balks, G.G.C. Claridge, N. Matsuoka, M. McLeod, M. Ramos, E. Serrano, D. Smith, G. Vieira, and others.

References

Berg, T.E. & Black, R.F. 1966. Preliminary measurements of growth of nonsorted polygons, Victoria Land, Antarctica. American Geophysical Union, *Antarctic Research Series* 8: 61-108.

Black, R.F. 1973. Growth of patterned ground in Victoria Land, Antarctica. In: *Permafrost: North American Contribution, Second International Conference; Genesis, Composition, and Structure of Frozen Ground and Ground Ice, National Academy of Sciences, Washington, DC*, 193-203.

Blume, H.-P., Kuhn, D. & Bölter, M. 2002. Soils and landscapes. In: L. Beyer & M. Bölter (eds.), *Geoecology of Antarctic Ice-Free Coastal Landscapes*. Berlin: Springer-Verlag.

Bockheim, J.G. 1995. Permafrost distribution in the Southern Circumpolar Region and its relation to the environment: a review and recommendations for further research. *Permafrost & Periglacial Processes* 6: 27-45.

Bockheim, J.G., Campbell, I.B. & McLeod, M. 2007. Permafrost distribution and active layer depths in the McMurdo Dry Valleys, Antarctica. *Permafrost & Periglacial Processes* 18: 217-227.

Bölter, M., Blume, H.-P., Schneider, D. & Beyer, L. 1997. Soil properties and distributions of invertebrates and bacteria from King George island (Arctowski Station), maritime Antarctic. *Polar Biology* 18: 295-304.

Campbell, I.B. & Claridge, G.G.C. 2006. Permafrost properties, patterns and processes in the Transantarctic Mountains region of Antarctica. *Permafrost & Periglacial Processes* 17: 215-232.

Cannone, N., Ellis Evans, J.C., Strachan, R. & Guglielmin, M. 2006. Interactions between climate, vegetation and active layer in Maritime Antarctica. *Antarctic Science* 18(3): 323-333.

Chambers, M.J.G. 1966b. Investigations on patterned ground at Signy Island, South Orkney Islands: II. Temperature regimes in the active layer. *British Antarctic Survey Bulletin* 10: 71-83.

Denton, G.H., Bockheim, J.G., Rutford, R.H. & Andersen, B.G. 1992. Glacial history of the Ellsworth Mountains, West Antarctica, pp. 403-432. *In* Webers, G.F., Craddock, C. & Splettstoesser, J.F. (eds.) *Geology and paleontology of the Ellsworth Mountains, West Antarctica*. Geol. Soc. Am. Memoir 170.

Denton, G.H., Bockheim, J.G., Wilson, S.C. & Schlüchter, C. 1986. Late Cenozoic history of Rennick Glacier and Talos Dome, northern Victoria Land, Antarctica. In: Stump, E. (ed.) *Geological Investigations of Northern Victoria Land*. American Geophysical Union, Antarctic Res. Ser. 46:339-375.

Everett, K.R. 1976. *A survey of the soils in the region of the South Shetland Islands and adjacent parts of the Antarctic Peninsula*. Institute of Polar Studies, Report No. 58, Ohio State University, Columbus, OH, 44

Estimation of Ice Wedge Volume in the Big Lake Area, Mackenzie Delta, NWT, Canada

Jenifer A. Bode
Department of Geography, University of Calgary, Calgary, Canada
Brian J. Moorman
Department of Geography, University of Calgary, Calgary, Canada
Christopher W. Stevens
Department of Geoscience, University of Calgary, Calgary, Canada
Steve M. Solomon
Natural Resources Canada, Halifax, Nova Scotia, Canada

Abstract

With potential development of the Mackenzie Gas Pipeline in northern Canada, it becomes increasingly necessary to understand all aspects of the permafrost environment affected by this project. A major concern with development is terrain disturbance within the Kendall Island Bird Sanctuary, resulting in an alteration of the subsurface thermal regime. Warming of the subsurface could lead to the melting of excess ground ice causing further subsidence. A combination of Ground Penetrating Radar (GPR) and remote sensing data were used to map the distribution of excess ground ice. The volume of wedge ice was calculated and then combined with a high-resolution digital elevation model to determine the location and amount of potential subsidence that could be induced by melting of subsurface excess ground ice. Although the distribution of excess ice in the Big Lake area is not uniform, its presence is substantial enough that melting may result in significant terrain alteration.

Keywords: Big Lake; digital elevation model; ground penetrating radar; ground subsidence; ice wedges; Mackenzie Delta.

Introduction

Several large hydrocarbon fields have been discovered in the Mackenzie Delta area, NWT, Canada (Fig. 1). One of these is the Taglu gas field which is estimated to contain 2.8 trillion cubic feet of natural gas and natural gas liquids (Imperial Oil Resources Limited 2004). The Taglu field is located within the Kendall Island Bird Sanctuary. Alteration of the landscape in this area could alter sensitive bird habitat.

There is concern that with alteration of the landscape there will be a disturbance of the subsurface thermal regime which could lead to the melting of ground ice. The objective of this research is to estimate the volume of ice contained within ice wedges in order to calculate the potential subsidence and terrain disturbance that could result from the warming of the subsurface. This study focuses solely on ice wedges as they contribute to significant volumes of excess ice in the study area.

Ice wedge formation has been widely studied (Mackay 1974, Murton & French 1993, Murton 2001). However, estimating ice wedge volume has remained difficult as measuring the depth and shape in the subsurface is usually limited to coring. Obtaining core data is expensive and logistically very difficult at Big Lake, so alternative methods were used in an attempt to quantify ice wedge volume. Their linear dimensions and width are in some cases relatively easy to measure photogrammetrically, but their depth is difficult to measure by drilling due to the narrow shape of the wedge.

Previous studies (Arcone et al. 1982, Kasper 1996, Hinkel et al. 2001, Fortier & Allard 2004, Munroe et al. 2007) have shown that it is possible to identify the location of ice wedges using Ground Penetrating Radar (GPR). However, estimates of ice wedge volume have not been determined using GPR. For this project we use GPR and a geographic information system to measure the length, width, and depth of the ice wedges and estimate the total volume of ice and maximum potential subsidence.

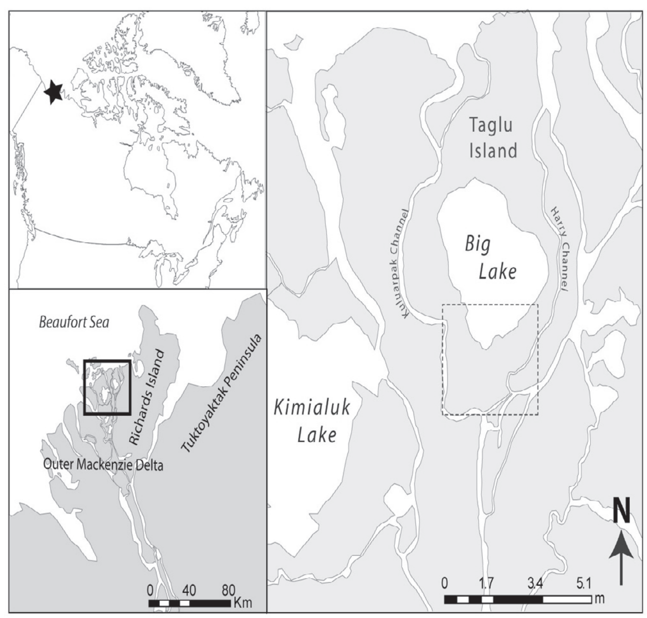

Figure 1. Location of the study area in the outer Mackenzie Delta, NWT, Canada. The study site, located south of Big Lake, is outlined with a dashed line.

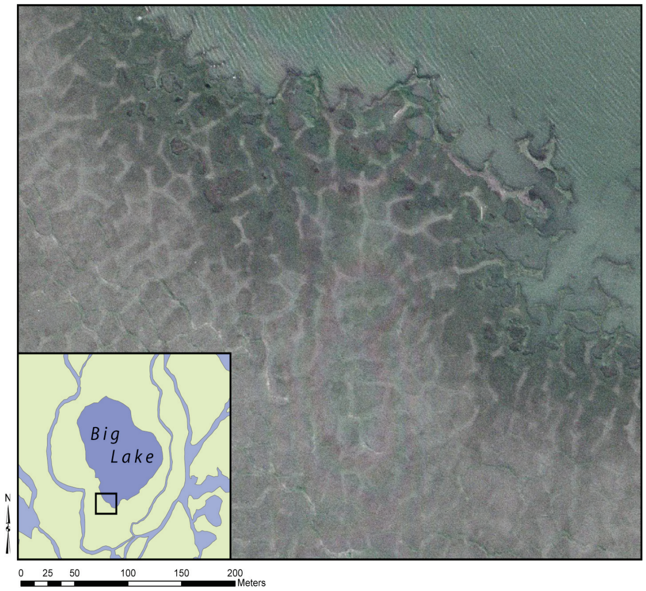

Figure 2. A portion of the aerial photo that shows the surficial expression of ice wedges in the southern portion of Big Lake.

Excess Ground Ice and Land Subsidence

Extraction of natural gas, and subsequent reduction of reservoir pressure, has previously been shown to cause subsidence of the overlying sediment (Geertsma 1973, Doornhof 1992, Teatini et al. 2005). At the Taglu site subsidence from gas extraction is estimated to be a maximum of 0.38 m in the center of the subsidence bowl (Haeberle et al. 2004). However, these estimates do not account for the thawing of permafrost and melting of excess ground ice (Haeberle et al. 2004, Haeberle et al. 2005). The center of the subsidence bowl is located just south of the southern shore of Big Lake; therefore it is likely that subsidence will lead to inundation of the surrounding terrain and expansion of the lake. With inundation, the water will act as a heat source and warm the subsurface (Williams & Smith 1989). If excess ground ice is present, a warming of the subsurface could result in a positive feedback mechanism of excess ice melt causing further subsidence.

Study Area

The Mackenzie Delta is the second largest arctic delta in the world and is a product of the largest river in Canada, the Mackenzie River. The delta is composed of many islands one of which is Taglu Island (Fig. 1). This region of the delta was likely ice free around 12.5 ka BP (Duk-Rodkin & Lemmen 2000). Permafrost beneath the Island extends 500–620 m (Taylor et al. 2000). On the southern tip of Taglu Island a Circumpolar Active Layer Monitoring (CALM) grid indicates an average active layer depth of 95 cm (average from 1998–2002)(Brown et al. 2003). Shallow drilling data indicated fine-grained sand overlain by silt and a thin layer of organic peat. Excess ground ice in the form of ice lenses ranges from 20–50% by volume in the upper 6 m (Traynor & Dallimore 1992).

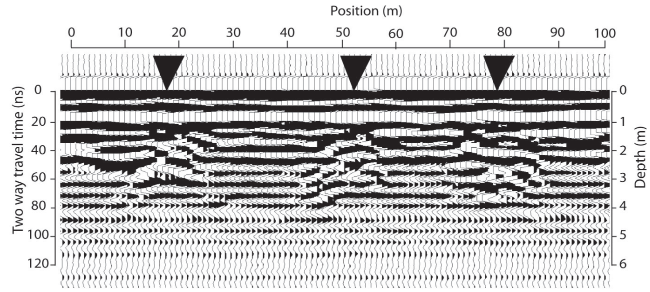

Figure 3. A 100 MHz GPR profile that shows the location of ice wedges. The ice wedges are indicated by the triangles above the profile.

The most prominent feature of Taglu Island is Big Lake which occupies 25% of the island (Fig. 1). Big Lake lies between two levees created by Kulurpak channel to the west and Harry channel to the east. The low lying land surrounding the lake is periodically flooded in the spring when the river overtops the levees. Flooding also occurs in the fall due to flooding from infrequent storm surges. However, Big Lake is cut off from the main channel for most of the year making it a low closure lake (Mackay 1963). The lake is surrounded by low centered, (Traynor & Dallimore 1992) non-oriented ice wedge polygons with an average diameter of approximately 20 m.

This study focuses on the southwestern shore of Big Lake where the estimated subsidence bowl is centered and the largest amount of data is available. The borders of the study area were determined by the availability of elevation data and the extent of the modeled subsidence bowl.

Methods

Volumetric estimates of ice wedges have previously been determined using aerial photos (Pollard & French 1980). However we use a combination of remote sensing and geophysical data to estimate the volume of ground ice. Aerial photography was used to determine the length and width of the ice wedges (Fig. 2) and GPR data were used to determine ice wedge depth. From these three variables, the volume of ice can be estimated using:

$$V = \frac{1}{2} * L * W * (D - D_{AL}) \quad (1)$$

where L is the total length of ice wedges visible on the aerial photographs, W is the average width of the ice wedges, D is the average depth of the ice wedges, and D_{AL} is the average active layer depth. This is assuming a triangular cross-section of the ice wedges. Field observations from the study area suggest that a triangular cross-section is a reasonable assumption (Mackay 1963).

The GPR response to ice wedges is based on the dielectric contrast between frozen sediment and ice. Radar patterns produced by ice wedges include secondary reflections from the reverberation of energy within the ice and hyperbolic reflections from the wedge acting as a point source (Arcone et al. 1982). Hyperbolas are frequently centered at the top

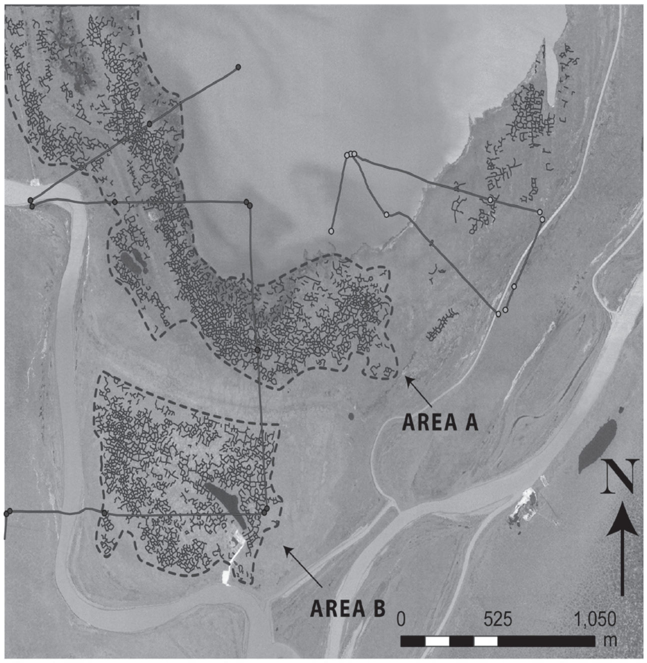

Figure 4. All the ice wedges digitized in the study area. The two areas where ice wedges are concentrated are outlined with the dashed line. Area A is the focus of this paper. The GPR transects surveyed in this study are indicated by the solid black lines.

(Fig. 3) and at the base of the ice wedge (Fortier & Allard 2004).

In March of 2007, GPR data was collected at the Taglu site using a PulseEKKO 100 with 100 MHz antennas and a 400 V transmitter. The GPR antennas were pulled behind a Tucker Sno-Cat® traveling at a constant speed of 5 km/hr. The vehicle was able to keep a steady speed higher than the resolution of the GPS. Data were collected in continuous mode and the average step size was 0.9 m. A total of 22 GPR transects were collected around the southern half of Big Lake (Fig. 4). The location of the GPR transects was determined with a GPS receiver that automatically tagged every trace with its position and elevation as it was collected. An average velocity for frozen sediment (0.1 m/ns) was used to convert travel time measurements to calculated radar depth.

Aerial photographs (Indian and Northern Affairs Canada 2004) of the southern portion of Taglu Island were used to identify the spatial extent of ice wedges (Fig. 4). The photographs were taken in August 2004 and have a resolution of 1.25 m. Every ice wedge was digitized to measure the length, which was used to calculate the total length of all visible ice wedges within the study area. To determine the average width, the trough of the ice wedge was measured from aerial photos. The trough width is not always equal to the actual ice wedge width however they are often comparable as shown in the data of Kokelj et al. (2007). Measurements were made at the mid-point between the junctions of the ice wedge using the measure tool in ArcGIS.

Ice wedge depths were calculated from the hyperbolic reflections caused by the base of the wedge. The depth to the bottom of the ice wedges was more difficult to determine since it was not always possible to interpret the basal

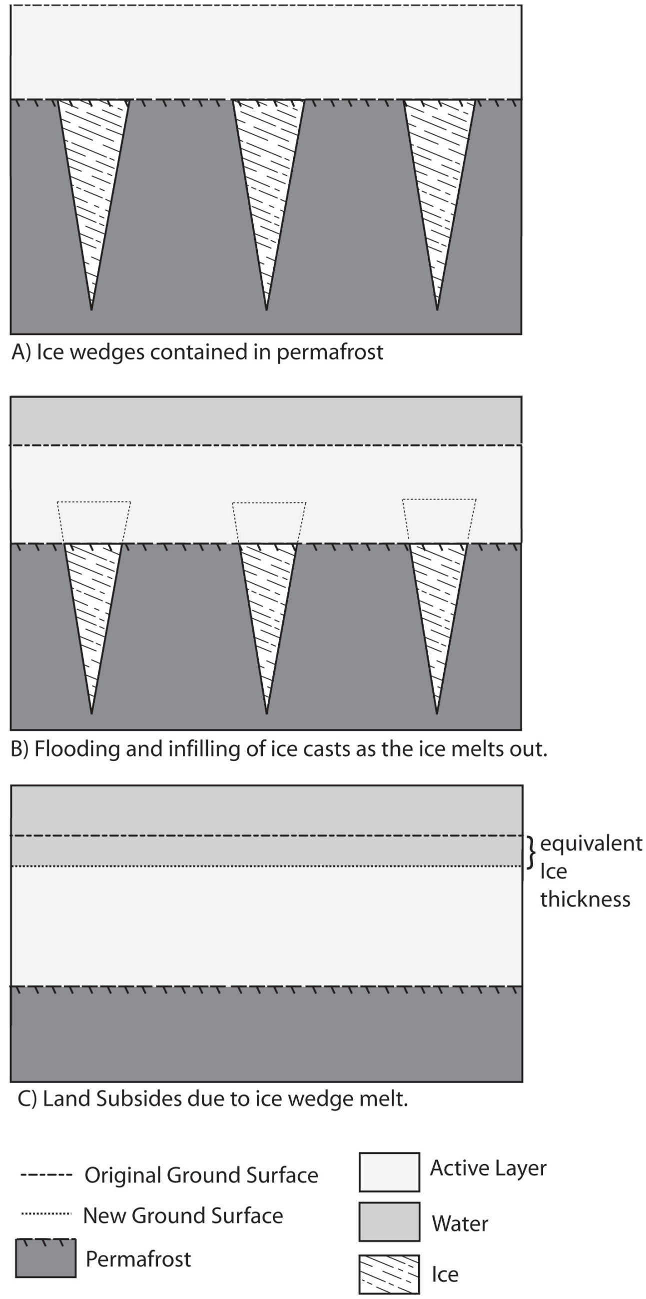

Figure 5: Schematic illustration of ground subsidence caused by flooding of the landscape (A), deepening of the active layer (B), and melt of the equivalent ice thickness (C).

reflections of the wedges from the GPR profile.

Here we consider the worst-case scenario where all of the volume of ice melts. Little research has been conducted to address the nature of ground subsidence caused by ice wedge degradation. Therefore, a uniform approach to ground subsidence was adopted. The term *equivalent ice thickness* was used to represent the estimated volume of ice wedge ice uniformly distributed over the study area (Fig. 5). The ice wedge volume was divided by the total area underlain by ice wedges in Area A to determine the equivalent ice thickness. The equivalent ice thickness was then applied uniformly over Area A and subtracted from a digital elevation model

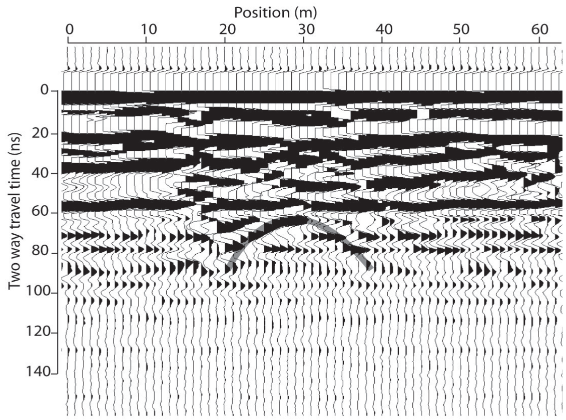

Figure 6. A portion of a GPR transect that shows the bottom of an ice wedge (highlighted). The bottom of the ice wedge is at the top of the hyperbola.

(DEM). The draft version of a DEM created from 1:30,000 air photos was obtained from the Northwest Territories Centre for Geomatics. The vertical accuracy of the DEM is ±1.5 m and is therefore not sufficient to obtain accurate results of subsidence due to ice wedge melting. However, we use it here for illustrative purposes since it is the best available dataset. DEMs developed from LiDAR are more appropriate for these types of analyses, but there are no publicly available data for this location.

Results

The ice wedges in the study area were primarily concentrated in two locations; the southwestern edge of Big Lake (Area A) and the southern portion of Taglu Island (Area B) (Fig. 4). Since the area of ice wedges closest to Big Lake would be most affected by lake expansion, Area A was the focus of this investigation. The total area of Area A is 2,940,040 m^2. The total length of ice wedges in this area was 95,525 m. The average width of the ice wedges was 3.9 m ±0.5 m (n = 225, max. = 5.8 m, min. = 1 m). The ice wedges ranged from 3.5 to 4 m in depth (n = 12) (Fig. 6). Minimum and maximum subsidence scenarios were both calculated as the number of ice wedge depth measurements was limited.

Using Equation 1 the volume of ice in Area A was calculated to be 471,655 m^3 using the minimum depth estimate and 754,650 m^3 using the maximum depth estimate. These volumes were then divided by the total area of Area A to calculate equivalent ice thicknesses of 0.17 m and 0.27 m for the minimum and maximum scenarios.

Figure 7 illustrates the effect of surface subsidence from the melt out of ice wedges on surface topography and shore location.

Discussion

The potential resultant area flooded by the melt out of ice wedges is likely to be irregular in character; however, with a uniform subsidence using the previously discussed equivalent ice thicknesses, a minimum of 274,790 m^2 of land would be flooded by ice melt alone (Fig. 7). With the

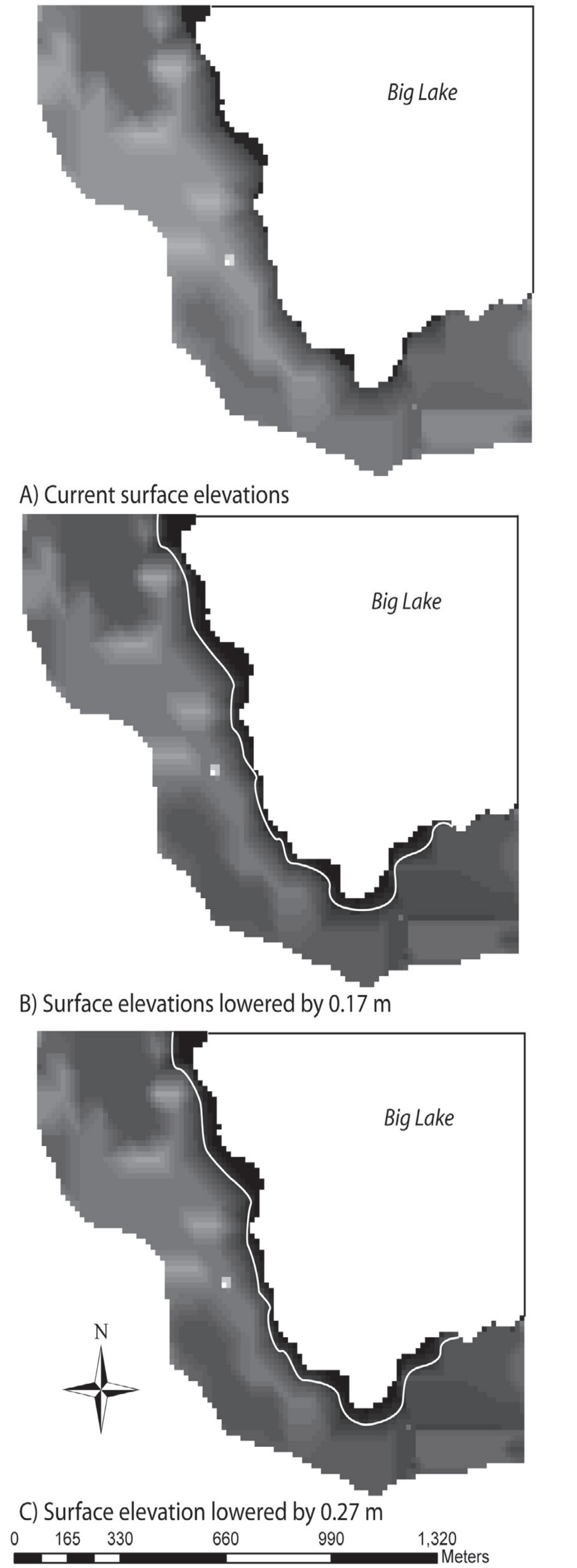

Figure 7. Topography of Area A to the southwestern edge of Big Lake. A) Displays the current terrain elevations (Northwest Territories Centre for Geomatics 2004), B) surface elevations minus 0.17 m and C) surface elevations minus 0.27 m. The 0.9 m white line in B and C indicates the extent of lake expansion. The water level at Big Lake, according to the dataset is 0.9 meters above sea level (m a.s.l.) therefore anything below 0.9 m a.s.l. will become flooded.

Figure 8. Flooded ice wedge polygons in the Mackenzie Delta. Subsidence appears to be spatially variable.

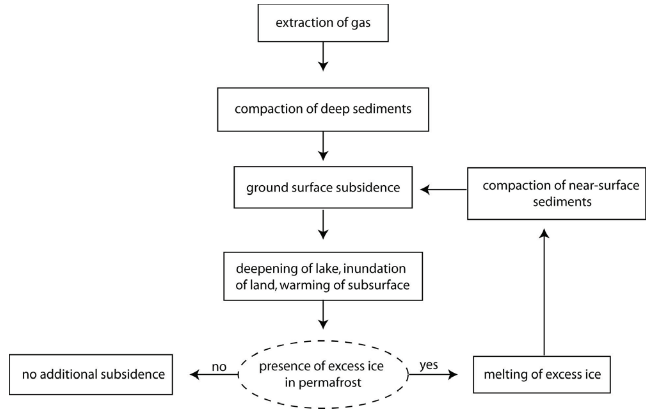

Figure 9. Flow chart illustrating the positive feedback that could be initiated by ground subsidence induced by natural gas extraction.

maximum depth scenario 343,715 m^2 would be flooded. The shoreline would move inland by over 75 m in some locations. These estimates are based on land below 0.9 m a.s.l. becoming flooded as that is the lake level from the DEM. Under a scenario of irregular subsidence concentrated at the zones immediately surrounding the central axes of the wedges, much greater flooding would occur reaching completely across Area A. Figure 8 illustrates another area in the Mackenzie Delta where irregular flooding of ice wedge polygons has occurred.

This study focused only on a small area on the southern part of Taglu Island due to the availability of elevation data and imagery. Ice wedges can also be seen on the northern portion of Taglu Island, therefore there is potential for ice wedge melt and flooding over a greater area surround the lake. Additionally, smaller bodies of ice, such as ice lenses, were resolved from GPR profiles. These ice lenses, if melted, would also cause ground subsidence.

For this initial estimate, subsidence was calculated using the equivalent ice thickness, therefore, the spatial variability in ice content is not taken into account. The actual character of subsidence may play a significant role in determining the resultant topography and the extent of flooding. Additionally, it is possible that the ice at depth could be maintained even with a deepening of the active layer. Consequently, we have calculated the worst case scenario where ice wedges completely melt. It should also be noted that these maps do not take into account the modeled subsidence bowl caused by natural gas extraction, as discussed earlier.

If considering the compounded effects of ground subsidence caused by both ice wedge melt and natural gas extraction over half of the study area would be flooded. Subsidence caused by gas extraction is estimated to be up to 0.38 m (Haeberle et al. 2004). If this subsidence were to occur a positive feedback loop could be initiated (Fig. 9). With initial subsidence, flooding could occur causing melt of excess ground ice leading to further subsidence and flooding. However, it must be acknowledged that there is also the potential that permafrost and ice wedges could remain stable and potentially even cool if flooding remains shallow.

Although the objectives of this research focused on assessing subsidence due to ice wedge melt, there are other potential causes of terrain disturbances. For example, climate warming could cause a deepening of the active layer and the melting of ground ice. Eustatic sea level rise and changes in the magnitude of seasonal flooding could also lead to excess ice melt. There are other processes that could result in changes of surface elevation such as isostatic rebound, sediment compaction, and frost heave.

This work builds on the study of Pollard and French (1980) which only used aerial photos and estimations of ice wedge depth. The result of this current research provides an initial attempt to estimate ice wedge volume using a combination of aerial photos and GPR data. Further verification of ice cross-sectional area, geometry near the junction of ice wedges, the character of ice wedge degradation due to flooding, and excess ice in other forms is required to further refine the quantification of excess ice and impact of subsidence and flooding.

Conclusions

Estimation of excess ice content from drilling is time consuming, difficult, expensive, and only provides point source data. Using GPR and aerial photographs, an estimation of ice wedge ice volume can be made over a large area in a relatively short time. The surficial expression of ice wedges at this location made it possible to measure their total length and width from aerial photographs. GPR was used successfully to identify the base of the ice wedges and determine ice wedge depth. By combining this data, the total volume of excess ice contributed by ice wedges was estimated. Applying these estimates to a DEM allowed for predictions to be made of the role of ice wedges may have on terrain subsidence and subsequent flooding. At the Taglu site the estimated ice volume is significant enough that if the subsurface warms and melts excess ice, subsidence leading to extensive flooding of land could occur.

Acknowledgments

Financial support for the research was provided by NSERC. The authors thank Chevron and the crew at Camp Farewell for accommodations and hospitality. The authors would also like to thank Steve Kokelj for providing insight and information.

References

Arcone, S.A., Sellmann, P.V. & Delaney, A.J. 1982. *Radar Detection of Ice Wedges in Alaska.* U.S. Army Cold Regions Research and Engineering Laboratory: CRREL Report 82-43, 15 pp.

Brown, J., Hinkel, K. & Nelson, F. (comp.). 2003. Circumpolar Active Layer Monitoring (CALM) program network: description and data. In: M. Parsons & T. Zhang (eds.), International Permafrost Association Standing Committee on Data Information and Communication (comp.). 2003. *Circumpolar Active-Layer Permafrost System, Version 2.0.* Boulder, CO: National Snow and Ice Data Center/World Data Center for Glaciology. CD-ROM.

Doornhof, D. 1992. Surface subsidence in The Netherlands: the Groningen gas field. *Geologie en Mijnbouw* 71: 119-130.

Duk-Rodkin, A. & Lemmen, D.S. 2000. Glacial history of the Mackenzie Region. In: L.D. Dyke & G.R. Brooks (eds.), *The Physical Environment of the Mackenzie Valley, Northwest Territories: A Base Line for the Assessment of Environmental Change.* Geological Survey of Canada Bulletin 547: 11-20.

Fortier, D. & Allard, M. 2004. Late Holocene syngenetic ice wedge polygons development, Bylot Island, Canadian Arctic Archipelago. *Canadian Journal of Earth Sciences* 41: 997-1012.

Geertsma, J. 1973. Land subsidence above compacting oil and gas reservoirs. *Journal of Petroleum Technology* 25: 734-744.

Haeberle, D.C., Pakal, R., Asmann, M. & Duffy, B.W. 2004. Taglu surface subsidence study. *Northern Gas Project Joint Review Panel.* http://www.ngps.nt.ca/ Upload/Proponent/Imperial %20Oil%20Resources%20 Ventures%20Limited/IORVL_R2_NRCAN_004%20 Attach_2.04-1_Taglu_Surface%20_Subsidence_ Study_Report. pdf. Retrieved February 25, 2007.

Haeberle, D.C., Hsu, S. & Asmann, M. 2005. Taglu surface subsidence study - addendum. *Northern Gas Project Joint Review Panel.* http://www.ngps.nt.ca/ Upload/ Proponent/Imperial %20Oil%20Resources%20Ventures%20Limited/IORVL_R2_NRCAN_004%20Attach_2.04-1_Taglu _Surface%20_Subsidence_Study_ Report_ Addendum.pdf. Retrieved February 25, 2007.

Hinkel, K.M., Doolittle, J.A., Bockheim, J.G., Nelson, F.E., Paetzold R., Kimble, J.M. & Travis R. 2001. Detection of subsurface permafrost features with ground penetrating radar, Barrow, Alaska. *Permafrost and Periglacial Processes* 12: 179-190.

Imperial Oil Resources Limited. 2004. *Application for the Approval of the Development Plan for Taglu Field: Project Description.* Calgary: Submitted to National Energy Board.

Indian and Northern Affairs Canada. 2004. *Mackenzie Valley Airphoto Project.* 2004, Airphoto 1:30,000 [Photo No. 500769]. Yellowknife, NWT.

Kasper, J. 1996. *Geomorphic, Geophysical and Quaternary Studies of Ice and Soil Wedge Features in the Foucault River valley, Northern Quebec.* Ph.D. Thesis. Université Laval, 277 pp.

Kokelj, S.V., Pisaric, M.F.J. & Burn, C.R. 2007. Cessation of ice-wedge development during the 20th century in spruce forests of eastern Mackenzie Delta, Northwest Territories, Canada. *Canadian Journal of Earth Sciences* 44: 1503-1515.

Mackay, J.R. 1963. *The Mackenzie Delta area, N.W.T.* Canadian Department of Mines and Technology Geographical Branch Memoir 8, 202 pp.

Mackay, J.R. 1974. *The Rapidity of Tundra Polygon Growth and Destruction, Tuktoyaktuk Peninsula-Richards Island Area, N.W.T.* Current research Part A Geological Survey of Canada paper 74-1A: 391-392.

Munroe J.S., Doolittle, J.A., Kanevskiy, M.Z., Hinkel, K.M., Federick, E.N., Jones, B.M., Shur, Y. & Kimble, J.M. 2007. Application of ground penetrating radar imagery for three-dimensional visualization of near-surface structures in ice-rich permafrost, Barrow, Alaska. *Permafrost and Periglacial Processes* 18: 309-321.

Murton, J.B. & French, H.M. 1993. Thaw modification of frost fissure wedges, Richards Island, Pleistocene Mackenzie Delta, western Arctic Canada. *Journal of Quaternary Science* 3: 185-196.

Murton, J.B. 2001. Thermokarst sediments and sedimentary structures, Tuktoyaktuk Coastlands, western arctic Canada. *Global and Planetary Change* 28: 175-192.

Northwest Territories Centre for Geomatics, 2004. *Mackenzie Valley Gas Project files, D5 Contours and DEMS.* Indian and Northern Affairs Canada.

Pollard, W.H. & French, H.M. 1980. A first approximation of the volume of ground ice, Richards Island, Pleistocene Mackenzie Delta, Northwest Territories, Canada. *Canadian Geotechnical Journal* 17: 509-516.

Taylor, A., Burgess, M.M., Judge, A.S. & Allen, V.S. 2000. Deep Ground Temperatures. In: L.D. Dyke & G.R. Brooks (eds.), *The Physical Environment of the Mackenzie Valley, Northwest Territories: A Base Line for the Assessment of Environmental Change.* Geological Survey of Canada Bulletin 547**,** 153-158.

Teatini, P., Ferronato, M., Gambolati, G., Bertoni, W. & Gonella, M. 2005. A century of land subsidence on Ravenna, Italy. *Environmental Geology* 47: 831-846.

Traynor, S. & Dallimore, S.R. 1992. *Geological Investigations of Proposed Pipeline Crossings in the Vicinity of Taglu and Niglintak Islands, Mackenzie Delta, NWT*. Geological Survey of Canada, Open File Report 2552, 109 pp.

Williams, P.J. & Smith, M.W. 1989. *The Frozen Earth: Fundamentals of Geocryology.* Cambridge: Cambridge University Press, 360 pp.

High-Resolution DEM Extraction from Terrestrial LIDAR Topometry and Surface Kinematics of the Creeping Alpine Permafrost: The Laurichard Rock Glacier Case Study (Southern French Alps)

Xavier Bodin, Philippe Schoeneich
University Paris Diderot (Paris 7)/Institute of Alpine Geography, Joseph Fourier University, Grenoble, France
Stéphane Jaillet
EDYTEM laboratory, University of Savoie, Le Bourget-du-Lac, France

Abstract

The most common landforms associated with the creep of Alpine permafrost are the rock glaciers, the morphology of which reflects the complex processes of the internal deformation of the ice and debris mixture. In the present study, a terrestrial LIDAR device was employed to scan, at a sub-decimeter resolution, the surface of the Laurichard active rock glacier (Southern French Alps). Two points-clouds were generated at one-year interval (Sept. 2005 and Sept. 2006) and processed in order to produce two high-resolution digital elevation models (DEMs) and to compare them. Different methods were used in order to extract small-scale topography, quantify interannual surface changes, and determine the kinematic behavior of the creeping mass. For a better understanding of rock glacier dynamics, the results have also been compared to the geodetic measurements annually over a 20-year period, and to the geophysical evidences of rock glacier internal structure.

Keywords: alpine permafrost; French Alps; high-resolution DEM; LIDAR; rock glacier morphology; surface kinematics.

Introduction

The long term, steady-state and slow deformation of ice-supersaturated sediments, which generates specific landforms called rock glaciers, is dependent on various parameters such as the ice/debris mixture thickness, the local slope angle, the ice and water content, or the depth of the basal shear zone (Haeberli 1985, Barsch 1992, Arenson et al. 2002, Haeberli et al. 2006). Recent investigations have also suggested that, at an interannual scale, the main controlling factor of rock glacier deformation rate may be the thermal state of the permafrost body (Ikeda 2004, Roer et al. 2005, Kääb et al. 2006).

Previous studies on rock glacier surface kinematics have classically used remote-sensing techniques (Kääb et al. 1998, Kaufmann et al. 2005), which provide a good spatial resolution but only on mid- to long-term trends of the creeping activity, or geodetic surveys (Delaloye 2004, Lambiel & Delaloye 2004, Kaufmann et al. 2006), which are often carried out at an annual time-scale but with a limited spatial resolution.

Recent development of the LIDAR (Light Detection And Ranging) technique allows fast and accurate acquisition of the topography with very high resolutions. Using terrestrial devices, several millions of points may be acquired in one day, and entire slopes (≈10^4 m^2) and landforms may be scanned. Therefore, it appears a promising tool to produce high-resolution digital elevation models (HR-DEMs) that have, until now, rarely been used to study surface changes and related processes in the glacial (Bauer et al. 2003, Avian & Bauer 2006) or periglacial geomorphology.

In this study, a medium-range terrestrial LIDAR was employed during two successive years to scan the surface of a rock glacier.

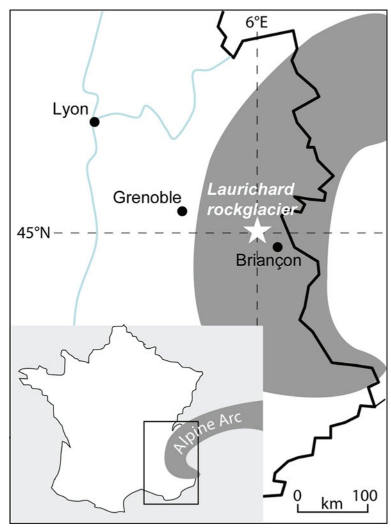

Figure 1. Location of the Laurichard rock glacier, in the Southern French Alps.

The investigated landform is the Laurichard rock glacier in the Southern French Alps (Fig. 1), which is a 500 m long, tongue-shaped, active rock glacier. As it is surveyed since 1979 with annual geodetic measurements of 28 marked blocks (Francou & Reynaud 1992), its mean surface velocities are known to range from 0.2 m/yr at the root and at the front to 1.2 m/yr in its steepest central part.

Beyond the necessity to test the applicability of the terrestrial LIDAR on a very rough and complex terrain, the main goals of this study were to perform multi-scale morphometric measurements, to quantify the interannual surface changes, and to determine the kinematic behavior of the creeping mass.

Acquiring High-Resolution DEM in an Alpine Environment

Data acquisition

The device (Ilris-3D, Optech; wavelength: 1500 nm) used in the present study is able to acquire 2500 points per second, with a centimetre accuracy (8 mm at 100 m) and at a maximal range of about 1000m. The limiting factors that can reduce the LIDAR measurements quality are the presence of non-reflective surfaces, such as snow, and the occurrence of very humid or foggy atmospheric conditions.

The small-scale morphology of the rock glacier, composed of extensive (longitudinal ridges) or compressive (transversal convex ridges and furrows) flow structures, has made it imperative to multiply the angles of view. Hence, during the two field campaigns (September 2005 and September 2006) four stations and 14 to 17 scenes (between 1 and 4 per station) were necessary each time to scan the whole surface of the rock glacier and to minimise shadowed areas (Fig. 2). In addition, five fixed points, outside the rock glacier, were measured with DGPS (Differential GPS), enabling a centimeter precision for the georeferencing of each DEM.

With a mean resolution of 7 cm (it varies according to the distance between the LIDAR and the target) two clouds of 10–15 millions points were generated.

Data processing

The raw datasets, that consist in x, y, and z coordinates (reflectance and colorimetric information have not been used), have to undergo several processing steps before being usable for further treatments. The PolyWorks (© InnovMetrics 2005) software, dedicated to the processing of 3D point clouds, was hence used to:

1. align and adjust the scenes together, thanks to common overlapping areas,
2. reduce the redundancy where a high density is not necessary,
3. grid the data to obtain either a polygonal model or a regularly spaced model,
4. georeference one polygonal model, thanks to using the DGPS points by the manual recognition of the blocks, and
5. align the two polygonal models on their common stable parts.

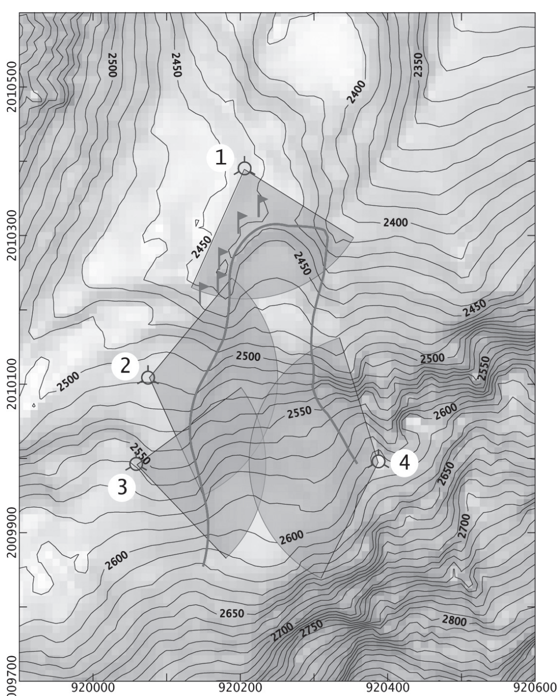

Figure 2. Position of the four stations (circles and numbers), of the corresponding scanning windows (circle portions) and of the fives fixed points (flag) used to scan the surface of the rock glacier (bold line). Geographic coordinates and elevations are in meters.

Finally, three types of processed data are available for further analysis: initial point clouds (17 in 2005, 14 in 2006, plus the 2 final aligned ones); two polygonal models (one per year); and two regularly-spaced models (one per year, at resolution of 0.5 and 1 m).

The Use of High-Resolution DEM to Quantify Rock Glacier Morphology and Surface Kinematics

Morphometric analysis of the rock glacier

Because of the presence of snow on the upper part of the rock glacier during the 2006 campaign, only the 2005 data were used.

First, a detailed map of the main morphological features has been established and verified in the field (Fig. 3). Interesting elements, such as the limits of the different flowing units or the variable roughness of the surface, can be extracted.

Second, the use of morphometric parameters has allowed a fine quantitative description of the rock glacier topography. Slope, microtopography (μz) after Kääb (2005), and roughness (ρz) index were computed along the main flow line by the following formulas:

$$\mu z_n = \frac{\sum_{n+2}^{n-2} z_n}{5} - \frac{\sum_{n+25}^{n-25} z_n}{51} \tag{1}$$

$$\rho z_n = z_n - \frac{\sum_{n+10}^{n-10} z_n}{21} \tag{2}$$

This allows several parts with homogeneous morphometric characteristics to be distinguished (Fig. 4):

a) the scree slope at the contact between the rock wall (slope >37°) is marked on its upper part by a deep concavity, which actually corresponds with the “randkluft” of the rock glacier (massive ice is commonly observed);
b) the upper convex part of the central slope where transversal microtopography is almost absent due to high, extensive flow;

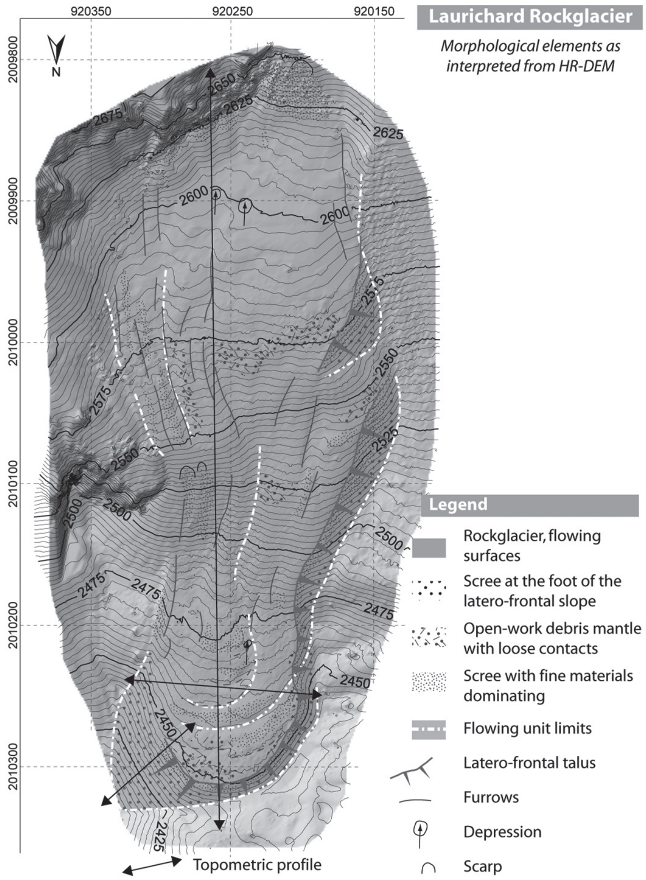

Figure 3. Morphological map of the rock glacier from the 2005 HR-DEM. Coordinates are in meters and equidistance of the contour lines is 2.5 m. Please note that, for aesthetic reasons, north as been placed at the bottom.

c) the lower concave part of the central slope, which is characterized by a high roughness, related to the presence of numerous large boulders and, at the bottom, by transverse ridges and furrows;

d) the gently sloping tongue of the rock glacier shows several ridges, and the roughness index suggests smaller boulders.

As a rock glacier is commonly interpreted as a creeping mixture of debris and ice (Haeberli 1985, Barsch 1992), it may be assumed that those morphometric measurements partly reflect the dynamics of the landforms.

Long-term deformation of the rock glacier

The digitizing of contour lines obtained through photogrammetric restitution of 1975 aerial photos (topographic map IGN 3436ET, 1:25000) has provided a DEM (at a grid resolution of 10 m) of the rock glacier region. The comparison between this 10 m DEM (which displays quite poor accuracy of +/-5m) and the 2005 HR-DEM allows us to roughly estimate the characteristics of the Laurichard rock glacier flow (Fig. 5). It appears that the frontal zone has advanced by about 11 m, displacing a volume of rock and ice of approximately 50,000 m^3 in 30 years. An interesting feature is the clear inflexion of the flow towards its right, in a local valley axis.

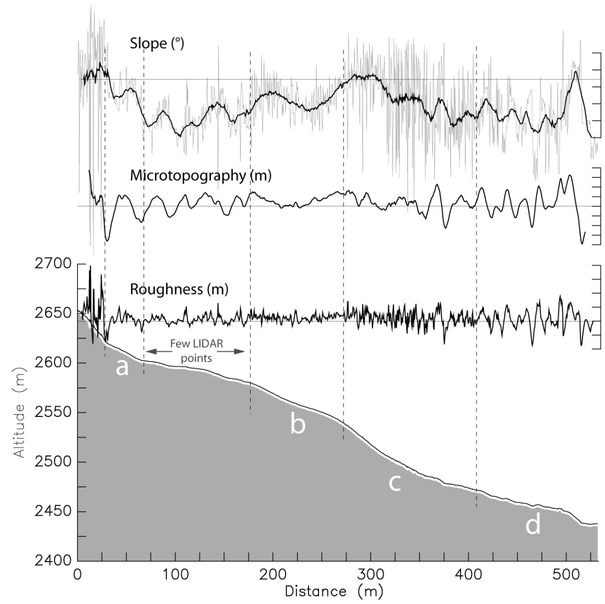

Figure 4. Longitudinal profile of the rock glacier with computed values of slope, microtopography, and roughness.

Interannual comparison of HR-DEM

Due to the coarse detritic cover of the rock glacier, made up of decimeter to meter-sized boulders without fine material, the surface roughness appears to be greater than the spatial resolution of the HR-DEM. Furthermore, the variability of the point density, from place to place and from one HR-DEM to the other, may lead to an heterogeneous quality of the reproduction of the surface by the models. Thus, as a smoothing of the "noisy" blocky surfaces would have induced an additional inaccuracy and would have limited the detection of infra-meter surface movements, direct comparisons were performed by two different means.

With the first method, the PolyWorks software computes the distance between each cell of the 2005 polygonal model and the closest cell of the 2006 polygonal models. A directional constraint is set by a 3D vector which specifies in which direction the comparisons have to be performed. Thus, maps of "directional differences" can be computed for various 3D vectors.

This method shows some of the main components of the surface movement, such as the downstream progression of the ridge that appears to be larger in the main flow axis of the landform (Fig. 8). The larger movement on the right side of the rock glacier seems also to be confirmed, and the fall of blocks from the top of the front or the individual movements of big boulders can be easily detected.

The second method consists in the use of topographic profiles along which 2005 and 2006 surfaces are compared. Vertical changes as well as horizontal differences can then be computed.

Specific patterns of rock glacier movement can therefore be visualized. The frontal advance is detected by the uprising of the surface, which decreases toward the foot of the talus (Fig. 6 A). Erosion by the fall of blocks from the upper part of the front is also perceptible at some places by a lowering

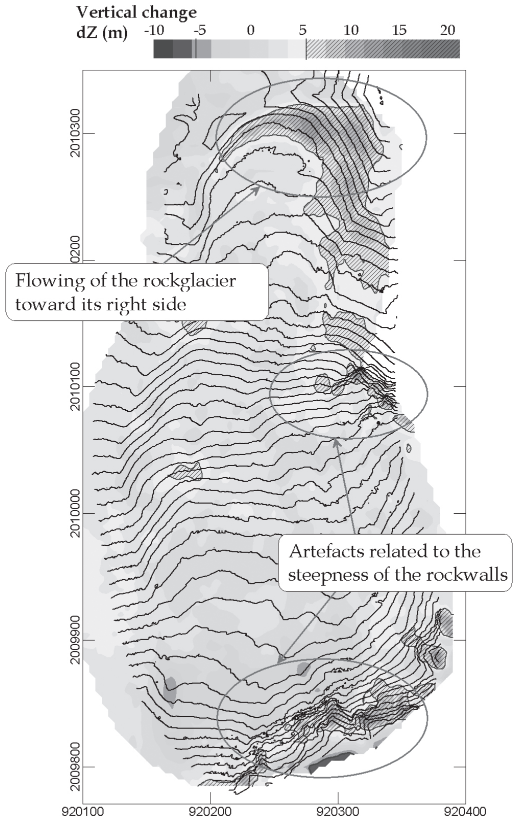

Figure 5. Vertical changes (in meters) between 2005 HR-DEM and 1975 DEM.

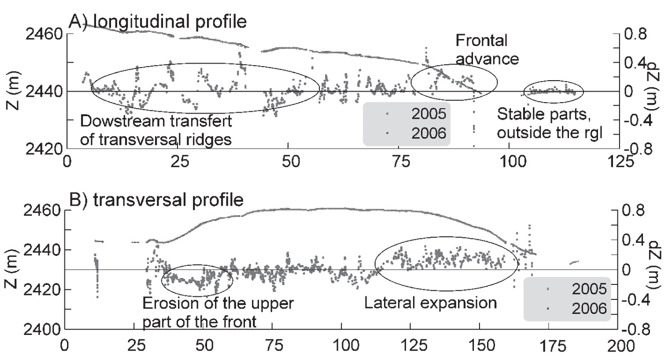

Figure 6. Vertical changes between 2005 and 2006 on a longitudinal and a transversal profile.

of the surface at the top and a subsequent rising at the foot, which corresponds to the deposit.

This method also permits to quantification of the downstream progression of the ridges (from 0.2–0.6 m/yr on the tongue) and the advance of the latero-frontal talus that appears to range from 0–0.6 m/yr (Fig. 7).

Discussion on the Rock Glacier Dynamics and Discussion

The rock glacier advance

The latero-frontal edges of the rock glacier were frequently perpendicular to the line-of-sight of the LIDAR, and this has locally improved the quality of the HR-DEM and facilitated surface changes quantification on those specific sectors.

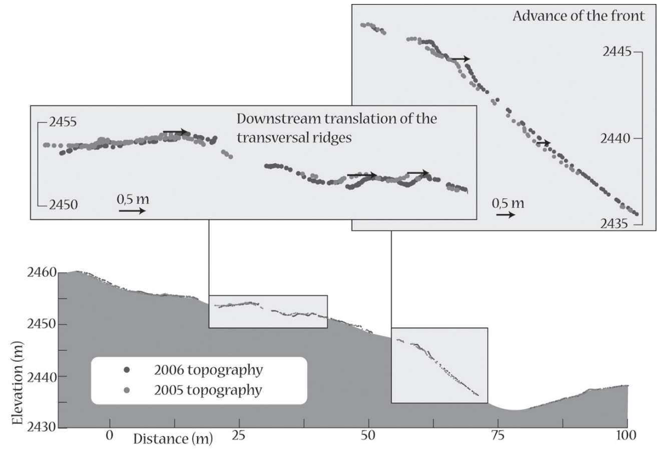

Figure 7. Surface changes between 2005 and 2006 on a longitudinal profile showing the tongue of the rock glacier.

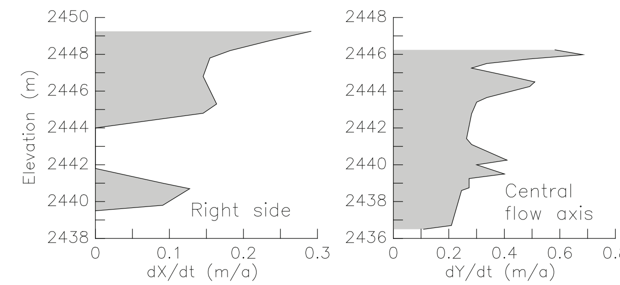

Figure 8. Vertical profiles showing the horizontal advance rate of the latero-frontal edges of the rock glacier (see Fig. 3 for location).

Hence, measure of the horizontal movement of visible boulders allows the drawing up ofvertical profiles of the advance of the rock glacier edges (Fig. 8). Those show an increase of the advance rate toward the top of the front, as well as marked ruptures that are visible at different levels in the profiles.

Although this kind of measurement has to be carefully interpreted due to the roughness of the surface and to individual boulder movements that may introduce noise in the values, several remarks can be made concerning the advance of the rock glacier.

First, the linear to parabolic shape of the vertical profiles is similar to those observed by Kääb & Reichmuth (2005) on the front of two rock glaciers. For the Murtèl case, they found that its frontal part is affected by a downslope creep of a surface layer (which acts as a "conveyor belt") and a thaw settlement that reveal an excess ice content of about 60%–70%.

Second, the presence of a non-moving layer is observed within the vertical profiles of the right side of the Laurichard rock glacier. This may approximately correspond to the level of the bedrock (as suggested by surrounding evidence) and may be interpreted as evidence of the presence, immediately above, of a shear zone (Arenson 2002) where a large part of the total deformation occurs.

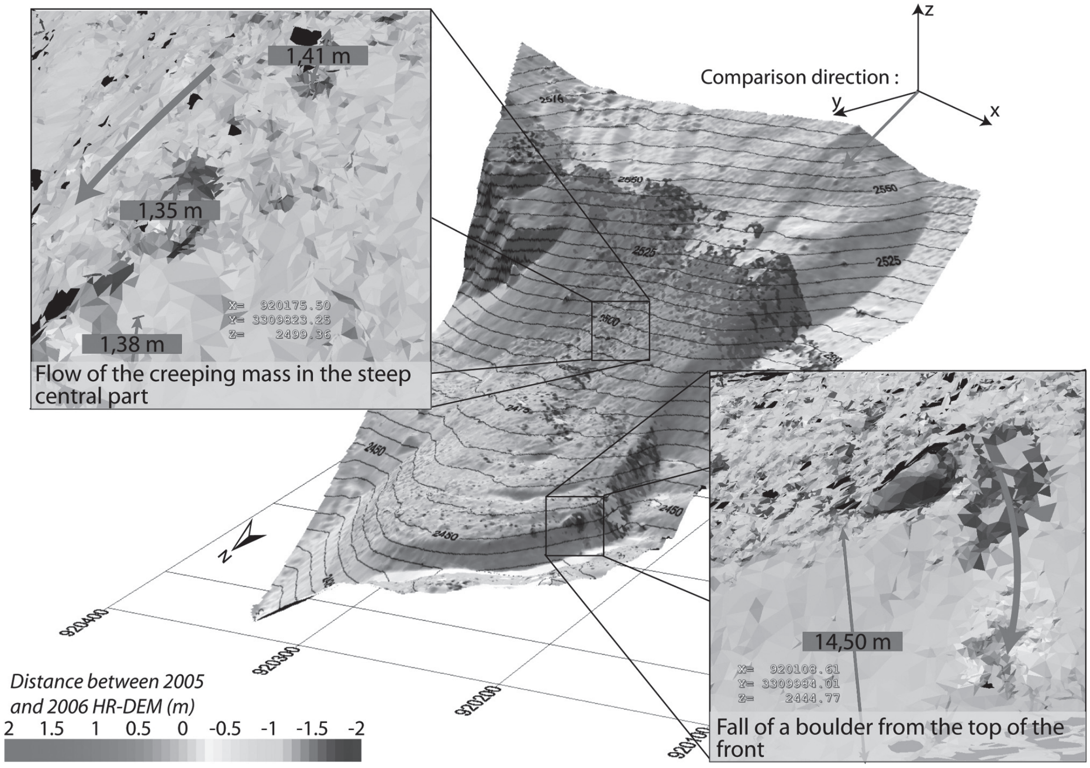

Figure 9. Map of the "directional difference" (direction of comparison shown in the upper right corner) between 2005 and 2006 HR-DEM. The inserts present some details of typical surface changes, such as the individual movements of boulders in the steep central part or the fall of a block from the front. The downstream progression of the ridge is also clearly visible.

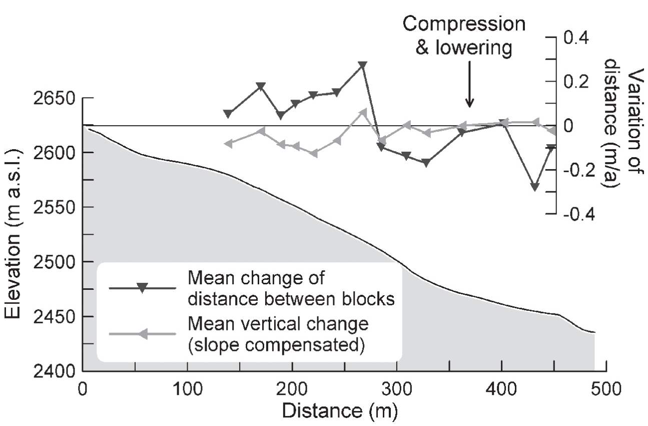

Figure 10. Surface variations of the Laurichard rock glacier after the long-term geodetic survey (mean 1986–2006 values).

Implications for the long-term geodetic survey

The annual measurements with the LIDAR device have suggested that the flow of the rock glacier may partly turn to its right, following a local valley axis. Between 1975 and 2005, the right side of the rock glacier advanced by about 14 m (+/-5 m) in that direction, and the corresponding 2005–2006 advance was around 0.3 m on the top of the latero-frontal talus.

Therefore it can be assumed that the surface changes observed with the long-term geodetic survey along the main axis of the rock glacier (Fig. 10) will reflect this specific behavior.

As a consequence, the small mean lowering of the surface (indicated by the calculated slope compensated variation of surface, data from 1986 to 2006) which accompanies the local compression of the tongue has to be interpreted in different ways. It may be a consequence of the global dynamics of the rock glacier, as well as an impact of the thaw settlement that would be associated to the global warming of the last two decades.

Conclusion

The terrestrial LIDAR technique has been employed to produce two high-resolution DEMs of the Laurichard rock glacier in two successive years. The morphology of the landform has been analyzed, thanks to mapping and to morphometric parameters. The depicted flowing structures clearly reveal the creep of the ice and debris mixture. This has also been studied through interannual comparisons of the HR-DEM, which allows general or detailed quantification of the surface kinematics of the rock glacier. By comparing with the results of a long-term geodetic survey, it appears that more detailed studies, for example with a regular (every 5 years) survey of the rock glacier, are necessary to develop models of the rock glacier dynamics.

Acknowledgments

This work has been possible thanks to collaboration between the Institute of Alpine Geography (Grenoble, France) and EDYTEM laboratory (Le-Bourget-du-Lac, France). The authors are indebted to R. Delunel, J. M. Krysiecki, and

A. Rabatel, as well as to the "Chalet-Laboratoire" of the Lautaret Pass (S. Aubert, P. Choler) for their help during the field campaigns. The unpublished data of the geodetic survey of Laurichard have been made available by the courtesy of L. Reynaud and E. Thibert.

References

Arenson, L., Hoelzle, M. & Springman S. 2002. Borehole deformation measurements and internal structure of some rock glaciers in Switzerland. *Permafrost and Periglacial Processes* 13: 117-135.

Avian, M. & Bauer, A. 2006. First results on monitoring glacier dynamics with the aid of terrestrial Laser Scanning on Pasterze Glacier (Hohe Tauern, Austria). *Grazer Schriften der Geographie und Raumforschung* 41: 27-36.

Barsch, D. (1992). Permafrost Creep and Rockglaciers. Permafrost and Periglacial Processes 3: 175-188.

Bauer, A., Paar, G. & Kaufmann, V. 2003. Terrestrial laser scanning for rock glacier monitoring. *8th International Conference on Permafrost, Zürich, Balkema:* 55-60.

Delaloye, R. 2004. *Contribution à l'étude du pergélisol de montagne en zone marginale*. PhD. Thesis. Université de Fribourg: 260 pp.

Francou, B. & Reynaud L.. 1992. 10 years of surficial velocities on a Rock glacier (Laurichard, French Alps). *Permafrost and Periglacial Processes* 3: 209-213.

Haeberli, W. 1985. *Creep of Mountain Permafrost: Internal Structure and Flow of Alpine Rock Glaciers*. Zürich, ETH. 142 pp.

Haeberli, W., Hallet, B., Arenson, L., Elconin, R., Humlum, O., Kaab, A., et al. 2006. Permafrost creep and rock glacier dynamics. *Permafrost and Periglacial Processes* 17(3): 189-214.

Ikeda, A. 2004. *Rock Glacier Dynamics near the Lower Limit of Mountain Permafrost in the Swiss Alps.* PhD. Thesis. University of Tsukuba: 107 pp.

Kääb, A. 2005. *Remote Sensing of Mountain Glaciers and Permafrost Creep.* University of Zürich: 266 pp.

Kääb, A., Frauenfelder, R. & Roer, I. 2006. On the response of rockglacier creep to surface temperature increase. *Global and Planetary Change* 56(1-2): 172-187.

Kääb, A., Gudmundsson, G.H. & Hoelzle, M. 1998. Surface deformation of creeping mountain permafrost. Photogrammetric investigations on Murtel rock glacier, Swiss Alps. *Proceedings of the Seventh International Conference on Permafrost, Yellowknife, Canada, Université de Laval*: 531-537.

Kääb, A. & Reichmuth, T. 2005. Advance mechanisms of rock glaciers. *Permafrost and Periglacial Processes* 16: 187-193.

Kaufmann, V., Ladstädter, R. & Kienast, G. 2007. 10 years of monitoring of the Doesen rock glacier (Ankogel group, Austria) - A review of the research activities for the time period 1995–2005. *5th ICA Mountain Cartography Workshop, Bohinj, Slovenia*: 128-144.

Kaufmann, V., Ladstädter, R. & Lieb, G.K. 2006. Quantitative assessment of the creep process of Weissenkar rock glacier (Central Alps, Austria). 8th International Symposium on High Mountain Remote Sensing Cartography, *Grazer Schriften der Geographie und Raumforschung, Band* 37, 77-86.

Lambiel, C. & Delaloye, R.. 2004. Contribution of RTK GPS in the study of creeping mountain permafrost. Examples from the Western Swiss Alps. *Permafrost and Periglacial Processes* 15: 229-241.

Roer, I., Avian, M., Delaloye, R., Lambiel, C., Dousse, J.-P., Bodin, X., et al. 2005. Rockglacier "speed-up" throughout European Alps - a climatic signal? *2nd European Conference on Permafrost, Potsdam, Alfred-Wegener-Stiftung:* 99-100.

Comparison of Exposure Ages and Spectral Properties of Rock Surfaces in Steep, High Alpine Rock Walls of Aiguille du Midi, France

Ralph Böhlert, Stephan Gruber, Markus Egli, Max Maisch, Dagmar Brandová & Wilfried Haeberli
Department of Geography, University of Zurich, Zurich, Switzerland

Susan Ivy-Ochs, Markus Christl
Institute of Particle Physics, ETH Zurich, Zurich, Switzerland

Peter W. Kubik
Paul Scherrer Institut, c/o Institute of Particle Physics, ETH Zurich, Zurich, Switzerland

Philip Deline
Laboratoire EDYTEM, Université de Savoie, Le Bourget-du-Lac, France

Abstract

Among various factors, permafrost and frost-thaw cycles play an important role for the stability of steep rock slopes in high alpine regions. Climate change in general and local temperature and precipitation trends in particular are likely to influence permafrost and, consequently, also the stability of rock walls. As stress relief following deglaciation can be excluded at Aguille du Midi (France), rockfall activity is mainly related to changes in permafrost and frost-thaw cycles. To put modern observations of possible climate-induced rockfalls into perspective, information on past rockfall activity is required. In this study, we investigated a combination of surface exposure dating and spectrometry to derive a correlation between rock surface ages and their spectral properties in homogenous lithology. The surface ages found varied from less than 2,000 years to around 40,000 years, and showed a clear correlation with reflectance behavior in the range 380–580 nm. These results may be a first step towards the possible generation of spatial data fields of age distribution in steep rock walls. This may provide deeper insights into spatial and temporal rock-wall development of permafrost in high alpine permafrost environments.

Keywords: cosmogenic nuclide dating; permafrost; reflectance spectroscopy; steep rock slope stability; surface exposure dating.

Introduction

Permafrost thaw is an important process which affects the stability of steep bedrock slopes in many alpine areas (cf. Haeberli et al. 1997, Gruber & Haeberli 2007). Slope failures, like rockfalls, landslides and debris flows, that are assumed to be triggered by changes in the permafrost conditions are known from numerous locations in high mountains and especially in the Alps (e.g., Haeberli 1992, Deline 2001, Noetzli et al. 2003, Schiermeier 2003, Gruber et al. 2004a). These processes cover magnitudes from small rockfalls to huge rockslides (Bergsturz). In comparison with debris-covered slopes, rock faces react quickly to climate change. This is due to the absence of a block layer (Mittaz et al. 2000, Hoelzle et al. 2001) and corresponding direct coupling of surface and subsurface conditions, combined with low water content and small transfer of latent heat during melt. This rapid reaction, together with the effect of destabilization, makes rockfalls due to permafrost degradation a likely and perceivable impact of climate change in the near future (Gruber et al. 2004a).

While recent advances in permafrost modeling have enabled the derivation of permafrost maps for steep bedrock (Gruber et al. 2004b), information about long-term rockfall activity is required to put recent observations and changes in temperature into a long-term perspective.

Besides radiocarbon dating and luminescence methods, the usage of cosmogenic nuclides has become a central technique to gain information about landform ages and landform-modification processes such as rockfalls. An overview of the spectrum of dated landforms and commonly used nuclides is given, for instance, in Gosse & Phillips (2001) and in Ivy-Ochs & Kober (2006). In relation to glacio-geomorphological questions, the determination of ^{10}Be- and ^{26}Al-concentrations in the surface of moraine boulders and polished bedrock is of great interest. Ivy-Ochs et al. (2006) summarized results from the European Alps. Whereas, numerous ages from late glacial moraines are available, data from polished bedrock (indicating deglaciation at higher altitudes) or from areas that were not glaciated during the Last Glacial Maximum (LGM) are sparse. Except for investigations in the Grimsel Pass region in central Switzerland (Ivy-Ochs 1996, Kelly et al. 2006), so far no dating has been carried out at higher-elevation sites.

Remote sensing techniques with multispectral and hyperspectral sensors are widely used to investigate different aspects of mountain areas. Kääb et al. (2005) provide an overview of air- and spaceborn remote sensing methods that are applicable for glacier and permafrost hazard assessment and disaster management. Other approaches discuss methodologies for mapping glacio-geological features such as trim lines or terminal moraines in order to reconstruct glacier changes and related past climate (e.g., Huh et al. 2006). Spectral field measurements and airborn hyperspectral data have enabled an approach to date and map other geomorphic features such as arid and semi-arid alluvial fans (Crouvi et al. 2006). The development of a rock coating significantly influences the overall reflectance of the surface. The redness of rock material or soil is directly related to the age. In oxidizing environments and increasing weathering time, color hues become redder and chromas become brighter (rubification). This fact is, among others, used in the calculation of the profile development index which gives a direct indication of soil age (e.g., Harden, 1982, Goodman et al., 2001).

In this paper, we present a pilot study to investigate the potential of combined imaging spectrometry and exposure dating to derive approximate surface ages in steep bedrock walls of homogeneous lithology. The geometric and radiometric correction of hyperspectral imagery over steep terrain is challenging but generally possible (cf. Gruber et al. 2003). The spatial data fields of estimated age resulting from this method would allow deriving the area and relative frequency of surfaces that belong to a certain age class and that are uninterrupted by older surfaces over a certain distance. This information is related to the frequency of rockfall events during a certain period and is a useful long-term background for assessing whether presently observable, large rockfall shows an unusual abundance as suggested by the relevance of permafrost for slope stability.

Our hypothesis is that the surface ages in this high alpine region can be directly related to the redness of the rocks. The redder a rock surface is, the higher the age that should be measured.

Geological and Physical Setting

Aiguille du Midi (3842 m a.s.l.) is situated some four kilometres south of Chamonix in the Western Alps in France. Whereas most of the peaks surrounding Chamonix are only reachable by making trips of several days with high alpine equipment, Aiguille du Midi is easily accessible by cable car and therefore an ideal study site.

Geologically, this area is part of the Mont-Blanc massif (Spicher 1980) and is made up of the so-called Mont-Blanc Granite with an age of roughly 300 Ma (von Raumer & Bussy 2004, Bussy et al. 2000). This granite type is of a very quartz-rich quality and thus suitable for surface exposure dating with ^{10}Be.

During LGM, the uppermost part of the Aiguille du Midi SSE-face, where the samples were taken, was most probably not glaciated. Paleogeographical reconstructions based on trimline mapping by Coutterand & Buoncristiani (2006) and Kelly et al. (2004) showed that Aiguille du Midi was, during this time, a Nunatak bounded in the east by the Mer de Glace, in the north by the Glacier de l'Arve, and in the west by the Glacier des Bossons. Apart from local glaciations in the less steep parts of the wall, the influence of glacial ice masses on exposure ages can be excluded.

We chose our sampling sites based on visually identifiable differences in color on photographs taken from a helicopter.

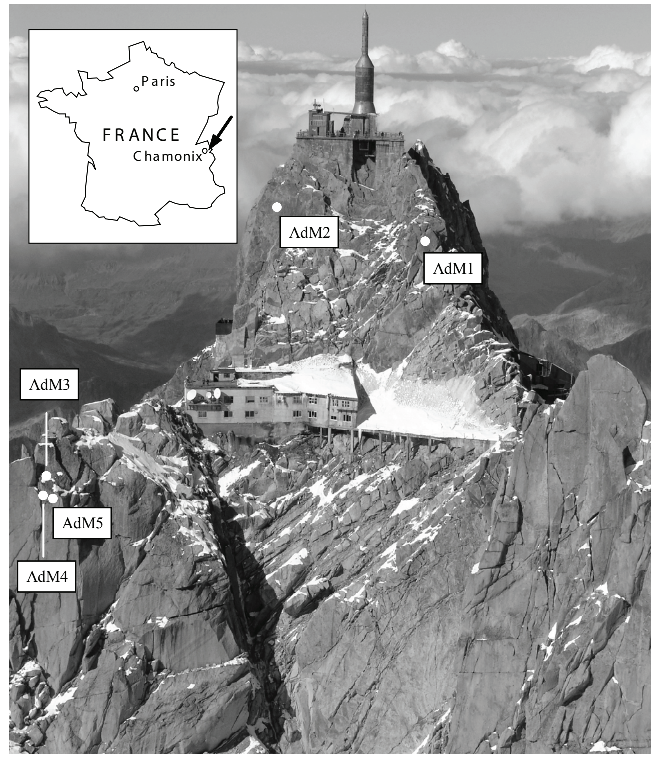

Figure 1. Overview of the sampling locations at Aiguille du Midi.

The hypothesis was that intensively red-colored parts in the rock wall were exposed to weathering over a longer time period than fresh gray ones, and consequently should have a higher age. This assumption is based on field observations at the adjacent Drus, where, besides several smaller events, a huge rockfall occurred in 2005 (Ravanel 2006). The gray-colored area that came to light clearly contrasts to the surrounding, more or less reddish, and obviously older parts of the wall.

Sample AdM1 was taken at a conspicuously red spot, whereas AdM2 was gathered from a gray part of the wall, where no red coloring was seen. AdM4 and AdM5 can be placed somewhere in between with respect to color. Thereby, sample AdM5 presented a more intensive coloration than AdM4. All these sampling places had a slope ≥ 79°. The slope at AdM3 was, however, only 49°. This sample was the only one that was partly covered by lichen, probably due to an increased water availability resulting from melting snow. For this reason spectral analysis was not applicable, and AdM3 was not taken into account for further interpretation. We concluded that the rock surfaces should have the following order of age: AdM1 > AdM5 >AdM4 > AdM2.

Rock samples were taken with hammer, chisel, and a drilling machine. After Masarik & Wieler (2003), marginal sampling places were excluded in order to avoid edge effects. To calculate the influence of shielding caused by the surrounding topography, azimuth-dependent angles were extracted from the map.

Methodology

Surface exposure dating

Approximately 500–1000 g of each rock sample were crushed and sieved. A grain-size fraction of 0.5 to 1 mm was used. Pure quartz was separated by selective chemical dissolution (Kohl & Nishiizumi 1992, Ivy-Ochs 1996). This method is based on the fact that feldspars and micas dissolve in 4% HF more quickly than quartz does. At least six HF steps were used to obtain very pure quartz as reflected by the low Al concentration (less than 100 ppm). ^{9}Be carrier was added to the dried quartz, which was then completely dissolved with concentrated HF in a microwave. Be and Al were separated using a cation exchange column. The Be hydroxides were precipitated, dried, and calcined at 850°C to BeO.

The ^{10}Be/^{9}Be ratios were measured at the ETH/PSI Zürich Tandem Accelerator Mass Spectrometry (AMS) Facility (Synal et al. 1997).

In order to calculate ^{10}Be ages, a simple exposure history was assumed, specifically that all ^{10}Be measured was produced in the rock surface during the latest period of exposure and that the rock surface did not suffer significant erosion. Any earlier exposure, even at greater depth below the original surface, will make the "measured" age an upper limit for the true exposure age of the sample's surface.

Ages were calculated using the ^{10}Be production rate of 5.1 ± 0.3 atoms gram-1 year-1 at sea level and high latitude (Stone 2000). Production rates were scaled to the specific sample locations according to Stone (2000) and corrected for sample thickness (assuming an exponential depth profile) and topographical (skyline) shielding (Dunne et al. 1999) (Table 2).

Laboratory reflectance spectroscopy

Rock surface spectra were measured in the laboratory using an ASD FieldSpec Pro Fr spectro-radiometer, a Spectralon reference panel, and a Thermo Oriel irradiance source. The hematite spectrum was taken from the Jet Propulsion Laboratory (JPL) Spectral Library (HEMATITE 0-1A). In order to identify absorption features for measurement, continuum removal was applied to the data. This is a means of normalizing reflectance spectra to allow comparison of individual features from a common baseline. Continuum removal (Clark & Roush 1984, Kruse et al. 1985, Green & Craig 1985) was performed in ENVI 4.1 to facilitate the comparison of individual absorption features between different objects. In this method, a convex hull (the continuum) of a reflectance spectrum is divided by the spectrum itself and thus results in values ranging from 0-1. The convex hull is built utilizing straight line segments that connect local reflectance maxima.

Elemental composition by X-ray fluorescence measurements

The elemental composition of the rock samples was analyzed by X-ray fluorescence (XRF) spectrometry. After crushing the rock samples to a size of <1mm, around 10 g of rock material were milled to <50 µm in a tungsten carbide disc swing mill (Retsch® RS1, Germany). 4 g of rock powder was mixed with 0.9 g of Licowax® C Micro-Powder PM (Clariant, Switzerland), pressed into a 32 mm pellet, and analyzed using an energy dispersive XRF spectrometer (SPECTRO X-LAB 2000, SPECTRO Analytical Instruments, Germany).

Table 1. Elemental composition of the samples.

	Samples Aiguille du Midi 1-5					Statistics	
Element [%]	AdM1	AdM2	AdM3	AdM4	AdM5	Mean	SD
CaO	0.87	0.87	1.44	1.17	1.31	1.13	0.26
MgO	0.62	0.60	0.37	0.39	0.56	0.51	0.12
K_2O	5.09	5.22	4.91	5.28	5.37	5.17	0.18
Na_2O	3.12	2.84	2.74	2.80	2.78	2.86	0.15
Al_2O_3	13.62	13.58	13.67	13.82	12.89	13.52	0.36
Fe_2O_3	1.43	1.64	1.85	1.70	2.23	1.77	0.30
SiO_2	70.32	68.73	67.27	70.09	66.56	68.60	1.67
MnO	0.02	0.03	0.033	0.04	0.049	0.04	0.01
P_2O_5	0.06	0.07	0.072	0.07	0.091	0.07	0.01
TiO_2	0.26	0.30	0.310	0.31	0.334	0.30	0.03
ZrO_2	0.02	0.02	0.022	0.02	0.022	0.02	0.00
BaO	0.07	0.08	0.098	0.08	0.080	0.08	0.01
Rb_2O	0.03	0.03	0.031	0.03	0.034	0.03	0.00
WO_3	0.05	0.05	0.045	0.06	0.036	0.05	0.01
LOI	3.43	0.55	0.63	3.57	0.53	1.74	1.61
Total	99.02	94.61	93.49	99.43	92.89		

Elemental composition of the samples based on XRF measurements. Values are converted into oxide contents. LOI = Loss on ignition. The low standard deviation (SD) values indicate a comparable composition and demonstrate the homogeneity of the lithology.

Table 2. List of samples and calculated surface exposure ages.

	Samples Aiguille du Midi 1-5				
	AdM1	AdM2	AdM3	AdM4	AdM5
Elevation (m a.s.l)	3800	3810	3750	3740	3740
Sample thickness (cm)	2.5	3.5	5.5	2.5	4.0
Surface dip (°)	85	85	49	79	79
Quartz (g)	58.13	57.03	58.26	56.77	56.68
^{10}Be (10^4 atoms g^{-1})	157.63	6.03	24.28	24.84	28.28
Measurement error (%)	3	9.2	5	4.6	5.2
Production rate not corrected (atoms g^{-1} yr^{-1})	75.59	76.00	73.57	73.17	73.17
Shielding factor	0.559	0.559	0.898	0.627	0.627
Production rate corrected for shielding, sample thickness and surface dip (atoms g^{-1} yr^{-1})	41.24	41.11	62.85	44.77	44.34
^{10}Be date (yr)	**38,600±1200**	**1,470±140**	**3,870±200**	**5,560±260**	**6,390±330**

Samples organized by sample name. The reference production rate is scaled for sample altitude and latitude after Stone (2000) and corrected for sample thickness (assuming exponential attenuation of cosmic rays at depth and an attenuation length of 150 g cm-2) and skyline shielding (Dunne et al. 1999).

Results

Elemental composition

Results from XRF measurements show after conversion into oxide contents a very similar composition (Table 1.). The high quartz content of the Mont-Blanc granite is represented by high amounts of SiO_2. Other important constituents of the rock samples are Al_2O_3 and potassium oxide. The total values of over 90% mean that almost all possible compounds were measured.

The comparable composition of the samples is an important indication that observed differences in color are not due to inhomogeneities in lithology.

Surface exposure ages and comparison with measured spectra

The intensively red colored sample AdM1 shows the highest age, followed by AdM5, AdM4, and AdM2, where no coloring occurred. This is in agreement with the above-stated hypothesis and the sample description (Table 2).

Generally, the ^{10}Be ages, especially AdM1, are remarkably old, and the differences in age are very big. But these ages have to be interpreted as maximum exposure ages of the rock surface, as long as erosional processes can be excluded.

Looking at the measured spectra (Fig. 2), a well-pronounced correlation between surface exposure ages and the corresponding spectral signature in the range of approximately 380–580 nm is identifiable after continuum removal. As a reference, a piece of unweathered fresh rock was also analyzed (AdMf).

According to the visual impression, the curve progression of AdM2 is shaped very similarly to the one of the unweathered sample. With increasing surface exposure ages and thus more pronounced weathering, a decrease in feature depth is ascertainable. A comparison with the continuum-removed spectrum of hematite permits the conclusion that the spectra evolution with increasing age is influenced, at least partly, by hematite formation (Fig. 2). Thus, hematite content and its effects on rock surface color can be interpreted as the main feature required in regard to the generation of spatial data fields of age distribution in rock walls.

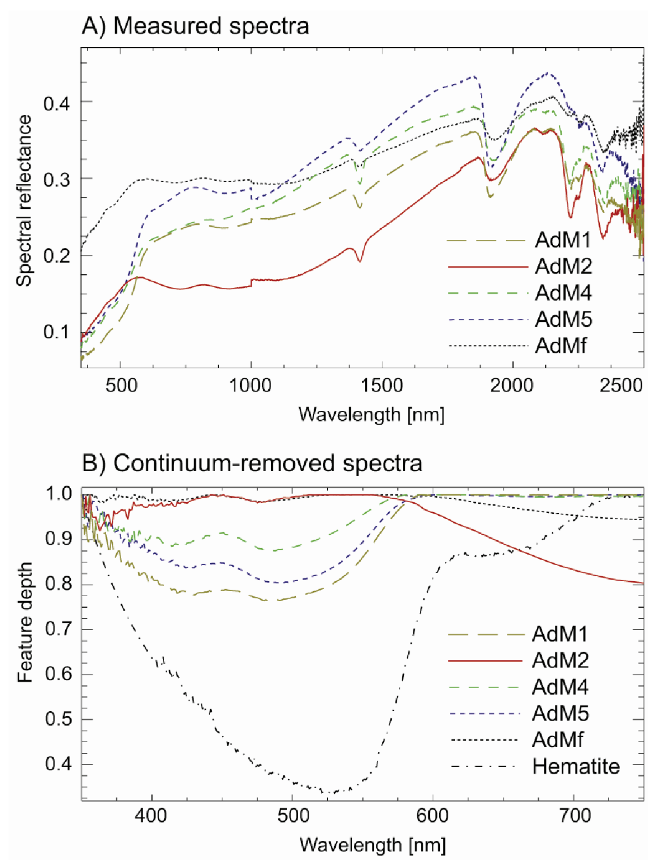

Figure 2. Measured and continuum-removed spectra. The arrow indicates the influence of the Fe-Oxide content with age.

Discussion and Conclusions

We showed that analyzing spectral properties of rock surfaces in steep walls with homogeneous lithology may be a tool to estimate the age distribution and related past rockfall activity in high alpine environments. The redder a rock surface, the longer this rock was exposed to weathering. In numerous cases, the correlation of rockfall initiation to changes in the permafrost conditions is rather weak, and related forecast and mitigation possibilities are limited (Gude & Barsch 2005). Not only permafrost thawing but also other processes like general frost-thaw activities (physical weathering), seismic (neotectonic) activity, or stress relief following deglaciation could induce rockfalls. Furthermore, non-erosive cold-based glacier ice can complicate the erosion history of rock surfaces (Briner et al. 2006). Due to the topographic situation of the investigated sites, however, at least one process affecting the stability of rock walls can be excluded. A stress-relief following deglaciation of (cold-based) glacier ice did not occur because no glaciers covered the rock walls during (and after) the LGM. Rockfall is predominantly due to permafrost changes and frost-thaw activities. Although neotectonic activities have been rather low, their influence on rockfalls cannot be fully excluded. The used approach, therefore, will not allow direct reconstruction of past permafrost conditions. However, it can give indications about past and present-day rockfall activities. From this, the influence of permafrost on rock wall stability can be deduced at least partially. Inasmuch as global warming in general and local temperature and precipitation trends in particular are likely to influence the permafrost significantly, the stability of rock walls will also be affected.

The relationships found look promising; however, they certainly represent only a first impression and further investigations in this field will be necessary to establish this approach as a commonly usable application. Doubtless, of great importance is the enlargement of the survey sample size in order to be able to generate statistical correlations between surface exposure ages and spectral properties. Therefore, the latter have to be translated into quantifiable values.

In the present study, we tried to keep as many factors constant as possible. Potential follow-up studies will have to deal with the influence of variable slope aspect and altitudes and different lithologies. Steep places at high elevations should be preferred. Sampling locations that are situated too low are not suitable due to lichen growth disturbing the spectral signal. The same is true for flat spots where snow cover can develop more easily and remain for a longer time. A fundamental problem will be the difficulty in accessing appropriate sites. There is, however, great potential for further efforts.

Acknowledgments

This research is supported by the Swiss National Science Foundation grant number 20-109565/1. We would like to thank Jürg Schopfer for providing support in the spectro lab. Easy access to Aiguille du Midi was possible thanks to the generous help of the Compagnie du Mont Blanc (Chamonix) and particularly of Emerick Desvaux. We are, furthermore, indebted to Anne Hormes and to an unknown reviewer for their helpful comments on an earlier version of the manuscript.

References

Briner, J.P., Miller, G.H., Davis, P.T. & Finkel, R.C. 2006. Cosmogenic radionuclides from fiord landscapes support differential erosion by overriding ice sheets. *GSA Bulletin* 118: 406-420.

Bussy, F., Hernandez, J. & von Raumer, J. 2000. Bimodal magmatism as a consequence of the post-collisional readjustment of the thickened variscan continental lithosphere (Aiguilles Rouges/Mont-Blanc massifs, western Alps). *Transactions of the Royal Society of Edinburgh: Earth Sciences* 91, 1-2: 221-223.

Clark, R.N., & Roush, T. L. 1984. Reflectance spectroscopy: Quantitative analysis techniques for remote sensing applications. *Journal of Geophysical Research* 89(B7): 6329-6340.

Couterrand, S. & Buoncristiani, J.-F. 2006. Paléogeographie du dernier macimum glaciere du Pleistocène de la Region du Mont Blanc, France. *Quartenaire* 17(1): 35-43.

Crouvi, O., Ben-Dor, E., Beyth, M., Avigad, D. & Amit, R. 2006. Quantitative mapping of arid alluvial fan surfaces using field spectrometer and hyperspectral remote sensing. *Remote Sensing of Environment*, 104: 103-117.

Deline, P. 2001. Recent Brenva rock avalanches (Valley of Aosta): New chapter in an old story? *Suppl. Geogr. Fis. Dinam. Quat.*: 55-63.

Dunne, J., Elmore, D. & Muzikar, P. 1999. Scaling factors for the rates of production of cosmogenic nuclides for geometric shielding and attenuation at depth on sloped surfaces. *Geomorphology* 27: 3-11.

Goodman, A.Y., Rodbell, D.T., Seltzer, G.O. & Mark, B.G. 2001. Subdivision of glacial deposits in southeaster Peru based on pedogenetic development and radiometric ages. *Quaternary Research* 56: 31-50.

Gosse, J.C. & Phillips, F.M. 2001. Terrestrial in situ cosmogenic nuclides: theory and application. *Quaternary Science Reviews* 20: 1475-1560.

Green, A.A., & Craig, M.D. 1985. Analysis of aircraft spectrometer data with logarithmic residuals. *Proceedings, AIS workshop, 8-10 April, 1985.* JPL Publication 85-41, Jet Propulsion Laboratory, Pasadena, California: 111-119.

Gruber, S. & Haeberli, W. 2007. Permafrost in steep bedrock slopes and its temperature-related destabilization following climate change. *Journal of Geophysical Research* 112, F02S18, doi:10.1029/2006JF000547.

Gruber, S., Hoelzle, M. & Haeberli, W. 2004a. Rock wall temperatures in the Alps: Modelling their topographic distribution and regional differences. *Permafrost Periglacial Processes* 15(3): 299-307.

Gruber, S., Hoelzle, M. & Haeberli, W. 2004b. Permafrost thaw and destabilization of Alpine rock walls in the hot summer of 2003, *Geophysical Research Letters* 31, L13504, doi:10.1029/2004GL020051.

Gruber, S., Schläpfer, D. & Hoelzle, M. 2003. Imaging spectrometry in high-alpine topography: The derivation of accurate broadband albedo. *Proceedings of the the 3rd EARSeL Workshop on Imaging Spectroscopy, Oberpfaffenhofen, Germany, 13–16 May 2003*: 10 pp.

Gude, M. & Barsch, D. 2005. Assessment of geomorphic hazards in connection with permafrost occurrence in the Zugspitze area (Bavarian Alps, Germany). *Geomorphology* 66: 85-93.

Haeberli, W., Wegmann, M. & Vonder Mühll, D. 1997. Slope stability problems related to glacier shrinkage and permafrost degradation in the Alps. *Eclogae Geologicae Helveticae* 90: 407- 414.

Haeberli, W., 1992. Construction, environmental problems and natural hazards in periglacial mountain belts. *Permafrost and Periglacial Processes* 3: 111-124.

Harden, J.W. 1982. A quantitative index of soil development from field descriptions: examples from a chronosequence in central California. *Geoderma* 28: 1-28.

Hoelzle, M., Mittaz, C., Etzelmüller, B. & Haeberli, W. 2001. Surface energy fluxes and distribution models of permafrost in high mountain areas: An overview of current developments. *Permafrost and Periglacial Processes* 12: 53-68.

Huh, K.I., Csatho, B., van der Veen, C.J. & Ahn, Y. 2006. Reconstructing Holocene glacier changes in west Greenland from Multispectral ASTER imagery. *EOS* 87, Fall Meeting Supplement, Abstract C11A-1134.

Ivy-Ochs, S. 1996: *The dating of rock surfaces using in situ produced 10Be, 26Al and 36Cl, with examples from Antarctica and the Swiss Alps*. Ph.D. thesis, ETH Zürich, No. 11763, 196 pp.

Ivy-Ochs, S., Kerschner, H., Reuther, A., Maisch, M., Sailer, R., Schaefer, J., Kubik, P.W., Synal, H.-A. & Schlüchter, C. 2006. The timing of glacier advances in the northern European Alps based on surface exposure dating with cosmogenic ^{10}Be, ^{26}Al, ^{36}Cl, and ^{21}Ne. In: L.L. Siame, D.L. Bourlès & E.T. Brown (Eds.), *In Situ-Produced Cosmogenic Nuclides and Quantification of Geological Processes: Geological Society of America Special Paper 415*: 43-60.

Ivy-Ochs, S. & Kober, F. 2006. Exposure geochronology. In: S.A. Elias (Ed.), *Encyclopedia of Quaternary Sciences:* 435-445.

Kääb, A., Huggel, C., Fischer, L., Guex, S., Paul, F., Roer, I., Salzmann, N., Schlaefli, S., Schmutz, K., Schneider, D., Strozzi, T. & Weidmann, Y. 2005. Remote sensing of glacier- and permafrost-related hazards in high mountain: an overview. *Natural Hazards and Earth System Sciences* 23: 1-28.

Kelly, M.A., Ivy-Ochs, S., Kubik, P.W., von Blanckenburg, F. & Schlüchter, C. 2006. Chronology of deglaciation based on 10Be dates of glacial erosional features in the Grimsel Pass region. Central Swiss Alps. *Boreas* 35: 634-643.

Kelly, M.A., Buoncristiani, J.-F. & Schlüchter, Ch. 2004. A reconstruction of the last glacial maximum (LGM) ice-surface geometry in the western Swiss Alps and contiguous Alpine regions in Italy and France. *Eclogae Geologicae Helveticae* 97: 57-75.

Kohl, C.P. & Nishiizumi, K. 1992. Chemical isolation of quartz for measurement of in-situ produced cosmogenic nuclides. *Geochemica et Cosmochimica Acta* 56: 3583-3587.

Kruse, F. A., Raines, G. L. & Watson, K. 1985. Analytical techniques for extracting geologic information from multichannel airborne spectroradiometer and airborne imaging spectrometer data. *Proceedings, International Symposium on Remote Sensing of Environment, Thematic Conference on Remote Sensing for Exploration Geology, 4th, Environmental Research Institute of Michigan, Ann Arbor:* 309-324.

Masarik, L. & Wieler, R. 2003. Production rates of cosmogenic nuclides in boulders. *Earth and Planetary Science Letters* 216: 201-208.

Mittaz, C, Hoelzle, M. & Haeberli, W. 2000. First results and interpretation of energy-flux measurements over Alpine permafrost. *Annals of Glaciology* 31: 275-280.

Noetzli, J., Hoelzle, M. & Haeberli, W. 2003. Mountain permafrost and recent Alpine rock-fall events: A GIS-based approach to determine critical factors. *8th International Conference on Permafrost, Int. Permafrost Assoc., Zurich, Switzerland*.

Ravanel, L. 2006. *Contribution à l'étude des écroulements dans les parois à permafrost de la haute montagne alpine. L'éxemple du Petit Dru (massif du Mont-Blanc) depuis la fin du Petit Age Glaciere*. Master's thesis, Université de Savoie, 116 pp.

Schiermeier, Q. 2003. Alpine thaw breaks ice over permafrost's role. *Nature* 424: 712.

Spicher, A. 1980. *Tektonische Karte der Schweiz*. Schweizerische Geologische Kommission (Hrsg.).

Stone, J.O. 2000. Air pressure and cosmogenic isotope production. *Journal of Geophysical Research* 105 (B10), 23: 753-759.

Synal, H. A., Bonani, G., Döbeli, M., Ender, R.M., Gartenmann, P., Kubik, P.W., Schnabel, Ch. & Suter, M. 1997: Status report of the PSI/ETH AMS facility. *Nuclear Instruments in Physics Research* B (123): 62-68.

von Raumer, J.F. & Bussy, F. 2004. Mont Blanc and Aiguille Rouges – Geology of their polymetamorphic basement (external massifs, France-Switzerland). *Mémoires de géologie (Lausanne)* 42, 203 pp.

—Plenary Paper—

Heat and Water Transfer Processes in Permafrost-Affected Soils: A Review of Field- and Modeling-Based Studies for the Arctic and Antarctic

Julia Boike

Alfred Wegener Institute for Polar and Marine Research, Telegrafenberg A43, 14473 Potsdam, Germany

Birgit Hagedorn

Environment and Natural Resources Institute, University of Alaska, Anchorage, Anchorage, 99501, USA

Kurt Roth

Institute of Environmental Physics, University of Heidelberg, 69120 Heidelberg, Germany.

Abstract

The main field experiments and modeling results of heat and moisture transfer processes of the Arctic and Antarctic are reviewed, following the historical development. Agreement exists that heat is mainly transferred via conduction in Arctic and Antarctic soils, but that latent heat and vapor migration are important factors for the thermal dynamic. Factors determining amount and type of heat transfer are soil water content and temperature gradient between atmosphere and soil.

Keywords: Antarctic; Arctic; heat transfer; permafrost; thermal processes; water transfer.

Introduction

An apparent discrepancy exists between numerical modeling results and field observations indicating water and vapor transfer in frozen soils. The latter includes depth hoar formation under snow, direct measurements of vapor flux out of the ground (e.g., Santeford 1978, Woo 1982), desiccation of upper soil layers (Hinzman et al. 1991) and ice growth from field and lab experiments (Parmuzina 1978, Chen & Chamberlain 1988) and accumulation of ice at the base of the active layer/top of permafrost (Yershov 1998, Solomatin & Xu 1994).

Due to page limits, we review available literature on heat and water transfer processes in Arctic and Antarctic soils only; thus results from alpine, high elevation and temperate regions are excluded from this paper. Furthermore, we limited the review of heat and water transfer modeling to studies for which field data are available.

The very different climate conditions in the Arctic and Antarctic are reflected in the soil systems. While Arctic soils generally have free liquid water in active layer during summer, Antarctic soils are hyperarid in the dry valleys around the Ross Sea but gradually approach wetter conditions towards the east and Antarctic Peninsula (Beyer et al. 1999 and references within). These differences are reflected in motivation and approaches to model water and heat transport processes thus both regions are described separately. A quantitative understanding of the processes underlying the thermal and hydraulic dynamics of permafrost soils is paramount to anticipate consequences of a changing atmospheric forcing as well as to improve the parameterization of the soil-atmosphere interaction in climate models.

Thermal dynamics of permafrost-affected soils

The major stages for the seasonal thermal dynamics of the active layer at a permafrost site consists of four different characteristic periods: (i) cold period, (ii) warming period, (iii) thawed period, (ix) isothermal plateau. During the *cold period*, temperatures are well below 0°C. Most of the soil water is frozen and the entire ground may be considered as a solid medium. With the sun rising in late spring and the onset of snow melt, ground temperatures rise quickly, soil water content changes following the soil freezing characteristic curve. This *warming period* is terminated by the thawing front, a macroscopic phase boundary that separates partially frozen ground from the completely unfrozen soil during the *thawed period.* The propagation of the thawing front consumes a large proportion of the energy input from the positive net radiation. As the energy balance becomes negative in fall, the soil cools down to 0ºC starting to freeze from the surface. Upon further cooling the reverse phase transition sets in, from liquid to solid. It releases large quantities of latent heat and thereby opposes the cooling. This leads to a rapid equilibration of the temperature at 0 ºC in the entire thawed zone, indicated by the practically vertical isotherms. This is often referred to as the closing of the zero-curtain (Outcalt et al. 1996, Outcalt et al. 1990). As the active layer turns isothermal, large quantities of latent heat need to be removed to allow further cooling. This leads to the *isothermal plateau* where soil temperatures stay near 0 ºC for an extended time. It is eroded from above and from below, where temperatures in the air and in the underlying perennial ice are well below the freezing point. Eventually, the isothermal plateau disappears, giving way to the *cooling period* where regular conduction removes the remaining surplus heat from the active layer. It is transferred through the snow layer, which is a major modulating factor, to the atmosphere.

While thermal processes may be the same in wet soils of east Antarctica and Antarctic Peninsula, in the hyperarid soils of dry valleys the isothermal plateau due to release of latent heat does not exist. However, based on changes in air temperature and lack of incoming radiation, temperature gradient in soils reverses in October, which causes a quasi-isothermal soil during a short period of time (Hagedorn et al. 2007, Pringle et al. 2003) but this isothermal temperature is well below 0ºC.

Heat and water transfer processes

Permafrost-affected soil can potentially have five components (soil matrix, ice, water vapour, water, air). Conduction, heat transfer through gradients, is widely accepted to be the dominant mechanism of heat transfer in soils. Other nonconductive heat transfer mechanisms associated with the convection of water, either in the liquid or in the vapor phase, are possible with appropriate gradients (pressure, gravitational, density, vapor pressure, and chemical). A good summary of potential heat transfer processes in permafrost affected soils is provided by Kane et al. (2001). They summarized the importance of non conductive heat transport based on data sets from Alaska as the following: (i) infiltration and refreezing of water in frozen soil accelerates warming of soil; (ii) free convection of fluids is not an important heat transfer process; (iii) migration of water and vapour could be important but has not been quantified yet. The large value of the enthalpy of evaporation, which exceeds that of melting by a factor of 7.4, makes vapor an efficient means for the transport of thermal energy.

Heat and Water Transfer Processes in Permafrost-Affected Soils: Arctic

Most of the available English-language literature up to the end of 1990s is reported from Alaskan sites and is based on temperature and electric potential measurements and one dimensional thermal diffusion modeling. When the snow cover becomes isothermal and snow melt starts during the warming period, the soil rapidly warms at all depths, presumably because of the infiltration and refreezing of snow melt water and of migrating vapor into the frozen soil. Most studies agree that nonconductive heat transfer processes must be responsible for the rapid warming of the soil (Putkonen 1998, Hinkel & Outcalt 1994).

Conversion of latent heat is thought to be most important during the summer when moisture evaporates from the surface and the active layer thaws. Evaporation consumes 25–50% of the total incoming energy at a Siberian study site on Northern Taymyr peninsula (Boike et al. 1998) and 30–65% in northern Alaska (Kane et al. 1990). According to Outcalt et al. (1998), evaporative cooling at the surface of the active layer was responsible for the deviation between observed and modeled soil temperatures of the active layer and upper permafrost. Thawing of the active layer is another important sink for thermal energy. It consumes up to 40% of the total net radiation at the Siberian site (Boike et al. 1998). Generally, a high percentage of the total heat flux into the ground (between 70 and 100% is converted into latent heat (Rouse 1984, Boike et al. 1998). Conduction of heat, transport of thermal energy by convection of water, either in the liquid or vapor phase, has been discussed. Hinkel et al. (1993) identified infiltration of summer precipitation as an effective method to transfer heat to the base of the active layer, especially in drained, organic soils. Pore water convection during the summer thaw period, driven by the density inversion of water, has been proposed as the initiator for the formation of sorted circles (Krantz 1990, Ray et al. 1983), but Hallet (1990) argued that this process is unlikely and that it has not been observed in finer-grained sediments typically found in patterned ground. Putkonen (1998) calculated a Peclet number much smaller than 1 for this site and concluded that advection of heat due to water motion is negligible.

When net radiation decreases during the fall, the soil is cooled to a practically isothermal condition, the so-called zero curtain at 0°C. The large amount of latent heat which must be removed from the profile through an almost isothermal soil stabilizes soil temperatures at 0° for a prolonged time. Hinkel & Outcalt (1993, 1994) suggested that internal distillation driven by osmotic gradients transfer heat across this isothermal zone. In contrast, Romanovsky & Osterkamp (2000) accurately predicted soil temperatures for sites in Central and North Alaska during the freeze back using a conductive heat exchange model by including effects of unfrozen water and therefore excluding moisture migrating as a transport mechanism. Snow melt infiltration was the only non conductive heat transfer responsible for soil warming.

Putkonen (1998) estimated that the maximal possible vapor and latent heat flux under given soil thermal properties was two orders of magnitude smaller than conductive heat transport, hence being insignificant for western Spitsbergen. Through the application of electronic instrumentation measurement techniques, such as Time Domain Reflectometry for determination of soil moisture in frozen soils, highly precise and frequent temperature and moisture data have been obtained from various field sites. Roth & Boike (2001) found an excellent agreement between projected and measured temperatures for the cold period which demonstrates that during this time, heat transport on Spitsbergen (Bayelva site) can be described by effective conduction. Furthermore, they found that the production of latent heat and the associated migration of water vapor is an important agent in the thermal dynamics at this site for all four periods and that it is the dominating process in the isothermal plateau since heat conduction is practically negligible there. Unimpeded vapor migration is possible down to some 0.9 m, restricted by a massive ice rich layer. This contrasts findings of sites for which it was stipulated that upon closing of the zero curtain, internal distillation and water advection cease for the rest of the winter (Hinkel & Outcalt 1994, Romanovsky & Osterkamp 2000).

Differences in latent heat production using the model by Roth & Boike (2001) were presented by Overduin & Kane (2006). Their patterned ground site, covered by mud boils, is located in Northern Alaska (Galbraith Lake). One of the contrasting differences in winter heat transfer processes was the continuous latent heat production after freeze back until spring in the middle part of the profile It is hypothesized that water advection in the frozen soils was possible through the unfrozen water film attached to the soil particles. Subsequent freezing of water was the source of the latent heat production, resulting in ice formation and large heave rates in the center of the mudboil. While these two Arctic sites are very similar in terms of soil parent material, surface cover and topography, the soil water/ice content and climate conditions vary. Firstly, the site at Galbraith lake is water saturated, thus the pore spaces are filled with ice during winter. The soil at the Bayelva site is water saturated only in the lower part of the profile below about 0.7 m depth. Secondly, Galbraith, located in the Arctic climate is much colder (average January air temp. ~ -24°C) compared to the warmer, maritime influenced Svalbard climate (average January air temp. ~ -13°C). In addition, Galbraith has no or little snow cover, whereas the Bayelva site experiences a snow depth up to about 1 to 1.5 m, modulating the ground thermal regime and thus reducing the thermal gradient between air and soil temperature. It is postulated that the large temperature gradient at Galbraith Lake was also responsible for the large heave (up to 12 cm) which is about an order of magnitude higher compared to the Bayelva site (about 2 cm).

Heat and Water Transfer Processes in Permafrost-Affected Soils: Antarctic

Due to the very dry climate in dry valley soils of Antarctica, the majority of water is present as ice which occurs 0.1 to 0.5 m below surface in approximately 36% of soils in Antarctica (Bockheim 2002). Liquid water is limited to scarce infiltration after snow events (Friedman 1978, Gooseff et al. 2003), water films adsorbed to grain boundaries (Anderson & Morgenstern 1973), and to brines in ice cement (Dickinson & Rosen 2003). Only a small fraction of water is present as water vapor, which is the phase that is transported between atmosphere, soil pore space and ice. The main motivation to study vapor transport and thermal regime in Antarctic soils of Dry Valleys is to estimate the stability of subsurface ice in Antarctic soils, since this ice is important for geomorphologic development of patterned ground formation, e.g. contraction cracks (Sletten et al. 2003) and since Antarctic soils are the best terrestrial analogue to Martian soils (Schorghofer 2005).

Sugden et al., (1995) and van der Wateren & Hindmarsh (1995) did the first back on the envelope calculation of vapor transport to evaluate the stability of ground ice using steady state vapor diffusion modeling. Both yielded very different results; Sudgen et al. (1995) used geothermal gradients to determine soil and ice temperature and assumed vapor saturated atmosphere. He estimated sublimation rates of 10^{-4}mm a^{-1}; van der Wateren & Hindmarsh (1995) used meteorological data and assumed vapor unsaturated atmosphere and estimated a rate of 1 mm a^{-1}. This fast sublimation rate could be confirmed in a more detailed modeling approach by Hindmarsh et al. (1998).

McKay et al. (1998) calculated vapor transport using soil temperature, air temperature and relative humidity records collected at Linnaeus Terrace (1550 to 1700 m elevation). Parameters like tortuosity and porosity were determined on investigated soil material. Thermal conductivity was modeled from temperature profiles and yielded 0.6±0.1 $Wm^{-1}K^{-1}$ for dry soil and 2.5±0.5 $Wm^{-1}K^{-1}$ for ice cement which are close to values determined by Putkonen et al. (2003). Based on Fick's diffusion they found that ice is lost at rates at ~0.2 mm a^{-1}, highlighting the very dry atmospheric conditions in the dry valleys. Based on a comparison between frost point of atmosphere and ice cemented soil they suggest that increase of 40% moisture to all humidity values could stabilize ground ice.

Schorghofer (2005) modeled ice sublimation in Beacon Valley (~1500 m asl.) constrained by climate and soil temperature data and found rates comparable to those of McKay et al. (1998). He found that advection caused by changes in surface pressure has negligible effect on sublimation. By exploring possible scenarios to stabilize subsurface ice, he suggests a decrease in annual air temperature by 5°C or increase in relative humidity of 50%, a rather unrealistic value.

Hagedorn et al. (2007) modeled vapor transport based on multi-year climate and soil temperature record in Victoria Valley which is about 400 m asl. and where ice occurs 0.2 to 0.4 m below surface. Vapor transport is calculated using Fick's diffusion incorporating a reaction term for ice precipitation and allowing vapor diffusion into the ice cement. Initially a linear vapor density gradient between ice cement and atmosphere was assumed. Using this approach they yielded sublimation rates close to those observed by McKay et al (1998). However, part of the vapor is transported from ice surface into the ice cement and most of it precipitates in upper ice cement slowly closing the pore space. Transient ice will form in dry soil during winter but completely disappears during beginning of summer. Snow cover will reduce vapor loss to atmosphere but to completely offset sublimation rates it would need to remain for several months. As suggested by McKay et al. (1998) and Schorghofer (2005) they also found that decreasing air temperature or increasing moisture will reduce sublimation but those scenarios do not seem to be very realistic under current climatic conditions. The most likely process which stabilizes ground ice in Antarctica seems to be occasional recharge by snow melt water.

Studies modeling thermal conductivity and heat fluxes based on field measurements are rare in Antarctic soils of the Dry Valleys. Putkonen et al. (2003) measured the sensible heat flux based on the difference between measured net radiation and ground heat flux in Beacon Valley using in situ measurements of soil thermal properties and 1-dimensional thermal conductivity model (Putkonen 1998). At this site, soils consist of ~20 cm dry sublimation till underline by massive ice. They found that mean annual ground heat flux is close to zero indicating long term thermal equilibrium. The annual mean net radiation is positive (24 Wm^{-2}) suggesting a net advection of sensible heat into atmosphere from this area. Measured values for thermal conductivity in dry debris are ~2 times smaller (0.2 $Wm^{-1}K^{-1}$) as values found from modeling (see above 0.4 $Wm^{-1}K^{-1}$). The difference between modeled and measured values may well be in the range of the instrument uncertainty.

Pringle et al. (2003) used temperature data collected on three sites from Table Mountain with different lithology and ice contents to calculate apparent thermal diffusivity (ADT). They found strong dependence of ADT with abundance of ice and determined an ice-fraction dependency of heat capacity of 1.7 to 1.8 $MJm^{-3}\,°C^{-1}$ causing a range of conductivity of ice rich soils between 2.5 to 4.1 $Wm^{-1}\,°C^{-1}$. Pringle et al. (2003) treated the heat transfer as purely conductive due to the very dry conditions and absence of liquid water. The lower value of heat conductivity is in good agreement with values from Putkonen et al. (2003) found for the massive ice. The generally low thermal conductivity found in Antarctic soils is an order of magnitude lower as in Arctic soils (6-26 times lower) reflecting the very dry conditions.

Summary and Future Potentials

Arctic versus Antarctic heat and water transfer processes

Other than during freeze back and snow melt infiltration, heat is largely transferred through conduction in soils at both regions. In non saturated Arctic soil, vapor migration occurs during all thermal periods while water advection occurs in frozen saturated soils. In dry Antarctic soils, vapor diffusion is a main process of water transport. The total amounts of water transferred are generally rather small; however, over longer terms could be significant, for example for the formation of patterned ground features (for example circles, ice wedges).

Snow melt is an important event for recharge of ground ice in Antarctica and a significant latent heat input for Arctic soils.

Factors affecting the heat transfer processes

The main factors determining the heat transfer are (i) phase composition of soil (specifically available pore space) which enables vapor diffusion and/or water advection (ii) the temperature gradient between atmosphere and soil which is largely affected by the snow cover.

What should happen next?

We need further detailed case studies (experimental and modeling) to face the challenge of highly nonlinear and strongly coupled processes which lead to a complex phenomenology. We still lack accurate methods for measuring relevant state variables of the system, for example the phase density of ice or water vapor, and even more so by the lack of sufficiently accurate instruments for measuring fluxes of thermal energy and of water. The processes of water and heat dynamics in permafrost soils, i.e. their potential relative weight should be assed quantitatively which is a topic of a future publication

Acknowledgments

We would like to thank Pier Paul Overduin for discussion about this topic.

References

In the following, references are organized geographically (Arctic versus Antarctic). Not all literature from Alaska is cited in the text since many references are repetitive.

Arctic

Boike, J., Roth, K. & Overduin, P.P. 1998. Thermal and hydrologic dynamics of the active layer at a continuous permafrost site (Taymyr Peninsula, Siberia). *Water Resources Research* 34(3): 355-363.

Chen, G. & Chamberlain, E.J. 1988. Observations of moisture migration in frozen soils during thawing. *Proceedings of the Fifth International Conference on Permafrost, V. 1, Trondheim, Norway, 2–5 August 1988:* 308-312.

Hallet, B. 1990. Self-organization in freezing soils: From microscopic ice lenses to patterned ground, *Can. J. Phys*. 68: 842-852.

Hinkel, K.M., Outcalt, S.I. & Nelson, F.E. 1990. Temperature variation and apparent diffusivity in the refreezing active layer, Toolik Lake, Alaska. *Permafrost and Periglacial Processes* 1: 265-274.

Hinkel, K.M. & Outcalt, S.I. 1993. Detection of nonconductive heat transport in soils using spectral analysis. *Water Resour. Res*. 29: 1017-1023.

Hinkel, K.M., Outcalt, S.I. & Nelson, F.E. 1993. Near-surface summer heat-transfer regimes at adjacent permafrost and non-permafrost sites in Central Alaska. *Proceedings of the Sixth International Conference on Permafrost, Beijing, China, 5–9 July 1993:* 261-266.

Hinkel, K.M. & Outcalt, S.I. 1994. Identification of heat transfer processes during soil cooling, freezing, and thawing in Central Alaska. *Permafrost and Periglacial Processes* 5: 217-235.

Hinkel, K.M. & Outcalt, S.I. 1995. Detection of heat-mass transfer regime transitions in the active layer using fractal geometric parameters. *Cold Regions Science Technology* 23: 293-304.

Hinkel, K.M. 1997. Estimating seasonal values of thermal diffusivity in thawed and frozen soils using temperature time series. *Cold Regions Science Technology* 26: 1-15.

Hinzman, L.D., Kane, D.L., Benson, C.S. & Everett, K.R. 1991. Hydrologic and thermal properties of the active layer in the Alaskan Arctic. *Cold Regions Science and Technology* 19: 95-110.

Kane, D.L., Gieck, R.E. & Hinzman, L.D. 1990. Evapotranspiration from a small Alaskan arctic watershed. *Nordic Hydrol*. 21: 253-272.

Kane, D.L., Hinzman, L.D. & Zarling, J.P. 1991. Thermal response of the active layer to climatic warming in a permafrost environment. *Cold Regions Science and Technology* 19: 111-122.

Kane, D.L., Hinkel, K.M., Goering, D. J., Hinzman, L.D. & Outcalt, S.I. 2001. Non-conductive heat transfer associated with frozen soils. *Global and Planetary Change* 29: 275-292.

Krantz, W.B. 1990. Self-organization manifest as patterned ground in recurrently frozen soils. *Earth Sci. Rev*. 29: 117-130.

Nelson, F.E., Outcalt, S.I., Goodwin, C.W. & Hinkel, K.M. 1985. Diurnal thermal regime in a peat-covered palsa, Toolik Lake, Alaska: *Arctic* 38(4).

Osterkamp, T.E. & Romanovsky, V.E. 1999. Evidence for warming and thawing of discontinuous permafrost in Alaska. *Permafrost Periglacial Processes* 10: 17-37.

Outcalt, S.I. & Hinkel, K.M. 1989. Night-frost modulation of near-surface soil-water ion concentration and thermal fields. *Physical Geography* 10: 336-348.

Outcalt, S.I., Nelson, F.E. & Hinkel, K.M. 1990. The zero-curtain effect: Heat and mass transfer across an isothermal region in freezing soil. *Water Resources Research* 26(7): 1509-1516.

Outcalt, S.I. & Hinkel, K.M. 1996. Thermally driven sorption, desorption, and moisture migration in the active layer in Central Alaska. *Physical Geography* 17: 77-90.

Outcalt, S.I., Hinkel, K.M., Nelson, F.E. & Miller, L.L. 1998. Estimating the magnitude of coupled-flow effects in the active layer and upper permafrost, Barrow, Alaska U.S.A. *Proceedings of the Seventh International Conference on Permafrost*: 869-873.

Overduin, P.P. & Kane, D.L. 2006. Frost boils and soil ice content: Field observations. *Permafrost and Periglacial Processes* 17: 291-307.

Parmuzina, O.Y. 1980. Cryogenic texture and some characteristics of ice formation in the active layer (in Russian). In: A.I. Popov (ed.), *Problems of Cryolithology*, V. 7. Moscow: Moscow Univ. Press, 1978, 131-152 (English translation *Polar Geogr. Geol*.: 131-152).

Putkonen, J. 1998. Soil thermal properties and heat transfer processes near Ny-Alesund, Northwest Spitsbergen, Svalbard. *Polar Research* 17(2): 165-179.

Ray, R.J., Krantz, W.B., Caine, T.N. & Gunn, R.D. 1983. A model for sorted patterned-ground regularity. *J. Glaciol*. 29: 317-337.

Romanovsky, V.E. & Osterkamp, T.E. 1995. Interannual variations of the thermal regime of the active layer and near-surface permafrost in northern Alaska. *Permafrost and Periglacial Processes* 6: 313-335.

Romanovsky, V.E. & Osterkamp, T.E. 2000. Effects of unfrozen water on heat and mass transport processes in the active layer and permafrost. *Permafrost and Periglacial Processes* 11: 219-239.

Roth, K. & Boike, J. 2001. Quantifying the thermal dynamics of a permafrost site near Ny-Ålesund, Svalbard. *Water Resources Research* 37(12): 2901-2914.

Rouse, W.R. 1984. Microclimate of arctic tree line 2. Soil microclimate of tundra and forest. *Water Resour. Res*. 20: 67-73.

Santeford, H.S. 1978. Snow soil interaction in interior Alaska. In: S.C. Colbeck & M. Ray (eds.), *Modeling of Snow Cover Runoff.* Cold Reg. Res. and Eng. Lab., Hanover, New Hampshire, 311-318.

Solomatin, V.I. & Xu, X. 1994. Water migration and ice segregation in the transition zone between thawed and frozen soil, *Permafrost Periglacial Processes* 5: 185-190.

Woo, M.K. 1982. Upward flux of vapor from frozen materials in the High Arctic. *Cold Regions Science Technology* 5: 269-274.

Yershov, E.D. 1998. *General Geocryology.* New York, NY: Cambridge Univ. Press.

Antarctic

Anderson, D.W. & Morgenstern, N.R. 1973. Physics, chemistry, and mechanics of frozen ground: A review. *Proceedings of the Second International Conference on Permafrost, Yakutsk, USSR*. Washington, DC: National Academy of Sciences Press.

Beyer, L., Bockheim, J.G., Campbell, I.B. & Claridge, G.G.C. 1999. Review: Genesis, properties and sensitivity of Antarctic Gelisols. *Antarctic Science* 11(4): 387-398.

Bockheim, J.G. 2002. Landform and soil development in the McMurdo Dry Valleys, Antarctica: A regional synthesis. *Arctic Antarctic and Alpine Research* 34: 308-317.

Dickinson, W.W. & Rosen, M.R. 2003. Antarctic permafrost: An analogue for water and diagenetic minerals on Mars. *Geology* 31: 199-202.

Friedman, E.I. 1978. Melting snow in the dry valleys is a source of water for endolithic microorganisms. *Antarctic Journal of the United States* 13: 162-163.

Gooseff, M.N., Barrett, J.E., Doran, P.T., Fountain, A.G., Lyons, W.B., Parsons, A.N., Porazinska, D.L., Virginia, R.A. & Wall, D.H. 2003. Snow-patch influence on soil biogeochemical processes and invertebrate distribution in the McMurdo Dry Valleys, Antarctica. *Arct. Antarct. Alp. Res*. 35: 91- 99.

Hagedorn, B., Sletten, R.S. & Hallet, B. 2007. Sublimation and ice condensation in hyperarid soils: Modeling results using field data from Victoria Valley, Antarctica. *Journal of Geophysical Research* 112.

McKay, C.P., Mellon, M.T. & Friedman, E.I. 1998. Soil temperature and stability of ice-cemented ground in McMurdo Dry Valleys, Antarctica. *Antarctic Sciences* 10: 31-38.

Pringle, D.J., Dickinson, W.W., Trodahl, H.J. & Pyne, A.R. 2003. Depth and seasonal variations in the thermal properties of Antarctic Dry Valley permafrost from temperature time series analysis. *J. Geophys. Res*. 108(B10): doi:10.1029/2002JB002364.

Putkonen, J.K., Sletten, R.S. & Hallet, B. 2003. Atmosphere/ice energy exchange through thin debris cover in Beacon Valley, Antarctica. *Proceedings of the Eighth International Conference on Permafrost, Zürich, Switzerland.*

Schorghofer, N. 2005. A physical mechanism for long-term survival of ground ice in Beacon Valley, Antarctica. *Geophys. Res. Letters* 32: L19503, doi:10.1029/2005GL023881.

Sletten, S.R., Hallet, B. & Fletcher, R.C. 2003. Resurfacing time of terrestrial surfaces by the formation and maturation of polygonal patterned ground. *Geophys. Res*. 108(E4), 8044: doi:0.1029/2002JE001914.

Sugden, D.E., Marchant, D.R., Potter, N., Souchez, R.A., Denton, G.H., Swisher, C.C. III. & Tison, J.-L. 1995. Preservation of Miocene glacier ice in East Antarctica. *Nature* 376: 412-414.

van der Wateren, D. & Hindmarsh, R. 1995. Stabilists strike again. *Nature* 376: 389-391.

Estimation of Hydraulic Properties in Permafrost-Affected Soils Using a Two-Directional Freeze-Thaw Algorithm

W. Robert Bolton
Alfred Wegener Institute for Polar and Marine Research
Julia Boike
Alfred Wegener Institute for Polar and Marine Research
Pier Paul Overduin
Alfred Wegener Institute for Polar and Marine Research

Abstract

In this study, a two-directional freeze-thaw (TDFT) algorithm is used to estimate the hydraulic conductivity and storage capacity of permafrost-affected soils. The physically based TDFT algorithm is based upon the Stefan equation. The algorithm is driven by both the surface temperature and temperature at a specified depth and uses physical properties of the soil (bulk density, porosity, soil moisture, organic and mineral fraction, and freezing temperature of water) as input variables. The TDFT is tested in a wet valley bottom and along a relatively dry hill slope in the Imnavait Creek Watershed, Alaska. Results indicate that the timing of thaw/freezeback periods, the maximum thaw depth, and latent heat effects are accurately simulated. Using the TDFT algorithm to derive hydraulic variables is an improvement from the previous methods used to represent the active layer in hydrological modeling studies.

Keywords: active layer; hydraulic conductivity; hydrologic modeling; permafrost; porosity.

Introduction

In (sub-) arctic environments, most biologic, geomorphic, hydrologic, and ecologic processes take place within the active layer —the thin soil layer above the permafrost that seasonally freezes and thaws (Kane et al. 1991, Hinzman et al. 1998, Woo 2000). The depth of the active layer, as well as the rate of seasonal freezing and thawing, is dependent upon a number of factors including soil properties (thermal conductivity, bulk density, moisture content, vegetation type/thickness), meteorologic conditions (air and surface temperature, presence of snow cover), and disturbance (either anthropogenic or natural disturbance such as wildfire) (Woo 1986). As each of these factors are spatially and temporally variable, the position of the freeze-thaw interface is also spatially and temporally variable (Woo & Steer 1983).

Hydrologically speaking, the (sub-) arctic environment is unique in that the thermal and hydrologic regimes of the soil (permafrost versus non-permafrost) can vary greatly over short horizontal spatial scales, with depth, and over time. It is well documented that the hydraulic conductivity of ice-rich permafrost soils can be several orders of magnitude lower than their unfrozen counterparts (e.g., Burt & Williams 1976, Kane & Stein 1983). Furthermore, ice-rich conditions at the freeze-thaw interface significantly reduce the permeability of the soil, effectively limiting the soil water capacity of the soil (Dingman 1975, Woo 1990).

However, the point and hill slope scale understanding of permafrost soils, specifically the effect of the freezing and thawing of the active layer on hydrologic proceses, have not been adequately or systematically incorporated into meso-scale hydrologic models (Vörösmarty et al. 1993). Representation of the active layer in previous modeling studies includes switching soil properties for the winter and summer periods (Sand & Kane 1986) and use of a simple square root of time function to estimate the active layer depth (Zhang et al. 1998, Schramm et al. 2007). Thermal models are absent in most hydrologic models because of computational time requirements and complexities in model coupling.

Fox (1992) introduced a physically-based one-directional freeze-thaw (ODFT) algorithm for estimating the position of the freeze-thaw interface. The ODFT is driven by surface temperature. Woo et al. (2004) modified the ODFT by inverting the equations and driving the algorithm in two-directions by using temperatures at the surface and at a specified depth in the soil column. This two-directional freeze-thaw (TDFT) algorithm improves the representation of the freeze-thaw interface during the freezeback period.

The objective of this paper is to present a method for estimating hydraulic conductivity and effective porosity (proxy for soil storage capacity) using the TDFT algorithm.

Methods

Overview of the TDFT algorithm

The main difference between frozen and thawed soils is the difference in hydraulic conductivity and storage capacity, both a function of amount of pore ice in the soils (Woo 1986). In our conceptualization of the arctic hydrologic regime, frozen soils are represented with a very low hydraulic conductivity, while thawed soils within the active layer are represented with a larger hydraulic conductivity. Effective porosity (P_{eff}) is used as a proxy for storage capacity. In frozen soils, the presence of pore ice reduces the effective porosity of the soil.

The freeze-thaw interface in the active layer is determined using the TDFT algorithm. The physically-based TDFT algorithm is based upon the Stefan's equation of heat conduction (Jumikis 1977). One of the assumptions of the Stefan equation is that sensible heat effects are negligible. This assumption typically holds in soils with high moisture contents (Lunardini 1981). The algorithm requires inputs for each soil layer: specified depth, bulk density, porosity, fraction of organic and mineral soils, soil moisture content, the threshold for freezing the soil moisture, and minimum unfrozen water content in frozen soils. For each soil layer, the thermal conductivity and the energy required to freeze or thaw that soil layer is calculated. The algorithm is driven by the surface temperature and temperature at the bottom of the soil column. At each time step, the energy available to freeze/thaw the soil is determined using a simple 'degree-day' formulation. The amount of energy available is compared to the amount of energy required to freeze/thaw a soil layer. The total amount of freezing or thawing of the soil layers is determined by the total amount of energy available from the surface and at the bottom of the soil column. The procedures for determining the thermal conductivity, the energy available for freezing/thawing the soils, and determination of the total freezing and thawing of the soil layers are described in detail in Woo et al. (2004). In our formulation, the TDFT is slightly modified such that soil thawing from the bottom of the soil column is not allowed.

Estimation of hydraulic properties

The next steps are to estimate the freeze-thaw interface, the hydraulic conductivity, and the effective porosity. After each time step, the total thawed thickness and frozen thickness (D_t and D_f, respectively) of each soil layer are determined. The position of the freeze-thaw interface is estimated for each soil layer, from the surface downward, by evaluating the thermal condition of the neighboring soil layers. For example, if soil layer X_{+1} is completely frozen ($D_t = 0.0$), while soil layer X_{-1} is completely thawed (D_t = soil layer thickness), then we assume that the active layer is developing and the position of the freeze-thaw boundary is located at D_t depth from the top of the soil layer, X. By evaluating each soil layer after each time step, multiple freeze-thaw interfaces within the soil column are possible.

Once the D_t and D_f are determined for each soil layer, the hydraulic conductivity for each soil layer is estimated using a simple weighting function. For each soil layer, the frozen and thawed hydraulic conductivity are specified. If the entire soil layer is either frozen or thawed, the appropriate hydraulic conductivity is assigned to that soil layer. If the freeze-thaw interface is located within a soil layer, the horizontal (K_H) and vertical hydraulic (K_V) conductivities are determined using simple weighting functions:

$$K_H = \frac{K_f D_f + K_t D_t}{D} \tag{1}$$

$$K_V = \frac{D}{\left[\dfrac{D_f}{K_f} + \dfrac{D_t}{K_t}\right]} \tag{2}$$

where $K_{f,d}$ are the frozen and thawed hydraulic conductivities, and D is the total thickness of the soil layer.

The effective porosity for each soil layer is simply estimated from the fractional components of the soil layer:

$$P_{eff} = 1.0 - F_m - F_o - F_{ice} \tag{3}$$

where $F_{m,o,ice}$ are the fractional components of mineral, organic, and ice.

Results

Evaluation of the TDFT

The TDFT algorithm is tested in the Imnavait Creek Watershed, Alaska (68°30′N, 149°15′W). Two sites, one in a valley bottom and one along a hill slope, are selected for testing. Compared with the hill slope site, the valley bottom site has a thick surface organic layer (0.3 m versus 0.2 m) and has a high soil moisture content. Table 1 shows the soil properties used to test the TDFT. The soil moisture content of each soil layer is the linear interpolation of field measurements to the center of each soil layer.

The surface temperature sensors used in the valley and hill slope sites are located at 2 and 7 cm below the land surface, respectively. Ground temperature measurements, located at 98 and 69 cm below the ground surface, were used for valley bottom and hill slope sites. In our simulations, the ground temperature can only be used in the soil freezing process (soils are not allowed to thaw from depth).

Initial simulations resulted in an underestimation of the maximum thaw depths at each site, probably as a result of underestimation of the amplitude of fluctuation of the ground surface temperature. The timing of the beginning of thaw/freezeback process was also slightly offset from measured field data. To better estimate ground surface temperatures, the near-surface soil temperatures were estimated via extrapolation of amplitude to the surface (Fig. 1). This resulted in an amplification of annual surface temperature fluctuation by 5% at the valley bottom and by 38/27% for temperatures above/below 0°C at the hill slope site. We explain the difference in amplitude by differences in near-surface moisture availability. Compared to the dry hill slope site, the wet valley bottom site has a high thermal diffusivity in the near surface soils. The combination of the high thermal diffusivity as well as the near proximity to the ground surface result in a much smaller surface temperature adjustment at the valley bottom site. Figure 2 displays the simulated freeze-thaw interface compared with measured soil temperatures and soil moisture content at each site.

Table 1: Soil properties of the valley bottom and hill slope sites.

Layer	Soil Depth (cm)	Valley Bottom Site: Bulk Density (kg/m^3)	Porosity (%)	Organic / Mineral Fractions	SMC / SMC min	Hill Slope Site: Bulk Density (kg/m^3)	Porosity (%)	Organic / Mineral Fractions	SMC / SMC min
1	10	150	80	0.20 / 0.0	0.45 / 0.05	150	80	0.20 / 0.0	0.40 / 0.06
2	10	260	63	0.37 / 0.0	0.60 / 0.15	560	63	0.37 / 0.0	0.40/ 0.04
3	10	855	55	0.25 / 0.2	0.55 / 0.14	1530	40	0.0 / 0.6	0.38 / 0.10
4	10	1530	48	0.0 / 0.48	0.48 / 0.14	1530	40	0.0 / 0.6	0.40 / 0.12
5	10	1530	40	0.0 / 0.6	0.40 / 0.06	1530	40	0.0 / 0.6	0.40 / 0.12
6	10	1530	40	0.0 / 0.6	0.40 / 0.06	1530	40	0.0 / 0.6	0.40 / 0.12
7	10	1530	40	0.0 / 0.6	0.40 / 0.05	1530	40	0.0 / 0.6	0.40 / 0.12
8	15	1530	40	0.0 / 0.6	0.40 / 0.05	1530	40	0.0 / 0.6	0.40 / 0.12

SMC / SMC min: Volumetric soil moisture content / Volumetric unfrozen water content of frozen soil.

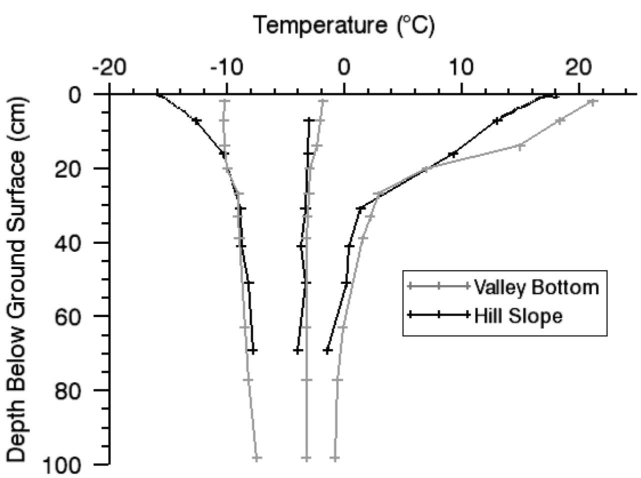

Figure 1. Trumpet curves showing the minimum, maximum, and average temperatures at the valley bottom site (light line) and hill slope site (dark line) for 2003. The "+" indicates location of measurements.

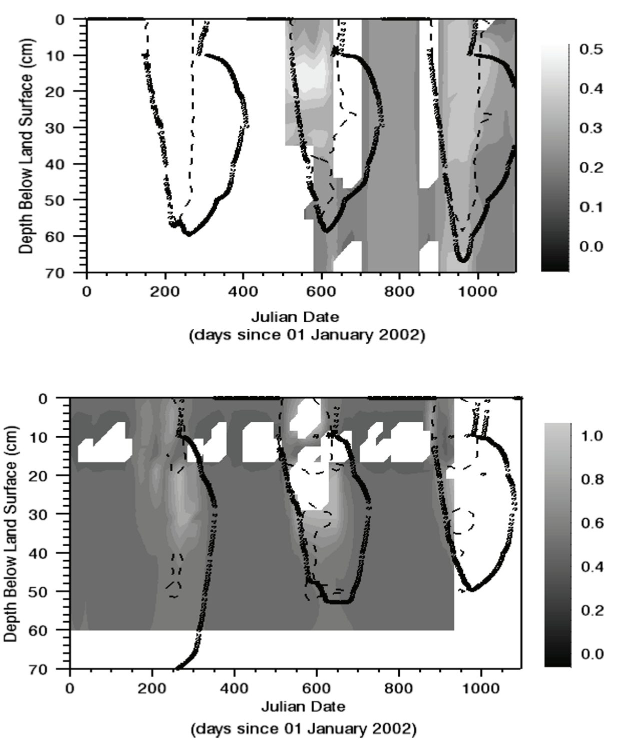

Figure 2. Comparison of the simulated freeze-thaw interface (dark dots) in the valley bottom (top panel) and hill slope (bottom panel) sites with the -0.1°C isotherm (dark dashes) and unfrozen soil moisture content (background). Color bar indicates volumetric soil moisture content. Solid white regions indicate missing data.

For these simulations and comparisons, daily temperature and soil moisture data measured at 12:00 are used. Results indicate that for most years, the TDFT algorithm is able to simulate the beginning of thaw, the maximum thaw depth, and freezeback period. The latent heat effect during the freezeback period is also represented. Estimated porosities derived from these simulations are shown in Figure 3.

Discussion and Conclusions

The seasonal freezing and thawing of the active layer and the associated changes in hydraulic properties are defining features of arctic hydrologic systems. Despite the known importance of the active layer in hydrologic systems, it has been poorly represented in meso-scale hydrologic models. The TDFT algorithm provides a foundation for estimating the freezing and thawing of the soils, hydraulic conductivity, and storage capacity of the soils.

The TDFT, based upon the Stefan equation, assumes that sensible heat effects are negligible. Care must be taken when applying the TDFT in drier areas, where sensible heat fluxes may be an important component of the energy balance. A basic understanding of the physical system being modeled is critical before applying the TDFT.

Using the TDFT to estimate hydraulic properties is an improvement over previously used methods in that 1) changes in the thermal and hydrologic regimes are continuously and adequately captured over time; 2) the ability to simulate the freezeback period allows for longer (year-to-year) simulations, whereas the other methods such as using the

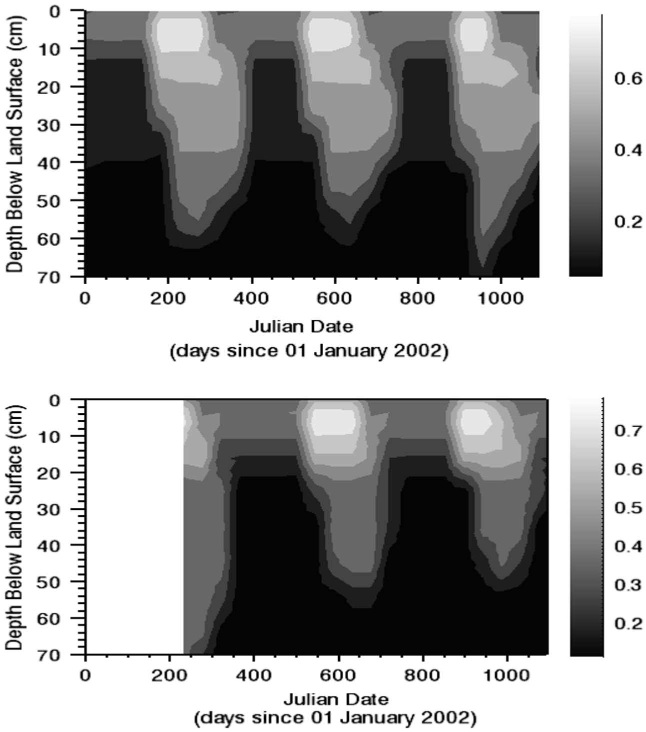

Figure 3. Simulated soil porosity at the valley site (top panel) and hill slope (bottom panel). Solid white regions indicate missing data.

square root of time function is only able to simulate the thawing process; 3) the TDFT is physically based, requiring no prior calibration; and 4) the TDFT is computationally cheap.

The depth and rate of thawing/freezing of the active layer are both spatially and temporally variable. As a result the hydraulic properties of the soils are spatially (x-, y-, and z-directions) and temporally (both short and long term) variable. Accurate freeze-thaw boundary simulations using the TDFT algorithm are highly dependent upon accurate surface temperature data. In order to take full advantage of the TDFT derived variables in (spatially-distributed) meso-scale models, a method needs to be developed to obtain accurate spatial and temporal surface temperatures from within the modeling area.

Acknowledgments

We gratefully acknowledge financial support by a Heimholtz Young Investigator Grant (VH-NG 203) awarded to Julia Boike. We also appreciate the helpful suggestions of the reviewers.

References

Burt, T. & Williams, P. 1976. Hydraulic conductivity in frozen soils. *Earth Surficial Processes* 1(4): 349-360.

Dingman, S.L. 1975. *Hydrologic effects of frozen ground.* Special Report 218. U.S. Army Cold Regions Research and Engineering Laboratory.

Fox, J.D. 1992. Incorporating freeze-thaw calculations into a water balance model. *Water Resources Research* 28: 2229-2244.

Hinzman, L., Goering, D. & Kane, D. 1998. A distributed thermal model for calculating soil temperature profiles and depth of thaw in permafrost regions. *Journal of Geophysical Research* 103(D22): 28,975-28,991.

Jumikus, A.R. 1977. *Thermal Geotechnics*. Rutgers University Press, 375 pp.

Lunardini, V. 1981. *Heat transfer in cold climates.* New York: Van Nostrand Reinhold, 731 pp.

Kane, D., Hinzman, L. & Zarling, J. 1991. Thermal response of the active layer to climatic warming in a permafrost environment. *Cold Regions Science and Technology* 19(2): 111-122.

Kane, D.L. & Stein, J. 1983. Water movement into seasonally frozen soils. *Water Resources Research* 19(6): 1547-1557.

Sand, K. & Kane, D.L. 1986. Effects of seasonally frozen ground in snowmelt modeling. In: D.L. Kane (ed.), *Proceedings of the Cold Regions Hydrology Symposium.* American Water Resources Association, 321-327.

Schramm, I., Boike, J., Bolton, W.R. & Hinzman, L. 2007. Application of TopoFlow, a spatially distributed hydrologic model to the Imnavait Creek Watershed, Alaska. *Journal of Geophysical Research* 112:G04S46, doi:10.1029/2006JG000326.

Vörösmarty, C., Gutowski, W., Person, M., Chen, T.-C. & Case, D. 1993. Linked atmosphere-hydrology models at the macroscale. In: W. Wilkinson (ed.), *Macroscale Modeling of the Hydrosphere.* No. 214 in International Association of Hydrological Sciences, 3-27.

Woo, M.-K. 1986. Permafrost hydrology in North America. *Atmosphere-Ocean* 24(3): 201-234.

Woo, M.-K. 1990. Permafrost hydrology. In: T. Prowse, C. Ommanney, & M.-K. Woo (eds.), *Northern Hydrology, Canadian Perspectives, Proceedings of the Northern Hydrology Symposium.* Canadian National Hydrology Research Institute Science Report 1: 63-76.

Woo, M.-K. 2000. Permafrost and Hydrology. In: N. Nuttal & T.V. Callaghan (eds.),, *The Arctic: Environment, People, Policy.* Harwood Academic Publications, 57-96.

Woo, M.-K., Arain, M.A., Mollinga, M. & Yi, S. 2004. A two-directional freeze and thaw algorithm for hydrologic and land surface modeling. *Geophysical Research Letters*: L12501, doi:10.1029/ 2004GL019475.

Woo, M.-K. & Steer, P. 1983. Slope hydrology as influenced by thawing of the active layer. *Canadian Journal of Earth Science* 20: 978-986.

Zhang, Z., Kane, D. & Hinzman, L. 2000. Development and application of a spatially-distributed Arctic hydrological and thermal process model (ARHYTHM), *Hydrological Processes* 14: 1017-1044.

Engineering Solutions for Foundations and Anchors in Mountain Permafrost

Ch. Bommer
WSL, Swiss Federal Institute for Snow and Avalanche Research SLF, 7260 Davos Dorf, Switzerland

H.R. Keusen
Geotest AG, 3052 Zollikofen, Switzerland

M. Phillips
WSL, Swiss Federal Institute for Snow and Avalanche Research SLF, 7260 Davos Dorf, Switzerland

Abstract

Various technical solutions for foundations and anchors of infrastructures in permanently frozen ground are examined. Focus is placed on different categories of infrastructures and their sensitivity to changing subsurface conditions, primarily caused by modifications in the ice and water contents of the permafrost. The requirements for infrastructures with high safety standards such as cableway stations and pylons are determined by factors including the mass of the building, its serviceability, dynamic forces engendered by the cable mechanism, and the bearing capacity of the ground. In contrast, the conditions for a structure such as an alpine hut are mainly given by the relatively low mass of the building, snow loads, wind effects, and the bearing capacity of the ground. It is crucial that design considerations involve an integral approach and take into account the influences of global warming and the more intensive time and cost factors required to complete a project.

Keywords: anchor; bearing capacity; foundation; mountain permafrost; serviceability.

Introduction

Changing subsurface conditions represent the main problem for infrastructures in mountain permafrost. The reasons for changing subsurface conditions can be global warming, construction work, an existing infrastructure, or a combination of these, and can lead to permafrost ice warming, melting, and finally to complete degradation. After the soil and rock characteristics, ice content and temperature strongly affect the subsurface conditions and play a vital role in controlling the deformation behaviour and the bearing capacity of infrastructures.

On the other hand, the serviceability determines the maximal allowable vertical and horizontal displacements of an infrastructure. The serviceability requirements depend on building categories (Table 1). Cableway stations and pylons or pipelines are highly sensitive to differential displacements, resulting in a higher urgency for repairs after displacements, whereas communication structures (e.g., telecommunication antennae) or alpine huts and mountain restaurants react less delicately. Therefore, the building category controls the differential deformation sensitivity or the serviceability respectively.

Combining the controlling subsurface conditions with the serviceability of an infrastructure is an essential step in the development of an adequate foundation concept. In addition, the mass of the building, snow loads, dynamic loads and the influences of present and future global warming must be considered. Depending on the subsurface and load conditions, anchor reinforcements for the foundation may be necessary. In this paper, we examine engineering solutions for foundations and anchors for various building categories in mountain permafrost.

Design Considerations

Time and cost intensity

The time and cost intensity required for the construction of infrastructure in mountain permafrost is higher in comparison with infrastructure located in permafrost-free terrain. The site investigation in particular requires a longer period of time. If the first site study indicates a possible permafrost occurrence, the preliminary study should take in account further *in situ* investigations to determine the characteristic geotechnical parameters. In addition to the typical examinations regarding the foundations, measurements of temperature and deformation should be carried out for at least one year prior to construction. With the resulting data, a first evaluation of the ice content, ground temperature, active layer thickness and deformation rate can be carried out. Sustainable design considerations can only be ensured with this crucial information.

The following additional factors can also have a time and cost-increasing effect: the obtention of approval to build outside an official construction zone; the environmental impact assessment of the projected structure; climatic conditions such as snow, air temperature or altitude; the logistics like accessibility and transportation; and the short time frame available for construction at high altitudes. All these factors account for a significantly higher time and cost intensity for infrastructures in mountain permafrost.

Effects on the ground and structure

For the design of infrastructure in mountain permafrost it is important to consider the effects on the ground. The main effects are due to the dead and live loads induced by an infrastructure. Other effects include heat input/thermal disturbance from building activity or the long-term thermal and mechanical influences of the infrastructure itself and those caused by global warming. Excavation activities also affect the ground. A warming of the excavated slope can cause instabilities and rockfall. In summary, there are mechanical influences (load), which change the stress condition, and there are thermal influences (heat exchange), which can change the geotechnical parameters of the ground. An appropriate design must take into account the geotechnical and thermal effects with respect to the bearing capacity, sliding and toppling (ultimate limit state [ULS]). The definition of ULS is satisfied if all design loads are below the ground resistance calculated for the section under consideration (Swisscode SN 505267).

The effects of modifications on the structure itself are as important as the effects on the ground. The allowable effects with respect to the deformation and creep rates are dependent on the serviceability of the infrastructure, which is usually defined in the service criteria agreements (Swisscode SN 505267) as an allowed inclination angle of a structure due to differential settlements. This inclination angle consists of a ratio of the differential settlement to the size (length) of the structure. In Table 1 the sensitivity limits for serviceability are given for different building categories. Not incorporated in Table 1 is the time factor, such as how fast a displacement takes place. Other effects on the structure, such as natural hazards in the vicinity or geotechnical and technical difficulties, are determined by the risk analysis. The aim of the latter is to identify all kinds of risks that could influence both the construction and use of an infrastructure. A consideration of all these effects on the structure is necessary for the design with respect to the serviceability (serviceability limit state [SLS]).

The ultimate and serviceability limit states result in two allowable values for the foundation pressure or anchor tension. Depending on the smaller value, the size and shape of a foundation or the type and length of an anchor are determined. Hence, only an integral design consideration, which includes all the above-described factors, ensures the sustainability of an infrastructure.

Table 1. Assessment of different building categories with the sensitivity limit for serviceability and the need for repairs.

Building categories	Sensitivity limit for serviceability		Urgency for repairs after displacement
	Uniform displacement	Differential displacement[1]	
Cableway station	moderate	high	high
Cableway pylon	moderate	high	high
Communication structure	low	high	moderate
Mountain hut	low	moderate	low
Mountain restaurant	low	moderate	moderate
Pipeline	high	high	high
Snow supporting structure	low	moderate	moderate

[1] e.g., leading to tilting and cracking of the structure.

Impact of global warming

Global warming shows an elevation dependency, whereby the warming at high elevation sites in the Alps may be more pronounced than at low elevations (Beniston & Rebetez 1996). The exact consequences are difficult to define, but the general warming tendency will lead to long-term degradation of mountain permafrost and a deepening of the active layer. Warming permafrost ice increases the creep ratio and decreases shear strength, which can lead to more pronounced mass movements. Melting of the permafrost ice induces horizontal (creep) and vertical displacements (settlement) and elevated pore water pressures (Andersland & Ladanyi 2004, Esch 2004). Ice segregation can cause uplift of infrastructures and terrain and lead to rock instabilities. These various impacts of global warming on an infrastructure in mountain permafrost must be considered during the design process with respect to the total service life of a building.

Technical Solutions

Shallow foundations

Foundation systems depend on load and subsurface conditions as described above. A shallow foundation transfers building loads to the ground very near the surface. Shallow foundations include, for example, single foundations, strip foundations, and slab-on-grade foundations. Therefore, if the subsurface consists of stable rock or the design loads are rather small, a shallow foundation type is suitable. In mountain permafrost, shallow foundations are common, because the subsurface conditions often consist of stable rock with high strength. On this account, cableway stations and pylons, mountain restaurants, and huts are often built with a shallow type of foundation such as single, strip or slab-on-grade foundations. Figure 1 shows the strip foundation of the

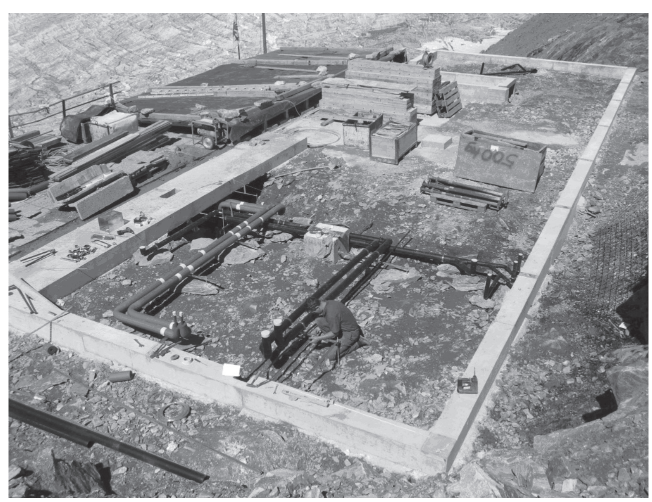

Figure 1. Strip foundation of new Finsteraarhorn mountain hut, Swiss Alps (Photograph: Ruch Architects, Meiringen 2003).

new Finsteraarhorn SAC (Swiss Alpine Club) mountain hut in the Swiss Alps.

Other reasons to choose a shallow foundation wherever possible are the complicated accessibility and transportation of heavy equipment for the excavation and material to the construction site. Shallow foundations are less complicated to implement than deep ones and therefore cheaper compared to all other types of foundations.

Deep foundations

As their name suggests, deep foundations are distinguished from shallow foundations by the depth to which they are embedded into the ground. The main reasons a geotechnical engineer would recommend a deep foundation over a shallow one are large design loads, high ice contents, warm permafrost at shallow depth or other site constraints such as unstable and complex geology. Deep foundations in mountain permafrost include drilled piles, shafts and piers. Drilled micropiles are often used for the construction or restoration of cableway stations and pylons. Permafrost degradation and active layer deepening can lead to a decrease in the bearing capacity of the ground, requiring additional anchors for the stabilisation of an existing structure – depending on the building category and its sensitivity limit for serviceability. In mountain permafrost the most practicable way to carry out this type of stabilisation is to drill a hole, place a threaded bar (micropile) and inject grout under high pressure into the surrounding clefts and fissures to increase the stability and bearing capacity. This is not a sustainable solution but it helps to allow continuation of the operation of an infrastructure without altering its location. For cableway stations and pylons in particular, this approach represents a cost-efficient and thus attractive way of restructuring.

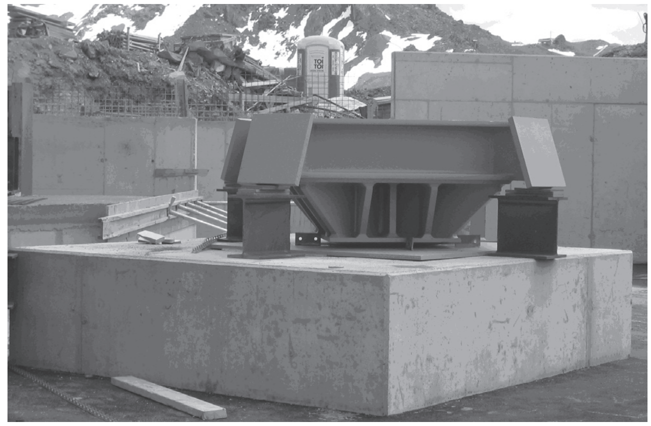

Figure 2a. Point bearing of a steel structure on a single concrete foundation, Ischgl, Austria (Photograph: M. Walser, Ischgl 2004).

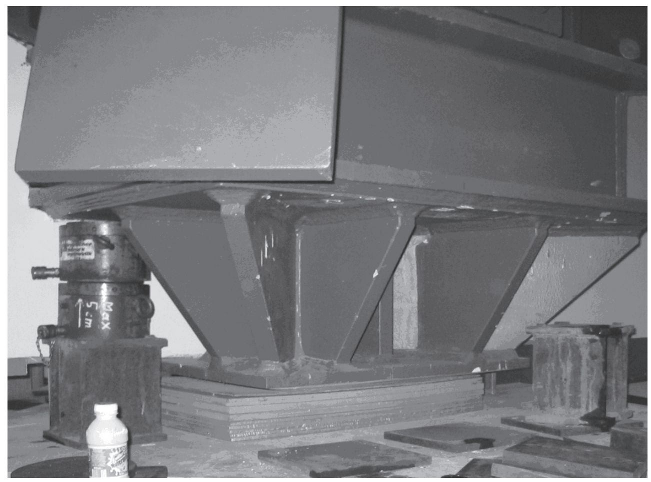

Figure 2b. Repositioning point bearing with hydraulic press, inserted steel plates, Ischgl, Austria (Photograph: M. Walser, Ischgl 2005).

Flexible structures

The latest technical experiences indicate that for locations with ice-rich permafrost, flexible systems are best adapted to meet the serviceability requirements. Laterally adjustable cableway pylons or three-point bearings for structures such as cableway stations (Phillips et al. 2007, Walser, pers. com.) and mountain restaurants are examples of these. Differential settlements within a three-point bearing do not generate internal constraints; this type of system can therefore extend the service life of a structure. Figure 2a shows one of the three-point bearings of a mountain restaurant in Ischgl, Austria. If settlement occurs, the steel construction can be uplifted hydraulically and steel plates can be inserted between the concrete support and the steel structure (Fig. 2b). The repositioning in this particular case takes place once a year and can be carried out in a few hours.

Snow nets (snow supporting structures) represent another flexible solution that is ideal for mountain permafrost. The hinged supports are mounted on ball joints, which allow them to swivel in a certain range. This behavior is particularly useful in creeping permafrost terrain and raises the service life of this type of avalanche defense structure (Phillips 2000). Experience in the Swiss Alps over the last decade shows that it is not sustainable to construct snow nets if the creep rates exceed 5 cm/year (Margreth 2007) and that floating foundations (steel bed plates) should be used in strongly creeping permafrost (Phillips & Margreth 2008, this proceedings).

Substrate structure

It is common practice to modify the substrate structure if necessary by replacing poorly graded material or broken rock with a well-graded gravely material. The modified substructure helps to uniformly distribute the load over an inhomogeneous surface. Compaction should take place in layers with a water content of the material close to the w_{opt} (Phillips et al. 2007). This facilitates the compaction work and increases the compactness of the packing (Soil Compaction Test, ASTM D698, Proctor 1933). A reinforcement consisting of steel nets or geotextile is possible. The reinforcement increases the bearing capacity, resulting in a higher design load and an even load distribution.

Insulation and cooling systems

To prevent heat transfer into the permafrost body (e.g.,

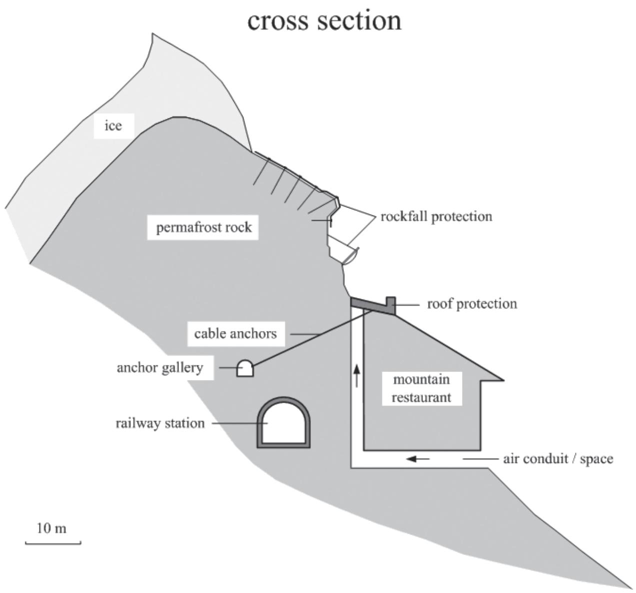

Figure 3. Scheme of air conduits, anchorage and anchor gallery, Jungfraujoch, Switzerland (after Keusen & Amiguet 1987).

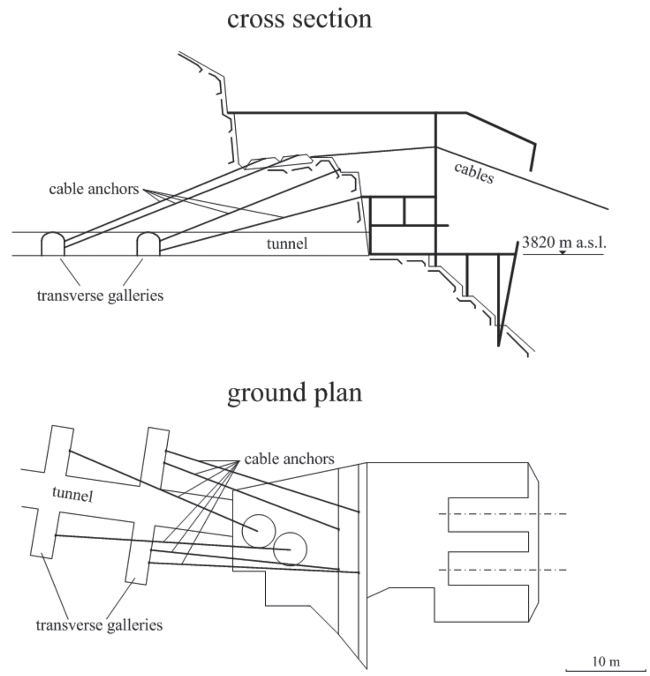

Figure 4. Scheme of anchorage including the transverse galleries, Klein Matterhorn, Switzerland (after Keusen & Haeberli 1983).

hydration heat emanating from curing concrete or conductive heat transfer from a heated structure above), a layer of insulation with high compressive strength (e.g., extruded polystyrene) should be placed between the foundation and the ground. Air conduits/spaces beneath a foundation and external wall represent another solution to protect the underlying permafrost (Fig. 3). These passive cooling systems are common, whereas experience with more sophisticated passive cooling systems (e.g., thermosyphons) is practically non-existent in the Alps. Active cooling systems (e.g., powered ventilation system) are used in individual cases but are not widespread in mountain permafrost infrastructures.

Anchors

Ground anchors normally consist of steel reinforcing bars or cables with a grout coating or a grout anchorage body (tieback). Rock or soil anchors can be installed prestressed or non-prestressed, respectively—prestressed is common practice. The non-prestressed are soil or rock nails and usually fully grouted. The force transmission of an anchor is based on a frictional bond between the grout and the surrounding ground. Anchors therefore react in a sensitive manner to changing subsurface conditions such as permafrost warming accompanied by loss of ice. The main implication of warming is reduced shear strength of anchors that can lead to a decreasing external bearing capacity and consequently, to accelerated deformation or failure of the supported structure.

The subsurface conditions, the size of the induced force and the risk potential of a failing structure determine the anchoring concept. In mountain permafrost most of the designed anchors are tied in bedrock. High stress and strain anchors with a large risk potential, such as those used for cableway stations and other exposed infrastructures, should be installed within an anchor gallery to avoid problems associated with injection anchors (e.g., freezing of grout, changing subsurface conditions) and to allow anchor replacements. Where possible, monitored anchors and load cells should be used. Figures 3 and 4 show two possible solutions for anchor galleries. In Figure 3, the rockfall and snow load roof protections of the mountain restaurant, Jungfraujoch, Switzerland, anchored with several high stressed cable anchors are illustrated (Keusen & Amiguet 1987). Figure 4 shows the traverse galleries from the access tunnel, used for anchorage of the cables and steel construction of the cableway station, Klein Matterhorn, Switzerland (Rieder et al. 1980, Keusen & Haeberli 1983). Drilling and prestressing of the anchors as well as the continued observation of the anchors occurs from the anchor gallery. This design approach ensures reliable monitoring, resulting in a higher factor of safety. Small stress and strain anchors such as those used for mountain huts, defence and communications structures, with a smaller risk potential, can be carried out with standard anchors without an anchor gallery. Margreth (2007) describes the important criteria and implications to install an anchor in mountain permafrost such as e.g., warming of the mixing water to a certain temperature to allow the curing of the injected grout in the anchor hole before freezing takes place.

In either case a monitoring and maintenance concept is highly recommended. It is compulsory for all prestressed permanent anchors to have accessible anchor heads over their service life. For high stress and strain anchors a permanent monitoring with load cells is a desirable objective. Likewise, there should be an anchor system redundancy, in order to allow maintenance work without safety reduction or interruption of operation.

Conclusions

The design consideration has to incorporate that the time and cost factors are higher for construction of an infrastructure in mountain permafrost in comparison with an infrastructure located in permafrost-free terrain. In particular the logistics such as the accessibility and transportation contribute to increasing time and cost for infrastructures in mountain permafrost. The necessity of undertaking extensive geotechnical investigations at least one year in advance of the start of construction also significantly extends the design and construction phase. The influences of present and future global warming, including the natural hazards involved, must be considered in the design of mountain infrastructure as well.

Various engineering solutions in mountain permafrost are affected by global warming and have been modified or restructured. Flexible technical solutions are well adapted to permafrost undergoing modification. In some cases, inappropriate technical solutions have been used and various mistakes have been made. Hence, development of guidelines for infrastructures in mountain permafrost is necessary to limit both cost and risk factors. The Swiss Federal Institute for Snow and Avalanche Research SLF is currently developing recommendations for infrastructures in alpine permafrost which should be published in 2009.

Acknowledgments

This research is supported by the Swiss Federal Office of Transportation FOT, armasuisse Real Estate and the Canton Valais. It is carried out in collaboration with the Swiss Alpine Club. The authors are thankful to W.J. Ammann and other anonymous reviewers of this paper for their helpful comments and suggestions.

References

Andersland, O.B. & Ladanyi, B. 2004. *An Introduction to Frozen Ground Engineering, XII*. Hoboken, New Jersey: John Wiley & Sons, Inc., 363 pp.

Beniston, M. & Rebetez, M. 1996. Regional behavior of minimum temperatures in Switzerland for the period 1979–1993. *Theoretical and Applied Climatology* 53(4): 231-243.

Esch, D.C. (ed.). 2004. *Thermal analysis, construction, and monitoring methods for frozen ground.* Technical Council on Cold Regions Engineering monograph. Reston, VA: American Society of Civil Engineers, 492 pp.

Keusen, H.R. & Amiguet, J.-L. 1987. Geologie, Felseigenschaften, Permafrost. *Schweizer Ingenieur und Architekt* (30-31): 905-906.

Keusen, H.R. & Haeberli, W. 1983. Site investigation and foundation design aspects of cable car construction in alpine permafrost at the „Chli Matterhorn," Wallis, Swiss Alps. *Permafrost Fourth International Conference*: 601-604.

Margreth, S. 2007. Defense structures in avalanche starting zones. *Technical Guideline as an aid to enforcement*. Bern and Davos: FOEN, SLF, 101 pp.

Phillips, M. 2000. *Influences of snow supporting structures on the thermal regime of the ground in alpine permafrost terrain.* Davos: Swiss Federal Institute for Snow and Avalanche Research SLF, 146 pp.

Phillips, M., Ladner, F., Müller, M., Sambeth, U., Sorg, J. & Teysseire, P. 2007. Monitoring and reconstruction of a chairlift midway station in creeping permafrost terrain, Grächen, Swiss Alps. *Cold Regions Science and Technology* 47(1-2): 32-42.

Phillips, M. & Margreth S. 2008. Effects of ground temperature and slope deformation on the service life of snow-supporting structures in mountain permafrost: Wisse Schijen, Randa, Swiss Alps. *Proceedings of the Ninth International Conference on Permafrost, Fairbanks, Alaska, June 29–July 3, 2008* (this proceedings)

Proctor, R.R. 1933. Fundamental principles of soil compaction. *Engineering News-Record* (9-13).

Rieder, U., Keusen, H.R. & Amiguet, J.-L. 1980. Geotechnische Probleme beim Bau der Luftseilbahn Trockener Steg-Klein Matterhorn. *Schweizer Ingenieur und Architekt* (18): 428-431.

Swisscode, SN 505267, 2003. *Geotechnical Design SIA 267.* Zurich: Swiss Society of Engineers and Architects, 104 pp.

Carbon, Nitrogen, and Phosphorus Interactions in the Hyporheic Zones of Arctic Streams that Drain Areas of Continuous Permafrost

William B. Bowden, Morgan J. Greenwald
Rubenstein School of Environment & Natural Resources, University of Vermont, Burlington, VT, USA
Michael N. Gooseff
Department of Civil & Environmental Engineering, Pennsylvania State University, University Park, PA, USA
Jay P. Zarnetske
Department of Geosciences, Oregon State University, Corvallis, OR, USA
James P. McNamara, John Bradford, Troy Brosten
Department of Geosciences, Boise State University, Boise, ID, USA

Abstract

In arctic streams, permafrost may influence hydrological and biogeochemical processes that control carbon and nutrient dynamics. We examined interactions among these processes in a fast-flowing, cobble-bottom stream and a slow-flowing, peat-bottom stream near Toolik Lake, within the foothills region of the Brooks Range, Alaska. Using a combination of ground penetrating radar, physical probing, and conservative solute injection experiments, we found that the thaw depths within the cobble-bottom stream were considerably deeper than in the peat-bottom stream. The maximum extent of hyporheic penetration followed a similar trend, but in both streams the hyporheic depth was less than the maximum extent of thaw. Hyporheic regeneration of N and P (estimated as mass fluxes) were in reasonable stoichiometric agreement. However, regeneration of C (estimated by whole-stream metabolism) was much greater than regeneration of either N or P, indicating considerable internal recycling of these essential elements.

Keywords: biogeochemistry; hyporheic zones; nutrients; thaw bulbs; tundra streams..

Prior to our current research, virtually nothing was known about hyporheic dynamics in Arctic streams draining areas with continuous permafrost. Substantial evidence from temperate streams suggests that the hyporheic zone can be an important site of organic matter turnover and a source of regenerated nutrients. However, permafrost exerts strong influences on surface processes that we initially thought might alter the structure and function of the hyporheic zone in Arctic streams. However, initial results reported by Edwardson (1997) and Edwardson et al. (2003) showed that hyporheic dynamics in the Kuparuk River, on the eastern North Slope of Alaska, were similar to those observed in temperate streams. In particular, we found that geomorphic profiles of stream channels (longitudinal more so than lateral) provide the necessary hydraulic gradients to drive hyporheic exchange through the streambed, as shown by Harvey and Bencala (1993) and Kasahara and Wondzell (2003). We also showed that biogeochemical processing in the hyporheic zone was important, potentially supplying from 14 to 162% of the benthic N uptake requirements in the Kuparuk River.

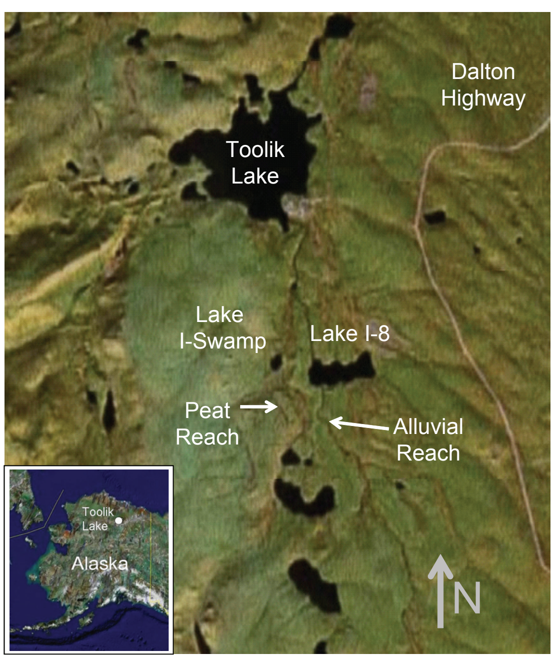

Figure 1. Location of the study streams. (Colored illustration available on CD-Rom.)

The purpose of this paper is to integrate the results of our work on hyporheic dynamics in tundra streams with results from a separate study of whole-stream metabolism in similar streams. These two studies provide insight into interactions among carbon, nitrogen, and phosphorus dynamics in the hyporheic zones of arctic tundra streams that overlie continuous permafrost.

Site Description and Methods

Study sites

The study area (Fig. 1) was located on the North Slope of the Brooks Range in Alaska, near the Toolik Field Station (68°38′N, 149°36′W), about 180 km south of the Arctic Ocean. Two common stream geomorphologic types occur on the tundra landscapes in this area: (a) high-gradient, alluvial streams with alternating riffle-pool sequences and (b) low-gradient, peat-bottom streams with a "beaded" morphology in which large, deep pools are connected by narrow, deep runs. We located two streams that represent these contrasting tundra stream types and that lie parallel to each other within a series of lakes and connecting streams that flow north into Toolik Lake. Kling et al. (2000) referred to these two stream reaches as the inlets to Lakes I-8 and I-Swamp in the I-Series. These two streams are of the same order, have the same aspect, and drain similar landscapes. They differ in that the alluvial reach has a higher gradient and drains an area that has no lakes, while the peat stream has a lower gradient and drains an area with several lakes.

Ground penetrating radar

We used ground penetrating radar (GPR) to establish the boundary between the thawed sediments in the active layer under the stream (the thaw bulb) and permafrost (Bradford et al. 2005, Brosten et al. 2006). We used a commercial pulsed radar system with 200 MHz antennas and high-powered transmitter (1000V) to maximize penetration beneath the streambed. The antennas and GPR control equipment were placed in the bottom of a small rubber boat, and pulled steadily across the stream and banks on either side while triggering the radar at a constant rate. While acquiring data, we were careful to maintain a steady pull rate while minimizing downstream drift. Additional details of GPR data acquisition are provided by Bradford et al. (2004). In addition to acquiring the radar profiles, we measured depth to permafrost on the stream banks and shallow (<0.5 m) margins of the streams by pressing a metal probe through the active layer to the point of refusal.

Solute injection experiments

We performed solute injection experiments (SIEs) using Rhodamine WT (RWT) in June and August 2005 in each stream to determine the extent of hyporheic exchange within the thaw bulb. A metering pump dripped RWT into the stream at a constant rate at the top of the reach until the surface water RWT concentration reached a plateau in the fully mixed zone of the streams (20–50 downstream from the injection point). During each SIE, and for a period following the tracer injection, surface and subsurface water were sampled at regular intervals. Subsurface samples were obtained via a set of nested mini-piezometers that spanned the depth of the thawed zone in each stream (3 depths in the alluvial stream and 2 depths in the peat stream). For the alluvial SIE, samples were taken every 20 min for the first hour, and every 30 min hourly thereafter, until the end of the experiment (~2.5 h). The peat SIE was longer, and so the later samples were taken approximately every two hours to the end of the experiment (6 and 9.7 h in two experiments). Samples were returned immediately to the laboratory for analysis of RWT concentration using a Turner Designs 10-AU fluorometer. For each mini-piezometer location, a tracer breakthrough curve (RWT concentration vs. time) was obtained for the surface water and each subsurface location sampled for each SIE. We used these data to establish the depth and timing of surface water penetration into the hyporheic zone of the two stream reaches. Details for these approaches are provided in Zarnetske (2006), Zarnetske et al. (2007), and Greenwald (2007).

Water chemistry

Four times during the summer of 2005 (Alluvial: 29 June, 4 July, 1 August, 15 August; Peat: 27 June, 1 July, 29 July, 10 August), surface and subsurface water from 9 sub-sites within both streams were sampled and analyzed for concentrations of nitrate (NO_3), ammonium (NH_4), soluble reactive phosphorus (SRP), dissolved oxygen (DO) and dissolved organic carbon (DOC). For each stream, the results from the first two sampling dates were averaged and reported as June data, and the results from the last two sampling dates were averaged and reported as August data. Early summer chemistry data were paired with the June SIE data, and late summer chemistry data were paired with the August SIE data.

Concentrations of DO in surface and subsurface water samples were measured in the field with a WTW Oxi 340i handheld dissolved oxygen meter. The reported accuracy for this dissolved oxygen meter is +0.01 mg/L (WTW, Weilheim, Germany). However, under the conditions in which we used this equipment, we assumed a more conservative estimate of accuracy of +0.1 mg/L. All other water samples were filtered through 0.45 µm, 25 mm diameter, cellulose acetate syringe filters and kept on ice for transport to the laboratory.

Ammonium and SRP analyses were done within 48 hours at the Toolik Field Station. Ammonium analyses were performed using the orthophthaldialdehyde (OPA) method (Holmes et al. 1999). SRP analysis was performed using the colorimetric molybdate blue method (Murphy and Riley 1962). Nitrate samples were immediately frozen at the field station, then transported to the University of Vermont's Rubenstein Ecosystem Science Laboratory in Burlington, Vermont, USA, where they were analyzed within 6 months by the cadmium reduction technique (Askew & Smith 2005, p. 123). DOC samples were preserved with 6N hydrochloric acid to a pH of 2, transported to the Ecosystems Center in Woods Hole, Massachusetts, USA, and analyzed by the persulfate-ultraviolet method within 6 months (Baird 2005, p. 23). We combined the RWT tracer and water chemistry data to estimate net nutrient regeneration rates using methods described by Greenwald (2007).

Whole-stream metabolism

We calculated net ecosystem metabolism (NEM) with the whole-stream, open-system, single station approach described by Marzolf et al. (1994) as refined by Young and Huryn (1998). We measured reaeration using the sound pressure method developed for these streams by Morse et al. (2007). Estimates of ecosystem respiration (ER) were corrected for the presence of low light levels at solar midnight, as described by Cappelletti (2006). Gross primary production is the difference between NEM and ER (where ER <0; i.e., a consumption of DO).

Results and Discussion

Stream characteristics

Despite their close proximity (less than 1 km), the two study streams were geomorphically distinct. Both streams are underlain by permafrost. However, the gradient of the alluvial stream was 0.7%, and the substrate was a mix of cobble and boulders, while the gradient of the peat stream was 0.03%, and the substrate was a mix of peat and silt (Fig. 2).

We used ground penetrating radar (GPR) to image the progression of thaw depth from May–September 2004 in the thawed zone under the alluvial and peat streams (Brosten et al. 2007). Permafrost depths interpreted from GPR data were constrained by both recorded subsurface temperature profiles and by pressing a metal probe through the active layer to the point of refusal. We found that the thaw bulb developed differently within the two stream environments. Thaw depths within the alluvial stream increased in thickness up to 2.5 m by the end of the summer (Fig. 3) but to a maximum of only 1.5 m (and generally <1 m) in the peat-bottom stream (Fig. 4). By late August and early September, the alluvial site began to refreeze. while the peat-bottom site continued to thaw; thaw depths had not receded at the peat-bottom sites by our last site visit in September. These results indicate distinctly different responses to the seasonal thermal input. Rapid heat absorption and loss occurs in the cobble-bottom alluvial stream while peat insulates the permafrost and introduces a lag in the seasonal thermal profile.

Using conservative tracer additions, we found that transient storage indicators such as mean storage residence time, storage zone area, hydraulic retention, and storage exchange rates were sensitive to discharge and strongly correlated with total stream power (Zarnetske et al. 2007). However, the relationship between transient storage and extent of thaw was less clear. Transient storage indicators increased with increasing thaw depths under base- and low-flow conditions, but these relationships diminished at high flow. We found good correlations between the Darcy-Weisbach friction factor of these channels and several metrics of transient storage, in agreement with previous studies (e.g., Bencala & Walters 1983, Harvey & Wagner, 2000). We found that stream power was a good predictor of transient storage characteristics because it normalizes simple characteristics of hydraulics and morphology, thereby allowing better comparisons across streams that differ widely in these characteristics (Fig. 2). Our results in arctic streams are comparable to those in temperate streams (Legrand-Marcq & Laudelout 1985, D'Angelo et al. 1993, Harvey et al. 2003) indicating that our findings are likely transferable to non-

A

B

Figure 2. Overview of the alluvial (A) and peat (B) stream reaches. (Colored illustration available on CD-ROM.)

A B

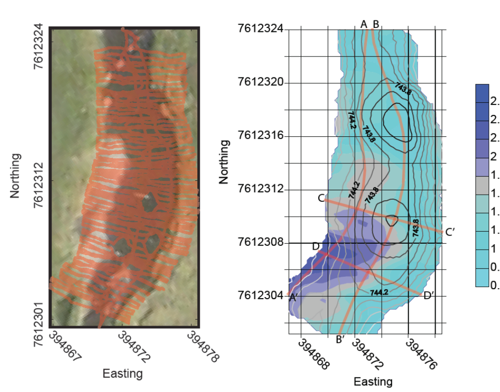

Figure 3. Thaw depth thickness in the alluvial reach. The left panel (A) shows an areal view of the reach with the GPR tracks (light grey) overlain. The right panel (B) shows an interpretation of the maximum thaw depth thickness in August 2005. (Colored illustration available on CD-Rom.)

A B

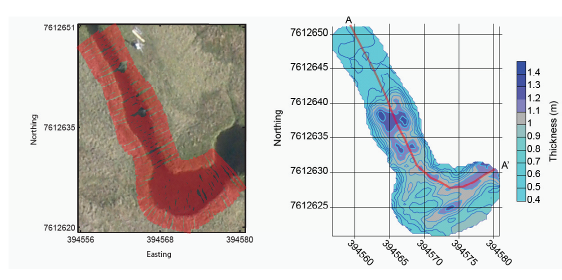

Figure 4. Thaw depth thickness for a portion of the peat reach. The left panel (A) shows an areal view of the reach with the GPR tracks overlain. The right panel (B) shows an interpretation of the maximum thaw depth thickness in August 2005. (Colored illustration available on CD-ROM.)

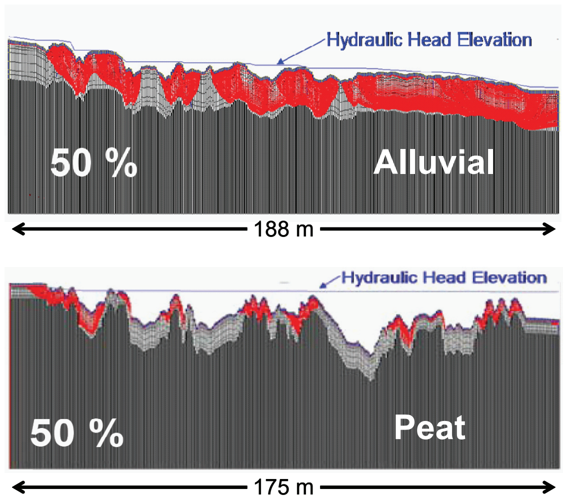

Figure 5. Zones of hyporheic exchange (black flow lines) in the alluvial (upper panel) and peat (lower panel) reaches for combined MODFLOW and MODPATH simulations in which the active layer (grey areas) was 50% of the observed maximum in each reach. See Zarnetske (2006) for details. (Colored illustration available on CD-ROM.)

arctic streams.

Hyporheic exchange depths in the cobble-bottom and peat-bottom streams (Fig. 5) were constrained in part by depths of thaw beneath these two streams and in part by the texture of the substrate, both of which are controlled by stream gradient. In the cobble-bottom stream–which had a greater depth of thaw–stream water penetrated the hyporheic zone to a depth of up to 54 cm. In the peat-bottom stream, which had a much shallower depth of thaw, the actively functioning hyporheic zone was limited to a depth of 10 cm or less. In both streams, we found that the maximum extent of hyporheic penetration was much less than the maximum extent of thaw.

Combining our estimates of hydraulic exchange between the open channel and the hyporheic zone with analyses of hyporheic nutrient concentrations in these reaches (Table 1) provided an estimate of hyporheic regeneration. Total N regeneration in the alluvial reach was about 9.3 µmoles m^{-2} h^{-1}, primarily as nitrate (7.9 µmoles m^{-2} h^{-1}). The P regeneration rate was 0.54 µmoles m^{-2} h^{-1} for N:P regeneration molar ratio of 17:1. Total N regeneration in the peat stream was 5.3 µmoles m^{-2} h^{-1} based on a release of ammonium (6.8 µmoles m^{-2} h^{-1}) and an uptake of nitrate (-1.5 µmoles m^{-2} h^{-1}). The P regeneration rate was very low, at 0.05 µmoles m^{-2} h^{-1} for an N:P regeneration molar ratio of 105:1. Thus, hyporheic regeneration in the alluvial reach was in approximate stoichiometric balance (16:1), while regeneration of P in the peat stream was considerably less than expected.

The ratios of N and P regeneration can also be compared to estimates of hyporheic C processing based on whole-stream estimates of ecosystem respiration measured in these stream reaches in a previous year (W.B. Bowden, unpublished data, 2001). Cappelletti (2006) observed that even in a modestly productive river (the Kuparuk River), the vast majority of total ecosystem respiration could be attributed to hyporheic respiration. Ecosystem respiration in both stream reaches was similar at ~30 mmoles m^{-2} h^{-1}. Thus, the observed C regeneration ratios relative to N and P were roughly 3 orders of magnitude greater than the expected C:N (~7:1) and C:P (~106:1) ratios. This suggests that a considerable quantity of N and P liberated in the course of decomposition in the hyporheic zones of these streams is reutilized before it leaves the hyporheic system.

These results show that gradient strongly influences the spatial and temporal extent of thawed sediments in streams that drain permafrost-dominated landscapes. Gradient controls substrate particle sizes, which in turn controls the hydraulic and—peat is deposited—the thermal conductivities of stream substrates. Thus, steeper streams have coarser substrates and conduct heat energy and water more effectively to depth than is the case in less-steep streams that accumulate fine organic sediments. The result is that the thaw bulb (active layer) below alluvial streams is deeper than it is beneath peat streams. For similar reasons, the zone of active hyporheic exchange is thicker in alluvial streams than it is in peat streams. However, we found that the thaw depth was thicker than the zone of active hyporheic exchange in both stream types.

The hyporheic zones in these streams were biogeochemically active. In the alluvial reach, the hyporheic zone was a source of NH_4, NO_3, and PO_4 and a sink for DO. In the peat stream, the hyporheic zone was a strong source of NH_4, a weak source of PO_4, and sink for NO_3 and DO. The total regeneration of N and P was in reasonable stoichiometric balance in the alluvial reach, while in the alluvial reach less P was regenerated than expected based on the N regeneration. However, based on C regeneration (respiration), far less N and P were regenerated from the hyporheic zones of either stream than expected. This suggests the potential for substantial re-immobilization of N and P mineralized from organic matter decomposition in the hyporheic zones of these streams. The relative importance of net nutrient regeneration from the hyporheic zones of these streams versus internal recycling of nutrients within these hyporheic zones is still poorly known. In addition, it is not clear how factors such as geomorphic form, stream network characteristics (e.g., stream order), or landscape characteristics (e.g., young versus old glacial ages) influences this balance.

Table 1. Connectedness-weighted, season-averaged concentrations of nutrients in the hyporheic zones of the alluvial and peat stream reaches. See Greenwald (2007) and Greenwald et al. (in press) for details about seasonal nutrient concentrations.

	Stream type	
Nutrient	Alluvial	Peat
Nitrate (µM)	5.75	7.49
Ammonium (µM)	0.20	0.52
Phosphate (SRP) (µM)	0.02	0.03

Acknowledgments

We thank Julia Larouche, Kenneth Turner, Joel Homan, Tom Crumrine, and Adrian Green for field and laboratory assistance and Alan Howard for statistical advice. Kenneth Edwardson contributed valuable information and insight to our comparisons of net nutrient regeneration rates in North Slope streams. We also thank the staff of the Toolik Field Station and VECO Polar Resources for logistical support. The material presented in this paper is based upon work supported by the National Science Foundation under Grant No. OPP-0327440.

References

Askew, E.F. & Smith, R. 2005. Inorganic nonmetallic constituents. In: A.D. Eaton, L.S. Clesceri, E.W. Rice & A.E. Greenberg (eds.), *Standard Methods for the Examination of Water and Wastewater*. Baltimore, MD: Port City Press, 123.

Baird, R.B. 2005. Aggregate organic constituents. In: A.D. Eaton, L.S. Clesceri, E.W. Rice & A.E. Greenberg (eds.), *Standard Methods for the Examination of Water and Wastewater.* Baltimore, MD: Port City Press, 23.

Bencala, K.E. & Walters, R.A. 1983. Simulation of solute transport in a mountain pool-and-riffle stream: a transient storage model. *Water Resources Research* 19: 718-724.

Bradford, J.H., McNamara, J.P., Bowden, W.B. & Gooseff, M.N. 2005. Imaging depth-of-thaw beneath arctic streams using ground-penetrating radar. *Hydrological Processes* 19(14): 2689-2699.

Brosten, T.R., Bradford, J.H., McNamara, J.P., Zarnetske, J.P., Gooseff, M.N. & Bowden, W.B. 2006. Profiles of temporal thaw depths beneath two arctic stream types using ground-penetrating radar. *Permafrost and Periglacial Processes* 17: 341-355.

Cappelletti, C. 2006. *Photosynthesis and respiration in an arctic tundra river: modification and application of the whole-stream metabolism method and the influence of physical, biological, and chemical variables*. M.Sc. Thesis. Burlington, VT: University of Vermont.

D'Angelo, D.J., Webster, J.R., Gregory, S.V. & Meyer, J.L. 1993. Transient storage in Appalachian and Cascade mountain streams as related to hydraulic characteristics. *Journal of the North American Benthological Society* 12: 223-235.

Edwardson, K.J. 1997. *Characterizations of hyporheic influences on the hydrology and biogeochemistry of arctic tundra streams.* M.Sc. Thesis. Durham, NH: University of New Hampshire.

Edwardson, K.J., Bowden, W.B., Dahm, C. & Morrice, J. 2003. The hydraulic characteristics and geochemistry of hyporheic and parafluvial zones in arctic tundra streams, North Slope, Alaska. *Advances in Water Resources* 26: 907-923.

Harvey, J.W. & Bencala, K.E. 1993. The effect of streambed topography on surface-subsurface water exchange in mountain catchments. *Water Resources Research* 29: 89-98.

Harvey, J.W., Conklin, M.H. & Koelsch, R.S. 2003. Predicting changes in hydrologic retention in an evolving semi-arid alluvial stream. *Advances in Water Resources* 26: 939-950.

Harvey, J.W. & Wagner, B.J. 2000. Quantifying hydrologic interactions between streams and their subsurface hyporheic zones. In: J.B. Jones & P.J. Mulholland (eds.), *Streams and Ground Waters*. San Diego, CA: Academic Press, 3-44.

Holmes, M., Aminot, A., Kerouel, R. Hooker, B.A. & Peterson. B.J. 1999. A simple and precise method for measuring ammonium in marine and freshwater ecosystems. *Canadian Journal of Fisheries and Aquatic Science* 56(10): 1801-1808.

Greenwald, M.J. 2007. *Hyporheic exchange and biogeochemical processing in arctic tundra streams.* MSc. Thesis. Burlington, VT: University of Vermont.

Greenwald, M.J., Bowden, W.B., Gooseff, M.N , Zarnetske, J.P., McNamara, J.P., Bradford, J.H. &. Brosten, T.R. In press. Hyporheic exchange and water chemistry of two arctic tundra streams of contrasting geomorphology. *Journal of Geophysical Research – Biogeosciences*.

Kasahara, T. & Wondzell, S.M. 2003. Geomorphic controls on hyporheic exchange flow in mountain streams. *Water Resources Research* 39: 1005, doi:1010.1029/2002wr001386.

Kling, G.W., Kipphut, G.W., Miller, M.C. & O'Brien, W.J. 2000. Integration of lakes and streams in a landscape perspective: the importance of material processing on spatial patterns and temporal coherence. *Freshwater Biology* 43: 477-497.

Legrand-Marcq, C. & Laudelout, H. 1985. Longitudinal dispersion in a forest stream. *Journal of Hydrology* 78: 317-324.

Marzolf, E.R., Mulholland, P.J. & Steinman, A.D. 1994. Improvements to the diurnal upstream-downstream dissolved oxygen change technique for determining whole-stream metabolism in small streams. *Canadian Journal of Fisheries and Aquatic Sciences* 51: 1591-1599.

Morse, N., Bowden, W.B., Hackman, A., Pruden, C., Steiner, E. & Berger, E. 2007. Using sound pressure to estimate reaeration in streams. *Journal of the North American Benthological Society* 26(1): 28-37.

Murphy, J. & Riley, J.P. 1962. A modified single solution method for the determination of phosphate in natural waters. *Anayitica Chimica Acta* 27: 31-36.

Young, R.G. & Huryn, A.D. 1999. Effects of land use on stream metabolism and organic matter turnover. *Ecological Applications* 9: 1359-1376.

Zarnetske, J.P., Gooseff, M.N., Brosten, T.R., Bradford, J.H., McNamara, J.P. & Bowden, W.B. 2007. Transient storage as a function of geomorphology, discharge, and permafrost active layer conditions in Arctic tundra streams. *Water Resources Research* 43: W07410, doi:10.1029/2005WR004816.

Zarnetske, J.P., Gooseff, M.N., Bowden, W.B., Greenwald, M.J., Brosten, T.R., Bradford, J.H. & McNamara, J.P. Influence of morphology and permafrost dynamics on hyporheic exchange in arctic headwater streams under warming climate conditions. *Geophysical Research Letters* (in review).

Zarnetske, J.P. 2006. *Headwater hyporheic zones in a warming arctic climate: an assessment of hyporheic dynamics across distinct geomorphic and permafrost conditions.* M.Sc. Thesis. Logan, UT: Utah State University.

Geomorphology and Gas Release from Pockmark Features in the Mackenzie Delta, Northwest Territories, Canada

R.G. Bowen
Diversified Scientific Solutions, 3439 Fulton Road, Victoria, B.C., V9C 3N2
S.R. Dallimore, M.M. Côté, and J.F. Wright
Geological Survey of Canada- Pacific, P.O. Box 6000, Sidney, B.C., V8L 4B2
T.D. Lorenson
United States Geological Survey, 345 Middlefield Road, M.S. 999, Menlo Park, CA 94025

Abstract

Field investigations were undertaken to study the geomorphology and permafrost conditions of more than 20 methane-venting pockmark features in a pond west of Middle Channel, Mackenzie Delta. The flux of methane to the atmosphere from these pockmarks is estimated to be 5.07×10^5 m^3 yr^{-1}. Terrestrial permafrost around the pond is ~60 m thick and likely formed within Holocene deltaic sediments. However, the site is located only 2 km from a major permafrost boundary where permafrost thickens over a short distance to more than 400 m. Mean annual pond-bottom temperature is above 0°C, creating the potential for talik formation, and hence gas migration pathways, beneath the pond. Isotopic analysis indicates that the methane is of thermogenic origin, and is similar in composition to the gas of the nearby Niglintgak gas field.

Keywords: climate change; gas hydrates; Mackenzie Delta; methane seeps; pockmarks.

Introduction

Interest in the occurrence of greenhouse gases within permafrost, particularly methane, has grown in recent years with the consideration of the effects of climate warming and the continued expansion of engineering activity in the Arctic. The potential release of methane as free gas fluxing from arctic lakes is recognized as a possible positive climate change feedback mechanism (Walter et al. 2006), as is gas release from dissociating gas hydrates beneath transgressed areas of the Arctic Shelf (Taylor et al. 2002, Paull et al. 2007). Gas leakage from deeper hydrocarbon occurrences are also of interest in areas underlain by large sedimentary basins. Finally, shallow occurrences of free gas have been recognized as a potential geohazard to hydrocarbon exploration and development (Collett & Dallimore 2002).

This paper describes a number of small gas seeps and one prolific seep which occur in a pond in the outer Mackenzie Delta, NWT, Canada (Fig. 1A). The site is of historical interest, as natural gas was first observed discharging from the pond in 1963 by Dr. Ross Mackay (pers. com. 1991). During the course of three field seasons approximately twenty small gas seeps and one large seep have been investigated. The large seep has a conical bed form depression similar to pockmark features described offshore (Hovland & Judd 1988). This paper describes permafrost conditions, geomorphology and geotechnical properties of the site, and quantifies the geochemistry and gas flux from the large seep.

Permafrost and Physiographic Setting

The depth of ice-bonded permafrost in the outer Mackenzie Delta has been estimated from geophysical well logs, hydrocarbon exploration wells (Smith & Judge 1993), and deep sounding electromagnetic transects (Todd & Dallimore 1998). Ground temperature data are also available from instrumented wells (Taylor et al. 1998). Using these data, the base of ice-bonded permafrost and intervals where stable methane hydrate can occur was modeled with physiographic boundary constraints.

Permafrost distribution beneath terrestrial areas is variable (Fig. 1A), reflecting a complex Quaternary paleoclimate and depositional history (Taylor et al. 1996). To the east of Middle Channel, older pre-Holocene sediments outcrop or occur at shallow depths beneath a thin veneer of Holocene deltaic sediments. Permafrost beneath land areas is 250 to 600 m thick. To the west of Middle Channel, Holocene deltaic sediments dominate the near-surface geology, and permafrost thins over a few kilometers to approximately 60 m (Fig. 1B). Reflecting this spatial change in ground temperatures, methane hydrate is not stable to the west of Middle Channel, whereas to the east, the base of the methane hydrate phase boundary may be 400 to 700 m deep (Fig. 1C).

The pond containing the pockmarks is 3 km from the Beaufort Sea and is connected to Middle Channel to the east via a small side channel and to the Beaufort Sea via a meandering channel to the west. The pond is tidally influenced and is highly turbid in summer due to the inflow of silt-laden Mackenzie River waters. The terrain in the vicinity of the pond is <2 m above sea level, and thus the site is susceptible to flooding during river breakup and Beaufort Sea storm surges. Pond sediments consist of uniform, dark brown mud with occasional organic inclusions including twigs and rootlets.

Estimates of the shallow terrestrial ground temperature regime are available from a temperature cable ~5 km south

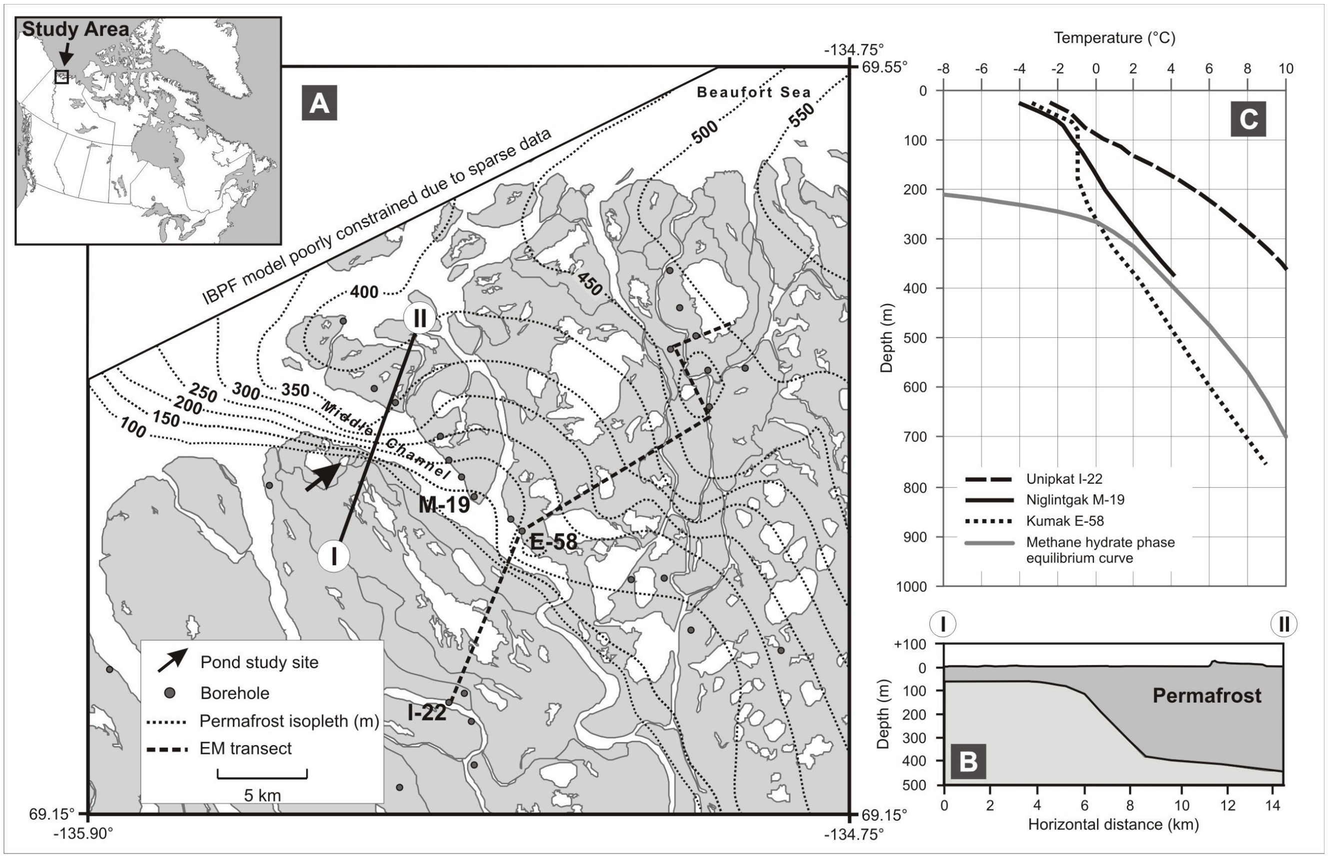

Figure 1. (A) Outer Mackenzie Delta near Middle Channel showing pockmark research site. Contours are of the base of ice-bonded permafrost, modeled using interpretations from geophysical well logs (Smith & Judge 1993), a deep sounding electromagnetic transect (Todd & Dallimore 1998), and boundary constraints established from the surficial geology. (B) The depiction of the base of permafrost from point I to II has been derived from the modeled data. (C) Ground temperatures from three instrumented wells (Taylor et al. 1998), methane hydrate phase equilibrium curve is from Sloan (1998).

of the pond site (Dyke, pers. com.) and a deeper installation 12 km south of the site (Dallimore & Matthews 1997). These studies reveal mean annual ground temperatures of this portion of the outer Mackenzie Delta are -4 to -6°C. Mean annual air temperatures measured at a site 20 km to the east are approximately -11°C (National Snow and Ice Data Centre 2007).

Vemco Minilog-T temperature loggers (temperature range -4 to +20°C, resolution 0.1°C) were deployed at the bed of the large pockmark site to record daily bottom water temperatures. The annual mean bottom temperature from August 10, 2006, to August 10, 2007, at ~9 m depth was 4.1 ± 0.1°C. Water depths of the main pond are generally <1.5m, and as a result, late winter ice typically contacts the bed in these areas lowering the annual mean temperatures to 2 to 3°C.

Bathymetry and Pockmark Morphology

The pond investigated in this study is heart-shaped and 25 hectares in surface area. Water depths vary from 1–2 m with the exception of the large seep/pockmark feature which is ~10 m deep. During the summers of 2006 and 2007, ~20 small but continuously active seeps were observed within the pond. Typically these seeps had surface bubble plumes which were 0.5 to 1.5 m in diameter. Physical inspection of six of these seeps revealed that sediment strength in the vicinity of the seeps was very weak, with 0.3 to 1.0 m deep conical depressions in the pond bed. Many seeps were discharging gas through orifices that were approximately 5 cm in diameter. In addition to the continuous seeps, small episodic gas discharges were observed throughout the pond, and occasionally on land, suggesting that gas is venting to the surface over a large area.

A boat equipped with a LCX-19C sonar and Global Positioning System (GPS) system was used to collect a series of survey transects over the large seep and the surrounding area. The bubble plume area at the surface of this seep varied from 2 to 5 m in diameter. The plume within the water column was visible from the sonar acoustic data as an area of intense acoustical backscatter due to the sonic reflection of the bubbles. Examination of the sonar data adjacent to the plume as well as several data points that penetrated the plume enabled the construction of depth interpolations, where the sonar data were giving false bottom data due to the strong reflection of bubbles from the plume. A digital terrain model was generated from the corrected sonar data (Fig. 2). The pockmark feature was ~10 m deep and conical in shape with a diameter of about 24 m at 3.5 m depth tapering to a flatter base of ~5 m diameter. The slopes were relatively steep with average dips of 20 to 25° (mean 22.4 ± 0.7°). The volume below a depth of 3.5 m was approximately 5400 m³.

Bearing Strength of Pockmark Sediments

A Seabed Terminal Impact Newton Gradiometer (STING) was used to estimate the dynamic bearing strength of the lake bed sediments across the main pockmark feature. This device measures the kinematic dynamics of the probe during the deceleration as it penetrates bottom sediments (Mulhearn 2002). The STING was configured with a 1 m shaft and a 35 mm foot. A boat survey transect was established using a taught surface line. The instrument was allowed to free-fall from the water surface at 1–3 m intervals along the transect line. Each point on the transect consisted of four discrete drops that were averaged to yield a mean. The instrument sampled every 0.0005 seconds allowing construction of a bearing strength vs. depth profile.

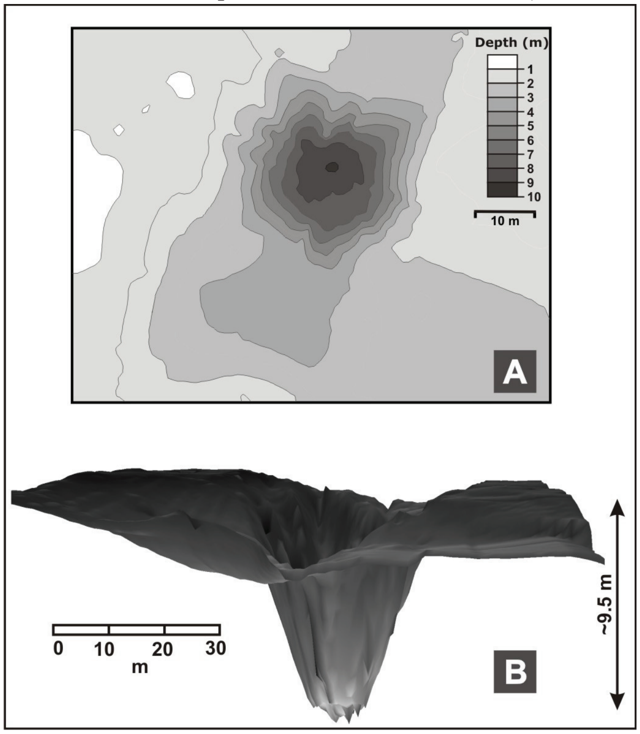

Figure 2. (A) Plan view and (B) sun-shaded perspective view of seep digital elevation model generated from sonar transects.

Figure 3 shows an east–west transect of 12 STING deployments across the pockmark feature. With the exception of deployments 11 and 12, the sediments from 0–25 cm depth are very weak, with bearing strengths below 20 kPa. At many sites (i.e., deployment 5, 6, 7, and 9, 10) the water sediment interface is barely discernible, and the bearing strength vs. depth shows only a small increase to maximum depth of penetration (limited by frictional effects). Several deployments do show some change in bearing strength vs. depth which are interpreted to be harder sediment layers. No STING measurements were obtained outside of the pockmark. However, estimates of the surface bearing strength in the shallow areas of the pond were made by several walking/wading transects. For the most part, the sediment interface could bear a person's weight, suggesting that near-surface bearing strengths likely exceed 200 kPa. STING data from the channel to the south of the pond showed near-surface bearing strengths as high as 400 kPa.

Gas Flux Measurements

Summer

An instrument was developed to measure gas flux from the large seep site (Fig. 4). The flux instrument, which was modified over several field seasons, consisted of a gas collection funnel and a chimney assembly.

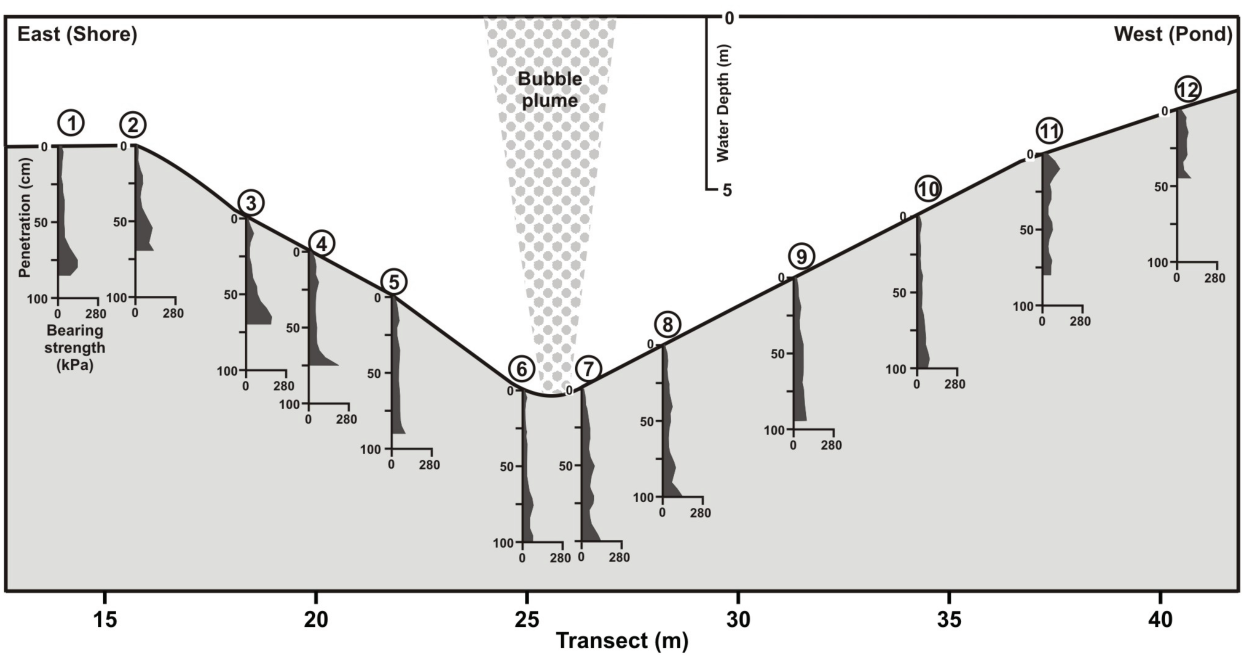

Figure 3. Seabed Terminal Impact Newton Gradiometer (STING) transect of seep. Profiles are averaged from four individual penetrations at each site.

Gas flow was measured with an airflow anemometer which was installed in the centre of the 10 cm chimney assembly. Anemometers are routinely used by industry for measuring flow through ducts. The anemometer internally logged data at 1-second intervals. To verify this measuring technique, the anemometer was calibrated at the Alaron Instruments wind tunnel calibration facility with an estimated instrument accuracy of ±3%. Calibration coefficients were applied to the raw data to produce corrected data. Further bench testing of the chimney assembly was undertaken by utilizing a 10 cm tube outfitted with a calibrated ultrasonic time of flight system. Airflow was measured by both the anemometer and the ultrasonic system with flux results yielding equal values at steady state flow.

The gas plume consisted of an upwelling convection current of gas bubbles and entrained water. The plume diameter and intensity at the surface varied constantly, shifting its position as much as 2 m over intervals of minutes. For this reason the collection funnel deployed in 2007 had a 9 m cross-sectional dimension with much of the funnel submerged to reduce wind and wave loading.

Figure 4. Seep collection flux meter used in 2007. Instrument consists of a 9 m collection funnel, most of which is submerged to reduce wind and wave loading, and a 10 cm chimney assembly in which the airflow anemometer was housed.

Figure 5 presents data from a 40 min deployment in August 2007. The data show 1-minute averaged flux rates between 0.36 and 0.86 m^3min^{-1}, with mean of 0.59 m^3min^{-1} and a standard deviation of 0.09. Marked increases and decreases in flux over a period of minutes are consistent with visual observations at the surface and measurements with a smaller collection funnel carried out in 2006.

Fall/winter

Field visits to the pond seep site were carried out in the fall and late winter. In late October, approximately 10 cm of ice had formed over the main pond, covering all but the main pockmark area where turbulence had resulted in a 19 m diameter ice-free area as measured by a laser range finder. While in some other locations in the outer Mackenzie Delta, holes in the ice persist through the winter, by March the only evidence of the large seep was a slight doming of the ice surface and the conspicuous occurrence of tension cracks radiating out from the dome. Drilling through the ice near the centre of the seep revealed ice thickness of less than 50 cm; in contrast, typical pond ice thicknesses were 1.2–1.8 m. While preparing for a through-ice ROV deployment in March 2007, a pressurized pocket of gas was penetrated at the ice-water interface which discharged a column of gasified water ~10 m high for about 1 minute.

Attempts to measure winter flux were undertaken by placing the chimney assembly directly over a 25 cm auger hole through the ice. The flow rates varied significantly as gas accumulated under the ice plate before venting in strong bursts. These bursts were short-lived lasting about 1 second followed by short periods with low flow, or even back flow, as water drained back into the auger hole. Burst intervals were

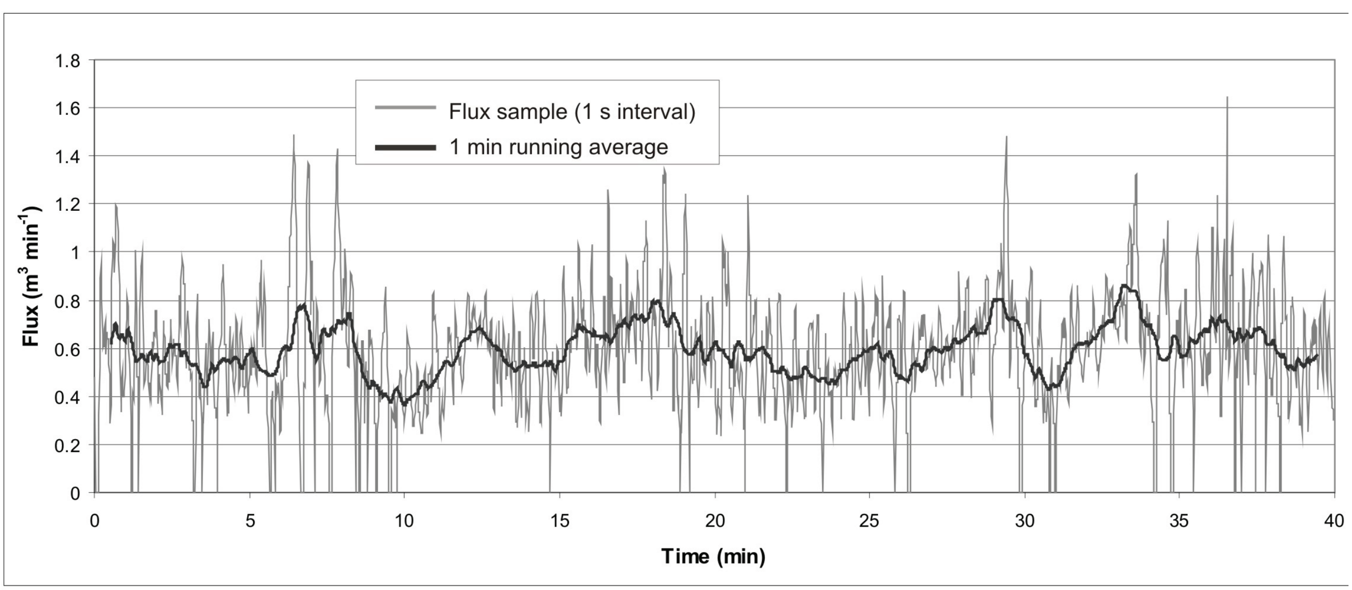

Figure 5. Flux data collected in August 2007. Grey line depicts flux data sampled at 1 s sampling interval. Black line shows the 1 min running average flux.

Table 1. Seep gas analysis from large pond seep.

Sample	CO_2 (ppm)	CO_2 *13C (ppt)	CH_4 (ppm)	CH_4 *13C (ppt)	C_2H_6 (ppm)	C_2H_6 *13C (ppt)
[1]SS-1	1030	-36.2	884400	-43.6	63	N/D
SS-2	1940	-48.8	849100	-43.2	230	-27.8
SS-3	1960	-24.5	976800	-43.0	140	N/D
[2]Nig field	9000	N/D	981900	N/D	6900	N/D

[1] SS = Gas samples collected from large seep; [2] Nig = Niglintgak gas field sample (Shell Canada Ltd. 2004a); N/D = no data

every 2–5 seconds as observed from recorded video. The measured gas flux values were influenced by the constrains of the ice plate, the possible release of gas through the radial ice cracks and the small diameter of the auger hole and were therefore too complex to resolve credible flux rates.

Geochemistry

The * ^{18}O and *D composition of mixed waters collected over the seeps were found to be identical to local surface water elsewhere in the pond and channels. This suggests that there are no large discharges of deeper connate waters associated with the seeps. The hydrocarbon gases from the pond seep are mainly methane with minor higher hydrocarbon homologues (Table 1). The carbon isotopic content of the methane suggests that it is of thermogenic origin. The carbon dioxide isotopic composition, however, is very light. Under some circumstances, if methane oxidation is a dominant process, then methane of microbial genesis may be mistaken for thermogenic methane. While the carbon dioxide isotope values are unusual, further evaluation of the data shows that the volume of methane is quite large relative to carbon dioxide, which is the opposite of what would be expected from the process of methane oxidation. In addition, the ethane carbon isotopic composition is of thermogenic origin. Thus the balance of data suggests the hydrocarbon gases have a thermogenic origin. The Niglintgak gas field produces a similar dry gas and may be the ultimate seep gas source.

Discussion

Formation of pockmark features

The presence of free gas in unconsolidated sediments can reduce the effective stress regime and, in turn, the sediment-bearing capacity. Identification of small orifices with almost no sediment strength, and the weak bearing strengths recorded by the STING survey over the large seeps suggest this possibility. Video from a winter ROV survey showed light sediment and fine organic material being liberated from the sediment interface into the water column by gas discharge. In some cases, gas discharge was associated with exposed root mats and organic debris which were free of sediment. The weakening of the strength of the sediments and the force of gas bubbles at the sediment interface provide a mechanism for the mobilization and exhumation of the bottom sediments and seems a possible factor in the formation of the pockmark features described.

A simple three-dimensional model can be constructed assuming 60 m of ice-bonded terrestrial permafrost with mean annual temperatures of -4°C, a basal temperature regime of 1°C for the 600 m diameter pond and 4°C for the 30 m diameter main pockmark. Applying a similar modeling methodology to that described by Taylor et al. (this volume) a through-going talik is created through the terrestrial permafrost if the pond existed on the landscape for 1000 years. The gas migrations appear to be associated with networks of root mats and organic debris. These networks may create vertical gas migration pathways, which may be a factor affecting the location of the seep/pockmarks within the larger pond.

Source of gas feeding the seeps

The seeps described in this paper are quite remarkable in both the volume of gas released and their apparent longevity. Based on an average flux rate of 0.59 m^3min^{-1}, the large seep is releasing 3.10 x 10^5 m^3 of methane (2.99 x 10^5 m^3 at 0°C, 1 bar) on an annual basis. Short-term flux measurements carried out on several of the small seeps suggest rates for some of these are as high as 0.13 m^3min^{-1}. In total, for the entire pond area (1 large seep, 20 small seeps), we estimate at least 5.07 x 10^5 m^3 (at STP) of gas is released annually. As the large seep feature has a similar appearance, and is virtually in the identical location to that observed by Dr. Mackay in 1963, it is not unreasonable to assume that during the past 44 years 2.23x10^7 m^3 (at STP) or almost 0.8 billion ft^3 of gas has been released from the 21 seeps. Clearly a significant source of gas accumulation is feeding these seeps continuously.

The closest known conventional gas field is the Niglintgak field located approximately 5 km to the east. This field, which contains approximately 2.8 x 10^{10} m^3 (~1 TCF) of recoverable gas, forms one of three anchor fields for the proposed Mackenzie Valley Gas pipeline project. The gas-bearing horizons occur at 760 m depth (Shell Canada Ltd. 2004b), with a similar dry gas chemistry to the pond seep samples (Table 1). Smith and Judge (1993) have identified gas hydrates in several Niglintgak wells at depths as shallow as 660 m. Assuming vertical gas migration is most likely where permafrost is absent and gas hydrate is not stable, the abrupt transition to the west of Middle Channel (Fig. 1) is an obvious potential lateral migration path to the near surface. However, further investigation is required to confirm this.

Conclusions

The following conclusions can be drawn from this study:

1) Approximately 20 small and 1 very large gas seeps have been characterized at a small terrestrial pond in the outer Mackenzie Delta;
2) The hydrocarbon gases being released are predominantly methane with minor higher hydrocarbon homologues (Table 1). The carbon isotopic content of methane and ethane indicates that the gas is of thermogenic origin;

3) Pockmark features are formed in the pond bed by vertical gas migration, causing sediment weakening and exhumation. The small seeps typically have small 0.5–1.0 m deep pockmarks, while the large seep has a 10 m deep pockmark;
4) Flux of methane to the atmosphere from these seeps is estimated to be 5.07 x 10^5 m^3 annually which, when considered over 44 years of activity, suggests a large supply of gas at depth;
5) The permafrost setting of the pond likely exerts control over the migration of gas to the surface with the site occurring at a major permafrost/gas hydrate boundary. The proximity of a large gas field down-dip and the similarity of gas geochemistry suggests a candidate for the source of the gas is the Niglintgak gas field.

Acknowledgments

The fieldwork is supported by the Polar Continental Shelf Project and the Aurora Research Institute. Financial support has been provided by the Panel for Energy Research and Development and the Geological Survey of Canada. Larry Greenland and William Hurst are thanked for their excellent field assistance. Mark Nixon's knowledge and field experience were very much appreciated. Dr Ross Mackay is gratefully acknowledged for his suggestion to embark on the study.

References

Collett T.S. & Dallimore, S.R. 2002. Detailed analysis of gas hydrate induced drilling and production hazards. *Proceedings of the Fourth International Conference on Gas Hydrates, Yokohama, Japan, May 19-23, 2002*: 1:47-52.

Dallimore, S.R. & Matthews, J.V., Jr. 1997. The Mackenzie Delta borehole project. Environmental Studies Research Funds Report No. 135, National Energy Board, Calgary, CD-ROM.

Hovland, M. & Judd, A.G. 1988. *Seabed Pockmarks and Seepages. Impact on Geology, Biology and the Marine Environment*. London: Graham & Trotman Ltd., 293 pp.

Mulhearn, P.J. 2002. *Influences of penetrometer probe tip geometry on the bearing strength estimates for mine burial prediction*. Australia: DSTO Aeronautical and Maritime Research Laboratory, 20 pp.

National Snow and Ice Data Centre. 2007. Geological Survey of Canada active-layer monitoring system documentation for Global Geocryological Database. http://nsidc.org/forms/ggd353_or.html

Paull, C.K., Ussler, W., Dallimore, S.R., Blasco, S.M., Lorenson, T.D., Melling, H., Medioli, B.E., Nixon, F.M., & McLaughlin, F.A. 2007. Origin of pingo-like features on the Beaufort Sea shelf and their possible relationship to decomposing methane gas hydrates. *Geophysical Research Letters* 34: (January 5, 2007) DOI 10.1029/2006GL027977.

Shell Canada Ltd. 2004a. Application for approval of the development plan for the Niglintgak field, Project Description, section 5.4 Functional Criteria. www.ngps.nt.ca/applicationsubmission/nig.html

Shell Canada Ltd. 2004b. Application for approval of the development plan for the Niglintgak field, Project Description, section 2.3 Petrophysics. www.ngps.nt.ca/applicationsubmission/nig.html

Sloan, E.D., Jr. 1998. *Clathrate Hydrates of Natural Gas*. New York: Marcel Dekker Inc., 705 pp.

Smith, S.L. & Judge, A.S. 1993. Gas hydrate database for Canadian Arctic and selected east coast wells. Geological Survey of Canada, Open File 2746, 54 pp.

Taylor, A.E., Dallimore, S.R., & Judge, A.S. 1996. Late Quaternary history of the Mackenzie-Beaufort region, Arctic Canada, from modelling of permafrost temperature. 2. The Mackenzie Delta-Tuktoyaktuk coastlands. *Canadian Journal of Earth Science* 33: 62-71

Taylor, A.E., Burgess, M.M., Judge, A.S., Allen, V. & Wilkinson, A. 1998. *Canadian Geothermal Data Collection - Deep permafrost temperatures and thickness of permafrost; Global Geocryological Database, CAPS version 1*. Colorado: International Permafrost Association and the National Snow and Ice Data Centre, CD-ROM.

Taylor A.E., Dallimore, S.R., Hyndman, R.D. & Wright, J.F. 2002. Comparing the sensitivity of terrestrial and marine gas hydrates to climate warming at the end of the last ice age. *Proceedings of the Fourth International Conference on Gas Hydrates, Yokohama, Japan, May 19-23, 2002*: 1:63-70.

Taylor, A.E., Dallimore, S.R. & Wright, J.F. This volume. Thermal impact of Holocene lakes on a permafrost landscape, Mackenzie Delta, Canada.

Todd, B.J. & Dallimore, S.R. 1998. Electromagnetic and geological transect across permafrost terrain, Mackenzie River Delta, Canada. *Geophysics* 63: 1914-1924.

Walter, K.M, Zimov, S.A., Chanton, J.P., Verbyla, D., & Chapin F.S., III. 2006. Methane bubbling from Siberian thaw lakes as a positive feedback to climate warming. *Nature* 443: 7 Sept 2006.

Current Capabilities in Soil Thermal Representations Within a Large-Scale Hydrology Model for Regions of Continuous Permafrost

Laura C. Bowling
Purdue University, West Lafayette, IN, USA
Keith A. Cherkauer
Purdue University, West Lafayette, IN, USA
Jennifer C. Adam
Washington State University, Pullman, WA, USA

Abstract

Despite the fact that warming in the Arctic has been greater than the global average and hydrological changes may provide important feedback responses to global climate, until fairly recently many global climate models that used to generate future climate projections have neglected the influence of permafrost on water and energy exchange in high latitude regions. At the scale of such models, the complexities of representing water and thermal exchange in permafrost systems are further compounded by the necessity for computational efficiency, coarse spatial resolution and the inability to fully describe the current state of the system. In this presentation, we explore successes and on-going challenges in simulating seasonal and decadal permafrost dynamics for the arctic region, with specific examples based on simulations using the Variable Infiltration Capacity (VIC) model, a macroscale land surface scheme. Considerable challenges still exist in appropriate definition of boundary conditions and with respect to near-surface runoff generation.

Keywords: Arctic; ground ice; hydrology; modeling; permafrost; wetlands.

Introduction

Observations of dramatic hydrologic change in permafrost environments in recent years have led to increased interest in the large-scale interactions of permafrost with surface water hydrology under a changing climate. Opposing changes in Siberian lake extent have been observed, which can be attributed to differences in discontinuous versus continuous permafrost by allowing or preventing drainage (Smith et al. 2005, Grippa et al. 2007). Observed trends in streamflow in some north-flowing arctic rivers, particularly in the winter season, may also be associated with increasing seasonal thaw and the melt of excess ground ice (Adam & Lettenmaier 2008, Cherry et al. 2006). In addition, there is continued evidence that the treatment of permafrost in the land surface schemes of global climate models can yield large sensitivities in remote teleconnections for future climate scenarios (Saha et al. 2006, Gagnon & Gough 2005). Although mathematical models of permafrost have existed for quite some time, many of these modeling efforts are poorly suited for investigating the complex interactions of the active layer hydro-thermal regime and water and energy interactions governing hydrologic response across the circumpolar arctic (Ishikawa & Saito 2006).

Representation of the spatial distribution of permafrost, particularly in alpine areas, has often relied on GIS-based empirical/statistical relationships to estimate the probability of permafrost presence at gridded locations based on proxy variables, such as snow basal temperatures (Julian & Chueca 2007), air temperature (Juliussen & Humlum 2007) and terrain parameters and land cover (Etzelmueller et al. 2007). These techniques have recently also been extended to non-alpine domains (Anisimov et al. 2002).

The state of the art in permafrost temperature modeling is typically associated with the detailed multi-dimensional modeling performed in the design of cold regions engineered structures (Zhang et al. 2006) or the evaluation of complex physical structures (Noetzli et al. 2007, Ling & Zhang 2004). Such models are often not capable of hydrologic analysis so physically detailed. Spatially distributed watershed models suitable for permafrost domains have also been developed (Zhang et al. 2000, Kuchment et al. 2000). These can be extremely useful for investigation of hydrothermal interactions at the scale of small watersheds, but more regional application is limited due to the required computational times.

Presently, the representation of permafrost within global climate models primarily includes a finite difference or finite element solution of the heat diffusion equation. The PILPS 2(e) land surface model intercomparison experiment compared simulated output from 23 land surface schemes applied to the Torne-Kalix River basin in Northern Sweden, an area of seasonally frozen ground. At the time of that experiment (2002), 16 of the 21 participating models represented soil freezing through some implementation of the heat diffusion equation (Bowling et al. 2003). The remaining models either did not include soil freezing or used a temperature index to restrict soil water movement. Due in large part to computational considerations, however, these early attempts at including physically-based permafrost algorithms within GCMs required simplifications regarding boundary and initial conditions, the energy effects of phase change and the number of solution elements.

The objective of this paper is to document the current representation of permafrost within the Variable Infiltration Capacity (VIC) model (version 4.1.0 r5), macroscale hydrology model/land surface scheme that has been adapted for applicability in arctic domains, and to explore the sensitivities and limitations of the current approach.

The Variable Infiltration Capacity Model

The variable infiltration capacity model

The Variable Infiltration Capacity (VIC) model is a water and energy balance hydrologic model suitable to application at large scales, typically applied at grid scales ranging from 0.125–2.0 degrees latitude by longitude (Nijssen et al. 2001, Su et al. 2005). It is similar to land surface parameterization schemes used in regional and global climate models, however, the VIC model is typically applied in an off-line mode, using historic meteorological observations or downscaled and bias-corrected climate model output, then calibrated and evaluated with respect to observed surface hydrology. General model structure is documented in Liang et al. (1994, 1996), Cherkauer and Lettenmaier (1999), and Cherkauer et al. (2003). In this section we wish to document the model structure as it pertains to simulation of surface water hydrology in permafrost domains.

Soil thermal solution

The core of the soil thermal solution is a finite-difference solution of the heat diffusion equation (Cherkauer & Lettenmaier 1999). The thermal solution takes into account the energy associated with phase change and freezing point depression by the soil matrix. Infiltration, percolation and baseflow are calculated based on the total and unfrozen soil moisture contents. The finite difference solution includes specification of thermal nodes that are independent of the model soil moisture layers, allowing for flexibility in the specified depth to the bottom boundary and number of solution nodes.

In addition, the bottom boundary condition can be specified as either a constant temperature or zero flux boundary. Typically, a constant temperature boundary condition is invoked by fixing the mean temperature of the annual thermal damping depth (approximately 3–4 m depth). A zero flux boundary condition is applied at a solution damping depth at least three times deeper than the thermal damping depth.

Figure 1 illustrates the influence of the bottom boundary condition on the equilibrium temperature profile. For the base simulation (gray, solid line) the model was run with a no flux boundary condition at a depth of 25 m, and spun-up for 100 years of constant 1998 weather conditions. Observed meteorology, soil temperature and soil conditions from the Betty Pingo research site, near Prudhoe Bay, Alaska, collected by the Water and Energy Research Center (WERC) at the University of Alaska Fairbanks (UAF) were used. The black line represents a similar simulation, using a 4 m damping depth, with the bottom temperature set equal to the final 4 m temperature derived from the no flux solution. The

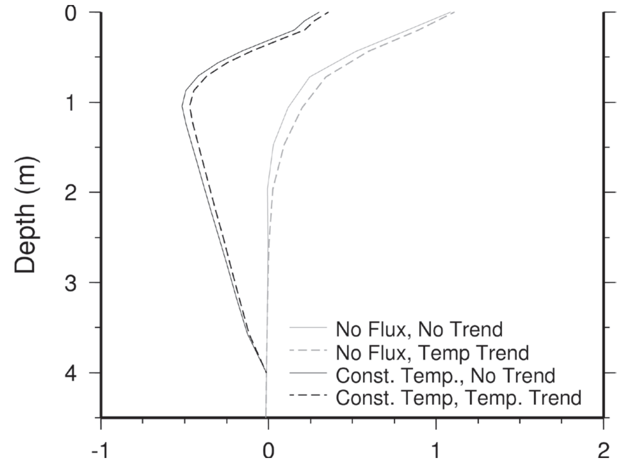

Figure 1. Illustration of the choice of boundary condition (no flux or constant temperature) on the soil temperature profile at equilibrium. Simulations were run for 100 years under constant 1998 conditions (solid lines). Simulations were then repeated (dashed) with an imposed air temperature trend of 0.094°C/decade.

dashed lines represent repeated 100 year simulations, with an imposed air temperature gradient of 0.094°C/decade, chosen to represent the recent observed rate of change in the Arctic (Polyakov et al. 2003). It was anticipated that this example would illustrate that under the imposed temperature trend, the no flux boundary condition would allow the profile temperatures to migrate away from the equilibrium solution, while the constant temperature boundary would not. What is perhaps more striking is that in both cases, the constant temperature solution diverges substantially from the no flux equilibrium profile, resulting in colder (and more reasonable) near-surface temperatures. The zero flux boundary condition appears to be allowing the accumulation of excess heat in the bottom of the soil column, leading to excessive warming in long-term simulations. This could illustrate that a constant flux boundary, that would pass this excess heat to the deeper soil layer would be more appropriate (Zhang et al. 2003). Or it may be due to solution error associated with the choice of damping depth such as that documented by Alexeev et al. (2007). Both of these will be explored in the future.

Solution dynamics and node distribution

The original VIC thermal solution used an explicit solution technique with iteration at the top boundary to close the surface energy balance. The imposed node distribution allowed for three fixed nodes in the top 20 cm of soil, with nodes linearly distributed between 20 cm and the specified damping depth. Both of these simplifying assumptions contributed to model instability, particularly in the presence of dry soils or extreme temperatures. Rather than solve the heat equation explicitly for each node, an implicit Newton-Raphson method has been implemented to solve soil temperatures and ice contents simultaneously. In the rare event of non-convergence, the method defaults to the explicit solution. Because the greatest variability in temperature occurs at the near surface thermal nodes, the nodes are distributed exponentially with depth.

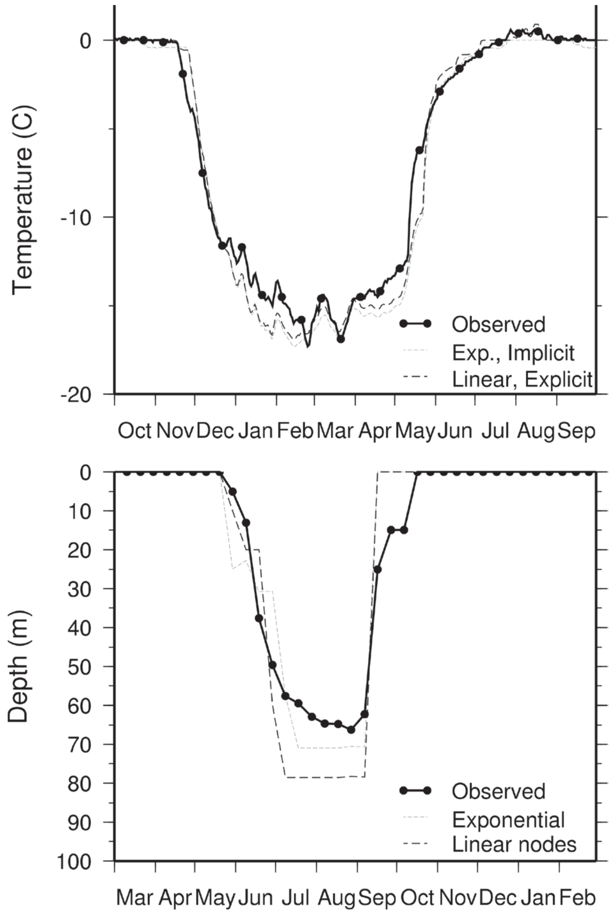

Figure 2. Example application of the VIC model to a point centered on the WERC Betty Pingo research site near Prudhoe Bay Alaska. (top) Simulated and observed 60 cm soil temperatures and (bottom) The location of the simulated and observed 0°C isotherm.

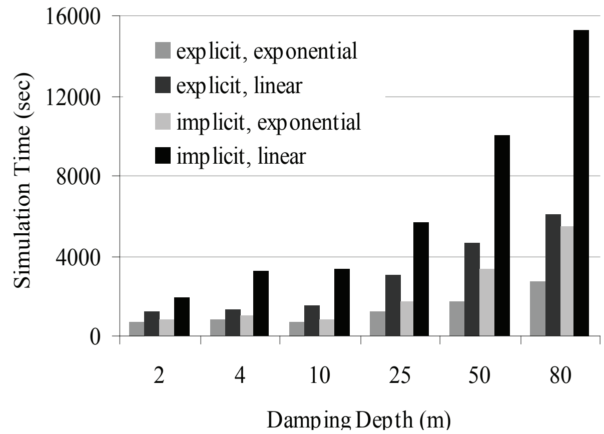

Figure 3. Comparison of system CPU times for a 100 year simulation with different damping depths using the explicit and implicit solutions and exponential and linear node distributions.

A grid transformation is performed in which the physical system exists in exponential space, while the heat equations are solved in linear space.

As shown in Figure 2 (top), when sufficient solution nodes are specified, there is negligible difference between the temperature solutions obtained from either the exponential or linear node distribution. This example utilized a constant temperature boundary at 4 m, with 20 solution nodes. Observed temperatures are taken from the WERC Betty Pingo site. The implicit or explicit solution also does not influence the predicted temperature. The benefit of the exponential node distribution is realized in more typical simulations, utilizing fewer nodes (Fig. 2). In this case, only 7 solution nodes were used, and it can be seen that by concentrating more nodes in the area of maximum change, the exponential node distribution is better able to capture the depth of the observed 0^oC isotherm.

Fewer solution nodes are advantageous with respect to total simulation time, as illustrated in Figure 3. In this case the model was run for several damping depths, with the number of solution nodes adjusted for each depth. With a linear distribution, the number of nodes was set equal to the damping depth plus 8, while only 1/3 as many nodes were used for the exponential distribution (with a minimum of 6 nodes). Overall the implicit solution is more time consuming than the explicit solution, in part because the implicit solution currently updates temperature dependent variables with each iteration, while the explicit scheme does not. By reducing the total number of solution nodes, however, the exponential distribution reduces the overall simulate time so that the implicit, exponential solution is faster than the explicit, linear solution.

Excess ground ice and ground subsidence

Excess ground ice, defined as an ice concentration above what could be held as liquid water in the soil column where the ground completely thawed, exists in various parts of the Arctic. As excess ice melts in response to climatic warming, the ground collapses and the excess meltwater is expelled to the surface. Because of ground subsidence, the water-holding capacity of the soil column is diminished. An excess ground ice and ground subsidence algorithm has been introduced to the VIC model. Each layer of the soil column is initialized with an ice fraction, which may exceed the soil porosity. Figure 4 illustrates how the expanded column depth is calculated based on the input soil column depth and ice fractions.

The expanded column depth does not change until the ice fraction to porosity ratio falls below a pre-specified ratio, f_{ice}. Even at very low temperatures, there can be a small amount of liquid water in the soil column due to freezing point depression (cf. Eq. 14 of Cherkauer & Lettenmaier 1999), therefore f_{ice} should be set to a value somewhere between 0.5 and just below 1.0, with a lower value causing subsidence to occur at warmer temperatures. After subsidence, all parameters dependant on the soil layers are updated.

Surface water interactions

As shown by Ling & Zhang (2003), shallow arctic thaw lakes can be significant sources of heat to sub-lake taliks and the surrounding permafrost. Surface water storage in small (sub-grid) lakes and wetlands is represented in the VIC model utilizing an input depth-storage relationship to determine

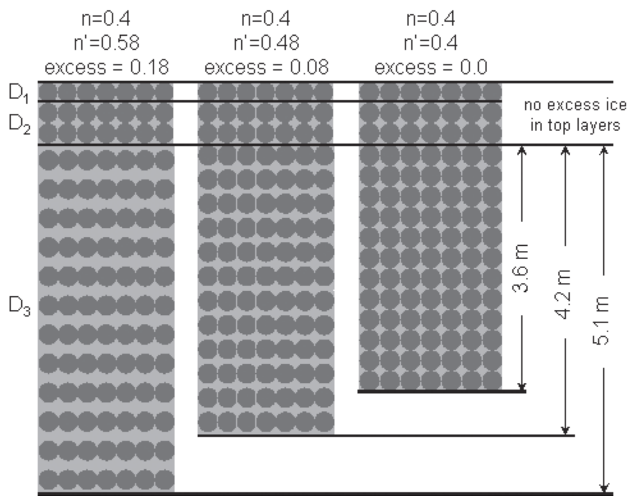

Figure 4. Example of an application of the VIC excess ice and subsidence algorithm in which the excess ice fraction in the third soil layer is initialized to 0.18 (left column). As the excess ice melts, the depth of the third soil layer decreases, and the effective porosity (*n'*) also decreases. Once effective porosity reaches soil porosity (*n*), the soil no longer subsides (right column).

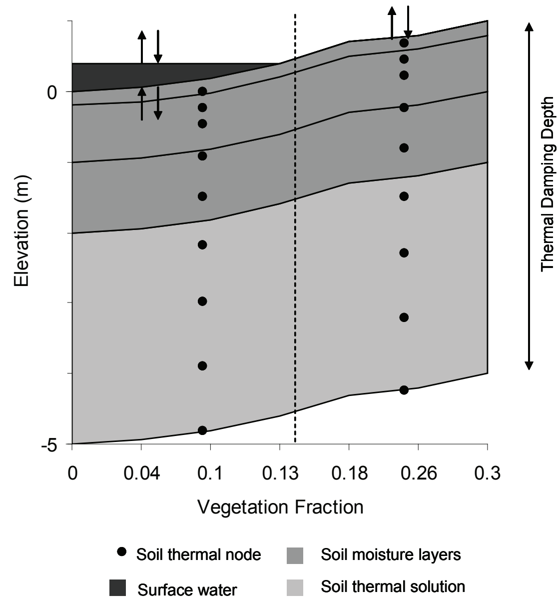

Figure 5. Illustration of the soil thermal solution for the wetland fraction of a VIC grid cell. The flooded fraction is determined using the land surface profile input as a depth-area curve. Soil temperatures are resolved independently for the flooded and upland fractions and then averaged.

spatial variability in surface water extent based on the stored volume (Cherkauer et al. 2003). The temperature profile and evaporation from stored water is resolved using an implicit one dimensional thermal model, based on Hostetler & Bartlein (1990). The original model assumed a no flux boundary condition at the lake bottom and did not resolve sub-lake soil temperatures. As illustrated in Figure 5, recent enhancements to the lake algorithm extend the thermal solution into the soil column, with a bottom boundary condition determined by the soil thermal model. Solar radiation through shallow water and conductive heat transfer from the water to the soil are balanced by the ground heat flux at the soil/water interface. The number of thermal solution nodes in the surface water is variable depending on water depth. To resolve energy instabilities in very thin water layers, the lake algorithm collapses to solve together with the surface soil layer, similar to the solution for thin snowpacks described by Cherkauer et al. (2003). This enhancement allows for exploration of the interaction of surface water storage and the soil thermal regime within the macroscale model. These interactions are further explored in Chiu et al. (these proceedings).

Discussion

Long-term simulation of the soil temperature profile requires a computational damping depth that greatly exceeds the thermal damping depth. The use of exponentially-distributed thermal nodes that are separated from the soil moisture layers results in reduced computation time, while the application of an implicit solver for the sub-surface heat equation results in greater numerical stability. There are still many issues to explore regarding the selection of appropriate damping depths and the start-up time required to

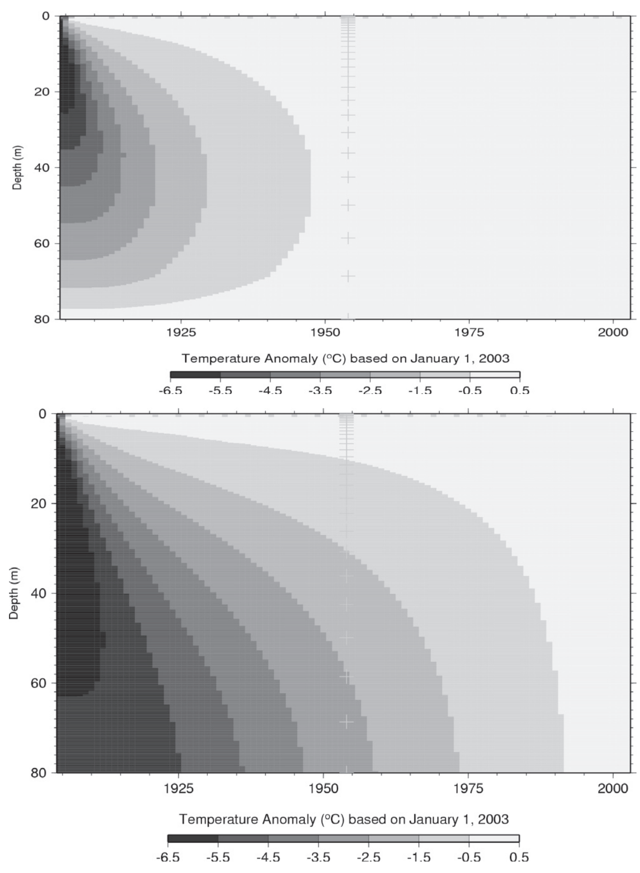

Figure 6. Assessment of the simulation time required to remove start-up anomalies with an implicit solution using exponentially-distributed nodes (shown by cross-hatches): constant temperature boundary condition (top), zero flux boundary condition (bottom).

reach stability. Figure 6 shows the temperature anomaly over time at each solution node for both the constant temperature and zero flux boundary conditions. The implicit solution and exponential node distribution were used in both cases. Temperature anomalies were calculated as the difference between the temperature on January 1 of each year, and the temperature on January 1 of the last year of simulation, so that small anomalies imply a temperature equilibrium has been reached. For the constant temperature scenario, equilibrium is reached after about 45–50 years of simulation. With the zero flux solution, it is not clear that equilibrium is reached after 100 years of simulation.

Summary

Recent studies have explored issues of computational stability, the role of excess ground ice, and permafrost/wetland interactions within the VIC land surface model. Representation of excess ground ice which exceeds the porosity of the undisturbed soil is essential for duplicating the water balance in some watersheds, especially those experiencing significant permafrost change. In other regions, the interaction between permafrost and surface water storage can be explored by resolving soil thermal fluxes under surface lakes and wetlands. These computational advances allow initial exploration of the role of large-scale permafrost-hydrology interactions on the dynamics of surface water and ground ice storage. Considerable challenges still exist in identifying the role of scale in permafrost representation, and with respect to near-surface runoff generation and the interactions between permafrost change and wetland extent.

Future work will proceed in several areas, including:

- Understanding of the problem of excessive warming in the no-flux boundary solution.
- Improved representation of runoff dynamics in permafrost areas, including the representation of subsurface water movement as a perched layer on top of the frozen transitional zone.
- Interaction between the ground subsidence algorithm and the wetland surface elevation profile, allowing dynamic increases in wetland extent associated with permafrost melt.

Acknowledgments

Funding for this research has been provided by NASA through the Northern Eurasia Earth Science Partnership Initiative (NEESPI). We acknowledge the efforts of M. Pan for implementation of the implicit solution method in the VIC model.

References

Adam, J.C. & Lettenmaier, D.P. 2008. Application of new precipitation and reconstructed streamflow products to streamflow trend attribution in Northern Eurasia. *Journal of Climate,* accepted.

Alexeev, V.A., Nicolsky, D.J., Romanovsky, V.E. & Lawrence, D.M. 2007. An evaluation of deep soil configurations in the CLM3 for improved representation of permafrost. *Geophysical Research Letters* 34(9): 9502.

Anisimov, O.A., Shiklomanov, N.I. & Nelson, F.E. 2002. Variability of seasonal thaw depth in permafrost regions: A stochastic modeling approach. *Ecological Modelling* 153(3): 217-227.

Bowling, L.C., Lettenmaier, D.P., Nijssen, B., Graham, L.P. et al. 2003. Simulation of high latitude hydrological processes in the Torne-Kalix basin: PILPS Phase 2(e) 1: Experiment description and summary intercomparisons. *Global and Planetary Change* 38(1–2): 1-30.

Cherkauer, K.A. & Lettenmaier, D.P. 1999. Hydrologic effects of frozen soils in the upper Mississippi River basin. *Journal of Geophysical Research 104*(D16): 19599-19610.

Cherkauer, K.A., Bowling, L.C. & Lettenmaier, D.P. 2003. Variable Infiltration Capacity cold land process model updates. *Global and Planetary Change* 38: 151-159.

Cherry, J.E., Alexeev, V., Liepert, B., Groisman, P. & Romanovsky, V. 2006. Acceleration of the arctic water cycle: Evidence from the Lena basin, Siberia. *EOS Transactions, American Geophysical Union* 87(52; Suppl.), Suppl. 26 Dec.

Etzelmueller, B., Farbrot, H., Gudmundsson, A., Humlum, O., Tveito, O.E. & Bjornsson, H. 2007. The regional distribution of mountain permafrost in Iceland. *Permafrost and Periglacial Processes* 18(2): 185-199.

Gagnon, A.S. & Gough, W.A. 2005. Climate change scenarios for the Hudson Bay region: An intermodel comparison. *Climatic Change* 69(2-3): 269-297.

Grippa, M., Mognard, N.M., LeToan, T. & Biancamaria, S. 2007. Observations of changes in surface water over the western Siberia Lowland. *Geophysical Research Letters* 34: L15403, doi:10.1029/2007GL030165.

Hostetler, S.W. & Bartlein, P.J. 1990. Simulation of lake evaporation with application to modeling lake level variations of Harney-Malheur Lake, Oregon, *Water Resources Research* 26 (10): 2603-2612.

Ishikawa, M., & Saito, K. 2006. Frozen ground sciences influencing climate and water cycle; reviews and perspectives. *Seppyo (Journal of the Japanese Society of Snow and Ice)* 68(6): 639-656.

Julian, A. & Chueca, J. 2007. Permafrost distribution from BTS measurements (Sierra de Telera, central Pyrenees, Spain); assessing the importance of solar radiation in a mid-elevation shaded mountainous area. *Permafrost and Periglacial Processes* 18(2): 137-149.

Juliussen, H. & Humlum, O. 2007. Towards a TTOP ground temperature model for mountainous terrain in central-eastern Norway. *Permafrost and Periglacial Processes* 18(2): 161-184.

Kuchment, L.S., Gelfan, A.N. & Demidov, V.N. 2000. A distributed model of runoff generation in the permafrost regions. *Journal of Hydrology* 240(1-2): 1-22.

Liang, X., Lettenmaier, D.P., Wood, E.F. & Burges, S.J. 1994. A simple hydrologically based model of land surface water and energy fluxes for GSMs. *Journal of Geophysical Research* 99(D7): 14,415-14,428.

Liang, X., Wood, E.F. & Lettenmaier, D.P. 1996. The soil moisture parameterization of the VIC-2L model: evaluation and modifications. *Global and Planetary Change* 13: 195-206.

Ling, F. & Zhang, T. 2003. Numerical simulation of permafrost thermal regime and talik development under shallow thaw lakes on the Alaskan Arctic coastal plain. *Journal of Geophysical Research* 108(D16): doi:10.1029/2002JD003014.

Ling, F. & Zhang, T. 2004. A numerical model for surface energy balance and thermal regime of the active layer and permafrost containing unfrozen water. *Cold Regions Science and Technology* 38(1): 1-15.

Nijssen, B., Schnur, R. & Lettenmaier, D.P. 2001. Global retrospective estimation of soil moisture using the Variable Infiltration Capacity land surface model, 1980-1993. *Journal of Climate* 14: 1790-1808.

Noetzli, J., Gruber, S., Kohl, T., Salzmann, N. & Haeberli, W. 2007. Three-dimensional distribution and evolution of permafrost temperatures in idealized high-mountain topography. *Journal of Geophysical Research* 112(F2): doi:10.1029/2006JF000545.

Polyakov, I., Bekryaev, R.V., Alekseev, G.V., Bhatt, U.S., Colony, R.L., Johnson, M.A., Makshtas, A.P. & Walsh, D. 2003. Variability and trends of air temperature and pressure in the maritime Arctic, 1875-2000. *Journal of Climate* 16 (12): 2067-2077.

Saha, S.K., Rinke, A., Dethloff, K. & Kuhry, P. 2006. Influence of a complex land surface scheme on arctic climate simulations. *Journal of Geophysical Research* 111(D22): doi:10.1029/2006JD007188.

Smith, L.C., Sheng, Y., MacDonald, G.M. & Hinzman, L.D. 2005. Disappearing Arctic Lakes, *Science* 308, 3 June: 1429.

Su, F., Adam, J.C., Bowling, L.C. & Lettenmaier, D.P. 2005. Streamflow Simulations of the Terrestrial Arctic Domain, *Journal of Geophysical Research* 110: D08112, doi:10.1029/2004JD005518.

Zhang, M., Yuanming, L., Fujun, N. & Shusheng, H. 2006. A numerical model of the coupled heat transfer for duct-ventilated embankment under wind action in cold regions and its application. *Cold Regions Science and Technology* 45(2): 103-113.

Zhang, Y., Chen, W. & Cihlar, J. 2003. A process-based model for quantifying the impact of climate change on permafrost thermal regimes. *Journal of Geophysical Research* 108(D22): doi:10.1029/2002JD003354.

Zhang, Z., Kane, D.L. & Hinzman, L.D. 2000. Development and application of a spatially-distributed arctic hydrological and thermal process model (ARHYTHM). *Hydrological Processes* 14(6): 1017-1044.

Effects of Soil Cryostructure on the Long-Term Strength of Ice-Rich Permafrost Near Melting Temperatures

M.T. Bray

University of Alaska Fairbanks, Departments of Civil and Environmental Engineering, Fairbanks, Alaska, USA

Abstract

Stress relaxation tests were performed to look at the effect of cryostructure on the long-term strength of ice-rich permafrost. Cryostructures of tested soils include micro-lenticular, remolded-massive, reticulate-chaotic, and wedge ice. Soils with remolded-massive structure shows long-term strengths three to four times greater than undisturbed soils, suggesting that data extrapolation from remolded soils to undisturbed soils can be non-conservative. Samples with reticulate-chaotic structure showed higher long-term strength in the tested temperature range than samples with micro-lenticular structure and wedge ice structure. Long-term strength relationships with temperature are presented.

Keywords: long-term cryogenic structure; cryostructure; ice-rich; long-term strength; permafrost; stress relaxation.

Introduction

Only a few published studies include information on the long-term strength behavior of ice-rich permafrost. In most cases, remolded samples are used for a variety of reasons. Remolded samples usually contain a *massive* cryostructure unless special efforts are made to create a different cryostructure. The cryostructure is the pattern of ice inclusion found in a frozen soil. Soils with *massive* structure may, but in many instances for ice-rich permafrost, do not represent the actual permafrost soil that is present. It has been recognized that the texture has an influence on the resulting strength and creep behavior (e.g., Sayles & Carbee 1981). A few studies have investigated the creep behavior of ice-rich permafrost samples (undisturbed cores) (Arenson & Springman 2005, McRoberts et al. 1978, McRoberts 1988, Savigny & Morgenstern 1986). Savigny & Morgenstern (1986) briefly explored the effects of cryostructure on the behavior of clay permafrost and found that the prominent ice veins or lenses had a large impact on the resulting creep behavior. Research in Russia showed that the orientation of segregated ice in frozen soil also had an impact on the shear strength (e.g., Pekarskaya 1965, Vialov et al. 1965). Shear strength in the direction of ice lenses was lower than the shear strength perpendicular to ice lenses.

The primary purpose of this program is to examine the impact of cryostructure on the long-term strength of ice-rich permafrost.

Materials and Methods

Soils and cryostructure

The soils used in this testing program are taken from the CRREL permafrost tunnel at Fox, Alaska. A detailed discussion of the permafrost geology and cryostructures is presented by Bray et al. (2006).

Permafrost in the CRREL permafrost tunnel is ice-rich, syngenetic permafrost deposit of Pleistocene age and is commonly referred to as the "Ice Complex" or "Yedoma" (Shur et al. 2004). This syngenetic permafrost deposit is characterized by sediments that typically contain 40–60% segregated ice by volume and large, 2–5 m wide, dark colored ice wedges. The syngenetic permafrost is representative of the original permafrost formed during deposition and sedimentation. The other defining feature of the tunnel is that extensive secondary modification occurred due to thermal-fluvial erosion that operated preferentially along the ice wedges. The resulting deposits are characterized by epigenetic permafrost with cryostructures that are different from the original syngenetic permafrost.

Cryostructures within the tunnel deposits are strong indicators of the original syngenetic and secondary refrozen deposits. *Micro-lenticular* cryostructure is the primary diagnostic cryostructure of the original permafrost. *Layered* and *lenticular-layered* cryostructures are also characteristic of the original permafrost. The modified permafrost deposits either contain *massive* or *reticulate-chaotic* cryostructures. In this study, soils with *micro-lenticular*, *massive* (i.e., *remolded-massive)*, and *reticulate-chaotic* cryostructures were used (Fig. 1). Also included is massive *wedge ice.*

Micro-lenticular cryostructure consists of thin, straight to wavy lenticular shaped ice lenses that essentially saturate the soil. Lenses are less than 0.5 mm in thickness and usually less than 4–10 mm long. Microscopic analysis shows that the soil particles are essentially suspended in an ice matrix. Typical water contents by weight are 90–130%. Frozen bulk densities range from 1.26 to 1.34 g/cm^3. *Horizontal micro-lenticular* and *vertical micro-lenticular* cryostructure is referred to below. Horizontal indicates ice lenses are perpendicular to applied principal stress. Vertical indicates ice lenses are parallel with applied stress.

Massive cryostructure consists of silt cemented together without visible segregated ice. Microscopic analysis from *massive* structures in the tunnel silts show that ice in excess of pores does exist, indicating that the soil was in a supersaturated condition when refrozen. This was confirmed by gravimetric water contents between 50–70%. Saturation for these soils is normally 30–40%.

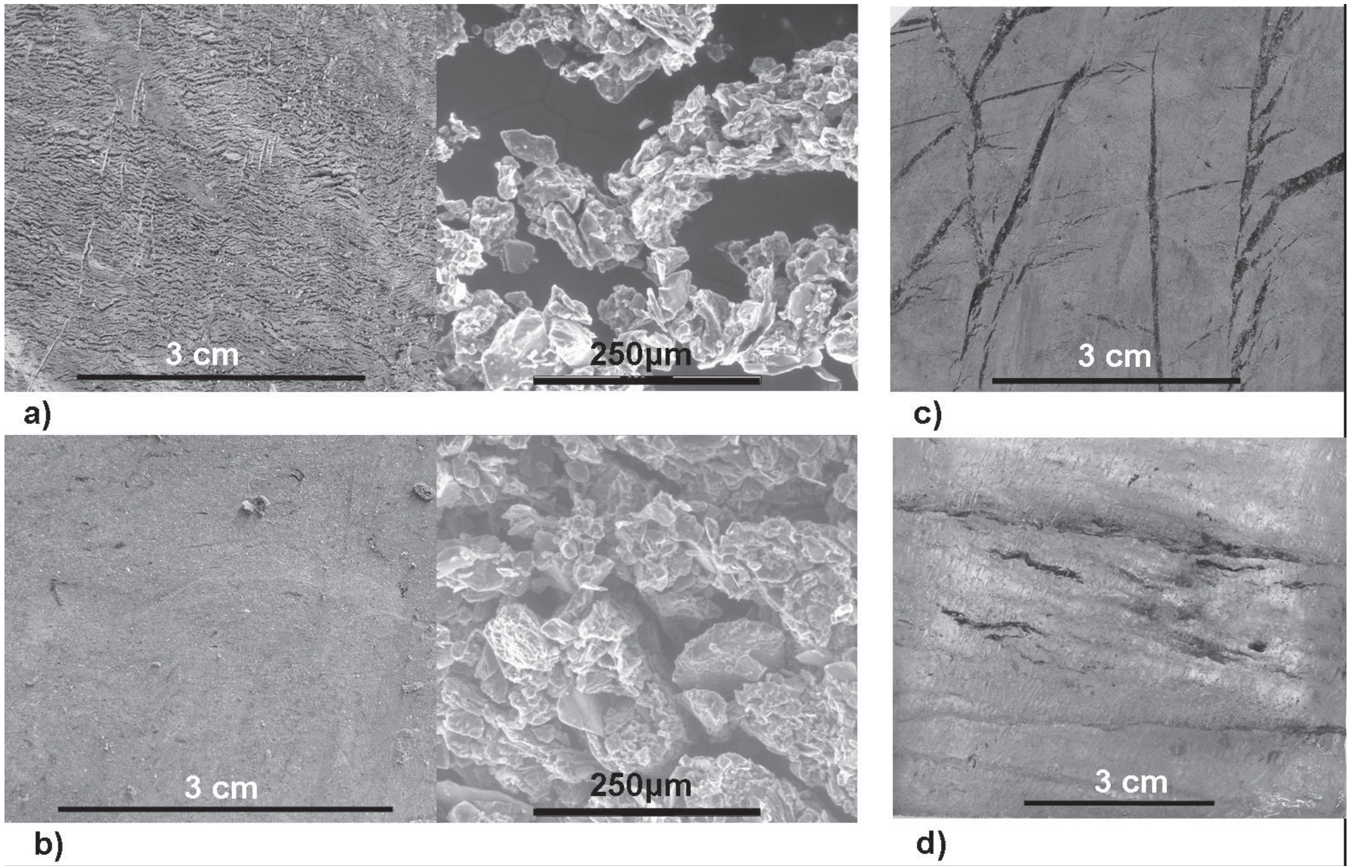

Figure 1. Images of cryostructures: a) *Micro-lenticular* cryostructure. To the right is a micro-scale image taken with an ESEM, b) *Massive* cryostructure. To the right is micro-scale image taken with an ESEM. c) *Reticulate-chaotic* cryostructure consists of larger ice lenses with massive soils between them, d) *Wedge ice*. Dark inclusions are foliation planes and sedimentation zones. Typically they run from 0° to 15°. Scales are indicated.

Remolded-massive structure represents a soil that has been reconstituted and then frozen quickly to produce *massive* cryostructure. A slurry was prepared and placed in a plastic cylinder. The sample was then vibrated to increase settlement. The sample was allowed to drain 24 hours under gravitation and then was frozen at -45ºC. The result was very little ice segregation and uniform *massive* silt. Frozen bulk densities range from 1.52 to 1.58 g/cm^3. Remolded samples were prepared from a slurry made of material from the CRREL tunnel, which had water contents ranging from 60–65%. Final drained water contents ranged from 48–52% by weight. This represents the lower range of water contents as seen from silts with *massive* structure found in the permafrost tunnel.

Reticulate-chaotic structure is characterized by randomly oriented ice lenses, 1–5 mm in thickness, and 1–5 cm in length. The silt between segregated ice lenses is *massive.* Frozen bulk density ranges from 1.33 to 1.51 g/cm^3. This structure most commonly occurs with clear ice deposits (non-foliated ice, thus not wedge ice) that we classify as thermokarst cave ice; another term used in the North American literature is *pool ice* (Mackay 1988 p. 87, 1997 p. 20). It occurs in the saturated sediments along the erosional-depositional surface. *Reticulate-chaotic* structure can be found in some silt deposits along the erosional surface without thermokarst cave ice, but it will always be found with thermokarst cave ice deposits in the tunnel. When found in association with thermokarst cave ice, the lenses are largest near the clear ice deposits.

Wedge ice was taken from large syngenetic ice wedges. They are brown to gray in color due to soil particles along foliations and organic staining. The wedges are generally 2–5 m in width with the bottom portions observed.

Testing

Undisturbed samples of syngenetic and epigenetic permafrost, along with samples remolded from the same silt, were tested. Relaxation tests were the main testing method and were performed on two electro-mechanical screw driven load frames.

All tests were conducted within a temperature range from -0.3°C to -3.1°C. Temperature stability was generally better than +/- 0.10°C for the duration of the tests. The two electro-mechanical screw driven frames were placed within a cold room that was maintained at -5°C. Insulated chambers were then placed around the sample. Temperature of the sample area was maintained using 20 liter recirculating water baths with temperature stability of +/- 0.10°C, by running the fluid through a convection driven heat exchanger located in the insulated chambers. These convection driven temperature controlled environments tended to promote substantial sublimation problems. In order to prevent sublimation of soil samples, latex membranes were placed around the sample with good results.

Relaxation tests

One of the primary focuses of the testing program was the utilization and application of relaxation tests. Relaxation tests allow for the testing of one sample as compared to a set of identical samples. The inherent variability of undisturbed soils made the use of relaxation tests an attractive alternative.

The relaxation tests were conducted by quickly loading (10–20 mm/min) the sample with a high capacity spring (approx. 71 kN/cm) placed in series with the sample to a prescribed stress level. The stress level was at least 50% of the instantaneous strength. The lower load applying platen was then fixed (stationary). As the elastic strain in the spring is released, the soil undergoes creep deformation and stress relaxation. Movement of the lower platen was monitored with an LVDT (i.e., machine relaxation) and two LVDT's were used to monitor the creep deformation occurring within the sample. The load was monitored with an electronic load cell. Temperatures were monitored by two thermistors at the sample surface. All data was automatically collected at 5 sec to 30 min intervals. Tests were typically run for 300 to 1000 hours. The longest test ran for about 2000 hours.

Long-Term Strength

The long-term strength can be defined as the stress above which deformations no longer attenuates (Tsytovich 1975, Vyalov 1980). Alternatively creep strengths are commonly predicted by recording the time to failure for a given stress. Failure is adopted as the transition from secondary to tertiary creep or a strain of 20% (Andersland & Ladanyi 1994). Strength versus time is plotted to represent ultimate creep strength. A direct experimental approach to determining the long-term strength is outlined by Tsytovich (1975) and Vyalov et al. (1966). The two approaches outlined are the ball plunger and the dynamometer, from which the long-term strength is defined as the stress at which deformation ceases (or a prescribed conditional stability is met). Thus, these approaches give directly the value of long-term strength.

The test procedures used in this work are similar to the dynamometer techniques. In many instances complete stabilization was difficult to reach, therefore two strain rates of 2.083 x 10^{-6} hr^{-1} and 2.083 x 10^{-7} hr^{-1} were considered as conditional stability states, as was done by Vyalov et al. (1966). The first strain rate condition will henceforth be referred to as "*stability condition 1*" and the second as "*stability condition 2*." Consequently, the definition of long-term strength in this work is the stress at which the conditional stability criterion is met.

Results and Discussion

Table 1, Figure 2, and Figure 3, show the long-term strengths as determined directly from relaxation tests based on the conditional stability criteria. Table 2 shows long-term

Table 1. Summary of long-term strengths for stability conditions 1 and 2.

Long-term strength (kPa) Stability Condition 1	Long-term strength (kPa) Stability Condition 2	Temperature (°C)
vertical micro-lenticular (VML)		
69.2	39.9	-0.77
46.0	23.0	-0.86
217.4	153.0	-2.78
horizontal micro-lenticular (HML)		
56.4	33.9	-.077
48.5	27.2	-0.82
162.3	113.1	-1.81
115.7	74.8	-1.86
127.2	84.7	-1.82
209.5	161.2	-2.81
remolded-massive (RM)		
72.5	60.7	-0.3
146.2	142.0	-0.5
136.0	130.2	-0.5
270.9	256.7	-1.0
259.0	236.6	-1.0
286.9	278.8	-1.0
532.8	506.2	-2.0
509.9	484.2	-2.0
695.4	654.6	-3.0
715.2	676.8	-3.0
reticulate-chaotic (RC)		
86.9	63.6	-0.88
154.7	118.0	-1.85
140.0	110.0	-1.85
183.3	138.2	-2.08
213.0	151.1	-2.79
wedge ice (IW)		
95.8	39.3	-0.44
131.0	63.0	-0.96
123.2	60.1	-0.95
101.3	42.5	-1.86
113.6	53.4	-1.86
117.7	58.6	-3.10
113.4	59.0	-3.10

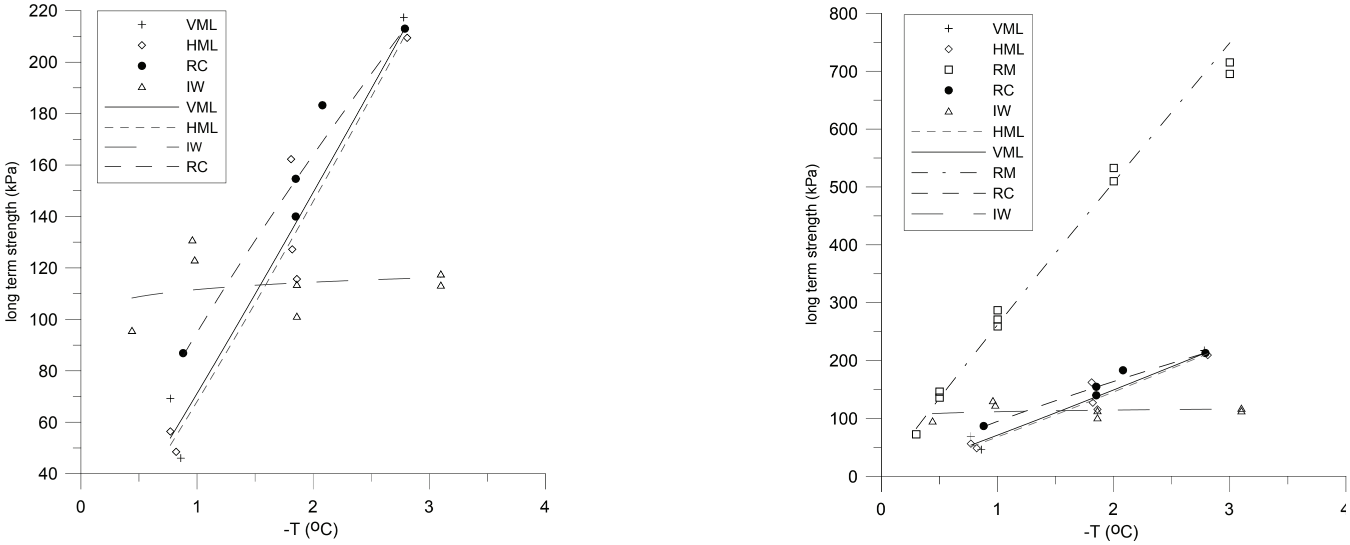

Figure 2. Long-term strength for stability condition 1.

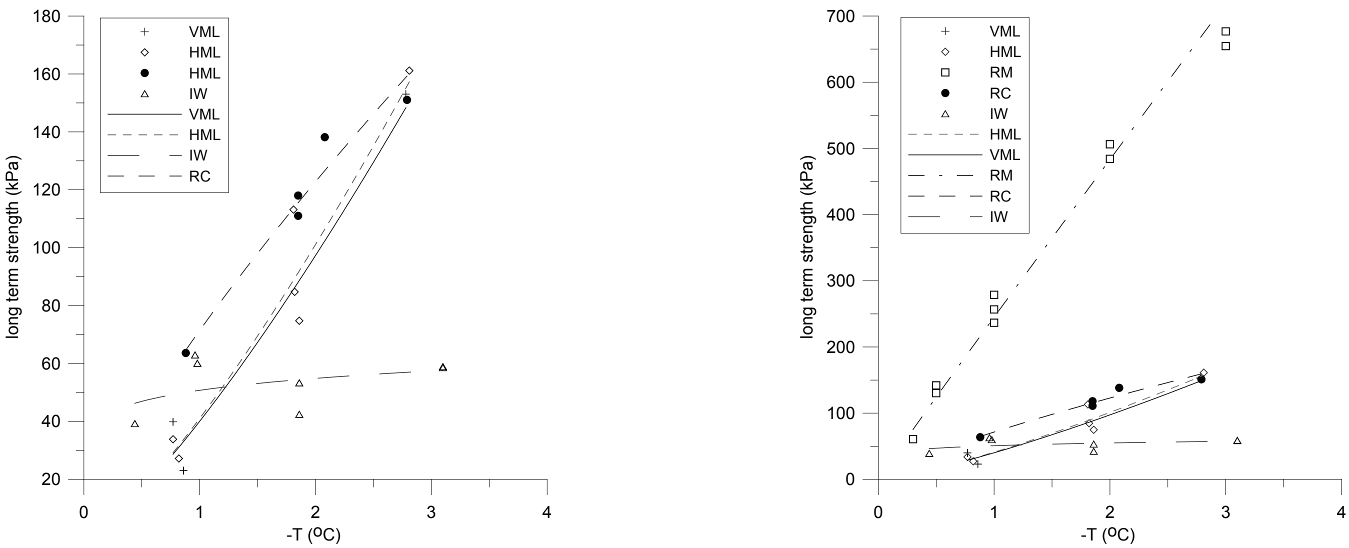

Figure 3. Long-term strength for stability condition 2.

strengths for Fairbanks silt from outside sources. Long-term strength as a function of temperature can be modeled by equation 1.

$$\sigma_{lt} = A\left|\theta\right|^{b} \tag{1}$$

where A and b are experimentally determined parameters. Values for A and b as a function of cryostructure are shown in Table 3 and 4. The value of σ_{lt} has units of kPa. A has units of kPa°C^{-b}. Temperature, θ, is the temperature in degrees Celsius below 0°C.

For soils with *micro-lenticular* structure, the value of b>1 results in concave upwards inflection of any extrapolation of the curve. The temperature range represented by this data is the zone of the most intense change in unfrozen water content. As the temperature decreases, the long-term strength generally increases at a slower rate. Therefore, extrapolation of the given equation to lower temperatures should give larger values of long-term strength than would be expected.

The long-term strength of soils with *vertical micro-lenticula*r (VML) and *horizontal micro-lenticular* (HML) structure are similar as seen from the parameters A and b as well as Figure 2 and Figure 3. Soil with *remolded-massive* (RM) cryostructure shows higher long-term strength as compared to natural soils; the strength is 3 to 4 times larger for RM soils than undisturbed soils. This is significant in that extrapolation of results from remolded soils to undisturbed soils is not conservative, based on our data.

In situ massive silts from the permafrost tunnel were not tested directly using the relaxation method. A small number of massive silt specimens were tested under uniaxial constant stress conditions. Results suggest that the in situ massive silts show higher deformation for a given stress than soils with micro-lenticular structure. Results from soils with *remolded-massive* structure should not be extrapolated to the in situ massive silts.

Table 2. Long-term strength data summary for Fairbanks silt and other ice-rich silt.

long-term strength (kPa) stability condition 1	long-term strength (kPa) stability condition 1	Temperature (ºC)	soil	source	comments
319.7	228.5	-2.0	Fairbanks silt	Yuanlin & Carbee 1987	low density, remolded
62.9	35.4	-1.7	Fairbanks silt	Thompson & Sayles 1972	Lab test on undisturbed cores
46.8	26.3	-1.7	Fairbanks silt	Thompson & Sayles 1972	Permafrost tunnel closure rates
*note: above values are based on steady state power law creep relationships					
100 Year Strength Approximations					

$\sigma_{100\ yrs}$	Temperature (ºC)	soil	source	comments
191.2	-0.5	Fairbanks silt	Yuanlin & Carbee 1987	med. density, remolded
343.2	-1.0	Fairbanks silt	Yuanlin & Carbee 1987	med. density, remolded
608.0	-2.0	Fairbanks silt	Yuanlin & Carbee 1987	med. density, remolded
864.0	-3.0	Fairbanks silt	Yuanlin & Carbee 1987	med. density, remolded
29.3	-1.7	Fairbanks silt	Ladanyi et al. 1991	pressuremeter relaxation, field, med. strains
133.8	-1.7	Fairbanks silt	Ladanyi et al. 1991	pressuremeter relaxation, field, low strains
171.0	-1.0	Norman Wells silt	McRoberts et al. 1978	lab tests, undisturbed cores, ice-rich
220.0	-3.0	Norman Wells silt	McRoberts et al. 1978	lab tests, undisturbed cores, ice-rich

Soils with *reticulate-chaotic* (RC) structure show a slight increase in long-term strength over soils with *micro-lenticular l*structure under the temperature range tested. Extrapolation of the RC curve to colder temperatures would suggest lower long-term strengths.

The *wedge ice* (IW) shows small increase of long-term strength with temperature. Significant scatter of experimental data exists. Only at -0.44ºC is a drop in strength observed. Under the temperature range observed, the long-term strength can be considered constant. At a temperature of approximately -1.5ºC, the long-term strength of *wedge ice* falls below that of the ice-rich soils. The largest drop in long-term strength for the stability condition 2 is for *wedge ice.*

Comparison with previous works

Table 2 shows strength data for Fairbanks silt (Ladanyi et al. 1991, Thompson & Sayles 1972, Yuanlin & Carbee 1987) along with data for ice-rich silts (McRoberts et al. 1978). Data is reduced from steady state creep rates and primary creep equations. Yuanlin & Carbee (1987) worked with remolded Fairbanks silt from the permafrost tunnel. For low density (1.07–1.10 g/cm^3), the strength corresponding to stability conditions 1 and 2 were 319.7 kPa and 228.5 kPa at -2°C. Values were obtained from tests with strains rates greater than 2.88 x 10^{-4} hr^{-1}. Hundred year long-term strength (data extrapolated to 100 years) for medium density silt (1.18–1.23 g/cm^3) yielded strengths of 191.2 kPa, 343.2 kPa, 608.0 kPa, and 864 kPa at temperatures of -0.5°C, -1°C, -2°C, and -3°C, respectively. The strength data for soils with *remolded massive* structure falls between the low and medium density silts. The dry densities for soil with *remolded-massive* structure are close to the low density silts.

Ladanyi et al (1991), performed in situ pressuremeter relaxation tests in the permafrost tunnel. For medium strains, 100 year strength is equal to 29.3 kPa. For low strains, the 100 year strength is equal to 133.8 kPa. Test temperatures varied from -1.7°C to -2°C. Thompson & Sayles (1972) measured closure rates of the permafrost tunnel and performed laboratory creep tests of undisturbed soil cores. Based on steady state creep rates for laboratory tests, the strengths are 62.9 kPa and 35.5 kPa (for strain rate of 2.083x10^{-6} hr^{-1} and 2.083x10^{-7} hr^{-1}, respectively) at -1.67°C. Test strain rates were greater than 0.0018 hr^{-1}. Steady state creep conditions for the tunnel closure data yielded strength values of 46.8 kPa and 26.3 kPa. McRoberts et al (1978) reported 100 year strengths for ice-rich Norman Wells silt with strength value of 171 kPa and 220 kPa at temperatures of -1°C and -3°C, respectively. Based on water contents listed in the field study reports from the permafrost tunnel, the soil tested was most likely *micro-lenticular*. Detailed permafrost descriptions were not available. Generally, the field tests yielded lower strengths as compared to the relaxation tests in this study. It is important to note that results of the laboratory tests on undisturbed soils are extrapolations from higher strain rates under which the tests were conducted to lower strain rates. Experience indicates that extrapolation to lower strain rates generally will yield lower strengths. The low strain conditions (Ladanyi et al. 1991) are in the same range as soils with *micro-lenticular* structure. The -1°C strengths are generally higher for ice-rich Norman Wells silt as compared to soils with *micro-lenticular* and *reticulate-chaotic* structure. The -3°C long-term strengths are comparable.

Conclusions

The aim of this study was to explore the effects of the cryostructure on the long-term strength of ice-rich permafrost soils. Long-term strength data directly from relaxation tests yield comparable results to other testing methods. Soils with *remolded-massive* structure had long-term strengths 3 to 4 times greater than the undisturbed soils. In the temperature

Table 3. Experimental parameters A and b for Eq. 1 for stability condition 1.

Cryostructure	Temp range (°C)	A (kPa˚C^{-b})	b (dimensionless)
VML	-0.77 to -2.78	40.057	1.2806
HML	-0.77 to -2.81	41.043	1.3004
RM	-0.3 to -3.0	244.980	0.9798
RC	-0.88 to -2.79	0.1128	0.7817
IW	-0.44 to -3.10	50.747	0.0365

Table 4. Experimental parameters A and b for Eq. 1 for stability condition 2.

Cryostructure	Temp range (°C)	A (kPa˚C^{-b})	b (dimensionless)
VML	-0.77 to -2.78	40.057	1.2806
HML	-0.77 to -2.81	41.043	1.3004
RM	-0.3 to -3.0	244.980	0.9798
RC	-0.88 to -2.79	0.1128	0.7817
IW	-0.44 to -3.10	50.747	0.0365

range tested, soils with *reticulate-chaotic* structure have greater long-term strength than soils with *micro-lenticular* structure or *wedge ice.* The long-term strength for *wedge ice* had little temperature influence in studied range. Soils with *horizontal* and *vertical micro-lenticular* structure had similar long-term strength patterns.

Acknowledgments

This research was funded by NSF Alaska EPSCOR grant 0701898. Dr. Yuri Shur's advice and feedback are appreciated.

References

Andersland, O.B. & Ladanyi, B.L. 1994. *An Introduction to Frozen Ground Engineering.* New York: Chapman & Hall, 352 pp.

Arenson, L.U. & Springman, S.M. 2005. Triaxial constant stress and constanst strain rate test on ice-rich permafrost samples. *Canadian Geotechnical Journal* 42: 412-430.

Bray, M.T., French, H.M. & Shur, Y. 2006. Further Cryostratigraphic Observations in the CRREL Permafrost Tunnel, Fox, Alaska. *Permafrost and Periglacial Processes*, 17: 233-243.

Ladanyi, B., Touileb, B. & Huneault, P. 1991. Pressuremeter stress relaxation testing in a permafrost tunnel. *Proceedings of the Geotechnical Engineering Congress, Boulder, CO, 1991,* 1-11.

Mackay, J.R. 1988. Catastrophic lake drainage, Tuktoyaktuk Peninsula area, District of Mackenzie. *Current Reasearch, Part D, Geological Survey of Canada, Paper* 88-1D: 83-90.

Mackay, J.R. 1997. A full-scale experiment (1978-1995) on the growth of permafrost by means of lake drainage, western Arctic coast: a discussion of the method and some results. *Canadian Journal of Earth Sciences,* 34: 17-34.

McRoberts, E.C. 1988. Secondary creep interpretation of ice-rich permafrost. *Proceedings of the Fifth International Conference on Permafrost, Trondheim, Norway, August 2-5, 1988*: 1137-1142.

McRoberts, E.C., Law, T.C. & Murray, T.K. 1978. Creep tests on undisturbed ice-rich silt. *Third international permafrost conference* 1: 539-545.

Pekarskaya, N.K. 1965. *Shear strength of frozen ground and its dependence on texture*. CRREL, Technical translation AD 715 091. Hanover, NH: 97 pp.

Savigny, K.W. & Morgenstern, N.R. 1986. Creep behaviour of undisturbed clay permafrost. *Canadian Geotechnical Journal* 23(4): 515-526

Sayles, F.H. & Carbee, D.L. 1981. Strength of frozen silt as a function of ice content and dry unit weight. *Engineering Geology* 18: 55-65.

Shur, Y., French, H.M, Bray, M.T. & Anderson, D.A. 2004. Syngenetic permafrost growth: cryostratigraphic observation from the CRREL tunnel near Fairbanks, Alaska. *Permafrost and Periglacial Processes* 15(4): 339-347.

Thompson, E.G. & Sayles, F.H. 1972. In situ creep analysis of room in frozen soil. *Journal of the Soil Mechanics and Foundation Division* 98: 899-915.

Tsytovich, N.A. 1975. *The Mechanics of Frozen Ground.* Washington, DC: Scripta Bood Compnay, 426 pp.

Vialov, S.S., Gmoshinskii, V.G., Gorodetskii, S.E., Grigorieva, V.G., Zaretskii, Iu.K., Perkarskaya, N.K. & Shusherina, E.P. 1965. The strength and creep of frozen soils and calculations for ice-retaining structures. *Izd Akademii Nauk SSR Moscow (1962), CRREL Translation 76,* Hanover, NH: 301 pp.

Vyalov, S.S., Gorodetskii, S.E., Ermakov, V.F., Zatsarnaya, A.G. & Pekarskaya, N.K. 1966. *Methods of Determining Creep, Long-Term Strength, and Compressibility Characteristics of Frozen Soils.* Moscow: Nauka, 109pp. NRC technical translation 1364.

Vyalov, S.S., Dokuckayev, V.V. & Sheynkman, D.R. 1980. Ground-ice and ice-rich ground as structure foundations. *CRREL Translation 737*. Hanover, NH: 159 pp.

Yuanlin, Z. & Carbee, D.L. 1987. *Creep and Strength behavior of frozen silt in uniaxial compression: CRREL Report 87-10.* Hanover, CRREL, 67 pp.

Warming of Cold Permafrost in Northern Alaska During the Last Half-Century

Max C. Brewer
U. S. Geological Survey, 4200 University Drive, Anchorage, Alaska 99508-5021, USA
Huijun Jin
State Key Laboratory of Frozen Soils Engineering, 326 W. Donggang Rd., Lanzhou 730000 China

Abstract

Climatic warming has not resulted in measurable thawing of the cold (-5 to -10°C) permafrost in northern Alaska during the last one-half century. The maximum depths of summer thaw at five locations near Barrow, Alaska, in 2005 were within the ranges of the depths obtained at those exact same locations during the early 1950s. However, there has been a net warming of about 2°C at the upper depths of the permafrost column at two of the locations. Thawing of permafrost from above (increase in active layer thickness) is determined by the summer thawing index for the specific year, while any warming or cooling of the upper permafrost column results from the cumulative effect of changes in the average annual air temperatures over a period of years, assuming no change in surface conditions. Theoretically, thawing from the base of permafrost should be negligible even in areas of thin (about 100-200 m) permafrost in northern Alaska.

Key words: cold permafrost; climatic warming; northern Alaska; thawing.

Introduction

The U.S. Geological Survey (USGS) initiated a program for studying permafrost temperatures, based at Barrow, in northern Alaska beginning in 1949. The objective was to assist the U.S. Navy in solving some of the engineering problems being encountered in their oil and gas exploration of Naval Petroleum Reserve No. 4 (NPR-4). It rapidly became apparent that several areas of science and engineering would be involved in the solution of the problems. The Navy's problems included drilling bits frozen into wellbores, well-casing collapse, saline waters encountered in seismic shot holes in supposedly deep permafrost areas, obtaining year-around water supplies, obtaining electrical grounds for communications, overland transportation, and differential settlements and frost heaves in airstrips and in building foundations and floors.

Barrow is on the coast at the northernmost point (71°20′N) of land in Alaska (Fig. 1). It has an arctic marine climate with short, cool (maximum temperature +24°C, average about 4°C) summers and long, cold (minimum temperature -49°C) winters. The average annual air temperature was -12.2°C during the period from 1922 to 2004. The sun sets for the year on November 19 and does not show above the horizon again until January 24; it rises on May 10 and does not set again until August 2. Precipitation is light, about 53 mm of "drizzle-type" rain in summer, and 244 mm in the form of hard-packed snow, density about 0.4 g cm^{-2}, in winter (Black 1954), but the evaporation rate is low. Light winds are almost constant, fall storms are common, and blizzards occur frequently during the winter. The ocean is frozen over for 8 to 10 months of the year. The inland coastal plain is a flat-lying, treeless, roadless, tundra-covered area with a vast multitude of shallow lakes and ponds. For biologically oriented scientists, it is a priceless wetland; for engineers, it is a mosquito-infested swamp land in summer and a desolate wasteland in winter, although that is the best season for trafficability. For the Eskimo people it is, and has been for more than 6,000 years, home. The permafrost table is at depths ranging from 0.3 to about 1.0 m.

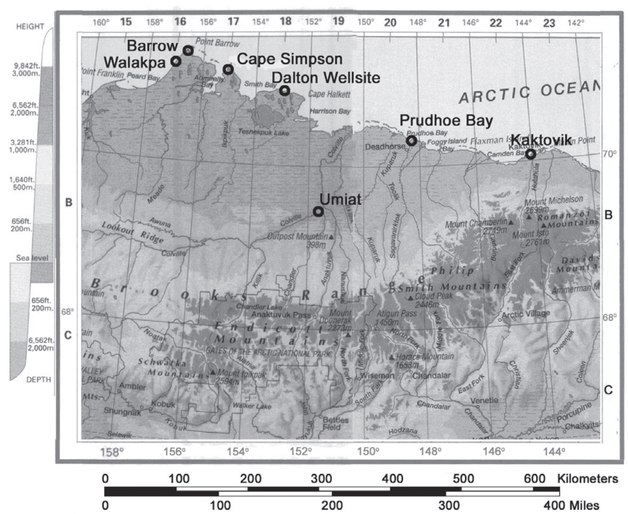

Figure 1. Permafrost study areas.

The permafrost temperatures were obtained using thermistor cables permanently frozen into the boreholes with readings obtained weekly in the shallow (0.3 to 40 m) holes, less frequently in the deeper (200 to 2000 m) oil wells abandoned during the late 1940s and the 1950s. The deeper measurements were concentrated on the solution of the problem of well-casing collapse. One very important scientific finding from those studies was that when the geothermal gradients from depth were projected upwards in some of the wells, they suggested a warming of 2 to 4°C in the upper approximately 100 m of the permafrost column (Brewer 1958a, Lachenbruch & Brewer 1959, Lachenbruch et al. 1962, Lachenbruch and Marshall, 1986, Lachenbruch et al. 1987). Lachenbruch (pers. com.) calculated that, for the warming from surface effects to have reached depths on the order of 100 m, the warming would need to have commenced about the year 1860, the estimated end of the Little Ice Age.

During the next century, an even greater change in climate in Alaska has been projected by some researchers, often using 1980 (at Barrow, the end of a mini-cooling period (Fig. 2)) as a temperature reference base. By 2100, the IPCC and HadCM2 modeling have projected a warming of 2.8°C (in the range of 1.1 to 5.0°C) in spring, summer, and fall, and 5.6°C (with a range of 2.2 to 8.9°C) in winter. Earlier measurements in more than 100 boreholes with depths ranging from 0.3 to 30 m, to more than 100 m, and on some occasions up to 650 m, on the North Slope in the 1950s and early 1960s were obtained by scientists from the USGS (Brewer 1958a, b, Lachenbruch & Brewer 1959, Lachenbruch et al. 1962, Lachenbruch and Marshal 1986, Lachenbruch et al. 1982, 1988). In addition, yearly permafrost temperature measurements were obtained along the Trans-Alaska Pipeline and at other locations in Alaska in the late 1970s (Osterkamp et al. 1994, Osterkamp & Romanovsky 1999) by a research team led by Jerry Brown, which re-occupied some of the earlier Barrow boreholes (Jin & Brewer 2002, Jin et al. 2002, Romanovsky et al. 2002), by Clow, who took over the Lachenbruch and Brewer ONPRA permafrost temperature measurement program on the Arctic Coastal Plain and Foothills (Clow & Urban 2002), and by other individuals. However, the IPCC appears to have ignored the fact that Alaska is a big area (1.5 million km^2), is surrounded on three sides by oceans/seas, that the state essentially has five climate zones, and that a cooler summer, when thawing occurs, and a warmer winter can produce a positive average annual air temperature (AAAT). Some of the reports contain a paucity of information regarding surface conditions in the areas where the temperatures were measured; the difference in snow conditions, especially the densities, preferring to use the term "temperature offset" to encompass the unknowns; vegetative covers; active layer conditions; or differences in elevations.

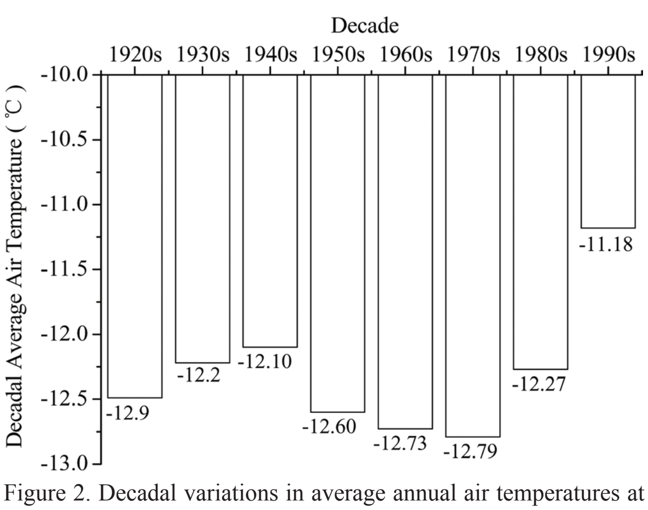

Figure 2. Decadal variations in average annual air temperatures at Barrow, Alaska, during the 20th Century.

Weather Bureau records (Fig. 2) for Barrow, Alaska, from 1922 to date indicate a decadal warming trend from the 1930s through the 1940s, a cooling from about 1950 through about 1975, the year that a major portion of the construction equipment and materials could not reach Prudhoe Bay because of the Arctic Ocean pack ice, followed by a warming trend that accelerated in the 1990s. Romanovsky provided the authors with a copy of the AAATs for Barrow from 1922 to 2004 that indicated no overall average change in the AAATs during that period.

Many modelers on climatic-warming-related degradation of permafrost have predicted significant and rapid losses of permafrost, both in thickness and areal extent in Alaska and in other regions. In so doing, the modelers have had to make many assumptions, including that the changes in air temperatures and the changes in depths to the permafrost table move in lock-step. However, the rate of dispersing the heat received downward in the permafrost profiles and the thicknesses of those profiles to absorb the heat are important factors. Of even greater importance are the complicated interactions between the atmosphere and the permafrost table, particularly those impacts involved because of the intervening poorly understood and little-studied active layer.

Study Regions

The wide, flat-lying, tundra-covered coastal plain of northern Alaska is characterized by "cold (-5 to -10°C) permafrost"; a multitude of 1- to 3-m-deep lakes; grasslands interspersed with areas of low-center ice-wedge polygons; high-center polygons adjacent to small breaks in topography, often associated with lake basins or minor drainage patterns; and meandering streams. The vegetation overlying the dominant silts and fine sands is thin (5 to 10 cm), as are the peats which are often confined to the low-center polygonal areas. MacCarthy (1952) reported an average of approximately 1 m per year of coastal erosion between Barrow and Kaktovik, approximately 560 km to the east. However, the averaging obscures the fact that the natural erosion geographically has been very uneven during the 20th century. Reportedly, the erosion has been as much as 800 m in the area of Cape Halkett (200 km east) since 1913 and a recorded 400 m at the Dalton Wellsite (Fig. 1) since 1980. The Native coastal settlements of Birnik, dating back 800 to 1000 years, and at Walakpa with an age of approximately 6,000 years still remain. The bluff at Walakapa, 17 km southwest of Barrow, retreated a measured 10.2 m between 1951 and 1997.

Umiat (69°22′N, 152°08′W, 81 m in elevation) is located in the Colville River Valley, which traverses the rolling hill country on the northern front of the Brooks Range. The vegetation tends to be tall grasses and low shrubs with birch near the river.

While the Alaskan arctic and subarctic meteorological data are sparse geographically and of limited history, the Weather Bureau's reported average annual air temperatures (AAATs) through 1954 for Barrow (-12.2°C), Kaktovik (-12.0°C), and Umiat (-12.1°C) 120 km inland were very similar, even though the first two have arctic marine environments and the latter the greater extremes of an arctic continental climate. The similar AAATs obscure the fact that the cumulative centigrade degree days of thawing for Barrow averaged 268, and for Umiat 916 during the 1950s.

Because the wind blows almost continually at Barrow, Umiat, and Kaktovak, the snow crystals are broken up and packed much like fine sand, and the snow pack develops a density of about 0.4 g cm^{-3}. The majority of the snowfall arrives during three periods: early fall before the air temperatures drop much below -20°C, during the annual early January warming period of two to three weeks, and in the late spring (April and May). Thus, its cumulative effect as a ground insulator is highly variable. Another imponderable cumulative effect is the amount of evaporative cooling of the ground resulting from the frequency, sometimes almost daily, of the July, August, and occasionally early September "drizzle-type" precipitation with the ever-present windy conditions.

Methodology

The shallow temperature cables, permanently installed, were used to investigate temperatures beneath various natural surface environments (dry grasslands, wet meadows, low- and high-center polygons, old poorly vegetated beach ridges, an active beach, shallow and moderate-to-deep lakes and lagoons, lake and ocean ice, and the near-shore Arctic Ocean) and beneath engineering structures (various types and sizes of buildings, airstrips, roads, various thicknesses of gravel fill, and beneath a recently artificially drained shallow (0.5 m) lake). Most of these study sites were located within about 8km of the Barrow Weather Station (71°18′N, 156°47′W) and thus were assumed to be impacted by relatively similar air temperatures, precipitation, and winds. The accuracy of the thermistors was 0.02°C, their sensitivity was 0.006°C. Similar shallow temperature study programs, on much reduced scales, were initiated near Umiat in 1951. The depths of thaw measurements data presented are from some of those studies, plus updates from 2001 and 2005 in northern Alaska.

Results and Discussions

Permafrost

"Cold (-10 to -5°C) permafrost," ice-wedge polygons, and wetlands are prominent characteristics of the Alaskan Arctic. The measured thicknesses of permafrost vary greatly at the same latitude, from less than 200m to an unusual thickness of 685m in the Prudhoe oilfield. Lachenbruch et al. (1987) believe that thickness resulted from anomalous thermal conductivity because of the unusual thickness of gravel swept down from the Brooks Range by the Sagavanirktok River. At Umiat, the thickness of permafrost ranges from 213 to 322m within a horizontal distance of 2.4km. That rapid change in the thickness may have resulted from changes in the course of the Colville River. Brewer (1958a) also found that the temperatures at depths of 20 m (depth of significant annual change of 0.01 to 0.03°C) within a radius of 8 km from the Weather Bureau Station at Barrow varied from -7.3 to -10.7°C, to +1.0°C beneath a freshwater lake 2.8 m in depth.

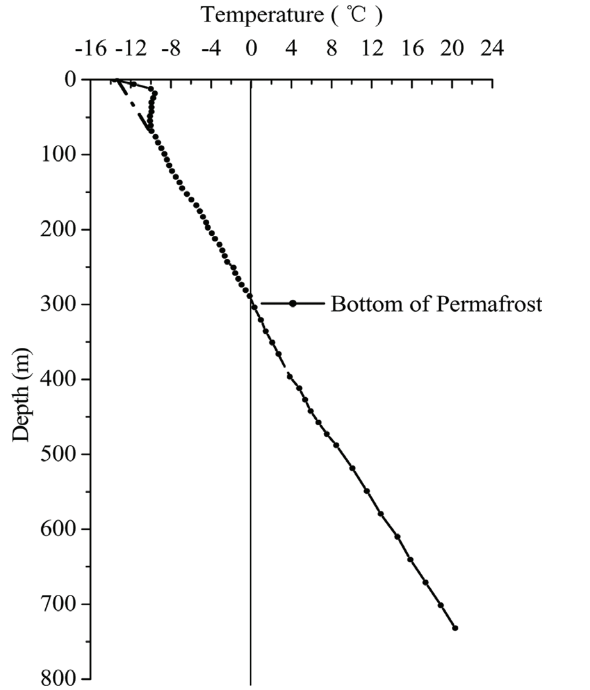

Figure 3. Thermal profile for Simpson 28 Well 112 km southeast of Barrow, Alaska. The broken line at depths of 0-80 m is the linear projection based on the thermal gradient from below.

The geothermal profile for Simpson Well 28 (Fig. 3) obtained two years after installation of the cables in the wellbore and, projected upwards, is one of those used by Brewer (1958b), Lachenbruch & Brewer (1959), and Lachenbruch et al. (1962) to suggest a warming of the upper part of the permafrost by 2 to 4°C during the previous century. The consistent slope of the profile below 70m suggests a remarkably steady surface environment (air temperature, precipitation, and vegetative cover) for the previous several centuries.

The geothermal profiles in Figure 4 were obtained at the end of the unusually warm 1954 summer, from within a horizontal radius of approximately 5 km near Barrow. The figure is intended to illustrate the relative impacts of various natural surface covers on the near-surface temperatures. The temperatures at 2 m are at the maximum for the year although, because of the phase lag, those below that depth will continue to rise for several weeks or months thereafter.

The permafrost temperatures at a red grass low-center polygonal area in 1954, and from a replacement cable installed in the same spot by Kenji Yoshikawa in 2001, are shown in Figure 5 (Romanovsky et al. 2002). The cumulative maximum warming indicated was 1.69°C at about the 11 m depth. The vegetative cover in Figure 5, except for the wetness (a bit drier), the area was little changed after 47 years. However, the data in Table 1 indicate a minor greater measured maximum depth of thaw (thickness of the active layer) in 1954.

The 1950s cooling (0.80°C at a depth of 4.7 m) beneath the adjacent, unusually wide polygonal trough, about 10 m distant, was much greater than at the same depth beneath the polygon. This was in spite of the fact that the trough quickly accumulated a thickness of about 1.0 m of drifted, hard-packed snow (insulating effect is over compensated by the additional time required for melting (Drew et al. 1958)), whereas the top of the polygon rarely had more than 4 to 10 cm of snow cover in winter due to the ever-prevailing winds. Permafrost temperatures at depths of 30 m at other Barrow installations indicate a cooling of 0.23 to 0.30°C during the period 1953-1960.

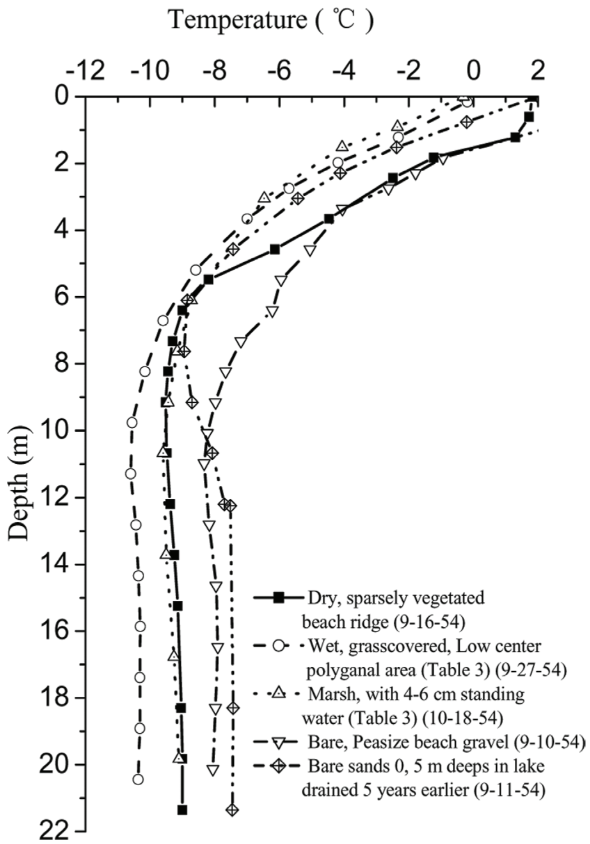

Figure 4. Geothermal profiles beneath different surface covers within a radius of 5 km, Barrow, Alaska.

The temperature profiles (Fig. 6), obtained weekly from a frozen-in cable beneath a high-center polygon, indicate a cooling of the permafrost of about 0.37°C, at 4.7m, between the years 1953 and 1960. A repeat of the measurements in 2001 indicates a cumulative warming of the permafrost at that depth of 1.66°C during the intervening 41 years.

Table 1. Maximum depths (cm) of thaw, Barrow, Alaska.

Date	Dry, high-center polygon with good drainage	Date	*Low-center polygonal area with 4-10 cm standing water	Date	Marsh with 4-6 cm standing water and moss/grass
9-08-52	48.3	9-01-52	25.4	9-07-53	26.7
9-07-53	55.9	9-07-53	27.3	7-27-54	26.7
9-14-54	63.5	8-23-54	30.5	9-15-56	26.7
8-25-56	41.3	8-25-56	25.4	8-05-57	28.6
		9-07-57	33.0	8-18-58	31.8
				9-15-59	29.2
Averages	52.3		28.3		28.3
9-08-05	47.2		34.0		19.1**

* No visible change in surface cover during 1951-2005. This site is shown in Figure 5 and 6.

** Area had more and taller grasses in 2005.

The year 1953 had a very cool summer, and 1954 and 1957 had unusually warm summers.

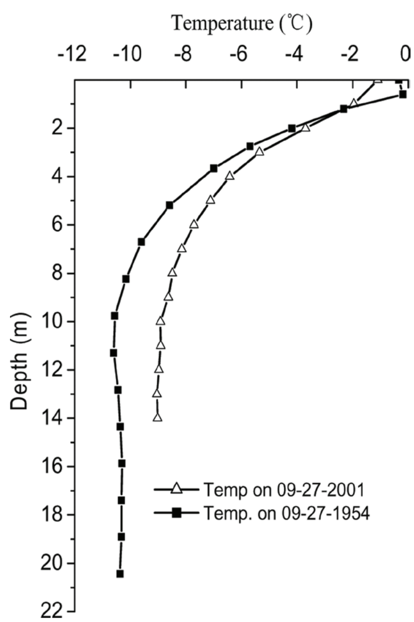

Figure 5. Geothermal profile beneath low-center polygon area with 4-10 cm standing water at Barrow, Alaska. This site had the coldest temperature measured at 20 m in Northern Alaska.

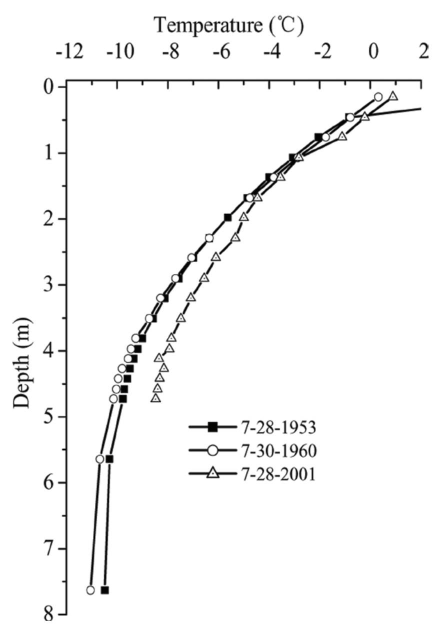

Figure 6. Geothermal profiles for a high-center polygon, Barrow, Alaska.

An illustration of the impact on permafrost temperatures resulting from modifying the surface is shown in Figure 7. Tracked personnel vehicles, traversing a moderate slope at Umiat during a spring/summer, caused the tundra in the trail to become badly damaged. The thermistor cables installed beneath the bare trail and in an adjacent undamaged area two years later indicated that the active layer beneath the trail had deepened from about 0.6m to about 1.5m, but that the annual permafrost temperatures had decreased by about 1.3°C at 6.1m. In other words, the active layer was increasing in thickness at the expense of thawing a bit of the upper permafrost, while at the same time the annual average temperatures of the underlying permafrost were decreasing. The same phenomena occur in gravel fills at Barrow, and it was the basic tenant behind the construction, in 1955, of the permanent roads and airstrips for the radar stations along the Alaskan Arctic coast and for the permanent drilling pads and other facilities constructed in the Prudhoe Bay oilfields. The 1.5m of fill cools and brings the top of the permafrost into the base of the fill in cold permafrost areas, thus providing a solid foundation.

Depths of thaw

Since deepening of the active layer and/or permafrost thaws only when the temperatures are above freezing for an extended period of time, the annual change in the thawing index tends to provide far greater insights regarding the near-surface permafrost than do the changes in the annual average air temperatures.

The cumulative °C-days of thaw at Barrow in 1950 and 1952 (Table 2) were about the same, approximating the decadal average, but the average annual air temperature in 1952 was 2°C colder than in 1950, indicating colder winter air temperatures, which have nothing to do with the thawing of permafrost or the active layer.

The maximum depths of summer thaw were obtained using a pointed steel rod, 0.64 cm in diameter, pushed to refusal (sounded like hitting concrete) at an average of 4 points at about 1 m distance surrounding the thermistor cables (Tables 1 and 3). The measurements generally were made in early September, as there usually is little thaw of permafrost, or warming of lake (Brewer 1958b, Drew et al. 1958), after the first week in August in northern Alaska.

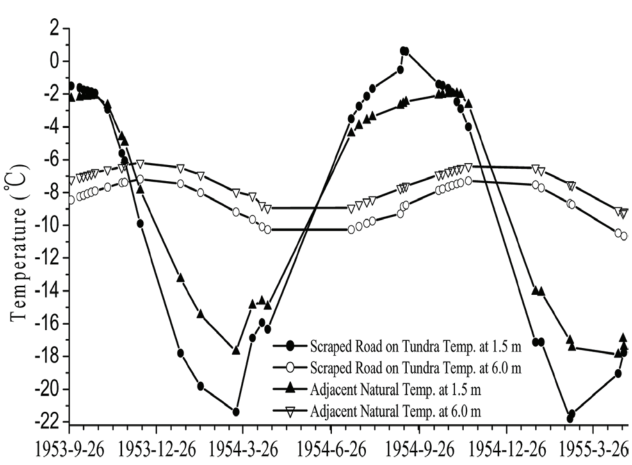

Figure 7. Time-temperature series beneath damaged and adjacent undamaged tundra, 1953-1955, Umiat, Alaska.

Summary and Conclusions

Observation over the last 50 years indicates that in Arctic Alaska there definitely has been a warming of the upper layer of permafrost, and just as definitely there has been no thawing of the permafrost during the same 50 years because the depths of thaw have remained unchanged.

Projecting temperatures upwards in permafrost is a relatively easy and scientifically repeatable way to study climate change because the equilibrium geothermal profile has long been established, the impacts of the active layer are avoided, and only heat conduction is involved. This was the approach used by Brewer and Lachenbruch in 1958, 1959, and 1962 when they noted an apparent warming of 2-4°C in the upper permafrost. The big problem is bridging the complicated active layer, which is subject to short-term cyclical changes and numerous unknown factors, to connect with the atmosphere where most climatic measurements are being obtained.

Table 2. Average annual air temperature (AAAT) and thawing index (TI) at Barrow, Alaska during 1950-1960.

Year	AAATs (°C)	TI (°C·d)
1950	-10.6	284
1951	-11.4	448
1952	-12.8	264
1953	-13.3	186
1954	-11.8	472
1955	-14.8	116
1956	-13.9	121
1957	-12.3	324
1958	-11.5	384
1959	-13.6	198
1960	-13.3	154
1950-1960 Average	-12.7	268
2000	-11.8	304
2001	-11.9	220

Table 3. Maximum depths (cm) of thaw in adjacent dry and wet areas (Figure 7 and text), Barrow, Alaska.

Date	Grass-covered, high-center Polygon	Adjacent 1- m deep wet polygonal trough
09-05-53	29.2	33.0
09-04-54	36.8	
08-22-55	28.6	
09-14-56	31.8	
09-09-57	41.7	
09-10-58	33.0	35.6
09-11-59	25.4	26.7
09-10-60	27.9	27.9
1953-1960 average	31.8	30.8
9-08-05	28.2	36.1

Brewer (1958b), Lachenbruch & Brewer (1959), and Lachenbruch et al. (1962) discussed an apparent warming of permafrost in Arctic Alaska beginning about 1860, the estimated end of the Little Ice Age, without making any predictions regarding the future. But many recent publications have discussed air temperature warming in Arctic Alaska beginning about 1980, the end of a mini-cooling period at Barrow (Fig. 2), projecting temperatures forward and suggesting worldwide implications. Projecting forward from an extreme point in a cycle would appear to be of questionable scientific validity.

Chronicling climatic change is a long-term multi-faceted endeavor that necessitates the observation of numerous potentially impinging aspects of nature, not just changes in temperature. Obtaining those needed observations sometimes is hampered by the fact that advancements in the technologies in instrumentation, communications, and transportation have outstripped the willingness and ability of researchers to obtain field observations, i.e., one can rapidly acquire data without the needed field environmental information concerning how the data may have been or are being compromised by extraneous factors.

The many mixed views on the changes in permafrost and its distribution under a changing climate have highlighted the paucity of integrated scientific knowledge and information, due to a lack of long-term observations, as recorded by Hinzman et al. (2005).

A determination of the actual effects of the active layer, which lies between the permafrost and the atmosphere and hence the correlations between the permafrost and climatic change, is the biggest problem. At least a proximate solution, which cannot be derived by imagery or modeling, is critical.

References

Black, R.F. 1954. Permafrost: a review. *Bulletin of the Geological Society of America* 65: 839-856.

Brewer, M.C. 1958a. The thermal regime of an arctic lake. *American Geophysical Union, Transactions* 39: 278-294.

Brewer, M.C. 1958b. Some results of geothermal investigations of permafrost in northern Alaska. *American Geophysical Union, Transactions* 39: 19-26.

Clow, G.D. & Urban F.E. 2002. Large permafrost warming in Northern Alaska during the 1990s determined from GTN-P borehole temperature measurements. *American Geophysical Union, Fall Meeting 2002, Abstract* #B11E-04.

Drew, J.V., Tedrow, J.C.F., Shanks, R.E. & Koranda, J.J. 1958. Rate and depth of thaw in Arctic soils. *American Geophysical Union, Transactions* 39: 697-701.

Hinzman, L.D., Bettez, N.D., Bolton, W.R. & Chapin, F.S. 2005. Evidence and implications of recent climatic change in Northern Alaska and other Arctic regions. *Climatic Change* 72: 251-298.

Jin, H.J. & Brewer, M.C. 2002. Correlating changing annual air and permafrost temperatures in northern Alaska. *Abstracts: AGU Fall Meeting*, San Francisco, CA, 6-10 December 2002.

Jin, H.J., Brewer, M.C. & Perkins, R.A. 2002. Ground Temperatures across the Old and New Roads at Mile 130, Richardson Highway during 1954-1962. *Cold Regions Engineering: Cold Regions Impacts on Transportation and Infrastructure*: *Proceedings of the 11th International Conference*, May 20–22, 2002, Anchorage, Alaska. K.S. Merrill (ed.). ASCE, Washington D.C., 724-735.

Lachenbruch, A.H. & Brewer, M.C. 1959. Dissipation of the temperature effect of drilling a well in Arctic Alaska. Washington D.C.: *U. S. Geological Survey Bulletin*, 1083-C, USGPO, 73-109.

Lachenbruch, A.H., Brewer, M.C., Greene, G.W. & Marshall, B.V. 1962. Temperatures in permafrost. *Temperature: Its Measurement and Control in Science and Industry*, Vol. 3. New York: Reinhold Publishing Co., 791-803.

Lachenbruch, A.H., Sass, J.H., Marshall, B.V. & Moses, T.H. Jr. 1982. Permafrost, heat flow, and the geothermal regime at Prudhoe Bay, Alaska. *Journal of Geophysical Research* 87(B11): 9301-9316.

Lachenbruch, A.H. & Marshall, B.V. 1986. Changing climate geothermal evidence from permafrost in the Alaskan Arctic. *Science* 234: 689-696.

Lachenbruch, A.H., Sass, J.H., Lawver, L.A. & Brewer, M.C. 1987. Temperature and depth of permafrost on the Alaskan arctic slope. In: Tailleur I. and Weimer P. (eds.), *Alaskan North Slope Geology*, Vol. 2. Society of Economic Paleontologists and Mineralogists, Pacific Section: Bakersfield, CA, USA, 545-558.

Lachenbruch, A.H., Cladouhos, T.T. & Saltus, R.W. 1988. Permafrost Temperature and the Changing Climate. In: *Permafrost, 5th International Conference on Permafrost*, Vol. 3. S. Kaare (ed.). Trondheim, Norway: Tapir Publishers, 9-17.

MacCarthy, G.R. 1952. Geothermal investigations on the Arctic slope of Alaska. *American Geophysics Union Transaction* 33: 589-593.

Osterkamp, T.E., Zhang, T. & Romanovsky, V.E. 1994. Evidence for a cyclic variation of permafrost temperatures in Northern Alaska. *Permafrost and Periglacial Processes* 5: 137-144.

Osterkamp, T.E. & Romanovsky, V.E., 1999. Evidence of warming and thawing permafrost in Alaska. *Permafrost and Periglacial Processes* 10(1): 17-37.

Romanovsky, V.E., Yoshikawa, K., Brewer, M.C., Jin, H.J. & Brown, J. 2002. A permafrost observatory at Barrow, Alaska. In: *Proceedings of the Arctic System Science Program All-Hands Workshop*, February 20-23, 2002. J. Overpeck (ed.). Fairbanks, AK: Arctic Research Consortium of the United States, 196.

Characterization and Classification of Topsoils as a Tool to Monitor Carbon Pools in Frost-Affected Soils

Gabriele Broll
University of Vechta, Vechta, Germany
Charles Tarnocai
Research Branch, Agriculture and Agri-Food Canada, Ottawa, Canada

Abstract

Many frost-affected soils contain large pools of carbon that are very sensitive to climate change. Detailed mapping of topsoils and their spatial variability could help to improve the reliability of soil carbon data. The topsoil, which acts as the interface between vegetation and subsoil, is an indicator of ecosystem change. The objective of this paper is to give an overview of developments in topsoil/humus form characterization and classification. This information can be used to show the spatial variability of topsoils and, thus, carbon pools, as well as the biological activity in the Arctic. Identification, sampling, and analysis of representative pedons for the soil and humus forms will improve the quality of the data required for upscaling and, additionally, will provide information on the soil biocoenoses, all interacting organisms living in soil. Special requirements for frost-affected sites should be considered when topsoils are mapped.

Keywords: carbon stocks; permafrost-affected soils; seasonally frozen soils; soil biocoenoses; topsoil.

Introduction

Many frost-affected areas (perennially or seasonally frozen) with large carbon stocks are very sensitive to climate change. Topsoils or humus forms are the interface between vegetation and subsoil (Fig. 1). They can act as indicators for changes of ecosystems driven by climate change or land-use change. Up to now new approaches of international working groups to characterize and to classify topsoils and/or humus forms are ignoring frost-affected sites. On the other hand, topsoils of subarctic and arctic sites will probably change quickly due to climate warming, wild fires, and flooding.

Objectives of this paper are:

- To present developments in characterization and classification of topsoils and humus forms, which could be used in the Arctic and Subarctic;
- To show examples for spatial variability of topsoils and thus carbon pools as well as biological activity in the Arctic and Subarctic;
- To present ideas how knowledge about topsoils can help to improve the interpretation of carbon data, which is of special interest for the northern environment containing large carbon pools.

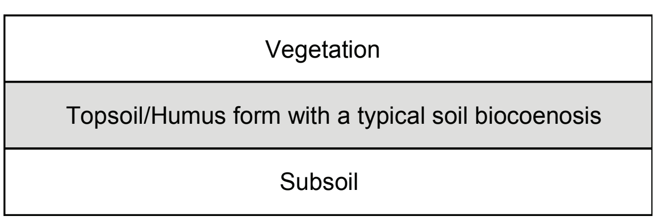

Figure 1. Topsoil as interface between vegetation and subsoil, acting as habitat for a typical soil biocoenosis and being a product of the soil organisms based on litter input and mineral components.

Characterization, Classification, and Indicator Function

Topsoils and humus forms include litter (L), in many cases organic horizons (OF/F, OH/H), and the A horizon. In agricultural areas, the A horizon is in almost all cases the only part of the topsoil. Thus, soil structure and the quality of the soil organic matter as results of the soil biological activity can be used for characterizing the topsoils. In forests usually different organic layers indicate different decomposition rates. Modeling approaches focusing on organic layers help to improve predictions for changes of carbon pools in the environment (e.g., Akselsson et al. 2005). In the Subarctic and Arctic there are different types of topsoils, from the more or less pure geological substrate to thick organic layers.

The topsoil acts as habitat for the soil organisms, and at the same time it is a product of the soil organisms. The humus form is the mirror of the soil biocoenosis, their composition, and their activity result in different decomposition rates. So why not look for the soil organisms and their activity directly? It is time-consuming as well as costly and requires specialists. This should be done for representative monitoring sites which could then serve as reference sites. Humus forms can be used as indicators for environmental change instead of the soil organisms themselves. Humus form data could be made available for large areas within a relatively short time. Their description is quite easy to learn and probably new remote sensing methods will be available in the future, but first, worldwide accepted guidelines for characterizing and classifying topsoils have to be developed.

A first step in this direction was made in cooperation with the FAO that has a draft for characterizing topsoils. One outcome of a FAO project was that in principle, a great coincidence between characterizations of humus types and

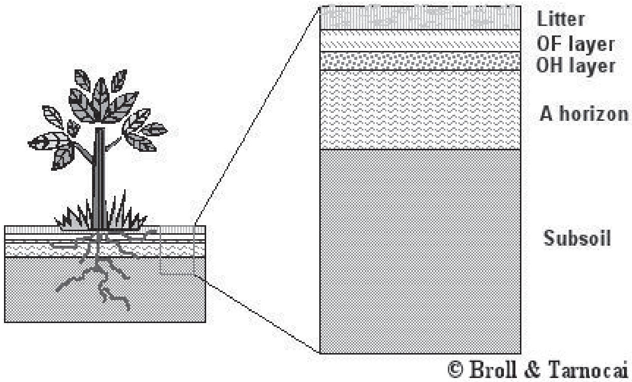

Figure 2. Appearance of carbon in the vegetation and in different soil horizons; example for non-frost-affected soils.

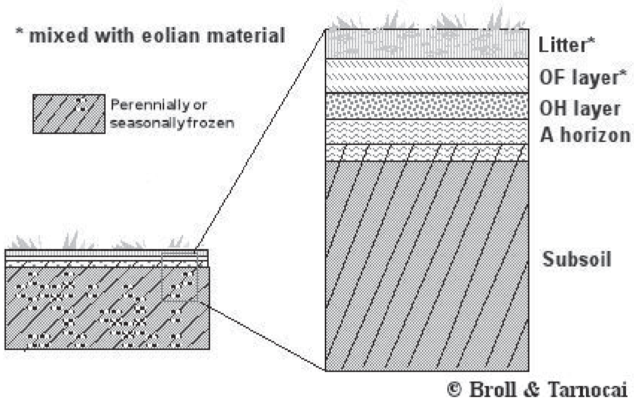

Figure 3. Appearance of carbon in the vegetation and in different soil horizons; example for static frost-affected soils.

Figure 4. Turbic cryosols and static cryosols at Pangnirtung Pass on Baffin Island, Canadian Arctic.

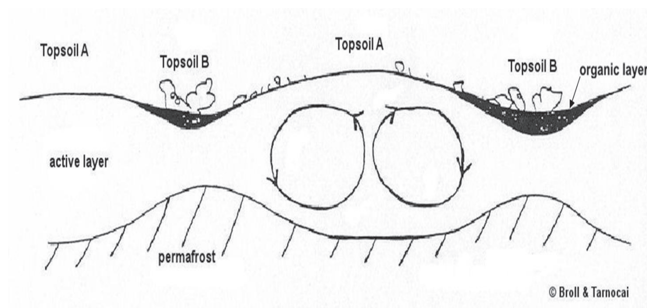

Figure 5. Turbic cryosol with two different topsoils occurring regularly in the landscape (modified after: Heal et al. 1998).

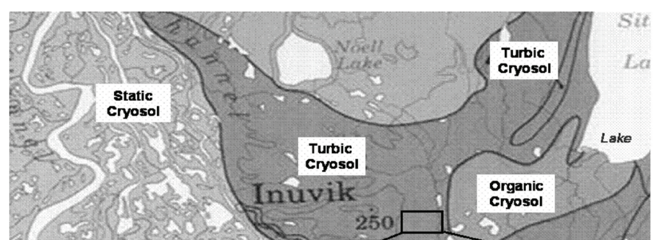

Figure 6. Distribution of Cryosols, topsoils, and soil biocoenoses in the Canadian Arctic (Mackenzie River delta area).

topsoils exists which appears to be an appropriate basis for further correlation, and, finally, incorporation in the World Reference Base for Soil Resources. This could promote worldwide use of this system. In case of forest sites, the topsoil characterization can be improved by incorporation of humus typology using qualifiers for the organic layers. In case of grassland or arable land usually lacking organic layers, topsoil characterization can be improved by using qualifiers for soil biological activity in the A horizon. The biological qualifiers provide a good basis for soil quality assessment besides chemical and physical qualifiers (Broll et al. 2006).

Looking at the carbon pools specifically in non-frost-affected soils, carbon is stored in the vegetation, in the organic layers, in the A horizon, and in the subsoil, where generally only small amounts of carbon are found (Fig. 2). The carbon stocks in the topsoil depend on site conditions such as moisture.

Looking at frost-affected soils of the Arctic, especially those perennially frozen, only little amounts of carbon are stored in the actual vegetation but large amounts can be stored in the soil, both in the topsoil and in the subsoil (Figs. 3, 4).

The topsoil can have, for example, a thick moss layer on wet sites. In the boreal region, about one-third of the carbon is in the vegetation and two-thirds in the soil. Very often the topsoil in the Arctic is enriched with eolian material. Due to formerly warmer climate along with high production of biomass, large amounts of carbon can be found also in the subsoil, where the carbon is stored in the permafrost.

Turbic Cryosols (cryoturbated, permafrost-affected soils) (Fig. 4) contain larger amounts of carbon than Static Cryosols (non-cryoturbated, permafrost-affected soils) (Tarnocai et al. 2003, Tarnocai & Broll 2008) and show even more specific

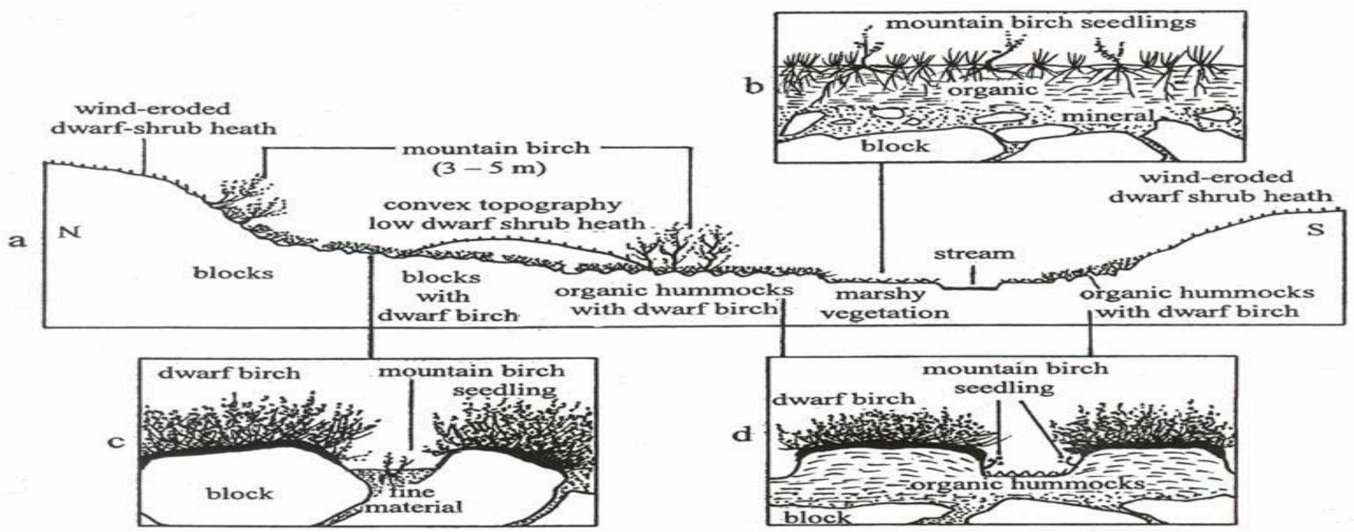

Figure 7. Spatial variability: Topsoils and carbon sequestration depending on microtopography in the Finnish Subarctic (Holtmeier et al. 2003).

Figure 8. Landscape mosaic in the treeline ecotone on Mt. Rodjanoaivi, subarctic Finland.

properties concerning carbon pools. Organic layers are drawn into the subsoil due to cryoturbation and, on the other hand, geological substrate-like till can be brought to the surface producing topsoil with very low amounts of carbon. Moreover, carbon can be enriched above the permafrost table.

In case of Static Cryosols, topsoils are relatively homogenous. In case of Turbic Cryosols two different topsoils occur (Figs. 4, 5). These topsoils are not unique for certain areas like Pangnirtung Pass on Baffin Island (Fig. 4); they are widespread in the Arctic. These frequently appearing features can be mapped in the field as well as by remote sensing and thus used for modeling and upscaling.

Spatial Variability and Upscaling

Turbic Cryosols show a regular pattern of topsoils due to cryoturbation (Figs. 5, 6). Because of insulation effects of the organic layer, the active layer under topsoil B is shallower than that under topsoil A. In general, topsoil A has low amounts of carbon whereas topsoil B contains high amounts of carbon (Broll et al. 1999). In case of climate warming, cryoturbation will stop and vegetation succession will start from topsoil B to topsoil A. At the optimum stage the plant cover will be continuous, and it will be very difficult to tell the differences between the two topsoils at the surface. On the other hand, this can be very helpful for a quick monitoring of environmental change in the Arctic.

Detailed investigations of topsoils including soil organisms (species, activity) on representative sites would enable making predictions for soil biocoenosis, decomposition, etc. for large areas. This could be interesting, especially in those areas where detailed soil mapping is already available like in the Mackenzie River delta area (Fig. 6). Similar approaches are tested in temperate regions already (Beylich et al. 2006).

This approach of upscaling soil ecological properties via topsoil mapping is relatively easy on flat areas. In mountainous areas the relief plays an important role for the distribution of soils especially because of creating different drainage and thus soil moisture conditions. This affects the topsoils and the related carbon stocks (Figs. 6, 7).

Although those sites like in the Finnish Subarctic looks quite heterogenous; a regular pattern can be identified which occurs all over in the Subarctic: dry wind-exposed heath, boulders with fine material in between, small organic hummocks etc. (Figs. 6, 7) (Broll et al. 2007).

Because topsoils are habitats for characteristic soil biocoenoses, soil ecological processes like decomposition are correlated with the topsoil type (Nadelhoffer et al. 1992, Broll 1994, Müller et al. 1999) Since the topsoil pattern shows a certain regularity, geostatistical methods could be applied to get from the plot scale to the landscape scale (Joschko et al. 2007).

Conclusions

- Topsoils are good indicators for ecosystem changes in the Arctic and Subarctic.
- Detailed information on topsoils in soil mapping protocols can improve the data quality for upscaling of carbon data, can help modeling soil ecological processes and provide information on the soil biocoenoses.
- Combination of spatial soil data with spatial humus form data and vegetation data could help to reduce the number of carbon analysis or help to extrapolating existing data.
- Identification and characterization of topsoils should be included in the Minimum Soil Dataset for Cryosols to provide first information on the biological activity of the site.
- Some existing long-term monitoring sites already include the characterization of topsoils. This knowledge can also be applied to the Arctic.

References

Akselsson, C., Berg, B., Meentemeyer, V. & Westling, O. 2005. Carbon sequestration rates in organic layers of boreal and temperate forest soils – Sweden as a case study, *Global Ecology and Biogeography* 14: 77–84.

Beylich, A., Broll, G., Höper, H., Römbke, J., Ruf, A., & Wilke, B.-M. 2006. Boden als Lebensraum für Bodenorganismen: Bewertung im Rahmen von Planungsprozessen. *Bodenschutz* 2: 49-53.

Broll, G. 1994. Influence of the Soil Mosaic on Biodiversity at Heath Sites in the European Subarctic. *Transactions 15th World Congress of Soil Science (Mexico)*, Vol. 4a, 220-231.

Broll, G., Brauckmann, H.-J., Overesch, M., Junge, B., Erber, C., Milbert, G., Baize, D. & Nachtergaele F. 2006. Topsoil characterization – recommendations for revision and expansion of the FAO-Draft (1998) with emphasis on humus forms and biological features. *Journal of Plant Nutrition and Soil Science* 169(3): 453-461.

Broll, G., Holtmeier F.-K., Anschlag, K., Brauckmann, H.-J., Wald, S. & Drees B. 2007: Landscape mosaic in the treeline ecotone on Mt Rodjanoaivi, Subarctic Finland. *Fennia* 178(2) (in press).

Broll, G., Tarnocai, C. & Müller, G. 1999. Interactions between vegetation, nutrients and moisture in soils in the Pangnirtung Pass area, Baffin Island, Canada. *Permafrost and Periglacial Processes* 10: 265-277.

Heal, O.W., Broll, G., Hooper, D.U., McConnell, J., Webb, N.R. & Wookey, P.A. 1998. Impacts on global change on tundra soil biology. In: O.W. Heal, T.V. Callaghan, J.H.C. Cornelissen, C. Körner, & S.E. Lee (eds.), *Global change in Europe´s cold regions.* Ecosystems Research Report No. 27, Brussels, 65-134.

Holtmeier, F.-K., Broll, G., Müterthies, A. & Anschlag, K. 2003. Regeneration of trees in the treeline ecotone: northern Finnish Lapland. *Fennia* 181: 103-128.

Joschko, M., Oehley, J., Gebbers, R., Wiemer, M., Timmer, J. & Fox, C. 2008. A spatial approach to soil ecological experimentation at landscape scale. *Journal of Plant Nutrition and Soil Science* (in press).

Müller, G., Broll, G. & Tarnocai, C. 1999. Biological activity as influenced by microtopography in a Cryosolic soil, Baffin Island, Canada. *Permafrost and Periglacial Processes* 10: 279-288.

Nadelhoffer, K.J., Giblin, G.R., Shaver, G.R. & Linkins, A.E. 1992. Microbial processes and plant nutrient availability in arctic soils. In: F.S. Chapin (ed.), *Arctic ecosystems in a changing climate. An ecophysiological perspective.* San Diego, California: Academic.

Tarnocai, C. & Broll, G. 2008. Soil Organic Carbon Stocks in the Northern Permafrost Region and Their Role in Climate Change. *Proceedings of the Ninth International Conference on Permafrost*, *Fairbanks, Alaska, June 29–July 3, 2008* (this proceedings).

Tarnocai, C., Kimble, J. & Broll, G. 2003. Determining carbon in Cryosols using the Northern and Mid Latitudes Soil Database. In: M. Phillips, S. Springman, & L.U. Arenson (eds.), *Proceedings of the Eighth International Conference on Permafrost*, *Zurich, Switzerland, 21–25 July 2003.* Lisse: Balkema Publishers, 1129-1134.

The International Permafrost Association: 1983–2008

Jerry Brown, President IPA
International Permafrost Association, Woods Hole, MA, USA

Hugh French, Professor Emeritus, Past President IPA
Departments of Geography and Earth Sciences, University of Ottawa, Ottawa, Canada

Cheng Guodong, Academician, Past President IPA
CAREERI, Chinese Academy of Sciences, Lanzhou, China

Abstract

The International Permafrost Association (IPA) was founded in July 1983, at Fairbanks, Alaska, during the Fourth International Conference on Permafrost. The four founding members were Canada, China, the USSR, and the United States. The IPA presently has 26 members. The primary purposes of the IPA are to convene international conferences to facilitate communication and to develop and exchange information related to permafrost research and engineering. Beginning in 1963, international permafrost conferences have been held in Canada, China, Norway, USSR (Russia), Switzerland, and the United States. Working groups, task forces, and committees undertake specific projects and collaborate with other international organizations. Accomplishments include establishment of the Global Geocryological Data (GGD) system, an international permafrost glossary, a permafrost map of the Northern Hemisphere, an inventory of carbon content of northern soils, bibliographies, and publication of *Frozen Ground*. Several major international programs and long-term observing networks initiated by the IPA contribute to the 2007–2008 International Polar Year (IPY).

Keywords: frozen ground; history; IPA; IPY; permafrost; periglacial.

Background

The geopolitical situation that evolved after the Second World War focused attention upon the high northern latitudes. Russian experience of permafrost conditions was more extensive, more advanced, and better documented than in North America (e.g., see Shiklomanov 2005). For example, the Permafrost Institute, a branch of the USSR Academy of Sciences, Moscow, had been established in Yakutsk, Siberia, in 1939, and Russian language permafrost texts had been published from the 1930s onwards (e.g., see Sumgin 1927/37, Shvetsov 1956). By the late 1940s and early 1950s, the importance of the Russian permafrost literature was beginning to be appreciated in North America (Muller 1943, see French & Nelson 2008). As a consequence, the USA and Canadian governments established research agencies and organizations to promote scientific understanding of these regions.

In the USA, the Snow, Ice and Permafrost Research Establishment (SIPRE) and the Arctic Construction Frost Effects Laboratory, later to become the Cold Regions Research and Engineering Laboratory (CRREL), in Hanover, New Hampshire, and the Arctic Research Laboratory (ARL) in Alaska, were established, and the U.S. Geological Survey began extensive field investigations. In Canada, the Division of Building Research (DBR), National Research Council of Canada (NRCC), the Polar Continental Shelf Project (PCSP) and the Geological Survey of Canada (GSC) started to support permafrost-related investigations in the north. The Arctic Institute of North America (AINA) was set up as a bi-national organization with headquarters in Montreal and Washington. Several monographs and publications document some of these early North American undertakings (see French & Nelson 2008).

The First International Conference on Permafrost (ICOP), held at Purdue University, Indiana, in 1963, was an initiative to promote communication and understanding between Soviet and North American permafrost scientists and engineers. This was the first major contact between Russian and western scientists (Brown & Walker 2007). The Second ICOP was held in Yakutsk, Siberia, in 1973, where it was mutually agreed that further conferences would be advantageous to all concerned. At the Third ICOP in Edmonton, Canada, in 1978, the desirability of establishing an organizational structure that would ensure the continuation of these conferences was discussed. Accordingly, the NRCC, through its Bureau of International Relations and the DBR, established a task force in 1981 to draft a set of organizational rules. This was chaired by Lorne Gold, Head of the DBR, NRCC, and the members were Fred Roots, Science Advisor, Environment Canada, John Fyles, Head of the Division of Terrain Sciences, Geological Survey of Canada, and Hugh French, Chairman, Permafrost Sub-committee, ACGR, NRCC. Representatives of the Bureau of International Relations, NRCC, provided advice at meetings of the group.

Formation of the IPA

At the Fourth ICOP in 1983, held at the University of Alaska-Fairbanks, Alaska, Hugh French, leader of the Canadian delegation, convened a special meeting of the leaders of the official delegations from the USA, USSR, and China. Professor T.L. Péwé (USA), Academician P.I. Mel'nikov

(USSR), and Professor Shi Yafeng (China) attended this meeting together with advisors (Fig. 1). Unofficially, these four countries subsequently became known as the "Big Four." It was agreed to form an international association.

The primary mandate of the newly formed association was to organize and promote international conferences on permafrost at regular five-year intervals. A secondary role was to encourage and facilitate the international exchange of scientific information among permafrost scientists and engineers. The agreement to form the association was announced at the closing ceremony; the Executive Committee consisted of Academician Mel'nikov, President, Professor Péwé, Vice-President, and Professor J. Ross Mackay, Secretary-General. The terms of office were for five years. The NRCC, through its Bureau of International Relations, agreed to provide funding to support the activities of the Secretary-General. The creation of the IPA Council was announced, and countries wishing to join the Association were asked to name an organization or representative. The Council was to meet at regular intervals, minimally at the beginning and end of each international conference on permafrost. At the closing ceremony it was immediately clear that, in addition to USA, Canada, China, and the USSR, a number of other countries were interested in becoming members of the IPA.

Figure 1. Participants in the founding meeting of the IPA, held at Fairbanks, Alaska, in 1983. Front row: Louis DeGoes, Li Yusheng, Shi Yafeng, J. Ross Mackay, P.I. Mel'nikov, T.L. Péwé, G.H. Johnston, N.A. Grave. Back row: Zhao Yuehai, Cheng Guodong, H.M. French, Jerry Brown. Photograph taken by J.A. Heginbottom.

Three of the first acts of the Association in Fairbanks were to: (1) modify the constitution to allow for a Second Vice-President, (2) appoint a Nominations Committee in order to allow a new Executive to be elected at the 1988 Conference, and (3) plan to seek affiliation with other international scientific bodies. Dr. Kaare Flaate (Norway) was elected to the Executive Committee as a second Vice-President, and Norway agreed to host the Fifth ICOP in Trondheim in 1988.

The detailed history of the IPA is chronicled in its News Bulletin *Frozen Ground,* which started as informal notes by the Secretary General in 1986, and became a formal publication starting in 1989. All issues are found on the IPA website. The following sections report on the development and accomplishments of the Association. Hereafter, specific issues of *Frozen Ground* are cross-referenced, for example, as (FG 30). The following presents both administrative details and some of the major accomplishments of the IPA since 1983.

Administrative Activities

Council, Executive Committee, and Secretariat

Membership on the Council is through adhering national or multinational organizations as full voting members or as non-voting associates or individuals in countries where no Adhering Body exists. The IPA is governed by its Council and elected Executive Committee officers. Members of the Executive Committee are listed in Table 1. The Council currently consists of representatives from 24 Adhering Bodies and two Associate members having an interest in any aspect of theoretical, basic, and applied frozen ground research, including permafrost, seasonal frost, artificial freezing, and periglacial phenomena.

Attendance at the first council meeting on August 5, 1987, in Ottawa, Canada, included 15 Adhering Bodies together

Table 1. Executive Committees of the International Permafrost Association 1983–2008

	1983–1988	1988–1993	1993–1998	1998–2003	2003–2008
President	P.I. Mel'nikov U.S.S.R.	T.L. Péwé USA	Cheng Guodong China	H.M.French Canada	J. Brown USA
Vice President	T.L. Péwé USA	Cheng Guodong China	N.N. Romanovskii Russia	F.E. Are Russia	C. Harris U.K.
Vice President	K. Flaate Norway	V.P. Mel'nikov U.S.S.R	H.M. French Canada	W. Haeberli Switzerland	G. Perlshtein Russia
Secretary General	J. Ross Mackay Canada	J. Ross Mackay Canada	J. Brown USA	Replaced by Secretariat	Replaced by Secretariat
Members				J. Brown, USA T. Mølmann, Norway Zhu Yuanlin, China	H.-W. Hubberten Germany D.W. Hayley Canada Zhu Yuanlin Ma Wei, China

with representatives from France (joined 1988) and Sweden (joined 1990) as observers. Other members soon followed: Denmark (1989), Spain and Southern Africa (1993), Mongolia and Kazakhstan (1995), Austria (1998), Iceland (2003), and New Zealand (2005). Portugal and South Africa were approved as Associate members in 2005. Each member pays an annual membership fee established by the Council.

The Constitution and Bylaws were adopted at the first council meeting. Since then, five modifications have been approved (December 1992, June 1998, March 2003, June 2005, Potsdam; and May 2006). These largely involved membership and working party activities.

The Council elects the Executive Committee and approves the formation and review activities of Committees, Working Groups, and Task Forces. It also approves the venue for each ICOP. The Council met in ten locations:

Ottawa, Canada (1987, FG 2).
Trondheim, Norway (1988, FG 4).
Quebec City, Canada (1990; FG 7).
Beijing, China (1991 during INQUA, FG 10).
Washington, DC (1992 during INQUA, FG 12).
Beijing, China (1993, FG 14).
Berlin, Germany (1995 during INQUA, FG 18).
Yellowknife, Canada (1998, FG 22).
Zurich, Switzerland (July 2003, FG 27).
Potsdam, Germany (June 2005, FG 29).

Starting in 1990, the Council issued a series of recommendations that include specific activities and topics of international scope (see summaries of Council meetings in *Frozen Ground*). These include statements on mapping, long-term monitoring, modeling, climate change, data acquisition and archiving, terminology, coordination with other international organizations and programs including both the Northern and Southern Hemisphere, and mid- and low-latitude mountains and plateau regions.

The Executive Committee is elected by Council every five years. Although members do not represent their own country, the four countries with significant areas of permafrost have always been represented on the Committee. A representative from the forthcoming international conference is also a member. A geographic and disciplinary balance of membership is also maintained. The first formal meeting of the Executive Committee took place in Oslo in September 1985. The Council has met formally 27 times.

The Secretary General first resided at the University of British Columbia, Canada (J. Ross Mackay, 1983–1993) and then in Washington DC, USA (Jerry Brown, 1993–1999). In 1998 the position of Secretary General was replaced by a Secretariat. This was initially located at the Institute of Geography, University of Copenhagen, Denmark (1999–2001) and is now at the University Centre on Svalbard (UNIS), Norway (2001–2009). Hanne H. Christiansen has been responsible for the Secretariat since 1999. In both locations, national research agencies and institutions have provided financial support. Major responsibilities include preparation and distribution of *Frozen Ground*, maintenance of the IPA webpage, coordination of administrative, Executive Committee and Council affairs, and international representation. The IPA web is currently hosted by the Department of Geosciences, University of Oslo.

International affiliations

The IPA became an Affiliated Organization of the International Union of Geological Sciences (IUGS) in July 1989. In 1996 the IPA and the International Geographical Union (IGU) signed an agreement that formalized a joint Periglacial Commission. This agreement recognized the longtime relationships between periglacial and permafrost researchers, the foundations of which are recorded in the pages of the Polish journal *Builetyn Peryglacjalny*. The IGU-IPA agreement was modified in 2004 with the formation of the new Commission on Cold Regions Environments.

Agreements also exist to share joint working groups, committees, or projects with the International Union of Soil Science (IUSS), the Scientific Committee for Antarctic Research (SCAR), and the International Arctic Science Committee (IASC). A Memorandum of Understanding was signed in 2004 between IPA and the World Climate Research Programme project “Climate and Cryosphere” (CliC). Although no formal agreement exists with the International Union of Quaternary Research (INQUA), close working relations are maintained with the Quaternary communities. Similarly, ties are maintained with the International Society for Soil Mechanics and Geotechnical Engineering (ISSMGE) and the newly formed International Association of Cryospheric Sciences.

Technical Activities

Conferences and workshops

Starting in 1983, the International Permafrost Association assumed responsibility for scheduling the ICOP meetings at five-year intervals. A written invitation for the proposed conference is required for IPA Council approval. The President of the IPA formally convenes the opening and closing sessions of each conference. In 1998 an International Advisory Committee for ICOP was formed to facilitate continuity in the planning of conferences. The host country is responsible for the financial support, technical organization, and publications. Field trips in or to permafrost areas are required as part of the program. The host country is responsible for the organization and financing of the conferences. The eight international conferences to date are:

First: 11–15 November, 1963, Purdue, Indiana, USA.
Second: 12–20 July, 1973, Yakutsk, Siberia, USSR.
Third: 10–13 July, 1978, Edmonton, Alberta, Canada.
Fourth: 17–22 July, 1983, Fairbanks, Alaska, USA.
Fifth: 2–5 August, 1988, Trondheim, Norway.
Sixth: 5–9 July, 1993, Beijing, China.
Seventh: 23–27 June, 1998, Yellowknife, Canada.
Eighth: 20–25 July, 2003, Zurich, Switzerland.

Over the span of these forty years, approximately 2500 individuals from 36 countries have participated in the eight conferences. Short reports on each conference, including numbers of attendees, papers in proceedings, field trips, and related publications for all eight conferences are reported elsewhere (Brown & Walker 2007). From 2008 onwards, conferences will take place on a four-year cycle with an official intervening regional conference. During the Eighth ICOP, the Troy L. Péwé Award was established to recognize the best presentation by a young researcher.

The IPA has also sponsored a number of regional permafrost conferences. These include the Fourth Canadian permafrost Conference (Québec, 1990), two European permafrost conferences (Rome, 2001: Potsdam, 2005), and the First Asian Conference on Permafrost (Lanzhou, 2006). In addition, the annual Russian geocryology conferences (e.g., Pushchino; Salekhard), and several cryopedology and soils meetings (e.g., Copenhagen, Syktyvkar, Madison, Arkhangelsk) have been sponsored by the IPA.

Workshops also play an important role in implementing IPA-related projects. The following are the major such meetings; results are reported in *Frozen Ground*:

Global Geocryological Data workshop (1994).

International workshop on processes and ability to detect change (1995).

Mountain permafrost and monitoring (1997).

International workshop on permafrost monitoring and databases (2000).

International symposium on mountain and arid land permafrost (2001).

Circumpolar Active Layer Monitoring (CALM) workshop (2002).

Arctic Coastal Dynamics workshops (annual 1999-2006).

Permafrost and Climate in the 21st Century (PACE21) workshop (2004).

Antarctic workshops (2004, 2007).

Asian permafrost mapping workshop (2006).

Working parties

Since 1998 many of the IPA activities between conferences have been undertaken by committees, working groups, and task forces (collectively referred to as *working parties*). Annual reports of working parties are published in *Frozen Ground* and archived on the IPA website. At the 1988 Council meeting in Trondheim, three standing committees and six working groups were established. New working groups were added and some goals modified prior to, or at, the 1993 Council. During the intervening years and at the 1998 Yellowknife Council meetings, major revisions were made to the organization of working parties. New guidelines were developed and included the formation of Task Forces (see FG 22). During the 2003 Council meeting, several Task Forces became working groups, and existing working groups were redefined. A total of ten working groups, several with subgroups, are presently active and are joint with other international organizations:

Standing Committees:

Data, Information and Communication

International Advisory Committee for International Permafrost Conferences

Working Groups:

Antarctic Permafrost and Periglacial Environments (SCAR)

Coastal and Offshore Permafrost (IASC and LOICZ)

Cryosols (IUSS)

Glaciers and Permafrost Hazards in High Mountains (IACS)

Isotopes and Geochemistry of Permafrost

Mapping and Modeling of Mountain Permafrost

Periglacial Landforms, Processes and Climate (IGU)

Permafrost and Climate (IGU)

Permafrost Astrobiology

Permafrost Engineering (ISSMFE)

Since 1998, working party reports covering the previous five years have been published as part of the program for the international conferences on permafrost. In 2007 a review was undertaken by an ad hoc committee on working parties to provide recommendations on the present activities and future directions. These will be discussed at the 2008 Council meetings. Future activities will be approved between then and the next regional and international conferences in 2010 and 2012, respectively.

Major Accomplishments

By 1988 the IPA was serving as a catalyst and organizer of several major international activities.

Database

A common challenge facing many field-oriented disciplines is access to international data sets and the subsequent preservation or archiving of these data. The lack of readily available, international permafrost-related data sets was recognized by the IPA prior to, and during, the 1988 Trondheim conference. A Working Group on Permafrost Data was formed and an international data workshop was subsequently convened in 1994 in Olso. The result was development of the Global Geocryological Database (GGD), the basis of which is identification and description of data sets beginning in a metadata format. The National Snow and Ice Data Center took the lead in populating the GGD with both metadata and data. For the 1998 and 2003 conferences, the compilations of the GGD were provided on CD-ROM, entitled Circumpolar Active-Layer Permafrost System (CAPS) (Barry et al. 1995, NSIDC 1998, IPA SCDIC 2003, Parsons et al. 2008). The CAPS/GGD products are available on line at the NSIDC Frozen Ground Data Center.

Terminology

By the time the IPA was established, it was clear that the major terminological problem associated with permafrost, as defined in North America, Russia, and China, arose from the fact that ground at or below 0°C may, or may not, be frozen. Put simply, permafrost is not necessarily frozen because soil and rock, for a variety of reasons (salts, pressure, etc.), may exist in an unfrozen state at temperatures below 0°C. This prompted the Permafrost Subcommittee of the Associate Committee on Geotechnical Research, NRCC, to establish a terminology working group in 1985. In its report (ACGR 1988), "cryotic" terminology was re-introduced in an attempt to accommodate the unfrozen nature of certain permafrost situations. The IPA Council approved a Working Group on Permafrost Terminology in 1988 and encouraged production of a multi-language glossary of permafrost and related ground ice terms (van Everdingen 1998). Although this glossary did not resolve the problem, the permafrost community has, for the first time in its history, a working document that describes permafrost terminology in twelve languages. This represents a major achievement.

International permafrost map

Prior to 1983, the mapping of permafrost had been undertaken using different classifications by different national organizations. The need existed for a circum-arctic map based on a common classification. An informal group representing members of the United States Geological Survey (USGS), the Geological Survey of Canada, and the Institute for Hydrogeology and Engineering Geology (VSEGINGEO), Russia, was spearheaded by the IPA Secretary General (J. Brown) and started work in the early 1990s. A generalized legend based on permafrost continuity, ground ice content, and physiography was applied to existing permafrost maps and, after several meetings and numerous editorial discussions by the authors and the USGS cartographers, a map at 1:10,000,000 was finalized and published (Brown et al. 1997). It was subsequently digitized and made available in ArcInfo. The digitized product has been used extensively by the modeling communities and others involved in climate research. Building on this existing map, a new international map based on spatial and temperature variations of permafrost terrain is a logical next step.

Observational networks

The IPA has taken the leadership in initiating and coordinating several international, long-term monitoring networks and related data acquisition programs. The IPA entered into a cooperative partnership with the World Meteorological Organizations (WMO) and the Food and Agriculture Organization (FAO) of the United Nations to facilitate development and coordination of the Global Terrestrial Network for Permafrost (GTN-P) (Burgess et al. 2000). The GTN-P consists of two components: the borehole measurements or Thermal State of Permafrost (TSP) and the Circumpolar Active Layer Monitoring (CALM) network. Both TSP and CALM are included in the IPA-coordinated International Polar Year (IPY) Project 50 "Permafrost Observatory Project: A Contribution to the Thermal State of Permafrost." This currently consists of 150 CALM sites (Nelson et al. 2004, Shiklomanov et al. 2008) and approximately 500 borehole temperature sites in both hemispheres. Also included are the boreholes developed under the PACE program (Harris 2008) and the Norwegian TSP boreholes. At least 15 countries are participating in GTN-P, primarily with national funding.

A second major network exists in the Arctic Coastal Dynamics (ACD) program. Following a 1999 workshop, a science plan under the Working Group on Coastal and Offshore Permafrost was developed and project status was approved by the International Arctic Science Committee. There are approximately 30 key coastal sites located around the Arctic Ocean. ACD developed a database of several thousand coastal segments.

Publications

In addition to those previously mentioned, numerous publications have arisen from IPA working parties, projects, and related activities. Some of these include:

Bibliographies of published literature (e.g. Brennan 1983, 1988, 1993, Mullins 2003).

An annotated bibliography on climate change (Koster et al. 1994).

Soil carbon map (Tarnocai et al. 2003).

Periglacial manual (IPA web accessible).

In addition, the Wiley journal *Permafrost and Periglacial Processes (PPP)* has published a number of special issues on mountain permafrost (PPP3), climate change (PPP4), grèzes litées (PPP6), frozen ground (PPP7), cryostratigraphy (PPP9), cryosols (PPP10), PACE (PPP12), hydrology, climate and ecosystems (PPP14); periglacial processes and instrumentation (PPP14), CALM (PPP15), PACE21: mountain permafrost (PPP15), and a special issue in honor of J. Ross Mackay at the time of his 90th birthday (PPP18).

Several other journals serve the international geocryology communities. For example, since 2002, the *Reports on Polar Research* of the Alfred Wegener Institute for Polar and Marine Research (Bremerhaven, Germany) have contained an annual issue devoted to the results of the ACD workshops. Other journals have also devoted special issues to IPA-sponsored activities: these include the *Norwegian Journal of Geography, Polar Geography and Geology, Southern African Journal of Science, Global and Planetary Change, Cold Regions Science and Technology,* and *Journal of Geophysical Research.*

Conclusions

The International Permafrost Association has established itself as a productive international organization.

Geocryology is now recognized as a cold-climate discipline that integrates permafrost science and permafrost engineering. Permafrost is recognized as an important component of the cryosphere.

Specific achievements under the IPA include the production of a multi-language glossary, publication of a digitized, circum-arctic map of permafrost and related ground ice conditions, and the establishment of the global geocryological database system and several monitoring networks.

The IPA legacy that is resulting from both the IPY and existing activities includes: (i) establishment of networks of active layer and permafrost temperature observatories, (ii) development of a sustainable geocryological database, and (iii) fostering a new generation of geocryologists through the activities of the Permafrost Young Researchers Network.

These collective activities will further develop and sustain international activities, particularly those related to the state and fate of permafrost in relation to a changing climate.

Acknowledgments

The IPA and this report contribute to the activities of the International Polar Year. Numerous individuals and organizations have contributed to the success of the IPA. Special thanks must go to the Bureau of International Relations, National Research Council of Canada, for the initial funding of the activities of the IPA Secretary General, Professor J. Ross Mackay, between 1983 and 1993, and to the U.S. National Science Foundation, USA, for funding the activities of the IPA Secretary General, Jerry Brown. Since 1998, Hanne H. Christiansen has been responsible for the successful operation of the IPA Secretariat, assisted by Angélique Prick (2005–2007), and most recently by Herman Farbrot. Funding of this Secretariat has been provided by the Danish Polar Centre, Barlindhaug, and the Research Council of Norway. Ole Humlum (University of Oslo) has provided valuable assistance and support for the IPA webpage.

References

Associate Committee on Geotechnical Research 1988. *Glossary of permafrost and related ground-ice terms*. National Research Council of Canada. Ottawa, Technical Memorandum No. 1242, 156 pp.

Barry, R.G., Heginbottom, J.A. & Brown, J. 1995. Workshop on Permafrost Data Rescue and Access. 3-5 November 1994, Oslo, Norway. *Glaciological Data Report GD-28.* World Data Center for Glaciology (Snow and Ice), Boulder, CO, 134 pp.

Brennan, A.M. 1983. Permafrost bibliography update, 1978-1982. *Glaciological Data Report GD-14*. World Data Center for Glaciology (Snow and Ice), Boulder, CO, 336 pp.

Brennan, A.M. 1988. Permafrost bibliography update, 1983-1987. *Glaciological Data Report GD-21*. World Data Center for Glaciology (Snow and Ice), Boulder, CO, 225 pp.

Brennan, A.M. 1993. Permafrost bibliography update, 1988-1992. *Glaciological Data Report GD-26.* World Data Center for Glaciology (Snow and Ice), Boulder, CO, 401 pp.

Brown, J., Ferrians, O.J., Jr., Heginbottom, J.A. & Melnikov, E.S. 1997. Circum-Arctic map of permafrost and ground-ice conditions. *U.S. Geological Survey Circum-Pacific Map CP-45*, 1:10,000,000, Reston, Virginia.

Brown, J. & Walker, H.J. 2007. Report from the International Permafrost Association: A brief history of the International Permafrost Conferences (1963-2003). *Permafrost and Periglacial Processes* 18: 385-392.

Burgess, M. Smith, S.L., Brown, J., Romanovsky, V., & Hinkel, K. 2000. Global Terrestrial Network for Permafrost (GTNet-P): Permafrost monitoring contributing to global climate observations. *Geological Survey of Canada, Current Research 2000-E14*, 8 pp.

French, H.M., & Nelson, F.E. 2008. The permafrost legacy of Siemon Muller (*this proceedings*).

Harris, C. 2008. Recent warming of European Permafrost: evidence from PACE boreholes and other monitoring networks (*this proceedings*).

IPA Standing Committee on Data Information and Communication, comp. 2003. *CAPS: Circumpolar Active-Layer Permafrost System, Version 2.0*, M. Parsons & T. Zhang (Eds.), National Snow and Ice Data Center, Boulder, CO, CD-ROM.

Koster, E.A., Nieuwenhuijzen, M.E. & Judge, A.S. 1994. Permafrost and Climatic Change: An Annotated Bibliography. *Glaciological Data Report GD-27*. World Data Center for Glaciology (Snow and Ice), Boulder, CO, 94 pp.

Mullins, T. 2003, Permafrost and Frozen Ground Bibliography, 1978-2003. *Glaciological Data Report GD-31*. World Data Center for Glaciology (Snow and Ice), Boulder, CO, 1128 pp.

National Snow and Ice Data Center 1998. *CAPS: Circumpolar Active-Layer Permafrost System, Version 1.0.* National Snow and Ice Data Center, Boulder, CO, CD-ROM.

Nelson, F.E. (Ed.) 2004. Special Issue: Circumpolar Active Layer Monitoring (CALM) Workshop. *Permafrost and Periglacial Processes* 15(2): 99-188.

Parsons, M.A. et al. 2008. Managing Permafrost Data: Past Approaches and Future Directions (*this proceedings*).

Shvetsov, P.F. 1956. *Basic concepts and terms in geocryology.* Inst. Merzlotovedeniya, Akad. Nauk SSSR, 16 pp. (in Russian).

Shiklomanov, N.I. 2005. From exploration to systematic investigation: Development of geocryology in 19th- and early-20th century Russia. *Physical Geography* 26: 249-263.

Shiklomanov, N., Nelson, F.E., Streletskyi, D.A., Hinkel, K.M. & Brown, J. 2008. The Circumpolar Active Layer Monitoring (CALM) Program: Data Collection, Management, and Dissemination Strategies (*this proceedings*).

Sumgin, M.I. 1927, 1937. Soil Permafrost within the USSR. *Vladivostok: 1st edition; Moscow-Leningrad: 2nd edition, Acad. Nauk SSSR*, 372 pp. (in Russian).

Tarnocai, C., Kimble, J. & Broll G. 2003. Determining carbon stocks in Cryosols using the northern and mid Latitudes soil database. *Proceedings of the Eighth International Conference on Permafrost, Zurich, Switzerland, July 21-25, 2003:* 1129-1134.

van Everdingen. R.O. 1998. *IPA Multi-Language Glossary of Permafrost and Related Ground-Ice Terms in Chinese, English, French, German, Icelandic, Italian, Norwegian, Polish, Romanian, Russian, Spanish and Swedish.* Arctic Institute of North America, Calgary, Canada.

Experimental Study of the Thermal Conductivity of Frozen Sediments Containing Gas Hydrates

B.A. Buhanov
Department of Geocryology, Geological Faculty, Moscow State University, Russia
E.M. Chuvilin
Department of Geocryology, Geological Faculty, Moscow State University, Russia
O.M. Guryeva
Department of Geocryology, Geological Faculty, Moscow State University, Russia
P.I. Kotov
Department of Geocryology, Geological Faculty, Moscow State University, Russia

Abstract

In this paper, the authors present the results of laboratory measurements of the thermal conductivity of artificial hydrate-bearing sediments under frozen conditions and atmospheric pressure. Frozen hydrate-saturated samples were maintained in a quasi-stable condition due to the so-called "self-preservation" effect of gas hydrates at negative temperatures. We determined the structure and thermal and physical properties of gas hydrate-bearing sediments, including the thermal conductivity. The results were then compared to properties of similar frozen sediments containing no methane hydrate. Experimental data showed that the thermal conductivity is very different for hydrate-bearing sediments in the self-preserved state than for similar ice-bearing sediment samples. This difference depends on the type of sediments and on structure-textural transformations which occur in the porous medium during self-preservation of hydrate-bearing samples. This difference increases with increasing hydrate saturation and volumetric hydrate content and with the decrease of dry density.

Keywords: frozen sediment; gas hydrate; hydrate-bearing sediments; self-preservation; thermal conductivity.

Introduction

Gas hydrates are ice-like crystalline substances that form from water and gas (of comparatively low molecular weight) under certain thermobaric conditions. Gas hydrates are a highly concentrated source of natural gas (mainly methane), and are considered to represent a promising new energy resource due to their extensive geographic occurrence. It is known that gas hydrates can exist naturally at both positive and negative temperature. According to drilling data and other indirect indicators, gas hydrates occur in permafrost environments in several regions of North Siberia and in on-shore/off-shore regions of the Canadian Arctic (Judge et al. 1994; Judge & Majorowicz 1992, Yakushev & Chuvilin 2000). Most known concentrations of permafrost gas hydrate occur below the permafrost table (e.g., Mallik), at temperatures well above 0°C (Henninges et al. 2005) However, several occurrences of intrapermafrost gas hydrates have been documented (Dallimore & Collett 1995, Dallimore et al. 1996, Ershov et al. 1991). It is difficult to identify and quantify gas hydrates occurring within frozen sediments using traditional geophysical techniques (mainly seismic) because of the similar geophysical response of gas hydrates and pore ice in frozen sediments. This is assumed to be due to the similarity between many of the physical properties of ice and gas hydrates (Table 1). However, the authors note that the thermal conductivity of ice and gas hydrate differ significantly, raising the possibility of employing thermal conductivity measurements to identify gas hydrates occurring within permafrost.

The anomalously low thermal conductivity of gas hydrates was discovered by Stoll & Bryan (1979), and was later confirmed by many other studies (Sloan 1998). Experimental data indicate that the thermal conductivity of gas hydrate (~0.5 $Wm^{-1}C^{-1}$) is similar to that of water (~0.6 $Wm^{-1}C^{-1}$), and is approximately 5 times lower than the thermal conductivity of ice (~2.2 $Wm^{-1}C^{-1}$).

The first technical study of the thermal properties of gas hydrate-bearing sediments was conducted by Groysman (1985), in which he compared the thermal properties of gas hydrate-bearing sandstone in the frozen and unfrozen states. These experiments indicate that the heat capacity per unit mass of frozen and gas hydrate-bearing sandstone differed little from each other, but the thermal conductivity of a gas hydrate-saturated sandstone was 70% lower than that of the frozen (ice-bearing) sample (Groysman 1985). Asher (1987) experimentally showed that the thermal conductivity of frozen sand is 80% higher then that of hydrate-saturated sand, but did not present any quantitative data about the degree of hydrate saturation of the investigated sediments. Wright et al. (2005) employed a needle probe to measure the thermal conductivities of laboratory specimens and recovered core from the gas hydrate-bearing reservoir at the Mallik gas hydrate production research site in Canada's Mackenzie Delta. Their measurements were obtained within a temperature-controlled pressurized test chamber designed to maintain thermodynamically stable gas hydrate.

Table 1. Comparison of physical properties of ice, SI and SII hydrate (Sloan 1998).

PROPERTY	ICE	STRUCTURE I	STRUCTURE II
Number of H_2O molecules	4	46	136
H_2O diffusion jump time (μsec)	21	>200	>200
Dielectric constant at 273 K	94	~58	~58
Isothermal Young's Modulus at 268 K (10^9 Pa)	9.5	8.4 (est)	8.2 (est)
Poisson's ratio	0.33	~0.33	~0.33
Bulk modulus at 272 K (GPa)	8.8	5.6	N/A
Shear modulus at 272 K (GPa)	3.9	2.4	N/A
Velocity ratio (comp./shear) at 272 K	1.88	1.95	N/A
Linear thermal expansion at 200 K (K^{-1})	56 x 10^{-6}	77 x 10^{-6}	52 x 10^{-6}
Adiabatic bulk compression at 273 K (GPa)	12	14 (est)	14 (est)
Speed Long Sound at 273 K (km/sec)	3.8	3.3	3.6
Density (g/cc)	0.917	0.91 (at 273 K)	0.94 (at 273 K)
Thermal conductivity at 263 K ($Wm^{-1}C^{-1}$)	2.23	0.49±0.02	0.51±0.02

Their data also indicated that the thermal conductivity of frozen (ice-bearing) samples is considerably higher than that of the same samples containing gas hydrate at temperatures above 0°C. They presented data on the thermal conductivity of frozen hydrate-bearing sediments with values 20–25% higher than the thermal conductivity of the unfrozen hydrate-bearing samples. Their results suggest that the thermal conductivity of gas hydrate-bearing sediments in the frozen/unfrozen state is dependent on the relative proportions of gas hydrate/ice and gas hydrate/water, respectively.

Waite et al. (2007) also used the needle probe technique to study the thermal conductivity of gas hydrate, and demonstrated weak temperature and pressure dependencies for thermal conductivity of gas hydrate. On the basis of the experimental data and analysis of published works they concluded that the thermal conductivity of hydrate-containing sediments at positive temperatures does not depend on the ratio of hydrate and water in the porous media.

Gas hydrates in frozen sediments can exist in a "relict" state for long periods of time due to the self-preservation effect (Ershov et al. 1991, Dallimore et al. 1996). The determination of in situ thermal conductivity anomalies may represent a potential exploration tool for gas hydrate identification and quantification within the upper horizons of permafrost. This notion forms the motivational basis for undertaking the experimental study of the thermal conductivity of frozen, hydrate-containing sediments under the non-equilibrium conditions ($p<p_{eq}$), as presented in this paper.

Methods

To facilitate the study of thermal conductivity of frozen hydrate-bearing sediments at negative temperature, we prepared artificial hydrate-saturated samples of sand, silty sand, and sandy loam, including samples collected from permafrost regions. A summary of sample characteristics is presented in Table 2.

For each individual laboratory test, a sample holder containing a test specimen was loaded into a high-pressure cell designed for the formation of gas hydrate within artificial or natural porous media, under controlled pressure and temperature conditions (Chuvilin & Kozlova 2005). After hermetically sealing the test cell, the cell was purged of air and charged with methane gas by slowly increasing cell pressure to about 8–10 MPa. The cell was maintained at room temperature while temperature and pressure conditions were stabilized, after which the cell was cooled to about 1–2°C. Under these conditions the process of gas hydrate formation was spontaneously initiated, as indicated by a sharp pressure drop within the cell. After the termination of hydrate accumulation within the sediment, the test cell was cooled to about -7 to -8°C, freezing any residual pore water which had not transformed to gas hydrate. The test cell was then transferred to a cold room maintained at a temperature of about -8°C. The cell was subsequently depressurized to 1 atmosphere, after which the test cell was opened and the sample removed.

The self-preservation effect of gas hydrates at negative temperatures facilitates the maintenance of the frozen hydrate-bearing samples in a quasi-stable state (at atmospheric pressure) during subsequent measurements of thermal conductivity. This also facilitates determination of the composition, structure and selected properties of gas hydrate-bearing samples, including the thermal-conductivity (λ), gravimetric water content (W_g), density and gas content. Definition of the sample's gas content was carried out by means of measurement of gas released in the course of defrosting of the sample placed in saturated NaCl solution. Then we calculated dry density (ρ), porosity (φ), volumetric hydrate content H_v ($H_v=V_H \cdot 100\% / V_{sam,}$ where V_H is volume of hydrate, V_{samp} is volume of the sample), hydrate saturation S_h ($S_h = H_v / φ$,%); ice saturation S_i ($S_i = I_v / φ$,% where I_v is volumetric ice content). The results were then compared to measurements of the properties in samples without methane hydrates.

Thermal conductivity measurements were obtained using the thermal properties analyzer KD2, which is a registered trademark of Decagon Devices, Inc. The pocket-sized KD2 uses a single sensor (needle probe) to measure thermal conductivity and thermal resistivity of the test sample.

Table 2. Characteristics of soils.

Type of sediment	*Particle size distribution, %*			*Particle density, ρ_s, g/cm³*	*Plastic limit, W_p, %*	*Liquid limit, W_L %*	*Salinity, %*
	1–0.05 mm	0.05–0.001mm	<0.001 mm				
Silty sand	84	14	2	2.65	-	-	0.089
Sand	94.8	3.1	2.1	2.65	-	-	0.012
Sandy loam	41.8	53.7	4.5	2.7	20	33	0.693

The unit employs the transient line heat source method to calculate and display the thermal conductivity within 90-seconds. A detailed description of the transient line heat source method is presented by Bristow et al. 1994.

The small-diameter needle probe (1.2 mm diameter by 65 mm long) results in very little compaction during installation and allows for a short heating time, thereby minimizing any thermally-induced disturbance to gas hydrate or ice in the vicinity of the probe. The KD2 needle probe contains both a heating element and a thermistor. The controller module contains a battery and a 16-bit microcontroller, which automatically calculates the thermal-conductivity from temperature-time data.

The KD2 is rated for operation across a temperature range from -20 to +40°C, and measures thermal conductivity in the range from 0.01 to 2.0 $Wm^{-1}C^{-1}$ with a rated accuracy of ±5% to about 2.0 $Wm^{-1}C^{-1}$ with an accuracy ± 10%.

During the measurement, temperature increases by about 0.5°C. Since the sample temperature during measurement is in the range of -7 to -8°C, we assume that this small temperature increase does not significantly influence the phase composition of water either through ice melting or hydrate decomposition. Since the measurement is obtained at atmospheric pressure (i.e., outside of the gas hydrate pressure-temperature stability field), some portion of the hydrate in sediment pores dissociates progressively with time. However, the rate of dissociation is assumed to be very slow due to the self-preservation effect and according to our estimation does not influence the thermal field of the sample during the 90 second period of measurement.

To facilitate insertion of the needle probe, a small hole was drilled into the frozen test sample, the diameter of which corresponded to the diameter of the probe. The chilled needle probe was inserted full-length into the hole, such that a tight fit was obtained. Thermal contact between the probe and the sediment was maximized by use of a thermal paste with a thermal conductivity of 1.0 $Wm^{-1}C^{-1}$. For each sample, multiple measurements of thermal conductivity were obtained over a reasonable time period that allowed any thermal disturbances within the test sample to dissipate between measurements. With constant negative ambient temperatures being maintained, subsequent consecutive measurements were made at longer time intervals to document the change in thermal conductivity with time (assuming slow but progressive gas hydrate dissociation under the "self-preserved" condition). At the same time the gas content was determined with accuracy of 2–3%.

The KD2 thermal analyzer was also employed to measure the thermal conductivity of frozen control sediments having similar physical properties but without hydrate.

Results of Experimental Research

Frozen hydrate-containing samples of sand, silty sand, and sandy loam were prepared for thermal conductivity measurement. For each sample tested, we determined water content, dry density, porosity, gas hydrate saturation, and ice saturation. Thermal conductivity measurements (Table 3) were obtained using a needle probe and KD2 thermal analyzer.

Data from experiments indicate that the thermal conductivities of hydrate-bearing sediments were considerably lower than those obtained for similar ice-bearing sediments. The maximum difference (by more than a factor of 5) was observed for silty sand with an initial water content of 21%, and a high pore hydrate-saturation. We speculate that this large difference in measured thermal conductivities may be a reflection of the comparatively low thermal conductivity of methane hydrate forming on the surfaces bridging individual sediment particles within the bulk sediment. In the experiments conducted by Wright et al. (2005) the difference in the thermal conductivities of hydrate-saturated sand vs. frozen sand containing no hydrate is noticeably smaller, not exceeding 70%. However their data were obtained for thermodynamically stable gas hydrate under controlled temperatures and elevated pressures (in the order 5–8 MPa). In our case, thermal conductivity measurements were obtained at atmospheric pressure and freezing temperatures favourable for the self-preservation of pore-space gas hydrate. It is possible that the structural characteristics of sediments containing self-preserved gas hydrate are significantly different than the structural characteristics of sediment containing thermodynamically stable gas hydrate. One plausible explanation may be the formation of numerous microcracks and pinholes within the gas hydrate crystal matrix during partial dissociation of hydrate in the self-preserved condition. The formation of such microcracks in hydrates following depressurization to one atmosphere has been described previously by Ershov et al. (1990). The presence of microcracks in pore-space gas hydrate may result in a substantial reduction of the thermal conductivity of hydrate-bearing sediments, in comparison to frozen samples containing no gas hydrate.

The smallest differences between the thermal conductivity

Table 3. Thermal conductivity for frozen hydrate-saturated sediment samples (t = -7 to -8°C).

Type of sediment	Wg, %	Dry density, ρ_s, u.f.	Porosity, ϕ, u.f.	Hv,%	Sh, %.	Si, %	λ_{hyd}, $Wm^{-1}C^{-1}$	λ_{fr} $Wm^{-1}C^{-1}$
Sand	10	1.23	0.55	12	23	6	0.76	1.30
Silty sand	10	1.52	0.42	8	20	23	1.07	1.74
	15	1.51	0.43	13	32	32	0.5	1.9
	17	1.53	0.42	14	40	34	0.46	2.14
	21	1.37	0.48	25	52	18	0.44	2.32
Sandy loam	17	1.55	0.42	22	59	16	1.24	1.93
	17	1.55	0.42	15	34	35	1.59	1.93

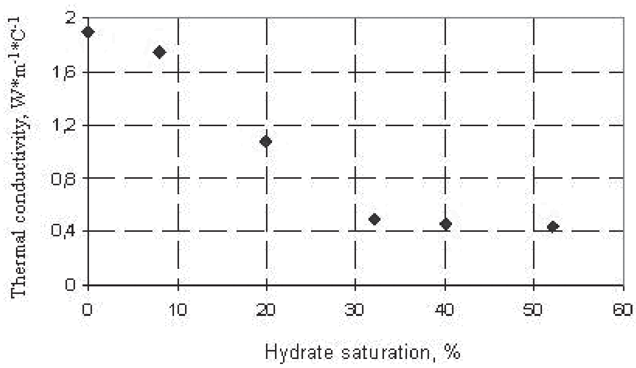

Figure 1. Influence of hydrate saturation on thermal conductivity in frozen silty sand sample (t = -7 to -8°C).

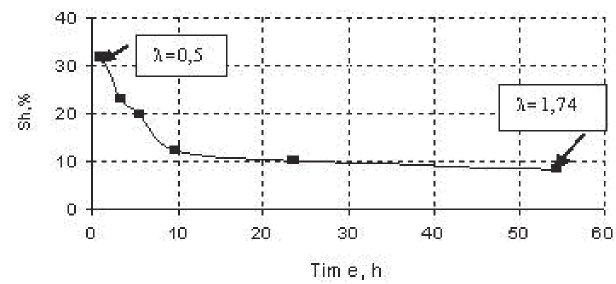

Figure 2. Methane hydrate dissociation kinetic in frozen silty sand sample and thermal conductivity (t = -7 to -8°C).

of frozen hydrate-bearing vs. ice-bearing samples (30–50%) were observed in samples of sandy loam (Table 3), characterized by comparatively high dry density (1.55 g/cm^3) and low porosity (~0.42). This result may be explained by the absence of hydrates at contacts between sediment particles, despite the relatively high hydrate content. Comparatively little difference in the thermal conductivity of frozen hydrate-bearing vs. ice-bearing samples was observed for sand having an initial water content of 10%. Note that hydrate saturation of this sample was 2.5 times lower than that of the silty sand having an initial water content of 21%. The large difference between the thermal conductivity of frozen hydrate-bearing and ice-bearing samples representing more dispersed sediments may be associated with structure-textural peculiarities in sediments containing self-preserved pore-space gas hydrate. However, this question requires additional investigation.

Thus, our data indicate that for self-preserved gas hydrate at atmospheric pressure, higher hydrate-saturation is associated with decreased thermal conductivity (Fig. 1).

Additional experiments to measure thermal conductivity during dissociation of pore-space hydrate in silty sand (W_{in}=15%) were conducted at negative temperatures (Fig. 2). Note that the degree of pore saturation with hydrate decreases over time as a result of the slow dissociation of pore hydrate in the self-preserved state, accompanied by an apparent increase in thermal conductivity from 0.5 $Wm^{-1}C^{-1}$ at the beginning of the experiment, to 1.74 $Wm^{-1}C^{-1}$ at the end of the testing period

The observed increase in thermal conductivity at the end of the experiment can be explained by a progressive decrease in the amount of pore-space hydrate and a corresponding increase in the amount of pore ice as dissociation progresses at temperatures below 0°C. Ice is exposed to processes of metamorphism which causes decrease of its porosity. Given that the process of hydrate dissociation in porous media at atmospheric pressure is poorly understood, it is desirable to undertake special micro-morphological studies designed to clarify the specifics of thermal conductivity in frozen hydrate-bearing sediments under non-steady state conditions.

Conclusion

A technique for obtaining rapid measurements of the thermal conductivity of self-preserved hydrate-bearing sediments at atmospheric pressure were was established.
Experimental data confirm that the thermal conductivity of self-preserved hydrate-bearing sediments is considerably lower than that of similar ice-bearing sediments, and that this discrepancy increases with increasing of hydrate saturation and volumetric hydrate content, and with decreasing dry density. This difference is also more apparent in uniform sands than in more dispersed sediments such as sandy loam.

Experimental results show that the thermal conductivity of frozen hydrate-containing soils increases with time because of the pore gas hydrate dissociation at non-equilibrium conditions.

Our results show the possibility of using thermal conductivity to single out frozen hydrate containing layers both in stable and metastable states.

Acknowledgments

This research was funded by the program Russian Foundation Basic Research No. 05-05-39019 and No. 06-05-91573. We thank the anonymous referees for various suggestions to improve the manuscript. Special thanks to J.F. Wright for his valuable advice and help to correct the English.

References

Asher, G.B. 1987. *Development of a computerized thermal conductivity measurement system utilizing the transient needle probe technique: an application to hydrates in porous media*. Dissertation T-3335, Colorado School of Mines, Golden, Colorado.

Bristow, K.L., White, R.D. & Kluitenberg, GJ. 1994. Comparison of single and dual probes for measuring soil thermal properties with transient heating. *Australian Journal of Soil Research* 32: 447-464.

Chuvilin, E.M. & Kozlova, E.V. 2005. Experimental estimation of hydrate-containing sediments stability. *Proceedings of the Fifth International Conference on Gas Hydrates. Thermodynamic Aspects. V.5. Trondheim, Norway:* 1562-1567.

Dallimore, S.R. & Collett, T.S. 1995. Intrapermafrost gas hydrates from a deep core hole in the Mackenzie Delta, Northwest Territories, Canada. *Geology* 23: 527-530.

Dallimore, S.R., Chuvilin, E.M., Yakushev, V.S. Grechischev, S.E., Ponomarev, V. & Pavlov A. 1996. Mackenzie Delta, N.W.T., Canada. *Proceedings of the 2nd International Conference on Natural Gas Hydrates, France, Toulouse*: 525-531.

Ershov, E.D., Lebedenko, Yu.P, Chuvilin, E.M. & Yakushev, V.S. 1990. Experimental investigations of microstructure of ice–methane hydrate agglomerate. *Engineering Geology* 3: 38-44 (in Russian).

Ershov, E. D., Lebedenko, Yu.P., Chuvilin, E.M., Istomin, V.A. & Yakushev V.A. 1991. Peculiarity of gas hydrates existence in the permafrost. *Reports of Academy of Sciences USSR* 321: 788-791 (in Russian).

Groysman, A.G. 1985. *Thermophysical properties of gas hydrates*. Novosibirsk, 94 pp.

Henninges, J., Schrötter, J., Erbas, K. & Huenges, E. 2005. Temperature field of the Mallik gas hydrate occurrence – implications on phase changes and thermal properties. In: S.R. Dallimore and T.S. Collett (eds), *Scientific Results from the Mallik 2002 Gas Hydrate Production Research Well Program, Mackenzie Delta, Northwest Territories, Canada*. Geological Survey of Canada, Bulletin 585.

Judge, A.S., Smith, S.L. & Majorowicz, J.A. 1994. The current distribution and thermal stability of gas hydrates in the Canadian Polar Regions. *Proceedings of the Fourth International Offshore and Polar Engineering Conference, Osaka, Japan, The International Society of Offshore and Polar Engineers:* 307-313.

Judge, A.S. & Majorowicz, J.A. 1992. Geothermal conditions for gas hydrate stability in the Beaufort-Mackenzie area: the global change aspect. *Global and Planetary Change* 98: 251-263.

Sloan, E.D. 1998. Physical/chemical properties of gas hydrates and application to world margin stability and climatic change. In: J.-P. Henriet & J. Mienert (eds.), *Gas Hydrates: Relevance to world margin stability and climate change.* Geological Society, London, Special Publication 137: 31-50.

Stoll, R.D. & Bryan, G.M. 1979. Physical properties of sediments containing gas hydrates. *Journal of Geophysical Research* 84: 1629-1634.

Waite, W.F., Stern, L.A., Kirby, S.H., Winters, W.J. & Mason, D.H. 2007. Simultaneous determination of thermal conductivity, thermal diffusivity and specific heat in sI methane hydrate. *Geophysical Journal International* 169: 767-774.

Wright, J.F., Nixon, F.M., Dallimore, S.R., Henninges, J. & Côté, M.M. 2005. Thermal conductivity of sediments within the gas-hydrate-bearing interval at the JAPEX/JNOC/GSC et al. Mallik 5L-38 gas hydrate production research well. In: S.R. Dallimore & T.S. Collett (eds), *Scientific Results from the Mallik 2002 Gas Hydrate Production Research Well Program, Mackenzie Delta, Northwest Territories, Canada*. Geological Survey of Canada, Bulletin 585.

Yakushev, V.S. & Chuvilin, E.M. 2000. Natural gas and hydrate accumulation within permafrost in Russia. *Cold Regions Science and Technology* 31: 189-197.

Permafrost Dynamics Within an Upper Lena River Tributary: Modeled Impact of Infiltration on the Temperature Field Under a Plateau

Sergey Buldovich
Moscow State University, Geological Faculty, Moscow, Russia
Nikolai Romanovskiy
Moscow State University, Geological Faculty, Moscow, Russia
Gennadiy Tipenko
Institute of Environmental Geoscience, Russian Academy of Sciences, Moscow, Russia
Dmitry Sergeev
Institute of Environmental Geoscience, Russian Academy of Sciences, Moscow, Russia
Vladimir Romanovsky
Geophysical Institute, University of Alaska Fairbanks, USA

Abstract

In southern Yakutia where permafrost is discontinuous, the numerous taliks on the watershed divide surface provide ideal conditions for groundwater feeding. This groundwater discharges locally in the bottom of valleys. Climate change produces differences in permafrost configuration (geometry). It affects the interaction between underground and fluvial waters through changes in the volume of talik reservoirs. This interaction leads to changes in river discharge, especially in the winter. To describe this interaction, the authors developed an efficient numerical method for solving coupled groundwater flow and phase-change heat transfer problems in porous media. The first results of modeling showed that the watershed divides without permafrost became colder because the descending cold infiltration water is directed toward the ascending heat flow. The developed approach seems to be instrumental in analyzing the peculiarities of discharge dynamics of the Lena River tributaries.

Keywords: climate change; discontinuous permafrost; groundwater flow; numerical modeling; water infiltration.

Introduction

Introduction

The problem of discharge dynamics of the great Siberian rivers and the affect on permafrost conditions is the topic of this paper.

The site of our investigation is located on a plateau with monoclinal bedding of Mesozoic rock in the upper part of the Lena basin. The study area is situated in uplands and mountain foothills where permafrost is the warmest in the region (it is still widespread but discontinuous). This region is between the Aldan and Timpton Rivers (centered at 57°N and 125°E), and, more specifically, within the basin of the Chulman River, right tributary of the Aldan River which is a right tributary of the Lena River. Geologically, this region is located in the central part of the Mesozoic Chulman Depression. This territory is well-studied in geocryological and hydrogeological aspects and is representative in Southern Yakutia as the region with discontinuous permafrost (Chizhov et al. 1975). The water catchment areas are situated predominantly at 850–950 m a.s.l.. The typical depth of valleys is 150–200 m. Locally, the valley depth increases up to 950 m. The density of the river network is very high. The water-collecting areas are flat and have the width of 2–3 km. The steepness of slopes is 10–20º. Permafrost distribution is closely related with different elements of the relief. It exists under slopes and in the valley bottoms. The permafrost thickness varies from ten m to 100–150 m and more. The mean annual permafrost temperatures (MAPT) vary from -0.5 to -2.0ºC rarely to -5.0ºC. The permafrost-free flat surfaces of hilltops are the areas where snowmelt and rain waters percolate into the deeper rock horizons. In these areas the active layer in well-drained coarse sediments, and weathered bedrock is very deep (down to 5 m).

The long-term dynamics of precipitation regime and river discharge demonstrate a tight correlation during most of the year. However, they have opposite tendencies in June and September–October. This fact shows the complexity of water balance within the Southern Yakutia watersheds. Here the groundwater (interpermafrost and subpermafrost) storage and icings are important components of the regional discharge. Recently observed total increase in the annual amount of precipitation goes together with a relatively stable dynamics of evapotranspiration (Berezovskaya et al. 2005).

We suppose the principal factor of river discharge tendencies is an interaction between variable permafrost massifs and underground water-flow intensity. Such assertion has no evident analogs in recent investigation results and requires combined theoretical and field studies.

In this paper, we present some preliminary results of permafrost-hydrosphere interaction modeling.

Methods

Problem definition

We developed a schematization of permafrost-hydrogeological and meteorological conditions and governing pro-

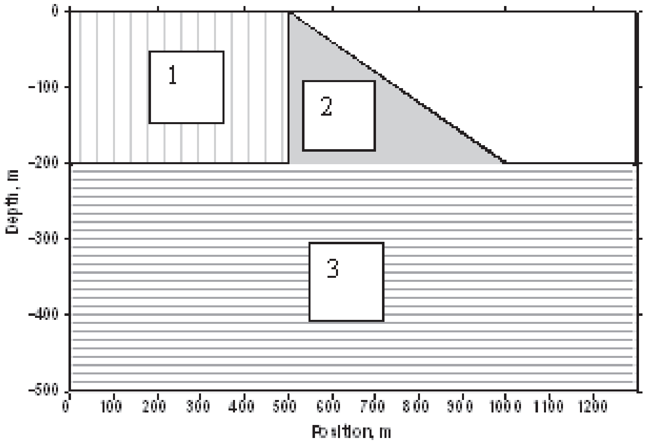

Figure 1. The geometry of the computational domain.

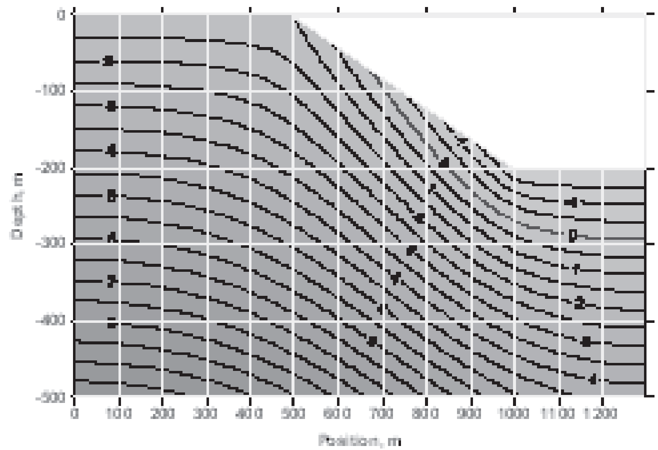

Figure 2. Temperature field without water-flow.

cesses that were used for the formulation of a mathematical model. This model allows the assessment of river discharge dynamics under the influence of permafrost and climate change in the upper part of the Lena River basin.

The hydrogeological setting depends on permafrost conditions. In spring and summer, the feeding of the groundwater takes place due to vapor condensation and percolation of snowmelt and rain waters through the vast watershed taliks situated on the flat hilltops. The vertical zones of air-dry fractured bedrock, periodical saturation, and constant saturation are located within unfrozen massifs of intensively fractured and weathered bedrock. The area and volume of the above-mentioned zones constantly change during the year. In spring, the snowmelt water and atmospheric precipitation start to infiltrate into and through a thick zone of airing (50–150 m and more) and increase the volume of saturation by the groundwater zone. The water movement is very fast and is accompanied by increasing water level in the massif of bedrock and by forming so-called infiltration knolls (reaching up to tens of meters in thickness). Groundwater feeding by atmospheric precipitation stops when the air temperature drops below 0°C in early winter and the active layer freezing starts. Starting from this moment, the gradual decrease of infiltration knolls begins. It is linked with groundwater discharge through open river taliks on the valley bottoms and icing forming. The groundwater transit pass way under the slopes is situated below the bottom of ice-bonded permafrost. This intensive flow of subpermafrost groundwater eventually forms a layer with high water permeability. However, in the lower parts of the slopes, the subpermafrost water head has a level up to 10 m above the permafrost table.

The analysis of available data shows that climate change can affect the groundwater recharge, out-flow, and discharge by the following factors or processes: (1) the expansion or contraction of the area of watershed open taliks; (2) a shift in the duration and timing of seasonal freezing and thawing that controls the time of infiltration and feeding of the groundwater reservoirs; and (3) changes in the amount of atmospheric precipitation.

In an epoch of climate warming and increased precipitation, we should expect the increase in the groundwater discharge in the valleys. There is a very important problem about the time lag of the pressure water waves. They form during the summer under the watershed divides and move toward the valley bottoms during the autumn and early part of the winter.

Research Strategy

The goal of the research presented here is to evaluate the impact of climate and permafrost changes on hydrological dynamics. To achieve this goal, we developed an efficient numerical method for solving coupled fluid flow and the phase-change heat transfer problem in porous media.

Because of the baffling complexity of the problem, the calculations were organized in three stages. *Foremost, we solved the two-dimensional heat transfer problem while taking into account the permanent continuous annual infiltration*. The goal of this stage was the retrieval of equilibrium spatial configuration of permafrost massif under condition of water flow in zones of suspended water and water saturation. In considered conditions, the influence of convective heat transfer on the permafrost develops not only because of the convective transport of the heat, but also because of the redistribution of the direction and intensity of the geothermal heat flow. As a result of this stage, the calculated configuration (geometry) of the permafrost massif in the computational domain was used as the base for the *second stage of modeling, when we are solving the phreatic flow problem with variable infiltration feeding*. In this case, the shape of the ice-bonded permafrost massif was assumed stable because the typical time of its change is much larger than the time scale of changes in the groundwater flow field. The model will allow understanding of the groundwater head level regime within the watershed divide taliks, the transfer of the head wave along the way of water flow under the permafrost, and water discharge dynamics in the valley during the year. Lastly, at *the third stage of modelin,g we plan to investigate the seasonal freezing as well as the full dynamics of the permafrost and taliks-configuration*

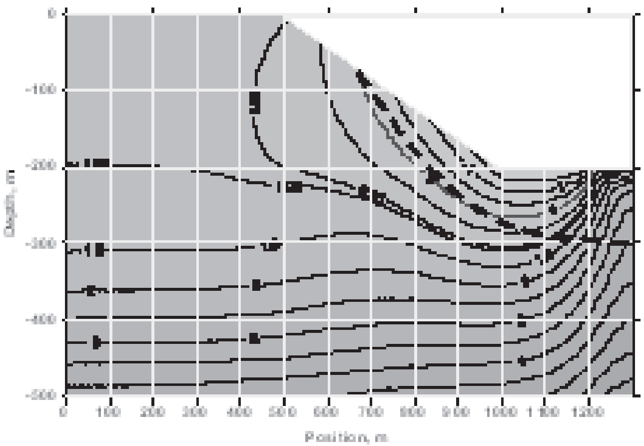

Figure 3.The temperature field in the run with a water-flow. The dashed line shows the zero-temperature isotherm for the run where the convection was not taken into account.

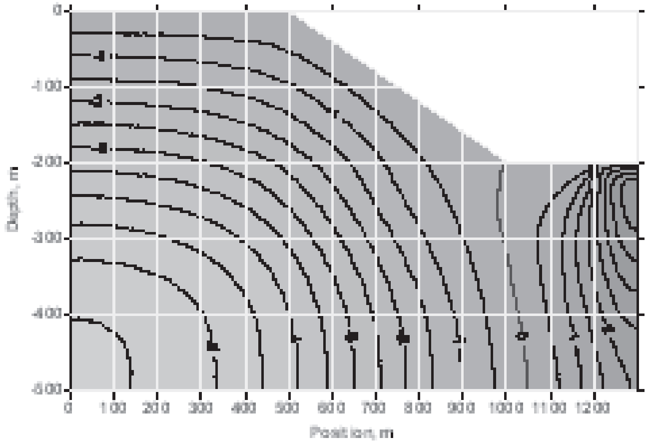

Figure 4. The difference in the temperature between "convective" and "conductive" runs.

development by taking into account the variability of climate and convective heat transfer in the bedrock. The seasonal freezing affects the period, the area, and the patterns of groundwater infiltration. The area of taliks within the watershed divide, and the amount of precipitation controls the volume of groundwater reservoir (storage).

Thus, these three stages of modeling will allow the obtaining of quantitative characteristics of the link between climate change and the hydrological dynamics within a typical site in the southern part of the Lena River basin.

Methods of Modeling and Assumptions

We performed the first stage of the modeling with the following principal simplification to describe the natural conditions. The original numerical model was prepared by G.Tipenko (Sergueev et al. 2003). We assumed that the temperature and water-flow fields can be represented by the two-dimensional vertical section across a river valley because of the elongated shape of the watershed divides. The hydrological and thermal physical properties of sediments and bedrock are sectionally continuous and isotropic.

Because the divide valley is symmetrical, we modeled a fragment between the vertical axis of the watershed divide and the center of an adjacent valley (Fig. 1). The geometry of this area corresponds to a real relief fragment near the town of Chulman in southern Yakutia. The calculation domain contains three blocks (Fig. 1). The width of the flat divide surface is 1000 m (block #1), the horizontal lengths of the slope is 500 m, and the valley depth is 200 m (block #2). The width of the valley's bottom is 600 m. The bottom of the computation area is at 300 m below the bottom of the valley and at 500 m below the top of the divide surface (block #3).

The position of low limit of permeability corresponds to the real data about zone of active water exchange in this region (about 200–300 m).

At the first stage of modeling we use some simplifications of real rules of the water migration. The zone of suspended water is replaced by the zone of full saturation (block #1). Within this zone an effective permeability of rocks was selected to ensure the correspondence to unit value of head gradient as in condition of descending water flow. Thus in condition of flow norm as W_{in} m/year the hydraulic conductivity in the zone of suspended water should be $k_f = W_{in}/365$ m/day (W_{in} is the rate of the infiltration).

The block #2 is water-impermeable because it represents permafrost; therefore there is not any infiltration in the upper part of the valley slope. This assumption explains the absence of the horizontal spread of water from the block #1.

The hydraulic conductivity of the seepage is determined by the reverse calculation from the shape of seepage level surface under the watershed divide under condition of infiltration. We use the value of transmissivity T = 45 m^2/day. This value corresponds to the hydraulic conductivity k_f = 0.15 m/day in condition of seepage thickness at 300 m. It corresponds very well with real mean conductivity of terrigenous rocks in southern Yakutia.

The left- and right-side borders of the computational area are "heat-proof" (zero value of heat flux in the "Second Type" boundary conditions). At the bottom of the computational domain, we set the heat flux q_{dp} = 0.043 W/m^2. At the upper boundary, we prescribed the "First Type" boundary condition as the temperature +1ºC at the hilltop divide surface and some rule of variability of temperature in the valley system. Within the entire bottom of the valley, the surface temperature was set at -2ºC. On the slopes, the temperature has a linear spatial trend from +1ºC on the limit of the hilltop divide surface to -2ºC at the foot of the slope. The chosen initial ground conditions values are theoretically typical for the area (Chizhov et al. 1975).

The surface of the slope and the lower and side limits of the computational domain are hydraulically impermeable. On the top of the divide and at the bottom of the valley we use the "First Type" hydraulic boundary conditions as head values that correspond to the altitude of the relief surface. The permafrost is also impermeable to water-flow in our model.

Results

To describe the influence of infiltration and convective heat transfer on the temperature field dynamics in the thawed zone, we implemented the plain conductive heat transfer computation as the first step of modeling. Here we did not have a riverbed talik in the valley. In this case, we obtained the maximal thickness of the permafrost at 93 m (Fig. 2).

At the second step of modeling, we increased the surface temperature in the 100-m band from the middle part of the river main channel in the valley up to +2ºC. This increase was held for a sufficient time for the occurrence of the riverbed talik as the zone of subpermafrost water discharge and icing formation that exists in reality.

At the third step of modeling, we resolved a coupled groundwater flow and phase-change heat transfer problem in porous media. The surface temperature in the middle part of the valley was +0ºC. The calculation was performed for the 10,000 yr time period to reach the new equilibrium for the temperature field (Fig. 3) and obtain the field of the water head that corresponds to the new geometry of the permafrost massif.

The numerical modeling resulted in following qualitative and quantitative conclusions. Because the descending cold infiltration water is directed toward the ascending heat flow, the watershed divides without permafrost became colder. This cooled area exists not only in the zone of suspended water, but also in water-saturated rock massif up to 200 m below the surface of saturation. This effect is a result of high importance of the vertical component of the water flow in the area between model blocks 1 and 3 where the groundwater flow changes its direction. As a result, a non-gradient temperature field was formed in the zone of suspended water.

The migration of groundwater from cooled divide massif to the valley was accompanied by temperature decrease under the slope and increase in permafrost thickness there. In the valley the convective open talik became stable, and temperature around it increased in comparison with the case without convective heat transfer. This change was not only a consequence of the convective heat flux, but also a result of decrease in the geothermal heat flux from the lower part of the calculation domain because it was shifted from the watershed to the valley.

The influence of the water-flow on the temperature field was illustrated by calculation of the difference between "convective" and "conductive" runs (Fig. 4). The considerable decrease in the temperature in the zone of descending groundwater flow and vertical heat flux from the bottom was obviously noticeable (left part of the figure). On the contrary, in the zone of water discharge into the riverbed talik, the temperature increased (right part of the figure). The separation zone, where the influence of the water-flow on the temperature is insignificant, was located under the lower part of the slope.

Conclusion

The basic conclusion from our numerical modeling is that *even at large depth the temperature distribution and the permafrost configuration (geometry) are sensitive to the percolation of surface water from snowmelt and from liquid precipitation and to amount and pass ways of groundwater infiltration within the thawed zones in sediments and fractured bedrock*. As a result of permafrost degradation related to climate warming, the areas of groundwater feeding and the reservoir capacity of fissured/fractured bedrock increase in size and the river discharge changes.

Considered mechanisms of interaction between permafrost and underground discharge have a regional importance.

We are planning to study these effects during the next stage of modeling. The model must be calibrated using real hydrological and hydrogeological data. A proposed approach could be used to explain the complicated picture of real tendencies in relationships between changes in atmospheric precipitation and river discharge.

Acknowledgments

This work is supported by grants from NASA THP Discovery Investigation "Current climate changes over Eastern Siberia and their impact on permafrost landscapes, ecosystem dynamics, and hydrological regime" and "Permafrost Dynamics within the Northern Eurasia Region and Related Impacts on Surface and Sub-Surface Hydrology" and by research grants from the Russian Fund of Basic Research (#06-05-64959a and 05-05-64390a).

References

Berezovskaya, S., Yang, D. & Hinzman, L. 2005. Long-term annual water balance analysis of the Lena River. *Global and Planetary Change* 48: 84-95.

Chizhov, A.B., Buldovich, S.N. & Chizhova, N.I. 1975. Hydrogeological condition of Chulman Depression. In: *Southern Yakutia*. MGU Publ: 291-311 (in Russian).

Sergueev, D., Tipenko, G., Romanovsky, V. & Romanovskii, N. 2003. Mountain permafrost thickness evolution under influence of long-term climate fluctuations (results of numerical simulation). *Proceedings of the Eighth International Conference on Permafrost, Switzerland, July 2003*, 2: 1017-1021.

Permafrost Distributions on the Seward Peninsula: Past, Present, and Future

Robert C. Busey
International Arctic Research Center, University of Alaska Fairbanks, USA

Larry D. Hinzman
International Arctic Research Center, University of Alaska Fairbanks, USA

John J. Cassano
UC Boulder, Colorado, USA

Elizabeth Cassano
UC Boulder, Colorado, USA

Abstract

Current observations show the Seward Peninsula sits on the margin of the continuous/discontinuous permafrost transition in western Alaska, U.S.A. This region of subarctic Alaska could be viewed as a proxy for a warmer Arctic, due to the broad expanses of tussock tundra, invading shrubs, and fragile permafrost. With average annual air temperatures just below freezing and very warm permafrost, the area is susceptible to dramatic change in response to a warming climate. Ground temperatures were estimated using observed meteorological and GCM-simulated forcing of the TTOP soil temperature model, making it possible to investigate the potential rate and mechanisms of change in frozen ground distribution past, present, and future.

Keywords: climate change; IPCC projections; numerical soil temperature model; permafrost; TTOP.

Introduction

The Seward Peninsula of Alaska, USA is located in the western part of the state (Figure 1). As estimated by the International Permafrost Association (2003), the northern part of the peninsula is underlain by continuous permafrost while the southern part, with its higher mean annual air temperatures and a maritime coast, is underlain by discontinuous permafrost.

Villages on the peninsula are located primarily near the coast, but many subsistence activities take place in the interior. Active local economic development includes placer and hard rock gold mining, as well as reindeer herding. Future mining will create a need for a denser road network. With ground underlain by warm permafrost, the economic cost of maintaining current and establishing new infrastructure is expected to rise in a warmer climate due to thawing of permafrost. The economic future of the peninsula is dependent on an accurate projection of permafrost distribution and state.

Permafrost sensitivity is affected by changes in a transitional climate and will shape the economic future on the peninsula. In this paper, permafrost extent is estimated for three periods: the early 20th century, the early 21st century, and the late 21st century using the TTOP numerical model.

Methods

Detailed knowledge about permafrost is difficult to ascertain without extensive research. To develop a better understanding of permafrost distribution on the larger scale we often use models. A model is a way of simplifying the complex natural environment into something more manageable.

In this study, permafrost thermal composition on the Peninsula is estimated using the TTOP numerical model with a spatial resolution of 100 m. The TTOP model is one way of determining the thermal offset between the ground surface and the top of the permafrost table (Smith & Riseborough 1996). TTOP was originally developed by Smith & Riseborough (1996) and is an equilibrium numerical model, which assumes quasi-steady state conditions for each year (Riseborough 2007). The TTOP model was selected because it is numerically efficient so performing calculations over a large domain such as the Seward Peninsula at a relatively high horizontal resolution is not an obstacle. In this study, to reduce the impact of interannual climate variation, several years are averaged together. The three time periods modeled in this study show thermal change over centennial scales. The components of the thermal offset calculation are outlined in Equation 1 below.

$$
\begin{aligned}
T_T &= \frac{n_T k_T I_{AT} - n_F k_F I_{AF}}{k_F P}, T_T < 0 \\
T_T &= \frac{n_T k_T I_{AT} - n_F k_F I_{AF}}{k_T P}, T_T > 0
\end{aligned} \tag{1}
$$

In Equation 1, T_T is the temperature at the top of the perennially frozen or unfrozen ground (°C). Each variable on the right-hand side of Equation 1 is a function of spatial position except the annual cycle (365 days), P. I_{AT} and I_{AF} are the annual air temperature thawing and freezing indices (°C-days), which are calculated for each time period using another model, MicroMet—a quasi-physically-based program that uses climate forcing to distribute meteorological parameters across a physical domain and will be described in more detail below (Liston & Elder 2006). The annual freezing index is the summation of mean daily air

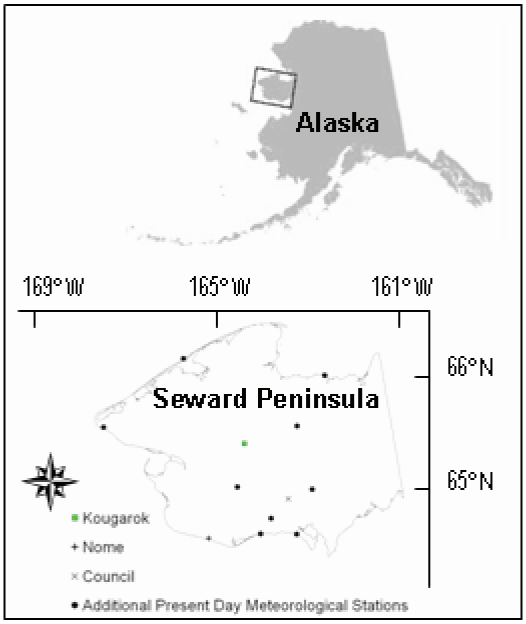

Figure 1 The study area, Seward Peninsula in Western Alaska, USA. Model comparison data are from Kougarok, the square in the interior of the Peninsula. Verification data comes from Kougarok and Council, the *x* symbol in the interior of the peninsula. Nome, the largest community on the peninsula, is the + symbol along the southern coast of the peninsula.

temperatures below freezing at a single point for a one-year period. The annual thawing index is the sum of average daily air temperatures above freezing over the year. N-factors are a way of relating air temperature to soil surface temperature, simplifying the heat transfer relationship between air and the soil surface (Lunardini 1978). N-factors parameterize effects such as radiative heating, evaporative cooling in summer, or snow insulation in winter. For the above freezing and below freezing air-soil surface interface relationship, n-factors are represented as n_T and n_F, respectively (Lunardini 1978). In this study, these two components vary as a function of the primary vegetation group in each cell. In the TTOP equation, thawed and frozen bulk thermal conductivities of the soil in the active layer are represented by k_T and k_F. These two thermal conductivity parameters vary spatially across the peninsula and are based on values from a soil classification map created by the Natural Resources Conservation Service (Van Patten 1990). The next several sections will discuss these components in more detail.

To calculate the annual freezing and thawing air temperature indices across the peninsula (I_{AT} and I_{AF} from Equation 1), the program MicroMet was used. MicroMet is a quasi-physically-based meteorological forcing model (Liston & Elder 2006). MicroMet distributes common meteorological variables, like air temperature, relative humidity, precipitation (solid and liquid), wind speed, and wind direction, across a physical domain. Originally developed for a domain on the North Slope of Alaska, it has been used successfully in other Arctic areas and locations around the world (Liston & Elder 2006). Quasi-physically-based means the point data (e.g., from a meteorological station) are adjusted through physical parameterizations to a common elevation of sea level when appropriate, such as with air temperature. Next, these point data are gridded horizontally across the domain using the Barnes objective distribution scheme (Barnes 1973, Koch et al. 1983). Finally, the interpolated data are adjusted vertically back to a realistic topographic distribution using the model and elevation data from the digital elevation. In this study, MicroMet distributes the meteorological data daily in one-year intervals. At the end of each one-year period the annual freezing and thawing air temperature indices (I_{AF} and I_{AT}) are calculated for each point in the Seward Peninsula domain.

GIS components

When applying the TTOP equations across the Seward Peninsula domain several variables vary spatially. Both MicroMet and TTOP use a Digital Elevation Model (DEM) with the same 100 m horizontal resolution. In addition, a vegetation map is used both by MicroMet (for solid precipitation distribution) and TTOP (the n-factor values are a function of vegetation type). The plant types in this digital map include three types of tundra in varying degrees of wetness, forest, shrub land, water bodies, and barren lands (Thayer-Snyder 2005). The vegetation type in each pixel controls the n-factors (n_t and n_f in Equation 1). Surface n-factor relationships in each vegetation class are primarily calculated using several years of data collected by our established long-term meteorological stations (http://www.uaf.edu/water/projects/atlas/atlas.html) on the peninsula and are supplemented with n-factor values compiled by Lunardini (1978).

The U.S. Natural Resources Conservation Service (NRCS) completed an extensive soil examination covering the Seward Peninsula area (Van Patten 1990). This digital map of peninsula soils serves as the basis for estimating subsurface thermal properties (k_t and k_f in Equation 1). These data are generally qualitative and are divided into 24 landscape groups. In the report, each landscape group has at least one subsurface soil profile typical to that class. To make this map useful in the permafrost extent modeling, quantitative data collected by Ping et al. (2005) was used to estimate thermal conductivity of the mineral soils identified by Van Patten (1990). Using the mineral content of the soil from Ping et al (2005), bulk thermal conductivity over the active layer was estimated using Johansen's method outlined in Farouki (1981). In addition, surface vegetation and subsurface organic layer thermal conductivity were measured by our group during the 2007 field season on the northern part of the peninsula. These values were used for all organic soils mentioned in the typical soil profiles of Van Patten (1990). Frozen organic thermal conductivity is estimated using prior work by Hinzman et al. (1991).

Early 20th century permafrost extent

For the early 20th century permafrost distribution, a single meteorological record from the peninsula (Nome) is available from the National Climate Data Center. Using

MicroMet, annual freezing and thawing air indices for the hydrologic years 1908 to 1918 are calculated. The mean annual air temperature over this period for the Kougarok site is -2.9°C. Since there is just a single point in the domain, MicroMet performs only a vertical temperature adjustment (using the adiabatic lapse rate) across the peninsula. The period 1908 to 1918 was chosen as the earliest continuous segment in the Nome period of record. In summer when sea ice is absent, Nome has a maritime climate rather than the continental climate that is typical of the interior of the peninsula. Temperatures in Nome are also warmer compared to the northern coast of the peninsula. Using only one station observation therefore leaves considerable uncertainties, but it is the only record available for this era.

Present-day permafrost extent

Present-day permafrost extent is estimated using data from significantly more meteorological stations in the region. Data sources include the Natural Resources Conservation Service (NRCS) Snow Telemetry (SNOTEL) sites, Bureau of Land Management (BLM) Remote Automated Weather Stations (RAWS), National Weather Service (NWS) sites, and University of Alaska Fairbanks Water and Environmental Research Center (WERC) sites.

All of these sites record hourly air temperature, relative humidity, wind speed, and wind direction. Additionally, many, but not all, log precipitation. The period of interest is an average of the hydrologic years 2001 to 2004 with the mean annual air temperatures over this period -3.2ºC (Table 2). The recent period was selected because a number of new meteorological stations came online during this time compared to the previous decade.

Late 21st century permafrost extent

Permafrost temperatures at the end of the 21st century are estimated using output from the 13 Intergovernmental Panel on Climate Change (IPCC) fourth assessment report (AR4) General Circulation Models (GCMs) (2007). See Table 1 for a list of the GCMs. These models show considerable variability in their climate projections. For example, at the Kougarok K2 station grid point, the intermodel variation in mean air temperature ranged from -8.7°C (FGOALS 1.0g) to 4.6°C (IPSL CM4). The climate forcing for the GCM output is based on the SRES A1B scenario and encompasses the interval 2092 to 2100 with the exception of the NCAR model, which has an interval of 2092 to 2099. The A1B scenario is driven by technological and economic advancement across the globe with a balanced increase in energy use. Grid points from the GCM output located over the Seward Peninsula are used by MicroMet to downscale meteorological parameters on the peninsula.

For the future distribution experiments, MicroMet is run with data from each GCM individually. An average temperature at the top of the permafrost for each GCM is computed and then averaged over the decade to smooth interannual variability. Finally, a multi-model mean of these late 21st century runs is computed for brevity.

Table 1. IPCC AR4 Models used for late 21st century extent and mean air temperature over the period 2092 to 2100 at Kougarok site K2.

IPCC SRES A1B GCMs	Mean Air Temperature, Degrees Celsius
Canadian Centre for Climate Modelling and Analysis (Canada) CGCM 3.1	2.7
Centre National de Recherches Météorologiques (France) CNRM CM3	-3.2
Commonwealth Scientific & Industrial Research Organization (Australia) Mk 3.0	0.6
Geophysical Fluid Dynamics Laboratory (USA) CM 2.0	-1.7
Geophysical Fluid Dynamics Laboratory (USA) CM2.1	-0.3
Goddard Institute for Space Studies (USA) AOM	-0.4
Goddard Institute for Space Studies (USA) Model E R	-4.7
Institute of Atmospheric Physics (China) FGOALS 1.0g	-8.7
Institut Pierre Simon Laplace (France) IPSL CM4	4.6
Center for Climate System Research (Japan) 3.2 medres	0.3
The Max Planck Institute for Meteorology (Germany) Echam 5	-1.3
Meteorological Research Institute (Japan) MRI CGCM2.3.2a	-4.9
National Center for Atmospheric Research (USA) NCAR CCSM3.0 (2092–2099 mean)	-0.7

Results

Permafrost temperatures for the early 21st century (2001–2004) are shown in Figure 2. For verification, observed temperature data from two pairs of meteorological stations operated by WERC in Kougarok and Council were compared to the calculated TTOP model results for the present TTOP model output. Kougarok and Council are located in the interior of the peninsula as seen in Figure 1. These four sites are located in three different vegetation types as well as three separate soil classes. A Mann-Whitney *U* test, similar to Student's *t* test but more appropriate for these data, is true at the 0.1 significance level, suggesting good agreement between the calculated TTOP temperature and the observed top of permafrost temperature. With regard to the precision of the modeling results, the mean absolute error is 1.8°C. Site-specific information is shown in Table 2, which is an overview of the climate and permafrost temperatures at one of the Kougarok sites.

In Figure 2, areas with above-freezing TTOP temperatures, which could indicate a talik below the active layer and thawing permafrost or a permafrost-free area, are generally limited to mountains and related features. However, in the south, some areas with a thicker organic base are also estimated to be experiencing thaw.

Table 2. Climate statistics at Kougarok site K2.

K2 Site	Mean Annual Air Temperature	Observed TTOP	Calculated TTOP	Difference (Observed – Calculated)
		Degrees Celsius		
2001	-2.5	-3.7	-3.0	-0.7
2002	-4.4	-2.7	-4.6	1.9
2003	-2.1	-2.5	-3.0	0.4
2004	-3.7	--	-4.6	--

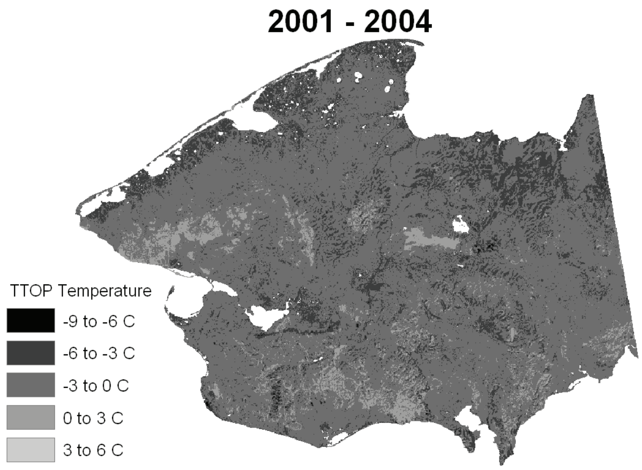

Figure 2. Present-day estimated permafrost temperatures.

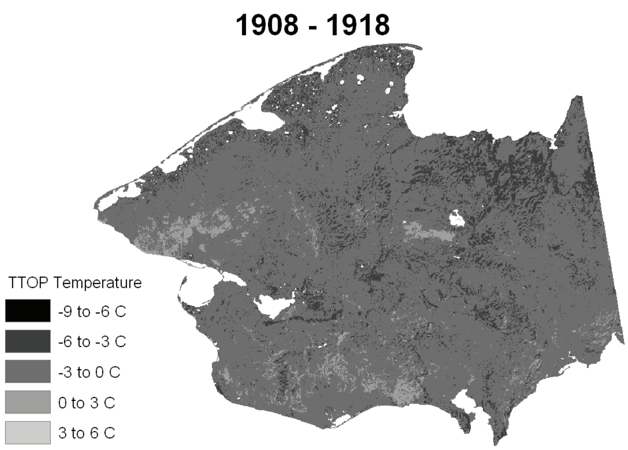

Figure 3. Early twentieth century estimated permafrost temperatures.

One current MicroMet limitation is the lack of an algorithm for calculating wintertime temperature inversions. If included, there would potentially be more land surface estimated as underlain by continuous permafrost in the interior. Winter temperature inversions occur when air temperatures are well below freezing and there has been no wind, which allows air temperatures to stratify vertically with the coldest temperatures at the lowest elevations. Steep thermal gradients develop until the wind mixes the air column again. This is not expected to be a major limitation, as the Seward Peninsula seldom experiences calm winds for extended periods. It is possible that for estimating present

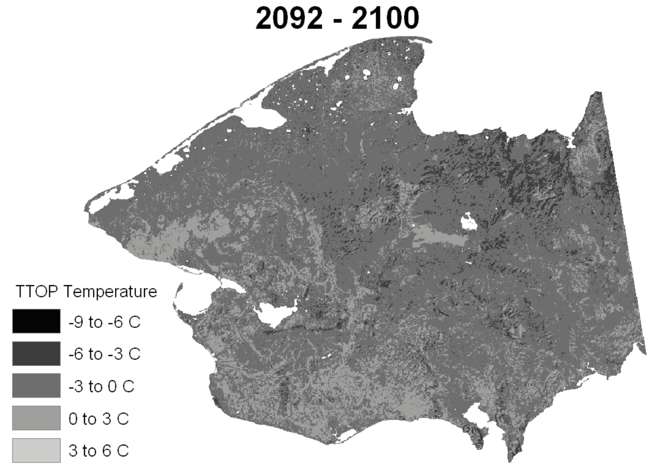

Figure 4. Late 21st century estimated permafrost temperatures.

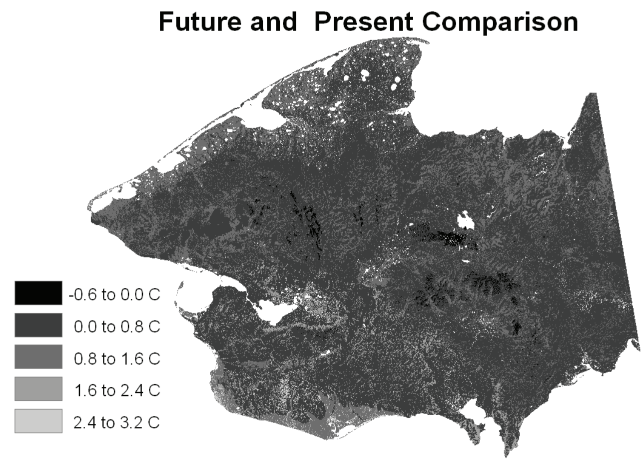

Figure 5. Temperature difference between the future distribution and the present distribution. Higher temperatures represent warmer future conditions.

extent satellite measured ground surface temperatures could allow consideration of winter inversions in future research.

Modeled permafrost temperatures for the early 20th century (1908–1918) displayed in Figure 3 are similar to the present day TTOP results (Fig. 2). In reality the TTOP temperatures for this earlier time should be a bit lower due to using a single weather station in Nome as the only climate forcing point in the domain used by MicroMet. Points further north in the interior would better capture the continental climate for the landscape away from the ocean. Additional experiments are planned to test this hypothesis. Another similarity to the present is that only the mountainous areas, which are dominated by coarse mineral soil, are thawed or thawing. This is probably related to the reduced water content in these coarse soils and the corresponding higher thermal conductivity compared to the valley bottoms, where there is a thick layer of organic mat above the fine-grained mineral soil. About 8% of the area has TTOP temperatures above freezing.

In contrast, permafrost extent for the end of this century (2092–2100) shown in Figure 4 based on the IPCC SRES A1B scenario shows much warmer temperatures across the peninsula. Much of the near-surface landscape in the south and low-lying areas will likely have temperatures at the base of the active layer rise above freezing.

A summary figure comparing the difference between the late 21st century results of the IPCC SRES A1B scenario to the present estimated TTOP temperatures is shown in Figure 5. A plot comparing the early 20th century permafrost temperatures to the present is not shown because the temperatures were similar. In Figure 5, the greatest difference in temperature is concentrated along the coasts. Several small areas in Figure 5 show colder temperatures between the future and the present. These are high in the mountains and are probably skewed by the IAP FGOALS 1.0 g GCM, which predicts future air temperatures 5° colder than the present. Additionally, the increase of thawing landscape between now and the future begins to encompass more of the lower, flatter terrain that is also ice-rich. Charon (1995) estimated permafrost thickness on Cape Espenberg, the northernmost part of the peninsula, to be 158 m. Thus, permafrost is unlikely to thaw completely, but the surface conditions, where there is the highest diversity of plants and organisms, will change.

Conclusion

Permafrost temperatures over the Seward Peninsula of Alaska were modeled over 3 time intervals approximately 80 years apart. Early 20th century simulated permafrost conditions are similar to current estimated permafrost temperatures. When conducting numerical modeling, it is important to start with a simulation that estimates the present conditions well. Comparison of permafrost temperatures modeled with TTOP to observations from four UAF WERC climate stations on the peninsula shows they are statistically similar. In the future, permafrost degradation is likely to accelerate (Fig. 5). This will probably result in additional thermokarst development, because much of the areas predicted to warm are ice-rich valley bottoms. Higher permafrost temperatures and unfrozen talik formation will likely have a mixed effect on local industry, such as mining and reindeer herding, on the peninsula. The logistics of getting to these locations will increase in difficulty, since road maintenance costs are likely to be higher.

Acknowledgments

Support for this research was provided by the U.S. National Science Foundation under the Arctic System Science Programs (Grant Number OPP-0328686 and OPP-0229649). We would like to thank the people of the Seward Peninsula for assisting us in conducting this research. We also acknowledge international modeling groups for providing their data for analysis and the Program for Climate Model Diagnosis and Intercomparison for collecting and archiving the model data.

References

Barnes, S.L. 1973. *Mesoscale Objective Analysis Using Weighted Time-series Observations*. NOAA Tech. Memo. ERL NSSL-62, National Severe Storms Laboratory, Norman, OK 73069, 60 pp. [NTIS COM-73-10781].

Charon, S.D. 1995. *Changes in late Pleistocene and Holocene sedimentation, North Killeak Lake, Bering Land Bridge, National Preserve, Western Alaska.* M.S. Thesis, University of Massachusetts Amherst.

Farouki, O. 1981. *Thermal Properties of Soils.* U. S. Army Cold Regions Research and Engineering Laboratories, Hanover, NH. CRREL Monograph 81-1.

Hinzman, L.D., Kane, D.L., Gieck, R.E. & Everett, K.R. 1991. Hydrologic and thermal properties of the active layer in the Alaskan Arctic. *Cold Regions Science and Technology* 19: 95-110.

International Permafrost Association Standing Committee on Data Information and Communication (comp.). 2003. *Circumpolar Active-layer Permafrost System, Version 2.0.* M. Parsons & T. Zhang (eds.). Boulder, CO: National Snow and Ice Data Center/World Data Center for Glaciology. CD-ROM.

IPCC. 2007. *Climate Change 2007: The Physical Science Basis. Contribution of Working Group I to the Fourth Assessment Report of the Intergovernmental Panel on Climate Change.* S. Solomon, D. Qin, M. Manning, Z. Chen, M. Marquis, K.B. Averyt, M. Tignor & H.L. Miller (eds.). Cambridge, United Kingdom and New York, NY, USA: Cambridge University Press, 996 pp.

Koch, S.E., DesJardins, M. & Kocin, P.J. 1983. An interactive Barnes objective map analysis scheme for use with satellite and conventional data. *J. Clim. and Appl. Meteorol*. 22: 1487-1503.

Liston, G.E. & Elder, K. 2006. A meteorological distribution system for high-resolution terrestrial modeling (MicroMet). *Journal of Hydrometeorology* 7: 217-234.

Lunardini, V.J. 1978. Theory of n-factors and correlation of data. *Proceedings of the Third International Conference on Permafrost, Edmonton, Alberta, July 10–13, 1978:* 41-46.

Ping, C., Michaelson, G.J. & Dai, X.Y. 2005. *NSF-ATLAS Winter C-flux Project.* URL: http://www.joss.ucar.edu/atlas/seward_cd/tables/group_ps.htm. Boulder, CO, variously paged. November 2

Riseborough, D.W. 2007. The effect of transient conditions on an equilibrium permafrost-climate model. *Permafrost and Periglacial Processes* 18: 21-32.

Smith, M.W. & Riseborough, D.W. 1996. Permafrost monitoring and detection of climate change. *Permafrost and Periglacial Processes* 7: 301-310.

Thayer-Snyder, C.R., Maier, H.A & Walker, D.A. 2005. *A Preliminary Landsat MSS-Derived Land-Cover Map of the Seward Peninsula, Alaska.* http://www.geobotany.uaf.edu/. Fairbanks, AK, variously paged. November 2

Van Patten, D. 1990. *Soil investigation of Seward Peninsula area, Alaska*. USDA-NRCS (SCS). U.S. Gov. Print. Office, Washington, DC.

Soil and Permafrost Properties in the Vicinity of Scott Base, Antarctica

I.B. Campbell
Land & Soil Consultancy Services, Nelson, New Zealand
G.G.G.Claridge
Land & Soil Consultancy Services, Nelson, New Zealand

Abstract

The southern tip of Ross Island is the location of two bases: Scott Base and McMurdo Station. The soils in this area are formed from thin volcanic drift over volcanic bedrock materials, and the active layer averages around 30 cm thick. The permafrost is predominantly ground ice, but ice wedges are present and extend into the volcanic bedrock. Extensive ground surface modifications have resulted in loss of permafrost ice, the formation of hummocky and patterned ground, and extensive surface soluble salt precipitation. Low albedo contributes to soil warming and moisture evaporation. Chemically, the soils are influenced by their proximity to the sea. They contain small amounts of soluble salts and are strongly alkaline. They are very little weathered and most of the clay fraction is derived from mechanical rock breakdown. Significant contaminations with heavy metals, wood, metal and fabric materials, and hydrocarbons have resulted from human occupation.

Keywords: Antarctic permafrost; Antarctic soils; human disturbance; Ross Island; Scott Base.

Introduction

Ross Island is a large volcanic island (area approximately 1350 km^2) situated at the southern margin of the Ross Sea and at the edge of the Ross Ice Shelf (Fig. 1). It comprises several extinct volcanoes and the active Mt. Erebus, 3740 m in elevation. Small ice-free areas occur in eastern and northwestern coastal areas (the location of several penguin rookeries), around the central summit crater, and at the southern tip of the island at the end of the narrow Hut Point Peninsula. Permanent research station occupation was established on the southeastern end of Hut Point Peninsula at Scott Base and at McMurdo Station on the southwestern end (some 4 km apart) in 1956/57 but at that time, little consideration was given to the nature of the soils, the permafrost or other environmental issues that are at the forefront today.

Since establishment of these bases, considerable land surface changes have occurred through construction of roads and pipelines, ground surface leveling for building sites and storage of materials, installation of communications, and extensive ground scraping for aggregate requirements, coupled with retreat of snow and ice cover. These have dramatically altered the original permafrost conditions in the modified areas.

The advent of the Antarctic Treaty (1959) and the Protocol on Environmental Protection to the Antarctic Treaty System (1991) have now provided a framework within which environmental management is expected to occur. This report gives an outline of the soil and permafrost conditions observed in the southern Ross Island area to provide a basis for future management considerations. Information and data have been obtained from general observations since the 1970s as well as from experimental, soil sampling, and monitoring activities through the 1990s.

Environmental Background

Ross Island is part of the McMurdo Volcanics Group, the rocks at Hut Point Peninsula being primarily scoriaceous flows and tuffs around 1.5 my old (Kyle 1981). The present hilly topography has been little modified by glacial erosion and is largely inherited from the previous volcanic activity with cones and craters forming distinctive local features. The soil forming material is a patchy thin cover of till, dominated by fragmental volcanic rock with a stony sandy gravel texture that becomes coarser with increasing depth (Table 1). Small partly rounded basaltic clasts are sometimes present, and also some granite and sandstone in the upper horizons. The latter rock materials are believed to be derived from the mainland, some 70 km to the west during the last glacial period (Ross Glaciation, Denton et al. 1971) when ice filled McMurdo Sound and covered Hut Point Peninsula.

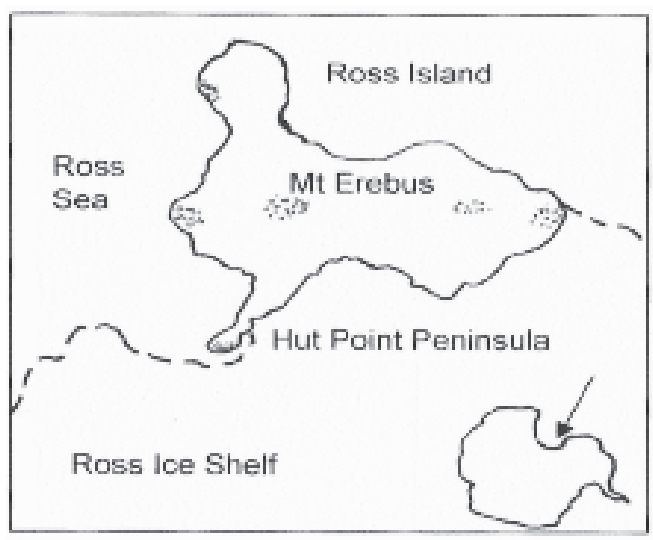

Figure 1. Location map. Scott Base is situated on the southeastern end of Hut Point Peninsula. Dotted areas are bare ground locations.

Table 1. Particle size fractions for a typical soil from volcanic materials near Scott Base.

	Weight fractions % of whole soil				
Depth cm	75 -2mm	75 -20mm	20 -5mm	5 -2mm	<2mm
0-0	42	4	18	20	58
0-7.5	56	37	19	--	44
7.5-15	65	36	10	19	35
15-30	74	46	12	16	26
30-45	61	34	13	14	39

Figure 2. Average active layer thickness and active layer and permafrost H_2O% (gravimetric) for 21 dry sites (left) and 21 wet sites (right).

The major features of the climate of the Hut Point Peninsula area are a mean annual temperature of -20°C at Scott Base (-18°C at McMurdo) and precipitation equivalent of about 200 mm. Temperatures average from around -30°C in winter months to -4°C in December and January but with occasional days in which summer temperatures may reach +6°C. Precipitation is difficult to assess accurately as much snow accumulates as drift from surrounding sea ice. Periodic summer snowfalls occur, however. Much of the landscape is snow covered in early December with maximum thaw taking place by late December to early January. The December/January thaw period is usually accompanied by small water flows from thawing snow banks, etc., but most of the snow is lost by ablation with only occasional surface soil moistening. Vegetation is restricted to sparse moss and lichen patches.

Soils

The soils of the Hut Point Peninsular area are unweathered and belong to weathering stage I which includes soils less than 50,000 years old (Campbell & Claridge 1975, 1987). They typically have a boulder or pebble pavement of angular scoriaceous basalt which is unweathered apart from a patina or thin varnish that gives upper black coloured clast surfaces a distinct luster. Ventiforms are absent although some clast abrasion is occasionally seen. The undersides of surface clasts commonly have a thin grayish brown calcareous coating and occasionally a thin precipitate of soluble salts. The carbonate was thought to have been derived from wind-deposited dusts originating from the mainland (Blakemore & Swindale 1958) but given the granite erratics that are present and the known fluctuations of the Ross Ice Shelf, the carbonate may have originated from the till materials. Below the stony surface pavement, the soil is grayish brown (10YR 5/2-2.5Y5/2) loose sandy stony gravel with the coarse fraction increasing with depth (Table 1).

Figure 3. Ice wedge formed in tuffaceous volcanic bedrock in a cut section for pipeline construction, near Scott Base.

A weakly-developed vesicular structure, formed as a result of freezing when the soil is moist, may be present in the top few centimeters. The soil passes abruptly into hard ice-cemented and unweathered permafrost. The active layer thickness ranges from near ground surface alongside permanent snow patches to around 60 cm on well-drained windy surfaces that have little snow accumulation. In well-drained sites, the soils have a low moisture content (gravimetric), averaging around 0.5% in the surface horizon and increasing with depth to around 8% above the permafrost.

Permafrost Properties

Physical characteristics

The permafrost in the Hut Point Peninsula region has been observed in the course of a number of investigations including general soils investigation, leaching and contamination studies (Claridge et al. 1999, Sheppard et al. 2000), from experimental disturbance of permafrost (Balks et al. 1995), as part of long-term monitoring studies (Paetzold et al. 2000), and from casual observations during domestic activities.

Examinations from shallow drilling (approximately 1.5 m deep) showed that the average depth of the permafrost table was approximately 30 cm at well-drained sites such as ridge surfaces (Fig. 2). In gullies or nivation cirques where water flows are occasionally present, the active layer thickness averaged 18 cm. At the edge of a permanent snow pack, the permafrost table was at the ground surface but increased to 20 cm some 20 m from the snow pack. The frozen water content (gravimetric) of the permafrost increases from around 10% near the permafrost table to 140% at greater depths with ice layering commonly occurring as ground ice. Our shallow drilling revealed that ground ice was present in the volcanic rock below the cover materials, with ice wedges and sand wedges being observed in the volcanic bedrocks in excavated

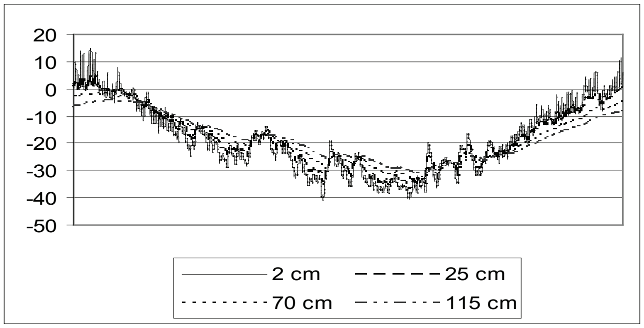

Figure 4. Hourly plots of temperatures (°C) at four depths in 2002 from the CALM site near Scott Base.

roadway sections (Fig. 3). In some places, massive stagnant ice was observed in exposures where regolith removal had given rise to accelerated thaw and ground slumping.

Thermal characteristics

Soil temperature plots from hourly measurements in 2002 at a CALM recording site near Scott Base (Paetzold et al. 2000) are shown in Figure 4. Mean annual soil and permafrost temperatures at four of the depths (2, 25, 70, and 115 cm) from which temperatures were recorded are all similar (approximately -18°C) and are close to the mean annual 1992 air temperature recorded at the site (-19.3°C). The 2 cm depth temperatures range from 14.2°C (January 11) to -40.7°C in mid June. At 115 cm, (approximately 85 cm below the permafrost table, the annual temperature ranged from -4°C to -19°C. At the 2 cm depth, there were 45 freeze/thaw cycles through the period from December 2 to January 31 with soil temperatures remaining above 0°C periodically for 15 days. As soil warming commences after the winter minimum temperatures, the temperature at all depths is briefly isothermal (-23°C) around late August and again in late February when the temperature was -6°C (Fig. 4). In summer months, diurnal temperature changes may reach 16°C while in winter months temperature changes in excess of 20°C occur over short periods due to weather events.

Experimental soil and permafrost disturbance

The moisture content, evaporation rate and soil radiation balance were investigated at an experimental site near Scott Base in January, 1994 (Balks et al. 1995, Campbell et al. 1997). The active layer (approximately 30 cm) was removed from 300 m^2 of eastward-facing, gently-sloping ground and observations were made and compared with those from an undisturbed immediately adjacent similar-sized area.

Observations from neutron probe access tubes to 1.2 m depths in the undisturbed sites showed low moisture contents in the active layer, very high ice contents in the upper part of the permafrost, and decreasing amounts with increasing depth. At the disturbed site, thawing of the permafrost began immediately with some of the thaw water apparently accumulating in the upper permafrost zone, judged by the neutron probe measurements which showed considerably higher moisture/ice contents compared with the undisturbed site. Over the following six years, ice was lost from the disturbed site at a diminishing rate as measured by the amount of ground shrinkage against the access tubes (Fig. 5).

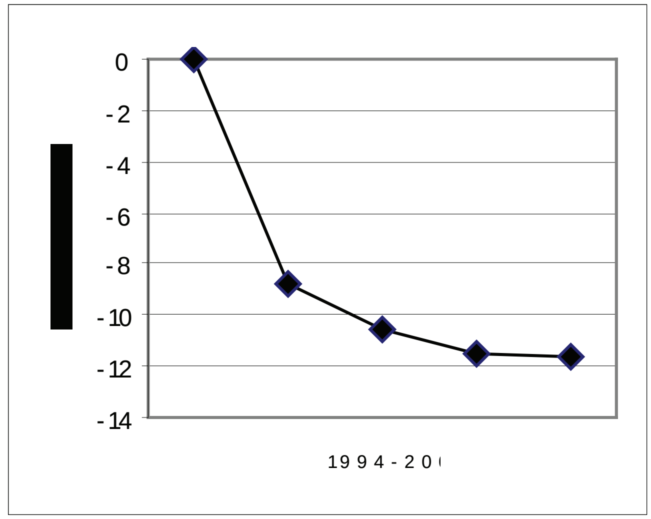

Figure 5. Average ground shrinkage values for 7 tube sites over 6 years at an experimental site near Scott Base.

Evaporation rates were measured on undisturbed and the disturbed soil using small lysimeters over six days (Balks et al 1995). For the undisturbed dry soil, the evaporation loss was less than 0.1 mm/day and 1.1 mm/day at a site that was wetted from an adjacent snow melt. For the disturbed soils, initial evaporation rates of 1.5 mm/day and 3 mm/day were measured, but these rates declined as the soil surface became lighter-coloured on drying. These rates are similar to those observed in moist soils in the Dry Valley region (Campbell 2003).

The soil radiation balance was also measured at the disturbed and undisturbed sites (Balks et al. 1995, Campbell et al. 1997) over four days, and albedo measured during the 3-hour period of highest solar angle averaged 0.048 on the undisturbed surface with a similar value on the moist disturbed surface. On the dried disturbed surface, the values averaged 0.112 with more solar radiation being reflected from the disturbed dry surface than the undisturbed and the disturbed moist surface.

Disturbances caused by logistical activities

Soil and permafrost disturbance from logistical activities are widespread in the southern Hut Point Peninsula area and have primarily been caused by ground scraping to provide fill material for construction sites. In some places, only shallow scraping occurred with the active layer being removed but at other sites, repeated ground scraping into the scoria bedrock has removed meters of material. The shallow scraping was observed to result in rapid permafrost thaw with ground shrinkage causing patterned ground to form within three years, due to melting of ice wedges. It was noted that, in places, the ground surface was partly covered with large rock slabs indicating that the ice wedges and ground ice were largely within the volcanic bedrock. A reticular

Table 2. Components of the <2 µm fraction. Mc mica, Vt vermiculite, Chl chlorite, FeC iron-rich chlorite, Sm smectite, Qtz quartz, Fel feldspar, Hb hornblend, SRO short-range order material.

Depth	Mc	Vt	Chl	FeC	Sm	Qtz	Fel	Hb	SRO
cm	% of <2 mm fraction								
0-4	30		10	25	5	15	15		
4-30	30	5	5	20	7	15	15	5	
30-90	10	5		5	5	5	15		55
>100	10	3	2	5	5	5	15		55

Table 3. Composition of water extracts of soil, ms conductivity of 1:5 soil water extract $mScm^{-1}$.

Depth	pH	EC	Na	Ca	Mg	K	Cl	SO_4	CO_3
cm		mS	Millimoles charge/100g (me%)						
0-5	9.1	186	185	8.3	7.8	1.6	120	1.0	81.7
5-30	9.1	4.2	59	4.3	0.9	0.3	17	0.1	47.4
30-90	9.2	3.5	16	1.3	0.4	0.2	9.9	0.15	8.4
>100	9.4	3.2	16	1.2	0.4	0.7	10.8	0.1	7.7

patterned ground network was present in a few places on the deeply cut surfaces near McMurdo Station suggesting that ice wedges may at times penetrate some depth into the bedrock. At one locality on a ridge that had been scraped, grey quartzofeldspathic sand was noted in a crack that was presumed to be the remains of a sand wedge. Scraping on sloping ground that was underlain by stagnant ice resulted in extensive instability in the early 1980s, with repeated ground slumping and formation of thermokarst terrain (Campbell & Claridge 2003). In most places, ground disturbance is followed by the precipitation of a surface cover of soluble salts.

Examinations of areas in which fill materials have been deposited have not revealed any indications of recent ice accumulation consistent with the reformation of icy permafrost. The gravimetric moisture content was found to vary with depth and probably reflects the moisture content of the materials when deposited.

Soil Chemical Properties

Soil chemistry and mineralogy

The soils at southern Ross Island are very little weathered and contain only small amounts of the fine-earth fraction. Extractable Fe_2O_3, the usual measure of mineral breakdown, and release of iron is also very low, about 0.3% of the fine earth fraction, while clay contents (<2 µm) are around 6%, relatively high for Antarctic soil indicating mechanical breakdown of rock particles, largely the glassy component of the basaltic scoria parent material. The clay fraction of the surface material (Table 2) (0–30 cm) contains mica (illite?), chlorites, and some smectite, as well as clay-size quartz and feldspar, all consistent with much of the clay fraction, apart from the smectite, being derived from materials transported from the mainland, rather than from breakdown of the basaltic rocks. The smectite could have been derived from weathering of the glassy material in the basalt but this has not been investigated.

Within the ice-cemented permafrost, which was accessed by drilling, the clay fraction is dominated (50%) by palagonitic material showing only short-range order and may have been derived from breakdown of glassy material within the basalt.

The soils of the southern Ross Island area are heavily influenced by their proximity to the ocean, in contrast to most of the soils from the Transantarctic Mountains (Campbell & Claridge 1987). They are strongly alkaline, with pH values above 9. They contain moderate amounts of water-soluble salts (Table 3), in contrast to some of the older soils of the Transantarctic Mountains, and the salts are dominantly chlorides of sodium with lesser amounts of calcium and magnesium. The proportion of sulphate ion is very low while nitrate is below the limit of detection.

There is very little difference in the composition of the salts in the active layer of the soil and the salts in the underlying permafrost which was sampled to 1.5 m. At a site where the active layer had been removed and the underlying permafrost had thawed and a new active layer formed, the salts contained within the thawed permafrost had migrated to the surface giving an extensive surface efflorescence of halite. At sites that had not been scraped, only very small efflorescence's were visible. The ions within the surface efflorescence's are in the same proportion as those within the soil indicating no differences in mobility of the ions over the distances involved.

It is not clear whether the salts within the permafrost are residual and relate to previous glacial conditions or whether the salts may migrate into the permafrost under current conditions as thin films of concentrated solutions with low melting points as described by Ugolini & Anderson (1973).

Lithium chloride-leaching experiments

In order to assess the potential for salts or contaminants to move within the soils at southern Ross Island, the mobility of lithium chloride, which was added to the soil surface, was studied (Claridge et al. 1999). In this experiment, lithium chloride solution was applied to the soil surface at two sites, one a dry ridge and the other a moist depression, then sampled over several years at and downslope from the application sites, then analysed for lithium.

The results of this experiment showed that at the dry sites, substances added to the soil surface, such as airborne salts or spilt contaminants, will mainly penetrate only a small distance into the soil, related to the particle size and permeability of the soil. A small proportion may penetrate further down by capillary action until the soil temperature reaches freezing point at the permafrost table. Solutions concentrated by freezing and evaporation may also enter the permafrost through cracks and pores as indicated by detectable lithium within the permafrost. At the moist site, lithium was detected several meters downslope after three years indicating that downslope movement of contaminants can occur given sufficient moisture.

Table 4. A 0-2 cm, B 2-10 cm, C 10-20 cm, D 20-30 cm. Con – control site; Sp – contaminated site; THP – total petroleum hydrocarbons (mg/kg);, hyd – hydrocarbon degraders (no./g).

	pH		Org C		THP		Hyd	
	Con	Sp	Con	Sp	Con	Sp	Con	Sp
			%			X10^4		X10^4
A	8.4	7.8	0.1	5.1	<20	3.3	3.3	1.3
B	9.1	8.8	0.1	3.4	<20	2.5	230	1.4
C	8.9	9.8	0.09	1.6	<20	0.1	13	8.3
D	9.3	9.8	0.06	0.08	<20	0.1	13	3.5

Contaminations of soils around Scott Base

Detailed studies of the contamination of soils around Scott Base were made by Sheppard et al. (2000). Day-to-day activities can result in many kinds of contaminants being added to the soil surface, more especially in the past when management procedures were less concerned with environmental protection. A range of macro-contaminants such as wood, plastic, fibre, metals, etc. as well as odours from fuel spills were detected. The organic carbon content in the soils adjacent to the base was generally higher than at undisturbed sites, indicating the presence of intrusive organic material, which may have ranged from wood fragments to exhaust materials.

Acid extracts of the soils, designed to estimate heavy metal contamination, showed that the soils adjacent to the base were measurably contaminated with Ag, As, Cd, Cu, Pb and Zn, with the highest amounts in sites where materials had been dumped or stored.

The saline, oxidizing, and alkaline environment of the soils and the variations of these conditions within the soil profiles were considered to cause the episodic mobilization and retention of heavy metals in response to freeze-thaw cycles and the movement of water through the soils. Heavy metals can be bound to the surface of the clay particles within the soil, such as the smectites or the short-range order of palagonitic clays, and this may prevent their removal, while the more soluble constituents may be leached out.

Effect of fuel oil spills

Accidental fuel spills can arise from a variety of causes and several spill sites have been noted around Scott Base (Aislabie et al. 2004). The most obvious affect on soil properties is that the soil becomes darker and absorbs more heat, so that soil temperatures may rise by as much as 10°C, possibly causing some thawing of the underlying permafrost. Fuel-affected soils are sometimes weakly hydrophobic with the potential to alter the soil moisture regime and change other soil properties, some of which are shown in Table 4. Hydrocarbon-contaminated sites have slightly lower pH values, especially in the surface layer, increased organic carbon contents, much higher total petroleum hydrocarbons (TPH), and very much larger contents, by five orders of magnitude, of hydrocarbon-degrading bacteria, although total bacterial counts are more or less the same.

If left undisturbed, fuel-contaminated sites have the potential to self-remediate, as the hydrocarbons are used as an energy source by some organisms, as discussed by Aislabie et al. (2004).

Hydrocarbon spills that are sufficiently large may wet the active layer and pond on the ice-cemented permafrost and spread over a much larger area than the surface spill. Liquid hydrocarbons may also penetrate into the permafrost along cracks and fissures filled with unfrozen saline solutions. While no major spills of this sort are known around Scott Base, they have been observed elsewhere in the McMurdo Sound region.

Conclusions

Properties of the soils at southern Ross Island reflect their youthfulness, being exposed to weathering since the retreat of Ross I ice in the late Last Glaciation. The permafrost table is present at a relatively shallow depth compared with that is soils of other coastal locations in the McMurdo Sound region because the combination of low albedo and high moisture availability results in more energy being expended in moisture phase change rather than in soil heating to greater a depth. Variations in depth to the permafrost table are due to differing site moisture availability. Soil disturbance and removal of the active layer soon results in permafrost thawing and ground instability with patterned ground forming where ice wedges have melted and ground slumping where massive stagnant ice is present. Ground ice and ice wedges are common in the volcanic bedrock.

The soils are strongly alkaline because of the marine influence, and salts have penetrated far into the underlying permafrost and are rapidly precipitated at the ground surface after the removal of metres of bedrock permafrost.

As well as the physical and chemical changes resulting from disturbance to the active layer and the permafrost, soils in the region are contaminated from a wide variety of macro-substances, and also by a range of heavy metals and hydrocarbons. Experiments have shown that the movement of contaminants through the soil is small in dry sites but greater in moist sites. The levels of hydrocarbons in the soils can be reduced by biodegrading bacteria.

Acknowledgments

The support provided by the New Zealand Antarctic Programme over a number of years and the contributions from various colleagues is gratefully acknowledged.

References

Aislabie, J.M., Balks, M.R., Foght, J.M. & Waterhouse, E.J. 2004. Hydrocarbon spills on Antarctic Soils: Effects on management. *Environmental Science and Technology* 38: 126.

Balks, M.R., Campbell, D.I., Campbell, I.B. & Claridge, G.G.C. 1995. *Interim results of 1993/94 soil climate, active layer and permafrost investigations at Scott Base, Vanda*

Station, and Beacon Heights, Antarctica. University of Waikato Antarctic Research Unit Special Report No. 1, 1-64.

Blakemore, L.C. & Swindale, L.D. 1958. Chemistry and clay mineralogy of a soil from Antarctica. *Nature* 182: 47-48.

Campbell, D.I., MacCulloch, R.J.L & Campbell, I.B. 1997. Thermal regimes of some soils in the McMurdo Sound region, Antarctica. In: W.B. Lyons & C Howard-Williams (eds.), *Ecosystem Processes in Antarctic Ice-free Landscapes.* Rotterdam: Balkema, 45-55.

Campbell, I.B. 2003. Soil characteristics at a long-term ecological research site in Taylor Valley, Antarctica. *Australian Journal of Soil Research* 41: 351-364.

Campbell, I.B. & Claridge, G.G.C. 1975. Morphology and age relationships in Antarctic soils. In: R.P. Suggate & M.M. Cresswell (eds.), *Quaternary Studies.* Royal Society of New Zealand Bull. 13, 83-88.

Campbell, I.B. & Claridge, G.G.C. 1987. *Antarctica: Soils, Weathering Processes and Environment*. Amsterdam: Elsevier, 368 pp.

Campbell, I.B. & Claridge, G.G.C. 2003. Thermokarst landforms in the Transantarctic Mountains region of Antarctica. *Proceedings of the Eighth International Conference on Permafrost, Zurich, Switzerland, July 21-25, 2003:* 119-124.

Claridge, G.G.C., Campbell, I.B. & Balks, M.R. 1999. Movement of salts in Antarctic soils: Experiments using chloride. *Permafrost and Periglacial Processes* 10: 223-233.

Denton, G.H., Armstrong, R.I. & Stuvier, M. 1971. The late Cenozoic glacial history of Antarctica. In K.K. Turekian (ed.), *The Late Cenozoic Glacial Ages.* Yale University Press, 267-306.

Kyle, P.R. 1981. Glacial history of the McMurdo Sound region as indicated by the distribution and nature of McMurdo Volcanic Group rocks. In: L.D. McGinnis (ed.), *Dry Valley Drilling Project.* Am. Geophys Union Antarct. Resc. Ser. 33, 403-412.

Paetzold, R.F., Balks, M.R., Aislabie, J., Kimble, J.M. & Campbell, I.B. 2000. In: J.A. Adams & A.K. Metherall (eds.), *Soil 2000: New Horizons for a new century. Australia and New Zealand Second Joint Soils Conference.* Christchurch: NZ Society of Soil Science , 167.

Sheppard, D.S., Claridge, G.G.C. & Campbell, I.B. 2000. Metal contamination of soils at Scott Base, Antarctica. *Applied Geochemistr.* 15: 513-530.

Ugolini, F.C. & Anderson, D.M. 1973. Ionic migration and weathering in frozen Antarctic soils. *Soil Science* 115: 461-470.

Patterned Ground Features and Vegetation: Examples from Continental and Maritime Antarctica

N. Cannone

Dept. Biology and Evolution, Ferrara University, Corso Ercole I d'Este, 32, 44100 - Ferrara, Italy

M. Guglielmin

DBSF, Insubria University, Via J.H. Dunant, 3, 21100 - Varese, Italy

Abstract

The relationships between vegetation patterns and periglacial features and their underlying ecology are still poorly understood and lack specific investigations in Antarctica. Here we present the preliminary results on vegetation colonization of different types of sorted patterned ground and gelifluction features (stone-banked lobes and terracettes) in two sites at James Ross Island and four sites in Northern Victoria Land. The paper aims to a) understand the relationships between the patterns of vegetation colonization and the investigated periglacial features; b) compare the characteristics of vegetation patterns in similar periglacial features in two geographically remote sites of Maritime and Continental Antarctica; and c) compare the observed patterns of vegetation with those described by literature for the High Arctic. Vegetation relations with the periglacial features show some common patterns between Maritime and Continental Antarctica. Frost creep/gelifluction processes and frost heave are much more effective than grain size as limiting factors for vegetation development.

Keywords: gelifluction features; Continental Antarctica; Maritime Antarctica; patterned ground; vegetation.

Introduction

Periglacial landforms are widespread in the polar regions of both hemispheres (French 2007). While several authors have focused on the relationships between vegetation colonization and the periglacial landforms in the Arctic (i.e., Britton 1957, Billings & Mooney 1959, Jonasson & Sköld 1983, Anderson & Bliss 1998, Matthews et al. 1998, Cannone et al. 2004, Walker et al. 2004), this topic has been poorly addressed in Antarctica (i.e., Heilbronn & Walton 1984). Moreover, to our knowledge, until now there are not specific investigations providing the comparison of the vegetation patterns in relation to periglacial landforms in Maritime and Continental Antarctica.

The aims of this paper are:

1) to understand the relationships between the patterns of vegetation colonization and the type and characteristics of the most widespread periglacial features;

2) to compare the characteristics of the periglacial features and of their related vegetation patterns in geographically remote sites of Maritime and Continental Antarctica: and

3) to compare the patterns observed in Antarctica with those described by literature for the High Arctic.

Study Areas

Two geographically remote areas of Antarctica were selected for this investigation (Fig. 1): James Ross Island, located on the eastern side of the Antarctic Peninsula and used as a template of Maritime Antarctica, and Northern Victoria Land, located at East Antarctica and used as a template of the conditions of Continental Antarctica.

Maritime Antarctica

At James Ross Island, two different sites (about 20 km from each other) were investigated: the Rink Plateau (named Rink in this paper) (63°55′S, 58°10′W) and Lachman Crags (named Lachman in this paper) (63°54′S, 57°35′W).

At James Ross the climate is a cold, dry maritime climate, with a mean annual air temperature of -6.7°C (referred to the period 1996–2004) (Mori et al. 2007) and mean annual precipitation of about 200 mm/yr water equivalent (Strelin & Sone 1998).

Rink site is a relatively high elevation plateau (400 m a.s.l.) delimited by a sharp and almost vertical scarp. This site is characterized by the occurrence of several periglacial features and a small ice cap located in the upper part of the plateau. The outcropping bedrock is composed of Cenozoic lavas and pyroclastites underlain by Cretaceous sedimentary rocks (Strelin & Malagnino 1992, Carrizo et al. 1998).

Lachman site includes different types of environments (i.e., valley bottoms, raised beaches, slopes) at elevations ranging between 0 and 200 m a.s.l. and characterized by a high frequency of periglacial features. The outcropping bedrock is volcanic with the occurrence of different types of deposits ranging from morainic and slope deposits, to raised beaches.

Northern Victoria Land

The climate of Northern Victoria Land is frigid Antarctic, with a mean annual air temperature of -18°C and precipitation, always in the form of snow, between 100 and 200 mm (Grigioni et al. 1992).

Four different sites were selected: Tarn Flat (74°59′S, 162°37′E), Boulderclay (74°44′S, 164°05′E), Gondwana (74°36′S, 164°12′E), and Apostrophe Island (73°30′S, 167°50′E).

All these sites are located along the coast, with the exception of Tarn Flat, at elevations ranging from 20 to 150 m a.s.l. These sites are characterized by the occurrence of different types of periglacial features occurring on different outcropping rock and deposits ranging from gabbro and metamorphic rocks (Apostrophe Island and Gondwana) to granites and morainic deposits (Tarn Flat and Boulderclay).

The vegetation both at James Ross and at Victoria Land is a cryptogamic nonvascular tundra, including different moss- and lichen-dominated associations (Longton 1979). Descriptions of the moss and lichen flora and of the main vegetation communities of Victoria Land have been provided by several authors (Kappen 1985, Castello & Nimis 1995, Seppelt et al. 1995, 1996, Seppelt & Green 1998, Smith 1999, Cannone 2005, 2006).

Methods

Geomorphology

The geomorphological study was performed by field surveys. All the periglacial landforms occurring in each selected study site were recorded and classified. Only in some representative cases, the groups of landforms selected for the vegetation survey were also morphometrically characterized through profiles and visual descriptions. In addition, the thickness of the active layer was measured by frost probing and, where logistical conditions allowed enough time, also by measuring the ground temperature at different depths following the method proposed by Guglielmin (2006).

Trenches were dug into the ground to investigate the internal structure of the features and for sampling.

Vegetation survey

The vegetation was sampled in 50 × 50-cm plots. Two (occasionally three) plots were set up at each of the selected landforms. All of the plots were located in morphologically homogeneous microhabitats within the landforms. All of the moss and lichen species occurring in the plot were recorded and their percentage cover estimated visually. Microtopography and surface-soil texture were assessed visually in each plot. Species nomenclature follows Castello & Nimis (2000), Øvstedal & Smith (2001) and Castello (2003) for lichens, and Ochyra (1998) and Seppelt & Green (1998) for bryophytes.

Results

Maritime Antarctica

At James Ross Island several types of periglacial features were analyzed, including sorted, patterned ground (debris island; sorted polygon; sorted stripes), terracettes, and stone-banked lobes (Rink & Lachman). The geomorphological survey pointed out that, within each site, the high- and low-centered patterned ground shows similar size (Table 1), which is about twofold larger at Lachman than at Rink. The measured frost table depth ranged from 40 cm at Rink and 80 cm at Lachman. In many cases, groundwater flow filled the trenches. The height of the investigated terracettes and of the stone-banked lobes ranges between a few decimeters up to 1.6 m. At Lachman, vegetation colonization shows clear patterns. The average total vegetation coverage is highest on the sorted stripes, decreases to the terracettes, and is lowest on the stone-banked lobes. High-centered and low-centered patterned ground show opposite colonization patterns, with the highest coverage on the border of the low-centered and on the center of the high-centered patterned ground (Table 1). The total vegetation coverage shows differences considering separately the different parts of the landforms (i.e., border and center of sorted patterned ground, tread and riser of both terracettes and stone-banked lobes, fine- and coarse-grained parts of the sorted stripes). As could be expected, the higher values of coverage characterize the elements with finer texture, ranging from the fine part of the sorted stripes (with the highest average coverage recorded >80%), to the treads of the terracettes and the center of sorted high-centered patterned ground (with similar values ranging around 35%), to the treads of stone-banked lobes (c. 25%). In the coarser sediments, vegetation coverage is relatively high on the border of sorted patterned ground (ranging from 14% on high-centered to 48% on low-centered). On the other hand, coverage decreases sharply when considering the coarse part of the sorted stripes and the treads of terracettes, while the riser of stone-banked lobes is devoid of vegetation. In the sorted stripes the vegetation (occurring only on the fine-grained part) is dominated by crustose microlichens with scattered mosses. Similar floristic composition and dominance (crustose microlichens such as *Psoroma*, foliose lichens as *Leptogium* and scattered mosses) characterize the flat part of the terracettes, the center of sorted patterned ground and the flat of stone-banked lobes. The border of sorted patterned ground is mainly colonized by different species of mosses and macrolichens (*Usnea* and *Stereocaulon*).

The high-centered patterned ground shows opposite vegetation colonization patterns between Lachman and Rink, where the stony border shows higher vegetation coverage (60%) than the finer center (1%). At Rink the low-centered patterned ground shows similar patterns to those of Lachman, although with lower vegetation coverage, with higher coverage on the border (21%) than the center (8%). However, the patterns of floristic composition are similar indicating similar environmental and ecological gradients but different intensity of ground disturbance. On the other hand, at Rink the center of all the patterned ground is mainly colonized by crustose microlichens (i.e., *Psoroma*) and mosses, and the vegetation of the borders is composed of mosses (more than 15%) and, only as subdominants, by macrolichens (*Usnea* and *Leptogium*). At Lachman the depressed fine center of the low-centered patterned ground is homogeneously colonized (average coverage 11%) by crustose microlichens (*Psoroma*, *Ochrolechia*) and mosses (*Andreaea*, *Polytrichum*) and by a black crust of *Nostoc*. The border of the low-centered patterned ground shows lower average vegetation coverage (48%) with the prevalence of mosses (*Bryum*, *Andreaea*) and of epilithic foliose and fruticose lichens (*Leptogium*, *Usnea*). Among the rarest periglacial features at Lachman, there are

Table 1. Average total vegetation coverage and floristic composition of the different elements of the investigated features at two sites (Rink and Lachman) of James Ross Island (Maritime Antarctica). The features are listed in order of decreasing total vegetation coverage (+ = less than 1%). Legend: A = Lachman; B = Rink; 1 = fine grained sorted stripes; 2 = tread terracettes; 3 = center of sorted patterned ground; 4 = tread stone-banked lobes; 5 = border of sorted patterned ground; 6 = coarse grained sorted stripes; 7 = riser terracettes; 8 = riser stone-banked, *low-centered patterned ground, ° high-centered patterned ground, ND not determinable.

Site	A	A	A	A	B	A	A	B	A	A
Feature Characteristics	1	2	3	4	5	5	6	3	7	8
% Total Vegetation Coverage	85	45	35° 11*	30	60° 21*	14° 48*	5	1° 8*	1	0
Mosses	10	5	10	5	15	15	5	5		
Fruticose lichens			1	+	5				+	5
Foliose lichens	+	5	1	5	5	5		+	+	
Crustose lichens	75	35	20	20	1	1	1	5	+	
Algae and Cyanobacteria			5		1	1	+	+		
% Blocks	10	10	10	15	75	45	65	15	75	70
Width (cm)	125	158	116°128*	78	52° 49*	116°128*	90	52° 49*	ND	ND
Length (cm)		125	163° 165*	284	75° 76*	163° 165*		75° 76*	ND	ND
% Pebbles	10	20	20	15	25	40	30	15	20	30
% Gravel	20	20	30	25	0	<5	<5	30	<5	0
% Sand and finer material	60	50	40	45	0	10	<5	40	<5	0

Table 2. Average total vegetation coverage and floristic composition of the different elements of the investigated features at four sites (Tarn Flat, Boulderclay, Gondwana, Apostrophe Island) of Victoria Land (Continental Antarctica). The features are listed in order of decreasing total vegetation coverage (+ = less than 1%). Legend: A = Tarn Flat; B = Boulderclay; C = Gondwana; D = Apostrophe Island; 1 = riser terracettes; 2 = tread stone-banked lobes; 3 = tread terracettes; 4 = border of sorted patterned ground; 5 = center of sorted patterned ground; 6 = tread stone-banked lobes; 7 = riser stone-banked lobes; ° high-centered patterned ground, ^ debris island, ND not determinable.

Site	D	D	D	C	B	A	A	C	C	C	A	A	C	C
Feature Characteristics	1	2	3	4	5	4	3	2	7	5	1	5	3	1
% Total Vegetation Coverage	45	45	35	30	25	20	15	15	10	5	1	1	1	1
Mosses	5	5	15	1	20			+	1	+				
Fruticose lichens	10	10		1										
Foliose lichens	10	20	1	5		5	5							
Crustose lichens	30	15	30	25	5	15	15	15	10	5	1	1	1	5
Algae and Cyanobacteria								+		+				
Width (cm)	4.5	1.2	4.5	148°	75^	80	80	265	ND	148°	80	80	127	ND
Length (cm)	2.7	4.3	2.7	183°	85^	40	40	295	ND	183°	40	40	92	ND
Height (cm)	29	n.d	n.d.	25°	n.d.	n.d.	n.d.	n.d.	28	25°	10	n.d-	n.d.	14
Slope (°)	27	5	2	1	0	1	5	24	42	2	40	1	6	44
% Blocks	65	45	20	85	5	95	35	30	65	10	70	5	40	65
% Pebbles	<5	10	15	5	15	<5	45	30	15	35	10	5	20	20
% Gravel	15	10	15	5	45	<5	5	30	10	30	10	10	20	10
% Sand and finer material	15	35	50	5	35	0	15	10	5	25	10	80	20	5

frost boils, developing on sandy ground close to the raised beach and showing occasionally salt efflorescence. These features are extensively colonized by mosses (*Polytrichum* spp. and *Dicranum* spp.) located on the raised centers.

Continental Antarctica

In Northern Victoria Land in order to achieve a comparable data set, we only considered the same types of periglacial features investigated in Maritime Antarctica. The features that were analyzed were sorted patterned ground (debris island at Boulderclay, high-centered patterned ground at Tarn Flat, Gondwana, Apostrophe Island), terracettes (Tarn Flat, Gondwana, Apostrophe Island), and stone-banked lobes (Gondwana, Apostrophe Island).

From the geomorphological point of view, the absence of low-centered patterned ground and the thinner frost table (from 15 to 50 cm of depth) is remarkable with respect to the values recorded in Maritime Antarctica. No groundwater flow was found in any of the trenches. The height of the investigated terracettes and of the stone-banked lobes is surely much smaller than in Maritime Antarctica, ranging between 10 cm up to 35–40 cm.

In Northern Victoria Land vegetation shows different colonization patterns with higher total vegetation coverage on the tread of terracettes, tread of the stone-banked lobes, and coarse border of high-centered patterned ground and debris island, whereas the riser of stone-banked lobes and terracettes are characterized by a very low total coverage.

Tarn Flat and Gondwana show similar patterns of vegetation colonization both for terracettes and high-centered patterned ground concerning the total coverage and the floristic composition. The tread of terracettes and the center of high-centered patterned ground in these sites are colonized by microcrustose lichens (*Lecidella siplei*), and the slope of terracettes and coarse border of patterned ground are characterized by epilithic foliose lichens (i.e., *Umbilicaria*) and crustose placodioid lichens (i.e., *Buellia frigida* and *Rhizocarpon* spp.). At Apostrophe Island the high-centered patterned ground shows vegetation patterns similar to those observed both at Tarn Flat and Gondwana.

On the contrary, at Apostrophe Island vegetation composition of the gelifluction features is different with the strong ingression of foliose (*Umbilicaria*) and fruticose (*Usnea*) lichens accompanied by crustose lichens (*Buellia frigida*) mainly on the risers of terracettes and on the treads of stone-banked lobes.

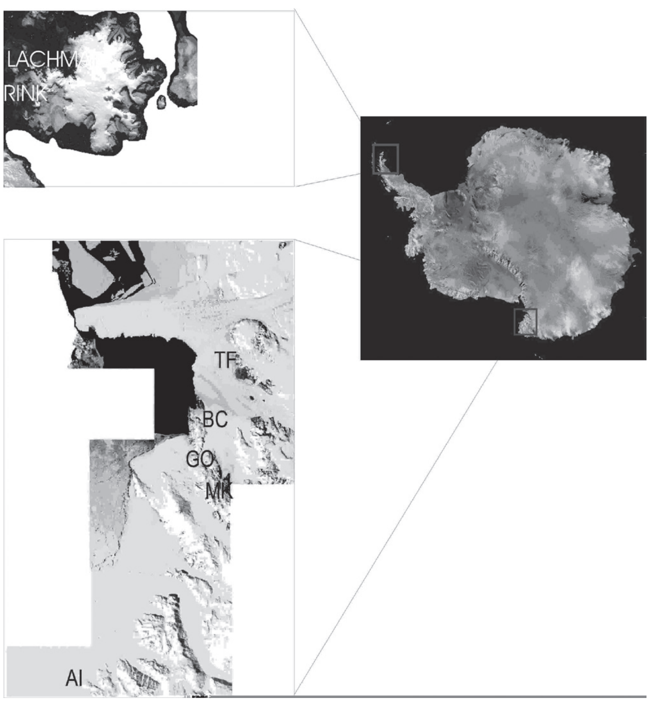

Figure 1. Location of the study sites at James Ross Island (Maritime Antarctica) and Victoria Land (Continental Antarctica). Legend: AI Apostrophe Island, BC Boulderclay, GO Gondwana, TF Tarn Flat. (Images from Landsat Image Mosaic of Antarctica, LIMA, International Polar Year 2007–2008 Project by BAS, USGS, NSF).

Discussion and Conclusions

The results obtained in all the investigated sites underline that grain size is not an effective factor in shaping the vegetation distribution patterns in the analyzed features.

The progressive decreasing sequence of vegetation coverage found through the periglacial landforms at Lachman suggest an important role of the frost creep/gelifluction processes as limiting factors for vegetation development. The estimated higher water content within the active layer and the higher height of the frost creep/gelifluction features in Maritime Antarctica than in Victoria Land can suggest that these processes are more intense in the former than in the latter areas. On the other hand, from the fabric of the pebbles in the trenches, the layer involved in the sorting or in the preferential orientation is much thinner (data not shown) than the recorded frost table depth. This pattern is opposite to what was already stressed by Cannone et al. (2004) for the High Arctic, where the substrate disturbance associated with gelifluction landforms does not affect the integrity of the upper soil layer.

Moreover, Northern Victoria Land (Gondwana and Tarn Flat) show similar conditions to what was found at Lachman. The higher vegetation cover of the gelifluction landforms at Apostrophe Island could be related more to the edaphic conditions of the site (high level of nutrients; higher water availability; see Cannone et al., in press) than to the active-layer thickness or to the depth of gelifluction processes.

The similar vegetation patterns at Rink (maritime Antarctica) and in all the selected sites at Northern Victoria Land are contrasting with those of Lachman.

At this site, the frost heave may be weaker than in the other sites not only due to milder conditions, but also due to the high salt content of the ground.

The analyses carried out at Victoria Land (as a template of Continental Antarctica) and at James Ross Island (as a template of Maritime Antarctica) indicate that there are some common patterns between these two geographically remote regions of Antarctica. In particular, the patterns of vegetation distribution (in terms of vegetation coverage, but not for the floristic composition) of the sorted patterned ground of Rink (James Ross Island) are more similar to those of all the investigated locations of Victoria Land than to the other site at James Ross Island (Lachman).

Similar evidences concern the colonization patterns of terracettes, with the patterns observed at Rink being more similar to those of Victoria Land than of Lachman.

On the other hand, the stone-banked lobes show similar trends in all the investigated sites, although at James Ross Island the differences between tread and riser are much more evident than at Northern Victoria Land.

Acknowledgments

Thanks to PNRA for the logistical support in Victoria Land. Thanks to DNA, PNRA and IAA for their logistical support and cooperation in Maritime Antarctica, with special reference to Dr. Jorge Strelin, Dr. Toni Curtosi, and Dr. Rodolfo del Valle. We want to thank also Enrique Serrano and an anonymous reviewer for their precious suggestions and comments.

References

Anderson, DG. & Bliss, LC. 1998 Association of plant distribution patterns and microenvironments on patterned ground in a polar desert, Devon Island, N.W.T., Canada. *Arct. Alp. Res.* 30: 97-107

Billings, W.D. & Mooney, H.A. 1959. An apparent frost-hummock sorted polygon cycle in the alpine tundra of Wyoming. *Ecology* 40: 16-20.

Cannone, N. 2005. Moss and lichen flora of Victoria Land Continental Antarctica along a latitudinal transect. *Terra. Antarctica Reports*, 11, 1-9.

Cannone, N. 2006. A network for monitoring terrestrial ecosystems along a latitudinal gradient in Continental Antarctica. *Antarctic Science*, 18(4): 549-560.

Cannone, N., Guglielmin, M. & Gerdol, R. 2004. Relationships between vegetation patterns and periglacial landforms in northwestern Svalbard. *Polar Biology* 27: 562-571.

Cannone, N., Wagner, D., Hubberten, H.W., & Guglielmin, M. 2007. Biotic and abiotic factors influencing soil properties across a latitudinal gradient in Victoria Land, Antarctica. *Geoderma*, in press.

Carrizo, H.G., Torielli, C.A., Strelin, J.A. & Muñoz, C.E.J. 1998. Ambiente eruptivo del grupo volcanico Isla James Ross en Riscos Rink, Isla James Ross, Antartida. *Revista de la Associación Geológica Argentina* 53: 469-479.

Castello, M. & Nimis, P.L. 1995. The lichen vegetation of Terra Nova Bay Victoria Land, Continental Antarctica. *Bibliotheca Lichenologica* 58: 43-55.

Castello, M. & Nimis, P.L. 2000. A key to the lichens of Terra Nova Bay Victoria Land, Continental Antarctica. *Italian Journal of Zoology*, Supplement, 1: 175-184.

French, H. 2007. *The Periglacial Environment* (3rd Ed.). London: John Wiley and Sons, 478 pp.

Grigioni, P., De Silvestri, L., Pellegrini, A. & Sarao, L. 1992. Some climatological aspects in the Terra Nova Bay area, Antarctica. In: M. Colacino, G. Giovanelli & L. Stefanutti (eds.), *Italian Research on Antarctic Atmosphere*. Bologna: SIF: 97-121.

Guglielmin, M. 2006. Ground surface temperature (GST), active layer, and permafrost monitoring in continental Antarctica. *Permafrost and Periglacial Processes* 17(2): 133-143.

Heilbronn, T.D. & Walton, D.W.H. 1984a. Plant colonization of actively sorted stone stripes in the Subantarctic. *Arct. Alp. Res.* 16: 161-172.

Jonasson, S. & Sköld, S.E. 1983. Influences of frost-heaving on vegetation and nutrient regime of polygon-patterned ground. *Vegetatio* 53: 97-112.

Kappen, L. 1985. Vegetation and ecology of ice-free areas of northern Victoria Land, Antarctica: 1. The lichen vegetation of Birthday Ridge and an inland mountain. *Polar Biology* 4: 213-225.

Matthews, J.A., Shakesby, R.A., Berrisford, M.S. & McEwen L.J. 1998 Periglacial patterned ground on the Styggedalsbreen Glacier foreland, Jotunheimen, Southern Norway: Micro-topographic, paraglacial and geoecological controls. *Permafrost Periglac.* 9: 147-166.

Mori, J., Fukui, K., Sone, T., Strelin, J., & Torielli, C. 2007. Internal structure of stone-banked lobes and terraces on Rink Plateau, James Ross Island, Antarctic Peninsula region. *Polish Polar Research* 281: 23-30.

Ochyra, R. 1998. *The Moss Flora of King George Island, Antarctica*. Cracow: Polish Academy of Sciences, W. Szafer Institute of Botany, 279 pp.

Øvstedal, D.O. & Smith, R.I.L. 2001. Lichens of Antarctica and South Georgia. Cambridge: Cambridge University Press, 405 pp.

Seppelt, R.D., Green, T.G.A. & Schroeter, B. 1995. Lichens and mosses from the Kar Plateau, Southern Victoria Land, Antarctica. New Zealand *Journal of Botany* 33: 203–220.

Seppelt, R.D., Green, T.G.A. & Schroeter, B. 1996. Additions and corrections to the lichen flora of the Kar Plateau, Southern Victoria Land, Antarctica. *New Zealand Journal of Botany* 34: 329-331.

Seppelt, R.D. & Green, T.G.A. 1998. A bryophyte flora for Southern Victoria Land, Antarctica. *New Zealand Journal of Botany* 36: 617-635.

Strelin J.A. & Malagnino, E.C. 1992. Geomorfologia de la Isla James Ross. In: C.A. Rinaldi (Ed.), *Geología de la Isla James Ross, Antártida*. Instituto Antártico Argentino, Buenos Aires: 7-36.

Strelin, J.A. & Sone, T. 1998. Rock glaciers on James Ross Island, Antarctica. In: A.G. Lewkowicz & M. Allard (Eds.), *Permafrost – Proceedings of the 7th International Permafrost Conference, Yellowknife, Canada. Collection Nordicana, Université Laval 57*: 1027-1032.

Walker, D.A., Epstein, H.E., Gould, W.A. et al. 2004. Frost boil ecosystems: Complex interactions between landforms, soils, vegetation and climate.

Rainfall-Runoff Hydrograph Characteristics in a Discontinuous Permafrost Watershed and Their Relation to Ground Thaw

Sean K. Carey

Department of Geography and Environmental Studies, Carleton University, Ottawa, Ontario, Canada K1S 5B6

Chris M. DeBeer

Centre for Hydrology, University of Saskatchewan, Saskatoon, Saskatchewan, Canada S7N 5C8

Abstract

Rainfall-runoff hydrographs were analyzed for 49 rainstorms over 5 years in a 7.6 km^2 alpine discontinuous permafrost watershed to assess the effect of seasonal thawing on hydrograph parameters. Hydrographs were analyzed for 11 common characteristics including runoff ratio, initial abstraction, recession coefficient, and several parameters related to shape of the hydrograph. Runoff ratios varied between 0 and 0.33 (average 0.09) and declined throughout the summer, reflecting increased active layer storage. Hydrograph recessions were steeper immediately post-freshet and flattened as the summer progressed, as flow pathways descended into soils with lower transmissivities. There was no relation between antecedent wetness and timing response, indicating that saturated areas of the catchment exist near the stream throughout the season, facilitating rapid runoff. Results indicate that at this scale, permafrost and active layer depth exert a strong influence on the stormflow hydrograph.

Keywords: discontinuous permafrost; hydrograph analysis; hydrology; recession; runoff.

Introduction

Watersheds underlain with discontinuous permafrost show a high degree of spatial variability in the timing and magnitude of hydrological processes (Carey & Woo 2001a, Spence & Woo 2003). Due to the relatively impermeable nature of permafrost, percolation is restricted and the soil storage capacity reduced, resulting in greater volumes of event water (both meltwater and rain) being conveyed to the stream from perched unconfined aquifers (Quinton & Marsh 1998, Carey & Woo 2001b). Following snowmelt, thaw of seasonally frozen ground increases the thickness of the active layer, enhancing basin storage and altering flow pathways (Bowling et al. 2003, Carey & Quinton 2004). As the ground thaws, the water table descends into deeper soil layers with reduced saturated hydraulic conductivity, stormflow response is dampened. In contrast, catchment areas without permafrost infiltrate and percolate meltwater and rainwater to the deeper regional groundwater table without generating significant lateral flow.

Rainfall-runoff events in permafrost basins are flashy, with accentuated peaks, extended recessions, and low baseflow contributions (Dingman 1973, McNamara et al. 1998). The mechanisms of runoff production in permafrost catchments has emphasized rapid surface and near-surface flow in porous organic soils that are ubiquitous surface cover, preferential flow pathways through interconnected surface depressions, soil conduits, and rills, particularly during the snowmelt period (Hinzman et al. 1993, McNamara et al. 1998, Quinton & Marsh 1999, Carey & Woo 2001a). As the active layer thaws and the saturated layer descends, rapid runoff declines and these runoff pathways become less effective in conveying water to the drainage network. In addition to changes in vertical soil hydraulic properties, the areal extent of runoff generation declines following snowmelt. When the saturated layer resides within near-surface organic soils, water from slopes and upland areas can be conveyed rapidly to the stream and the source area for runoff generation is relatively large and the basin is highly connected. However, as the water table drops into the mineral substrate, hill slopes and areas away from the stream become disconnected, reducing the contributing source area (Carey & Woo 2001b). The total percentage of the basin underlain by permafrost is important as seasonally frozen soils have predominantly vertical water flux throughout the year, and basin comparison studies in zones of discontinuous permafrost reveal significant differences in streamflow properties and hydrochemistry based upon permafrost disposition (McLean et al. 1999, Petrone et al. 2007).

A significant amount of research in discontinuous permafrost environments has investigated runoff mechanisms at the hillslope or plot scale (Carey & Woo 2001b, Spence & Woo 2003). This process information has not been linked to larger scale basin flow attributes. For example, in a continuous permafrost environment, McNamara et al. (1998) studied temporal variations in runoff properties over a cascading range of watershed scales and related hydrograph characteristics to the influence of permafrost. A similar exercise in discontinuous permafrost environments would provide validation that processes operating at small scales are manifested in the streamflow hydrology at the basin scale.

Hydrograph analysis continues to be a widely utilized and practical assessment tool of basin storages and in the calibration of many hydrological models (i.e. Tallaksen 1995, Szilagyi & Parlange 1998). Response times, runoff ratios and recession parameters provide first-order information as to catchment functioning. In this regard, hydrograph analysis remains a useful tool to evaluate whether conceptual and numerical models of runoff generation derived from plot and slope studies are applicable to the entire catchment, which integrates areas of seasonal and permafrost soils. It is the objective of this paper to evaluate five years of summer stormflow data to improve understanding of how heterogeneous discontinuous permafrost basins deliver water to the stream. Hydrograph parameters will be compared with precipitation characteristics and antecedent conditions such as flow and time of year (as a surrogate for ground thaw). The influence of increased basin storage on rainfall-runoff relations will be determined and results compared with knowledge of processes at smaller scales. The snowmelt period will not be considered.

Study Area

The study was conducted within Granger Basin (60º32′N, 135º18′W), a small headwater catchment of the Wolf Creek Research Basin, located approximately 15 km south of Whitehorse, Yukon (Fig. 1). The climate is subarctic continental, which is characterized by a large temperature range, low relative humidity, and low precipitation. Mean annual (1971–2000) temperature at the Whitehorse airport (706 m above sea level) is -0.7ºC, with mean January and July temperatures of -17.7ºC and +14.1ºC, respectively, although winter and summer extremes of -40ºC and 25ºC are not uncommon. Mean annual precipitation is 267.4 mm, of which 145 mm falls as rain.

The drainage area of Granger Basin is approximately 7.6 km^2, and the elevation ranges from 1310 to 2250 m a.s.l. The lower half of the basin and most of the stream channel has a fairly gentle slope (~4°), however the upper portion of the basin is considerably steeper (~15-25°). Throughout the basin there are several small (~0.01 km^2) ponds, and a permanent snowpack near the summit of Mount Granger.

Granger Basin lies within alpine and shrub-tundra ecological zones, with vegetation consisting predominantly of various willow (*Salix spp.*) and birch (*Betula spp.*) shrubs. A significant portion of the upper basin on the slopes of Mount Granger is covered with talus and bedrock outcrops. The lithology of the basin is predominantly sedimentary, comprising limestone, sandstone, shale, and conglomerate. A mantle of glacial till overlies most of the bedrock, ranging up to several meters in thickness. Fine-textured alluvium is found along much of the valley floor where the main channel resides, while colluvial deposits are more common along upper slopes away from the main valley. Soils are primarily orthic eutric brunisols with textures ranging from sandy loam to gravelly sandy loam. These are fairly well-drained soils with coarse parent materials. Surface organic soils range from 0.1 to 0.4 m in thickness, and are deepest in riparian areas and north-facing slopes throughout the basin, becoming thinner and more scattered in higher elevation and south-facing areas. Using the BTS method, it is estimated that approximately 70% of the basin is underlain with permafrost (Lewkowicz & Ednie 2004).

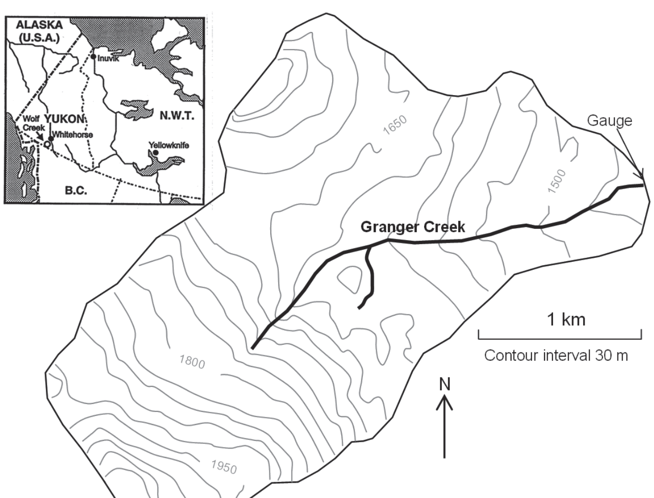

Figure 1. Map of Granger Basin. Inset is location within northwestern North America.

Methodology

Field data

Spring and summer discharge data were collected for Granger Creek over five years from 1999 to 2003 using an electronic stage recorder (Ott) placed inside a stilling well at the basin outlet. Measurements of stage were recorded at 15-minute intervals. A stage-discharge rating curve was developed by manual gauging of the stream at least 10 times per year. Rainfall data were collected using a Texas Instruments tipping bucket rain gauge, part of a nearby meteorology station (Fig. 1), measured rainfall depths in 0.1 mm increments and summed to the total number of these increments of each 30-minute period.

Hydrograph analysis

Hydrographs selected for analysis were taken after the snowmelt period (15 June) to eliminate diurnal fluctuations and mixed runoff signals. Visual inspection of the hydrographs was used to determine which events were suitable for analysis, and the selection criteria was based on distinct and isolated response events. In most cases, only storms >4 mm with one continuous or near continuous (<1 hour of no precipitation) event were chosen. In certain instances, additional precipitation following the peak in discharge prevented the determination of certain response factors. In these cases, the multiple input and flow peaks were treated as a single event to calculate runoff ratios and recession trends. Selected hydrographs were then isolated and analyzed separately.

The separation of stormflow runoff, *R*, and baseflow components was carried out using a straight line drawn from the initial rise in flow to the point of greatest curvature on the recession limb (Fig. 2). The rational for this procedure was that previous research in permafrost environments had justified this method based upon the properties of permafrost soils (McNamara et al. 1998, Carey & Woo 2001b).

Hydrograph parameters were determined as shown in Figure 2. Input starts at time t_{w0} and ends at time t_{we}, and total storm duration, T_w is given by, $T_w = t_{we} - t_{w0}$. Total precipitation

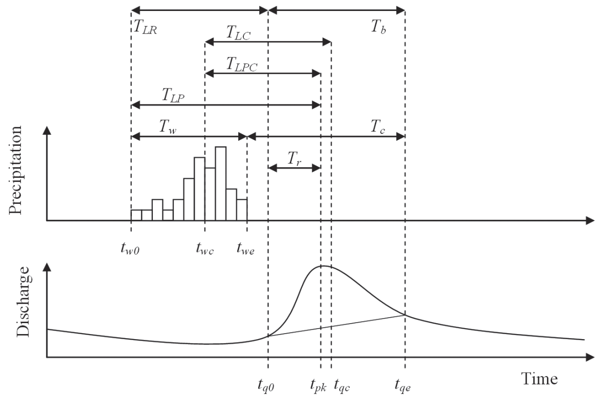

Figure 2. Hydrograph and precipitation parameters measured for analysis. Terms are provided in the text below.

is P_t. Stream response begins at time t_{q0} and ends at time t_{qe}, peaking at time t_{pk}. The time duration of the storm hydrograph is $T_b = t_{qe} - t_{q0}$. The time of rise specifies the period of increasing discharge, or rising limb, and is determined as: $T_r = t_{pk} - t_{q0}$. Time of concentration, T_c, defined as the time required for the water to travel from the most hydraulically distant part of the contributing area to the basin outlet is: $T_c = t_{qe} - t_{we}$. The time between the beginning of input and the initial hydrograph response, known as the response lag is: $T_{LR} = t_{q0} - t_{w0}$. Initial abstraction, P_{abst}, is as precipitation that falls prior to the initial rise in the storm hydrograph. The lag to peak discharge, T_{LP}, measures the time between the beginning of input and the hydrograph peak: $T_{LP} = t_{pk} - t_{w0}$. The center of mass, or centroid, of both input and runoff is useful in characterizing time lags. In determining the centre of mass, or centroid, for the input hyetograph, t_{wc}, the input values, W_i, measured for i = 1, 2, n time periods of equal length as:

$$t_{wc} = \sum_{i=1}^{n} W_i t_i \Big/ \sum_{i=1}^{n} W_i \qquad (1)$$

The centroid of the response hydrograph, t_{qc}, is determined in the same fashion, summing the event-discharge-weighted time values for equal length periods, and dividing by the sum of the event discharge values for each period:

$$t_{qc} = \sum_{i=1}^{n} Q_i t_i \Big/ \sum_{i=1}^{n} Q_i \qquad (2)$$

The centroid lag is defined as the period of time between the respective center of mass of the input and runoff events: $T_{LC} = t_{qc} - t_{wc}$. The centroid lag to peak is the interval from the input center of mass to the peak discharge: $T_{LPC} = t_{pk} - t_{wc}$.

Hydrograph recessions were analyzed for all of the selected stormflow events. The recession curve conveys information about watershed characteristics and storage properties, as it represents the natural storage that feeds the stream after the input has ceased. Numerous studies have focused attention on this part of the hydrograph, and many models have been develop to describe the decline in streamflow because of the importance in certain areas of hydrological application, including forecasting and water resource planning (see Tallaksen 1995 for review). Additionally, recession analysis has been used widely in permafrost environments (Dingman 1973, McNamara et al. 1998, Carey & Woo 2001b).

The most basic model for describing the recession is the linear-reservoir model of response, where water storage recharge and evaporation are neglected, given as:

$$q = q_0 e^{(-t/t^*)} \qquad (3)$$

where q is discharge, q_0 is the discharge at $t = 0$ (the beginning of the recession), t is time, and t^* is the recession parameter, also known as the turnover time, that describes the decay for the draining aquifer. The linear-reservoir model of watershed response has the advantage that it is simple and that t^* is a widely used parameter for inferring watershed characteristics. However, this model is recognized as being valid over a limited range of the recession period (Tallaksen 1995).

Results

Post-freshet hydrographs (15 July to 15 September) are shown above in Figure 3. The interruption in the hydrographs in August 2003 was due to mechanical failure of the logger. Maximum annual flows occurred during snowmelt freshet (not shown) in May and early July when 30 to 50% of the annual precipitation was released over a several-week period. Following freshet, streamflow gradually declined throughout the summer and fall, with rainfall-runoff stormflow events superimposed on the seasonal recession. Discharge rates were typically below 0.4 m^3s^{-1} following snowmelt, and gradually declined to ~0.05 m^3s^{-1} before stream gauging ceased prior to freezing. The 2000 hydrograph shows greater flows than other years, with baseflow rates of ~0.25 m^3s^{-1} in early summer, which later rose to 0.3 m^3s^{-1} triggered by a series of storms in late August. By late September 2000, the flow rate had fallen to ~0.2 m^3s^{-1}.

Rainfall from 15 June to 15 September over the five years was 141, 234, 141, 130, and 129 mm for 1999 to 2003, respectively. In 1999, 2001, and 2002, ~8 rainfall events following the snowmelt period were >4 mm in magnitude, whereas 2000 and 2003 were wetter with 15 and 13 events >4 mm, respectively. The average rainfall for all storms (including those not analyzed) over all years was 8.1 mm with a maximum of 31.8 mm. Rainfall intensities varied from 0.2–2.6 mm hr^{-1}, averaging 0.8 mm hr^{-1}. Storms selected for analysis ranged between 2 and 48 hours with an average of 6 hours.

Hydrograph timing response

During the 5-year study period, 49 rainfall-runoff stormflow events passed the selection criteria and were analyzed for response lags and time durations. A summary of the hydrograph parameters is presented in Table 1. A Spearman rank (Sr) correlation coefficient matrix ($p < 0.05$) of all measured variables was performed to explore relations among hydrograph parameters, rainfall and date (Table 2). Response lags (T_{LR}) ranged between 0 and 11.2 hours, with an average time of 2.4 hours. McNamara et al. (1998) reported a mean response time of 2.15 hours (range 0–6

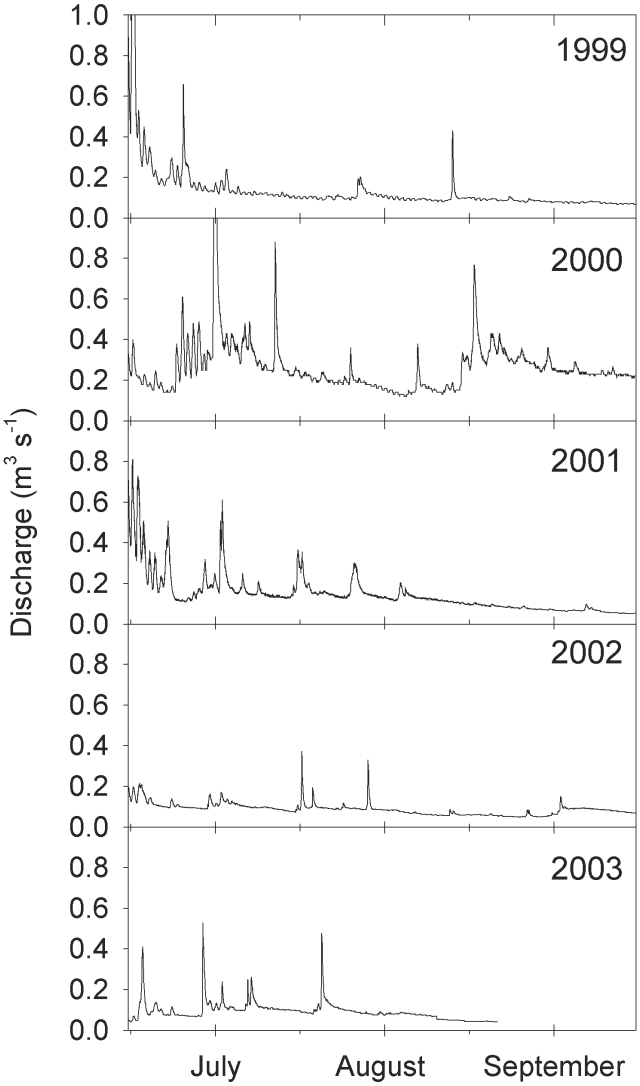

Figure 3. Post-freshet hydrographs (15 June–15 September) for Granger Basin, 1999–2003.

hours) for Imnavait Creek, a continuous permafrost basin (2.2 km²) in northern Alaska. Compared with temperate basins, the average response time was rapid, and the results are consistent with Church (1974) who also reported that rapid response times are a characteristic of northern rivers.

Initial abstractions (P_{abst}) were low, ranging from 0 to 4.1 mm with an average of 1.1 mm. An unexpected significant positive relation existed between P_{abst} and antecedent discharge, (Q_{ant}) (Sr = 0.32), indicating that more water was abstracted when the catchment was wettest. On the other hand, watershed wetness as represented 5-day antecedent rainfall (P_{5day}) showed no relation with P_{abst}. A lack of correlation between P_{abst} and wetness indices has been reported previously for subarctic and arctic watersheds (Dingman 1973, McNamara et al. 1998, Carey & Woo 2001b), and is typically attributed to limited subsurface storage capacity due to the presence of permafrost.

The time of rise (T_R) for most hydrographs was similar to the duration of precipitation (T_W). The lag to peak (T_{LP}), centroid lag to peak (T_{LPC}), and centroid lag (T_{LC}) were short,

Table 1. Summary of hydrograph parameters for 49 storms. Terms are defined in text.

Hydrograph Parameter	Mean	Standard Deviation	Maximum	Minimum
R/P_t	0.09	0.09	0.33	0.00
t^* (h)	41.70	32.20	163.10	7.70
P_{int} (mm)	0.79	0.84	5.20	0.18
P_{abst} (mm)	1.05	0.96	4.10	0.00
P_{5d} (mm)	7.72	6.81	29.30	0.00
T_w (h)	12.19	8.70	46.00	0.50
T_{LR} (h)	2.44	2.72	11.25	0.00
T_r (h)	9.56	6.52	33.50	2.00
T_{LP} (h)	11.83	6.47	34.75	3.50
T_{LPC} (h)	5.80	3.38	18.75	0.36
T_{LC} (h)	8.07	3.15	16.10	1.37
T_b (h)	25.21	13.81	72.50	6.50
T_c (h)	15.29	7.97	45.50	4.00

with averages of 11.8, 5.8, and 8.1 hr, respectively. This is in contrast to values of T_{LP} and T_{LC} of 17.8 and 34.8 hr for Imnavait Creek reported by McNamara et al. (1998). The centroid lag for Granger Basin was closer to the average of 19.5 hr reported by Holtan & Overton (1953) in a study of 40 streams in the conterminous United States, ranging from 76 km² to 3200 km² in basins that are much larger than the study catchment. Both T_{LP} and T_{LC} were positively correlated (Sr = 0.31 and 0.29, respectively) with Q_{ant}.

Runoff ratios (R/P_t) were highly variable, ranging between 0 and 0.33, with an average of 0.1. These values were low when compared with studies from other permafrost basins and hill slopes (Dingman 1971, Slaughter et al. 1983, Woo 1983, McNamara et al. 1998, Carey & Woo 2001b). Seasonally, higher runoff ratios were associated with early periods following melt when the frost and water table was near the surface, and ratios progressively diminished as summer progressed and the active layer thickened (Fig. 4a). A strong negative relationship existed between runoff ratio and Julian Day (Sr = -0.74). Runoff ratio increased with Q_{ant} (Sr = 0.55), yet there was no significant relation between runoff ratio and P_{5day}. Additionally, there was no relation between runoff ratio and total rainfall and rainfall intensity.

Streamflow recessions

Hydrograph recessions were observed to be temporally variable, with steeper recession limbs characteristic of earlier season discharge events that flattened out as summer progressed (Fig. 4b). Values of the t^* parameter ranged between 7.7 and 163.1 hr with an average of 41.7 hr, which compared well with other permafrost and organic-covered permafrost basins of similar area. For example, Dingman (1971) reported an average t^* of 39 hours for Glenn Creek, Alaska, while McNamara et al. (1998) found this value to be 30.2 hours for Imnavait Creek. There was a strong positive relationship between t^* and Julian Day (Sr = 0.69) indicating that as the season progresses and soils thaw, runoff reached the stream through deeper, less conductive soils. As would be expected, t^* increased with decreasing runoff ratio (Sr =

Table 2. Spearman rank correlation matrix. Values in bold are significant at the 95% confidence level. Terms defined in text.

	Julian Day	P_t	Q_{ant}	R/P_t	$t*$	P_{int}	P_{abst}	P_{5d}	T_w	T_{LR}	T_r	T_{LP}	T_{LPC}	T_{LC}	T_b	T_c
Julian Day	**1.00**	**-0.35**	**0.69**	**-0.74**	0.23	0.03	0.23	0.05	0.24	0.23	-0.12	-0.12	-0.25	-0.04	-0.01	-0.24
P_t		**1.00**	-0.10	**0.55**	0.11	0.13	**0.32**	**0.45**	0.19	0.24	0.17	**0.31**	0.23	**0.29**	0.20	0.17
Q_{ant}			**1.00**	**-0.66**	-0.07	-0.25	0.07	0.10	0.26	0.15	0.04	0.08	-0.11	0.12	0.06	-0.17
R/P_t				**1.00**	0.04	-0.02	-0.04	0.19	0.01	-0.13	0.26	0.20	0.25	0.24	**0.31**	**0.47**
$t*$					**1.00**	0.29	**0.30**	0.02	**0.61**	0.24	**0.46**	**0.44**	0.04	0.24	**0.53**	0.23
P_{int}						**1.00**	-0.21	0.12	**-0.44**	-0.26	-0.23	**-0.46**	**-0.43**	**-0.50**	**-0.29**	-0.14
P_{abst}							**1.00**	0.10	**0.50**	**0.68**	-0.11	0.21	0.02	0.27	0.08	0.07
P_{5d}								**1.00**	-0.04	0.17	-0.08	-0.03	0.08	0.08	-0.03	-0.06
T_w									**1.00**	**0.43**	**0.59**	**0.78**	**0.35**	**0.57**	**0.66**	0.23
T_{LR}										**1.00**	-0.18	**0.34**	0.04	0.14	-0.09	-0.12
T_r											**1.00**	**0.78**	**0.64**	**0.63**	**0.88**	**0.53**
T_{LP}												**1.00**	**0.69**	**0.68**	**0.67**	**0.41**
T_{LPC}													**1.00**	**0.60**	**0.41**	**0.33**
T_{LC}														**1.00**	**0.80**	**0.74**
T_b															**1.00**	**0.76**
T_c																**1.00**

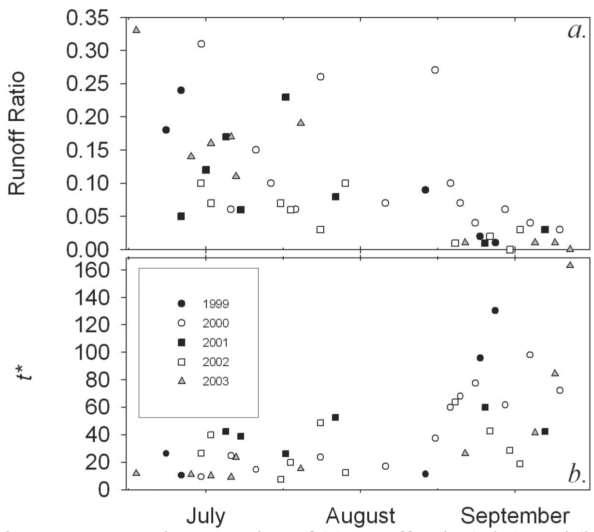

Figure 4. Seasonal progression of (a) runoff ratio (R/P_t), and (b) recession parameter, $t*$, for 49 stormflow events between 1999 and 2003.

-0.66). Recession constants were compared with total rainfall (P_t), antecedent wetness indices (Q_{ant}, P_{5day}), and other storm characteristics to assess for any influence of input volume, intensity, or watershed wetness, yet these relations were poorly defined and not statistically significant at the 95% confidence level.

Discussion and Conclusion

Simple analysis of stormflow hydrographs provide useful insight into the dynamics of runoff generation as permafrost-underlain catchments, unlike more temperate catchments, undergo significant physical changes throughout the summer due to ground thaw. For example, the decline in runoff ratio implies a widespread increase in soil storage capacity as the active layer becomes thicker and soils dry. Large rainfall events late in the summer must overcome significant storage deficits to generate even small volumes of runoff. Increasing $t*$ indicates water inputs take progressively longer to reach the stream due the gradual deepening of the flow pathways into less transmissive soil layers. Results from Granger Basin compare well with others reported in permafrost regions (Dingman 1973, Slaughter et al. 1983, McNamara et al. 1998) and support conceptual models of runoff generation being controlled by the relation between frost and water table positions for this environment (Carey & Woo 2001b).

Hydrograph lag-time indices had little correspondence with time of year or wetness, implying at the basin scale, these variables were not controlled explicitly by permafrost-related processes, but rather to other catchment characteristics (which may be affected by the presence of permafrost). The lack of correlation between response lags (T_{LR}), initial abstractions (P_{abst}), and measures of basin wetness such as antecedent discharge (Q_{ant}) and 5-day rainfall (P_{5day}) indicate that certain areas of the basin (footslopes of permafrost-underlain slopes and riparian areas) remain wet, contributing water rapidly to the stream after rainfall begins. The spatial extent of these wet areas expands and contracts away from the stream based on time of year and basin wetness, which is reflected by the declining trend in runoff ratios (R/P_t) throughout the summer. This process is similar to that reported by Quinton & Marsh (1998) and Carey & Woo (2001b), whereby hill slopes become effectively disconnected from the stream as the season progresses.

The recession coefficient, $t*$, was strongly related to time of year and runoff ratio, yet had no relationship with precipitation characteristics. Shallow thaw depths in the early summer lead to rapid drainage of the slopes through near-surface organic soils and preferential pathways that are well-linked. As the active layer deepens, the water table descends atop the frost table, and rainfall is able to percolate into deeper, less permeable, mineral soils. The hydraulic conductivity of mineral soils is typically orders of magnitude less than organic soils (Carey & Woo 2001b), resulting in increased transmission times to the stream and larger $t*$.

Hydrograph parameters investigated in Granger Basin, a discontinuous permafrost alpine basin, indicate that at the headwater scale, streamflow response reflects the influence of permafrost throughout the post-freshet season. Hydrological models that use these parameters in calibration must consider their temporal dependent nature.

Acknowledgments

This work is funded by research grants from the Natural Sciences and Engineering Research Council of Canada, the Canadian Foundation for Climate and Atmospheric Sciences, and the Northern Scientific Training Program. The support of Glenn Ford and Ric Janowicz of the Water Resource Branch, Yukon Environment, and John Pomeroy, University of Saskatchewan is gratefully acknowledged.

References

Bowling, L.C., Kane, D.L., Gieck, R.E., Hinzman, L.D. & Lettenmaier, D.P. 2003. The role of surface storage in a low-gradient Arctic watershed. *Water Resources Research* DOI: 10.1029/2002WR0014466.

Carey, S.K. & Quinton, W.L. 2004. Evaluating snowmelt runoff generation in a discontinuous permafrost catchment using stable isotope, hydrochemical and hydrometric data. *Nordic Hydrology* 35: 309-324.

Carey, S.K. & Woo, M-K. 2001*a*. Slope runoff processes and flow generation in a subarctic, subalpine environment. *Journal of Hydrology* 253: 110-129.

Carey, S.K. & Woo, M-K. 2001*b*. Spatial variability of hillslope water balance, Wolf Creek basin, subarctic Yukon. *Hydrological Processes* 15: 3113-3132.

Chacho Jr., E.F. & Bredthauer, S. 1983. Runoff from a small subarctic watershed, Alaska. *Proceedings, Fourth International Conference on Permafrost, National Academy Press, Washington, D.C.*, 115-120.

Church, M. 1974. Hydrology and permafrost with reference to northern North America, In: *Proc. Workshop Seminar on Permafrost Hydrology, Canadian National Committee*. Ottawa: IHD, 7-20.

Dingman, S.L. 1966. Characteristics of summer runoff from a small watershed in central Alaska. *Water Resources Research* 2: 751-754.

Dingman, S.L. 1973. Effects of permafrost on stream flow characteristics in the discontinuous permafrost zone of central Alaska. *North American Contribution to Second International Conference of Permafrost, National Academy of Sciences, Washington, D.C.,* 447- 453.

Hewlett, J.D. & Hibbert, H. 1967. Factors affecting the response of small watersheds to precipitation in humid regions. In: Sopper, W.E. & Lull, H.W. (eds.), *Forest Hydrology*. Oxford: Permagon Press, 275-290.

Hinzman, L.D., Kane, D.L. & Everett, K.R. 1993. Hillslope hydrology in an Arctic setting, *Proceedings, Sixth International Conference on Permafrost, South China Press, Beijing,* 257-271.

Kane, D.L. Bredthauer, S.R. & Stein, J. 1981. Subarctic snowmelt runoff generation. In: Vinson, T.S. (ed.), *Proceedings of the Specialty Conference on The Northern Community, ASCE, Seattle, Washington,* 591-601.

Kane, D.L., Hinzman, L.D., Everett, K.R. & Benson, C.S. 1989. Hydrology of Imnavait Creek, and arctic watershed. *Holarctic Ecology* 12: 262-269.

Lewkowicz, A.G. & Ednie, M. 2004. Probability mapping of mountain permafrost using the BTS method, Wolf Creek, Yukon Territory, Canada. *Permafrost and Periglacial Processses* 15: 67-80.

MacLean, R., Oswood, M.W., Irons III, J.G. & McDowell, W.H. 1999. The effect of permafrost on stream biogeochemistry: a case study of two streams in the Alaskan (U.S.A.) taiga. *Biogeochemistry* 47: 239-267.

McNamara, J.P., Kane, D.L., & Hinzman, L.D. 1998. An analysis of streamflow hydrology in the Kuparuk River Basin, Arctic Alaska: a nested watershed approach. *J. of Hydrol.* 206: 39-57.

Petrone, K.C., Jones, J.B., Hinzman, L.D. & Boone, R.D. 2006. Seasonal export of carbon, nitrogen, and major solutes form Alaskan catchments with discontinuous permafrost. *Journal of Geophysical Research* 111: DOI: 10.1029/2005JG000055.

Pomeroy, J.W. & Granger, R.J. (eds.) 1999. *Wolf Creek Research Basin: Hydrology, Ecology, Environment.* Saskatoon: Environment Canada, 160 pp.

Quinton, W.L. & Marsh, P. 1998. The influence of mineral earth hummocks on subsurface drainage in the continuous permafrost zone. *Permafrost and Periglacial Processes* 9: 213-228.

Quinton, W.L. & Marsh, P. 1999. A conceptual framework for runoff generation in a permafrost environment. *Hydrological Processes* 13: 2563-2581.

Slaughter, C.W. & Kane, D.L. 1979. Hydrologic role of shallow organic soils in cold climates. *Proceedings, Canadian Hydrology Symposium 79: Cold Climate Hydrology, National Research Council of Canada, Ottawa,* 380-389.

Slaughter, C.W., Hilgert, J.W. & Culp, E.H. 1983. Summer streamflow and sediment yield from discontinuous-permafrost headwater catchments. *Proceedings, Fourth International Conference on Permafrost, National Academy Press, Washington, D.C.,* 1172-1177.

Spence, C. & Woo, M-K. 2003. Hydrology of subarctic Canadian Shield: soil-filled valleys. *Journal of Hydrology* 279: 151-166.

Szilagyi, J. & Parlange, M.B. 1998. Baseflow separation based on analytical solutions of the Boussinesq equation. *Journal of Hydrology* 204: 251-260.

Tallaksen, L.M. 1995. A review of baseflow recession analysis. *Journal of Hydrology* 165: 349-370.

Woo, M.K. & Steer, P. 1982. Occurrence of surface flow on arctic slopes, southwestern Cornwallis Island. *Canadian Journal of Earth Sciences* 19: 2368-2377.

—*Plenary Paper*—

Innovative Designs of the Permafrost Roadbed for the Qinghai-Tibet Railway

Guodong Cheng
State Key Laboratory of Frozen Soil Engineering, Cold and Arid Regions Environmental and Engineering Research Institute, Chinese Academy of Sciences, Lanzhou, 730000, China

Qingbai Wu
State Key Laboratory of Frozen Soil Engineering, Cold and Arid Regions Environmental and Engineering Research Institute, Chinese Academy of Sciences, Lanzhou, 730000, China

Wei Ma
State Key Laboratory of Frozen Soil Engineering, Cold and Arid Regions Environmental and Engineering Research Institute, Chinese Academy of Sciences, Lanzhou, 730000, China

Abstract

Under global warming scenarios, the traditional method of simply increasing the thermal resistance by raising the embankment height and using insulating materials has been proven ineffective in warm and ice-rich permafrost areas and, therefore, could not be used in the Qinghai-Tibet Railway engineering. Instead, an alternative "cooled-roadbed" approach was developed and used to lower the ground temperature in order to maintain a perennially frozen subgrade. The concept that local and site-specific factors play an important role in the occurrence and disappearance of permafrost has helped us to devise a number of measures to cool down the roadbed. For example, we can adjust and control heat transfer by using different embankment configurations and fill materials. The Qinghai-Tibet Railway project demonstrates that a series of alternative roadbed-cooling methods can be used to lower the temperature of permafrost beneath the embankment and to stabilize the roadbed. These methods include solar radiation control using shading boards, heat convection control using ventilation ducts, thermosyphons, air-cooled embankments, and heat conduction control using "thermal semi-conductor" materials, as well as combinations of the above-mentioned three control measures. This roadbed-cooling approach provides not only a solution for engineering construction in sensitive permafrost areas, but also a countermeasure against possible global warming.

Keywords: cooled roadbed; global warming; Qinghai-Tibet Railway; warm permafrost.

Introduction

The Qinghai-Tibet Railway, 1142 km from Golmud to Lhasa, crosses 632 km of permafrost terrain of which 275 km is warm permafrost (mean annual ground temperature between 0 and -1°C) and 221 km is ice-rich permafrost (ice content >20% by volume). The section that is underlain by both warm and ice-rich permafrost is 134 km in distance (Wu et al. 2002). At the beginning of the Qinghai-Tibet Railway project, Chinese scientists and engineers were confronted with two unfavorable factors: the "warm" nature of the plateau permafrost and scenarios of global warming. Finding a solution for building the railway and keeping it operational and stable under such conditions became one of the greatest challenges (Cheng & Wu 2007). Observations along the Qinghai-Tibet Highway indicate that, after the road surface was paved with asphalt, talik pockets developed in 60% of the paved sections due to increased thawing. All that happened in warm permafrost areas. Approximately 85% of the damage to highway embankments is caused by thaw settlement of ice-rich permafrost (Wu et al. 2002). The performance of the Qinghai-Tibet Highway and other engineering structures in permafrost areas indicates that the traditional design method of simply increasing the thermal resistance by raising the embankment height and using insulating materials can no longer meet operational and safety needs. An alternative "cooled-roadbed" approach was developed and used to lower the underlying ground temperature, especially in areas of warm and ice-rich permafrost. Otherwise, it is difficult to maintain a stable roadbed (Cheng 2004a, 2005a). It has long been known that local and site-specific factors (e.g., slope aspect, soil type, etc.) have a significant impact on the occurrence and disappearance of permafrost. With the same concept, we devised and used a number of measures to cool down the roadbed for the Qinghai-Tibet Railway. These methods include adjusting and controlling the amount of solar radiation, heat convection, and heat conduction, as well as combinations of the above-mentioned measurements, by using different embankment configurations and fill materials (Cheng 2004b, 2005b).

Controlling Solar Radiation

The combination of low latitude and high altitude makes solar radiation on the Qinghai-Tibet Plateau one of the strongest in the world. Shading the surface from solar radiation can effectively lower the ground temperature (Kondratyev 1996). Feng et al. (2006) investigated the effect of awnings and measured the ground surface temperature at 14:00 over the course of a one-year period at the Fenghuoshan area. The surface temperature was 8–15°C lower inside the awnings than outside, and the maximum temperature difference can reach 24°C. But awnings are not suited on the plateau due to the strong wind. Consequently, shading boards were

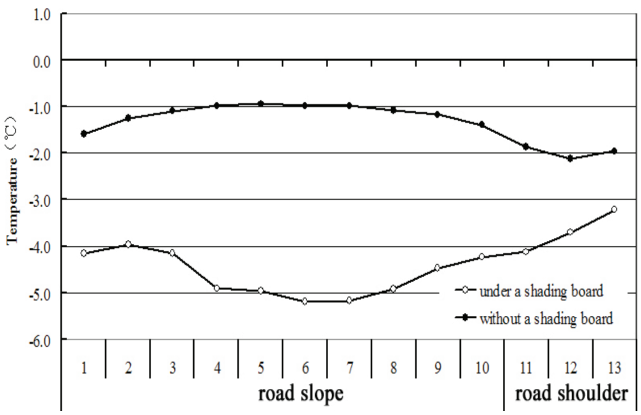

Figure 1. The variation of soil temperature under a shading board.

installed on embankment side slopes at Beiluhe to study the cooling effect. Observations show that the mean annual slope-surface temperature under the board was 3.2°C lower than that outside the board (Fig. 1) and 1.5°C lower than that of the natural ground surface (Yu et al. 2007a).

The original embankment fill may become loose and weak after undergoing repeated freeze–thaw cycles. Shading boards can reduce the number of these cycles and can also protect the embankment from the impact of wind action and erosion caused by the rain.

Altering Convection Patterns

Crushed rocks, ventilation ducts, and thermosyphons (or thermal tubes) were used in the Qinghai-Tibet Railway engineering to adjust and control convection patterns within embankments (Fig. 2).

Crushed rocks

On the Qinghai-Tibet Plateau, crushed rocks over permafrost act as “thermal semi-conductor” materials. In winter, the air is colder than permafrost; this induces R-B convection within the crushed rocks. As a result, permafrost releases heat into the air. In summer, the air is warmer than permafrost. Since the cold air is heavier and sinks to the bottom, no convective heat transfer takes place, and heat exchange is mainly in the form of conduction. Because of the small contact areas between the crushed rock and the low thermal conductivity of the air, the crushed rocks act as thermal insulators and reduce the amount of heat gained by the underlying permafrost from the air. The imbalance of increased heat releases in winter and reduced heat gains in summer produces a net heat release over the course of one year and thus lowers the underlying ground temperature (Cheng & Tong 1978, Goering & Kumar 1996, Goering 2003, Cheng et al. 2007a). When crushed rocks are placed on sloping surfaces, the chimney effect develops if the slope angle is sufficiently big. This chimney effect also lowers the underlying ground temperature (Cheng et al. 2007a).

On the Qinghai-Tibet Plateau, wind speeds are stronger in winter than in summer; 75% of the strong winds occur in winter. Therefore, wind-forced convection in crushed rocks

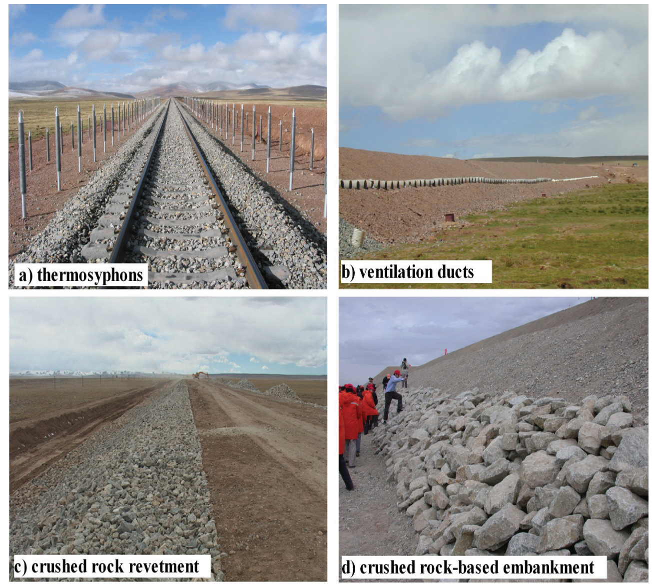

Figure 2. Measures adjusting and controlling convection.

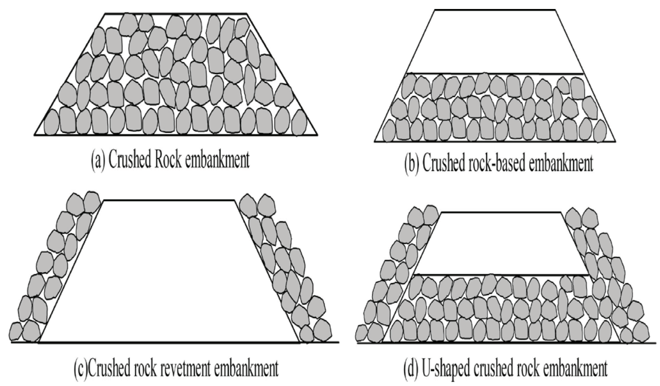

Figure 3. Different types of crushed-rock embankment.

is greater in winter than in summer, causing a cooling effect in the underlying ground (Cheng et al. 2007b).

The use of crushed rocks in embankments during the Qinghai-Tibet Railway construction took several different forms and configurations: crushed-rock embankment, crushed rock-based embankments, crushed-rock revetments embankments, and U-shaped crushed-rock embankments (Fig. 3).

Crushed rock-based embankments

The railway design standard in China requires that the soil layer beneath the railroad tracks be at least 2.5 m thick. A rock layer is often placed at the base of the embankment, so a crushed-rock embankment (Fig. 3a) is changed into a crushed rock-based embankment (Fig. 3b). This type of embankment covers 130 km of the Qinghai-Tibet Railway. The base of the embankment is usually between 1.0 and 1.2 m thick and consists of crushed rocks of 20–30 cm in diameter. The overlying soil layer ranges in thickness from 2.5 to 10 m.

Ground temperature monitoring was carried out on rock-based embankments at seven sites. Monitoring data

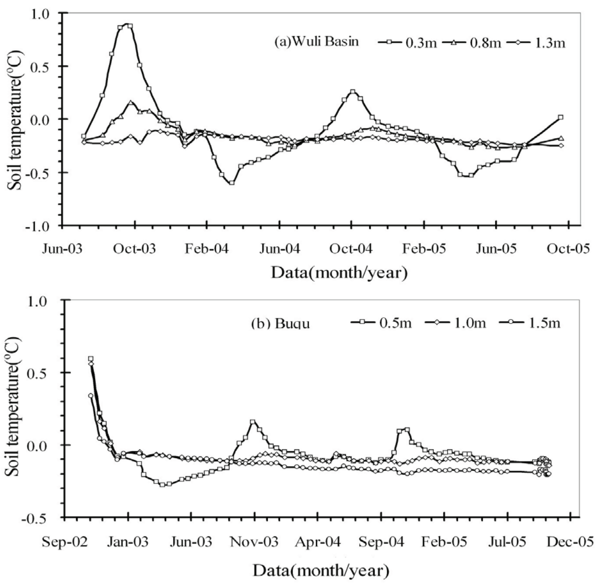

Figure 4. The variation of soil temperature under crushed rock-based embankment in warm permafrost areas.

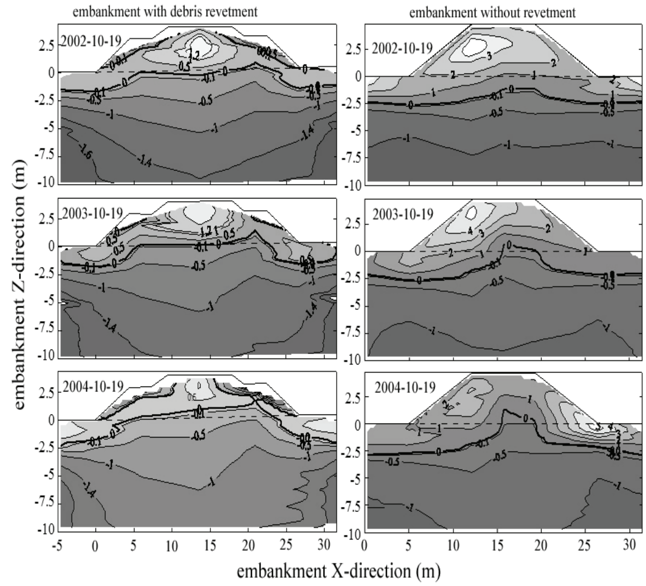

Figure 5. Comparison of soil temperatures under embankment with and without crushed-rock revetment.

indicates that the permafrost table beneath the embankment had raised at most sites by as much as between 1.8 and 2.6 m. Ground temperature near the permafrost table showed a cooling trend. However, at Wuli Basin and the Buqu River, where the mean annual ground temperature is warmer than -0.5°C, the ground temperature near the permafrost table did not show a clear cooling trend (Wu et al. 2006a) (Fig. 4), indicating that the cooling effect of crushed rocks is greatly reduced due to the overlying soil layer. Therefore, we cannot rely on the rock-based embankment alone to ensure a stable roadbed; additional cooling techniques are required.

A comparison study was made on the cooling effect of open and closed crushed rock-based embankment at Beiluhe. *Closed* means that the crushed rocks on the embankment side slopes are covered with a soil layer of 20 cm thick. *Open* means that the crushed rocks are not covered by a soil layer and are exposed to the air on either side of the embankment. At Beiluhe, the crushed-rock layer at the base is 1.2 m thick, consists of crushed rocks of 20–30 cm in diameter, and is overlain by a 2.5 m thick soil layer. At this site, wind speeds are also much higher in winter than in summer. For example, the average wind speed in winter is 5–8 m/s and is mainly from the east-northeast, roughly perpendicular to the embankment. The average wind speed in summer is 2–3 m/s and is mainly from the north-northwest. Observations indicate that, due to the overlying soil layer, natural convection in the closed rock layer is weak. On the other hand, the wind-forced convection dominates and is strong in the open crushed-rock layer. In the open crushed-rock layer, natural convection takes place in winter only when the wind speeds are low. Wu et al. (2006b, 2007) conclude that open crushed-rock layers at the base of the embankment have a greater cooling effect than its closed counterparts, because the ground temperature beneath open rock layers is 2–4°C lower than that beneath closed rock layers.

Crushed-rock revetments embankment

Crushed rocks are placed on embankment side slopes to cool down the roadbed (Fig. 3c). Approximately 37 km of the embankment along the Qinghai-Tibet Railway is covered with crushed-rock revetments. The revetment is 80–100 cm thick and is made up of crushed rocks of two different sizes: 8–10 cm and 20–30 cm in diameter.

A comparison is made between embankments with and without crushed-rock revetments at Beiluhe on the Tibet Plateau. At this site, the mean annual air temperature is -3.8°C, and the mean annual ground temperature is between -1.4 and -1.6°C. Two different rock sizes are used in the revetment. The side slopes of one section of the embankment are covered with rocks 5–8 cm in diameter. The revetment is 80 cm in thickness and is 4.1 m in height. A neighboring section is covered with rocks of 40–50 cm in diameter. The revetment is also 80 cm in thickness and is 4.8 m in height. The height of the traditional embankment (without a crushed-rock revetment) is 4.5 m. Temperature readings were taken from the 10 cm depth below the crushed-rock surface. The results show that summer temperature in the crushed-rock (5–8 cm in size) revetments, regardless of their aspect, is lower than that of the unrevetted counterparts, due to the insulating action of crushed rocks. In winter, the opposite is true, indicating the development of air convection in rock revetments (Saboundjian & Goering 2003). Temperature measurements from boreholes drilled at the center of the general and crushed-rock (5–8 cm in size) revetment embankments indicate that the magnitude of temperature decrease in the revetment embankment is greater than that in the general embankment. The temperature within 2 m of the surface is still decreasing under the revetment embankment, displaying a greater cooling effect (Fig. 5). Three years after completion of the above embankments, the permafrost table had risen slightly into the unrevetted embankment.

In contrast, the permafrost table had moved well into the embankment fill for most of the embankments with crushed-rock (40–50 cm in size) revetments. The overall temperature in the crushed-rock revetment embankment is lower than that in the general embankment. This demonstrates the cooling effect of crushed-rock (40–50 cm in diameter) revetments (Sun 2006).

Laboratory models and field data indicate that placing rock revetments of different thicknesses on embankment side slopes can reduce the differential thaw depth. This may help prevent differential thaw settlement and longitudinal cracking in the embankment (Yu 2006).

U-shaped crushed-rock embankments

As the cooling effect of crushed rocks is reduced due to the overlying soil layer, crushed rocks are placed on side slopes of rock-based embankments to form U-shaped crushed-rock embankments (Fig. 3d) in order to strengthen the thermal stability. Although it is too early to draw any conclusions, preliminary results show that it has an even greater cooling effect than both the rock-based and rock-revetted embankments (Ma et al. 2007).

Zhang et al. (2005, Niu et al 2006) completed a numerical simulation on three different embankments: the traditional embankment with ballasts, the rock-based embankment, and the U-shaped crushed-rock embankment. The objective was to evaluate the impact of future climatic warming on the embankment thermal regime. The model assumes an increase of 2.6°C in mean annual air temperature over the next 50 years. The initial mean annual air temperature used in the model is -4.0°C. The embankment height is 5.0 m; crushed rocks are 10 cm in size; the crushed-rock layer at the base is 1.5 m thick; the overlying soil layer is 3.5 m thick; the rock revetment is 1.6 m thick. The model shows that in 50 years, the permafrost table under the traditional embankment will be lowered to a depth of 7.4 m, and this will reduce the stability of the embankment due to the thaw settlement and subsidence. The permafrost table under the rock-based embankment will be very close to the natural ground surface, but its overall temperature will be warm and close to 0°C. For the U-shaped rock embankment, the permafrost table will be above the natural ground surface and in the base layers of crushed rocks. The overall temperature will be 0.25–0.3°C lower than the rock-based embankment, improving the thermal stability.

The crushed rocks layer used in the Qinghai-Tibet Railway engineering have a cooling impact on the underlying ground, but they are not as effective as theoretically predicted. This may have been caused by fine soil grains within the crushed rocks layer. These soil grains reduce the porosity of the rock layer and thus decrease the cooling effect. Fine-grained soils can find their way into the crushed-rock openings during the construction; wind can also blow them into the openings. Necessary measures should be taken in the future to prevent this from happening.

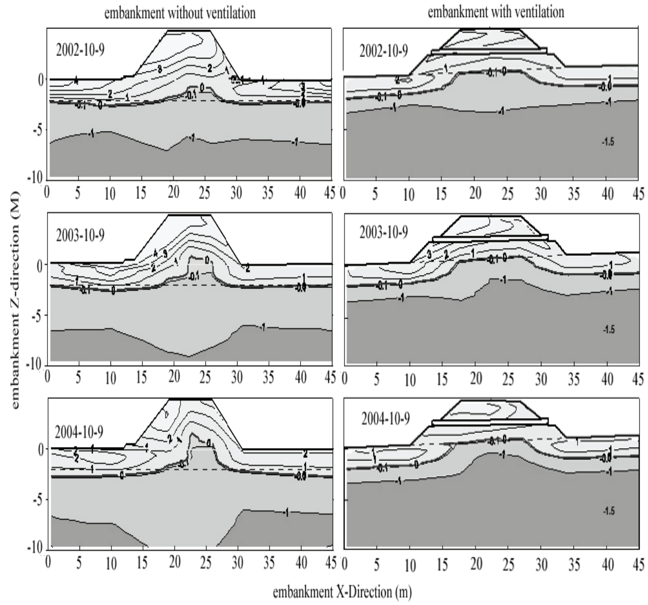

Figure 6. Comparison of soil temperature under embankment with and without ventilation ducts.

Ventilation ducts

Field experiments on ventilation ducts were carried out using PVC and concrete ducts at Beiluhe (Fig. 2b). These ducts are either 30 cm or 40 cm in diameter; the distance between two neighboring ducts is 2 times the duct diameter. They are buried into the embankment 0.5–0.7 m from the original ground surface.

The mean annual air temperature on the Tibet Plateau is, on average, about 3°C colder than the mean annual ground surface temperature. Consequently, embedding air ducts in embankments can effectively lower the underlying ground temperature. Field observations show that air ducts do lower ground temperatures. Ventilation ducts buried below and near the original ground surface have a greater cooling impact than those buried in higher positions (Niu et al. 2006). For embankments with ducts buried below and close to the original ground surface, the permafrost table moved up to the same level as the original ground surface three years after embankment construction (Fig. 6). The -1°C isotherm continued to rise, showing a clear cooling trend (Fig. 5). Temperature data indicate that the air temperature within the ventilation ducts is just 1.6–1.8°C higher than the air temperature, while the embankment surface temperature is 45°C higher, and the natural ground surface temperature is 2.5°C higher than the air temperature (Niu et al. 2007).

Air ducts increase the heat loss of the underlying soil during winter; they also increase the heat absorbed by the underlying soil in summer. To enhance the cooling effect of air ducts, an experiment was conducted to investigate the impact of a temperature-controlled ventilation system where one or both ends of the air ducts are installed with shutters that open and close automatically with changes in air temperature. The shutter has a temperature sensor and a control unit. It closes when the ambient air temperature is higher than a pre-set value. The temperature data measured from the inner walls of the ventilation ducts indicate that ducts with shutters are 1°C colder than those without. The mean annual ground temperature measured at a depth of 3.5 m beneath the embankment with shuttered air ducts is 0.45°C lower than that beneath the embankment installed with normal air ducts (Yu et al. 2007b).

To further improve the cooling effect, an experiment was carried out on an embankment ventilated by perforated air ducts at Beiluhe. Because of the holes in the duct wall, the heat exchange between the air inside the duct and surrounding soils is greatly increased, and the cooling effect is improved (Hu et al. 2004).

Thermosyphons

Thermosyphons were installed in over 34 km of the Qinghai-Tibet Railway embankment (Fig. 2a). Based upon the embankment height, thermosyphons of different length (7 m, 9 m, and 12 m) were inserted either vertically or at an angle into the shoulder or the foot of side slopes. The lower end is usually 2–3 m below the permafrost table.

Experiments on actual embankments at Qingshuihe show that thermosyphons do lower the ground temperature and make the permafrost table move upwards. As the "radius of influence" of a thermosyphon is about 1.8 m, the suggested distance between the thermosyphons is 3 m (Pan et al. 2003). Numerical modeling suggests that the cooling effect both in the embankment and at the foot of side slopes is greatest when the incline angle of the thermosyphons (installed at the foot of side slopes) is 25–30° (Yang et al. 2006).

Altering Heat Conduction

When water is frozen, its thermal conductivity increases by 4 times, from 0.45 to 2.2 W/m·K. This characteristic of water can be used to manufacture a material with a much greater thermal conductivity in the frozen state than in the thawed state. The material, similar to a "thermal semi-conductor" will lower the ground temperature by increasing heat loss in winter and decreasing heat gain in summer. Yu (2006) completed a laboratory experiment by placing layers of a water-absorbing material, separated by layers of air, in a sealed container. Water was added to the container. The result indicates that, when the material froze, its thermal conductivity changed from 0.11 W/m·K to 1.2 W/m·K, an increase of about 10 times. So far, this study has not been applied to cold regions engineering.

Combined Control Measures

The three different measures (e.g., adjusting radiation, adjusting convection, and adjusting conduction) can be combined in engineering practices to improve the cooling effect.

Dry bridges

Dry bridges totaling 125 km in length were built in ice-rich and extremely unstable permafrost sections along the Qinghai-Tibet Railway. Piles 1.2 m in diameter were buried 25–30 m into the ground to form a solid foundation. Since the dry bridges became operational, the deformation has been less than 2 mm on average, with a maximum of 5 mm.

Dry bridges can lower the ground temperature, as they can shade the ground from the sun; the air can freely flow through it. They possess good mechanical stability and can support heavy loads. They are effective means of ensuring the stability of roadbeds in ice-rich and sensitive permafrost. Dry bridges can also provide a migration route across the railroad for wild animals on the plateau. A numerical simulation on the dry bridge at Qingshuihe shows that the bridge has a cooling effect because the mean annual permafrost temperature under the bridge is lower than that without the bridge (Xiao et al. 2004).

Combining shading boards and crushed-rock revetments

Li et al. (2007) studied a different embankment configuration by combining shading boards with crushed-rock revetments. This configuration not only can shade the embankment from the sun but also can make good use of natural convection in crushed rocks to lower the ground temperature. The shading boards can also reduce the amount of fine-grained soil getting into the openings of crushed rocks. A numerical model was developed for this combined configuration to calculate the optimum values for the shading board height, for the thickness of rock revetments, for the embankment height, and for the size of crushed rocks. Li et al. (2007) proposed an optimum design for this type of embankment configuration.

Combining thermosyphons and insulating board

Wen et al. (2005) numerically simulated another embankment configuration that combines insulating board with thermosyphons. The board is embedded near the base of the embankment (0.5 m above the original ground surface). The model indicates that, assuming a mean annual air temperature of -3.5°C and a 2°C increase in air temperature on the plateau over the next 50 years, the stability of all three types of embankments (e.g., normal embankments, embankments installed with thermosyphons, and embankments with insulating boards) will without exception be compromised. However, if thermosyphons are combined with insulating board, the embankments will have a greater resistance to global warming and will remain stable.

Combining crushed-rock revetments and insulating board

Zhang et al. (2005) studied the effect when insulating board is embedded at a 0.8 m depth beneath the surface of rock-reveted embankments. The numerical model indicates that the temperature measured from the middle portions of the embankment is lower when insulating boards are used.

Conclusions

Under the global warming scenario, the "cooled roadbed" approach must be used for road design and construction in "warm" and ice-rich permafrost. This approach changes the design philosophy from traditional insulation to alternative cooling to better deal with possible global warming.

Combining solar radiation control, heat convection control, and heat conduction control can achieve a better cooling effect on the roadbed. Shading boards, crushed rocks, ventilation ducts, thermosyphons, and dry bridges were all used in the Qinghai-Tibet Railway engineering and have proven successful in lowering the ground temperature and in ensuring the roadbed stability.

Further studies are necessary to quantify and to optimize various measures employed in the Qinghai-Tibet Railway project.

Acknowledgments

The authors sincerely thank Dr. Baolai Wang for editing the English version of the article. This work was supported by a grant of the Knowledge Innovation Program of the Chinese Academy of Sciences (Grant no. KZCX1-SW-04) and the Outstanding Youth Foundation Project, the National Natural Science Foundation of China (Grant No. 40625004).

References

Cheng, G.D. & Tong, B.L. 1978. Experimental research on an embankment in an area with massive ground ice at the lower limit of alpine permafrost. *Proceedings of the Third International Conference on Permafrost, Ottawa.* National Research Council of Canada 2: 199-222.

Cheng, G.D. 2004a. Principle of thermal insulation for permafrost protection. *Cold Regions Science and Technology* 40: 71-79.

Cheng, G.D. 2004b. Influences of local factors on permafrost occurrence and their implications for Qinghai-Tibet Railway design. Science in China, Series D: *Earth Sciences* 47(8): 704-709.

Cheng, G.D. 2005a. Permafrost studies in the Qinghai-Tibet Plateau for road construction. *Journal of Cold Regions Engineering* 19(1): 19-29.

Cheng, G.D. 2005b. A roadbed cooling approach for the construction of Qinghai-Tibet Railway. *Cold Regions Science and Technology* 42: 169-176.

Cheng, G.D. & Wu, T.H. 2007. Responses of permafrost to climate change and their environmental significance, Qinghai-Tibet Plateau. *Journal of Geophysical Research* 112: F02S03, doi:10.1029/2006JF000631.

Cheng, G.D., Lai, Y.M., Sun, Z.Z. & Jiang, F. 2007a. The "thermal semi-conductor" effect of crushed rocks. *Permafrost and Periglacial Processes* 18: 151-160, doi:10.1002/ppp.575.

Cheng, G.D., Sun, Z.Z. & Niu, F.J. 2007b. Application of the roadbed cooling approach in Qinghai-Tibet railway engineering. *Cold Regions Science and Technology:* doi:10.1016/j.coldregions.2007.02.006 (in press).

Feng, W.J., Ma, W., Li, D.Q. & Zhang, L.X. 2006. Application investigation of awning to roadway engineering on the Qinghai-Tibet Plateau. *Cold Regions Science and Technology* 45: 51-58.

Goering, D.J. & Kumar, P. 1996. Winter-time convection in open graded embankments. *Cold Regions Science and Technology* 24(1): 57-74.

Goering, D.J. 2003. Passively cooled railway embankments for use in permafrost areas. *Journal of Cold Regions Engineering* 17(3): 119-133.

Hu, M.J., Wang, R., Ge, X.R., Shi, X.F. & Huang, M.K. 2004. An experimental study on the cooling effect of perforated ventilation pipes embedded in the Qinghai-Tibet Railway roadbed. *Chinese Journal of Rock Mechanics and Engineering* 23(24): 4195-4199 (in Chinese with English abstract).

Kondratyev, V.G. 1996. Strengthening railroad base constructed on icy permafrost soil. *Proceedings of the Eighth International Conference on Cold Regions Engineering, Fairbanks:* 688-699.

Li, N., Kang, J.M. & Quan, X.J. 2007. Study on cooling mechanism of a new type ripped-stone embankment in high temperature area. *Chinese Journal of Geotechnical Engineering* 29(3): 425-429 (in Chinese with English abstract).

Ma, W., Feng, G.L., Wu, Q.B. & Wu, J.J. 2007. Analyses of temperature fields under the embankment with crushed-rock structures along the Qinghai-Tibet Railway. *Cold Regions Science and Technology:* doi:10.1016/j.coldregions.2007.08.001 (in press).

Niu, F.J., Cheng, G.D., Xia, H.M. & Ma, L.F. 2006. Field experiment study on effects of duct-ventilated railway embankment on protecting the underlying permafrost. *Cold Regions Science and Technology* 45(3): 178-192.

Niu, F.J., Liu, X.F., Ma, W., Wu, Q.B. & Xu, J. 2007. Monitoring study on the boundary thermal conditions of duct-ventilated embankment in permafrost regions. *Cold Regions Science and Technology:* doi:10.1016/j.coldregions.2007.07.004 (in press).

Pan, W.D., Zhao, S.C., Xu, W.Z., Yu, S.S. & Ma, W.D. 2003. Application of thermal probe to enhance thermal stability of roadbeds in plateau permafrost areas. *Journal of Glaciology and Geocryology* 25(4): 433-438 (in Chinese with English abstract).

Saboundjian, S. & Goering, D.J. 2003. Air convection embankment for Roadway: A field experimental study in Alaska. *Publication at the 82nd Annual Meeting of the Trasportation Research Board, Washington, DC.*

Sun, Z.Z. 2006. *Study on the crushed rock revetment embankment in permafrost regions of Qinghai-Tibet Railway.* Ph.D. Thesis, Cold and Arid Regions Environmental and Engineering Research Institute, Chinese Academy of Sciences (in Chinese with English abstract).

Wen, Z., Sheng, Y., Ma, W., Qi, J.L. & Wu, J.C. 2005. Analysis on effect of permafrost protection by two-phase closed thermosyphon and insulation jointly in permafrost regions. *Cold Regions Science and Technology* 43: 150-163.

Wu, Q.B., Liu, Y.Z. & Zhang, J.M. 2002. A review of recent frozen soil engineering in permafrost regions along Qinghai-Tibet Highway, China. *Permafrost and Periglacial Processes* 13(3): 199-205.

Wu, Q.B., Cheng, G.D., Ma, W., Niu, F.J. & Sun, Z.Z. 2006a. Technical approaches on permafrost thermal stability for Qinghai-Tibet Railway. *Geomechanics and Geoengineering: An International Journal* 1(2): 119-127.

Wu, Q.B., Dong, X.F. & Jiang, G.L. 2006b. Cooling effect differences of soil beneath open and closed block-stone embankments. *Chinese Journal of Rock Mechanics and Engineering* 25(12): 2565-2571 (in Chinese with English abstract).

Wu Q.B., Cheng H.B., Jiang G.L., Ma W. & Liu Y. Z. 2007. Cooling mechanism of embankment with block stone interlayer in Qinghai-Tibet railway. *Science in China, Series E* 50(3): 319-328.

Xiao, J.Z., Lai, Y.M., Zhang, X.F., Yu, W.B. & Zhang, S.J. 2004. Three dimensional temperature character analysis of a dry bridge on the Qinghai-Tibet Railway. *Journal of Glaciology and Geocryology* 26(4): 426-434 (in Chinese with English abstract).

Yang, Y.P., Zhou, S.H. & Wei, Q.C. 2006. Effect simulation of different incline angles of thermosyphons used in Qinghai-Tibet railway permafrost embankment. *China Civil Engineering Journal* 39(3): 108-113 (in Chinese with English abstract).

Yu, Q.H. 2006. *Study on the heat conduction process of roadbeds in permafrost region and new control methods.* Ph.D. Thesis, Cold and Arid Regions Environmental and Engineering Research Institute, Chinese Academy of Sciences (in Chinese with English abstract).

Yu, Q.H., Niu, F.J., Pan, X.C., Bai, Y. & Zhang, M.Y. 2007a. Investigation of embankment with temperature-controlled ventilation along the Qinghai-Tibet Railway. *Cold Regions Science and Technology:* doi:10.1016/j.coldregions.2007.07.002 (in press).

Yu, Q.H., Pan, X.C., Cheng, G.D. & He, N.W. 2007b. An experimental study on the cooling mechanism of a shading board in permafrost engineering. *Cold Regions Science and Technology:* doi:10.1016/j.coldregions.2007.07.003 (in press).

Zhang, M.Y., Lai, Y.M., Liu, Z.Q. & Gao, Z.H. 2005. Nonlinear analysis for the cooling effect of Qinghai-Tibet Railway embankments with different structures in permafrost regions. *Cold Regions Science and Technology* 42: 237-249.

Does Permafrost Deserve Attention in Comprehensive Climate Models?

Jens Hesselbjerg Christensen and Martin Stendel
Danish Meteorological Institute, Copenhagen, Denmark

Peter Kuhry
Stockholm University, Sweden

Vladimir Romanovsky and John Walsh
University of Alaska Fairbanks, USA

Abstract

Traditionally, from a climate modeling perspective, permafrost is looked upon as a phenomenon impacted by climate change. However, it is well recognized that thawing permafrost may create climate feedback loops via changes in greenhouse gas emissions and surface hydrology. Only recently, these effects are being introduced in comprehensive climate models. The thermal properties of permanently frozen regions on the other hand have not been much explored in this context, mainly because models rarely resolve soil layers deeper than a few meters. One reason comes from the still rather poor ability of climate models to simulate realistic snowpack behavior, which is vital to allowing for a realistic depiction of below-surface properties. Here, we stress the sensitivities of near-surface atmospheric temperatures to inadequacies in the description of soil processes including retreat of permafrost to deeper layers under warming conditions.

Keywords: global climate; permafrost modeling; regional climate change; systematic errors.

Introduction

A major effort in the development of comprehensive climate models is devoted towards a reduction in systematic errors. In general, the better a model can reproduce in a satisfactory manner observed climate statistics, the higher its credibility in simulating climate change. But the demand for accurate representation of climate variables is changing steadily as the application of models for climate change research and demand for realistic climate projections increase. Efforts in the 1990s were concentrated on getting a realistic energy balance at the top of the atmosphere energy balance, along with a realistic annual cycle in mean climate variables such as mean sea level pressure, temperature, and precipitation. The field has moved forward, and focus is now set on other aspects of the climate system, including the ocean, sea ice, and land-surface processes. Furthermore, higher moments of climate variables are being assessed. This includes, for example, the ability to reproduce observed trends or the entire spectrum of daily precipitation intensities and temperature variables. The understanding of models' ability to reproduce these features has become the cornerstone in identifying model shortcomings and gives a clear hint to the modeler on where to improve model descriptions (e.g., IPCC 2007).

Despite the ongoing improvement of models and the associated enhanced credibility in climate change projections, the deficiencies in the models are still limiting their ability to provide detailed regional projections where systematic errors are indisputable. Examples are errors in the ability to capture the overall distribution of sea ice, the seasonality of snow cover, and more complex inefficiencies due to erroneous atmospheric or oceanic circulation. In applying such models to investigate the influence of anthropogenic climate changes, it becomes vital to keep in mind these model deficiencies as they may leave an imprint on the resulting climate projections. Here we discuss the complexity of such errors and how they may be interpreted. We focus on the role of permafrost as a key to improvement of model behavior in the Arctic and, hence, add to an improved understanding of the future behavior of permafrost in a warming world.

Understanding Modeled Climate Change

Global climate change in the Arctic

The ability to simulate present-day climate conditions by a climate model is well depicted by characteristics of the dynamics of the atmosphere. Hence, if the position of the storm tracks is erroneous, the details of the simulated climate cannot be accurate and must be erroneous even if the model validates well with statistical properties of temperature and precipitation, for example. To a certain extent, it simply must be an artifact of the way the model is constructed and less due to a correct depiction of the physical processes. Thus the ability to simulate aspects of the North Atlantic Oscillation (NAO) and atmospheric blocking events becomes of particular relevance for the Arctic. According to the recent Intergovernmental Panel on Climate Change (IPCC 2007), models have continued to improve in their ability to represent some of the main observed NAO-related characteristics. However, there are still major discrepancies in their ability to represent blocking frequency. The implications of this will tend to manifest themselves in inadequate depictions of precipitation and temperature patterns, but these may be obscured by the presence of other systematic errors, resulting in error cancellations, that may not easily be depicted from model validation analyses.

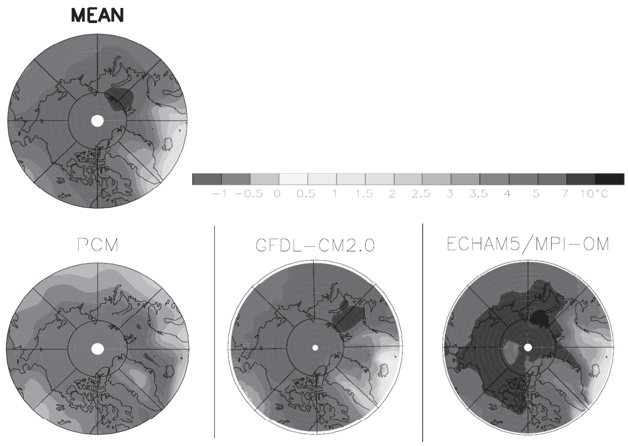

Figure 1. Maps of composite (based on 21 models) and 3 individual model simulated annual mean temperature change (2080–2099 vs. 1980–1999) for the IPCC A1B SRES scenario. From IPCC (2007).

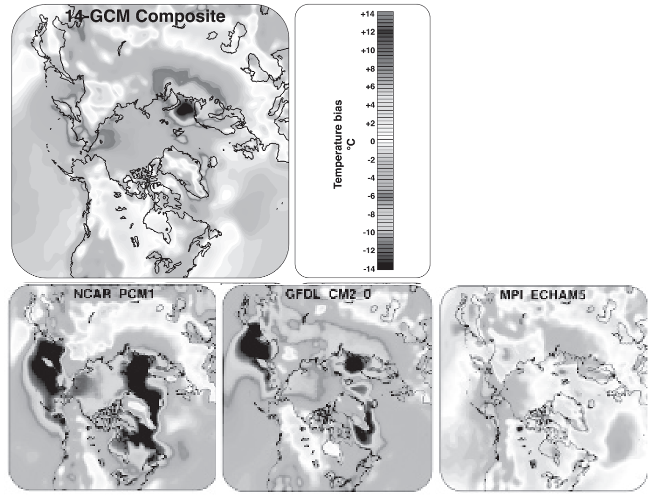

Figure 2. Maps of composite (based on 14 models) and 3 individual model temperature biases for winter (1958–2000). From Walsh et al. (2007).

Changes in temperature and sea ice

In IPCC (2007), the temperature within the Arctic is assessed to increase at a higher rate than globally, confirming results from previous IPCC reports and ACIA (2005). For the IPCC SRES A1B scenario, the annual mean Arctic temperature increase by the end of the 21st century is projected to be about twice that of the global mean (5°C–7°C vs. 2.5°C–3.5°C) (IPCC 2007, Christensen et al. 2007). Figure 1 shows an extract of an evaluation of 21 model simulations of global change under the A1B scenario (from Christensen et al. 2007), highlighting 3 models—the NCAR PCM, GFDL CM2.0, and MPI ECHAM5—as well as the 21-model mean. It is evident that these 3 individual models qualitatively show the same climate change response, but the magnitude of the change differs by several °C, with the PCM model exhibiting the lowest degree of warming, and the ECHAM5, the highest degree of warming, while the GFDL CM2.0 model is close to the ensemble mean.

It is interesting to note, however, that the projected climate signals to some degree are caused by quite different mechanisms. Figure 2 shows an extract of an analysis of the performance of 14 model simulations for the period 1958–2000 from Walsh et al. (2007). Again the ensemble mean behavior is shown along with the same 3 individual models. A common feature for most of the models, reflected by the ensemble mean, is a clear cold bias in the Barents Sea due to a tendency to simulate too much sea ice, with the MPI model being a clear exception. At the same time, the greatest warming by the end of the century is simulated exactly over this region in the ensemble mean as well as by the individual models. In the NCAR and GFDL models, this is partly reflecting the bias in present-day sea ice conditions, while in the MPI model this apparently cannot be the case. Note also that, in general, the largest warming occurs in the area with too much ice (strong cold bias) under present-day conditions, and in the NCAR model in particular, even though we here compare winter with annual mean. Thus, to some extent, the results are at the regional scale clearly subject to the systematic errors in the present-day simulations. Using an ensemble of models masks this deficiency.

Therefore, maps of warming must be carefully analyzed, and data cannot be used in a region with nonlinear feed backs such as the presence and absence of sea ice without further analysis.

Changes in snow conditions

Snow cover presents a challenge to models, and the issue is further complicated by a rather incomplete verification database. Apart from very few sites, the information available is only snow cover extent. While this is a similar challenge as for sea ice, there is much less constraint on the temperature below the snow seal. In the ocean, temperatures are well approximated by -1.7°C under sea ice, while soil temperatures can go well below -10°C in some places. Therefore, the ability to simulate snow cover realistically is essential.

According to the IPCC (2007), models are now more consistent in their simulation of snow cover than previously. Problems remain, however, and Roesch (2006) showed that the recent models predict excessive snow water equivalent in spring, likely because of excessive winter precipitation. The magnitude of these model errors is large enough to affect continental water balances. Snow cover area is well captured by the recent models, but interannual variability is too low during melt. Moreover, many models are able to reproduce the observed decline in annual snow cover area for the period 1979 to 1995, and most models capture the observed decadal-scale variability over the 20th century. Despite this, some of the models still exaggerate snow covered areas in spring and summer. This has obvious consequences for any analysis on permafrost-related properties using such models.

Implications for changes in permafrost

Re-inspection of Figure 1 reveals that the largest warming, apart from that occurring over the Arctic Ocean, is seen

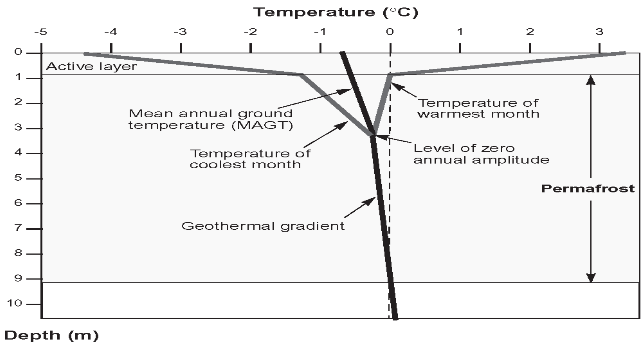

Figure 3. Schematics of temperature profiles at a permafrost site. Fat horizontal stippled line indicates an arbitrarily chosen lowest soil model level as typically represented in a climate model.

over the northern-most part of the continents, for several reasons. Firstly, the warming associated with the reduced sea ice cover simulated by all models has an impact mainly in spring and autumn. During these periods, relatively warm and moist air is more likely to influence these regions due to the lack of sea ice cover in a longer period, while in summer and winter the atmospheric conditions in this aspect will be more like present day. Thus the largest signal in the warming comes from the change in the seasonality of the sea ice. This in turn has implications for the poleward advection of heat in the shoulder seasons as well, leading to enhanced warming. But the albedo feedback from reduced snow cover from the return of sun light in spring to late autumn is also likely to contribute to the enhanced warming. Any bias in the seasonality of sea ice or snow cover will strongly impact this warming signal. This immediately implies that simulated permafrost properties are impacted by a model's ability to capture the present-day conditions as well as respond to increased greenhouse forcing in an adequate way.

Figure 3 illustrates the classical depiction of temperature profiles at a site underlain by permafrost. This schematic picture also shows how the typical representation of the soils in a GCM is handled. The lowest layer in the soil is located somewhere above the level with zero annual amplitude. Typically, GCMs adopt a zero heat flux adjustment at the lowest level in order to avoid an artificial energy source or sink. This implies that instead of allowing for heat penetration into the deeper soils, heat accumulates near the lowest level if the general model behavior reflects a warming, as indeed is the case unanimously in the Arctic under global warming. Therefore, in the model, once the possible nonlinear jump due to changes in snow cover conditions (earlier melt and later reoccurrence) has expressed itself at a grid point underlain by permafrost, heat can start to accumulate in the shallow soils, starting from below. This in turn will show up as a faster warm-up and, subsequently, thaw of the permafrost conditions than should be expected if the excess heat were allowed to propagate into greater depth. Recently, it has been demonstrated that indeed such behavior is found using the CLM land surface scheme (Alexeev et al. 2007, Nicolsky et al. 2007). Therefore, these authors proposed a procedure to parameterize the existence of deeper soil layers. In their idealized case study, the CLM was driven off-line with observations from one winter season, and the authors were able to show how heat was effectively transported to further depth, avoiding a pile-up of excess heat near the deepest model levels. The implications are important not only for the depiction of soil temperature behavior. Once a region experiences strong warming due to modified snow-cover insulation conditions, permafrost erroneously warms up too fast below the active layer, implying excess heat capacity during the cold season which in turn may lead to too-warm conditions close to the surface as well. Thus a feedback mechanism is initiated that may induce further warming, which at least partly is induced by the imperfect lower-boundary condition. The implications for the interpretation of direct GCM model-based soil temperatures are therefore severe; the induced warming and subsequent thawing of permafrost will take place too quickly. Moreover, when more advanced permafrost models are used to provide detailed information about changes in permafrost conditions, the simulated permafrost properties will be impacted by the biased precipitation, snow, and near-surface temperature provided to it by the GCM.

Conclusion

Here we have highlighted some of the well-known deficiencies of most state-of-the-art climate models. It is also clear, however, that some models appear to be less prone to some of the errors we have discussed here. In particular, a few of today's models are capable of reproducing crucial aspects of the climate system in the Arctic. In order to provide reliable climate change scenarios in areas underlain by permafrost, we have illustrated the need to single out some of today's GCMs that are representing with reasonable accuracy the atmospheric circulation, sea ice distribution, and general aspects of snow cover for the present climate Furthermore, we have demonstrated that there is a need to introduce a more sophisticated treatment of soil processes which includes information about soil thermal development even at considerable depth, as this has the potential to further improve the ability of climate models to simulate arctic climate, hence increasing credibility of arctic climate change projections.

Finally, the importance of permafrost in high-latitude climate change implies a need for accurate representations of the soil vertical profiles of conductivity, porosity, and other parameters affecting soil temperature and moisture content.

Acknowledgments

This research was partly funded by the Polar Earth Science Program, Office of Polar Programs, National Science Foundation (ARC-0612533), and by the EU Sixth Framework Programme, Global Change and Ecosystems sub-programme, CARBO-North Project (contract number 036993).

References

ACIA. 2005. *Arctic Climate Impact Assessment*. NY: Cambridge University Press, 1042 pp.

Alexeev, V.A., Nicolsky, D.J., Romanovsky, V.E. & Lawrence, D.M. 2007. An evaluation of deep soil configurations in the CLM3 for improved representation of permafrost. *Geophys. Res. Lett.* 34: L09502, doi:10.1029/2007GL029536.

Christensen, J.H., Hewitson, B., Busuioc, A., Chen, A., Gao, X., Held, I., Jones, R., Kolli, R.K., Kwon, W.-T., Laprise, R., Magaña Rueda, V., Mearns, L., Menéndez, C.G., Räisänen, J., Rinke, A., Sarr, A. & Whetton, P. 2007. Regional Climate Projections. In: S. Solomon, D. Qin, M. Manning, Z. Chen, M. Marquis, K.B. Averyt, M. Tignor, & H.L. Miller (eds.), *Climate Change 2007: The Physical Science Basis. Contribution of Working Group I to the Fourth Assessment Report of the Intergovernmental Panel on Climate Change.* Cambridge, UK, and New York, NY: Cambridge University Press.

IPCC. 2007. *Climate Change 2007: The Physical Science Basis. Contribution of Working Group I to the Fourth Assessment Report of the Intergovernmental Panel on Climate Change.* S. Solomon, D. Qin, M. Manning, Z. Chen, M. Marquis, K.B. Averyt, M. Tignor, & H.L. Miller (eds Cambridge, UK, and New York, NY: Cambridge University Press.

Nicolsky, D.J., Romanovsky, V.E., Alexeev, V.A. & Lawrence, D.M. 2007. Improved modeling of permafrost dynamics in a GCM land-surface scheme. *Geophys. Res. Lett.* 34:L08501, doi:10.1029/2007GL029525.

Roesch, A. 2006. Evaluation of surface albedo and snow cover in AR4 coupled climate models. *J. Geophys. Res.* 111:D15111, doi:10.1029/2005JD006473.

Walsh, J.E., Chapman, W.L., Romanovsky, V., Christensen, J.H. & Stendel, M. 2007. Global climate model performance over Alaska and Greenland. *J. Clim.* (in revision),